Modeling of active magnetic regenerators and experimental investigation of passive regenerators with oscillating flow

Lei, Tian; Engelbrecht, Kurt; Nielsen, Kaspar Kirstein; Veje, Christian T.

Publication date:
2016

Document Version
Publisher's PDF, also known as Version of record

Technical University of Denmark

Modeling of active magnetic regenerators and experimental investigation of passive regenerators with oscillating flow

PhD Thesis

Tian Lei

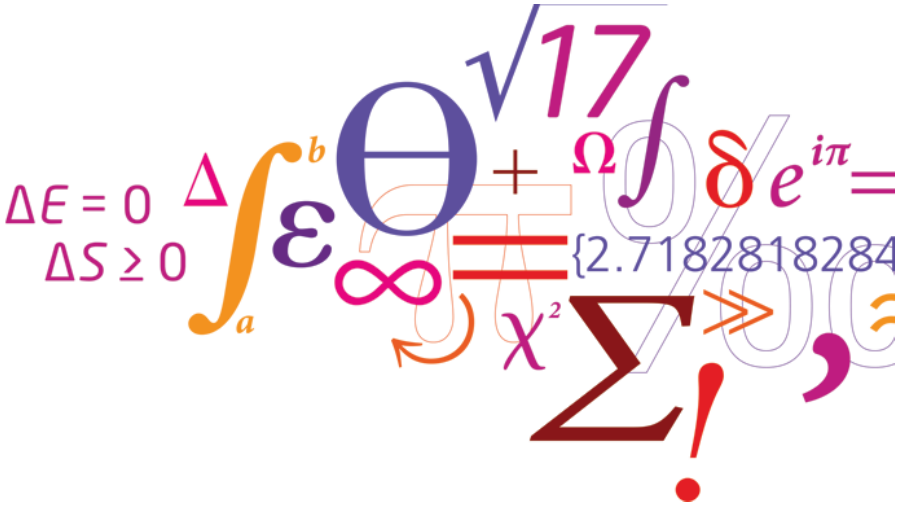

August 12th, 2016

DTU Energy
Department of Energy Conversion and Storage

Acknowledgments

I would like to express my special appreciation and thanks to my supervisors Dr. Kurt Engelbrecht, Dr. Kaspar K. Nielsen and Dr. Christian T. Veje for their support and supervision. I appreciate all their contributions of time, ideas and constructive discussions to help me overcome the difficulties during my research.

This dissertation would not have been possible without the help of the colleagues and the friends at DTU Energy. Special thanks to Mr. Henrique Neves Bez, Mr. Andrea R. Insinga, Dr. Stefano Dall'Olio, Dr. Christian Bahl, Dr. Dan Eriksen, Dr. Rasmus Bjørk and Prof. Dr. Nini Pryds for long term collaboration in the same project. I am very grateful to their support and help. Mr. Jørgen Geyti's engineering expertise makes it possible to build up the experimental test apparatus in this study and Mrs. Anita Voss supports me to solve many problems. I would also like to thank Mr. Stefano Soprani and Ms. Kristina Navickaité for the valuable discussions in the laboratory "Neutron house".

I have been so fortunate to have several opportunities to work and discuss with many international scholars and experts. I want to thank Prof. Dr. Gregory F. Nellis and Prof. Dr. John M. Pfotenhauer for their supervision and supportive guidance during my external study at the University of Wisconsin-Madison. I had a really nice time with the friends in Madison, which is a beautiful city full of the summer sunshine. It is also a nice experience to learn the system integration from Dr. Maryamsadat Tahavori and Dr. Konstantin Filonenko from the University of Southern Denmark, and Mr. Hicham Johra from the Aalborg University. Dr. Andrej Kitanovski, Dr. Jaka Tušek and Dr. Urban Tomc from the University of Ljubljana collaborate closely with us and provide many valuable advices on my work. Dr. Alexander Barcza from the Vacuumschmelze GmbH & Co. KG prepared the materials and regenerators for the tests in this thesis and his comments are always inspiring. I also exchange many ideas on numerical modeling with Dr. Bárbara Torregrosa-Jaime from the Universitat Politècnica de València and Prof. Dr. Andrew Rowe from the University of Victoria.

I want to thank my parents for their long term support, no matter where I am. Most of all my special thanks go to my loving, supportive and encouraging wife, Minfei. Because of your love and support, I feel motivated and encouraged every time I face with problems, which means more to me than you will ever know.

Finally, I would like to acknowledge the support from the ENOVHEAT project which is funded by Innovation Fund Denmark. I also greatly appreciate a travel grant from the Otto Mønsteds Fund for supporting my external study in U.S.

Abstract

This thesis presents numerical modeling of active magnetic regenerator (AMR) and passive regenerator tests with oscillating flow. The work serves to investigate and improve the understanding of emerging concepts and technologies in the area of magnetic refrigeration.

The discretization scheme of a one dimensional (1D) AMR model is improved for decreasing spurious temperature oscillations in the numerical solution. This transient AMR model is further modified for simulating tapered regenerators, heat loss through the housing wall and regenerators using mixed materials.

Magnetocaloric materials (MCM) with a first or second order phase transition (FOPT or SOPT) exhibit different characteristics in isothermal entropy change ΔS_{iso}, adiabatic temperature change ΔT_{ad} and temperature dependence of the magnetocaloric effect (MCE). A theoretical study quantifies the impact of these parameters, showing that all of them are equally important. Based on measured magnetocaloric properties of $La(Fe,Mn,Si)_{13}H_y$ and Gd, a thorough investigation on how to layer typical FOPT or SOPT materials is implemented. For those regenerators, the sensitivity to the working temperature and the Curie temperature variation is evaluated. A concept of mixing FOPT and SOPT materials is also investigated.

Furthermore, the entropy production rates due to insufficient heat transfer, viscous dissipation and axial conduction, as well as the total entropy production rate, are calculated and compared for analyzing different loss mechanisms and optimizing AMRs. The impacts of the heat loss through the regenerator housing and the dead volume are also quantified. A multi-parameter optimization reveals the optimal dimensions and operating parameters for different regenerator geometries.

In order to evaluate different regenerator geometries, including the emerging epoxy bonded bed and different heat transfer fluids, a passive regenerator test apparatus is constructed and an experimental investigation is presented. The flow and heat transfer characteristics of different regenerators are estimated by presenting the measured and deduced indicators, including the pressure drop, friction factor, effectiveness, heating power and overall Nusselt number.

Finally, based on the research in this thesis, the perspectives and some suggestions for the future work are given.

Resumé (Danish)

Emnet for denne ph.d. afhandling er numerisk modellering af den aktive magnetiske regenerator (AMR) samt eksperimentelle tests af passive regeneratorer med periodisk varierende væskestrømning. Det primære formål med dette arbejde er at udforske og forbedre nye koncepter og teknologier indenfor magnetisk køling.

Den numeriske diskretisering af en endimensionel (1D) AMR model er blevet forbedret, således, at ufysiske temperaturvariationer i den numeriske løsning elimineres. Yderligere tilføjelser til den transiente AMR model er blevet implementeret, således, at modellen nu kan håndtere trapez formede regeneratorer, varmetab gennem regeneratorvæggen samt regeneratorer med varierende materialer.

Magnetokaloriske materialer (MCM) klassificeres typisk som 1. eller 2. ordens (efter ordenen af deres faseovergang). De magnetokaloriske egenskaber, isoterm entropiændring, ΔS_{iso}, samt adiabatisk temperaturændring ΔT_{ad} er markant forskellige for de to klasser af MCMer. Via et teoretisk studie vises det i afhandlingen, at disse egenskaber bør betragtes med lige stor vægt. Et dybdegående studie omhandlende hvordan man organiserer regeneratorer med hhv. 1. og 2. ordens materialer baseret på eksperimentelle målinger af hhv. $La(Fe,Mn,Si)_{13}H_y$ (1. ordens) og Gd (2. ordens) præsenteres i afhandlingen. Det vises, at regeneratorens ydeevne er en funktion af arbejdstemperaturen samt Curie (overgangs-) temperaturvariationen i materialerne. En konceptuel regenerator med en kombination af 1. og 2. ordens materialer foreslås som en potentiel fremtidig regenerator kandidat.

Den aktive magnetiske regenerator evalueres ydermere på basis af en entropiminimeringsstrategi, hvor entropigeneration fra utilstrækkelig varmetransport, viskøs opvarmning samt aksial termisk ledning inkluderes. Betydningen af varmetab fra regeneratorens indkapsling samt såkaldt dødt volumen kvantificeres. Endelig udføres en multiparameter optimering med hensigten at finde de optimale operations- og geometriske parametre for en AMR.

Et testapparat til evaluering af passive regeneratorer opbygges, testes og valideres. Dette eksperimentelle udstyr bruges til at sammenligne forskellige regeneratorgeometrier inklusive de nye innovative regeneratorer, som er delvist limet sammen med epoxy, samt forskellige varmetransportvæsker. Væske- og varmetransport egenskaberne evalueres på basis dels af målte størrelser (tryktab, regenerator effektivitet samt tilført varme) og afledte størrelser (friction factor samt Nusselt-tallet).

Endelig perspektiveres forskningen præsenteret i denne afhandling og forslag anvises til fremtidigt arbejde.

List of publications

Papers published in peer-reviewed international scientific journals

T. Lei, K. K. Nielsen, K. Engelbrecht, C. R. H. Bahl, H. Neves Bez and C. T. Veje, Sensitivity study of multi-layer active magnetic regenerators using first order magnetocaloric material $La(Fe,Mn,Si)_{13}H_y$, *Journal of Applied Physics*, **118**, 014903, (2015). Attached in section A.1.

T. Lei, K. Engelbrecht, K. K. Nielsen and C. T. Veje, Study of geometries of active magnetic regenerators for room temperature magnetocaloric refrigeration, *Applied Thermal Engineering*, in press, (2015). Attached in section A.2.

T. Lei, K. Engelbrecht, K. K. Nielsen, H. Neves Bez and C. R. H. Bahl, Study of multi-layer active magnetic regenerators using magnetocaloric materials with a first and second order phase transition, *Journal of Physics D: Applied Physics*, **49**, 345001, (2016). Attached in section A.3.

Papers submitted to peer-reviewed international scientific journals

T. Lei, J. M. Pfotenhauer, W. Zhou, Analysis and comparison of novel phase shifters for Stirling pulse tube cryocooler, *Cryogenics*, under review, (2016). Attached in section A.4.

C. R. H. Bahl, K. Navickaité, H. Neves Bez, **T. Lei**, K. Engelbrecht, R. Bjørk, K. Li, Z. Li, J. Shen, W. Dai, J. Jia, Y. Wu, Y. Long, F. Hu, B. Shen, Operational test of bonded magnetocaloric plates, *International Journal of Refrigeration*, under review, (2016). Attached in section A.5.

Papers published in conference proceedings or presented in conferences

T. Lei, K. Engelbrecht, K. K. Nielsen, et al., Optimization of multi-layer active magnetic regenerator towards compact and efficient refrigeration, *The 29th International Conference on Efficiency, Cost, Optimisation, Simulation and Environmental Impact of Energy Systems*, Portorož, (2016). Attached in section A.6.

T. Lei, K. K. Nielsen, K. Engelbrecht, et al., Modelling and simulation of regenerators with complex flow arrangements for active magnetocaloric refrigeration, *Proceedings of the ASME 12th Biennial Conference on Engineering Systems Design and Analysis*, Copenhagen, (2014). Attached in section A.7.

T. Lei, K. Engelbrecht, K. K. Nielsen, et al., Modelling and comparison studies of packed screen regenerators for active magnetocaloric refrigeration, *Proceedings of the 6th IIF-IIR International Conference on Magnetic Refrigeration*, Victoria, (2014). Attached in section A.8.

M. Tahavori, C. Veje, **T. Lei**, K. K. Nielsen and K. Engelbrecht, Computationally efficient model of an active magnetocaloric regenerator. *Proceedings of the 5th IEEE International Conference on Control Systems, Computing and Engineering*, Batu Ferringhi, (2015). Attached in section A.9.

Papers accepted by conference proceedings

H. Neves Bez, K. Navickaité, **T. Lei**, K. Engelbrecht, A. Barcza and C. R. H. Bahl, Epoxy-bonded La(Fe,Mn,Si)$_{13}$H$_z$ as a multi-layered active magnetic regenerator, *The 7th IIF-IIR International Conference on Magnetic Refrigeration at Room Temperature*, Turin, (2016). Attached in section A.10.

M. Tahavori, K. Filonenko, C. T. Veje, **T. Lei**, K. Engelbrecht and C. R. H. Bahl, A cascading model of an active magnetic regenerator system, *The 7th IIF-IIR International Conference on Magnetic Refrigeration at Room Temperature*, Turin, (2016). Attached in section A.11.

Contents

CHAPTER 0

Nomenclature

0.1 Nomenclature

a_s	Specific surface area [1/m]
a_{wf}	Specific surface area of the housing in contact with the fluid [1/m]
a_{wa}	Specific surface area of the housing in contact with the ambient environment [1/m]
$\mathbf{A}$	$N_x \times N_x$ diagonal matrix
A_c	Cross sectional area of the regenerator [m^2]
A_{cw}	Cross sectional area of the housing wall [m^2]
$A_{i,j}$	Coefficient of the equation set
B	Applied magnetic field [Tesla]
$\mathbf{B}$	N_x-element vector
$B_{i,j}$	Constant of the equation set
Bi	Biot number
c_f	Specific heat capacity of the fluid [J/(kg·K)]
c_H	Specific heat capacity of the magnetocaloric material at constant magnetic field [J/(kg·K)]
C_{max}	Maximum heat capacity rate [W/K]
C_{min}	Minimum heat capacity rate [W/K]
c_w	Specific heat capacity of the wall material [J/(kg·K)]
C^*	Ratio of the minimum to maximum heat capacity rate
D_{avg}	Average particle diameter [m]
D_c	Micro-channel diameter [m]
D_h	Hydraulic diameter [m]
D_L	Characteristic dimension length [m]
D_{sc}	Wire diameter of the woven screen [m]
D_{sp}	Sphere diameter [m]
E_{reg}	Internal energy in the regenerator [J]
f	Frequency [Hz]
f_F	Friction factor
Gz	Graetz number
h	Heat transfer coefficient [W/(m^2·K)]
h_f	Specific enthalpy of the fluid [J/kg]
h_{in}	Specific enthalpy of the inflow [J/kg]
h_{out}	Specific enthalpy of the outflow [J/kg]
h_V	Volumetric heat transfer coefficient [W/(m^3·K)]

h_{wa}	Heat transfer coefficient between the wall and ambient [W/(m^2·K)]
h_{wf}	Heat transfer coefficient between the wall and fluid [W/(m^2·K)]
H	Magnetic field strength [A/m]
H_f	Final magnetic field [A/m]
H_i	Initial magnetic field [A/m]
H_{p1}	Plate thickness of the parallel plate matrix [m]
H_{p2}	Flow channel height of the parallel plate matrix [m]
H_{r1}	Flow channel height of the rectangular micro-channel matrix [m]
H_{r2}	Flow channel width of the rectangular micro-channel matrix [m]
i	Spatial node number
I	Spatial node indicator
j	Temporal node number
k	Thermal conductivity [W/(m·K)]
k_{disp}	Thermal conductivity due to axial dispersion [W/(m·K)]
k_f	Thermal conductivity of the fluid [W/(m·K)]
k_s	Thermal conductivity of the magnetocaloric material [W/(m·K)]
k_{stat}	Static thermal conductivity of the regenerator [W/(m·K)]
L	Regenerator length [m]
m	Specific magnetization [A·m^2/kg]
$\dot{m}_f$	Mass flow rate [kg/s]
m_s	Solid mass [kg]
M	Volume magnetization [A/m]
M_{irr}	Irreversible volume magnetization [A/m]
M_{neg}	Volume magnetization when demagnetized [A/m]
M_{pos}	Volume magnetization when magnetized [A/m]
M_{sc}	Mesh number of the woven screen [1/m]
n	Layer sequence number
N_L	Number of layers
N_t	Number of time steps
N_x	Number of spatial nodes
Nu	Nusselt number
Nu$_o$	Overall Nusselt number
P	Pressure [Pa]
Pr	Prandtl number
$\dot{q}$	Heat flow rate [W]
$\dot{q}_c$	Specific cooling power [W/kg]
$\dot{q}_h$	Specific heating power [W/kg]
$\dot{Q}_c$	Cooling power [W]
$\dot{Q}_h$	Heating rejection or heating power [W]
R_a	Aspect ratio
R_{DV}	Dead volume ratio
Re	Reynolds number
Re$_h$	Reynolds number based on the hydraulic diameter
s	Specific entropy [J/(kg·K)]
s_s	Specific entropy of the solid refrigerant [J/(kg·K)]

$\dot{S}_g$	Irreversible entropy production rate [W/K]
S_p	Piston stroke [m]
$S_{p,ac}$	Entropy production rate due to axial conduction [W/K]
$S_{p,ht}$	Entropy production rate due to insufficient heat transfer [W/K]
$S_{p,vd}$	Entropy production rate due to viscous dissipation [W/K]
$S_{p,tot}$	Total entropy production rate [W/K]
St	Stanton number
t	Time [s]
T	Temperature [K]
$\mathbf{T}$	N_x-element vector
T_a	Ambient temperature [K]
T_c	Cold end temperature [K]
T_{Curie}	Curie temperature [K]
T_f	Fluid temperature or final temperature [K]
T_h	Hot end temperature [K]
T_i	Initial temperature [K]
T_s	Solid temperature [K]
$T_{Schumann}$	Temperature predicted by the Schumann model [1] [K]
T_w	Wall temperature [K]
u	Specific internal energy [J/kg] or velocity [m/s]
u_f	Specific internal energy of the fluid [J/kg]
u_s	Specific internal energy of the solid [J/kg]
U	Utilization ratio
v_p	Piston velocity [m/s]
v_s	Superficial velocity (open velocity) [m/s]
V_r	Regenerator volume [m^3]
W_p	Plate width [m]
x	Axial position [m]
x_p	Piston displacement [m]

0.2 Abbreviations

1D	One dimensional
2D	Two dimensional
AMR	Active magnetic regenerator
CD	Center differential
CFC	Chlorofluorocarbon
CFL	Courant-Friedrichs-Lewy number
CHX	Cold end heat exchanger
COP	Coefficient of performance of a refrigerator
COP_{HP}	Coefficient of performance of a heat pump
CV	Check valve
CYL	Cylinder
DSC	Differential scanning calorimeter

EG	Ethylene glycol
EPM	Entropy production minimization
FOPT	First order phase transition
GWP	Global warming potential
HCFC	Hydrochlorofluorocarbon
HFC	Hydrofluorocarbon
HT	Heater
LE	Linear encoder
MC	Monotonized central-difference
MCE	Magnetocaloric effect
MCM	Magnetocaloric material
MCR	Magnetocaloric refrigeration
MT	Motor and crank system
NTU	Number of transfer units
NTU_o	Overall number of transfer units
ODP	Ozone depletion potential
P	Pressure gauge
REG	Regenerator
RMSD	Root-mean-square deviation
SOPT	Second order phase transition
SS	Stainless steel
T	Thermocouple
TEV	Total energy deviation
TVD	Total variation diminishing
VSM	Vibrating sample magnetotometer

0.3 Greek letters

α	Aspect ratio of the micro-channel or coefficient in the Ergun equation
β	Coefficient in the Ergun equation
γ	Shape factor of the magnetocaloric effect [K]
δ_L	Monotonized central-difference limiter at left boundary
δ_R	Monotonized central-difference limiter at right boundary
$\Delta\dot{q}$	Error in heat flow rate [W]
ΔS_{iso}	Isothermal entropy change [J/(kg·K)]
Δt	Time step [s]
ΔT	Temperature span [K]
ΔT_{ad}	Adiabatic temperature change [K]
ΔT_{Curie}	Curie temperature variation [K]
Δx	Spatial node length [m]
ε	Porosity of the regenerator bed
η	Effectiveness
η_c	Effectiveness of the cold-to-hot blow
η_h	Effectiveness of the hot-to-cold blow

θ	Tapered angle [°]
θ_L	Coefficient for calculating δ_L
θ_R	Coefficient for calculating δ_R
μ_0	Vacuum permeability $4\pi\times10^{-7}$ [T·m/A]
μ_f	Dynamic viscosity [mPa·s]
ξ	Volume fraction
ρ_f	Density of the fluid [kg/m^3]
ρ_s	Density of the magnetocaloric material [kg/m^3]
ρ_w	Density of the wall material [kg/m^3]
τ	Period time [s]
χ	Correction factor of internal temperature gradient in Ref. [2]
ω	Angular velocity [rad/s]

CHAPTER 1

Introduction

This chapter introduces the works implemented during the Ph.D. project and a background on room temperature magnetocaloric refrigeration (MCR). In Section 1.1, the outline of this thesis is presented. The basic thermodynamics of the magnetocaloric effect (MCE) are reviewed in Section 1.2, as a general introduction to this study. Recent developments in magnetocaloric materials and magnetic refrigerators, particularly in the last decade, are briefly reviewed in Sections 1.3 and 1.4, respectively. Finally, this chapter is summarized in Section 1.5.

1.1 Outline of the dissertation

This dissertation is presented based on the Ph.D. project at the Department of Energy Conversion and Storage, Technical University of Denmark (DTU). It lasted from August 2013 to August 2016, focusing on the study of active magnetic regenerators by numerical modeling and passive regenerator tests.

This dissertation is structured into seven chapters. Chapter 1 gives an introduction to the magnetocaloric effect and a brief review of the magnetocaloric materials and magnetic refrigerators for room temperature application. Chapters 2 - 4 summarize the study on numerical modeling of AMRs and Chapters 5 - 6 present the passive regenerator tests.

In detail, Chapter 2 presents an improved one dimensional AMR model. The original transient model solves the energy equations of the fluid and solid refrigerant for predicting the temperature distribution in both temporal and spatial domains, and then outputs the performance indices after reaching periodic steady state. To avoid spurious temperature oscillations in the original numerical scheme, the discretization method is improved by introducing monotonized central-difference (MC) limiter. The AMR model is also modified for simulating the tapered regenerator, heat loss through the housing wall as well as regenerators packed with mixed materials. Chapter 3 presents a study on multi-layer AMRs using magnetocaloric materials with a first and second order phase transition. A series of parameter studies are performed to investigate how to choose and layer the FOPT, SOPT or mixed materials and the sensitivity of those AMRs. The simulation tool is also applied to predict the performance of a small magnetic refrigerator and a future 2 kW magnetic heat pump. Chapter 4 analyzes the main loss mechanisms based on the method of entropy production minimization (EPM) and presents a multi-parameter optimization of AMRs using different geometries. In addition, the influence of the heat loss through the housing wall and the dead volume based on numerical modeling is estimated.

Chapter 5 introduces the construction of a passive regenerator test apparatus and a corresponding measurement / control system. The methodology for evaluating the passive regenerators is also described in detail. Chapter 6 presents the test results of passive regenerators with oscillating flow. The flow and heat transfer characteristics of the regenerator packed with stainless steel particles and epoxy bonded La(Fe,Mn,Si)$_{13}$H$_y$ are identified by presenting the measured and deduced indicators, including the pressure drop, friction factor, effectiveness ratio, heating power and overall Nusselt number. Different heat transfer fluids are also tested and discussed.

Chapter 7 summarizes the findings of this thesis and provides the perspectives and some suggestions for future work.

1.2 Fundamentals of magnetocaloric effect

The magnetocaloric effect is a phenomenon that a temperature change is associated when a magnetocaloric material undergoes a magnetization or demagnetization processes. Although many papers referred to E. Warburg (in 1881) as the discoverer of magnetocaloric effect, Smith [3] argued that the discovery should be attributed to P. Weiss and A. Piccard in 1917. [1] It debates that E. Warburg could not have observed the magnetocaloric effect in iron at room temperature, while Weiss and Piccard first discovered the magnetocaloric effect in nickel. What Warburg actually did observe was heating due to hysteresis.

The first important application of the MCE is the adiabatic demagnetization refrigerator for obtaining temperature close to absolute zero. The concept was proposed by Giauque in 1927 [4] and experimentally tested by Giauque and MacDougall in 1933 [5]. By adiabatically demagnetizing $Gd_2(SO_4)_3 \cdot 8H_2O$ from a starting point at about 1.5 K, an ultra-low temperature of 0.25 K was attained [5]. Giauque was recognized with the Nobel prize in 1949 for the outstanding and pioneering works. This ultra-low temperature refrigeration technology has been developed and applied extensively. Now the refrigeration temperature ranges from mK to liquid nitrogen temperature around 80 K for cryogenic applications. From the 1970s, the MCE was further applied and rapidly developed in the field of room temperature refrigeration. Brown in 1976 [6] built a room temperature magnetic refrigeration system and a temperature span of 47 K has been achieved using 1 mm thick gadolinium (T_{Curie}=293 K) plates with a magnetic field source of 7 T. In 1983, Barclay introduced the concept of the active magnetic regenerative refrigerator, which has been widely used in magnetic refrigerators.

Most of modern MCR systems consist of the following components: regenerators loaded with magnetocaloric materials, permanent magnets, a driven system generating the periodically changing magnet field, as well as a fluid control system for distributing the heat transfer liquid. Although alternative concepts, such as applying superconducting magnets and using pressurized gases as the heat transfer fluid, have been studied, this dissertation mainly focus on room temperature systems using permanent magnets and heat transfer liquids.

[1] Indirect reference is used since the original papers are in German and French.

Compared with the vapor refrigeration system, the magnetocaloric refrigerators exhibit many advantages, including high theoretical efficiency and avoidance of gaseous refrigerants. Although traditional refrigerants such as chlorofluorocarbons (CFCs) and hydrochlorofluorocarbons (HCFCs) with ozone depletion potential (ODP) and global warming potential (GWP) are being replaced by hydrofluorocarbons (HFCs), HFCs have high GWP and still draw serious environment concerns. Another interesting point is that future MCR systems can be integrated directly with cooling water distribution systems or the ground loop of a heat pump. This configuration may reduce the system complexity and the total cost, as well as the irreversible loss due to the approach temperature in the heat exchangers. However, a clear gap still exists between these conventional cooling devices and available MCR systems. For example, in Europe and North America commercial residential air-conditioners generally have COPs of 2.5-3.5 over a temperature span of 20-30 °C [7], which has not been seen in available MCR prototypes. The advantages of MCR systems and some potential points for improvement are summarized in Table 1.1.

Table 1.1: Advantages and desired improvements of magnetocaloric refrigerators.

Advantages	High theoretical efficiency Avoidance of vapor refrigerant Environment friendly fluid Low system pressure Easy integration with the distribution system
Desired improvements	Improvement of the cooling capacity and efficiency at large temperature span Cost reduction and recycling of the permanent magnets and magnetocaloric materials Development of the control strategy Long term operation Improvement of energy density

The basis of magnetic refrigeration is the magnetocaloric effect, which has been qualitatively explained and quantitatively described using the thermodynamic equations. In a qualitative explanation, the total specific entropy of a magnetic material can be separated into three components [8]: (1) the magnetic specific entropy representing the freedom of the electronic spin systems; (2) the lattice specific entropy due to the lattice vibrations; (3) the electronic specific entropy due to the electrons. The magnetic specific entropy is strongly associated with the applied magnetic field. The other two components, the lattice specific entropy and the electronic specific entropy, are independent of the magnetic field, but vary in connection with the temperature. During a magnetization process, the electronic spin systems inside an MCM tend to align according to the direction of the magnetic field, leading to a reduction in the overall freedom and thus the magnetic specific entropy. Conversely the demagnetization process results in an increase in the magnetic specific entropy. The total specific entropy of an MCM at constant pressure can be described by [8]:

$$s_{tot}(T,H) = s_{mag}(T,H) + s_{lat}(T) + s_{ele}(T) \tag{1.1}$$

The adiabatic magnetization process is associated with a raised temperature caused by an increase in the lattice and electronic specific entropy, due to the decreased magnetic specific entropy and the constant total specific entropy. The temperature increase is the so-called adiabatic temperature change ΔT_{ad}, which is an important parameter for evaluating MCMs. Inversely, the MCM temperature decreases upon an adiabatic demagnetization process. Without the magnetic hysteresis, a magnetized MCM could return to its initial condition being removed from the magnetic field adiabatically. In an isothermal magnetization process, the change in the total specific entropy equals to that in the magnetic specific entropy, which is another important parameter, i.e., isothermal entropy change ΔS_{iso}.

Figure 1.1 illustrates the thermodynamic processes, isothermal entropy change ΔS_{iso} and adiabatic temperature change ΔT_{ad} based on the entropy data of gadolinium. Note that the isothermal entropy change ΔS_{iso} is always negative and it is normally the specific value, which is the ratio of the entropy change to the MCM mass.

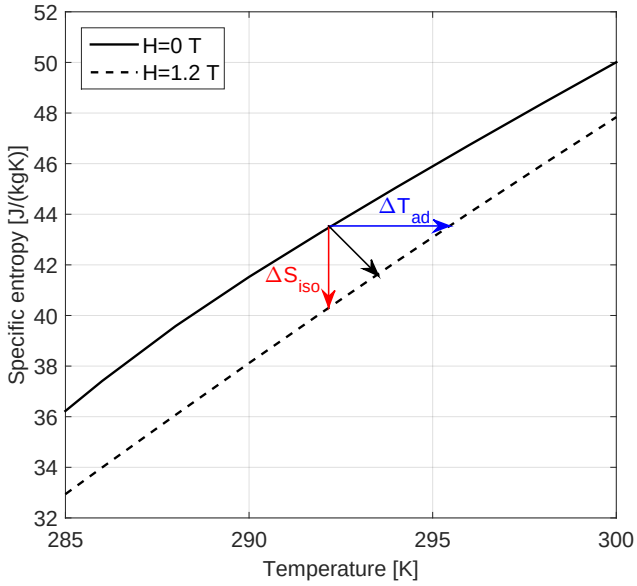

Fig. 1.1: Isothermal entropy change ΔS_{iso} and adiabatic temperature change ΔT_{ad} of gadolinium in the temperature-entropy ($T-S$) diagram. The red, blue and black arrows represent the isothermal, adiabatic and "polytropic" processes, respectively.

The differential of the total specific entropy $ds(T,H)$ is expressed by:

$$ds(T,H) = \left(\frac{\partial s}{\partial T}\right)_H dT + \left(\frac{\partial s}{\partial H}\right)_T dH \tag{1.2}$$

where T and H are the temperature and magnetic field, respectively.

The specific heat c_H of an MCM at constant magnetic field is defined as:

$$c_H(T,H) = T\left(\frac{\partial s}{\partial T}\right)_H \tag{1.3}$$

According to the definition, the isothermal entropy change Δs_{iso} is formulated by [9]:

$$\Delta s_{iso}(T, H_i : H_f) = s(T, H_f) - s(T, H_i) \tag{1.4}$$

The isothermal entropy change can also be calculated based on Eqns. 1.3 and 1.4 by:

$$\Delta s_{iso}(T, H_i : H_f) = \int_0^T \frac{c_H(T, H_f)}{T} dT - \int_0^T \frac{c_H(T, H_i)}{T} dT \tag{1.5}$$

Since the adiabatic process requires:

$$ds(T,H) = \left(\frac{\partial s}{\partial T}\right)_H dT + \left(\frac{\partial s}{\partial H}\right)_T dH = 0 \tag{1.6}$$

Then, the adiabatic temperature change ΔT_{ad} is stated as:

$$\begin{aligned} \Delta T_{ad}(T_i, H_i : H_f) &= T_f - T_i \\ &= -\int_{H_i}^{H_f} \left[1/\left(\frac{\partial s}{\partial T}\right)_H\right] \left(\frac{\partial s}{\partial H}\right)_T dH \\ &= -\int_{H_i}^{H_f} \frac{T}{c_H(T,H)} \left(\frac{\partial s}{\partial H}\right)_T dH \end{aligned} \tag{1.7}$$

where T_i and T_f are the initial and final temperature in the adiabatic process, respectively. As pointed out in Ref. [9], the integral in Eqn. 1.7 is not independent of the integration path. ΔT_{ad} is obtained from the relevant isentrope as shown in Figure 1.1.

Besides, the Maxwell relation [9] gives:

$$\left(\frac{\partial s}{\partial H}\right)_T = \mu_0 \left(\frac{\partial m}{\partial T}\right)_H \tag{1.8}$$

where μ_0 is the vacuum permeability $4\pi\times10^{-7}$ T·m/A and m is the specific magnetization with a unit of A·m^2/kg.

Therefore, the isothermal entropy change and adiabatic temperature change can be rewritten in the following forms:

$$\Delta s_{iso}(T, H_i : H_f) = \int_{H_i}^{H_f} \mu_0 \left(\frac{\partial m}{\partial T}\right)_H dH \tag{1.9}$$

$$\Delta T_{ad}(T_i, H_i : H_f) = -\int_{H_i}^{H_f} \frac{T}{c_H(T,H)} \left[\mu_0 \left(\frac{\partial m}{\partial T}\right)_H\right] dH \tag{1.10}$$

Rather than an ideal isothermal or adiabatic process, a magnetic "polytropic" process as shown in Figure 1.1 is always undergoing in AMRs or a differential scanning calorimeter (DSC), due to the limited but inevitable heat transfer with the environment. The concept of the polytropic process is originally used to describe the compression of the near-ideal gases.

The isothermal entropy change and the adiabatic temperature change can be indirectly estimated from the entropy data by integrating the measured specific heat c_H. The measurement of c_H is usually implemented by a DSC [10, 11], which measures the heat flux upon an MCM given a fixed heating or cooling temperature rate at constant magnetic field. Normally a Peltier element is used as the heat flux sensor. For materials with magnetic hysteresis, both heating and cooling curves are required for determining ΔS_{iso}, which are the cooling curve at high field and the heating curve at low field [11]. The heating curve represents the transition from paramagnetic to ferromagnetic phase, and vice versa.

The magnetization data are usually measured by a vibrating sample magnetotometer (VSM). In the VSM, an MCM sample is vibrated in the constant magnetic field, leading to a changing magnetic flux, and then an induced voltage in a pickup coil close to the sample. By using this method, the magnetization data can be deduced by capturing the voltage signals. During the measurement, the sample is cooled down by low temperature nitrogen gas to obtain the temperature dependence and an electromagnet is used as the magnetic field source. The magnetization data sometimes can be used to determine the entropy data based on the Maxwell relation.

Direct measurement of the isothermal entropy change can be done by measuring the heat flux upon an MCM sample with a Peltier element and a DSC, where the applied magnetic field is varied and the temperature is kept constant [11, 12]. Although it is hard to maintain an ideally isothermal condition, the direct measurement of the isothermal entropy change is relatively accurate due to a small temperature change around room temperature.

Direct measurement of the adiabatic temperature change has been done by measuring the samples temperature change upon the changing applied magnetic field. A high vacuum is built for simulating the adiabatic condition. In the case of using a thermocouple to measure ΔT_{ad}, the contact of the thermocouple and the sample will reduce the accuracy [13].

The internal energy of a magnetocaloric material undergoing an irreversible process is:

$$\rho_s \frac{\partial u_s}{\partial t} = \rho_s T_s \frac{\partial s_s}{\partial t} + \mu_0 H \frac{\partial M}{\partial t} - \rho_s T_s \frac{\dot{S}_g}{m_s} \tag{1.11}$$

where ρ_s, u_s, t, T_s, s_s, μ_0, H, M, $\dot{S}_g$ and m_s are the density of the solid refrigerant, internal energy of the solid refrigerant, time, solid temperature, specific entropy of the solid refrigerant, vacuum permeability, internal magnetic field strength, volume magnetization, irreversible entropy production rate and solid refrigerant mass, respectively.

Rewriting Eqn. 1.11 gives:

$$\rho_s \frac{\partial u_s}{\partial t} - \mu_0 H \frac{\partial M}{\partial t} = \rho_s T_s \frac{\partial s_s}{\partial t} - \rho_s T_s \frac{\dot{S}_g}{m_s} \tag{1.12}$$

The terms on the left side of the solid energy equation represent the internal energy and the magnetic work, respectively. Based on Eqns. 1.2, 1.3 and 1.12, the equation can be expressed as:

$$\begin{aligned} \rho_s \frac{\partial u_s}{\partial t} - \mu_0 H \frac{\partial M}{\partial t} &= \rho_s \left[T_s \left(\frac{\partial s_s}{\partial T_s} \right)_H \frac{\partial T_s}{\partial t} + T_s \left(\frac{\partial s_s}{\partial H} \right)_{T_s} \frac{\partial H}{\partial t} - T_s \frac{\dot{S}_g}{m_s} \right] \\ &= \rho_s \left[c_H \frac{\partial T_s}{\partial t} + T_s \left(\frac{\partial s_s}{\partial H} \right)_{T_s} \frac{\partial H}{\partial t} - T_s \frac{\dot{S}_g}{m_s} \right] \end{aligned} \tag{1.13}$$

A method suggested by Brey et al. [14] for evaluating the magnetic hysteresis is to assume:

$$T_s \frac{\dot{S}_g}{m_s} = M_{irr} \left| \frac{\partial \mu_0 H}{\partial t} \right| \tag{1.14}$$

where the irreversible volume magnetization M_{irr} is defined in order to recover the area swept by a given hysteresis curve. The irreversible volume magnetization M_{irr} can be calculated according to:

$$M_{irr}(T_s, H) = \left| \frac{M_{pos}(T_s, H) - M_{neg}(T_s, H)}{2} \right| \tag{1.15}$$

where M_{pos} is the volume magnetization when the change in field with time is positive and M_{neg} is the volume magnetization when the change in field with time is negative.

In case without magnetic hysteresis and a reversible processes is assumed, $\dot{S}_g$=0.

1.3 Magnetocaloric materials

This section introduces the commonly seen magnetocaloric materials for room temperature applications and their performance. The magnetocaloric material first discovered with a transition temperature around room temperature is gadolinium. Urbain et al. [9] [2] studied the ferromagnetism of pure Gd with the Curie temperature of about 293 K. Except for the relatively high ΔS_{iso} and ΔT_{ad}, Gd has a density of 7900 kg/m^3, relatively high thermal conductivity of around 11 W/(m·K), high strength, relatively good malleability and smaller MCE attenuation within a large temperature region, making it still competitive among the advanced magnetocaloric materials till now.

A series of magnetocaloric materials for room temperature application have been developed in the past decades. The magnetocaloric materials can be classified according to the order of the transition, e.g., the first and second order phase transition. During the ferromagnetic to paramagnetic transition, the magnetization of SOPT materials is a continuous function to zero as the temperature approaches the Curie temperature T_{Curie} [9]. SOPT materials exhibit a moderate isothermal entropy change ΔS_{iso} and adiabatic temperature change ΔT_{ad}. For FOPT materials, the magnetization changes discontinuously and a latent heat is associated with the magnetic phase transition. FOPT materials usually exhibit much higher peak values in ΔS_{iso} than SOPT materials and have equivalent or lower ΔT_{ad} at the same time. For example, the maximum $|\Delta S_{iso}|$ of the typical SOPT material Gd is around 5 J/(kg·K) and the peak of ΔT_{ad} is around 4 K for a magnetic field change of 1.5 T [15], while the values are 10-20 J/(kg·K) and 4 K for a FOPT material La(Fe,Mn,Si)$_{13}$H$_y$ [11].

Besides Gd, LaCaSrMn [16], $Gd_{1-x}Er_x$ [17], $Gd_{1-x}Tb_x$ [18] and $Gd_{1-x}Y_x$ [19], are typical SOPT materials that have been implemented in AMR devices. Many research efforts have also been devoted to developing FOPT materials, including $Gd_5Si_2Ge_2$ [20, 21], La(Fe,Si)$_{13}$ [22, 23], MnFe(P,As) [24] and their derivatives. Typical properties of those FOPT and SOPT materials with Curie temperatures around the ambient temperature are summarized in Table 1.2 [3].

Except for the high isothermal entropy change and adiabatic temperature change, the temperature dependence of the MCE and the effective working temperature region are also vital parameters for obtaining large temperature span and cooling capacity. Using FOPT materials, the multi-layer design is thus necessary, due to the relatively narrower working temperature region of those materials. It is anticipated that much fewer layers are needed for the SOPT materials. Therefore, Chapter 3 investigate how to choose and layer proper materials in future prototypes.

Another important factor is magnetic hysteresis, which usually exists in the first order materials and it may cause a significant irreversible loss and a reduced refrigeration performance. The magnetic hysteresis may exist in both temperature and magnetization [13] and it could result in a reduction in the AMR efficiency [14]. The second-order materials usually present no magnetic hysteresis.

[2] Indirect reference is used since the original paper is in French.
[3] Some numbers are read approximately from the figures in the cited papers.

Table 1.2: Typical magnetocaloric materials with Curie temperatures around the ambient temperature.

Materials	Phase transition	ΔS_{iso} [J/(kg·K)]	ΔT_{ad} [K]	T_{Curie} [K]	Ref.
Gd	SOPT	5@1.5 T	4@1.5T	293	[25]
$Gd_{1-x}Y_x$	SOPT	-	4-5@1.9 T	260-300	[26]
$Gd_{1-x}Er_x$	SOPT	-	5@1.9 T	293	[27]
$Gd_{1-x}Tb_x$ (x=0.1)	SOPT	2.3@1 T	1.9@1 T	286	[28]
LaCaSrMn	SOPT	1.8-5.0@0.7 T	0.6-1.5@0.7 T	260-340	[16]
$Gd_5Si_2Ge_2$	FOPT	14@2 T	7.3@2T	278	[20]
$MnFe(P_{1-x}As_x)$ (x=0.55) $Mn_{1.1}Fe_{0.9}(P_{1-x}As_x)$ (x=0.53)	FOPT	11-12.5@1 T	2.8@1 T	292-306	[24]
$LaFe_{13-x-y}Co_xSi_y$ (x=0.86-0.94, y=1.01-1.08)	FOPT	5.1-6.1@2 T	2.1-2.3@2 T	276-289	[25]
$La(Fe_{1-x}Si_x)_{13}H_y$ (x=0.11-0.12, y=1-1.5)	FOPT	19-24@2 T	6.2-6.9@2 T	274-323	[29]
$La(Fe_{1-x}Co_x)_{11.9}Si_{1.1}$ (x=0.06, 0.08)	FOPT	9-12@2 T	-	274-301	[30]
$La(Fe,Mn,Si)_{13}H_y$	FOPT	10-20@1.5 T	4@1.5 T	272-312	[11]
$La_{1-x}Pr_xFe_{10.7}Co_{0.8}Si_{1.5}$ (x=0.2, 0.4, 0.5)	FOPT	7-8@2 T	-	272-280	[31]
FeRh	FOPT	12@5 T	-	300	[32]
$Ni_{52.6}Mn_{23.1}Ga_{24.3}$	FOPT	12@5 T	-	301	[33]

Except the magnetocaloric properties, the other properties, such as the thermal conductivity, thermal diffusivity, mechanical strength, corrosion and volume change during the magnetization process are also important for the system design. Moreover, constructing a porous regenerator bed with high heat transfer performance, low flow resistance and small axial conduction is vital to maximizing AMR performance with available materials.

1.4 Magnetocaloric refrigerators

Room temperature magnetocaloric refrigeration has developed rapidly in recent years and many prototypes with significant cooling capacity have emerged [34, 35, 36]. As an introduction, Figure 1.2 shows a typical four-step refrigeration process of an AMR. In operation, the MCMs are periodically magnetized and demagnetized with an associated temperature increase and decrease. During specific intervals, a heat transfer fluid is blown through the porous AMR bed to transport heat with the solid refrigerant, and the arrows in Figure 1.2 show the flow directions during the blow period. At the hot end, the outflow has a higher temperature than that of the hot end reservoir T_h, and rejects the excess heat $\dot{Q}_h$ to the reservoir. While the outflow at the cold end absorbs heat, which is cooling power $\dot{Q}_c$, from the cold end reservoir due to a temperature difference. The temperature span is $\Delta T = T_h - T_c$ and the COP is defined as $\dot{Q}_c/(\dot{Q}_h - \dot{Q}_c)$. The plots show the temperature distribution, the dashed line and solid line represent the status before and after each step.

The heat regeneration processes during the blow periods are crucial for obtaining a larger temperature span than the materials' adiabatic temperature span. As illustrated in Figures 1.2 and 1.3, the materials along an AMR are actually working in different temperature regions according to the temperature span. This also determines that the materials with different Curie temperatures should be layered in the order following the temperature span.

Depending on the relative movement between the permanent magnet and the active magnetic regenerators, the prototypes can be characterized into two groups, i.e., reciprocating and rotary systems. The reciprocating design is often seen in small testing systems with one or two regenerators running at low frequency (<1 Hz), while the medium / big systems generally use the rotary design at higher frequency. These two configurations would also generate different magnetic field profiles and torque conditions [37].

The oscillating flow can be generated in different ways, e.g., the reciprocating cylinder and the pump with rotary valves or sequential valves. There is also a common view that the inflow and outflow at each end should be separated to avoid the dead volume, which will be discussed in Chapter 4. To track the developments in magnetocaloric refrigerators, recent prototypes reported in the last decade are briefly reviewed below.

Zimm et al. [17] presented a rotary MCR system using Gd and LaFeSiH. The maximum temperature span was 24 K with a maximum cooling power of 50 W. Jacobs et al. [38] built a rotary prototype using six layers of LaFeSiH particles, producing 3042 W of cooling power at zero temperature span and 2502 W over a span of 12 °C with a COP around 2.

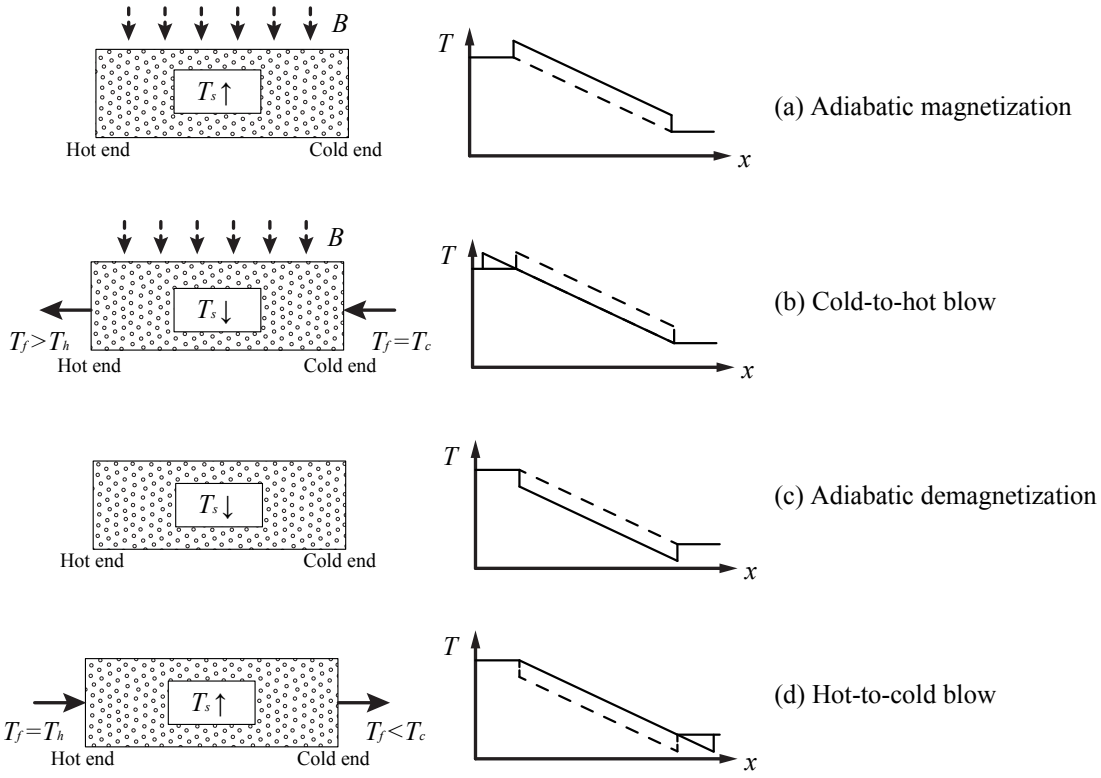

Fig. 1.2: Schematic diagram of an active magnetic regenerator undergoing a fourstep refrigeration process.

Rowe and Tura investigated the multi-layer regenerators using three materials in a 2-bed MCR system. Using a 2 T magnet assembly, a maximum temperature span of 50 K is realized in this refrigerator. Arnold et al. [39] presented a reciprocating MCR system using Gd and GdEr. This system realized in a maximum temperature span of 33 K with 2 T magnet, and then 59 K with a 5 T magnet. They further developed a 2-bed MCR system using a triple Halbach magnet assembly [40] and 650 g Gd, which realized a maximum temperature span of 33 K.

Tušek et al. [36] developed a rotary MCR prototype and analyzed the pros / cons of this magnetic refrigeration system. They also [41] presented an experimental comparison of MCRs using single layered Gd and multi-layer LaFeCoSi regenerators. The results showed that the Gd-based AMR produced a larger temperature span than the 4 or 7-layer LaFeCoSi AMRs. It indicates that the multi-layer AMR should be carefully designed and the layering strategy is important. This issue about how to design the multi-layer AMRs will be discussed in Chapter 3 in this thesis.

A rotary prototype exhibiting a no-load temperature span of over 25 K and maximum cool-

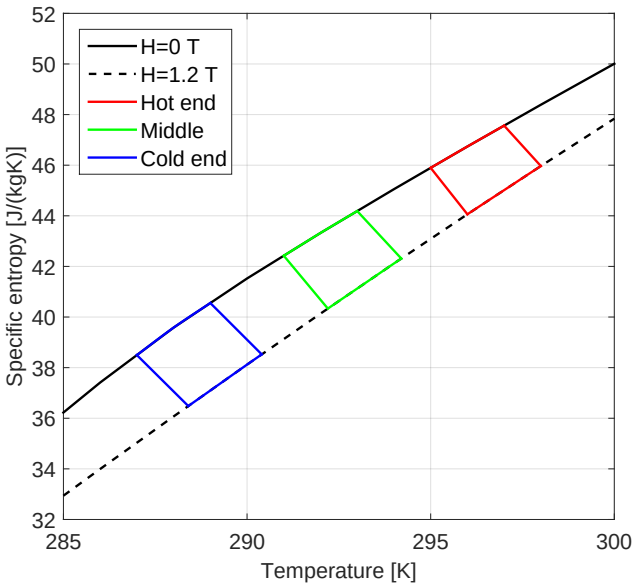

Fig. 1.3: Temperature - specific entropy loops of materials along a regenerator.

ing power of 1010 W using Gd spheres was developed by Engelbrecht et al. [42]. Eriksen et al. [19] presented a compact rotary MCR, which could realize a temperature span of 10.2 °C at a cooling load of 103 W and a COP of 3.1. The maximum temperature was 20 K. After further improvement, a maximum second-law efficiency of 18 % was obtained at a cooling load of 81.5 W, resulting in a temperature span of 15.5 K and a higher COP of 3.6 [43]. Neves Bez et al. [44] tested the multi-layer AMR using the first order material La(Fe,Mn,Si)$_{13}$H$_y$ and a maximum temperature span about 13-14 K was achieved using a 2-layer design, which is higher than the span of 10 K with Gd tested in the same test machine [45]. Recent results show that this reciprocating test machine could realize higher temperature span with AMRs using more layers.

Okamura et al. [46] reported a rotary MCR, which provided a maximum cooling power of 540 W with the largest temperature span of 21 K. Miyazaki et al. [36] constructed a rotary MCR using Gd and LaFeCoSi and this refrigerator could achieve a maximum temperature span of 7.6 K and a maximum cooling power of 150 W.

Capovilla et al. [47] reported a magnetic refrigerator prototype exhibiting maximum coefficient of 2.5 at 4 K temperature span and maximum zero-span cooling capacity of 150 W. Trevizoli et al. [48] presented an active magnetic regenerator test machine using a Halbach manet array. With Gd plates,this reciprocating machine realize a maximum temperature span of 4.45 K and a maximum cooling capacity of 3.9 W. Lozano et al. [49] built a rotary MCR system consisting of 24 regenerators packed with gadolinium spheres. For thermal loads of 200 and 400 W, the temperature spans are 16.8 K and 7.1 K, respectively, which correspond to COPs of 0.69 and 1.51.

Gatti et al. [50] presented a linear MCR system and some results of a rotary prototype, showing that a maximum temperature span of 30 K is realized. Aprea et al. developed a rotary MCR using 1.20 kg of Gd, which resulted in a maximum temperature span of 12 K and maximum cooling power of 200 W.

Different designs, such as the multi-layer design, using the FOPT materials, improved valve system, improved regenerator geometries, have been applied into those prototypes. This thesis also tries to further improve the understandings of those concepts and develop some new designs by theoretical and experimental investigation.

1.5 Summary

First this Ph.D. thesis is outlined and the work in each chapter is introduced briefly in Section 1.1. The fundamentals and thermodynamics of the magnetocaloric effect are reviewed in Section 1.2, as a general introduction to this study. The basic equations describing the solid refrigerant with the magnetization and heat transfer processes is built. The characterizations of the magnetocaloric materials are also summarized. Section 1.3 reviews the magnetocaloric materials with Curie temperature close to the room temperature. The characteristics of the FOPT and SOPT materials are emphasized, which also introduces the motive of the study on multi-layer AMRs. The recent MCR prototypes developed in the last decade have also been briefly reviewed in Section 1.4.

CHAPTER 2

Development of a one dimensional AMR model

This chapter introduces a one-dimensional numerical model of the AMRs developed at DTU and the improvements implemented during the Ph.D. project. The original numerical transient model solves two governing equations to obtain the temperature distribution in both fluid and solid domains [2, 51], and then output the performance indices after reaching convergence within a numerical tolerance.

The original discretization scheme, as shown in Section 2.1, has an energy conservation problem when evaluating a regenerator with varying cross sectional areas. It is solved by improving the spatial discretization of the heat conduction term, as shown in Section 2.2. Moreover, the regenerator housing is not taken into consideration and the boundary condition is adiabatic in the original model. Therefore, the heat loss from the housing wall to the ambient and the heat conduction in the wall are ignored. With the purpose of evaluating the influence of the regenerator housing, the 1D AMR model is further improved in Section 2.3 by introducing one more energy equation of the housing wall. In addition, Section 2.4 shows a revised solid equation for simulating AMRs using mixed materials in Chapter 3.

Furthermore, in Section 2.5, an advanced discretization method using monotonized central-difference limiter [52, 53] is applied to solve the problem of spurious oscillation in the numerical results and to decrease the numerical error. The model using the new scheme is validated against the Schumann analytical solution and compared with the originally established model using center differential (CD) method [2]. The results show that the introduced MC limiter could efficiently yield a stable solution and make the solutions total variation diminishing (TVD). Finally this chapter is summarized in Section 2.6. The content of this chapter is partially based on the papers attached in Sections A.7.

2.1 1D numerical AMR model

Many models have been developed to evaluate the AMR performance, including steady state models, one-dimensional models and two-dimensional (2D) models. With the development of the computational technology and the increase in computer capacity, 1D and 2D transient models are widely used for predicting cooling performance. Various numerical models of AMRs developed before 2013 have been well reviewed by Nielsen et al. [54]. References [2, 38, 55, 56, 57, 58, 59] presented typical 1D AMR model, and the examples of the 2D models can be found in References [60, 61, 62]. The 1D model exhibits advantages such as less

computation time, high efficiency and relatively high accuracy. This chapter presents the improvements of a 1D model, which has been used for the study of AMRs with different designs presented in the following chapters.

Although the assumptions and set up of different models could vary from each other, the basis is still similar. The core term is the one describing the magnetocaloric effect, which has been presented in Chapter 1 as:

$$\rho_s \frac{\partial u_s}{\partial t} - \mu_0 H \frac{\partial M}{\partial t} = \rho_s \left[c_H \frac{\partial T_s}{\partial t} + T_s \left(\frac{\partial s_s}{\partial H} \right)_{T_s} \frac{\partial H}{\partial t} - T_s \frac{\dot{S}_g}{m_s} \right] \tag{2.1}$$

where the entropy generation rate $\dot{S}_g$ is zero for a reversible process. The two terms on the left side of Eqn. 2.1 represent the energy storage and the magnetic work, respectively. The terms on the right side are widely used in various numerical models. Since $c_H = T_s \left(\frac{\partial s_s}{\partial T_s} \right)_H$, only the entropy data as a function of the temperature and the internal field are needed for modeling.

As presented in Chapter 1, the active magnetic regenerator is a porous medium consisting of magnetocaloric materials. The applied magnetic field changes periodically, synchronized with the periodical fluid blows in the interval between high and low fields. During the blow period, the fluid is blown through the porous bed, exchanging heat with the solid refrigerant. For the solid domain, except for the magnetic transition, more physical mechanisms such as the heat conduction and the convective heat transfer were considered in the energy equation:

$$\begin{aligned} \frac{\partial}{\partial x} \left(k_{stat} A_c \frac{\partial T_s}{\partial x} \right) &+ \frac{\mathrm{Nu} k_f}{d_h} a_s A_c \left(T_f - T_s \right) \\ &= A_c \left(1 - \varepsilon \right) \rho_s \left[c_H \frac{\partial T_s}{\partial t} + T_s \left(\frac{\partial s_s}{\partial H} \right)_{T_s} \frac{\partial H}{\partial t} - T_s \frac{\dot{S}_g}{m_s} \right] \end{aligned} \tag{2.2}$$

where x, k_{stat}, A_c, Nu, k_f, d_h, a_s, T_f and ε are the axial position, static thermal conductivity, cross sectional area of the regenerator, Nusselt number, thermal conductivity of the fluid, hydraulic diameter, specific surface area, fluid temperature and porosity of the regenerator, respectively. A_c, d_h, a_s, and ε reflect the geometry characteristics of a porous regenerator. For a given control volume, the fluid takes a fraction of ε, and the rest is solid. Here the porous medium is assumed locally homogeneous, and the velocity is uniform in this 1D model.

The heat transfer fluid is assumed incompressible, as an aqueous solution is normally used in MCR systems. Under this assumption, the continuity equation is eliminated and the mass flow rates at every position are the same. Except for the terms representing the heat conduction and the convective heat transfer, another two terms, the enthalpy flow $\dot{m}_f \left(\partial h_f / \partial x \right)$ and the viscous dissipation $\left| \left(\partial P / \partial x \right) \left(\dot{m}_f / \rho_f \right) \right|$ in the porous regenerator bed are considered. Therefore, the energy equation of the fluid is expressed as:

$$\frac{\partial}{\partial x}\left(k_{disp}A_c\frac{\partial T_f}{\partial x}\right) - \dot{m}_f\left(\frac{\partial h_f}{\partial x}\right) - \frac{\mathrm{Nu}k_f}{d_h}a_s A_c\left(T_f - T_s\right) + \left|\frac{\partial P}{\partial x}\frac{\dot{m}_f}{\rho_f}\right| = A_c\varepsilon\rho_f c_f\frac{\partial T_f}{\partial t} \tag{2.3}$$

where k_{disp}, $\dot{m}_f$, h_f ρ_f, c_f and $\partial P/\partial x$ are the thermal conductivity due to fluid dispersion, mass flow rate, specific enthalpy of the fluid, fluid density, specific heat of fluid and pressure drop. More details for the expressions of thermal conductivity due to fluid dispersion k_{disp}, static thermal conductivity k_{stat}, pressure drop $\partial P/\partial x$ and Nusselt number Nu are presented by Nielsen et al. [63].

In general, the center differential scheme and the implicit temporal discretization are used for discretizing the partial differential equations, e.g., Eqns. 2.2 and 2.3, in both space and time domains. The number of the spatial and temporal nodes (N_x and N_t) determines the Courant-Friedrichs-Lewy (CFL) number:

$$\mathrm{CFL} = u\frac{\Delta t}{\Delta x} = u\frac{\tau}{N_t}\frac{N_x}{L} \tag{2.4}$$

where u is the velocity magnitude, Δt is the time step and Δx is the spatial step. In a uniform meshing as shown in Figure 2.1, we have $\Delta t = \tau/N_t$ and $\Delta x = L/N_x$. However, a non-uniform meshing is sometimes applied for solving the non-linear problem, e.g., the non-linear response of the isothermal entropy changes when approaching the Curie temperature.

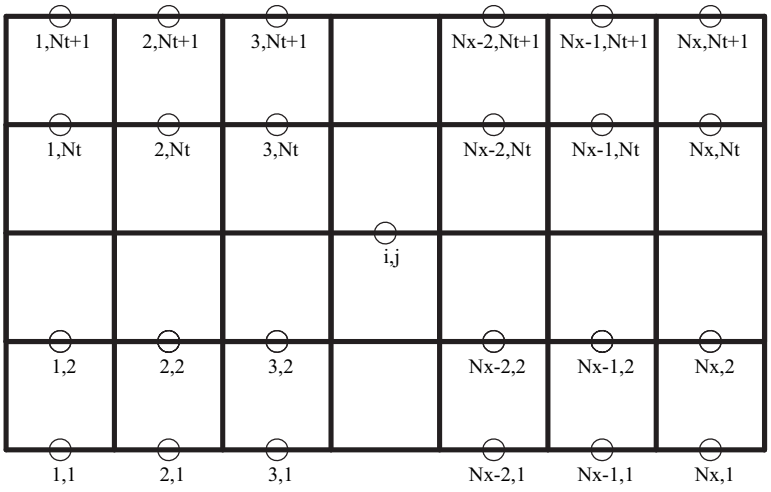

Fig. 2.1: Meshing of a 1D AMR model with temporal node number of N_t and spatial node number of N_x.

The CFL condition is needed for convergence while solving the partial differential equations numerically. In simulations, the convergence usually requires CFL$<<$1. A grid with high resolution is also required for high accuracy during simulation of the AMR performance. The number of temporal nodes N_t is always chosen according to the spatial node number N_x and the CFL condition. In the AMR model, the condition CFL$<$0.05 is reasonable if considering both the accuracy and the computation time. In the previous model, a uniform meshing was used. The non-uniform meshing scheme is also integrated into the model, although in most cases the uniform meshing is used.

By solving the coupled discretized equations, the temperature distribution can be calculated after each time step, given an initial condition. By using the information of the fluid temperature, the model will output the performance indices after reaching a numerical tolerance. The geometries, number of layers, materials, mass flow rate, applied magnetic field, and temperature span can be modified according to the evaluation of different designs.

2.2 Development of spatial discretization in conduction term

With the development of the magnetic refrigeration and the active magnetic regenerator, regenerators with different shapes have been developed and applied, for either maximizing the utilization of the magnetized area [17] or optimizing the construction of MCR prototypes. Although the influence brought by the regenerator housing [63] and the mal-distribution flow [64] have been discussed in the published paper, the study of AMRs with different shapes has not been well investigated.

However, the non-uniform shape of the regenerator brought significant numerical error during solving the conduction terms in the original model. The discretized equations based on the previous scheme are only capable of handling the regenerators with uniform cross sectional area, and the energy conservation of the conduction term fails handling AMRs with non-uniform shapes. Therefore, modifications are required in order to simulate those regenerators.

In the original model, the center differential scheme is used to discretize the conduction term with an implicit temporal discretization as:

$$\begin{aligned}\frac{\partial}{\partial x}\left(kA_c\frac{\partial T}{\partial x}\right) = \frac{1}{\Delta x}\Bigg[&\frac{k_{i-1,j}+k_{i,j}}{2}A_{c,i}\frac{T_{i-1,j+1}-T_{i,j+1}}{\Delta x}\\ &+\frac{k_{i,j}+k_{i+1,j}}{2}A_{c,i}\frac{T_{i+1,j+1}-T_{i,j+1}}{\Delta x}\Bigg]\end{aligned} \tag{2.5}$$

where the local thermal conductivity $k_{i,j}$ and the average cross sectional area $A_{c,i}$ of the node i are used.

For a regenerator with non-uniform shape, direct meshing using the previous scheme results in a node network as shown in Figure 2.2 (a), in which each node is still rectangular. The

interfaces between the neighboring nodes have different surface areas. Therefore, the heat conduction $\dot{q}$ from $i-1$ to i is not equal to that from i to $i-1$, as $A_{c,i-1} \neq A_{c,i}$:

$$\dot{q}_{i-1\to i} \neq \dot{q}_{i\to i-1} \tag{2.6}$$

$$\left|\frac{k_{i-1,j}+k_{i,j}}{2}A_{c,i-1}\frac{T_{i-1,j+1}-T_{i,j+1}}{\Delta x}\right| \neq \left|\frac{k_{i-1,j}+k_{i,j}}{2}A_{c,i}\frac{T_{i,j+1}-T_{i-1,j+1}}{\Delta x}\right| \tag{2.7}$$

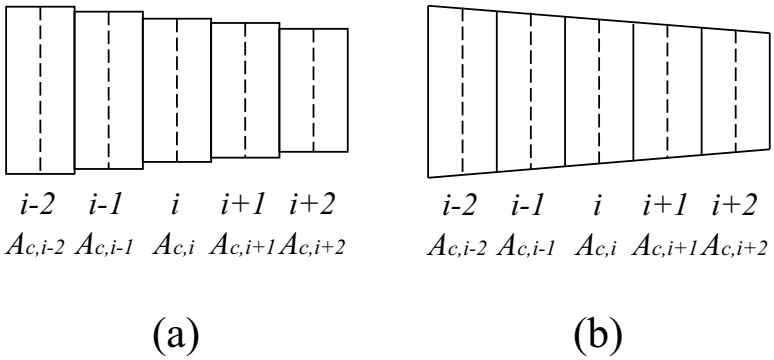

Fig. 2.2: Previous spatial discretization (a) and modified scheme (b) handling a tapered regenerator. The dashed lines represent the middle point of each node with an average cross sectional area of $A_{c,i}$.

The numerical error $\Delta\dot{q}$ is:

$$\Delta\dot{q} = \frac{k_{i-1,j}+k_{i,j}}{2}\left(A_{c,i}-A_{c,i-1}\right)\frac{T_{i,j+1}-T_{i-1,j+1}}{\Delta x} \tag{2.8}$$

This leads to a conservative problem in the original model and decreases the accuracy of the results. Although increasing node number could reduce the error, it may become significant during the numerical solving process, let alone the accumulating effect in the time domain. A solution for this issue is to use the average cross sectional area at the boundaries between two nodes as shown in Figure 2.2 (b). In this way, the heat conduction between the nodes i and $i-1$ becomes consistent:

$$\dot{q}_{i-1\to i} = \dot{q}_{i\to i-1} = \frac{k_{i-1,j}+k_{i,j}}{2}\frac{A_{c,i}+A_{c,i-1}}{2}\frac{T_{i,j+1}-T_{i-1,j+1}}{\Delta x} \tag{2.9}$$

In Table 2.1, an estimation of the accumulative error $\left(\int_x |\Delta\dot{q}|\right)/\dot{q}_0$ shows the old scheme could lead to a significant numerical problem, while this error is 0 for the improved scheme.

$\dot{q}_0$ is the conductive heat flow assuming $\theta = 0°$, which is 2.4 W in this case. Here a tapered regenerator, with a length of 0.05 m, an average cross sectional area of 400 mm^2 and a varying tapering angle θ, is assumed. The tapered angle θ is defined as the intersection angle between the hypotenuse and the horizontal line, as shown in Figure 2.3. The temperature span is 30 K and the thermal conductivity is fixed at 10 W/(m·K). It shows that the accumulative error cannot be neglected with large θ.

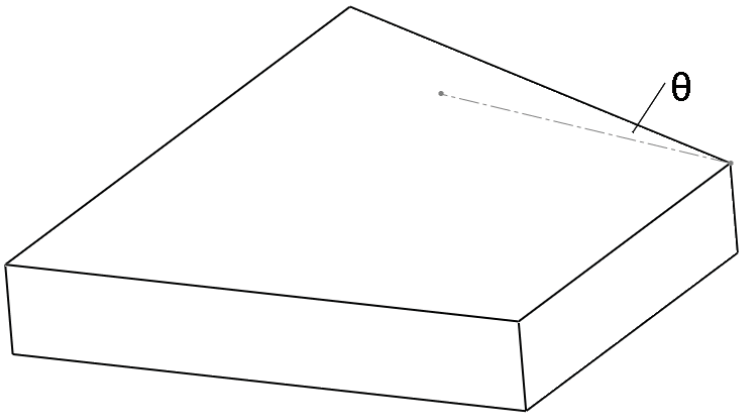

Fig. 2.3: Schematic diagram of a tapered regenerator with a tapered angle of θ.

Table 2.1: Accumulative error $(\int_x |\Delta\dot{q}|)/\dot{q}_0$ in the heat conduction term for a tapered regenerator using the previous model.

Tapered angle [°]	Accumulative error [-]
0	0.0%
5	21.7%
10	43.6%
15	66.3%
20	90.1%
25	115.4%
30	142.9%

2.3 Development of energy equation of housing wall

Several influences brought by the regenerator housing, such as the non-uniform velocity distribution in the cross sectional area, entrance effects and parametric losses to the ambient, have been considered in literature. Although the non-uniform velocity distribution and the entrance effect become less dominant due to the existence of the porous medium, the parametric losses and the conjugate loss sometimes cannot be neglected. Therefore, one additional

energy equation, describing the heat transfer with the housing wall and the internal heat conduction is developed and integrated with the original model.

First, the heat transfer between the wall and fluid is taken into account. Note it is difficult to identify the heat transfer coefficient between the fluid and housing wall h_{wf}, due to the presence of the porous medium. Therefore, only a theoretical prediction is presented in Chapter 4 by assuming different h_{wf}. Only a few particles are in contact with the wall and the contact area is relatively small. Therefore, the conduction between the particles and the housing wall is neglected. The second term is the heat conduction through the cross section of the wall, caused by the temperature gradient. The last ones are the natural convection with the ambient and the energy storage in the housing wall. In total, the energy equation of the housing wall could be set up as:

$$\begin{aligned} h_{wf}a_{wf}A_c\left(T_f - T_w\right) &+ \frac{\partial}{\partial x}\left(k_w A_{cw}\frac{\partial T_w}{\partial x}\right) \\ &+ h_{wa}a_{wa}A_c\left(T_a - T_w\right) = \rho_w A_{cw}c_w\frac{\partial T_w}{\partial t} \end{aligned} \tag{2.10}$$

where h_{wf}, a_{wf}, T_w, k_w, A_{cw}, h_{wa}, a_{wa}, T_a, ρ_w and c_w are the heat transfer coefficient between the wall and fluid, inner specific surface area of the housing, wall temperature, thermal conductivity of the wall, cross sectional area of the wall, heat transfer coefficient between the wall and ambient, outer specific surface area of the housing, ambient temperature, density of the wall material and specific heat capacity of the wall material, respectively.

Correspondingly, the new fluid energy equation becomes:

$$\begin{aligned} \frac{\partial}{\partial x}\left(k_{disp}A_c\frac{\partial T_f}{\partial x}\right) - \dot{m}_f\left(\frac{\partial h_f}{\partial x}\right) - \frac{\mathrm{Nu}k_f}{d_h}a_s A_c\left(T_f - T_s\right) \\ + \left|\frac{\partial P}{\partial x}\frac{\dot{m}_f}{\rho_f}\right| - h_{wf}a_{wf}A_c\left(T_f - T_w\right) = A_c\varepsilon\rho_f c_f\frac{\partial T_f}{\partial t} \end{aligned} \tag{2.11}$$

The modified model is based on the combined energy equations of the fluid, solid and the housing wall. The discretization of each term in the wall energy equation is presented as follows:

$$\frac{\partial}{\partial x}\left(k_w A_{cw}\frac{\partial T_w}{\partial x}\right)_{left} = \frac{1}{\Delta x}\left[\frac{k_{w,i-1,j} + k_{w,i,j}}{2}\frac{A_{cw,i-1} + A_{cw,i}}{2}\frac{T_{w,i-1,j+1} - T_{w,i,j+1}}{\Delta x}\right] \tag{2.12}$$

$$h_{wf}a_{wf}A_c\left(T_f - T_w\right) = h_{wf,i,j}a_{wf,i,j}A_{c,i}\left(T_{f,i,j+1} - T_{w,i,j+1}\right) \tag{2.13}$$

$$h_{wa}a_{wa}A_c\left(T_a - T_w\right) = h_{wa,i,j}a_{wa,i,j}A_{c,i}\left(T_a - T_{w,i,j+1}\right) \tag{2.14}$$

$$\rho_w A_{cw}c_w\frac{\partial T_w}{\partial t} = \rho_w A_{cw,i}c_{w,i,j}\frac{T_{w,i,j+1} - T_{w,i,j}}{\Delta t} \tag{2.15}$$

Rewriting the combined equations gives:

$$A_{i,i}T_{f,i,j+1} + A_{i,N_x+i}T_{s,i,j+1} + A_{i,2N_x+i}T_{w,i,j+1} = B_i \tag{2.16}$$
$$A_{N_x+i,i}T_{f,i,j+1} + A_{N_x+i,N_x+i}T_{s,i,j+1} + 0 \times T_{w,i,j+1} = B_{N_x+i} \tag{2.17}$$
$$A_{2N_x+i,i}T_{f,i,j+1} + 0 \times T_{s,i,j+1} + A_{2N_x+i,2N_x+i}T_{w,i,j+1} = B_{2N_x+i} \tag{2.18}$$

$$\begin{bmatrix} \mathbf{A_{i,i}} & \mathbf{A_{i,N_x+i}} & \mathbf{A_{i,2N_x+i}} \\ \mathbf{A_{N_x+i,i}} & \mathbf{A_{N_x+i,N_x+i}} & \mathbf{0} \\ \mathbf{A_{2N_x+i,i}} & \mathbf{0} & \mathbf{A_{2N_x+i,2N_x+i}} \end{bmatrix} \times \begin{bmatrix} \mathbf{T_{f,i,j+1}} \\ \mathbf{T_{s,i,j+1}} \\ \mathbf{T_{w,i,j+1}} \end{bmatrix} = \begin{bmatrix} \mathbf{B_i} \\ \mathbf{B_{N_x+i}} \\ \mathbf{B_{2N_x+i}} \end{bmatrix} \tag{2.19}$$

where A, T and B are the coefficient in the equation set, unknown temperature in next time node and constant term of the equation set, respectively. In addition, $\mathbf{A}$ is an $N_x \times N_x$ diagonal matrix as $i = 1 : N_x$. $\mathbf{T}$ and $\mathbf{B}$ are N_x-element vectors.

The temperature distribution $\mathbf{T}$ can be obtained by solving $\mathbf{T} = \mathbf{B}\mathbf{A}^{-1}$, and the rest of the solution process is similar to the original model.

2.4 Development of solid energy equation for simulating mixed materials

Various magnetocaloric materials have been tested for the application in the magnetocaloric refrigerators, which have been reviewed in Chapter 1. An important trend is to apply the MCM with a first order phase transition in future prototypes. However, the MCE of these materials is strongly temperature dependent, making the AMRs quite sensitive to the working temperature and the Curie temperature distribution [65]. To improve the stability of the MCR system using the FOPT materials, a study of mixing the SOPT and FOPT materials is done in this dissertation.

Correspondingly, in the numerical model, the solid equation is modified to simulate AMRs using the mixed materials. Assuming that the MCM A and B are used and they have the same temperature, the terms representing the magnetic transition in the solid energy equation can be rewritten as:

$$\begin{aligned} \rho_s \left[c_H \frac{\partial T_s}{\partial t} + T_s \left(\frac{\partial s_s}{\partial H} \right)_{T_s} \frac{\partial H}{\partial t} - T_s \frac{\dot{S}_g}{m_s} \right] = & \xi_A \rho_A \left[c_A \frac{\partial T_s}{\partial t} + T_s \left(\frac{\partial s_A}{\partial H} \right)_{T_s} \frac{\partial H}{\partial t} - T_s \frac{\dot{S}_{g,A}}{m_A} \right] \\ & + \xi_B \rho_B \left[c_B \frac{\partial T_s}{\partial t} + T_s \left(\frac{\partial s_B}{\partial H} \right)_{T_s} \frac{\partial H}{\partial t} - T_s \frac{\dot{S}_{g,B}}{m_B} \right] \end{aligned} \tag{2.20}$$

where ξ is the volume fraction of the material A or B.

In the heat conduction term, the solid thermal conductivity for the mixed materials is assumed to be:

$$k_s = \xi_A k_A + \xi_B k_B \tag{2.21}$$

2.5 Development of spatial discretization in ethalpy flow term

This section is devoted to the development in the spatial discretization method. The validation against the Schumann analytical solution and the comparison with the original model are presented.

Many methods are available for discretizing the partial differential equations in the spatial domain, such as the center differential scheme, upwind scheme, downwind scheme and other high-order schemes, etc. They have been chosen for different numerical models in terms of their characteristics.

2.5.1 Discretization using MC limiters

In the originally established AMR model, the center differential discretization and the implicit time discretization are used, which are efficient and easy for compiling. However, due to the discontinuity problem, e.g., the large temperature difference between incoming flow from the cold or hot reservoir and existing fluid in the regenerator bed, the solution of the conventional method shows spurious oscillation. The main concern is on the enthalpy flow term. The flux limiter method [53, 66] can be employed to capture sharper shock predictions without any misleading oscillations that would otherwise occur with high order spatial discretization schemes. Using a flux limiter, like the monotonized centered limiter [52], can make the solutions total variation diminishing [66]. In this section, the MC limiter is used to discretize the partial differential equations in the spatial domain. The implicit time discretization method is utilized as the original model did. The enthalpy flow term $\dot{m}_f \left(\partial h_f / \partial x\right)$ in the governing equation for liquid is discretized as follows.

If $\dot{m}_{f,j} > 0$, i.e. the fluid flows from the 1^{st} cell to the N_x^{th} cell (from hot to cold end), then,

$$\begin{aligned}\dot{m}_f \frac{\partial h_f}{\partial x} =& \frac{\dot{m}_{f,j}}{\Delta x}\Bigg\{h_{f,i,j} - h_{f,i-1,j} + \left(\frac{1}{2} - \frac{1}{2}\frac{\left|v_{s,i,j}\right|\Delta t}{\varepsilon_i \Delta x}\right)\left[\delta_{R,i,j}(h_{f,i+1,j} - h_{f,i,j})\right.\\ &\left.-\delta_{L,i,j}(h_{f,i,j} - h_{f,i-1,j})\right]\Bigg\}, \text{for } i = 2 : N_x - 1\end{aligned} \tag{2.22}$$

If $\dot{m}_{f,j} < 0$, we have:

$$\dot{m}_f \frac{\partial h_f}{\partial x} = \frac{\dot{m}_{f,j}}{\Delta x}\Bigg\{ h_{f,i+1,j} - h_{f,i,j} + \Big(\frac{1}{2} - \frac{1}{2}\frac{|v_{s,i,j}|\,\Delta t}{\varepsilon_i \Delta x}\Big)\big[\delta_{L,i,j}(h_{f,i,j} - h_{f,i-1,j}) - \delta_{R,i,j}(h_{f,i+1,j} - h_{f,i,j})\big]\Bigg\}, \text{for } i = 2 : N_x - 1 \tag{2.23}$$

δ_L and δ_R are the MC limiters:

$$\delta_{L,i,j} = max\Big(0, min\Big(\frac{1+\theta_{L,i,j}}{2}, 2, 2\theta_{L,i,j}\Big)\Big) \tag{2.24}$$

$$\delta_{R,i,j} = max\Big(0, min\Big(\frac{1+\theta_{R,i,j}}{2}, 2, 2\theta_{R,i,j}\Big)\Big) \tag{2.25}$$

$$\theta_{L,i,j} = \frac{h_{f,I,j} - h_{f,I-1,j}}{h_{f,i,j} - h_{f,i-1,j}} \tag{2.26}$$

$$\theta_{R,i,j} = \frac{h_{f,I+1,j} - h_{f,I,j}}{h_{f,i+1,j} - h_{f,i,j}} \tag{2.27}$$

$$I = i - 1, \text{if } \dot{m}_{f,j} > 0 \tag{2.28}$$

$$I = i + 1, \text{if } \dot{m}_{f,j} < 0 \tag{2.29}$$

Note that when $\dot{m}_{f,j} > 0$, $\theta_{L,i,j}$ of the 2^{nd} cell is:

$$\theta_{L,2,j} = \frac{h_{f,1,j} - h_{f,T_h}}{h_{f,2,j} - h_{f,1,j}}, \tag{2.30}$$

When $\dot{m}_{f,j} < 0$, $\theta_{R,i,j}$ of the cell $N_x - 1$ becomes:

$$\theta_{R,N_x-1,j} = \frac{h_{f,T_c} - h_{f,N_x,j}}{h_{f,N_x,j} - h_{f,N_x-1,j}}, \tag{2.31}$$

In fact, the commonly used schemes can also be expressed in a similar way:

$$\text{Upwind: } \delta(\theta) = 0 \tag{2.32}$$

$$\text{Cenered slope: } \delta(\theta) = 0.5(1+\theta) \tag{2.33}$$

$$\text{Upwind slope: } \delta(\theta) = \theta \tag{2.34}$$

$$\text{Downwind slope: } \delta(\theta) = 1 \tag{2.35}$$

To guarantee second order accuracy, Sweby suggested the following reduced portion of the TVD region, which is the grey region in Figure 2.4, as a suitable range for the flux limiting function [67]. Compared to the linear flux limiters, the MC limiter locating in the suggested region, leads to a stable solution essentially.

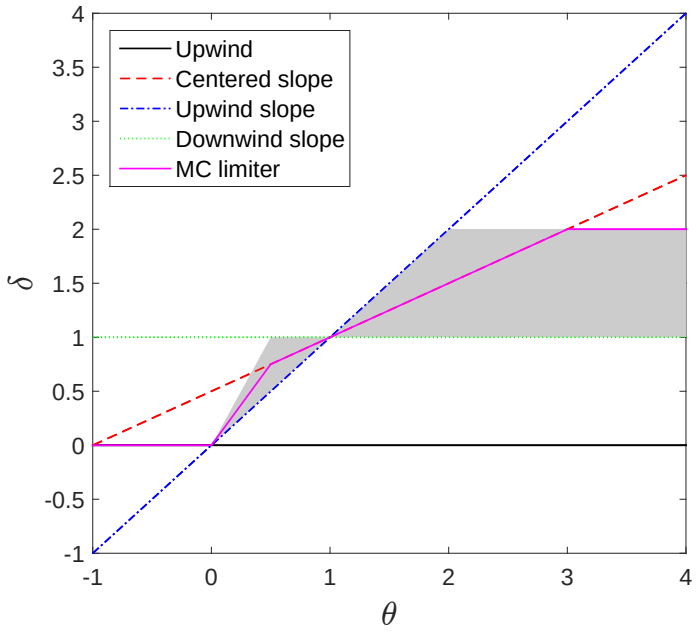

Fig. 2.4: Suggested reduced portion of the TVD region and flux limiters for different scheme [67].

2.5.2 Boundary conditions

The boundary conditions are important, sometimes vital, for obtaining correct and reasonable numerical solution. In the model of an AMR, the primary boundary condition is the mass flow rate, which is a function of time. In general, a refrigeration cycle of the AMR consists two blow periods and two dwelling periods. The two blows have opposite flow directions with balanced mass flow. Otherwise a reduced performance is foreseen if the mass flow is unbalanced [68].

Combined with the defined mass flow rate, the boundary conditions of the inflow temperature at the hot and colds of the AMR are:

$$\text{If } \dot{m}_{f,j} > 0, \text{ then } T(x=0,t) = T_h \tag{2.36}$$
$$\text{If } \dot{m}_{f,j} < 0, \text{ then } T(x=L,t) = T_c \tag{2.37}$$

That is, the inflow temperature is equal to the hot or cold reservoir temperature. In addition, the outflow at the cold end has a lower temperature than T_c, and it is higher than T_h at the hot end. Then, we can estimate the cooling power $\dot{Q}_c$ and the heat rejection $\dot{Q}_h$ by:

$$\dot{Q}_c = \sum_j -|\dot{m}_{f,j}|(h_{f,x=L,j} - h_{f,T_c})\Delta t \text{ where } \dot{m}_{f,j} > 0 \tag{2.38}$$
$$\dot{Q}_h = \sum_j |\dot{m}_{f,j}|(h_{f,x=0,j} - h_{f,T_h})\Delta t \text{ where } \dot{m}_{f,j} < 0 \tag{2.39}$$

Moreover, the boundary conditions at the first and last nodes of the regenerator have to be specified, which are influenced directly by the flow direction and the temperature boundary conditions.

If $\dot{m}_{f,j} > 0$, we have $\delta_{L,1,j} = 0$ and $\dot{m}_f \left(\partial h_f / \partial x\right)$ for the 1^{st} cell becomes:

$$\begin{aligned}\dot{m}_f \frac{\partial h_f}{\partial x} =& \frac{\dot{m}_{f,j}}{\Delta x}\Big\{h_{f,1,j} - h_{f,T_h} \\ &+\Big(\frac{1}{2} - \frac{1}{2}\frac{|v_{s,1,j}|\,\Delta t}{\varepsilon_1 \Delta x}\Big)\left[\delta_{R,1,j}(h_{f,2,j} - h_{f,1,j})\right]\Big\}\end{aligned} \tag{2.40}$$

$$\theta_{R,1,j} = \frac{h_{f,1,j} - h_{f,T_h}}{h_{f,2,j} - h_{f,1,j}} \tag{2.41}$$

If $\dot{m}_{f,j} < 0$, $\dot{m}_f \left(\partial h_f / \partial x\right)$ for the 1^{st} cell is:

$$\begin{aligned}\dot{m}_f \frac{\partial h_f}{\partial x} =& \frac{\dot{m}_{f,j}}{\Delta x}\Big\{h_{f,2,j} - h_{f,1,j} + \Big(\frac{1}{2} - \frac{1}{2}\frac{|v_{s,1,j}|\,\Delta t}{\varepsilon_1 \Delta x}\Big)\left[\delta_{L,1,j}(h_{f,1,j} - h_{f,T_h})\right. \\ &\left.-\delta_{R,1,j}(h_{f,2,j} - h_{f,1,j})\right]\Big\}\end{aligned} \tag{2.42}$$

$$\theta_{L,1,j} = \frac{h_{f,2,j} - h_{f,1,j}}{h_{f,1,j} - h_{f,T_h}} \tag{2.43}$$

$$\theta_{R,1,j} = \frac{h_{f,3,j} - h_{f,2,j}}{h_{f,2,j} - h_{f,1,j}} \tag{2.44}$$

If $\dot{m}_{f,j} > 0$, $\dot{m}_f \left(\partial h_f / \partial x\right)$ for the N_x^{th} cell is:

$$\begin{aligned}\dot{m}_f \frac{\partial h_f}{\partial x} =& \frac{\dot{m}_{f,j}}{\Delta x}\Bigg\{h_{f,N_x,j} - h_{f,N_x-1,j} + \left(\frac{1}{2} - \frac{1}{2}\frac{\left|v_{s,N_x,j}\right|\Delta t}{\varepsilon_{N_x}\Delta x}\right) \\ & \left[\delta_{R,N_x,j}(h_{f,T_c} - h_{f,N_x,j}) - \delta_{L,N_x,j}(h_{f,N_x,j} - h_{f,N_x-1,j})\right]\Bigg\}\end{aligned} \tag{2.45}$$

$$\theta_{L,N_x,j} = \frac{h_{f,N_x-1,j} - h_{f,N_x-2,j}}{h_{f,N_x,j} - h_{f,N_x-1,j}} \tag{2.46}$$

$$\theta_{R,N_x,j} = \frac{h_{f,N_x,j} - h_{f,N_x-1,j}}{h_{f,T_c} - h_{f,N_x,j}} \tag{2.47}$$

If $\dot{m}_{f,j} < 0$, we have $\delta_{R,N_x,j} = 0$ and $\dot{m}_f \left(\partial h_f / \partial x\right)$ for the N_x^{th} cell is:

$$\begin{aligned}\dot{m}_f \frac{\partial h_f}{\partial x} =& \frac{\dot{m}_{f,j}}{\Delta x}\Bigg\{h_{f,T_c} - h_{f,N_x,j} + \left(\frac{1}{2} - \frac{1}{2}\frac{\left|v_{s,N_x,j}\right|\Delta t}{\varepsilon_{N_x}\Delta x}\right) \\ & \left[\delta_{L,N_x,j}(h_{f,i,j} - h_{f,i-1,j})\right]\Bigg\}\end{aligned} \tag{2.48}$$

$$\theta_{L,N_x,j} = \frac{h_{f,T_c} - h_{f,N_x,j}}{h_{f,N_x,j} - h_{f,N_x-1,j}} \tag{2.49}$$

2.5.3 Other terms and iteration

The discretization treatments of the other terms are similar to those in the original model. By using those discretized equations, the temperature profiles on both fluid and solid (as well as wall) sides can be calculated after each time step. At the beginning of the computation, the initial fluid and solid temperatures are set to follow a linear distribution between the hot and cold reservoir temperature. The heat transfer fluid flows through the regenerator bed periodically, synchronized with the changing magnetic field. The temperature span is defined as $\Delta T = T_h - T_c$, which is the difference between the hot and cold reservoir temperatures. The computation is terminated when reaching a numerical tolerance. Finally, the cooling power $\dot{Q}_c$ and the heat rejection $\dot{Q}_h$ can be calculated by the periodical enthalpy flux at both sides. Also the indexes like pressure drop and COP, which is $\dot{Q}_c / (\dot{Q}_h - \dot{Q}_c)$, will be output in the end.

2.5.4 Validation and comparison

This section presents the validation of the introduced MC scheme against the Schumann analytical solution [1] and the comparison with the center differential method. The Schumann solution provides an accurate way to predict the temperature profiles inside the porous regenerator, where only the heat transfer and heat storage terms are considered.

Figure 2.5 shows such a regenerator model for the validation. The initial temperatures of the solid and fluid inside the regenerator are 270 K. A constant flow with a temperature of 300 K is blown through the regenerator bed by 100 s, raising both the solid and fluid temperatures.

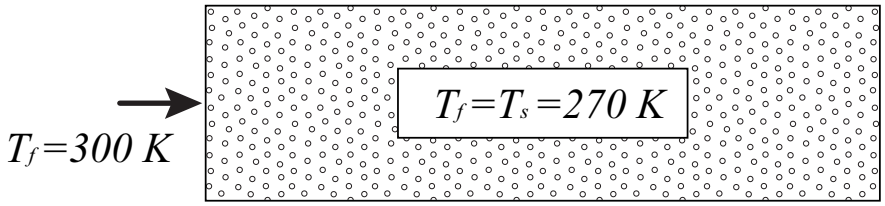

Fig. 2.5: Schematic diagram of a regenerator in the single blow test.

Then, the following equations are used here:

$$\frac{\mathrm{NTU}\dot{m}_f c_f}{L}\left(T_f - T_s\right) = A_c\left(1-\varepsilon\right)\rho_s c_s \frac{\partial T_s}{\partial t} \tag{2.50}$$

$$-\dot{m}_f \frac{\partial h_f}{\partial x} - \frac{\mathrm{NTU}\dot{m}_f c_f}{L}\left(T_f - T_s\right) = A_c \varepsilon \rho_f c_f \frac{\partial T_f}{\partial t} \tag{2.51}$$

where the number of thermal transfer units (NTU) and the volumetric heat transfer coefficient h_V are defined as:

$$\mathrm{NTU} = \frac{h_V A_c L}{\dot{m}_f c_f} \tag{2.52}$$

$$h_V = \frac{\mathrm{Nu}k_f}{d_h} a_s \tag{2.53}$$

The specific heat and density of the fluid and solid are constant and temperature independent. The mass flow rate is constant and the porosity is 0.36. The other parameters are listed in Table 2.2.

Figure 2.6 shows the impact of the meshing resolution on the temperature ramping curves, compared with the Schumann analytical solution for two different schemes. Total energy deviation (TEV) and root-mean-square deviation (RMSD) are also presented for evaluating the accuracy of those two methods. The TEV is essentially the numerical variation based on the energy conservation, which is defined as:

$$\mathrm{TEV} = \left| \int_0^t \dot{m}_f h_{in} dt - \int_0^t \dot{m}_f h_{out} dt - \Delta E_{reg} \right| \tag{2.54}$$

where h_{in} and h_{out} are the enthalpy inflow and outflow; ΔE_{reg} is the internal energy change of the regenerator. Note that there is no variation in the kinetic energy, since the flow resistance here is zero. Theoretically, TEV should be zero due to the energy conservation. In a numerical

Table 2.2: Modeling parameters for the validation and comparison.

Parameters	Value
Length of the regenerator	1 m
Cross sectional area of the regenerator	0.001 m^2
NTU	50
Mass flow rate	5 $kg/(m^2s)$
Initial fluid and solid temperature	270 K
Inflow fluid temperature	300 K
Flow period	100 s
Fluid density	1000 kg/m^3
Solid density	8900 kg/m^3
Specific heat of fluid	4200 J/(kg·K)
Specific heat of solid	500 J/(kg·K)

process, this parameter can be used to evaluate the accuracy of the model.

RMSD (root-mean-square deviation) represents the sample standard deviation of the differences between the predicted values and observed values. Here the predicted values are the Schumann analytical solution, therefore, we have:

$$\text{RMSD} = \sqrt{\frac{\sum_1^{N_x}(T - T_{Schumann})^2}{N_x}} \tag{2.55}$$

The ramping temperature curves in Figure 2.6 (a) shows that the CD method could lead to an overestimation of the fluid and solid temperature, at the inlet of the regenerator. In contrast, the MC limiter can neutralize this issue smoothly. The comparison with the Schumann solution also shows that the MC limiter realizes much smaller TEV and RMSD, meaning the new scheme has a higher accuracy. Furthermore, Figure 2.6 (b)-(d) shows the impact of the meshing resolution, using the same CFL number of about 0.07. The evenly meshed grid as shown in Figure 2.1 is used and the resolution increases with larger N_x and N_t. As expected, the ramping temperature curves of the CD scheme fit better with the analytical solution with increasing meshing resolution. Although both TEV and RMSD decrease significantly for the CD method, the MC limiter always performs better using the same grid resolution.

In Figure 2.6, small CFL of 0.07 is used, which is close to the real situation in the simulations of an AMR. High CFL is usually not recommended due to the issues such as low accuracy and increasing errors, although it can reduce the computation time significantly. Figure 2.7 shows the MC limiter is still performing well with high CFL, realizing small TEV and RMSD. Comparison between Figures 2.6 (d) and 2.7 (d) shows that high CFL can result in large deviation with the CD scheme, even using a grid with relatively high resolution.

The impact of the CFL number on the model performance is presented in Figure 2.8, where

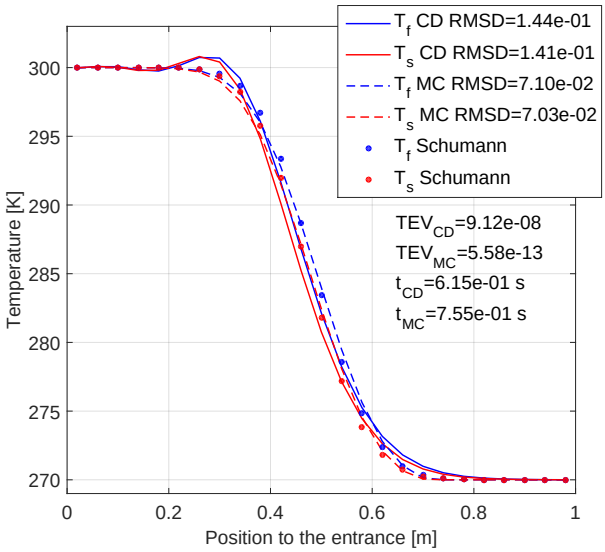

(a) N_x=25, N_t=500 and CFL=0.07

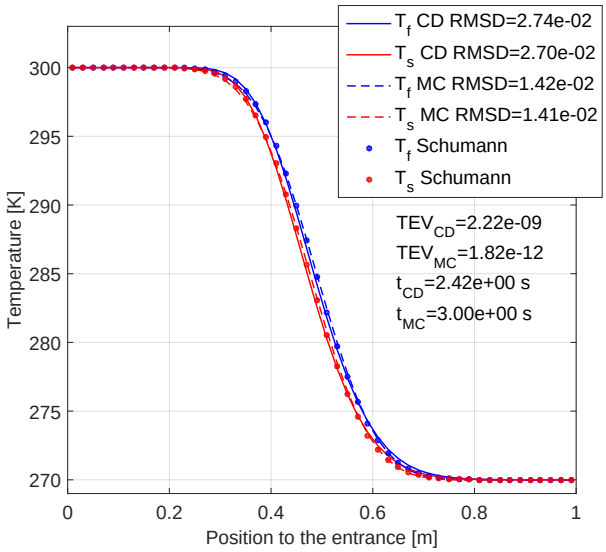

(b) N_x=50, N_t=1000 and CFL=0.07

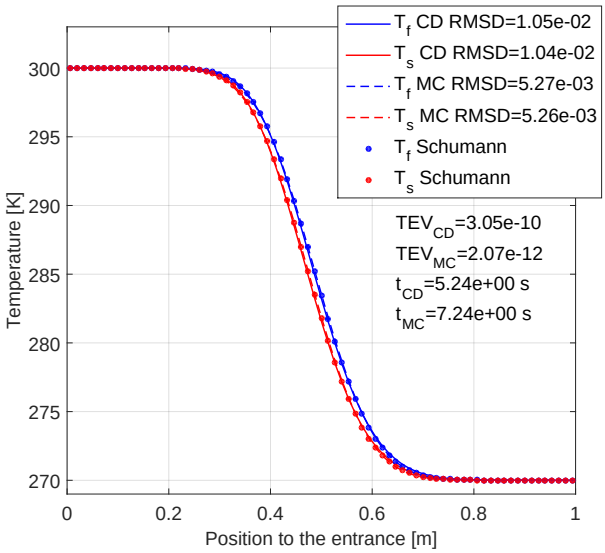

(c) N_x=75, N_t=1500 and CFL=0.07

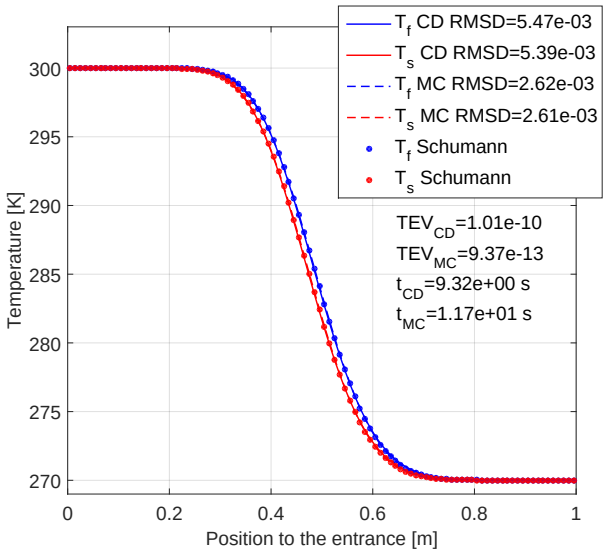

(d) N_x=100, N_t=2000 and CFL=0.07

Fig. 2.6: Impact of meshing resolution on numerical accuracy with a small CFL of 0.07.

four CFL numbers, 0.07, 0.35, 0.70 and 0.99, are used. Both TEV and RMSD become larger with an increase in the CFL number with the CD scheme. However, both indices did not change much in the model using the MC limiter. RMSD even decreases with a higher CFL. Figures 2.6-2.8 show that the utilization of MC limiter can eliminate the spurious oscillation in the numerical solution, presenting relatively high accuracy and robust performance in most cases.

The computation time of both schemes are also presented in Figures 2.6-2.8. It shows that the time consumption of the MC limiter is about 1/3 longer than that with the CD method. This is attributed to the introduction of the operator in Eqns. 2.22 - 2.29. The MC limiter is still an efficient scheme compared with the CD method, as the latter has to increase the meshing resolution to obtain the same accuracy.

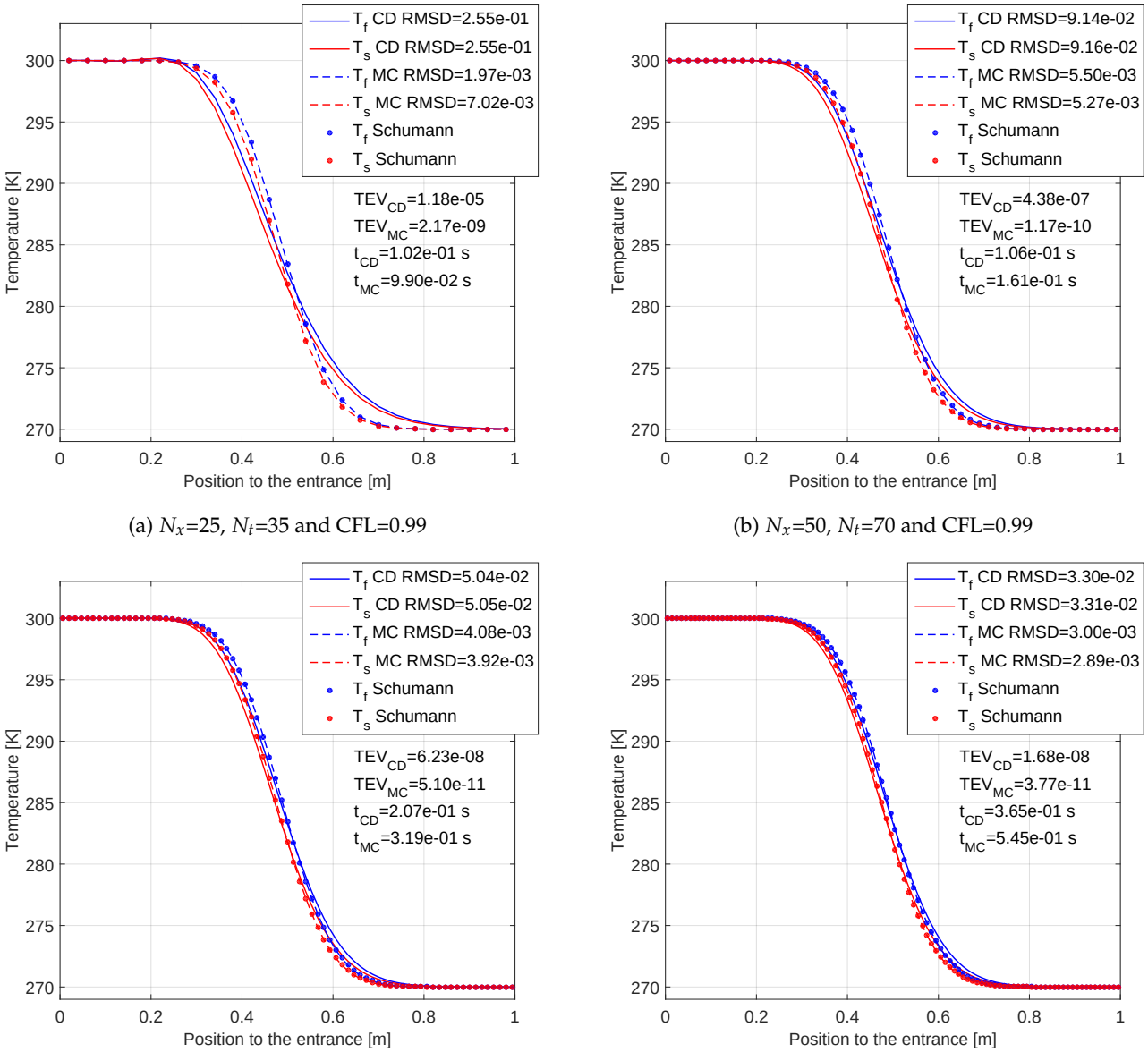

(a) N_x=25, N_t=35 and CFL=0.99

(b) N_x=50, N_t=70 and CFL=0.99

(c) N_x=75, N_t=105 and CFL=0.99

(d) N_x=100, N_t=140 and CFL=0.99

Fig. 2.7: Impact of meshing resolution on numerical accuracy with a large CFL of 0.99.

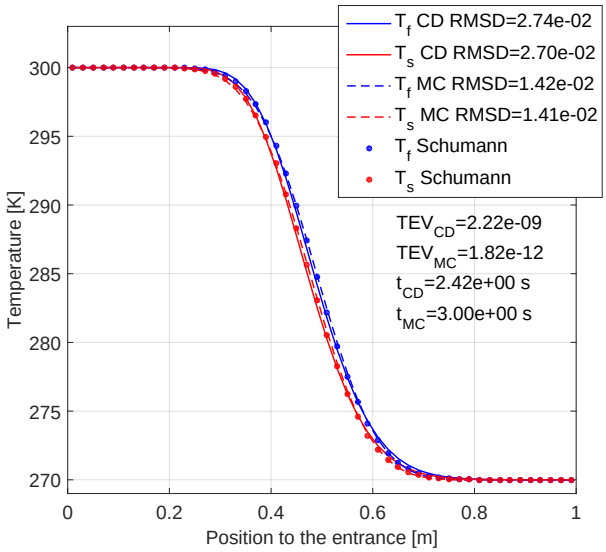

(a) N_x=50, N_t=1000 and CFL=0.07

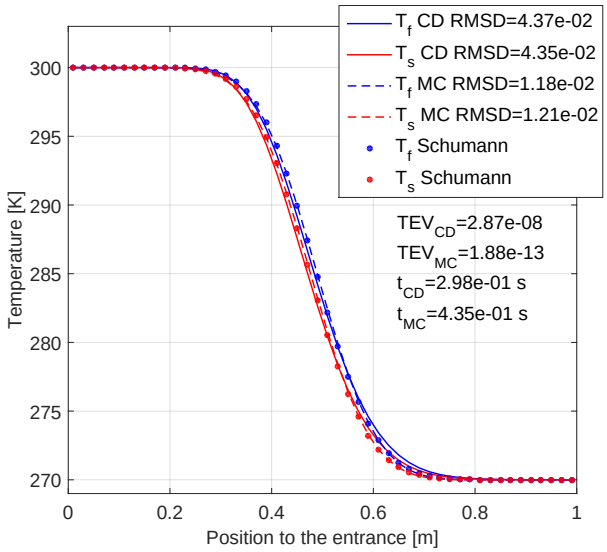

(b) N_x=50, N_t=200 and CFL=0.35

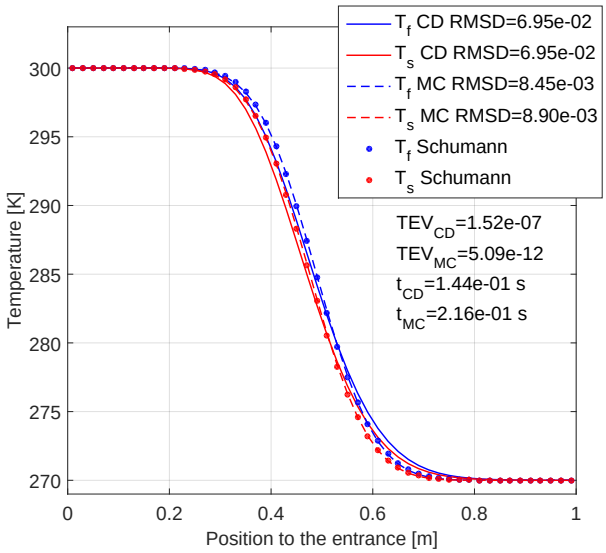

(c) N_x=50, N_t=100 and CFL=0.70

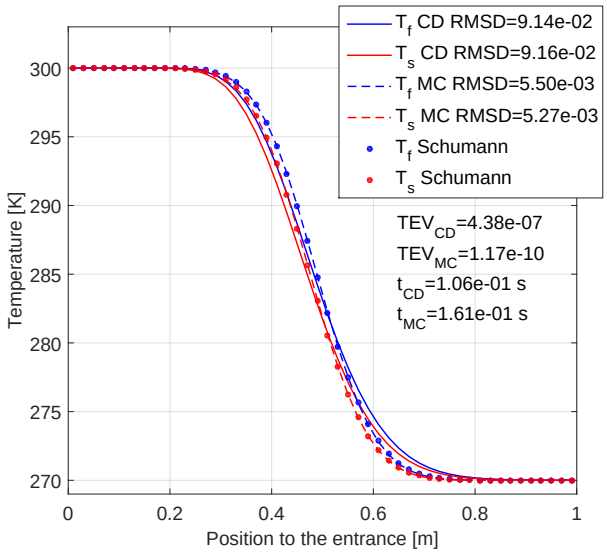

(d) N_x=50, N_t=70 and CFL=0.99

Fig. 2.8: Impact of CFL number on numerical accuracy with N_x=50.

2.6 Summary

In this chapter a 1D numerical model of the AMR is introduced. The previous established model faces several issues concerning regenerators with different shapes, the loss through the housing wall, the regenerators using mixed materials and the spurious oscillation in numerical solution.

Based on the energy conservation, the discretization of the heat conduction term is modified and the numerical error is eliminated by using the average cross sectional area between two nodes. Moreover, the energy equation of the housing wall is added into the combined set of the governing equations. The discretization and solving process are introduced in details. This allows the model to predict the losses brought by the wall. In addition, the energy equation of the solid is modified for simulating the regenerators using mixed MCMs.

Further, the MC limiter is introduced to the original model to solve the problem of the spurious temperature oscillation. Both the validation against the Schumann analytical solution and the comparison with the previous CD method show that the new scheme can provide a high accuracy and robust performance in most cases. Since the temperature dependence of the magnetocaloric effect is highly non-linear, especially for the materials with a first order phase transition, it is not recommended to use large time step with high CFL in the AMR simulation.

CHAPTER 3

Multi-layer AMR using magnetocaloric materials with first and second order phase transition

Magnetocaloric materials with a first order phase transition usually exhibit a large, although sharp, isothermal entropy change ΔS_{iso} near their Curie temperature T_{Curie}, compared with the materials with a second order phase transition. Experimental results in recent magnetocaloric refrigerators demonstrated the great potential of applying FOPT materials in future device [38, 44], but a thorough study on the impact of the moderate adiabatic temperature change and the strong temperature dependence of magnetocaloric effect is lacking. In addition, comparison of active magnetic regenerators using FOPT and SOPT materials is also of general interest.

This chapter presents the modeling results of multi-layer AMRs using the FOPT and SOPT materials based on the numerical model presented in Chapter 2. Section 3.1 quantifies the impact of isothermal entropy change, adiabatic temperature change and shape factor describing the temperature dependence of the MCE, by using artificially built magnetocaloric properties. In Section 3.2, based on measured magnetocaloric properties of $La(Fe,Mn,Si)_{13}H_y$ and Gd, an investigation on how to layer typical FOPT and SOPT materials with different temperature spans is carried out. Moreover, the sensitivity of the working temperature and the variation in Curie temperature distribution for both groups of AMRs is investigated. In the simulations, a concept of mixing FOPT and SOPT materials is also studied for improving the stability of layered AMRs. The simulation and experiment results are compared in Section 3.3 to validate the model. Predicted performance of an efficient 2 kW magnetic heat pump is presented in Section 3.4. This chapter is based partially on the papers attached in Sections A.1, A.3, A.6 and A.10.

3.1 Theoretical investigation on AMRs using different magnetocaloric materials

Many MCR systems use gadolinium, which is a typical SOPT material, as the solid refrigerant, including the first room temperature magnetic refrigerator presented by Brown [6]. During the ferromagnetic to paramagnetic transition, the magnetization of the SOPT materials goes continuously to zero, as the temperature approaches the Curie temperature T_{Curie} [9]. SOPT materials, including Gd and Gd alloys, exhibit moderate isothermal entropy change ΔS_{iso} and adiabatic temperature change ΔT_{ad}, which are the two most commonly used parameters for

evaluating MCMs. For the FOPT materials, the magnetization changes discontinuously and a latent heat is associated with the magnetic phase transition. The FOPT materials usually have much larger peak values in ΔS_{iso} than the SOPT materials and have equivalent or lower ΔT_{ad} at the same time. For example, the maximum $|\Delta S_{iso}|$ of the typical SOPT material Gd is around 5 J/(kg·K) and the peak of ΔT_{ad} is around 4 K for a magnetic field change of 1.5 T [15], while the values are 10-20 J/(kg·K) and 4 K for the FOPT materials La(Fe,Mn,Si)$_{13}$H$_y$ [11].

Many research efforts have been devoted into developing FOPT materials, such as $Gd_5Si_2Ge_2$ [21], La(Fe,Si)$_{13}$ [29] and MnFe(P,As) [24], or applying FOPT materials in an MCR prototype [38, 44]. Jacobs et al. [38] presented a rotary MCR device using six-layer LaFeSiH and it produced a cooling power of around 2500 W over a span of 11 K with a COP around 2, which demonstrates the significant potential. Neves Bez et al. [44] presents a single-regenerator magnetic refrigerator using two layers of LaFeMnSiH. This test machine could realize a no-load temperature span of 13 K, which is higher than a span of 9 K with only Gd [45].

Another distinguishing difference between the two groups of materials is that, both ΔS_{iso} and ΔT_{ad} of FOPT materials will decrease much faster as the temperature deviates from T_{Curie}. It indicates that the proper working temperature region of FOPT materials is thus much narrower than that for SOPT materials. Therefore, a single-layer AMR using one FOPT material is unable to realize a large temperature span ΔT. In order to improve that, a multi-layer design is required, in which MCMs with different Curie temperatures are aligned following the temperature gradient, as illustrated in Figure 3.1. Although the large ΔS_{iso} of FOPT materials is reported and emphasized extensively, the influence of moderate (or even lower) ΔT_{ad} and "sharp" temperature dependence of the magnetocaloric effect on the AMR performance are not well investigated. Engelbrecht and Bahl [51] studied the individual impact of ΔS_{iso} or ΔT_{ad} by holding the other parameter constant, and it was concluded that ΔT_{ad} can be more important than ΔS_{iso} in certain conditions. Brey et al. [14] evaluated the influence of ΔS_{iso} and ΔT_{ad} on the cooling power of a continuously layered AMR by scaling measured properties. Aprea et al. [69] investigated AMRs using four kinds of FOPT and SOPT materials based on a simplified model. However, the temperature dependence of the MCE, which differs a lot between FOPT and SOPT materials, has not been taken into account when evaluating AMRs in previous studies.

To further develop the understanding, the combination of ΔS_{iso}, ΔT_{ad} and the temperature dependence of the MCE affecting the cooling performance of multi-layer AMRs, is studied in this section based on artificially built magnetocaloric properties.

3.1.1 Artificially built magnetocaloric properties

As discussed in Chapter 2, the entropy data as a function of the internal magnetic field and temperature are mainly needed for modeling multi-layer AMRs using FOPT and SOPT materials. The two important parameters, isothermal entropy change ΔS_{iso} and adiabatic temperature change ΔT_{ad} of an MCM, are also closely connected and they are both derived from the entropy data by [9, 70]:

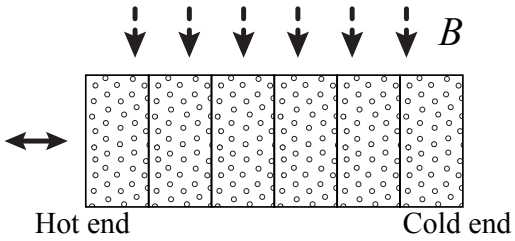

(a) Multi-layer magnetic regenerator

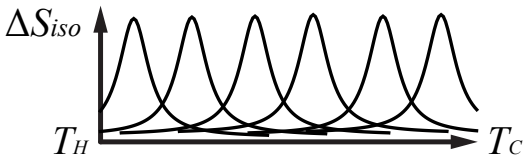

(b) ΔS_{iso} of each layer as a function of T

Fig. 3.1: Schematic diagram of a multi-layer regenerator (a) and maximum absolute isothermal entropy change of each layer along the regenerator (b), where the double sided arrow represents the periodical blows.

$$\begin{aligned}
\Delta S_{iso}(T_s; H_f, H_i) &= \int_{H_i}^{H_f} \left(\frac{\partial s_s}{\partial H}\right)_{T_s} dH \\
&= \int_0^{T_s} \frac{c_H(T_s, H_f)}{T_s} dT_s - \int_0^{T_s} \frac{c_H(T_s, H_i)}{T_s} dT_s \qquad (3.1) \\
\Delta T_{ad}(T_{s,i}; H_f, H_i) &= -\int_{H_i}^{H_f} \left[1/\left(\frac{\partial s_s}{\partial T_s}\right)_H\right] \left(\frac{\partial s_s}{\partial H}\right)_{T_s} dH \\
&= -\int_{H_i}^{H_f} \frac{T_s}{c_H(T_s, H)} \left(\frac{\partial s_s}{\partial H}\right)_{T_s} dH \qquad (3.2)
\end{aligned}$$

where T_s, H_f and H_i are the solid temperature, final magnetic field and initial magnetic field. The subscript i in $\Delta T_{ad}(T_{s,i}; H_f, H_i)$ represents the initial state.

In order to study the impacts of ΔS_{iso} and ΔT_{ad} as a combination, empirical methods, including holding one parameter constant [51] and scaling ΔS_{iso} or ΔT_{ad} [14], have been developed. However, the strong temperature dependence of the MCE is not taken into account. Therefore, the shape of the ΔS_{iso} curve is approximated as a Lorentzian curve with an assumed Curie temperature. The following modified Lorentzian equation is used to calculate the isothermal entropy change upon an increase of magnetic field from 0 to 1.5 T:

$$\Delta S_{iso,1.5T}(T_s) = -|\Delta S_{iso}|_{max} \frac{\gamma^2}{(T_s - T_{Curie})^2 + \gamma^2} \qquad (3.3)$$

where$|\Delta S_{iso}|_{max}$, T_{Curie} and γ are the maximum absolute isothermal entropy change, Curie temperature and shape factor of ΔS_{iso} curve.

Figure 3.2 presents the absolute value of ΔS_{iso} based on Eqn. 3.3, for$|\Delta S_{iso}|_{max}$ of 6 and 15 J/(kg·K) as well as γ from 4 to 10 K. The shape factor γ is introduced to adjust the temperature distribution and the shape of ΔS_{iso} curve. Smaller γ could lead to sharper ΔS_{iso} curve around the Curie temperature, and then narrower the working temperature region, which is similar to the case with FOPT materials. The isothermal entropy change upon a magnetic field change of H is calculated by:

$$\Delta S_{iso,1.5T}(T_s) = \left(\frac{H}{1.5}\right)^{2/3} \Delta S_{iso,1.5T}(T_s) \tag{3.4}$$

where the scaling coefficient $(H/1.5)^{2/3}$ is used due to the nonlinear magnetic field dependence of ΔS_{iso} [9]. Figure 3.3 (a) shows the absolute isothermal entropy change at different magnetic fields based on Eqns. 3.3 and 3.4, when$|\Delta S_{iso}|_{max}$ is 15 J/(kg·K) and γ is 4 K. In the following sections,$|\Delta S_{iso}|_{max}$ will represent the maximum isothermal entropy change when the maximum applied field is 1.5 T, without special description.

The specific heat at zero magnetic field as a function of temperature is defined as:

$$c_{H,0T}(T_s) = c_{H,max}\frac{\gamma^2}{(T_s - T_{Curie})^2 + \gamma^2} + c_{H,base} \tag{3.5}$$

where $c_{H,max}$ and $c_{H,base}$ are the maximum and background value of the specific heat at zero magnetic field.

Combining Eqns. 3.3 - 3.5 gives the entropy data as a function of the internal magnetic field and temperature. The adiabatic temperature change ΔT_{ad} can be further calculated by Eqn. 3.2. For a combination of ΔS_{iso} and ΔT_{ad},$|\Delta S_{iso}|_{max}$ is given and the desired ΔT_{ad} is obtained by iteration with adjusted $c_{H,max}$. Note that the temperature dependent curve of ΔT_{ad} also presents a sharp peak around the preset Curie temperature for a small γ as shown in Figure 3.3 (b), which is close to the actual situation. By using this method, the magnetocaloric properties with different combinations of ΔS_{iso}, ΔT_{ad}, γ and T_{Curie} are obtained, which cover most of FOPT and SOPT materials applied in room temperature MCRs.

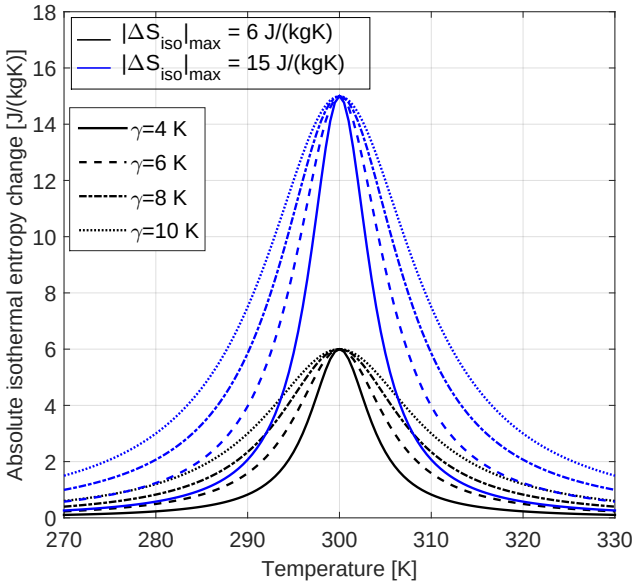

Fig. 3.2: Absolute isothermal entropy change $|\Delta S_{iso}|$ based on 3.3 as a function of temperature T for different shape factors γ upon a field change of 1.5 T, when the maximum absolute isothermal entropy change $|\Delta S_{iso}|_{max}$ is 6 and 15 J/(kg·K), respectively.

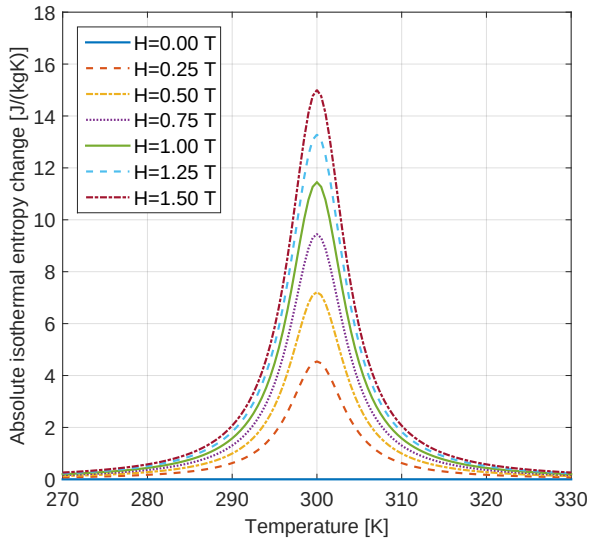

(a) Absolute isothermal entropy change

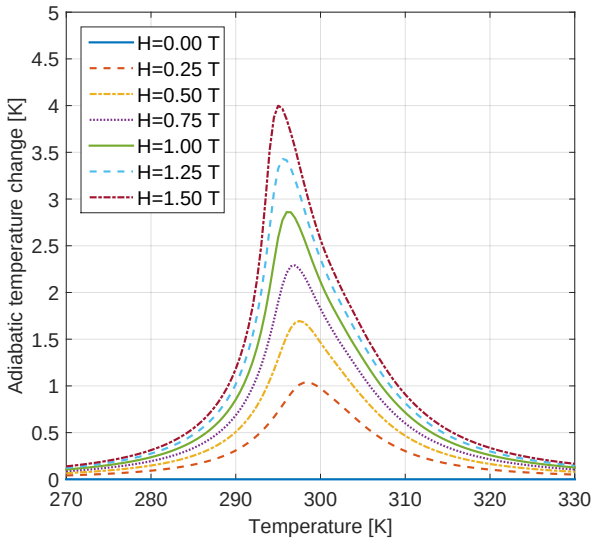

(b) Adiabatic temperature change

Fig. 3.3: Absolute isothermal entropy change $|\Delta S_{iso}|$ and adiabatic temperature change ΔT_{ad} ad as functions of temperature T and internal magnetic field H based on Eqns. 3.2 - 3.5. $|\Delta S_{iso}|_{max}$, ΔT_{ad}, and γ is 15 J/(kg·K), 4 K and 4 K respectively.

3.1.2 Modeling parameters

In the simulations, each regenerator has a length of 50 mm and a cross section of 625 mm^2. Packed spherical particle beds are used and the particle diameter is 0.3 mm. The maximum applied magnetic field is 1.4 T. The other operating and geometry parameters are listed in Table 3.1. For multi-layer AMRs, the thickness of each layer is assumed the same and the Curie temperature of the material in each layer follows:

$$T_{Curie,n} = T_h - (T_h - T_c)\frac{2n-1}{2n} \tag{3.6}$$

where n denotes the sequence number of each layer. Figure 3.4 shows an even Curie temperature distribution based on Eqn. 3.6.

Table 3.1: Parameters for modeling AMRs using magnetocaloric materials with different ΔS_{iso}, ΔT_{ad} and γ.

Parameter	Value
Maximum applied magnetic field	1.4 T
Heat transfer fluid	Aqueous solution with 20 % v/v ethylene glycol
Cross sectional area of regenerator bed	625 mm^2
Number of regenerator beds	12
Length of regenerator bed	50 mm
Sphere diameter	0.3 mm
Geometry of regenerator bed	Packed sphere bed
Porosity of regenerator bed	0.36
Frequency	2 Hz
Number of layers	1-40
Temperature span	1-30 K
Thermal conductivity of MCM	9.5 W/(m·K)
Density of MCM	7400 kg/m^3

Based on the observation that the materials from the same family behave quite similarly under the magnetization process and the peaks of both ΔS_{iso} and specific heat c_H are similar in magnitude and shape for a range of T_{Curie} [71], it is assumed that the material in each layer has the same $|\Delta S_{iso}|_{max}$ and $\Delta T_{ad,max}$ in this section. An example of the applied magnetic field and the mass flow rate is shown in Figure 3.5, where the positive nominal mass flow rate means the hot-to-cold blow and vice versa.

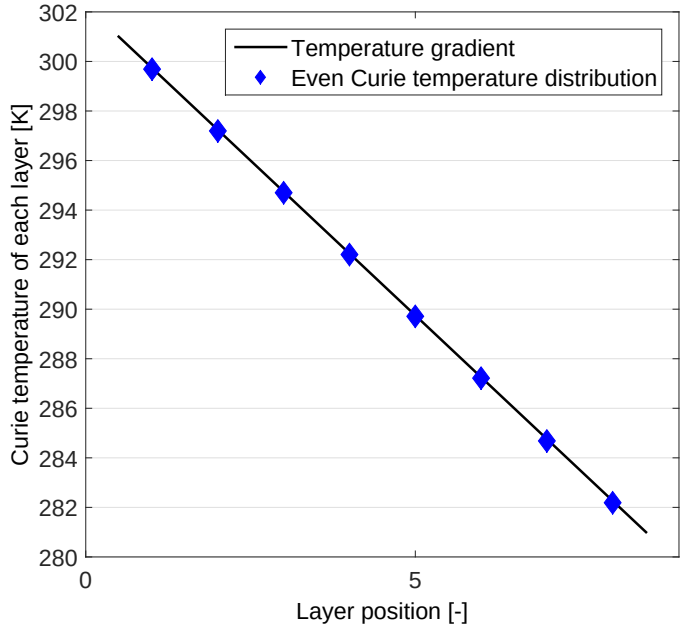

Fig. 3.4: Even Curie temperature distribution of an 8-layer AMR based on Eqn. 3.6. The hot and cold end temperatures are 301 K and 281 K, respectively.

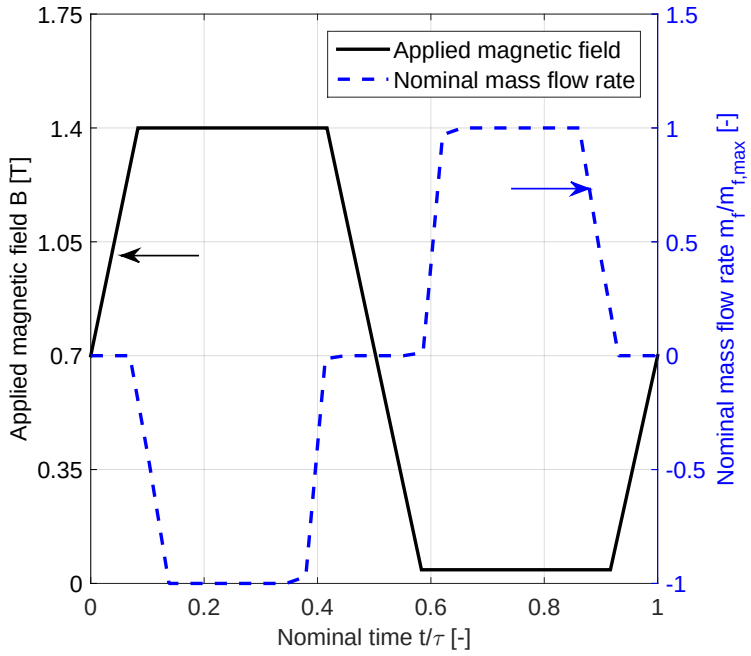

Fig. 3.5: Applied magnetic field and nominal mass flow rate as functions of nominal time.

3.1.3 Impact of isothermal entropy change, adiabatic temperature change and shape factor

Figure 3.6 presents a typical performance curve of the multi-layer regenerator, showing the specific cooling power, which is the cooling power generated with 1 kg MCM, and COP of a 40-layer regenerator for different mass flow rates.$|\Delta S_{iso}|_{max}$, $\Delta T_{ad,max}$ and γ of the simulated materials are 15 J/(kg·K), 5 K and 4 K, respectively. The temperature span is fixed at 20 K and the frequency is held constant at 2 Hz. Here the density and the thermal conductivity of these materials are assumed to be 7400 kg/m^3 and 9.5 W/(m·K) as shown in Table 3.1, which are averaged based on those of La(Fe,Mn,Si)$_{13}$H$_y$ and Gd [11, 25, 65].

Figure 3.7 shows the impact of ΔS_{iso} and ΔT_{ad} on the specific cooling power $\dot{q}_c$ of AMRs using materials with different shape factors, when the COP is 5. The mass flow rate is always optimized to reach the targeted COP. The number of layers N_L is 40, which indicates that the overall magnetocaloric effect varies along the regenerator quasi continuously and ideally. Since further increasing N_L does not significantly improve the AMR performance, N_L of 40 is chosen, with a compromised consideration of the computation time.

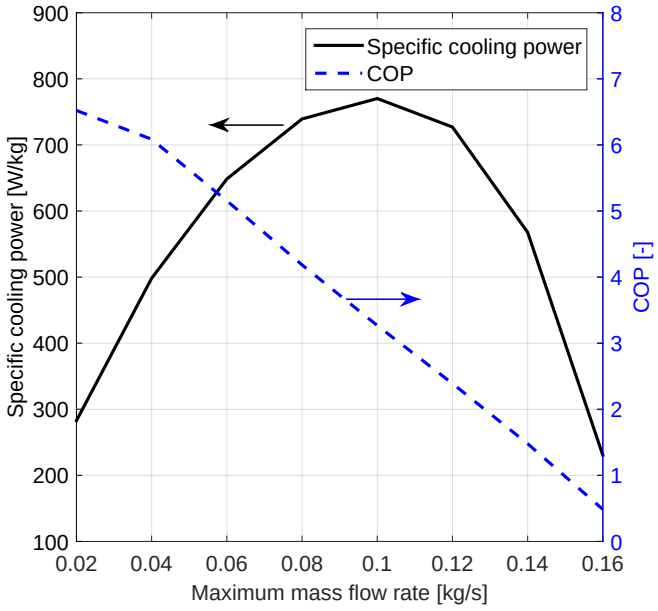

Fig. 3.6: Typical performance curve of specific cooling power $\dot{q}_c$ and COP of a 40-layer regenerator as a function of the maximum mass flow rate.

The results presented in Figure 3.7 (a) to (d) show that both ΔS_{iso} and ΔT_{ad} exert significant impact on the specific cooling power $\dot{q}_c$, which increases with ΔS_{iso} and ΔT_{ad} in general. Note that when one of the two parameters is relatively small (left and bottom in the figures), increasing the other one does not improve the performance much, which implies that influences brought by ΔS_{iso} and ΔT_{ad} should be equally emphasized.

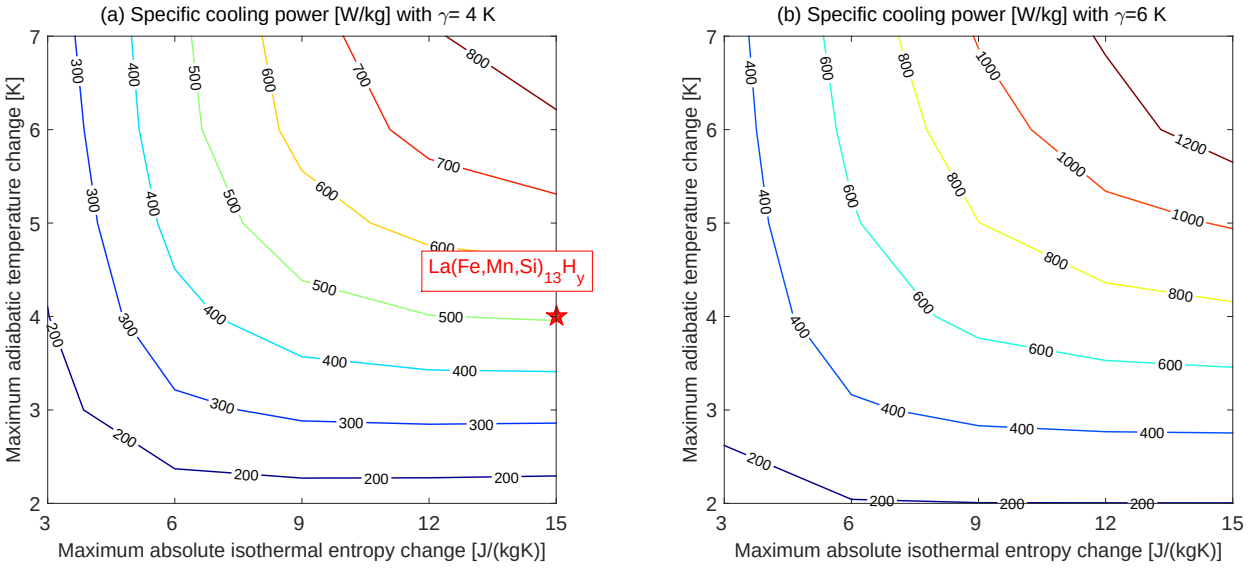

(a) γ=4 K

(b) γ=6 K

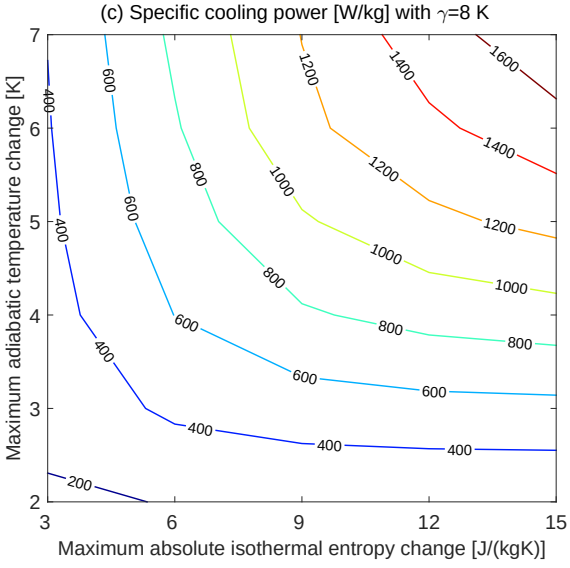

(c) γ=8 K

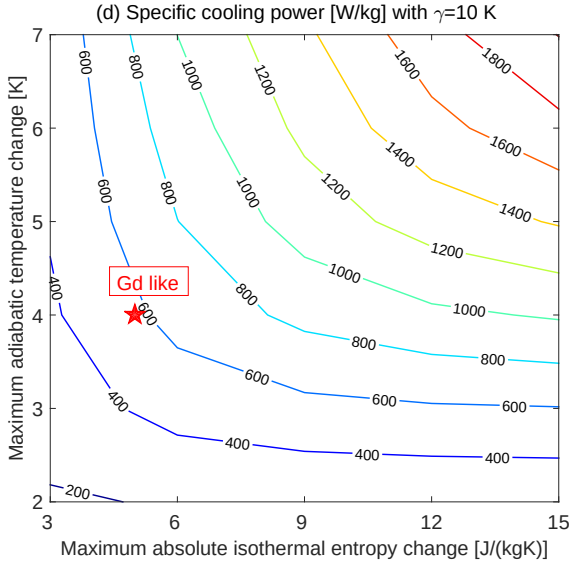

(d) γ=10 K

Fig. 3.7: Impact of maximum absolute isothermal entropy change $|\Delta S_{iso}|_{max}$ and maximum adiabatic temperature change $\Delta T_{ad,max}$ on specific cooling power $\dot{q}_c$ (contour lines) of AMRs using materials with different shape factors: (a) γ=4 K; (b) γ=6 K; (c) γ=8 K; (d) γ=10 K, when the COP is fixed at 5.

An interesting trend with different shape factors γ is observed. A smaller shape factor, which means sharper MCE curve and narrower working temperature region, will lead to a decrease in $\dot{q}_c$ even with the same$|\Delta S_{iso}|_{max}$ and $\Delta T_{ad,max}$. The maximum $\dot{q}_c$ of Figure 3.7 (d) is about 1900 W/kg, which is about twice of that in the case of Figure 3.7 (a), showing the significant impact brought by variation in γ.

The position representing materials similar to La(Fe,Mn,Si)$_{13}$H$_y$ or Gd are marked in Figure 3.7 (a) and (d), respectively. Here approximate values of ΔS_{iso}, ΔT_{ad} and γ for both materials are used for a theoretical prediction. AMR using La(Fe,Mn,Si)$_{13}$H$_y$-like materials gives a theoretical specific cooling power around 510 W/kg, which is close to the value of 580 W/kg for Gd-like materials, although the former presents much larger peak value in ΔS_{iso}. This may be attributed to the similar ΔT_{ad} for both materials and the difference in the shape factors. Compared to the results from Reference [14], the influence of ΔT_{ad} is further emphasized due to the introduction of the shape factor γ, which is closer to the real situation. The results show that not only the peak value of ΔS_{iso}, but also ΔT_{ad} and γ, which did not attract enough attentions in the previous literature, are also important for improving the AMR performance.

3.1.4 Impact of temperature span and number of layers

The continuously layered AMR is difficult to construct due to limits of fabricating the materials and tuning the Curie temperature. Besides investigating the theoretical maximum cooling performance, it is also interesting to explore how to layer the regenerators and how many layers are needed in a real AMR. Figure 3.8 presents a study on the impacts of number of layers for AMRs operating under different temperature spans. In the following studies, the mass flow is optimized for obtaining the highest specific cooling power. The Curie temperature of each layer is distributed evenly according to Eqn. 3.6. The maximum $|\Delta S_{iso}|$ and ΔT_{ad} are 15 J/(kg·K) and 4 K, respectively, upon a field change of 1.5 T. Four shape factors, from 3 to 9 K, are used.

The results in Figure 3.8 show that the specific cooling power decreases quickly with an increase in the temperature span and $\dot{q}_c$ increases with the increasing number of layers for all cases. However, for the materials with a larger shape factor of 9 K, the maximum specific cooling power (when N_L=40) is much larger. This may be attributed to the widely distributed magnetocaloric properties. The subplots at the bottom of Figure 3.8 (a) -(d) directly show the influence of the number of layers on the nominal cooling power $\dot{q}_c/\dot{q}_{c,N_L=40}$, which is the ratio of the specific cooling power to the maximum value when N_L is 40. Comparison shows that a smaller shape factor requires more layers to get close to the theoretical maximum performance, increasing the difficulties of constructing the multi-layer AMRs using the materials with small γ.

Based on the method presented in Reference [65], Figure 3.9 summarizes the value of 90% of the theoretical maximum specific cooling power and the corresponding number of layers needed to achieve that performance. It is aimed at proposing a reasonable number of layers without losing too much theoretical cooling capacity. The corresponding number of layers is obtained by interpolating the performance curve as a function of N_L, which could be a non-

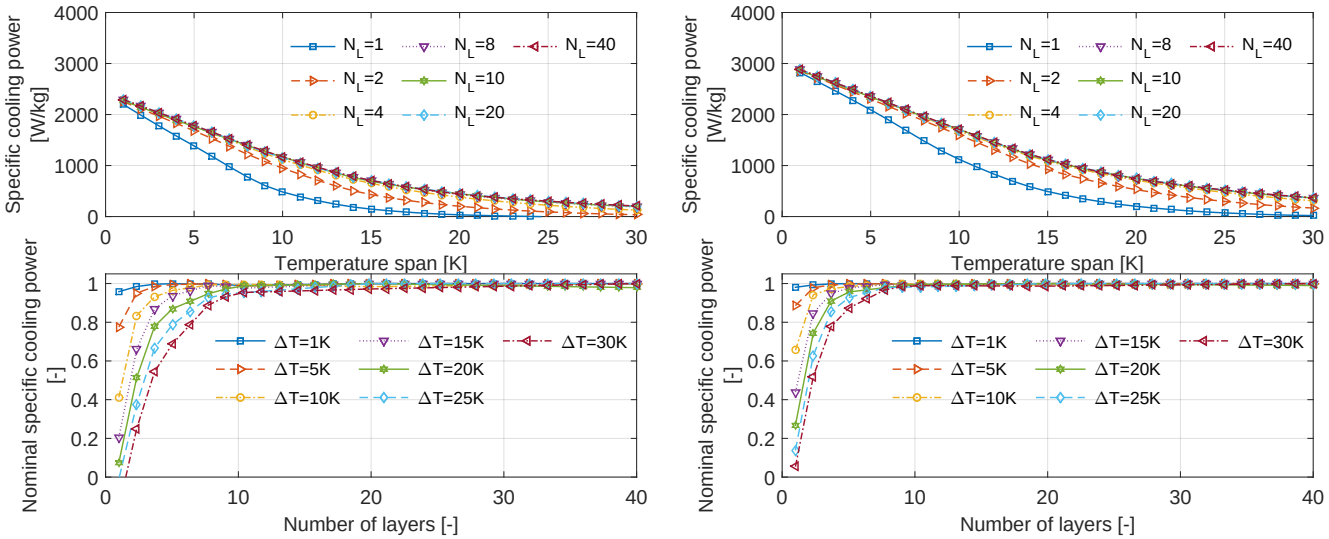

(a) γ=3 K

(b) γ=5 K

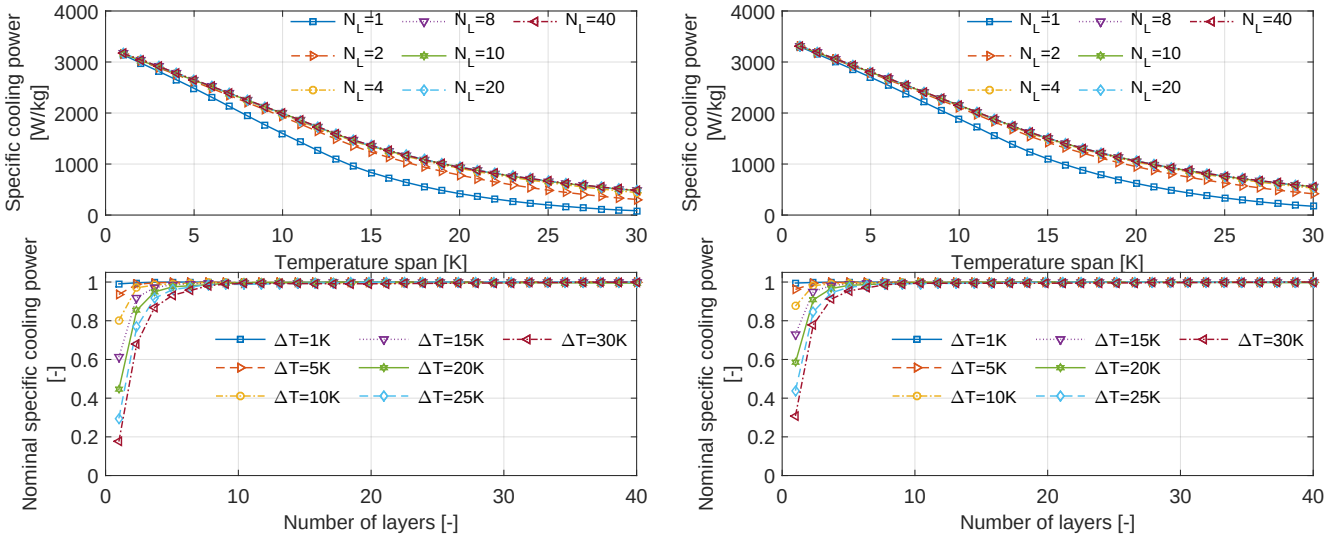

(c) γ=7 K

(d) γ=9 K

Fig. 3.8: Impacts of temperature span ΔT and number of layers N_L for multi-layer AMRs using materials with different shape factors: (a) γ=3 K; (b) γ=5 K; (c) γ=7 K; (d) γ=9 K, where $|\Delta S_{iso}|_{max}$ and $\Delta T_{ad,max}$ are 15 J/(kg·K) and 4 K, respectively.

integer in Figure 3.9, and the minimum N_L is 1. With increasing temperature span, the needed N_L becomes larger with a significant decrease in the specific cooling power in all cases. At the same time, smaller shape factors present lower cooling performance and larger number of necessary layers. For a temperature span of 30 K, about 7.6, 5.2, 4.0, 3.2 layers are needed to achieve the theoretical performance for γ =3, 5, 7 and 9 K, respectively. It shows the strong influence of γ on the system performance even with the same values of ΔS_{iso} and ΔT_{ad}.

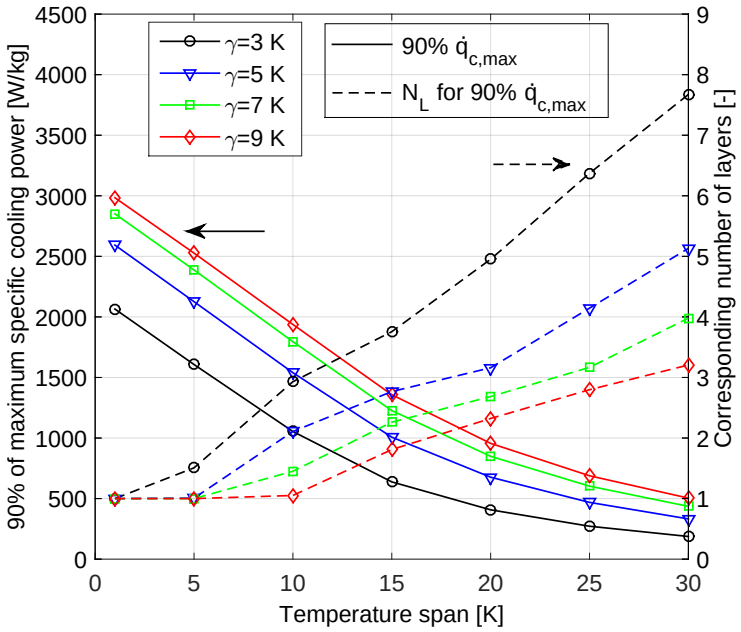

Fig. 3.9: 90% of the maximum specific cooling power $\dot{q}_{c,max}$ and corresponding number of layers N_L as functions of temperature span ΔT for multi-layer AMRs using materials with different shape factors γ. $|\Delta S_{iso}|_{max}$ and $\Delta T_{ad,max}$ are 15 J/(kg·K) and 4 K, respectively.

3.2 Multi-layer AMRs using La(Fe,Mn,Si)$_{13}$H$_y$ or Gd-like materials

Comparing AMRs using typical FOPT and SOPT materials are of significant importance for choosing proper materials in future MCRs. In this section, the measured magnetocaloric properties of two typical FOPT and SOPT materials, La(Fe,Mn,Si)$_{13}$H$_y$ and Gd, are applied, instead of the artificially built magnetocaloric properties presented in Section 3.1. The influences of the number of layers, temperature span and working temperature on the refrigeration performance are discussed, regarding two different groups of AMRs. In addition, a sensitivity study of variation in the Curie temperature distribution is presented. The concept of mixing FOPT and SOPT materials is also investigated, for improving the system stability.

3.2.1 Magnetocaloric properties of $La(Fe,Mn,Si)_{13}H_y$ and Gd

Although T_{Curie} of $La(Fe,Mn,Si)_{13}H_y$ is tunable and more than five materials with T_{Curie} around the room temperature have been characterized at DTU, existing measurements are still not enough for modeling multi-layer AMRs. Based on the observation that $La(Fe,Mn,Si)_{13}H_y$ materials behave quite similarly under the magnetization process and the peaks of both ΔS_{iso} and specific heat c_H are similar in magnitude and shape for a range of T_{Curie} [11, 71], it is assumed that the properties of the materials with different T_{Curie}, other than the characterized material, can be approximated by shifting one group of experimental data according to T_{Curie}. The base material has a T_{Curie} of 305.0 K, which is provided by Vacuumschmelze GmbH, Germany. The measured data of the specific heat at zero field and the absolute value of ΔS_{iso} presented in Figure 3.10 are obtained from the Lake Shore 7407 Vibrating Sample Magnetometer and a Differential Scanning Calorimeter at DTU [10]. The density of $La(Fe,Mn,Si)_{13}H_y$ is measured to be about 6900 kg/m^3. The properties of $La(Fe,Mn,Si)_{13}H_y$ are measured by a collaborated Ph.D. student Henrique Neves Bez from DTU Energy, whose work is appreciated. The thermal conductivity of $La(Fe,Mn,Si)_{13}H_y$ is assumed as 8 W/(m·K), which is close to the measured data of LaFeSi and LaFeSiH at the ambient temperature [72]. The properties of Gd can be reviewed in References [25]. The thermal conductivity and the density of Gd are estimated to be 11 W/(m·K) and 7900 kg/m^3. Although Gd has a fixed Curie temperature, its magnetocaloric properties are used to simulate similar materials with tunable T_{Curie}, e.g. Gd-Y alloys. The magnetic hysteresis of $La(Fe,Mn,Si)_{13}H_y$ is relatively small [11], so this effect is not taken into account here.

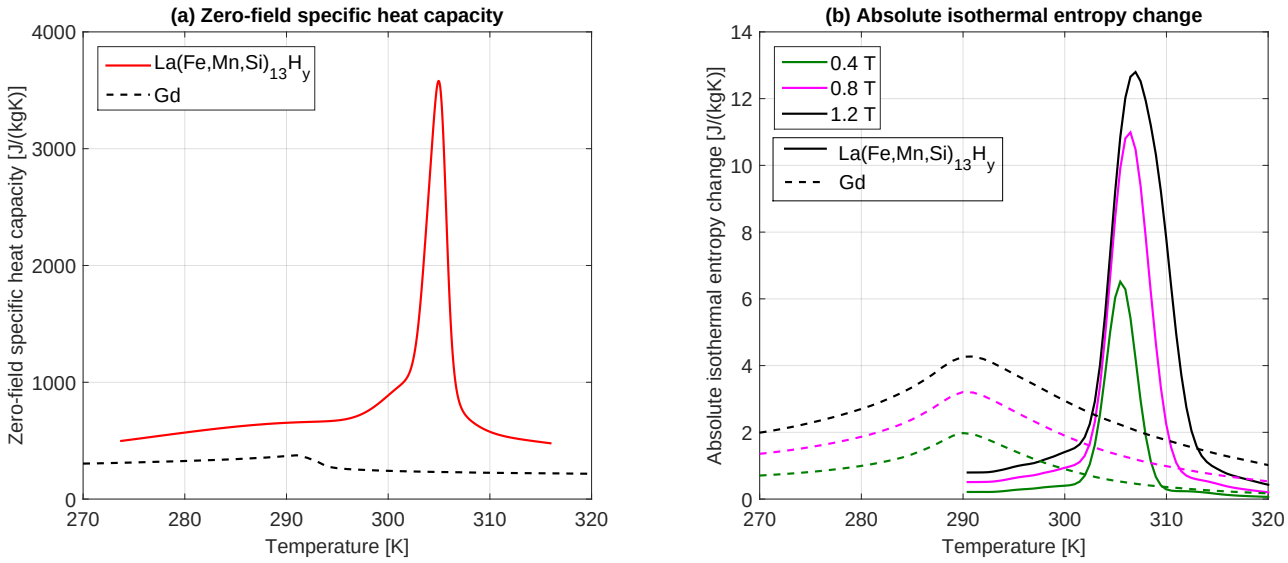

(a) Zero-field specific heat capacity

(b) Absolute isothermal entropy change

Fig. 3.10: Zero-field specific heat capacity (a) and absolute isothermal entropy change (b) of $La(Fe,Mn,Si)_{13}H_y$ with T_{Curie}=305 K and Gd with T_{Curie}=292 K.

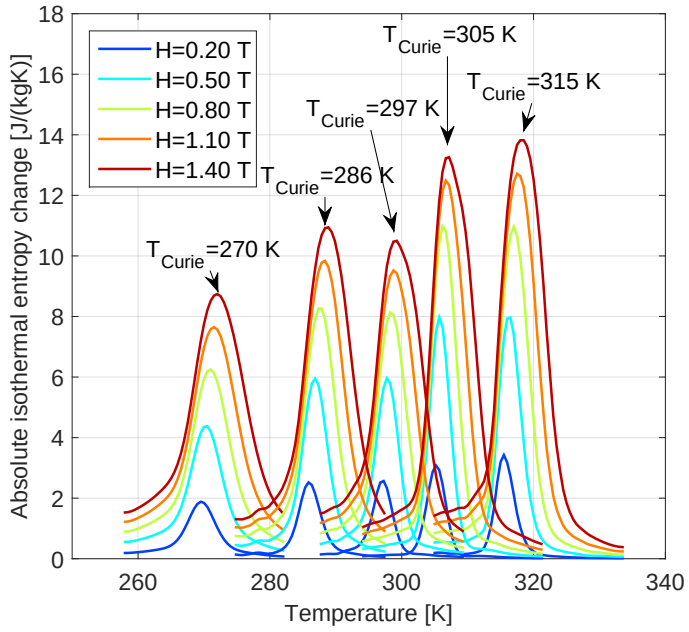

Fig. 3.11: Absolute isothermal entropy change of five $La(Fe,Mn,Si)_{13}H_y$ with different Curie temperatures.

3.2.2 Modeling parameters

Except for the material properties, the other modeling parameters are the same as those used in Section 3.1 and listed in Table 3.1.

3.2.3 Impact of number of layers and temperature span

The impact of the number of layers and the temperature span for multi-layer AMRs using La(Fe,Mn,Si)$_{13}$H$_y$ or Gd-like materials is presented in Figure 3.12. Increasing the number of layers or decreasing the temperature span leads to a higher specific cooling power for both cases generally. Although the maximum cooling power of AMRs using FOPT materials like La(Fe,Mn,Si)$_{13}$H$_y$ is larger than that with Gd-like materials, more layers are needed to approach the theoretical performance. It is preferable to use FOPT materials for obtaining a higher specific cooling power when the temperature span is less than 30 K, while the benefits become smaller when ΔT >30 K.

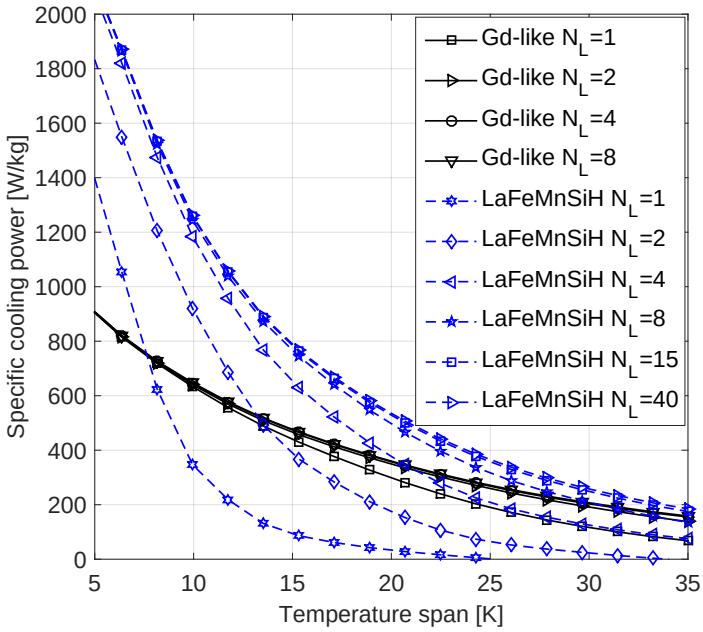

Fig. 3.12: Impacts of temperature span ΔT and number of layers N_L on maximum specific cooling power $\dot{q}_{c,max}$ of multi-layer AMRs using La(Fe,Mn,Si)$_{13}$H$_y$ or Gd-like materials, where LaFeMnSiH denotes La(Fe,Mn,Si)$_{13}$H$_y$.

As illustrated in Figure 3.13, the nominal specific cooling powers of AMR using La(Fe,Mn,Si)$_{13}$H$_y$ or Gd-like materials are presented, reflecting the direct influence of the number of layers. As predicted in Section 3.1, Gd-like materials, which have a widely distributed ΔS_{iso}, need much fewer layers, compared with the other group. The impact of number of layers on the COP

data is depicted in Figure 3.14, corresponding to the specific cooling power shown in Figures 3.12 and 3.13. It shows that Gd-like materials could realize a higher efficiency, although the maximum specific cooling power is lower. Note that Gd has superior magnetocaloric properties compared with most other SOPT materials with tunable Curie temperatures. Therefore the actual performance of AMRs using Gd-like materials will be somewhat lower than the theoretical prediction here.

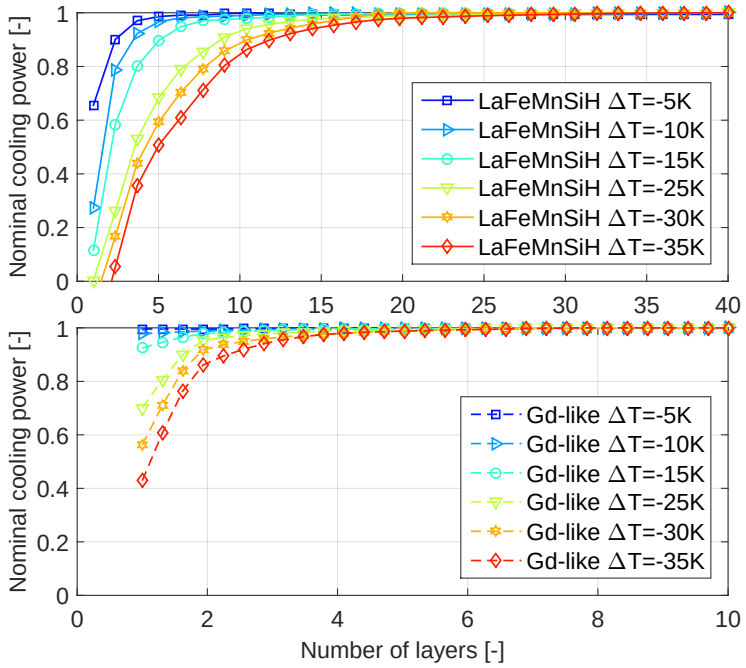

Fig. 3.13: Impacts of temperature span ΔT and number of layers N_L on nominal cooling power of multi-layer AMRs using La(Fe,Mn,Si)$_{13}$H$_y$ and Gd-like materials.

As shown in Figure 3.15, 90% of the theoretical maximum specific cooling power and corresponding number of layers for AMRs using La(Fe,Mn,Si)$_{13}$H$_y$ or Gd-like materials are presented. Higher cooling performance is observed in AMRs using La(Fe,Mn,Si)$_{13}$H$_y$. However, only 2-3 layers are needed for Gd-like materials to get close to the maximum performance when the temperature span is 30 K, while about 12 layers are required for La(Fe,Mn,Si)$_{13}$H$_y$. A concept of mixing FOPT and SOPT materials is proposed and further investigated here. La(Fe,Mn,Si)$_{13}$H$_y$ and Gd-like materials are mixed by volume fraction in each layer and their Curie temperatures are assumed the same. The results show that the number of layers could be reduced by sacrificing specific cooling power with the method of mixing more Gd-like materials. Although lower cooling performance is obtained, this concept could still bring certain benefits to the system including reducing the number of layers, which will be discussed in the following sections.

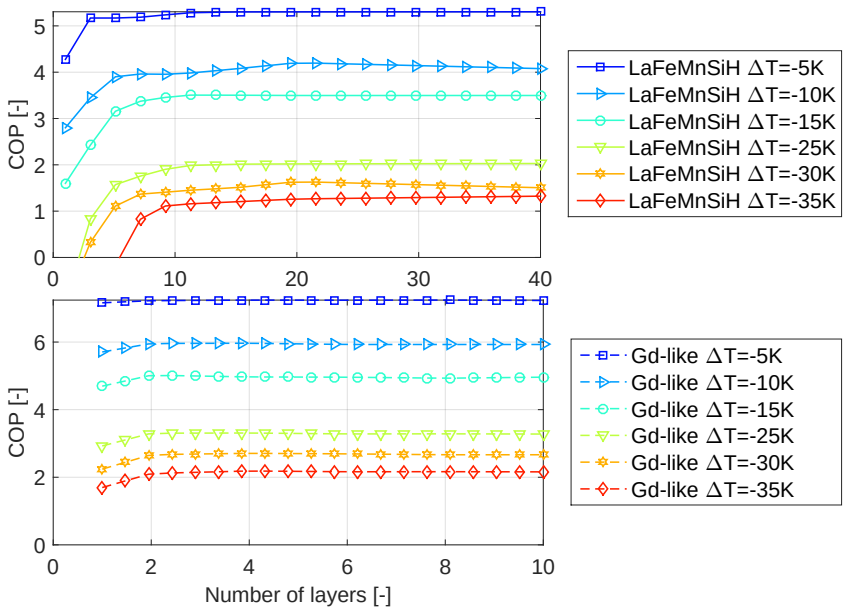

Fig. 3.14: COP of AMRs using La(Fe,Mn,Si)$_{13}$H$_y$ and Gd-like materials corresponding to Figures 3.12 and 3.13.

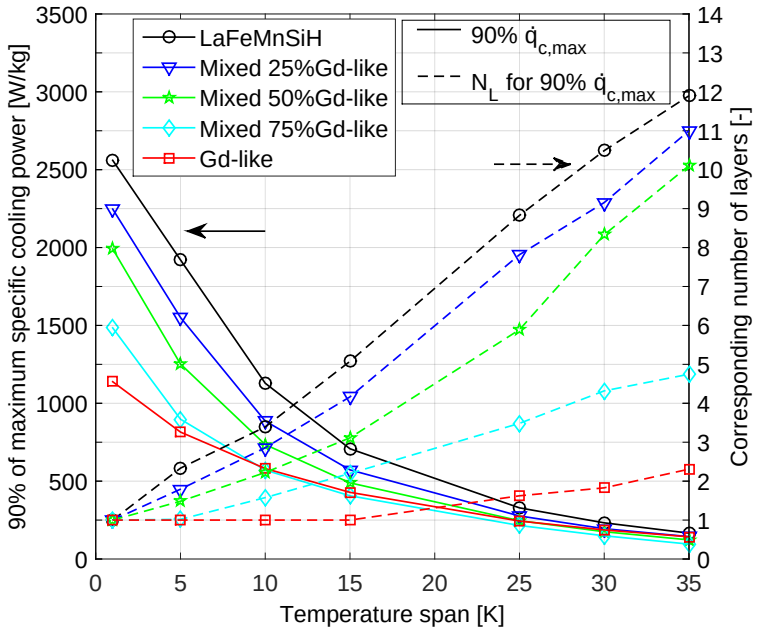

Fig. 3.15: 90% of the maximum specific cooling power $\dot{q}_{c,max}$ and corresponding number of layers N_L as functions of temperature span ΔT for multi-layer AMR using La(Fe,Mn,Si)$_{13}$H$_y$, Gd-like or mixed materials.

3.2.4 Sensitivity to working temperature

For most refrigeration devices, the system stability under fluctuating ambient temperatures is quite important, which depends on the climate and region. These varying operating conditions can cause performance issues for AMRs using FOPT materials, due to their relatively narrow MCE curve.

To investigate this effect, we simulate AMRs using FOPT, SOPT or mixed materials and the results are presented in Figure 3.16. The number of layers is fixed at 4, and the Curie temperature distribution is calculated based on Eqn. 3.6. The working temperature region is changed by shifting both cold and hot end temperatures, while the temperature span is kept constant at 15 K. In this way, the performance of AMRs using La(Fe,Mn,Si)$_{13}$H$_y$ degrades fast when the working temperature deviates from the designed region. Even a change of $\tilde{2}$-3 K will result in a significant decrease in performance. With an increasing volume fraction of Gd, the sensitivity of AMRs to the working temperature becomes smaller, although the peak performance decreases. Therefore, mixing FOPT and SOPT materials may be beneficial for resisting the variation in the ambient temperature and obtaining better performance than using only the SOPT materials. It can also be observed that the optimum working temperature regions are slightly different from that of the AMRs using different materials.

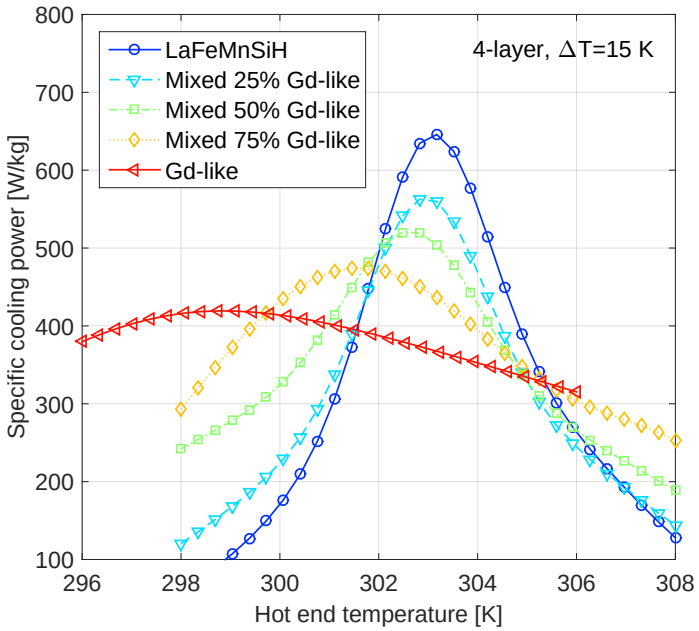

Fig. 3.16: Impact of working temperature (represented only by the hot end temperature T_h due to a fixed ΔT) on specific cooling power $\dot{q}_c$ of multi-layer AMRs using La(Fe,Mn,Si)$_{13}$H$_y$, Gd-like or mixed materials.

3.2.5 Impact of Curie temperature distribution

It is known that accurately tuning the Curie temperature during the manufacture of MCMs is difficult, and the impact of the Curie temperature variation is of interest for designing multi-layer AMRs. The section starts from studying the variation of T_{Curie} in a single layer, that is, the Curie temperature of a single layer will be shifted by a certain value and the Curie temperature is not evenly distributed anymore. The definition is illustrated in Figure 3.17.

The variation $\Delta T_{Curie,n}$ ranges from -2 to 2 K with an interval of 0.5 K, and a positive value means shifting to a higher temperature and vice versa. The number of layers is 8 and the temperature span is 15 K. Comparison between Figure 3.18 (a) and (b) shows that Gd-like materials can resist variations in the Curie temperature much better than FOPT materials like La(Fe,Mn,Si)$_{13}$H$_y$, and the performance change is less than 8 %. For the AMRs using La(Fe,Mn,Si)$_{13}$H$_y$, both positive and negative variation will result in lower cooling performance. And this influence becomes more sensitive when shifting the layers close to either end of the AMR, which should be more carefully handled than the layers in the middle. In both cases, the maximum cooling powers can be obtained with an approximately even Curie temperature distribution, which are around 790 W/kg and 470 W/kg for each group.

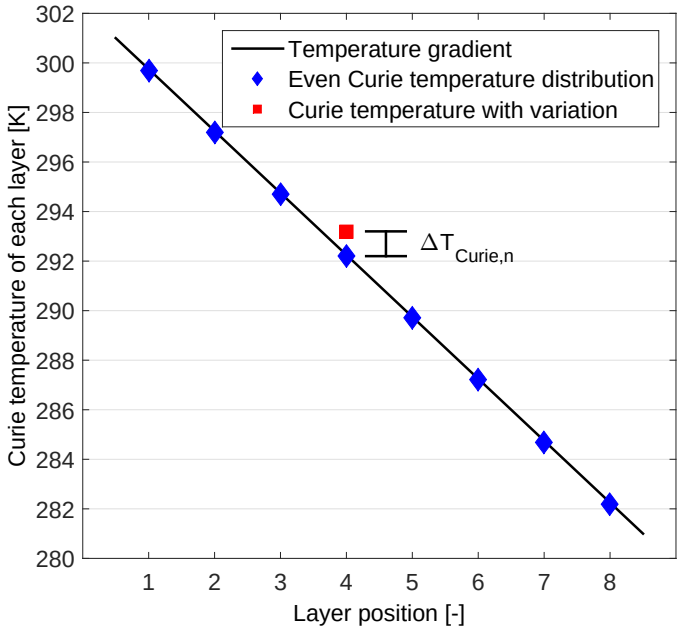

Fig. 3.17: Definition of Curie temperature variation $\Delta T_{Curie,n}$ in a multi-layer regenerator.

A further study is carried out based on the assumption that the Curie temperature variation $\Delta T_{Curie,n}$ follows a normal distribution. In this way, the standard deviation of $\Delta T_{Curie,n}$ could be utilized to describe how much $T_{Curie,n}$ deviates from the designed value and also the overall degree of deviating from an even distribution. The median of the normal distribution is 0

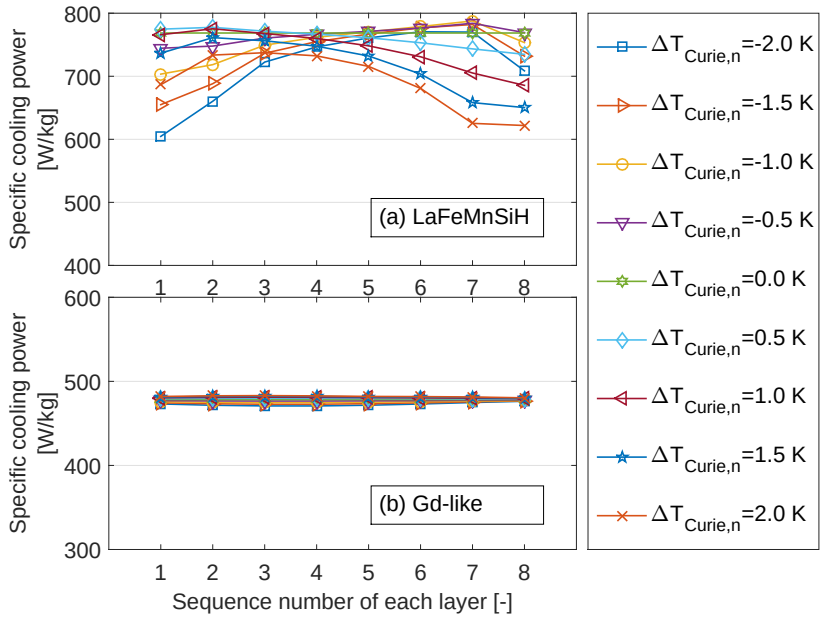

Fig. 3.18: Impact of Curie temperature variation $\Delta T_{Curie,n}$ of each layer on specific cooling power $\dot{q}_c$ of multi-layer AMRs using La(Fe,Mn,Si)$_{13}$H$_y$ or Gd-like materials.

K. This treatment allows a small random deviation in each layer, and makes the simulation more representative for real conditions in a commercial AMR. For each standard deviation, we randomly build 500 AMRs with different Curie temperature distributions and the results are presented in Figure 3.19. A box plot is implemented to show the probability of generated specific cooling powers. The concept of mixing materials is also studied. In Figure 3.19, the central mark of the box plot is the median value of a group of specific cooling powers for each standard deviation, and the box edges are the 25^{th} and 75^{th} percentiles. The whiskers show the most extreme data points without outliers and the crosses show the outliers. It can be seen that increasing the standard deviation reduces the median value of the specific cooling power significantly and also increases the risk of performance fluctuations for AMRs using La(Fe,Mn,Si)$_{13}$H$_y$. As the volume faction of Gd increases, the median value of $\dot{q}_c$ decreases, while the fluctuation in $\dot{q}_c$ becomes smaller. The results show that mixing FOPT and SOPT materials helps to improve the system stability regarding variations in the Curie temperature.

Figure 3.20 illustrates the combined impact of number of layers and the standard deviation. Both FOPT and SOPT materials are simulated for 4 and 8 layers. As the number of layers increases, the performance fluctuation decreases and the median value increases significantly for AMRs using La(Fe,Mn,Si)$_{13}$H$_y$. Therefore it is suggested to increase the number of layers as much as possible for improving the system stability. For Gd-like materials, the performance fluctuation is much smaller for both N_L=4 and 8, but the cooling capacity does not improve much.

The results from the maximum applied field of 1.2 T and 1.4 T are compared in Figure 3.21.

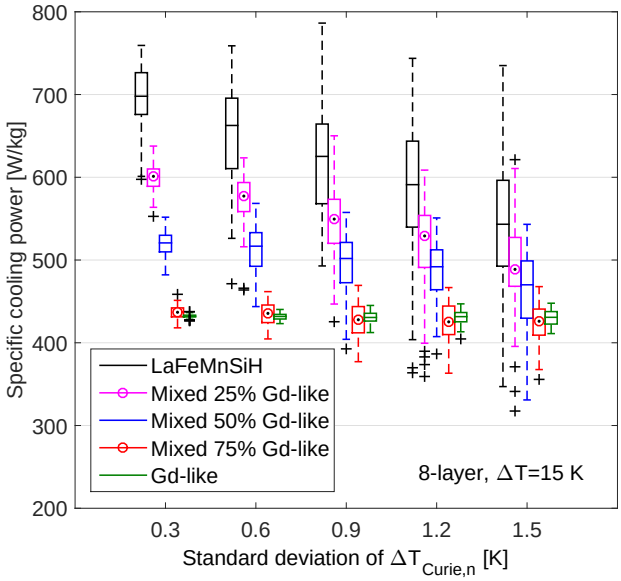

Fig. 3.19: Impact of standard deviation of $\Delta T_{Curie,n}$ on specific cooling power $\dot{q}_c$ of multi-layer AMRs using La(Fe,Mn,Si)$_{13}$H$_y$, Gd-like or mixed materials when $\Delta T_{Curie,n}$ follows a normal distribution. The central mark of the box plot is the median value of a group of $\dot{q}_c$ for each standard deviation, and the box edges are the 25^{th} and 75^{th} percentiles. The whiskers show the most extreme data points without outliers and the crosses show the outliers.

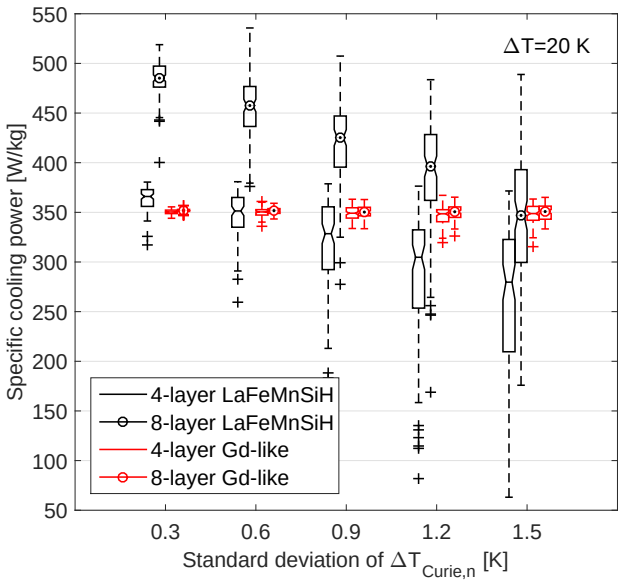

Fig. 3.20: Impact of number of layers N_L and standard deviation of $\Delta T_{Curie,n}$ on specific cooling power $\dot{q}_c$ of multi-layer AMRs using La(Fe,Mn,Si)$_{13}$H$_y$ or Gd-like materials.

The median cooling power increases at larger applied field for both groups of AMRs. But the performance increment for La(Fe,Mn,Si)$_{13}$H$_y$ is larger than Gd-like materials, indicating that a high flied is necessary for maintain the cooling capacity using the FOPT materials.

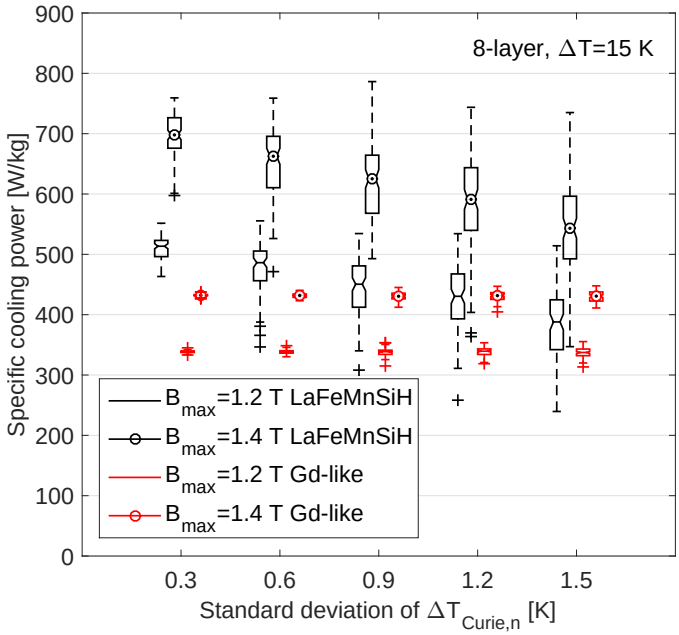

Fig. 3.21: Impact of maximum applied magnetic field and standard deviation of $\Delta T_{Curie,n}$ on specific cooling power $\dot{q}_c$ of multi-layer AMRs using La(Fe,Mn,Si)$_{13}$H$_y$ or Gd-like materials.

3.3 Comparison of experiment and simulation

Several regenerators using La(Fe,Mn,Si)$_{13}$H$_y$ have been tested in a small reciprocating magnetic refrigerator at DTU [44]. In this section, simulation results are compared to experimental data obtained from this test machine, which also verifies the impact of the working temperature as shown in Figure 3.16. The small test machine [45] consists of six main components as shown in Figure 3.22. A Halbach cylinder permanent magnet, generating an average magnetic flux density around 1.03 T, is used. The inner diameter and length of the regenerator housing for holding the magnetocaloric materials are 3.2 cm and 4.0 cm, respectively. A heater and a hot heat exchanger are used to simulate the cooling power and to maintain the hot end temperature, respectively. With the stationary magnet during operation, the piston and housing are moved reciprocally in the vertical direction, providing a periodically changing magnetic field and oscillating flows. There is a phase difference between the piston and housing movements for achieving a four-step refrigeration cycle as presented in Figure 3.23.

Two regenerators using La(Fe,Mn,Si)$_{13}$H$_y$ provided by Vacuumschmelze GmbH & Co. KG are tested by the collaborated Ph.D. student Henrique Neves Bez at DTU [44]. For the first

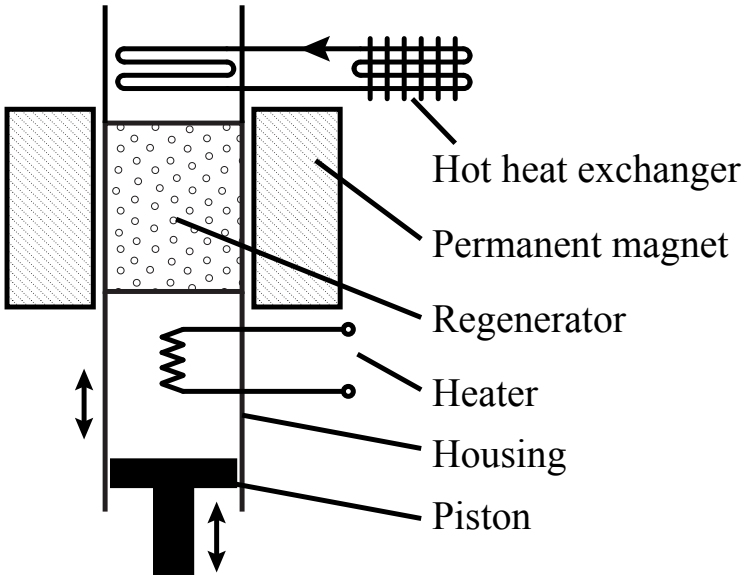

Fig. 3.22: Schematic diagram of a reciprocating one-bed test machine at DTU.

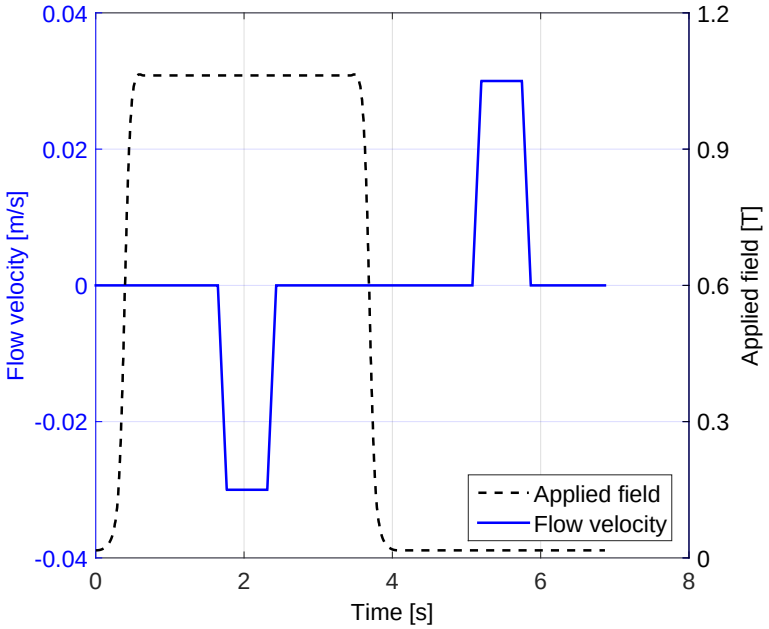

Fig. 3.23: Applied magnetic filed and fluid velocity as functions of time for the one-bed test machine.

one-layer regenerator, about 48 g materials with T_{Curie} =296.5 K is packed. The second one is loaded with two layers of materials, which have T_{Curie} =292.4 and 296.5 K, respectively. The mass of each layer is about 25 g. La(Fe,Mn,Si)$_{13}$H$_y$ are bonded with 3 wt. % epoxy and fixed into the housing. The heat transfer fluid is an aqueous solution with 20 v/v % ethylene glycol. The whole apparatus has been installed in a temperature controlled cabinet and the hot heat exchange is thermally contacted with the air in the cabinet. The hot end temperature is adjusted to control the working temperature. The cycle period is about 7 s and the temperature span is recorded by thermocouples with an estimated uncertainty $\pm$0.3 K. Figure 3.24 presents the no-load temperature span measured in the two regenerators. The 2-layer regenerator achieves larger temperature span than the 1-layer bed in general, and the maximum temperature spans for both regenerators are 11.1 and 8.2 K, respectively. As concluded in Section 3.2, both regenerators are very sensitive to the hot end temperature, i.e., the no-load temperature span decreases significantly when the working temperature is away from the materials' transition region. The simulation results are higher than the experimental measurement and it predicts the performance trend well. For the 2-layer regenerator, the peak in the simulation curve shifts to higher temperature region.

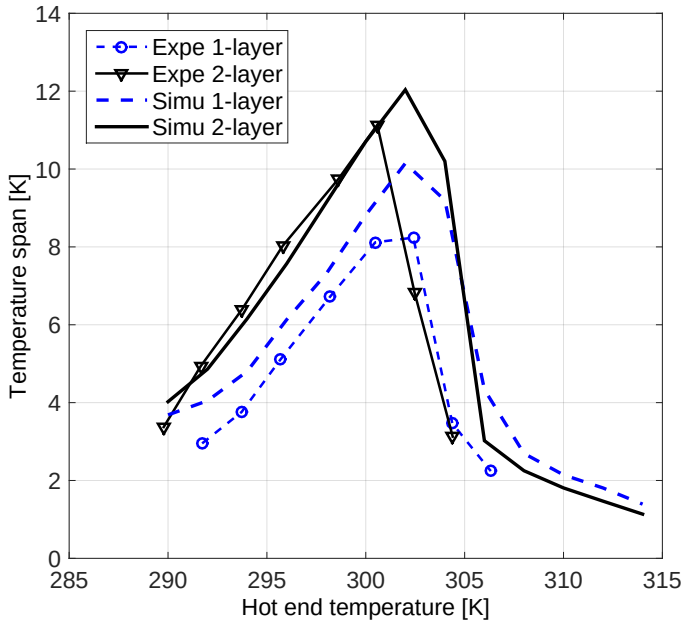

Fig. 3.24: Comparison of experiment and simulation results of zero-load temperature span for the one-bed test machine.

3.4 Predicted performance of ENOVHEAT heat pump

This project serves as a work package of the ENOVHEAT (Efficient Novel Magnetocaloric Heat Pumps) project. The final purpose is to design AMRs for a high-efficiency heat pump fulfilling the heating demand of a typical Danish house. This magnetic heat pump system is supposed to produce a practical performance with heating power $\dot{Q}_h$ of 2 kW and COP_{HP} of 5. The design and operation of both magnetic refrigerators and heat pumps are similar. The working temperature region is slightly different according to the ambient temperature. In addition, the load is applied at the cold end for a refrigerator, or at the hot end for a heat pump. Note that COP_{HP} is different from the COP of a refrigerator COP and it is defined as:

$$\mathrm{COP}_{HP} = \frac{\dot{Q}_h}{\dot{Q}_h - \dot{Q}_c} = \mathrm{COP} + 1 \tag{3.7}$$

As the ground heat source is integrated, a reasonable temperature span of 20 °C is considered. Based on the findings presented in 3.1 and 3.2, a general design of the magnetic heat pump is implemented and the typical performance is presented in Figure 3.25. In the design, 10-layer AMRs loaded with 2.8 kg $La(Fe,Mn,Si)_{13}H_y$ are used. It shows that at the optimal point, the ENOVHEAT pump could produce heating power of 2 KW over 20 °C and COP_{HP} above 5. Considering the trade-off between the heating power and COP_{HP}, the optimal operating frequency is about 2 Hz. The whole system is being in construction and it is expected to be tested in 2017.

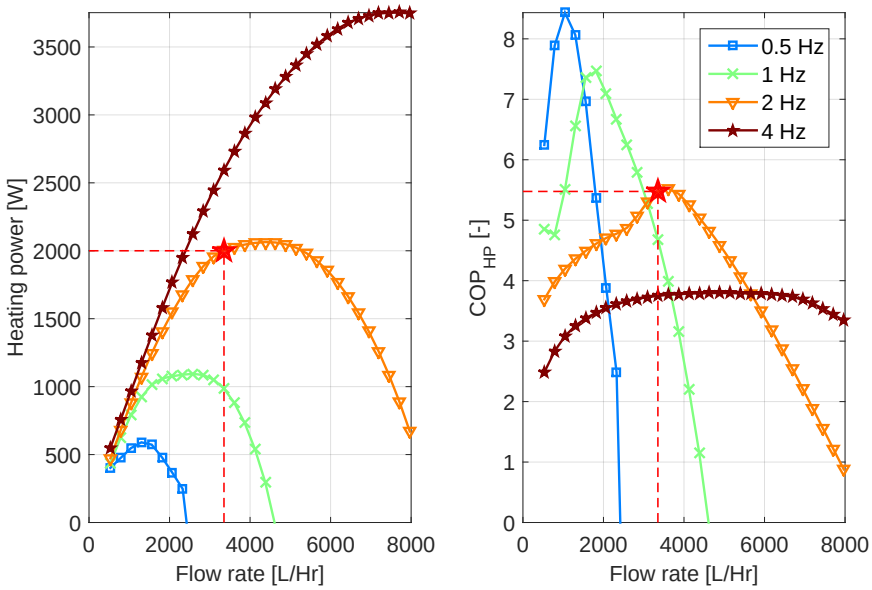

Fig. 3.25: Predicted performance of the ENOVHEAT heat pump.

3.5 Summary

In this section, AMRs using FOPT and SOPT materials are investigated based on a one dimensional numerical model. The results show that not only the isothermal entropy change ΔS_{iso}, but also the adiabatic temperature change ΔT_{ad} and the shape factor γ of MCE, have significant influence on the AMR performance. Although FOPT materials exhibit higher ΔS_{iso}, they sometimes could only produce equivalent performance compared to SOPT materials due to a similar or lower ΔT_{ad} and smaller shape factor γ. For materials with small γ, more layers are needed to achieve a high cooling power compared to those with larger γ.

The simulated results of multi-layer AMRs using typical La(Fe,Mn,Si)$_{13}$H$_y$ or Gd-like materials are presented and a concept of mixing FOPT and SOPT materials is investigated. Although La(Fe,Mn,Si)$_{13}$H$_y$ could realize higher specific cooling power than Gd-like materials, many more layers are needed to achieve the desired performance. From a practical point, around 10 to 12 layers may be suitable for a temperature span of 30 K with the FOPT material La(Fe,Mn,Si)$_{13}$H$_y$. At the same time, AMRs using typical FOPT materials are more sensitive to the working temperature and the Curie temperature variation. Even Curie temperature distribution is preferable in most cases. A standard deviation of 0.6 K could realize more than 15% reduction in the cooling performance. Mixing FOPT and SOPT could significantly reduce the required number of layers, show better resistance to fluctuating working temperatures, and be more robust to variations in the Curie temperature compared to FOPT materials, meanwhile realizing higher specific cooling power than SOPT materials.

Comparison of the simulation and experiment shows the model can predict the performance trends well. The results also verify the sensitivity of the AMR using FOPT materials to the working temperature. The predicted performance of a magnetic heat pump is presented, which could generate 2 kW heating power over a span of 20 °C with COP$_{HP}$ above 5.

CHAPTER 4

Loss analysis and geometry optimization of active magnetic regenerators

In the first section of this chapter, the influence of different loss mechanisms will be analyzed and quantified based on numerical modeling and entropy production minimization (EPM). In detail, a multi-variable optimization for maximizing COP is presented and the corresponding entropy production rates representing different loss mechanisms inside a typical AMR are compared in Section 4.1. In Section 4.2, the influence of the heat loss through the regenerator housing is analyzed, considering the heat transfer between the fluid and the wall, as well as that between the wall and the ambient. Section 4.3 addresses the impact of dead volume, which is represented by the empty space inside an AMR, on the cooling performance. The instantaneous temperature profiles along the regenerator are also illustrated to show the mixing effect caused by the dead volume. Section 4.4 shows the optimization of active magnetic regenerators using four different geometries and compares the maximum efficiencies in different cases. This chapter is based partially on the papers attached in Sections A.2, A.6, A.7 and A.8.

4.1 Entropy production minimization and analysis on loss mechanisms

Although recent MCR prototypes have realized kW-class refrigeration capacity [38, 42] and high COP in certain temperature spans [19, 43], a gap still exists between these conventional cooling devices and available MCR systems. To improve the performance, researchers have focused on various techniques, such as developing novel magnetocaloric materials [34, 35, 36], increasing the maximum applied magnetic field of the permanent magnet, reducing the parasitic losses by using novel designs and optimizing the regenerator geometry as well as related operating parameters. The last approach is of substantial interest to many machine designers since it is practical and important to get close to the best performance with existing materials and techniques.

From a thermodynamic viewpoint, the most obvious causes of reduced cooling capacity or efficiency of the AMRs include insufficient heat transfer between the fluid and solid refrigerant, viscous dissipation due to the pump work, axial conduction and heat loss to the ambient. The last issue, i.e., heat loss through the regenerator housing, will be discussed in Section 4.2. This section mainly focuses on the first three irreversible mechanisms, which are directly or indirectly related to the regenerator geometry and operating parameters. For example, smaller flow channels in a porous regenerator have a higher heat transfer coefficient

than larger channels. However, they also lead to an increase in the pressure drop and the viscous dissipation. Moreover, large power density requires high frequency operation, which may oppositely increase the risk of insufficient heat transfer due to the reduced blow time. Important parameters related to the regenerator geometry include the regenerator type, hydraulic diameter, porosity and aspect ratio. In addition, the frequency, average mass flow rate, temperature span and applied magnetic field are the key operating parameters. Since those parameters simultaneously affect the regenerator performance, the choice and optimization should be carefully done for achieving desired cooling performance.

Moreover, entropy production minimization is a powerful tool for quantitatively analyzing different loss mechanisms inside a thermal system. The second law of thermodynamics requires the entropy production in a natural process to be positive, and entropy production minimization can be used to obtain the optimal theoretical performance. This approach can also be used to quantify the irreversibility of various processes in the AMRs. The four main irreversible processes are summarized: (1) insufficient heat transfer process between fluid and solid refrigerant, as well as insufficient heat transfer processes at the hot or cold reservoirs; (2) viscous dissipation through the porous bed due to the flow resistance; (3) axial conduction through the bed and conduction due to fluid thermal dispersion; (4) other mechanisms such as irreversibility related to magnetization and demagnetization processes. The last issue is not discussed since it has less relation to this study. The following equations are used to calculate the entropy production rates for different irreversible processes based on the 1D numerical model [57, 73]:

$$\begin{aligned}
\dot{S}_{p,ht} &= \frac{1}{\tau}\int_0^\tau\int_0^L h a_s A_c \frac{(T_f - T_s)^2}{T_f T_s} dx dt \\
&+ \frac{1}{\tau}\int_0^\tau \left|\dot{m}_f\right| c_f \left(\ln\frac{T_C}{T_{f,x=L}} + \frac{T_{f,x=L}-T_C}{T_C} + \ln\frac{T_H}{T_{f,x=0}} + \frac{T_{f,x=0}-T_H}{T_H}\right) dt \quad (4.1)\\
\dot{S}_{p,vd} &= \frac{1}{\tau}\int_0^\tau\int_0^L \frac{\left|\dot{m}_f\right|}{\rho_f T_f}\frac{\partial P}{\partial x} dx dt \quad (4.2)\\
\dot{S}_{p,ac} &= \frac{1}{\tau}\int_0^\tau\int_0^L \left[k_{stat} A_c \frac{1}{T_s^2}\left(\frac{dT_s}{dx}\right)^2 + k_{disp} A_c \frac{1}{T_f^2}\left(\frac{dT_f}{dx}\right)^2\right] dx dt \quad (4.3)\\
\dot{S}_{p,tot} &= \dot{S}_{p,ht} + \dot{S}_{p,vd} + \dot{S}_{p,ac} \quad (4.4)
\end{aligned}$$

where $\dot{S}_{p,ht}$, $\dot{S}_{p,vd}$ and $\dot{S}_{p,ac}$ represent the entropy production rates due to insufficient heat transfer, viscous dissipation and axial conduction, respectively; $\dot{S}_{p,tot}$ is the total entropy production rate; L and τ are the regenerator length and the period of one cycle. By comparing those entropy production rates, the three loss mechanisms can be quantitatively measured.

Table 4.1 shows the details of the modeling parameters. In the simulation, Gd is used as the refrigerant and water mixture with 20 % v/v ethylene glycol as the heat transfer fluid. The magnetocaloric properties of Gd were presented in Chapter 3. The regenerator volume $V_r = LA_c$ is kept constant. Then, the aspect ratio $R_a = L/\sqrt{A_c}$ can fully describe the regenerator shape as shown in Figure 4.1, since a one-dimensional model is implemented here. The

temperature span is fixed from 280 to 300 K, corresponding to a COP of 14 for an ideal refrigerator. The profiles of the applied magnetic field and the nominal mass flow rate are shown in Figure 4.2. The optimization objectives usually include the specific cooling power $\dot{q}_c$, which is the cooling power generated with 1 kg MCM, and the COP. In this section the focus is to maximize COP for obtaining a constant specific cooling power. In a typical condition, the specific cooling power increases with the increment of averaged mass flow rate until reaching the maximum value. Therefore, the averaged mass flow rate can be specified when the specific cooling power is kept constant. Correspondingly the COP data are presented and compared. In this way, the frequency becomes the only operating parameter to be optimized.

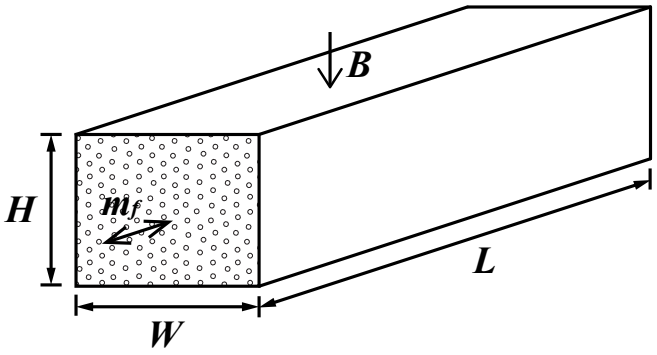

Fig. 4.1: Dimensions of an active magnetic regenerator.

Table 4.1: Main modeling parameters.

Parameter	Value
Maximum applied magnetic field	1.2 T
Number of regenerator beds	20
Volume of regenerator bed	22.5 cm^3
Temperature span	280-300 K
Aspect ratio	0.1-8
Frequency	0.3-10 Hz
Regenerator geometry	Packed sphere bed
Hydraulic diameter	0.10 mm
Porosity	0.36
Heat transfer fluid	Aqueous solution with 20 % v/v ethylene glycol
Magnetocaloric material	Gadolinium
Thermal conductivity of Gd	11 W/(m·K)
Density of Gd	7900 kg/m^3

Optimum performance of an AMR is presented and discussed in this section. To establish a reasonable comparison, the COP data for a desired specific cooling capacity of 100 W/kg are

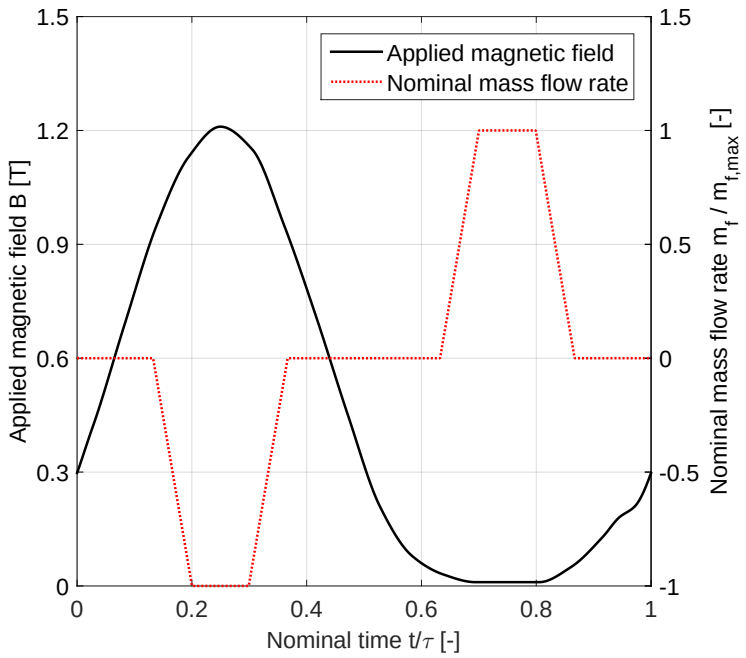

Fig. 4.2: Applied magnetic field B and nominal mass flow rate $\dot{m}_f/\dot{m}_{f,max}$ as a function of nominal time t/τ

compared and presented below. Figure 4.3 shows how the COP of regenerators using packed sphere bed varies with the frequency f and the aspect ratio R_a. The hydraulic diameter is 0.1 mm, which corresponds to a sphere diameter of 0.27 mm. In the simulation, the frequency ranges from 0.3 to 10 Hz and the aspect ratio from 0.1 to 8. In total, about 600 simulations were done to present the synthetic impacts of those two variables. For the packed sphere bed with a hydraulic diameter of 0.1 mm, the maximum COP is around 7.3 when the frequency is 1.6 Hz and the aspect ratio is 1.7 as shown in Figure 4.3. Too large or small frequency and aspect ratio can lead to a decrease in COP.

Figure 4.4 (a) shows the total entropy production rate $\dot{S}_{p,tot}$ as a function of frequency and aspect ratio, which has an inverse relationship compared to the results of COP in Figure 4.3. The minimum total production rate is also found when the frequency is around 1.6 Hz and the aspect ratio is 1.7, which fits the position of the maximum COP. As seen in Figure 4.4 (b), the entropy production rates due to insufficient heat transfer are strongly related to the frequency rather than the aspect ratio. In a typical case where the frequency increases from 0.3 to 10 Hz, the averaged mass flow rate only decreases approx.15% for obtaining a constant specific cooling power. It leads to about 8% decrease in the averaged heat transfer coefficient h_f. It is observed that the average value of $(T_f - T_s)^2/(T_f T_s)$ decreases slightly with increasing frequency when f <1 Hz, due to a relatively higher heat transfer coefficient. However, for f >1 Hz this term increases significantly, which is caused by the decreasing heat transfer time. As a result, $\dot{S}_{p,ht}$ decreases slightly when the frequency is less than 1 Hz, while it increases

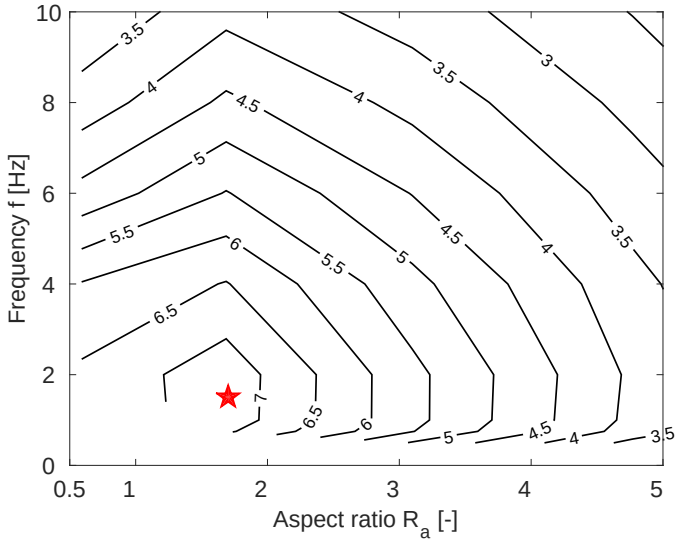

Fig. 4.3: COP as a function of frequency f and aspect ratio R_a for regenerators using packed sphere bed with D_h=0.1 mm.

dramatically with a further increasing frequency. In contrast, $\dot{S}_{p,vd}$ in Figure 4.4 (c) is more sensitive to the aspect ratio than the frequency, as the pressure drop strongly depends on the regenerator length and the average velocity through the bed. Since the axial conduction loss increases for larger cross sectional area and shorter length, $\dot{S}_{p,ac}$ increases significantly with decreasing aspect ratio. However the frequency does not affect $\dot{S}_{p,ac}$ much. In most cases, the entropy production rates representing insufficient heat transfer and viscous dissipation contribute most to the total entropy production rate, whereas the entropy production rate due to axial conduction becomes significant when the aspect ratio is smaller than 1.0. At the point of minimum total entropy production rate, the viscous dissipation contributes most to the lost; the second biggest lost is insufficient heat transfer, while the last is the axial conduction.

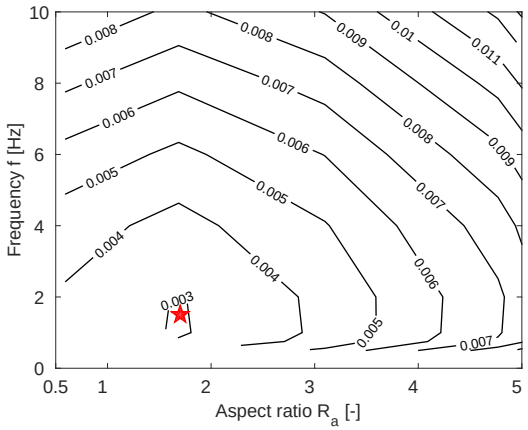

(a) Total entropy production rate consisted by three parts $\dot{S}_{p,tot}$

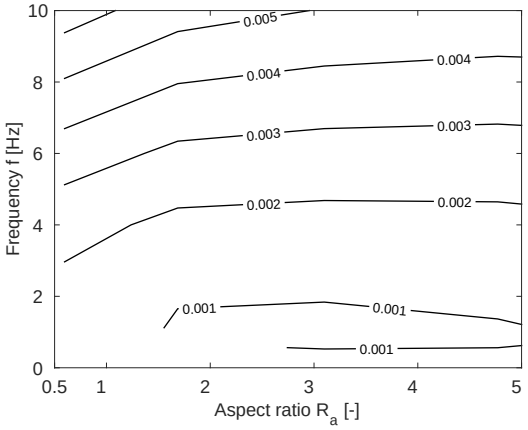

(b) Entropy production rate due to insufficient heat transfer $\dot{S}_{p,ht}$

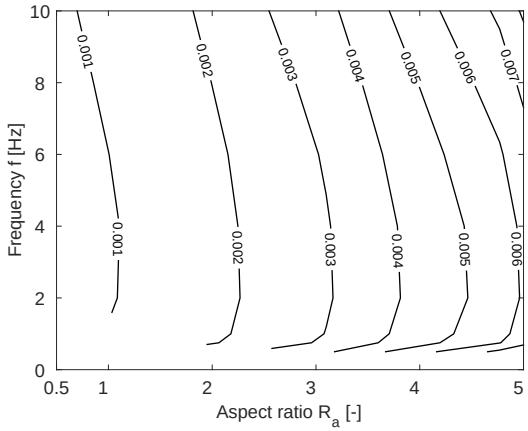

(c) Entropy production rate due to viscous dissipation $\dot{S}_{p,vd}$

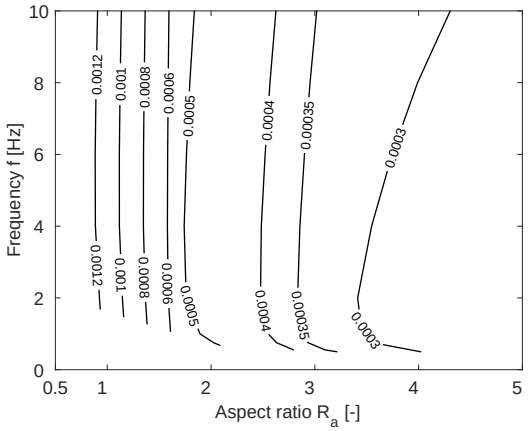

(d) Entropy production rate due to axial conduction $\dot{S}_{p,ac}$

Fig. 4.4: Corresponding entropy production rate as a function of frequency f and aspect ratio R_a for AMRs using packed sphere bed with D_h= 0.1 mm

4.2 Impact of heat loss through the regenerator housing

In the original model, an adiabatic boundary of the regenerator housing was assumed, and the heat loss through the wall was neglected. In order to estimate this factor, the 1D model is further modified as described in Section 2. Based on the model as shown in Figure 4.5, the energy equation of the wall is described by:

$$\begin{aligned} h_{wf}a_{wf}A_c\left(T_f - T_w\right) + \frac{\partial}{\partial x}\left(k_w A_{cw}\frac{\partial T_w}{\partial x}\right) &+ h_{wa}a_{wa}A_c\left(T_a - T_w\right) \\ &= A_{cw}\rho_w c_w \frac{\partial T_w}{\partial t} \end{aligned} \tag{4.5}$$

where the terms represent the heat conduction, heat transfer between the fluid and the wall, heat transfer between the wall and the ambient and energy storage, respectively. More details of the parameters were explained in Section 2.3.

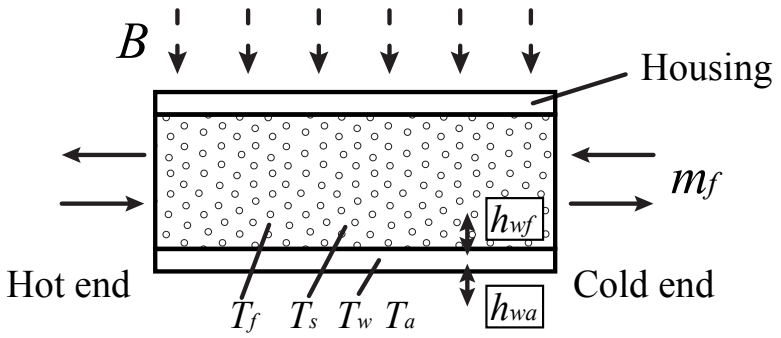

Fig. 4.5: Schematic diagram of an AMR with the housing wall, where the heat transfer between the wall and fluid, as well as that between the wall and the ambient, are considered.

In the model, h_{wf} is the convective heat transfer coefficient between the fluid and the wall and h_{wa} is the heat transfer coefficient between the wall and the ambient. The latter includes both effects of natural convection and forced convection, depending on the moving velocity of the regenerator. Since both h_{wf} is difficult to identify; only a theoretical prediction is presented by assuming different combination of h_{wf} and h_{wa}.

Figure 4.6 addresses the influence of h_{wf} on the specific cooling power and COP when h_{wa} is 100 W/(m^2·K). In the simulation, the aspect ratio is 0.6; the sphere diameter is 0.3 mm; the frequency is 2 Hz; the temperature span is 20 K. In addition, the nylon wall has a thickness of 3 mm; the thermal conductivity is 0.3 W/(m·K); the specific heat is 1670 J/(kg·K); and the density is 1200 kg/m3. In Figure 4.6, h_{wf} ranges from 0 to 6400 W/(m^2·K) and the increase in h_{wf} leads to a remarkable reduction in both specific cooling power and COP. The maximum specific cooling power decreases from 229 to 137 W/kg in the simulated range, showing the heat loss through the wall could exert a big influence. Note h_{wf}=0 represents the adiabatic condition, although h_{wa} is not zero.

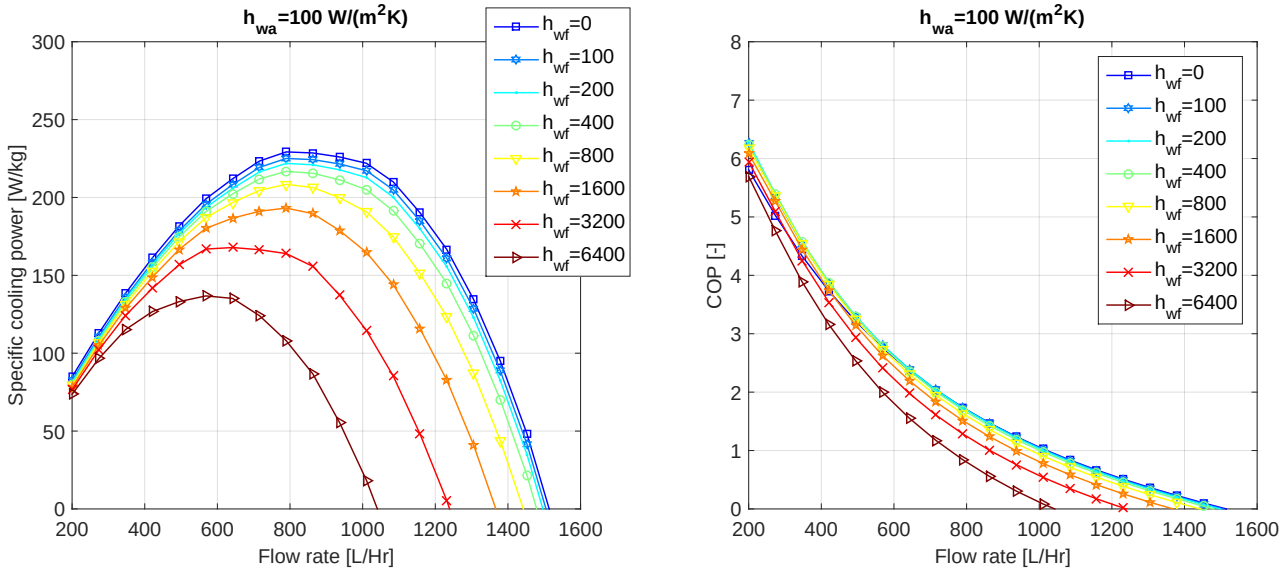

(a) Specific cooling power

(b) COP

Fig. 4.6: Impact of heat transfer coefficient h_{wf} between the wall and fluid on the performance of an AMR.

The impact of the heat transfer coefficient between the wall and the ambient h_{wf} is presented in Figure 4.7, when h_{wf} is fixed as 3200 W/(m^2·K). An interesting fact that the peak cooling power is much lower than that with the adiabatic wall condition (See the case in Figure 4.6 with h_{wf}=0 W/(m^2·K)), is noticed, even h_{wa} is zero and there is no heat loss from the housing to the ambient. This can be attributed by the heat leak along the wall due to the temperature gradient, and the temperature difference between the moving fluid and the wall. The latter is the conjugate loss and it sometimes becomes dominant, as the temperature of the periodical flow evolves dynamically as shown in Figure 4.8 and it could "transport" the heat much faster than the conduction. The results in Figure 4.7 illustrate the performance reduction with increasing h_{wa}. The peak specific cooling power drops from 175 to 118 W/kg and COP decreases in the meantime.

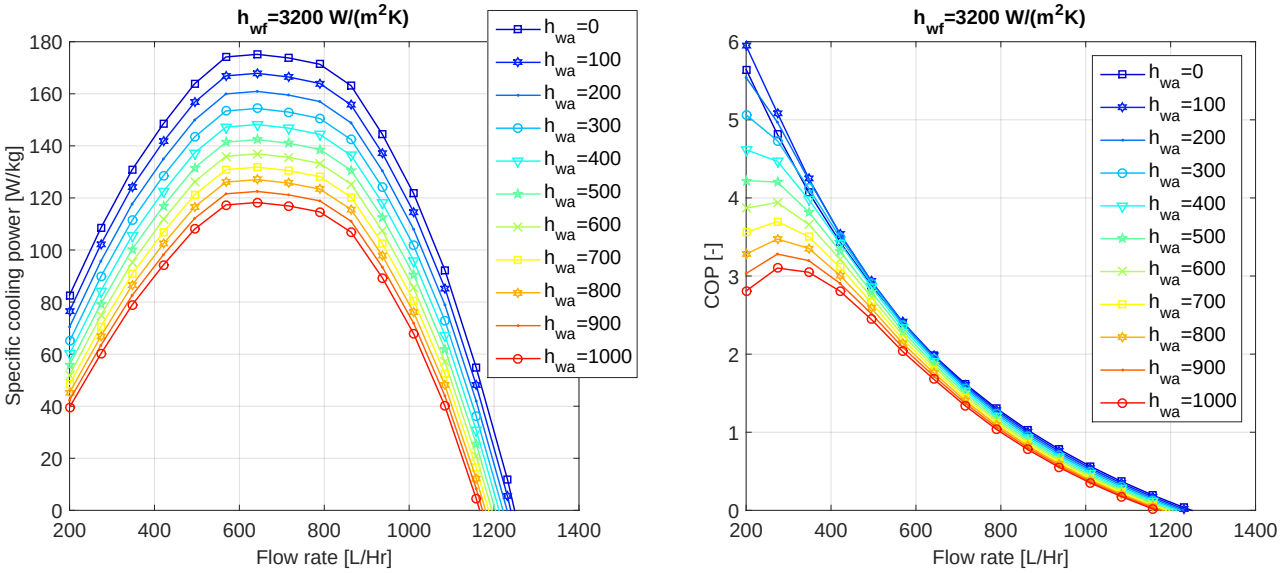

(a) Specific cooling power

(b) COP

Fig. 4.7: Impact of heat transfer coefficient h_{wa} between the wall and ambient on the performance of an AMR.

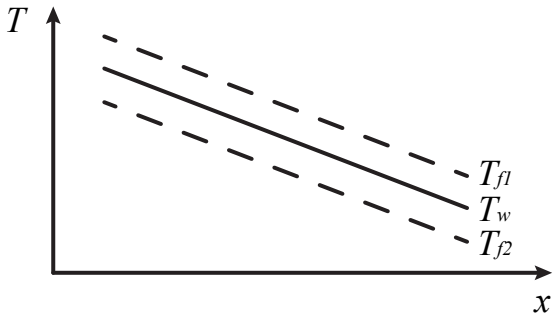

Fig. 4.8: Schematic diagram of conjugate loss in an AMR with the housing wall, where the wall temperature is assumed not changing.

4.3 Impact of dead volume

Usually there will be a small mixing chamber where the cold and hot fluid streams could mix at both ends and in the middle of the regenerator as shown in Figure 4.9. It could cause a substantial loss due to the mixing. From a regenerator stand-point, it is clear that such zones should be minimized, therefore, two channels are normally applied to separate the inflow and outflow at both ends and the whole regenerator is tightly packed with the MCM particles avoiding the dead volume. However, certain dead volume inevitably exists and it sometimes did not attract enough attention during the prototype design. To specify how much dead vol-

ume can be tolerated in terms of the impact on the performance from a practical point of view, a quantitative study is presented in this section.

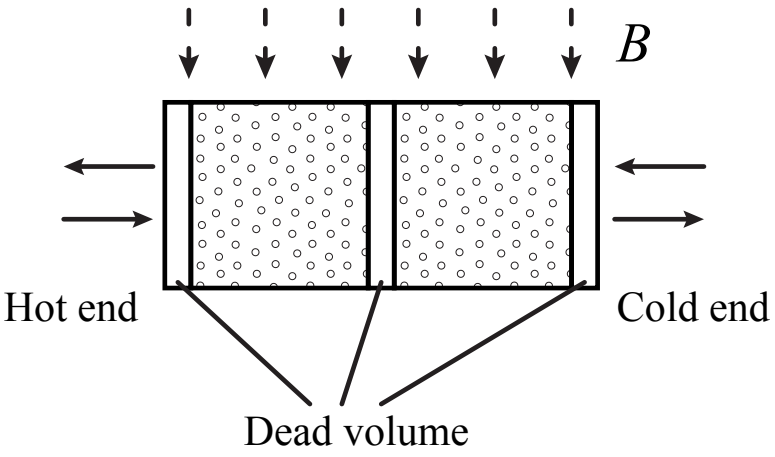

Fig. 4.9: Schematic diagram of dead volume in an AMR.

In the simulation, the amount of MCM is fixed while the dead volume ratio R_{DV}, which is the ratio of the dead volume to the total regenerator volume is adjusted. The dead volume ratio R_{DV} of 0.05 - 0.30 are assumed to exist in the regenerator. Figure 4.10 (a) and (b) show the performance of regenerator with different dead volume ratios when the temperature span is 20 K. Both cooling power and COP decrease with the increasing dead volume ratio, when the flow rate is relatively low. The trend of cooling power curve runs into an opposite way when the flow rate is high, however such a high flow rate is not commonly seen in real application. It can be concluded that the performance will degrade severely with a dead volume larger than 0.10.

With the dead volumes existing in the regenerator, the heat transfer liquid, which is left in the dead volume after hot / cold period, does not transfer heat in demagnetization / magnetization process because it is not in contact with magnetocaloric material. Therefore, this part of heat transfer liquid has a higher / lower temperature than that of the incoming cold / hot flow, which reduces enthalpy flux at each end and decrease the effectiveness of the regenerator. The temperature profiles along the regenerator with and without dead volume at typical time points are illustrated in Figure 4.11 to verify this effect. The dead volume of the regenerator in Figure 4.11 (a) is located in the middle of the regenerator. Compared with the case without dead volume, the temperature gradient of the regenerator with R_{DV}=0.30 shows a strong non-linear pattern, caused by the mixing effect in the dead volume.

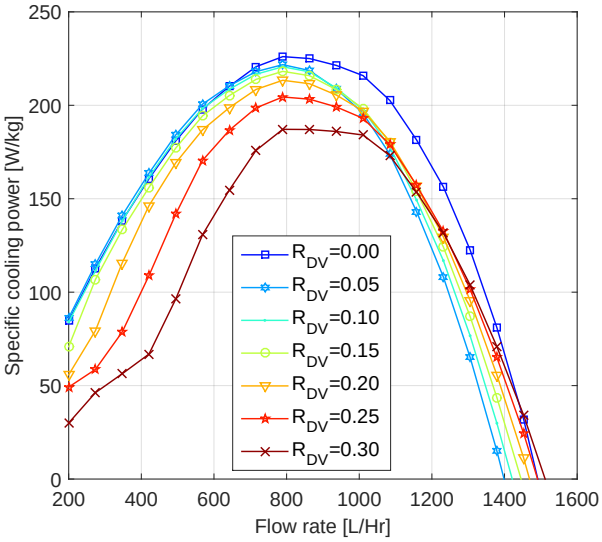

(a) Specific cooling power

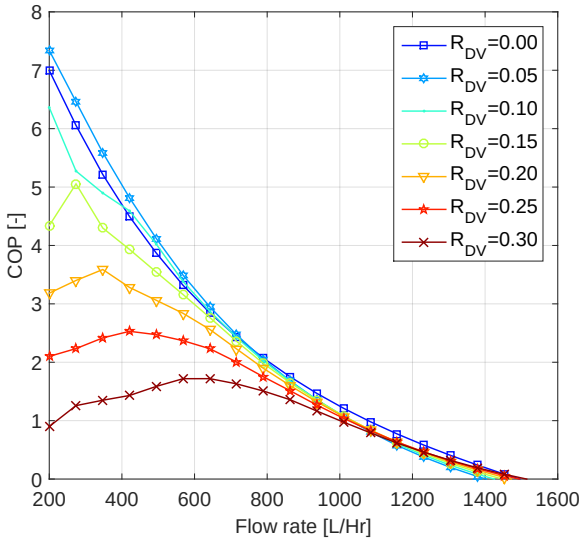

(b) COP

Fig. 4.10: Impact of dead volume ratio R_{DV} on the performance of an AMR.

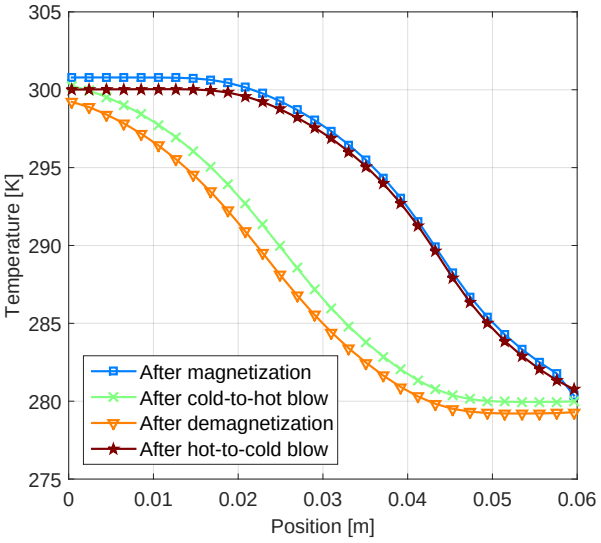

(a) Dead volume ratio R_{DV}= 0.00

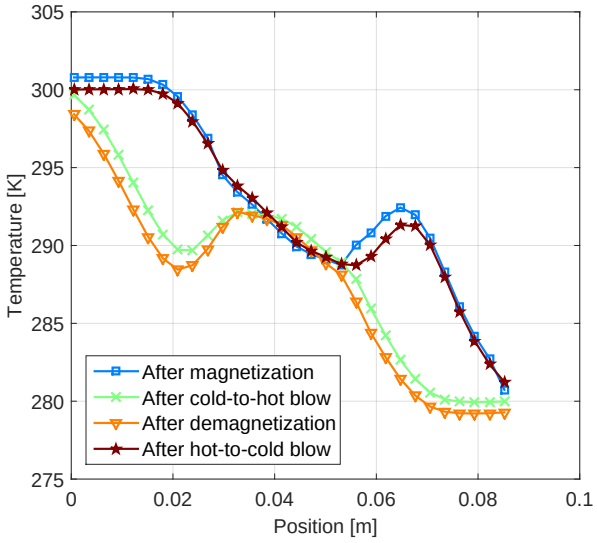

(b) Dead volume ratio R_{DV}= 0.30

Fig. 4.11: Fluid temperature profiles along the regenerator with R_{DV}=0.00 (a) and R_{DV}=0.30 (b), at four typical time nodes.

4.4 Optimization of regenerator geometries

Optimizing the regenerator geometry and related operating parameters is a practical and effective way to obtain the desired cooling performance, in addition to applying more advanced materials and layering AMRs. To investigate how to choose and optimize the AMR geometry, a quantitative study is presented by simulations in this chapter. Correlations for calculating the friction factor and heat transfer coefficient are reviewed and chosen for modeling different geometries. Moreover, the impacts of various parameters on the regenerator efficiency with a constant specific cooling capacity are simulated and presented. In addition, optimum geometry and operating parameters corresponding to the highest efficiency for different geometries are compared.

In general, good regenerator geometry requires sufficient heat transfer between the fluid and porous solid matrix, low pressure drop and small axial conduction. Among these issues, the insufficient heat transfer and the viscous dissipation are two major loss mechanisms, while the axial conduction should be stressed when dealing with short and bulky regenerators, as discussed in Section 4.1. In various prototypes, which were well reviewed in References. [34, 35, 36], the packed particle bed and parallel plate matrix were two commonly used geometries. Due to the advantages of easy construction and good heat transfer performance, the packed particle beds were widely implemented. However, the pressure drop over the packed particle bed and the viscous dissipation loss in packed particle bed are relatively large, which may cause a reduction in regenerator efficiency. Although the parallel plate matrix has much lower frictional pressure drop compared with the former, high heat transfer coefficient is difficult to obtain in experiments due to the limitation of fabricating small channels [64]. The micro-channel matrix for MCR application, which consists of numerous micro channels through a monolithic block, has been presented in a few papers [74, 75].

Radebaugh et al. [76] presented a comparison study on different regenerator geometries for regenerative refrigerators. For various geometries, the ratios of heat transfer modulus to friction factor $\mathrm{StPr}^{2/3}/f_F$, where St, Pr and f_F are the Stanton number, Prandtl number and friction factor respectively, were compared. The Stanton number is the ratio of the heat transferred into fluid to the thermal capacity of fluid. Their study showed that the parallel plate and micro-channel matrices were preferable concerning a balance between heat transfer and pressure drop. The worst groups included the rod bundle matrix, packed screen bed and packed sphere bed. The authors also argued that the parallel plate or micro-channel matrices were not suitable for the cryogenic regenerators because of their relatively large longitudinal conduction. In reality, the packed screen bed and packed sphere bed are widely used in regenerative heat engines or refrigerators instead of the parallel plate or micro-channel matrices. Barclay et al. [77] compared four different geometries for MCR application by using a simplified model, which included the packed sphere bed, parallel plate matrix and micro-channel matrix. The study presented optimal characteristic dimension and aspect ratio for different regenerator geometries at three frequencies. More recently, Li et al. [57] presented the optimization of the sphere diameter and aspect ratio for AMR using the packed sphere bed by a 1D model. Vuarnoz et al. [78] simulated the AMRs using a stacked wire matrix and compared the results with the packed sphere bed. Li et al. [79] compared the regenerators with the packed sphere bed and parallel plate matrix by simulation and the latter showed smaller total entropy pro-

duction rate and better performance. Tušek et al. [59] presented the optimization of an AMR with a packed sphere bed and parallel plate matrix in two operating frequencies based on a 1D model.

The study on the AMR geometry in the literature is insufficient as some interesting geometries like packed screen beds are not included. In the following section, a general analysis of regenerator geometries is presented. The correlations for estimating friction factor and heat transfer coefficient of different geometries are reviewed and proper ones are chosen for modeling. By using a one-dimensional model, the synthetic impacts of various parameters on regenerator performance are quantified and analyzed. Assuming a constant specific cooling power, the maximum COP of regenerators using different geometries are presented. Corresponding optimum geometry and operating parameters are compared.

In this section, five regenerator geometries, which are the packed sphere bed, parallel plate matrix, circular micro-channel matrix, rectangular micro-channel matrix and packed screen bed, are discussed. The schematic diagrams of different regenerator geometries are shown in Figure 4.12, where the dark area represents solid refrigerant and the remaining white space is the flow channel, where the flow direction is perpendicular to the schematic diagram except Figure 4.12 (e-2). Table 4.2 gives the important dimensions and the expressions of various characterizing parameters for different geometries, which include porosity , hydraulic diameter D_h and volumetric surface area a_s. The porosity is the void fraction of the porous regenerator; the hydraulic diameter is the ratio of the cross sectional area to the wetted perimeter of the cross-section of a flow channel times four; the volumetric surface area is the amount of surface area per unit volume.

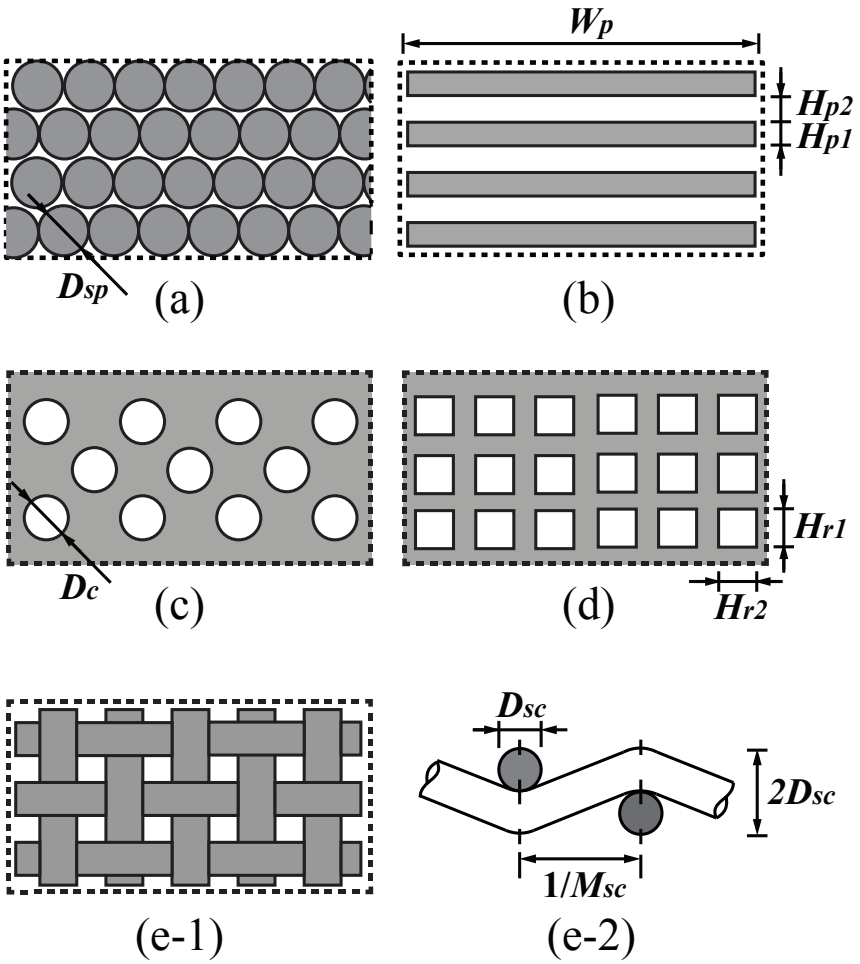

Fig. 4.12: Schematic diagram of different regenerator geometries including: (a) packed sphere bed; (b) parallel plate matrix; (c) circular micro-channel matrix; (d) rectangular micro-channel matrix; (e-1) and (e-2) top and side views of packed screen bed. Except (e-2), the flow direction is perpendicular to the schematic diagram. The dark region represents solid refrigerant, i.e., magnetocaloric material and the rest of the region represents flow channel.

Table 4.2: Parameters for characterizing different regenerator geometries.

Geometry	Dimensions	Porosity	Hydraulic diameter	Specific surface area
Packed sphere bed	D_{sp}	$\varepsilon = 0.36$	$D_h = \frac{2\varepsilon}{3(1-\varepsilon)} D_{sp}$	$a_s = \frac{4\varepsilon}{D_h} = \frac{6(1-\varepsilon)}{D_{sp}}$
Parallel plate matrix	H_{p1}, H_{p2}	$\varepsilon = \frac{H_{p2}}{H_{p1}+H_{p2}}$	$D_h = 2H_{p2}$	$a_s = \frac{4\varepsilon}{D_h} = \frac{2}{H_{p1}+H_{p2}}$
Circular micro-channel matrix	D_c	ε	$D_h = D_c$	$a_s = \frac{4\varepsilon}{D_h} = \frac{4\varepsilon}{D_c}$
Rectangular micro-channel matrix	H_{r1}, H_{r2}	ε	$D_h = \frac{2H_{r1}H_{r2}}{H_{r1}+H_{r2}}$	$a_s = \frac{4\varepsilon}{D_h} = \frac{2\varepsilon(H_{r1}+H_{r2})}{H_{r1}H_{r2}}$
Packed screen bed	M_{sc}, D_{sc}	$\varepsilon = 1 - \frac{\pi D_{sc} M_{sc}^2 \sqrt{D_{sc}^2 + M_{sc}^{-2}}}{4}$	$D_h = \frac{4\varepsilon}{a_s}$	$a_s = \pi M_{sc}^2 \sqrt{D_{sc}^2 + M_{sc}^{-2}}$

Here the "packed sphere bed" is used instead of the packed particle bed although the regenerator beds are typically packed with irregular particles in existing prototypes, since in this study all particles are assumed spherical with the same size. This kind of geometry can be easily constructed by packing small spheres into a regenerator housing. In addition, the porosity is assumed constant equal to 0.36 since the sphere diameter is much smaller than the housing diameter [80]. Therefore, the sphere diameter is the single characterizing parameter for the packed sphere bed. Under this assumption, the boundary effects are neglected, which means that the flow is assumed uniform in the cross section and in particular that no channeling of the fluid occurs. It can be seen that the hydraulic diameter of a packed sphere bed is proportional to the sphere diameter D_{sp} and the volumetric surface area has an inverse relationship with D_{sp} [81].

The parallel plate matrix can be built by stacking thin plates with a specified spacing from each other and the main dimensions are the plate thickness H_{p1} and flow channel height H_{p2}. The porosity and volumetric surface area is a function of H_{p1} and H_{p2}, assuming the plate width is much bigger than the channel size. For the circular micro-channel matrix, the hydraulic diameter is the same as the channel diameter D_c and the specific surface area can be calculated from the hydraulic diameter and porosity. The hydraulic diameter of the rectangular micro-channel matrix is related to the height and width of the flow channel (H_{r1} and H_{r2}). A square channel with $H_{r1} = H_{r2} = H_r$ gives $D_h = H_r$. Woven screens have been used for catalytic reaction for a long time, since they have highly ordered structures, high heat transfer rates and moderate flow resistances. Armour et al. [82] presented the equations for calculating different parameters by using a wire diameter D_{sc} and mesh number per meter M_{sc}, as shown in Table 4.2. Only the packed sphere bed can be characterized by only one parameter, and the other geometries need two variables for full identification. Therefore, two parameters, the hydraulic diameter and the porosity, are used to characterize the AMR geometries for reasonable comparison.

As numerous flow and heat transfer correlations for different geometries exist and there are few universally applicable correlations for modeling AMRs, a brief review of correlations is provided in the following. In a typical AMR, Gd is used as the solid refrigerant, while the heat transfer fluid could be aqueous solution with anti-freeze, which has a high Prandtl number around 5-7. Low Reynolds number (Re $<$100) flow is predicted as the typical operating conditions [63], which are considered in choosing the correlations.

The Ergun equation [83] is generally used to calculate the friction factor in a packed sphere bed, and the expression includes both viscous and kinetic effects as shown in Table 4.3. More correlations [84, 85, 86] are compared with the Ergun equation, and it turns out the latter presents a good estimation. Wakao et al. [87] in 1979 presented an expression for estimating the Nusselt number for the packed sphere bed. Engelbrecht [2] considered the internal temperature gradient inside the solid, and further correlated Wakao et al.'s correlation with the Biot number Bi, which is used in this study. The Fanning friction factor for laminar flow through the parallel plates was presented as $f_F = 24/\mathrm{Re}$ [88], and a similar expression can be found in Reference [89]. Different correlations for the heat transfer coefficient of the parallel plates were presented in References [89, 90, 91]. Among those, Nickolay et al. [90] presented a correlation of overall Nusselt number and it gave a good estimation compared with the others.

Nielsen et al. [61] found that the Biot number for a parallel plate matrix is much less than 1, which means the heat transfer inside the plate is faster than that across the boundary layer. Therefore, the correlation is not further modified here.

The Poiseuille law and its modified form [92, 93, 94] are generally used to calculate the friction factor for laminar flow through the micro-channel matrix. Comparing References [89, 93, 95, 96] shows that Hausen et al.'s correlation [95] is the best for calculating the heat transfer coefficient of the circular channel, and the one presented by Kays et al. [91] is used for the rectangular channel. Armour et al. [82] developed a flow friction correlation applicable to the flow through the most types of woven metal screens with different porosities. It gave the best estimation in contrast to References [97, 98, 99]. Park et al. [100] presented a heat transfer correlation based on experiments and it is chosen by comparing with other references [101, 102, 103].

The details of correlation comparison will not be presented in this section to avoid tedious enumeration. Only chosen correlations for different geometries are presented and compared. Figure 4.13 (a) and (b) show the friction factor f_F and Nusselt number Nuas a function of Reynolds number Re_h for different geometries, when the porosity is 0.36 and the hydraulic diameter is 0.20 mm. Here the friction factor, Nusselt number and Reynolds number based on the hydraulic diameter and the superficial velocity v_s are:

$$f_F = \frac{dP}{dx}\frac{2D_h}{\rho_f v_s^2} \tag{4.6}$$

$$\mathrm{Nu} = \frac{hD_h}{k_f} \tag{4.7}$$

$$\mathrm{Re}_h = \frac{\rho_f v_s D_h}{\mu_f} \tag{4.8}$$

$$v_s = \frac{\dot{m}_f}{\rho_f A_c} \tag{4.9}$$

where $\frac{dP}{dx}$, D_h, ρ_f, v_s, h, k_f, μ_f, $\dot{m}_f$ and A_c, are pressure drop over unit length, hydraulic diameter, density, superficial velocity, heat transfer coefficient, thermal conductivity of fluid, dynamic viscosity, mass flow rate and cross sectional area, respectively.

Table 4.3: Chosen correlations for different regenerator geometries.

Reference	Geometry	Characteristic dimension length	Reynolds number	Friction factor	Pressure drop	Remarks
Ergun et al. [83]	Packed sphere bed	$D_L = D_{sp}$			$\frac{dP}{dx} = 2\alpha \frac{(1-\varepsilon)^2 \mu_f v_s S_v^2}{\varepsilon^3} + \frac{\beta}{8} \frac{(1-\varepsilon)\rho_f v_s^2 S_v}{\varepsilon^3}$ $\alpha = (\pi/2)^2 \approx 2.5$, $\beta = 2.4$ and $S_v = 6/D_L$	Laminar and turbulent flow
Bejan [88]	Parallel plate matrix	$D_L = 2H_{p2}$	$\mathrm{Re} = \frac{\rho_f (v_s/\varepsilon) D_L}{\mu_f}$	$f_F = 24/\mathrm{Re}$	$\frac{dP}{dx} = 4 f_F [\frac{\rho_f (v_s/\varepsilon)^2}{2D_L}]$	Laminar flow
Poiseuille law (Asadi et al.) [92]	Circular micro-channel matrix	$D_L = D_c$	$\mathrm{Re} = \frac{\rho_f (v_s/\varepsilon) D_L}{\mu_f}$	$f_F = 64/\mathrm{Re}$	$\frac{dP}{dx} = f_F [\frac{\rho_f (v_s/\varepsilon)^2}{2D_L}]$	Laminar flow
Shah et al. [89]	Rectangular micro-channel matrix	$D_L = \frac{2H_{r1}H_{r2}}{H_{r1}+H_{r2}}$	$\mathrm{Re} = \frac{\rho_f (v_s/\varepsilon) D_L}{\mu_f}$	$f_F = 24(1 - 1.3553\alpha + 1.9467\alpha^2 - 1.7012\alpha^3 + 0.9564\alpha^4 - 0.2537\alpha^5)/\mathrm{Re}$ $\alpha = H_{r1}/H_{r2}$	$\frac{dP}{dx} = 4 f_F [\frac{\rho_f (v_s/\varepsilon)^2}{2D_L}]$	Laminar flow
Armour et al. [82]	Packed screen bed	$D_L = \frac{1-M_{sc}D_{sc}}{M_{sc}}$	$\mathrm{Re} = \frac{\rho_f v_s}{a_s^2 \mu_f D_L}$	$f_F = \frac{8.61}{\mathrm{Re}} + 0.52$	$\frac{dP}{dx} = f_F [\frac{\rho_f (v_s/\varepsilon)^2}{D_L}]$	$0.35 < \varepsilon < 0.76$ $0.1 < \mathrm{Re} < 1000$

Reference	Geometry	Characteristic dimension length	Reynolds number	Nusselt number	Heat transfer coefficient	Remarks
Engelbrecht [2]	Packed sphere bed	$D_L = D_{sp}$	$\mathrm{Re} = \frac{\rho_f v_s D_L}{\mu_f}$	$\mathrm{Nu} = \frac{2+1.1\mathrm{Pr}^{1/3}\mathrm{Re}^{0.6}}{1+\chi \mathrm{Bi}/5}$	$h_f = \frac{\mathrm{Nu} k_f}{D_L}$	Laminar flow
Nickolay et al. [90]	Parallel plate matrix	$D_L = 2H_{p2}$		$\mathrm{Nu} = [7.541^n + (1.841\mathrm{Gz}^{1/3})^n]^{(1/n)}$ $\mathrm{Gz} = \frac{2v_s A_c \rho_f c_f D_L}{k_f W_p L}$ and $n = 3.592$	$h_f = \frac{\mathrm{Nu} k_f}{D_L}$	$\mathrm{Gz} < 10^5$
Hausen et al. [95]	Circular micro-channel matrix	$D_L = D_c$	$\mathrm{Re} = \frac{\rho_f (v_s/\varepsilon) D_L}{\mu_f}$	$\mathrm{Nu} = 3.657 + 0.19\mathrm{C}^{0.8}/(1 + 0.117\mathrm{C}^{0.467})$ $\mathrm{C} = \mathrm{RePr}D_L/L$	$h_f = \frac{\mathrm{Nu} k_f}{D_L}$	Laminar flow and constant wall temperature
Kays and Crawford [91]	Rectangular micro-channel matrix	$D_L = \frac{2H_{r1}H_{r2}}{H_{r1}+H_{r2}}$		$\mathrm{Nu} = 8.235(1 - 1.883/\alpha + 3.767/\alpha^2 - 5.814/\alpha^3 + 5.361/\alpha^4 - 2/\alpha^5)$ $\alpha = H_{r1}/H_{r2}$	$h_f = \frac{\mathrm{Nu} k_f}{D_L}$	$\mathrm{Re} < 2200$
Park et al. [100]	Packed screen bed	$D_L = \frac{\varepsilon}{1-\varepsilon} D_{sc}$	$\mathrm{Re} = \frac{\rho_f (v_s/\varepsilon) D_L}{\mu_f}$	$\mathrm{Nu} = 1.315\mathrm{Pr}^{1/3}\mathrm{Re}^{0.35} \left(\frac{1-\varepsilon}{\varepsilon}\right)^{0.2}$	$h_f = \frac{\mathrm{Nu} k_f}{D_L}$	$0.40 < \varepsilon < 0.84$ $10 < \mathrm{Re} < 500$

Figure 4.13 (a) shows that the packed sphere bed exhibits the largest friction factor, and the second largest is the packed screen bed, whereas the other three have much lower flow resistance. On the contrary, higher Nusselt numbers can be observed in the packed sphere bed and packed screen bed than the other three geometries as shown in Figure 4.13 (b). Since higher Nusselt number Nu and lower friction factor f_F are desirable, the ratio of Nusselt number to friction factor Nu/f_F (see Figure 4.13 (c)) is utilized to evaluate the regenerator geometries. The parallel plate matrix gives the highest Nu/f_F in this comparison, and the lowest value is observed in the packed sphere bed. It is found that the circular and rectangular micro-channel matrices yield virtually the same friction factor and Nusselt number; therefore in this study only the results of the circular micro-channel matrix are presented and they are denoted as "micro-channel matrix". Since the static and dispersion conduction is relatively small, the related correlations for different geometries are not compared in this study and they can be found in References [84, 98, 104, 105, 106].

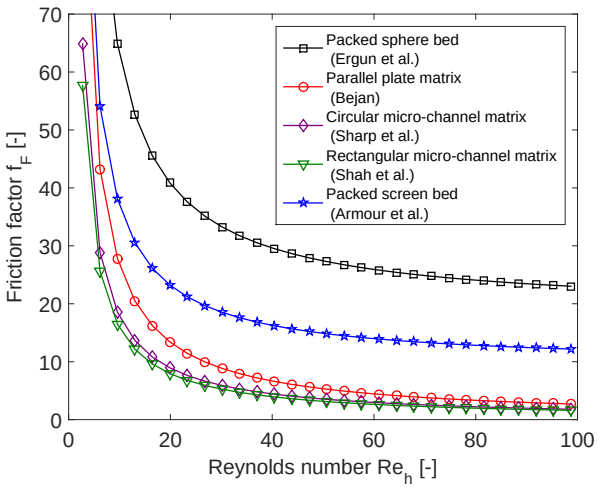

(a) Friction factor f_F

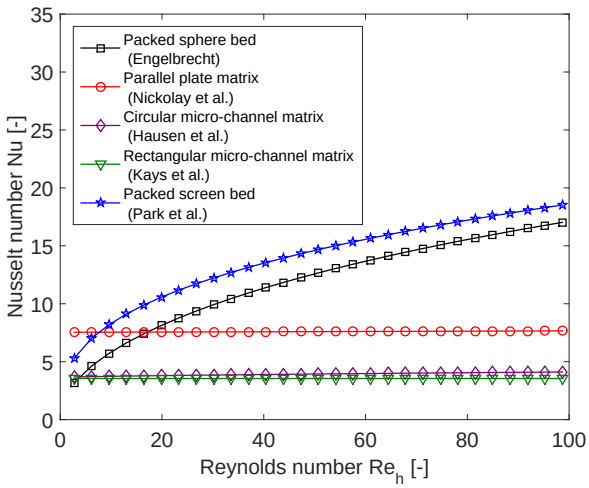

(b) Nusselt number Nu

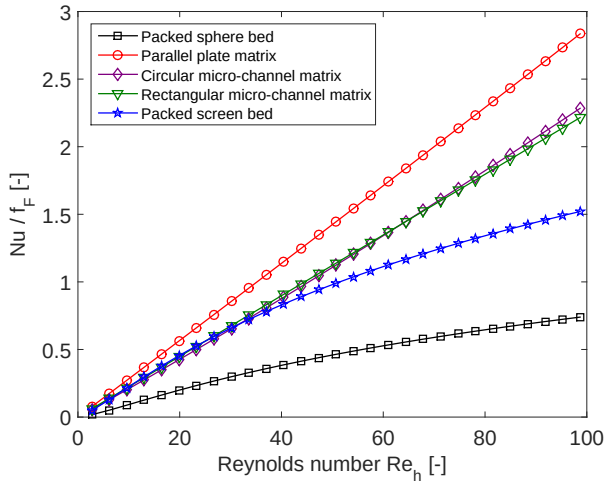

(c) Nu/f_F

Fig. 4.13: Nusselt number Nu, friction factor f_F, and ratio of Nusselt number to friction factor Nu/f_F as a function of Reynolds number Re_h for different geometries when porosity ε is 0.36 and hydraulic diameter D_h is 0.20 mm.

4.4.1 Packed sphere bed

The modeling parameters are listed in Table 4.1. Only the regenerator geometry and the porosity vary in the following sections. Figure 4.14 shows how COP of regenerators using packed sphere bed varies with the frequency f and the aspect ratio R_a. Four subgraphs represent different hydraulic diameters from 0.05 to 0.20 mm, which are corresponding to the sphere diameters from 0.14 to 0.57 mm. For each case, the frequency ranges from 0.3 to 10 Hz and the aspect ratio from 0.1 to 8. In total, about 1800 simulations were done to present the synthetic impacts of those three variables.

In general, it is found that not only the maximum COP, but also the optimum frequency and aspect ratio vary with the hydraulic diameter in Figure 4.14 (a)-(d). For the packed sphere bed with a hydraulic diameter of 0.05 mm, the maximum COP is around 6.9 when the frequency is 3.7 Hz and the aspect ratio is 0.7 as shown in Figure 4.14 (a). Too large or small frequency and aspect ratio can lead to a decrease in COP. The spindle shaped contour reveals that COP changes significantly with the aspect ratio; in contrast, it is less sensitive to the frequency. Figure 4.14 (b)-(d) shows that the maximum COP becomes 7.2, 6.5 and 4.8 when the hydraulic diameters are 0.10, 0.15 and 0.20 mm, respectively. Simultaneously the optimum frequency shifts to a lower value and the optimum aspect ratio becomes larger. In the case of a small hydraulic diameter, the pressure drop per unit length is relatively high; therefore a small aspect ratio is necessary in order to prevent the viscous dissipation from dominating. On the other hand, larger hydraulic diameter allows a longer regenerator, which in turn increases the risk of insufficient heat transfer. As a result, a relatively low frequency is desired in order to increase the heat transfer time and number of transfer units, defined as the ratio of the amount of heat transferred between solid and fluid to the thermal mass of the fluid moved. When the hydraulic diameter is larger than or equal to 0.15 mm, the COP becomes more sensitive to frequency instead of aspect ratio, as shown in Figure 4.14 (c) and (d).

Figure 4.15 summarizes the maximum COP and shows how optimum frequency and aspect ratio shift with the hydraulic diameter, by extracting the information from Figure 4.14 (a)-(d). The largest COP is 7.6 when the hydraulic diameter, frequency and aspect ratio are 0.075 mm, 2.3 Hz and 1.0, respectively.

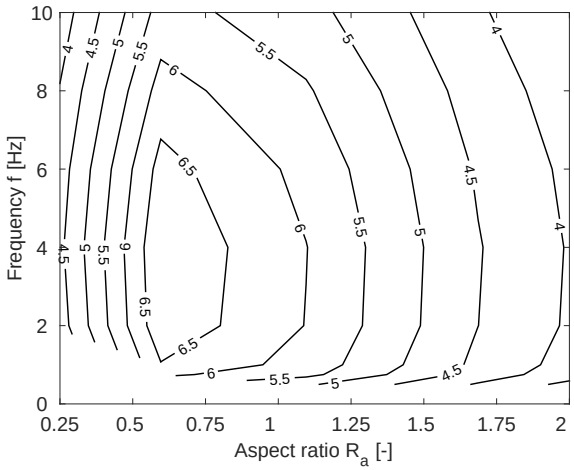

(a) D_h=0.05 mm

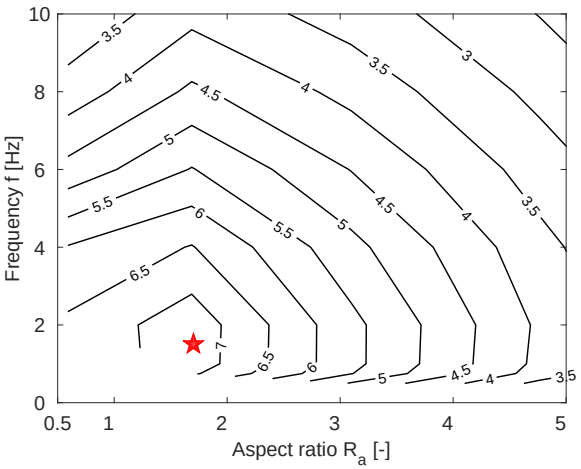

(b) D_h=0.10 mm

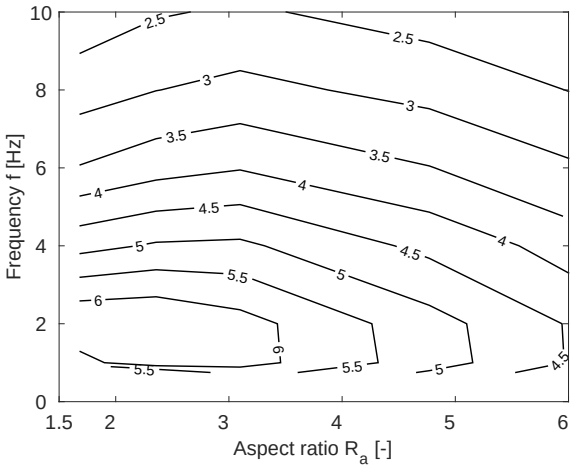

(c) D_h=0.15 mm

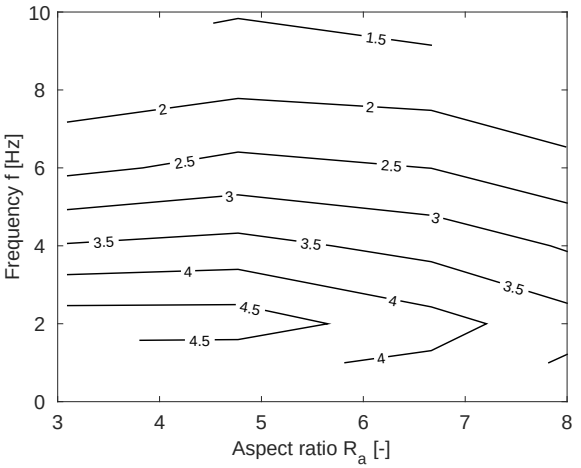

(d) D_h=0.20 mm

Fig. 4.14: COP as a function of frequency f and aspect ratio R_a for regenerators using packed sphere bed.

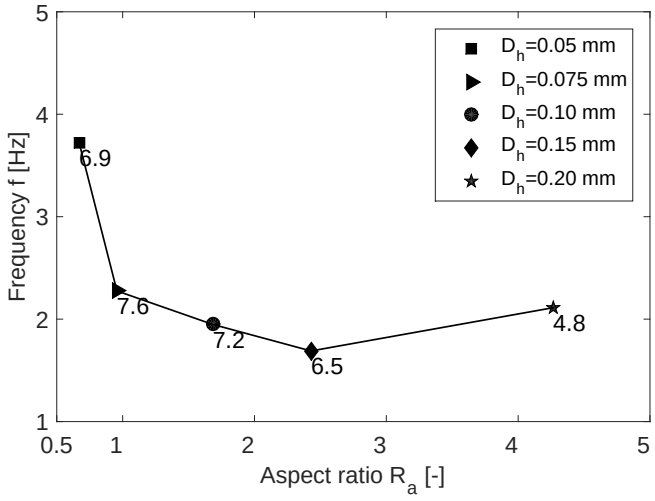

Fig. 4.15: Maximum COP (side-noted numbers) as well as optimum frequency f (vertical coordinate) and aspect ratio R_a (horizonal coordinate) for regenerators using packed sphere bed with different hydraulic diameter D_h

4.4.2 Parallel plate matrix

In contrast to the packed sphere bed, the porosity of the parallel plate matrix can be adjusted by changing the plate thickness and flow channel height. Therefore three porosities 0.36, 0.50 and 0.64 are studied and the results of optimum frequency and aspect ratio for different hydraulic diameters are presented in Figure 4.16. The curve representing the porosity of 0.36 shows a similar pattern to that of the packed sphere bed. The optimum aspect ratio increases with the hydraulic diameter, while the optimum frequency decreases to a minimum and then increases. The maximum COP is around 9.0, which is higher than that of the packed sphere bed, when the hydraulic diameter is 0.10 mm, the frequency is 4.7 Hz and the aspect ratio is 2.1. It is found that higher frequency is preferable for the parallel plate matrix compared with the packed sphere bed.

In general, the maximum COP increases and the optimum frequency becomes smaller with the increase of porosity, which can also be seen in some results from Reference [59]. The highest COPs of regenerators using a parallel plate matrix are 10.0 and 11.2 for the porosities of 0.50 and 0.64, respectively, corresponding to optimum hydraulic diameters of 0.10 and 0.15 mm. With the same hydraulic diameter, increased porosity will lead to a decrease in the plate thickness and solid mass, where a smaller mass flow rate is needed and this may make the COP higher with the same specific cooling power. However, the porosity should not be too high in a real design, because the power density per unit volume is decreased, which reversely requires a large magnet apparatus to obtain the same cooling power.

The optimum hydraulic diameter for a parallel plate matrix is around 0.10 - 0.15 mm and the corresponding flow channel height ranges from 0.05 to 0.075 mm. Besides, a uniform chan-

nel size in the parallel plate matrix is desired otherwise the flow mal-distribution may reduce the overall heat transfer coefficient and efficiency significantly [64]. Those requirements make the fabrication difficult and become the barriers for applying the parallel plate matrix in the real prototypes.

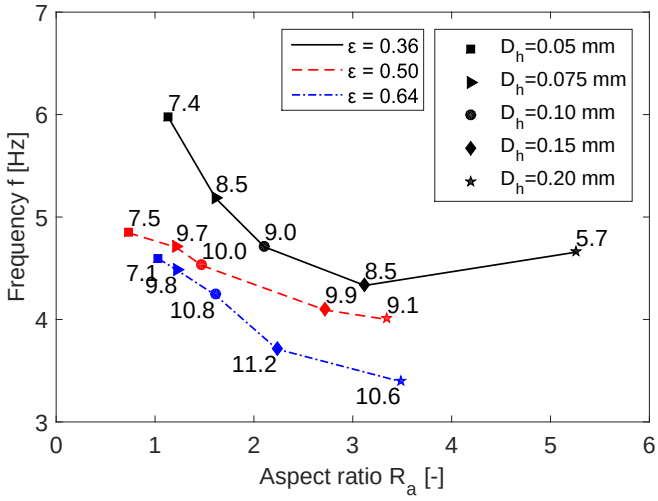

Fig. 4.16: Maximum COP (side-noted numbers) as well as optimum frequency f (vertical coordinate) and aspect ratio R_a (horizonal coordinate) for regenerators using parallel plate matrix under different hydraulic diameters D_h and porosities ε.

4.4.3 Micro-channel matrix

Since the circular and rectangular micro-channel matrices have similar characteristics, only the simulation results of the circular micro-channel matrix are presented. Figure 4.17 shows that the micro-channel matrix exhibits similar behavior as the parallel plate matrix. However, the best COP is lower, which is 7.8, 9.0 and 10.1 for different porosities. This is expected since the micro-channel matrix provides slightly smaller Nu/f_F compared to the parallel plate matrix. The optimum hydraulic diameter is 0.075 or 0.10 mm, which is also the optimal diameter of the circular channels.

Like the parallel plate matrix, the problems of fabrication and long term durability also exist. A regenerator with a monolithic perovskite structure fabricated by extrusion process has been tested [74] with a channel size around 1 mm. This was much larger than the optimum channel size in this study and in addition it revealed a problem of structure collapsing during sintering. Moore et al. [75] used selective laser melting technology to fabricate a wavy-channel block and an array of fin-shaped rods. The minimum channel diameter was around 0.8 mm and corrosion problems were reported.

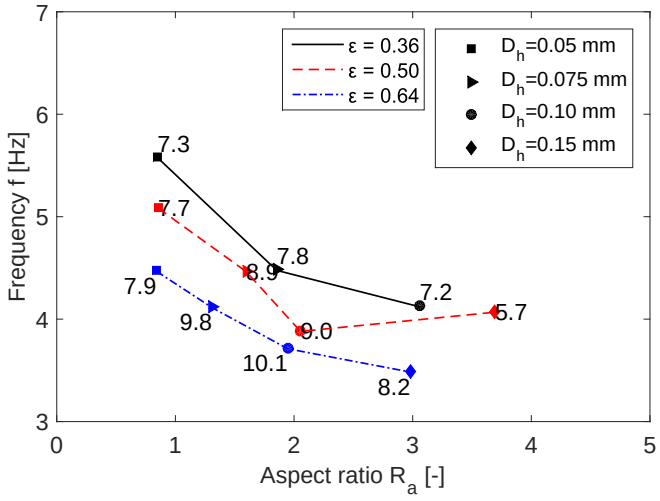

Fig. 4.17: Maximum COP (side-noted numbers) as well as optimum frequency f (vertical coordinate) and aspect ratio R_a (horizonal coordinate) for regenerators using micro-channel matrix under different hydraulic diameters D_h and porosities ε.

4.4.4 Packed screen bed

Compared with the packed sphere bed, the channels in the packed screen bed are more structured, giving an equivalent heat transfer performance but significantly lower pressure drop, as shown in Figure 4.13 (c). The tortuous structure is capable of relieving the problem of the flow mal-distribution as compared to the parallel plates. Another advantage of the packed screen bed is relatively low axial conduction due to the stacked structure, which is not discussed in detail here. Figure 4.18 shows the performance of AMRs using a packed screen bed. It can be seen that the optimum frequency approaches that of the packed sphere bed, which is lower compared with the parallel plate and micro-channel matrices. With a porosity of 0.36, the packed screen bed could provide the best COP around 7.7, which is higher than the packed sphere bed. At this point, the optimum frequency is 2.0 Hz and the aspect ratio is 3.3. With increased porosity, the best COP increases considerably to 8.9 and 9.6 for the porosities of 0.50 and 0.64, respectively.

Although it is difficult to fabricate the woven screens with existing MCM materials like Gd or ceramics, there is a probability of producing a similar geometry like a packed felt bed in the future. Table 4.4 summarizes the best COP of regenerators using different geometries and it is clearly seen that the other three geometries could provide higher efficiency at the optimum points compared with the packed sphere bed.

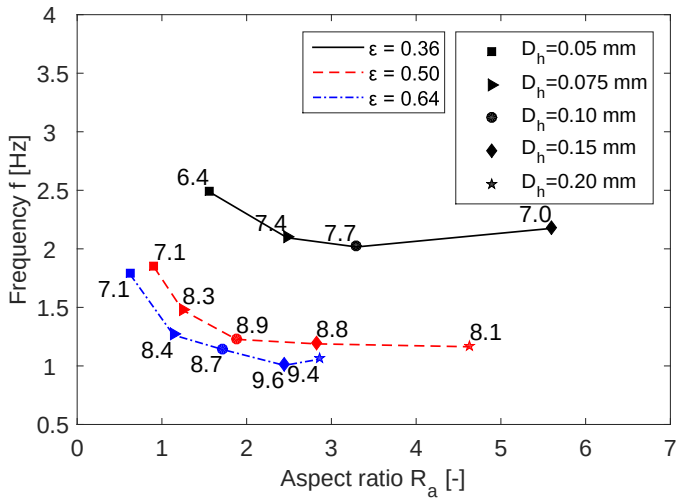

Fig. 4.18: Maximum COP (side-noted numbers) as well as optimum frequency f (vertical coordinate) and aspect ratio R_a (horizonal coordinate) for regenerators using packed screen bed under different hydraulic diameters D_h and porosities ε.

Table 4.4: Best performance and optimum parameters for different regenerator geometries.

Geometry	Porosity ε	Hydraulic diameter D_h [mm]	Aspect ratio R_a	Frequency f [Hz]	COP
Packed sphere bed	0.36	0.075	1.0	2.3	7.6
Parallel plate matrix	0.36	0.100	2.1	4.7	9.0
	0.50	0.100	1.5	4.5	10.0
	0.64	0.150	2.2	3.7	11.2
Micro-channel matrix	0.36	0.075	1.9	4.5	7.8
	0.50	0.100	2.1	3.8	9.0
	0.64	0.100	2.0	3.7	10.1
Packed screen bed	0.36	0.100	3.3	2.0	7.7
	0.50	0.150	1.9	1.2	8.9
	0.64	0.150	2.4	1.0	9.6

4.5 Summary

The analysis of loss mechanisms and the optimization of regenerator geometries for application in magnetocaloric refrigeration have been presented based on a 1D numerical model.

The entropy production rates due to the three main loss mechanisms, insufficient heat transfer, viscous dissipation and axial conduction, as well as the total entropy production rates, are calculated and compared. It is shown that insufficient heat transfer is more sensitive to the frequency while the viscous dissipation is more affected by the aspect ratio. The conduction loss becomes significant when the aspect ratio is less than 1.0. It is also found that the minimum total entropy production rate fits the maximum COP.

Moreover, the influence of heat loss through the regenerator housing is quantified. The heat transfer between the fluid and the wall could lead to a performance reduction, due to the heat transfer with wall and the heat conduction inside the wall, although the boundary to the ambient is adiabatic. The impact of the heat transfer between the wall and ambient is also evaluated, revealing a big negative influence on both specific cooling power and COP.

Another loss mechanism, that is, the dead volume, is discussed. With increasing dead volume ratio, both specific cooling power and COP decreases significantly when the flow rate locates in the design region. A tolerant maximum dead volume ratio of 0.10 is suggested for maintaining a proper cooling performance.

The optimization results show that with a specific cooling power of 100 W/kg, the maximum COP of regenerators using a packed sphere bed varies with the hydraulic diameter. The optimum frequency decreases while the optimum aspect ratio increases with the increasing of the hydraulic diameter. For a small hydraulic diameter of 0.05 mm, the COP changes significantly with the aspect ratio while it is less sensitive to the frequency. In contrast, the COP becomes more sensitive to the frequency when the hydraulic diameter is equal to or larger than 0.15 mm. For the packed sphere bed, the optimal COP is 7.6 when the hydraulic diameter, frequency and aspect ratio are 0.075 mm, 2.3 Hz and 1.0, respectively.

In general, the parallel plate matrix, micro-channel matrix and packed screen bed show better performance than the packed sphere bed. With a constant porosity, the optimum aspect ratio increases with the hydraulic diameter and the optimum frequency decreases in most cases. Higher porosity may result in an increase in the maximum COP and the optimum frequency becomes smaller. Although the regenerators based on parallel plates or micro-channels provide higher theoretical efficiency compared to packed sphere beds, the fabrication of small channel size with often very brittle composite magnetocaloric material and the effect of flow mal-distribution may become barriers to a real application. In contrast, the packed screen bed or similar matrix structure could be a promising geometry in that sense. The practical challenge in general is clearly to fabricate the required structures with the often very brittle composite magnetocaloric materials.

CHAPTER 5

Passive regenerator test apparatus

This chapter describes an experimental apparatus and the methodology for evaluating the flow and heat transfer characteristics of porous regenerators passively. That is, only the heat regeneration during oscillating flow is investigated and the magnetic field is not applied. Section 5.1. presents a brief introduction to the passive regenerator test and the study goals of Chapters 5 and 6. In Section 5.2, the construction of a regenerator test apparatus and an affiliated control / measurement system is described. Section 5.3 addresses the methodology and the data processing for characterizing different regenerators. Finally, the chapter is summarized in Section 5.4.

5.1 Introduction

The principle of heat regeneration and the regenerator has been extensively used in many thermal devices. The regenerator is a temporary heat storage system made of a porous solid matrix, as shown in Figure 5.1. The porous structure with a large specific surface area allows the fluid flow through and transfer heat with the solid matrix. Figure 5.2 gives the simulation result of a liquid saturated regenerator, for illustrating the oscillating flow operation. The model in Chapter 2 is modified and used here to simulate the passive regenerator, where the magnetocaloric effect is turned off. The fluid velocity curve in the simulation is close to a sinusoidal wave as seen in Figure 5.2 (a). Here positive velocity represents the hot-to-cold blow and vice versa. Figure 5.2 (b) shows the dynamic response of the inflow and outflow temperatures in one cycle, after periodic steady state is reached. During the hot-to-cold blow period illustrated in Figure 5.1 (a), the fluid with constant temperature, which is also the hot reservoir temperature T_h, is blown through the regenerator and cooled down by the solid matrix. In Figure 5.2 (b), the hot-to-cold blow locates at the time period from 0 to 0.5 s approximately. Conversely in the cold-to-hot blow, the fluid with a temperature of T_c (cold reservoir temperature) is heated up by the solid, as shown in Figure 5.1 (b) and Figure 5.2 (b) when the time ranges from 0.5 to 1.0 s.

Typical applications of regenerators include the active magnetic regenerators [35], regenerative heat engines / coolers [107], power-plants [108], internal combustion engines [109], desiccant cooling [110] and emerging compressed air storage systems [111], etc. Although the regenerators in those thermal systems usually perform multiple functions, the basic one is still heat regeneration. An excellent example is the regenerator inside the regenerative cryocooler [107], in which the gas is pre-cooled / heated up by the packed sphere bed or packed screen bed before the expansion / compression process. This heat regeneration process is crucial for the regenerative refrigerator to reach ultra-low temperatures.

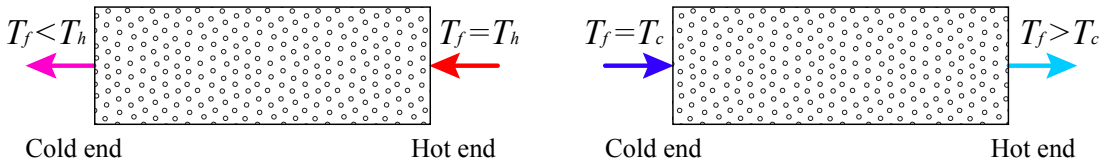

(a) Hot-to-cold blow (b) Cold-to-hot blow

Fig. 5.1: Schematic diagram of a regenerator in two blow periods.

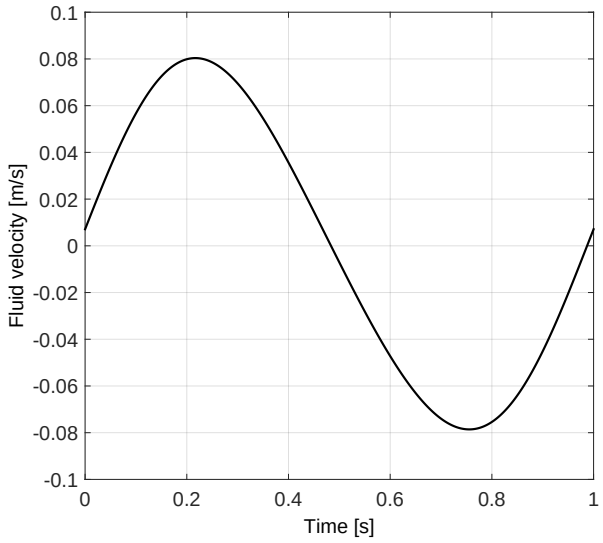

(a) Fluid velocity

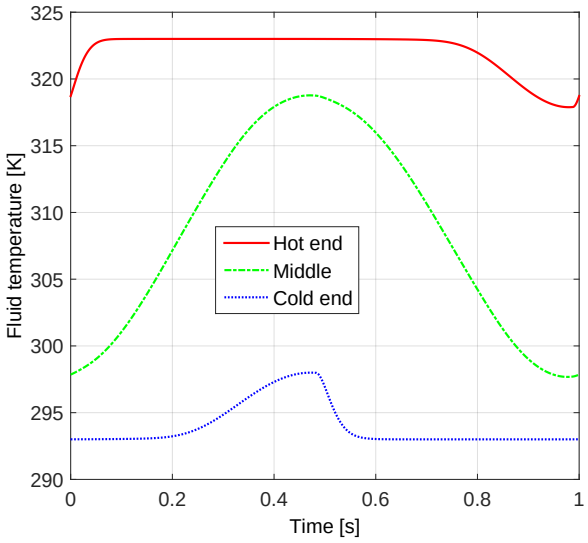

(b) Fluid temperature profiles along a regenerator

Fig. 5.2: Fluid velocity and temperature profiles along a regenerator with an oscillating flow based on numerical simulation.

As discussed in Chapter 4, a good regenerator in an MCR system requires the following characteristics: high heat transfer coefficient between fluid and solid, small thermal conduction in the axial direction, high volumetric heat capacity, which is the product of the density multiplied by the specific heat, and low flow resistance. Different parameters have been applied to evaluate those factors, such as the pressure drop ΔP, heat transfer coefficient h, effective thermal conductivity k_{eff}, effectiveness η, as well as the dimensionless group consisting of the Reynolds number Re_h, flow resistance f_F and Nusselt number Nu. A brief review is presented below, showing how to estimate some of the above-mentioned parameters.

The heat transfer coefficient between the solid and fluid h in the forced convection and the Nusselt number Nu are defined below:

$$h = \frac{\dot{Q}}{A(T_s - T_f)} \tag{5.1}$$

$$\mathrm{Nu} = \frac{hD_h}{k_f} \tag{5.2}$$

$$\tag{5.3}$$

where $\dot{Q}$, A, T_s, T_f, D_h and k_f are the heat flow, heat transfer area, solid temperature, fluid temperature, hydraulic diameter and thermal conductivity of the fluid, respectively. Those parameters can be estimated by either a unidirectional flow test with constant wall temperature / heat flux [96] [112], a single blow test [1] [113], or an oscillating flow test [114] [115]. In those tests, different approaches have been used to deduce h and Nu based on the measurement of the temperatures and the heat flux (optional).

The first approach, i.e., the unidirectional flow test with constant wall temperature / heat flux, has been extensively used to estimate the convective heat transfer coefficient in empty ducts or porous media. Park et al. [100] presented an apparatus to measure both the pressure drop and heat transfer coefficient of the packed screen bed. In the thermal test, a certain heat flux is applied from the thin wall to the test section with a unidirectional fluid flow. Afterwards, the temperature and the heat flux were recorded for deducing the heat transfer coefficient. Wakao et al. [87] did a comprehensive review on the heat transfer coefficient of the packed bed. A general correlation extending to the low Reynolds number region was proposed. Vafai [116] presented a thorough study of the convective flow and heat transfer in variable-porosity media. More examples are found in Refs. [96] and [112].

Schumann and Hausen [1, 95] developed the single blow test, which is an effective tool to estimate the heat transfer coefficient. In the test, the temperature of the regenerator bed is held constant and the fluid with another constant temperature is blown through the bed. The outflow temperature response is recorded and the heat transfer coefficient is deduced by matching the modeling results to the measured response. Heggs and Burns [113] reported this single blow experiment and compared four commonly used data reduction methods for predicting heat transfer coefficients. The least squares method was suggested for the data process. Engelbrecht [2] and Frischmann et al. [117] presented the experimental results of a single blow test of passive packed sphere regenerator using high Prandtl number fluids, where the conditions were close to those in AMRs.

The heat transfer performance can also be estimated by direct measurement of the temperature profiles inside the regenerator with an oscillating flow [97, 114, 115, 118]. Both the heat transfer coefficient h and effectiveness η can be deduced using this test. The effectiveness of a regenerator is the ratio of the amount of heat that is transferred during a blow process between the solid and the uid to the maximum possible heat transfer [119, 120].

Schopfer [114] studied the thermal-hydraulic properties of thermal regenerators under oscillating flow conditions. The dimensionless parameters, the friction factor and Nusselt number, in the microchannel and packed bed regenerators were estimated from an experiment based on a harmonic approximation technique. An interesting phase analysis was carried out

and it displayed the phase relation in such an oscillating flow system using liquid. Trevizoli et al. [115] presented a laboratory apparatus for testing passive regenerators using water as the thermal fluid. The fluid pumping power and the regenerator effectiveness as a function of operating parameters such as frequency and utilization ratio were presented. The results showed that a gadolinium sphere bed exhibiting a relatively large effectiveness imbalance due to strong temperature dependence of the specific heat capacity. Nielsen et al. [63] investigated the influences brought by the regenerator housing based on a 2D numerical model, especially at low Reynolds and large Prandtl numbers. The results showed that the regenerator effectiveness decreases significantly at low Reynolds numbers due to the thermal impact of the regenerator housing. Beck [121] investigated the transient operation of the regenerators and estimated the fraction of an operating cycle during which the regenerator will have reduced effectiveness. Daney [122] studied the ineffectiveness of regenerators with sinusoidal laminar flow through parallel plate, screen and packed sphere matrices. Tanaka et al. [97] evaluated the regenerator efficiency and the mean heat transfer coefficient by measuring the periodic temperature variation at both ends of the regenerators in an oscillating gas flow. Golombok et al. [123] investigated the convective heat transfer properties of a porous regenerator packed with metallic fiber material. The heat transfer coefficient was measured using a non-steady-state method based on cyclic counter-flow heat regenerator theory. In addition, the flow resistance can be calculated from the pressure drop over the regenerator measured in either the unidirectional flow [100] or the oscillating flow [115, 124].

Most of the existing studies were implemented using unidirectional flow and gas-saturated regenerators. Only a few works focused on the regenerator using high Prandtl number liquids with an oscillatory flow. Aimed at the applications of AMRs, this study experimentally investigates regenerators using heat transfer liquids with an oscillating flow. Moreover, the emerging epoxy bonded beds have been used to increase the mechanical strength of regenerators using FOPT materials such as $La(Fe,Mn,Si)_{13}H_y$. The active testing has been performed, but investigating the flow and heat transfer characteristics of such epoxy glued regenerator is not presented yet, which is one of the main purposes of this test apparatus.

5.2 Test apparatus

This section describes the construction of a passive regenerator test apparatus or an accompanying measurement / control system. In the design, the test apparatus is composed of five main sections: the oscillating flow generator, the regenerator test section with sensors, the cold heat exchanger with a cold reservoir, the heater with a power supply and the affiliated system for loading fluids / pressurizing. The schematic diagram and a photograph of the test apparatus with those five sections are presented in Figure 5.3.

In detail, the regenerator test section includes a porous regenerator bed (REG), four check valves (CV), thermocouples (T) and two piezoelectric pressure gauges (P), as shown in Figure 5.4. The oscillating flow generating section is made up of a motor-crank system (MT) and two cylinders (CYL 1 and 2). The cold heat exchanger (CHX) is double-pipe type. The cold water with constant temperature is circulated from the cold reservoir to the shell side of CHX, while

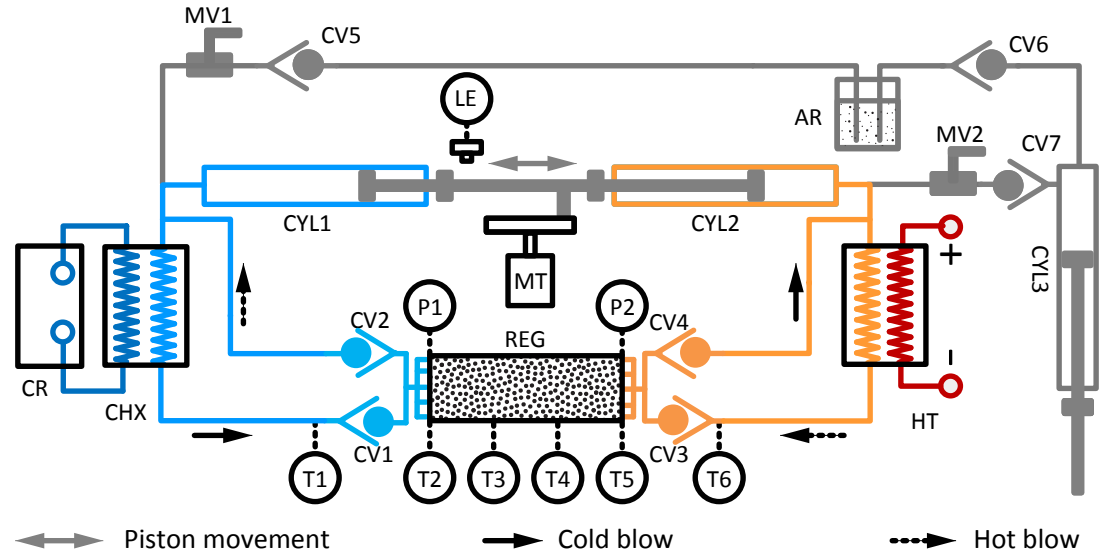

(a) Schematic diagram

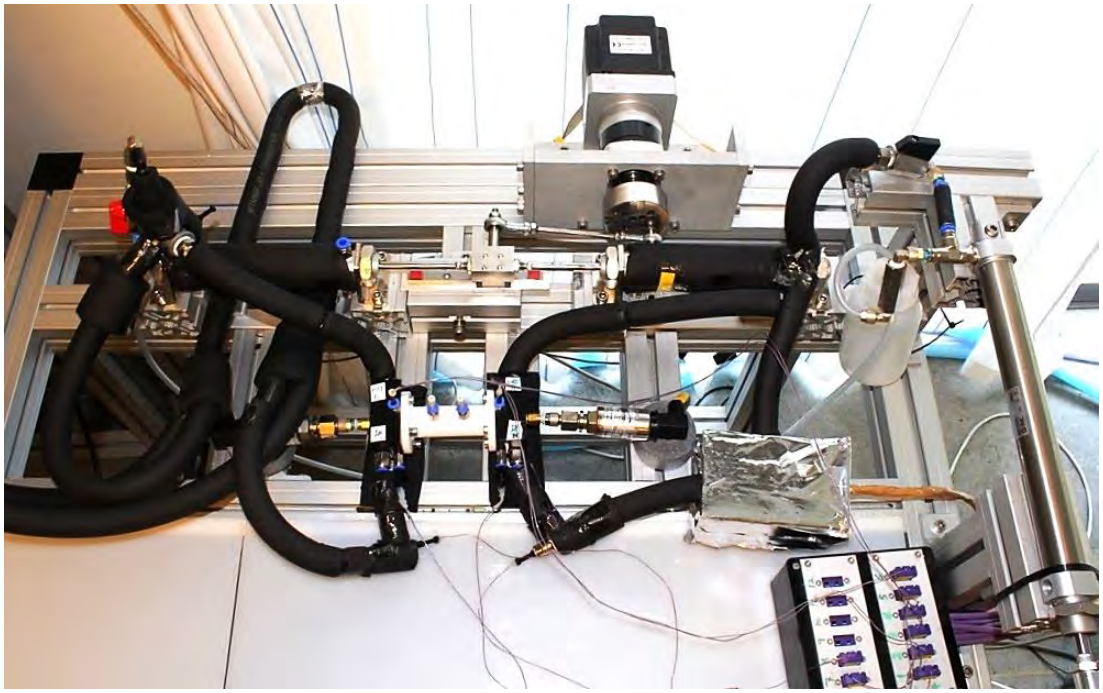

(b) Photograph

Fig. 5.3: Schematic diagram and photograph of the experimental apparatus for testing the passive regenerators using different porous geometries and heat transfer fluids. The labels represent: AR ambient reservoir; CHX cold heat exchanger; CR cold reservoir with circulating pump; CV check valve; CYL cylinder; HT heater; LE linear encoder; MT motor and crank; MV manual valve; P pressure gauge; REG regenerator; T thermocouple. The solid and dashed black arrows show the direction of the flow movement during the cold and hot blows, respectively.

the heat transfer fluid is cooled down flowing through the inner tube. At the hot end, the heater (HT) for heating up the fluid is made by inserting and sealing an electrical cartridge heater into a small enclosed chamber. The linear encoder (LE), thermocouples and pressure gauges are used to record the movement of the piston, flow temperatures as well as pressure drop over the regenerator. The main components are listed in Table 5.1.

Table 5.1: Main components in the passive regenerator test apparatus.

Items	Material or mode type
Filling materials	Stainless steel particles
	Epoxy bonded La(Fe,Mn,Si)$_{13}$H$_y$ regenerator
Regenerator housing	3D printed nylon by Sinterstation 2500+ selective laser sintering (SLS) printer
Regenerator lids	Acrylonitrile butadiene styrene (ABS) polymer
Check valves	SMC AKH check valve
Cold heat exchanger	Double-pipe type made of copper tubes
Cold reservoir	Julabo FP refrigerated circulator
Heater	Omega HDC00186 cartridge heater
Power supply	TTi CPX400DP DC power supply
Motor	Fulling 86BLS71 brushless DC motor
Gear box	OEM PS2-B gear box
Motor controller	Technosoft iPOS4808 BX-CAN intelligent servo drive
Cylinder	SMC CD85N20-100-B cylinder
Piping	RS polyurethane hose
Insulation	Insulation foam provided by Weiss Isolering A/S
Pressure gauge	Gems 2.5 bar pressure gauge
Thermocouple	Omega duplex insulated thermocouple wire
Data acquisition interface	National Instruments LabVIEW, NI cDAQ 9174, NI 9213 thermocouple module, NI 9203 current module

As shown in Figure 5.5, the motor-crank system drives two cylinders (CYL1 and CLY2) to absorb and push the fluid, respectively. The reciprocating movement generates an oscillating flow through the porous bed of the regenerator in one regenerative cycle. In the cold-to-hot blow period, represented by the solid arrow in Figure 5.3(a), the fluid is pushed from the CYL1 and cooled down to the CHX. Afterwards, it is blown through the CV1, REG, CV4 and stored in the CYL2 in the end. While in the hot-to-cold blow marked with dashed line, the fluid flow starts from the CYL2, and then the HT, CV3, CV2 and CYL1. The electric heater is used to heat the fluid during the hot-to-cold blow period. On each side of the regenerator, two check valves are set to separate the inflow and outflow, respectively. This configuration also ensures unidirectional flows in both cold heat exchanger and heater, as well as the constant inflow temperatures at both ends of the regenerator.

The piston displacement x_p as a function of time t and piston stroke S_p can be calculated by:

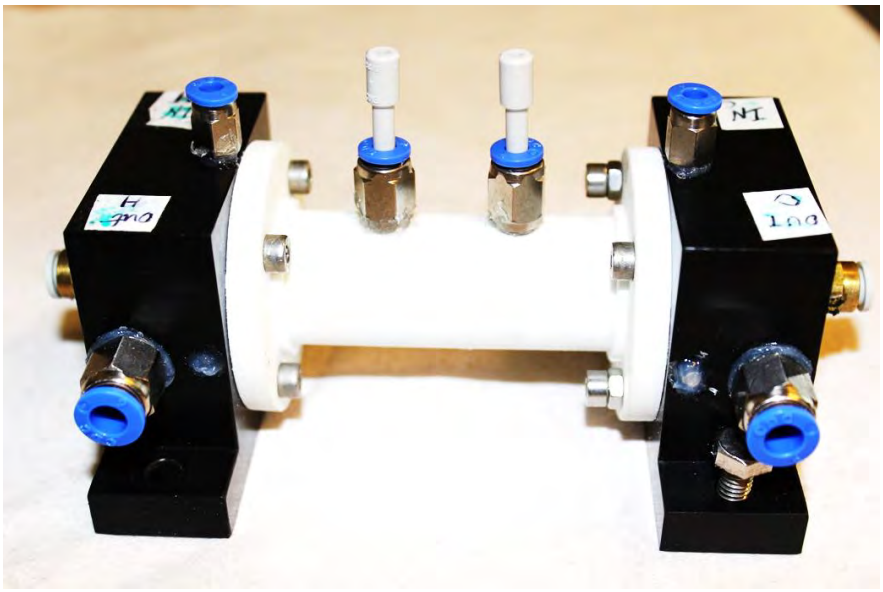

(a) Regenerator test section

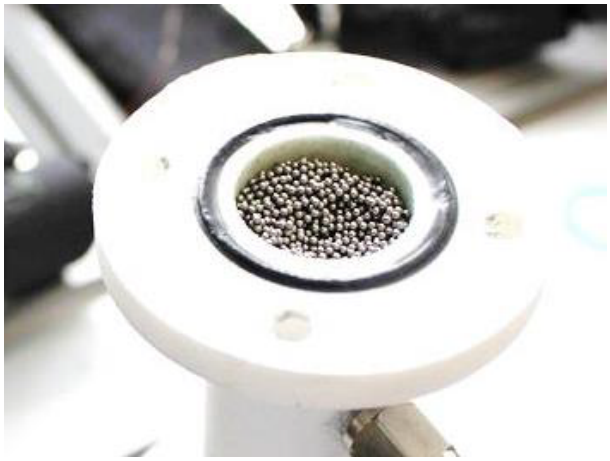

(b) Packed sphere bed

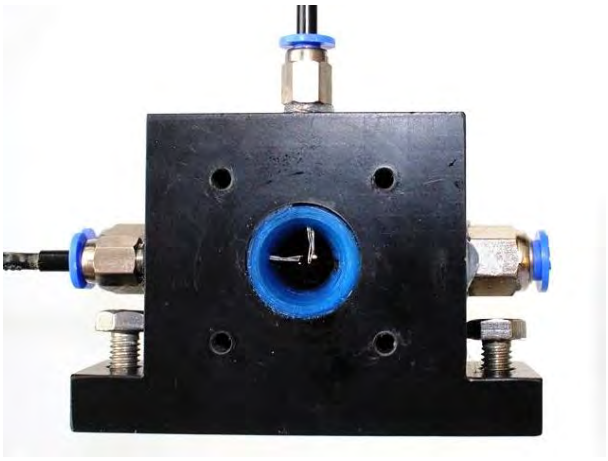

(c) Inserted thermocouples

Fig. 5.4: Photograph of the regenerator test section, packed sphere bed and inserted thermocouples.

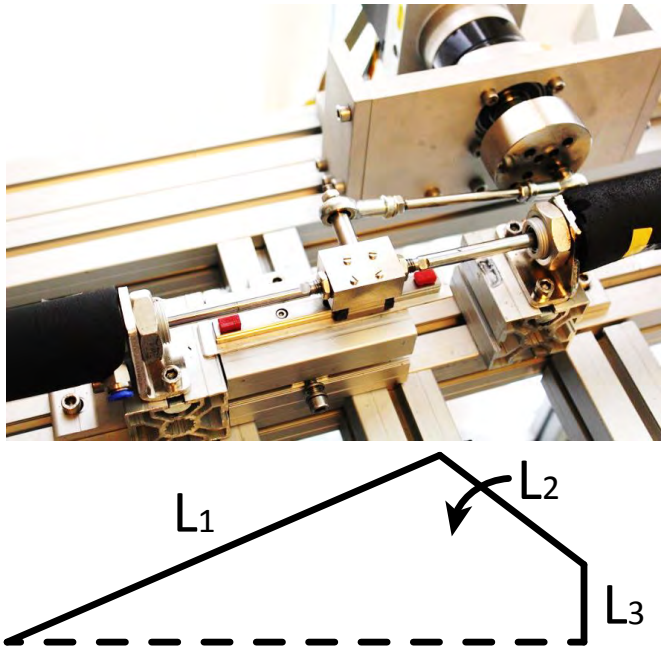

Fig. 5.5: Photograph and schematic diagram of the motor-crank system.

$$L_1 = \frac{S_p}{2} \tag{5.4}$$

$$x_p(t) = L_2 + L_1 - \sqrt{L_2^2 - (L_3 + L_1 sin\omega t)^2} - L_1 cos\omega t \tag{5.5}$$

where L_1, L_2 and L_3 are the length of the rotating arm, length of the swing arm and the displacement between the motor center and piston movement plane. A long swing arm, i.e., large L_1, is used to ensure $x_p(t)$ is an approximate sinusoidal wave. This movement is recorded by a linear encoder with an Arduino micro-controller and presented in Figure 5.6.

During operation, the outflow of the cold reservoir is held constant by a chilling system. The temperature span will be built up along the regenerator by applying a heating power at the heater section. After several cycles, the oscillating flow system will reach a periodical steady state with a certain temperature span. For each steady state, the temperature profiles along the regenerator, heating power and pressure drop are recorded for further analysis.

E-type thermocouples are used in the test apparatus and calibrated in a water bath before being applied. The temperature data are recorded by the NI 9213 thermocouple module and NI cDAQ 9174. The temperature span is limited to 60 °C and the measurement error is estimated as ± 0.3 °C. Figure 5.7 gives the time response of different thermocouples. In the test setup, the exposed thermocouples with a wire diameter of about 0.25 mm are used and they give a response time less than 0.15 s, which is almost the fastest response time.

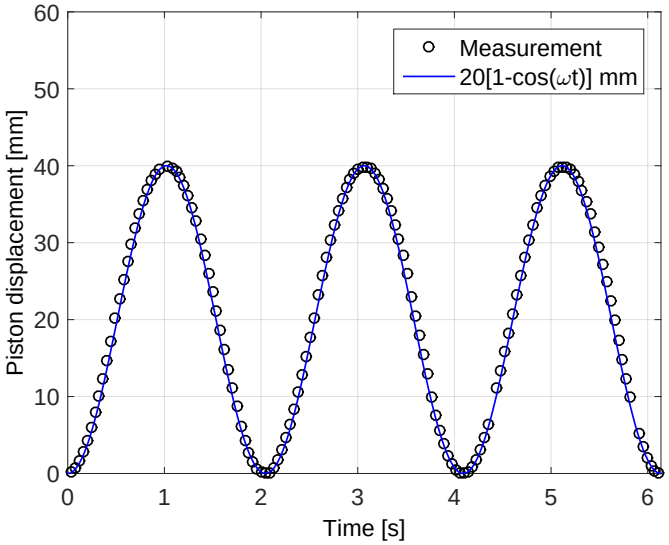

Fig. 5.6: Measured piston movement by a liner encoder and calculated positions assuming a long swing arm.

The calibrated pressure gauges have an accuracy of 0.25 % FS (full scale) and the signal is acquired by the NI 9203 current module. The response time of the pressure gauges is 0.5 ms. The power supply for the heater has a meter accuracies of $\pm$ 0.1% in voltage and $\pm$ 0.3 % in current.

Note that the two-cylinder design is adopted to avoid conduction losses through the piston rod and the shuttle loss caused by the temperature difference between the cylinder wall and the moving piston, which occurs in the one-cylinder design. To reduce the heat loss to the ambient, all the surfaces are thermally insulated by the insulation annular tube provided by Weiss Isolering A/S. In addition, a primary test is performed to specify the heat loss by changing the cold reservoir temperature and turning off the heating power. Due to the heat loss, a small temperature span is observed as shown in Figure 5.8 when the cold reservoir temperature deviates from the ambient temperature of about 25 °C. Therefore the temperature span is controlled to be close to the ambient temperature in the operation.

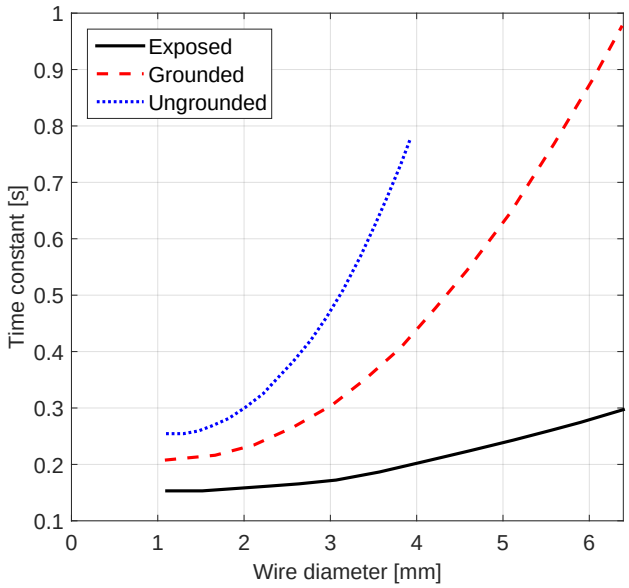

Fig. 5.7: Time response of metal sheathed thermocouple probe in water, where the time constant is defined as the time required to reach 63.2 % of an instantaneous temperature change. [125] ("Exposed" means that the wires are exposed to the environment; "grounded" means the wires contact with the metal sheath; "ungrounded" means the wires are isolated from the metal sheath.)

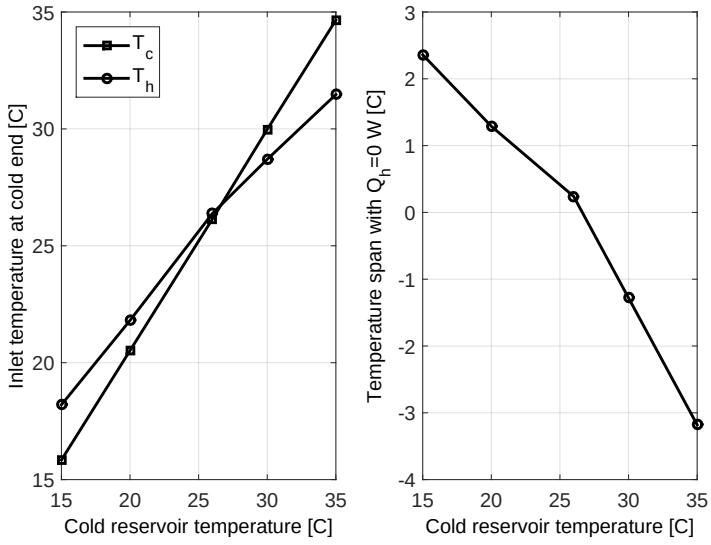

Fig. 5.8: Impact of cold reservoir temperature on temperature span, when the heating power is zero.

5.3 Methodology

Figure 5.9 shows an example of the measured pressure drop data as a function of time, as well as the piston velocity calculated from the measured piston displacement data. Both curves behave similarly to the sinusoidal wave. However, there is a certain phase difference between the piston velocity and the pressure drop over the regenerator, even though an incompressible fluid is used. This effect has been observed and mainly studied in gas-saturated regenerators. Schopfer [114] presented an analysis on the phase difference in the liquid-saturated regenerators. Note there are very few bubbles in the system, which can also influence the phase difference.

The original pressure drop is further fitted to a sinusoidal wave and the peak-valley amplitude, i.e., the maximum pressure drop, is presented in Chapter 6. Correspondingly, the maximum superficial velocity is used to calculate the Reynolds number for obtaining the dimensionless correlation.

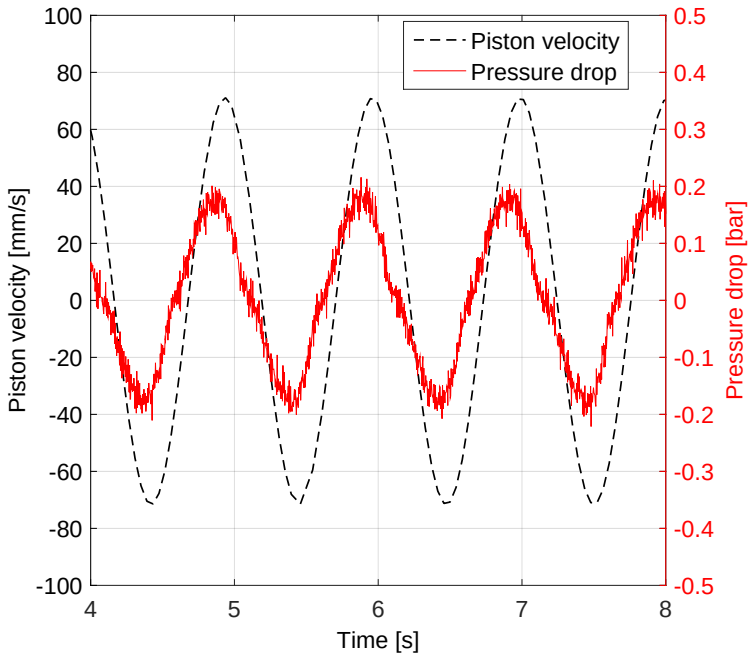

Fig. 5.9: Measured pressure drop and piston velocity calculated from the measured piston displacement.

The dimensionless friction factor is defined as:

$$f_F = \frac{dP}{dx}\frac{2D_h}{\rho_f v_s^2} \tag{5.6}$$

where dP/dx, D_h, ρ_f and v_s are the pressure drop per unit length, hydraulic diameter of the

channels, density and superficial velocity, respectively. Note that this definition varies in literature and the superficial velocity v_s, which is the product of the interstitial velocity multiplied by the porosity, is used here. In addition, the Reynolds number based on the hydraulic diameter and the superficial velocity is:

$$Re_h = \frac{\rho_f v_s D_h}{\mu_f} \tag{5.7}$$

$$v_s = \frac{\dot{m}_f}{\rho_f A_c} \tag{5.8}$$

where D_h, ρ_f, v_s, μ_f, $\dot{m}_f$ and A_c, are the hydraulic diameter, density, superficial velocity, dynamic viscosity, mass flow rate and cross sectional area, respectively.

An example of dynamic temperature profiles through the regenerator with an oscillating flow is illustrated in Figure 5.10, where T1 - T6 represent the positions from the cold to hot end as shown in Figure 5.4. Note that temperature profiles of passive regenerator are different from those in an active magnetic regenerator. In an active regenerator associated with the magnetocaloric effect, T2 should be lower than T1 and T5 higher than T6, representing the cooling load and the heat rejection at both ends, respectively. However, in a passive regenerator, the fluid rejects heat at the cold end, and absorbs heat at the hot end. Although the real AMR runs actively, the passive regenerator test can still be used to predict the general heat transfer characteristics of the regenerator.

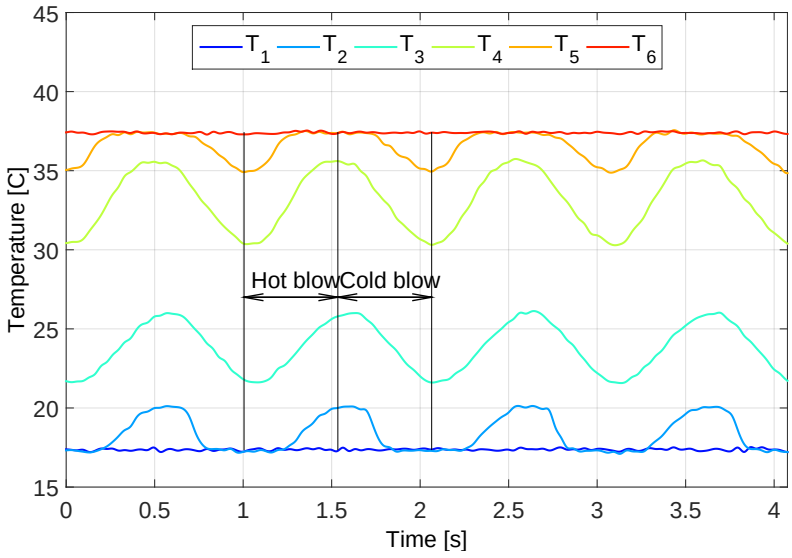

Fig. 5.10: Example of temperature profiles along a regenerator for calculating the effectiveness.

Moreover, the effectiveness can be calculated based on the measured temperature profiles.

Assuming that the specific heat capacity of the fluid is temperature independent, the effectiveness in each blow period is expressed as [115]:

$$\eta_c = \frac{2/\tau \int_0^{\tau/2} T_{f,h} dt - T_c}{T_h - T_c} \tag{5.9}$$

$$\eta_h = \frac{T_h - 2/\tau \int_0^{\tau/2} T_{f,c} dt}{T_h - T_c} \tag{5.10}$$

where $T_{f,h}$, $T_{f,c}$, T_h, T_c and τ are the outflow temperatures at both hot and cold ends, the inflow temperatures at both ends (or the reservoir temperatures) and the time period of one cycle. The effectiveness can be calculated from the temperature response and it directly reflects the heat efficiency of a regenerator. An ideal regenerator with infinite solid mass gives an effectiveness of 1, while real regenerators always give the effectiveness less than 1. In Figure 5.10, the hot-to-cold and cold-to-hot blow periods are marked and the effectiveness of two blows can be calculated based on Eqns. 5.9 and 5.10, where T_c, $T_{f,c}$, $T_{f,h}$ and T_h are T1, T2, T5 and T6, respectively.

Except for the effectiveness η, the dimensionless indexes, the utilization ratio U and the number of transfer units, will also be used for further analysis in this study. The utilization ratio is the ratio between the thermal mass of fluid moving through the regenerator to the total thermal mass of the regenerator solid. Due to a large heat capacity of water, the original definition of the utilization ratio in 5.11 is modified as shown below:

$$U_{original} = \frac{\dot{m}_f c_f \tau/2}{m_s c_s} = \frac{\rho_f c_f A_p S_p}{m_s c_s} \tag{5.11}$$

$$U = \frac{\dot{m}_f c_f \tau/2}{m_s c_s + \rho_f V_r \varepsilon c_f} = \frac{\rho_f c_f A_p S_p}{m_s c_s + \rho_f V_r \varepsilon c_f} \tag{5.12}$$

where c_f, c_s, m_s, A_p and V_r are the specific heat capacity of the fluid, specific heat capacity of the solid, solid mass, cross sectional area of the piston and regenerator volume, respectively. NTU describes the ratio of the amount of heat transferred between the solid and the fluid to the thermal mass of the fluid moved:

$$\text{NTU} = \frac{h a_s V_r}{\dot{m}_f c_f} \tag{5.13}$$

where a_s and V_r are the specific surface area and regenerator volume.

The effectiveness is a function of the utilization ratio and NTU, that is, $\eta = f(U, NTU)$. In general, high NTU and small utilization ratio lead to high effectiveness. High NTU means more heat is transferred and small utilization ratio indicates that less fluid is blown through the regenerator bed. Both effects lead to an outflow temperature closer to the reservoir temperature, therefore the effectiveness is closer to 1.

In many studies based on periodic flow heat exchangers and regenerators, the effectiveness η can be directly calculated from NTU and C^*. C^* is the ratio of the minimum to maximum heat capacity rate of the blown fluids. Those parameters form a dimensionless group describing the heat transfer phenomenon in heat regenerators. Kays and London [86] as well as Shah [126] presented the following empirical correlation, Eqn. 5.14, to demonstrate the effect of NTU_o and C^* on η of a heat regenerator:

$$\eta = \frac{1 - exp[-\mathrm{NTU}_o(1 - C^*)]}{1 - C^* exp[-\mathrm{NTU}_o(1 - C^*)]} \tag{5.14}$$

where NTU_o is the overall number of transfer unit. It can be rewritten as [86]:

$$\mathrm{NTU}_o = \frac{h a_s V_r}{C_{min}} = \frac{h a_s V_r}{(\dot{m}_f c_f)_{min}} \tag{5.15}$$

where h, a_s, V_r, $\dot{m}_f$ and c_f is the heat transfer coefficient, specific surface area, regenerator volume, mass flow rate and specific heat capacity.

In the test, the heat transfer fluid is an aqueous solution with 20 v/v % ethylene glycol (EG) and the properties are calculated based on the commercial software EES (Engineering Equation Solver) [127], which has a relatively high accuracy. The temperature dependences of the properties, including the density, thermal conductivity, dynamic viscosity and specific heat capacity, are presented in Figure 5.11. Measured on a viscometer (Anton Paar Lovis 2000 M/ME), the heat transfer fluid gives a density of 1031 kg/m^3 and a dynamic viscosity of 1.77 mPa·s, which are close to the calculated data presented in Figure 5.11. The regenerators are run with a temperature span less than 40 °C, and the largest change in the local fluid temperature is less than 15 °C. Besides, the variation in the specific heat capacity due to temperature is small as seen in Figure 5.11 (d). A temperature difference of 20 °C results in $C^* = C_{min}/C_{max} = 0.99$, which is close to 1. Therefore, Eqn. 5.14 describing the effectiveness can be rewritten as:

$$\eta = \frac{\mathrm{NTU}_o}{\mathrm{NTU}_o + 1} \tag{5.16}$$

Thus, NTU_o becomes:

$$\mathrm{NTU}_o = \frac{\eta}{1 - \eta} \tag{5.17}$$

Moreover, the specific surface area a_s is expressed as:

$$a_s = \frac{4\varepsilon}{D_h} \tag{5.18}$$

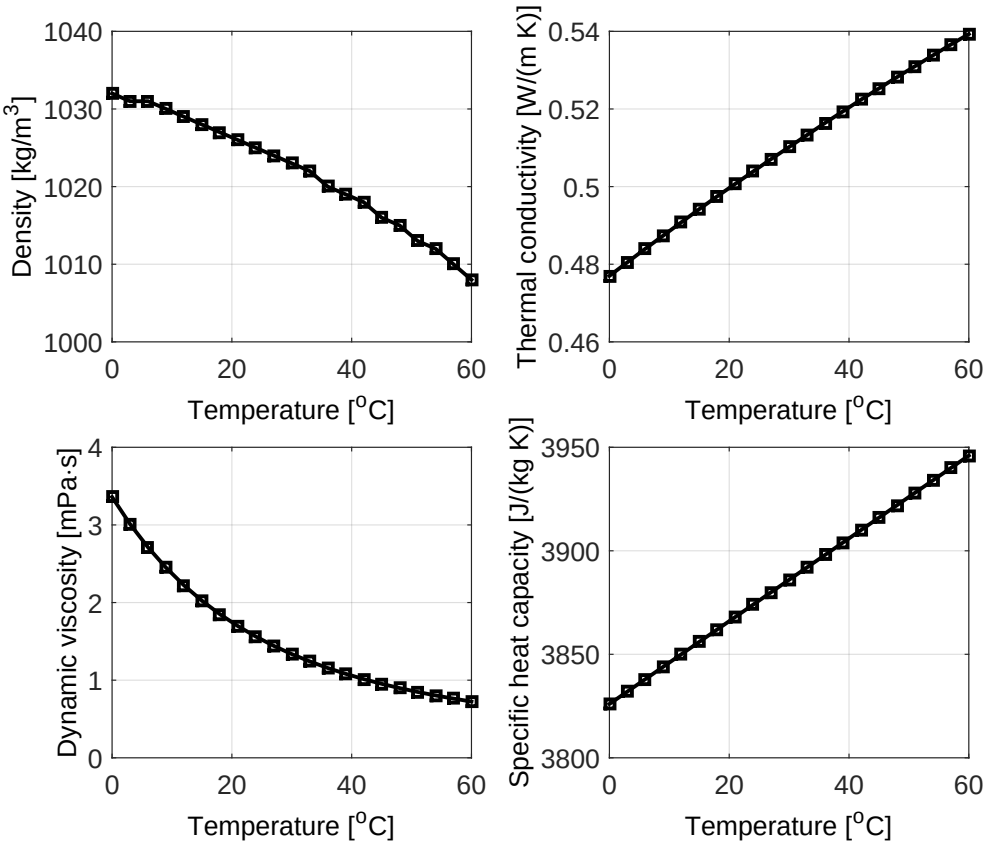

Fig. 5.11: Properties of aqueous solution with 20 v/v % ethylene glycol from EES [127].

Simplifying Eqns. 5.2, 5.15, 5.17 and 5.18 gives the overall Nusselt number Nu_o:

$$\mathrm{Nu}_o = \frac{\eta}{1-\eta}\frac{(\overline{\dot{m}_f c_f})_{min} D_h^2}{4\varepsilon V_r k_f} \tag{5.19}$$

Eqn. 5.19 can be used to estimate the overall Nusselt number in a regenerator with oscillating flow.

During operation, many parameters, such as the filling materials, regenerator size, frequency and stroke, can be changed to simulate different working conditions in AMRs. Corresponding outputs, including the pressure drop and temperature profiles, etc. are recorded or deduced to characterize regenerators. Table 5.2 summarizes those controllable variables and

outputs in the passive regenerator test.

Table 5.2: Variables and outputs of the passive regenerator test.

Variables	Outputs
Filling material and hydraulic diameter	Pressure drop and friction factor
Diameter and length of the regenerator	Temperature profiles
Piston stroke / displacing volume	Effectiveness of both blow periods
Frequency	Temperature span
Heating power	Utilization ratio
	overall Nusselt number

5.4 Summary

In the first section of this chapter, different methods to characterize the passive regenerators are briefly reviewed. The study objectives of Chapters 5 and 6, i.e., investigating passive regenerators using liquids in an oscillating flow and emerging epoxy glued regenerator, are introduced.

In addition, the construction of a passive regenerator test apparatus with a measurement / control system is described. The details of each section, which are the oscillating flow generator, the regenerator test section with measuring sensors, the cold heat exchanger with a cold reservoir, the heater with a power supply and the associated system for loading fluids, are presented. The main components used in the whole test apparatus are summarized.

Moreover, the methodology and the data processing for characterizing different regenerators are presented. Examples are given to show how to process the pressure drop data for calculating the friction factor, as well as to estimate effectiveness and overall Nusselt number.

CHAPTER 6

Experimental investigation of passive regenerators

This chapter presents the experimental investigation of passive regenerators based on the test apparatus described in Chapter 5. This study serves to provide a comparison of different regenerator geometries and heat transfer fluids for the design of upcoming MCR prototypes. Section 6.1 focuses on the experimental test of the commonly seen packed particle bed and the emerging epoxy bonded bed, by presenting the measured or deduced indices, including the pressure drop, friction factor, effectiveness, heating power and overall Nusselt number. Based on the same approach, the tests of different heat transfer fluids are implemented and the results are presented in Section 6.2. This chapter is summarized in Section 6.3.

6.1 Test of regenerator geometries

In this section, regenerators with different geometries, including packed particles and epoxy bonded beds, will be tested passively. The epoxy bonded beds are intended for increasing the mechanical strength of the regenerators. A typical case is the FOPT material La(Fe,Mn,Si)$_{13}$H$_y$. Although this material exhibits high entropy change as a promising material to be applied in future MCRs as discussed in Chapter 3, it has relatively low mechanical strength and may crack during the repeating de-/magnetization processes. For example, La(Fe,Mn,Si)$_{13}$H$_y$ exhibits a significant volume change up to $\approx$ 0.9 % during the magnetic phase transition [44], which may lead to the cracking of the particles and then the regenerator bed. To solve this problem, an approach of bonding MCM particles with the epoxy in the regenerator bed has been developed [38, 128, 129]. Bonded with small amount of epoxy, it is expected to increase the overall mechanical strength of the regenerator when keeping the continuous porous structure inside. Investigating the flow and heat transfer characteristics of such epoxy bonded regenerator is of importance for further application.

Several epoxy bonded La(Fe,Mn,Si)$_{13}$H$_y$ regenerators provided by Vacuumschmelze GmbH & Co. KG have been tested in a small magnetic refrigerator at DTU [44]. Figure 6.1 illustrates those regenerators bonded with different amounts of epoxy. The regenerator with 1 wt.% epoxy broke before the active testing as shown in Figure 6.1, while the others with more epoxy show better mechanical stability and maintain their structural integrity. The purpose of the regenerators shown in Figure 6.1 is to test different configurations in a small magnetic refrigerator and distinguish a regenerator optimal design that will be implemented in a scaled up magnetic heat pump. In addition to active testing of these regenerators, passive test is also important to isolate the heat transfer performance of each regenerator construction technique.

Fig. 6.1: $La(Fe,Mn,Si)_{13}H_y$ regenerators bonded with different amounts of epoxy for a reciprocating magnetic refrigerator at DTU.

As revealed in the literature, the cooling performance degrades with increasing amount of the epoxy [44], which may be attributed to the decreasing MCM volume and the possible reduction in the overall heat transfer performance. By improving the formulation of the epoxy glue, the mass can be reduced to as little as 1 wt.%, at the same time holding the mechanical strength. Therefore, 1 wt.% epoxy is applied in the regenerators tested in this study, which are more stable than the broken one shown in Figure 6.1. In general, 1-2 wt.% could be the optimal mass fraction considering the trade-off between the mechanical stability and the cooling performance for future application.

Two groups of $La(Fe,Mn,Si)_{13}H_y$ particles, i.e., irregular and spherical particles as shown in Figure 6.2 (a) and (b), are bonded with the epoxy and filled in regenerator housings for passive testing. Most particles in Figure 6.2 (a) have high degree of irregularity and the average size ranges from 0.2 to 0.9 mm. For the spherical particles, the size is about 0.4-0.8 mm. Both materials have Curie temperatures around 20 °C and densities about 7000 kg/m^3. In the first regenerator VAC-A, about 79 g of $La(Fe,Mn,Si)_{13}H_y$ irregular particles with 1 wt.% epoxy is loaded into a 3D-printed nylon housing, while 73 g of spherical particles are packed into the second regenerator VAC-B, using the same method. The housing has a length of 70 mm and a diameter of 20 mm. It is printed by the Sinterstation 2500 Plus Selective Laser Sintering (SLS) printer with a layer resolution of 0.1 mm. The housings are further treated to be watertight. The regenerators VAC-A and VAC-B have porosities around 0.46 and 0.48, respectively, which are estimated from the density and regenerator volume. The relatively high porosity is due to the relatively high irregularity of the particles and a low packing density.

As baseline experiments, four different stainless steel (SS) particles are also tested. Figure 6.3 presents the micrographs of those SS particles. Their sizes in the labels are determined by a homemade graphic analysis tool. The particle sizes of the first three groups are controlled by sieving. The last group uses 1 mm precise stainless steel balls, in which the diameter variation is quite small as shown in Figure 6.3 (d). For the regenerators using a packed particle bed, the SS particles are loaded randomly into the same housing and stopped by one piece of thin stainless steel woven screen at each end. About 112 - 116 g stainless steel particles are packed into those regenerators as illustrated in Figure 6.4. They give porosities around 0.34 - 0.37,

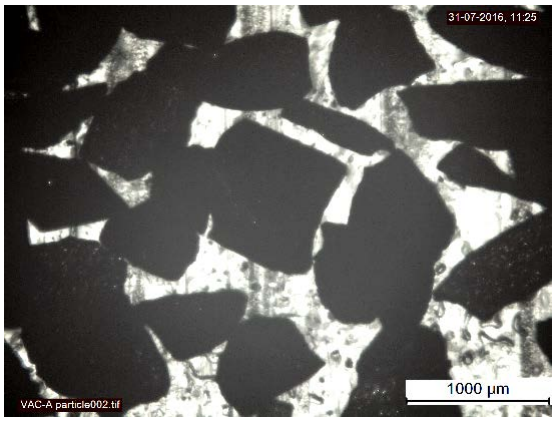

(a) $La(Fe,Mn,Si)_{13}H_y$ irregular particles

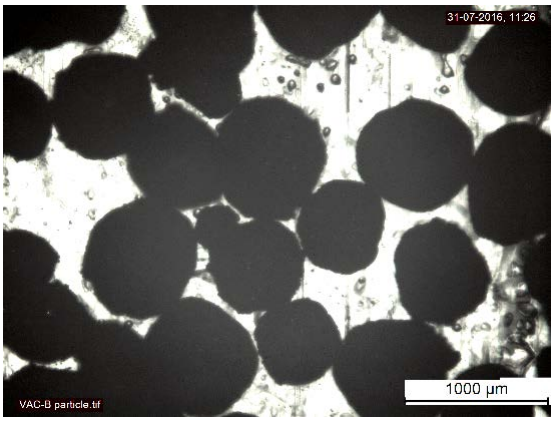

(b) $La(Fe,Mn,Si)_{13}H_y$ spherical particles

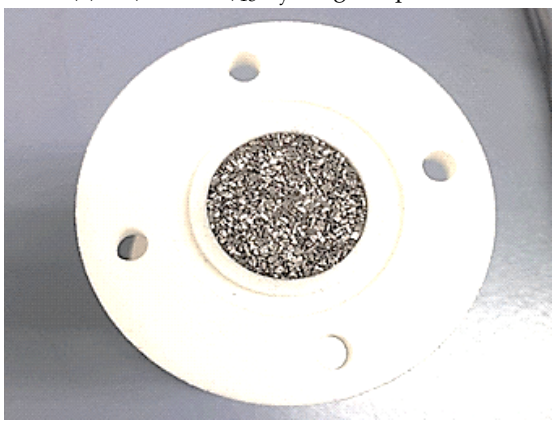

(c) Epoxy bonded regenerator loaded with $La(Fe,Mn,Si)_{13}H_y$ irregular particles (VAC-A)

(d) Epoxy bonded regenerator loaded with $La(Fe,Mn,Si)_{13}H_y$ spherical particles (VAC-B)

Fig. 6.2: $La(Fe,Mn,Si)_{13}H_y$ particles and epoxy bonded regenerators for passive testing.

although the particle sizes vary. This estimated porosity is close to the results reported in Ref. [130].

In this study, the regenerator volume is held constant. Direct comparison of the pressure drop, effectiveness and heating power reflects the overall flow and heat transfer performance, although the porosities of the packed particle beds and the epoxy bonded beds are different. Furthermore, the dimensionless groups, consisting of friction factor, overall Nusselt number and Reynolds number, are also presented here for general comparison.

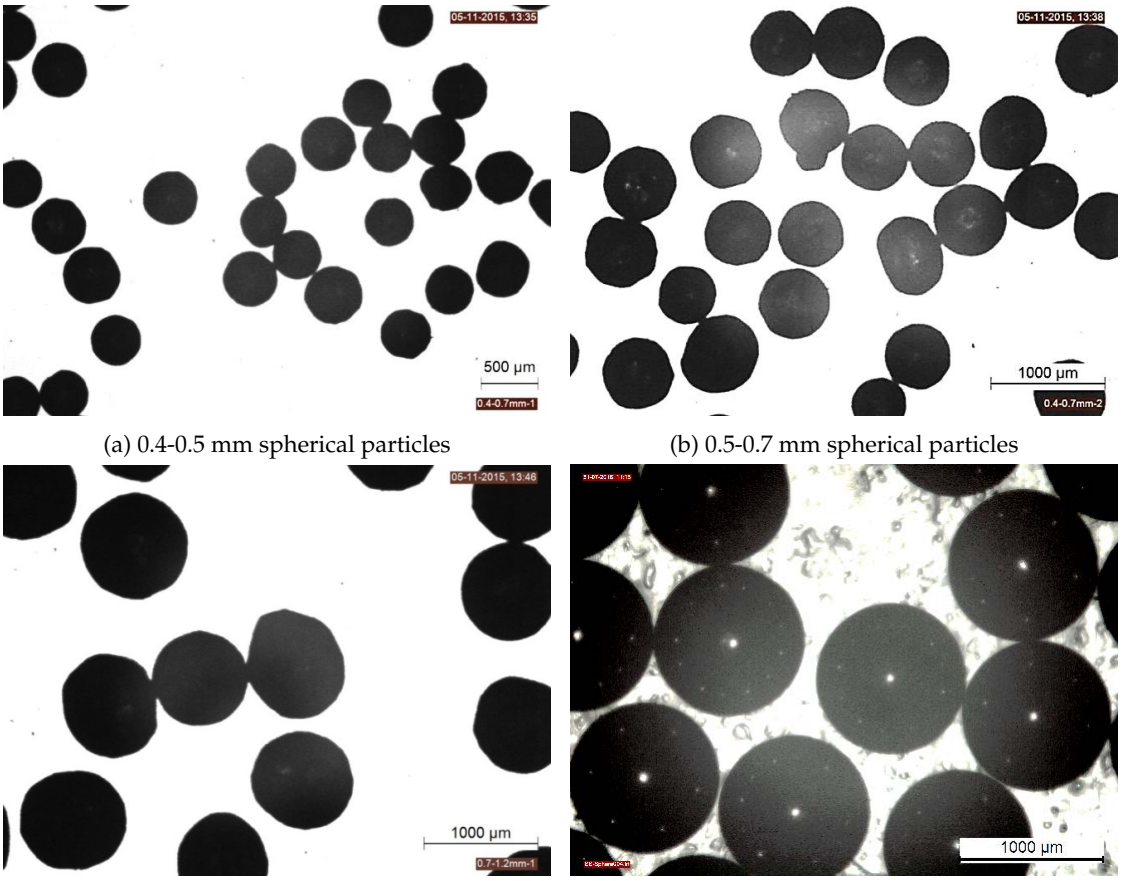

(a) 0.4-0.5 mm spherical particles

(b) 0.5-0.7 mm spherical particles

(c) 0.8-1.0 mm spherical particles

(d) 1mm precise balls

Fig. 6.3: Four stainless steel particles for the passive regenerator test.

As presented in Chapter 5, the effectiveness, overall Nusselt number, and friction factor can be estimated based on Eqns. 5.9, 5.10, 5.19 and 5.6, where the hydraulic diameter is necessary. For the packed bed with spherical particles, the hydraulic diameter is calculated by:

$$D_h = \frac{2\varepsilon}{3(1-\varepsilon)} D_{sp} \tag{6.1}$$

Fig. 6.4: A regenerator packed with stainless steel particles.

where D_{sp} is the sphere diameter.

The average particle diameters for the four stainless steel particles are estimated as 0.45, 0.6, 0.9 and 1.0 mm, respectively. This estimation is relatively accurate, due to a small variation in the particle sizes and the spherical shape.

However, the hydraulic diameter D_h and specific surface area a_s of two epoxy bonded $La(Fe,Mn,Si)_{13}H_y$ regenerators are difficult to identify. Here the average particle sizes are estimated to be 0.55 and 0.6 mm respectively, regardless of the particle size distribution. Eqn. 6.1 is still used to calculate the hydraulic diameters of those two beds, based on the estimated average particle sizes and porosities. Note that this estimation will bring a huge uncertainty into the calculation of dimensionless parameters. Therefore, the overall Nusselt number is used as an estimated comparison parameter for different regenerators and it is not meant as an accurate experimental measurement of the friction factor and overall Nusselt number for each regenerator.

The main parameters for testing the regenerators are listed in Table 6.1. In general, the utilization ratio is adjusted by changing the piston stroke, as shown in Eqn. 5.12. The velocity inside the regenerators depends on both the stroke and frequency. The maximum operating frequency is limited to 1.5 Hz in this study, as the flow resistance over the whole system increases significantly at high frequency.

Table 6.1: Main parameters for the passive regenerator test.

Parameter	Value
Filling material	0.4-0.5 mm stainless steel particles
	0.5-0.7 mm stainless steel particles
	0.8-1.0 mm stainless steel particles
	1 mm stainless steel precise balls
	Epoxy bonded $La(Fe,Mn,Si)_{13}H_y$ irregular particles
	Epoxy bonded $La(Fe,Mn,Si)_{13}H_y$ spherical particles
Material mass	112-116 g for packed particle beds
	73-79 g for epoxy bonded beds
Porosity	0.36-0.37 for packed particle beds
	0.46-0.48 for epoxy bonded beds
Piston stroke	10-40 mm
Piston diameter	20 mm
Volume of cold heat exchanger	14.1 cm^3
Volume of heater	10.8 cm^3
Heating power	0-120 W
Operation frequency	$<$1.5 Hz
Operation temperature	10-60 °C
Thickness of regenerator housing	3 mm
Diameter of regenerator	20 mm
Length of regenerator	70 mm
Heat transfer fluid	Aqueous solution with 20 v/v % ethylene glycol

6.1.1 Pressure drop and friction factor

High pressure drop leads to large pump power and viscous dissipation, which is one of the main losses in AMRs, as discussed in Chapter 4. Too high pressure drop over the regenerator is also a barrier for the system design, as the whole fluid distribution system and regenerator housings must be designed accordingly. In addition, increasing the thickness of the regenerator housing results in increased air gap in the magnetized volume, and then a significant decrease in the average applied magnetic field. Therefore, estimating the pressure drop over the regenerator bed should be carefully done during the design.

Figure 6.5 gives the maximum pressure drop data over the regenerators packed with different stainless steel particles. During the measurements, the stroke is adjusted from 15 to 40 mm and the frequencies are set from 0.50 to 1.25 Hz with a step of 0.25 Hz. As seen in the labels, the real frequency of the motor-crank system is slightly lower than the desired value. The cold reservoir temperature is set as 20 °C in all tests, which is close to the ambient temperature around 21 - 25 °C. The heat transfer fluid is an aqueous solution with 20 v/v % ethylene glycol. The results show that the pressure drop increases largely with increasing stroke S_p and frequency f, since the piston velocity $v_p \approx \pi f S_p cos(2\pi f t)$ is strongly related to these two parameters.

The pressure drop data over the epoxy bonded regenerators are presented in Figure 6.6. The regenerator VAC-B packed with spherical particles exhibits lower pressure drop than VAC-A generally. The pressure drop over VAC-A is close to the case with 0.5-0.7 mm SS spherical particles, comparing Figures 6.5 with 6.6. In addition, VAC-B and the regenerator packed with 0.8-1.0 mm SS spherical particles give similar pressure drop.

Eqns. 5.6 - 5.8 are used to calculate the dimensionless group of the friction factor and Reynolds number. In both calculations, the maximum pressure drop, maximum superficial velocity and measured properties of the heat transfer fluid are used. For all regenerator beds, the average particle diameters and porosities are used for calculating the hydraulic diameter based on Eqn. 6.1. The friction factors in packed particle beds and epoxy bonded beds are presented in Figure 6.7 (a) and (b), respectively. The results are also compared to the theoretical prediction based on the Erguns model, which is a classic correction predicting the pressure drop through a packed bed.

The Ergun equation includes both viscous and kinetic effects as:

$$\frac{dP}{dx} = 2\alpha \frac{(1-\varepsilon)^2 \mu_f v_s S_V^2}{\varepsilon^3} + \frac{\beta}{8} \frac{(1-\varepsilon)\rho_f v_s^2 S_V}{\varepsilon^3} \tag{6.2}$$

where $\alpha \approx 2.5$, β=2.4 and $S_V = 6/D_{sp}$ for packed beds. This correlation can also be used in case of high porosity, by adjusting and slightly. Therefore, $\alpha \approx 2.5$ and β=2.3 from Ref. [83] are used in Figure 6.7 (b).

Figure 6.7 (a) shows that the experimental results fit the Ergun equation well, meaning this model is suitable for estimating the pressure drop over packed spherical particle beds,

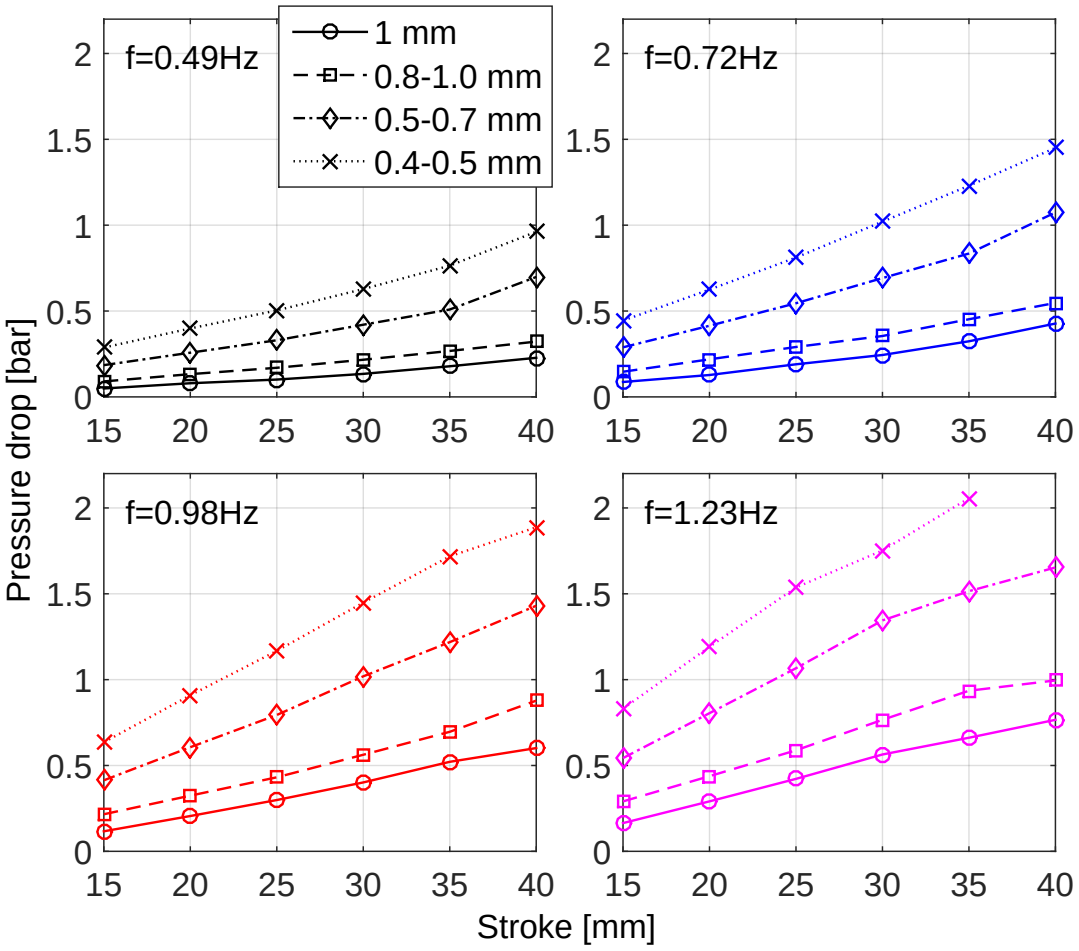

Fig. 6.5: Maximum pressure drop over regenerators packed with different SS particles at different strokes and frequencies.

regardless of a certain (small) variation in the bed shape and the particle sizes. As shown in Figure 6.7 (b), the measured friction factors of VAC-A and VAC-B are much higher than what predicted by the Ergun equation. Compared with the SS spherical particles, estimating D_h of the epoxy bonded beds has much bigger uncertainty, as the particle size distribution is not well known and the $La(Fe,Mn,Si)_{13}H_y$ particles are highly irregular. Furthermore, the epoxy occupies about 3% of the regenerator volume and its impact on the channel shape and sizes is not clear. This may introduce a considerable error into the calculated friction factor and it is impossible to propose the correlation for those epoxy bonded beds in this regard. Therefore, direct comparison of the pressure drop sometimes makes more sense for engineering application.

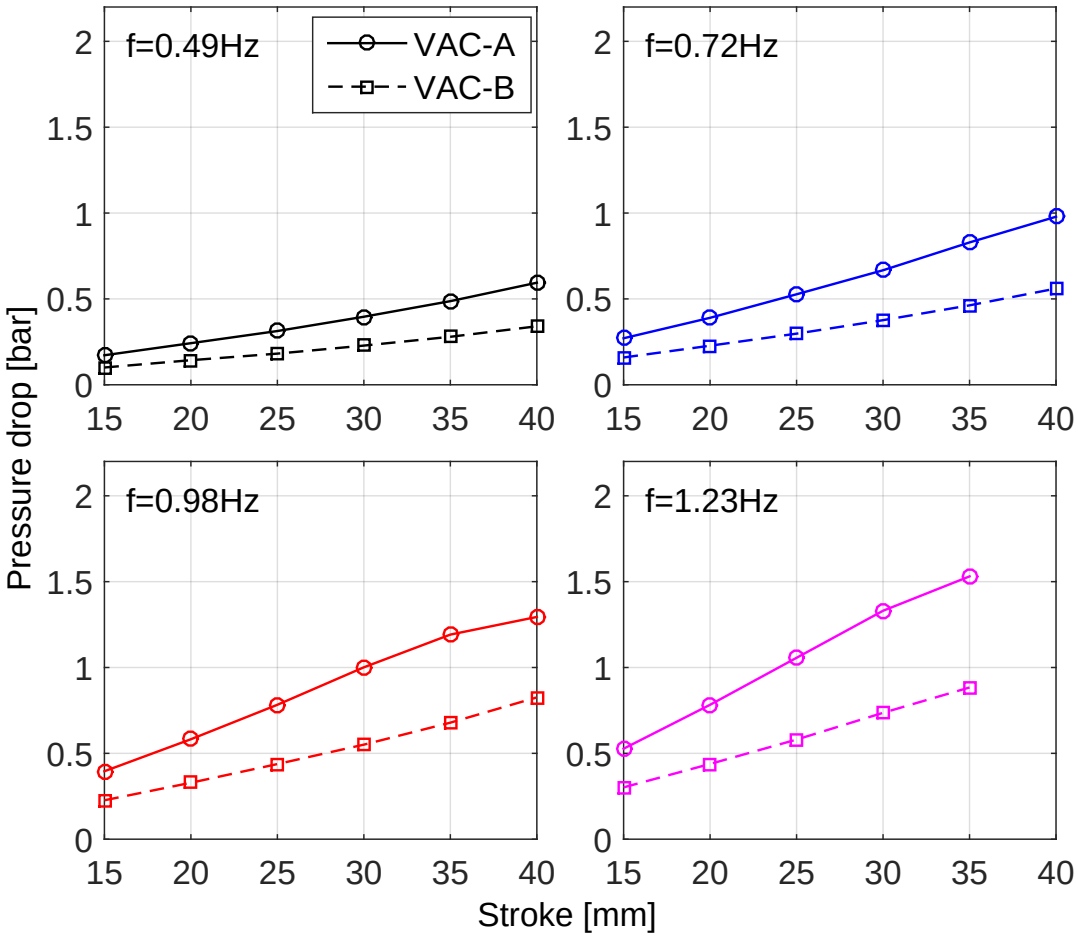

Fig. 6.6: Maximum pressure drop over epoxy bonded $La(Fe,Mn,Si)_{13}H_y$ beds at different strokes and frequencies.

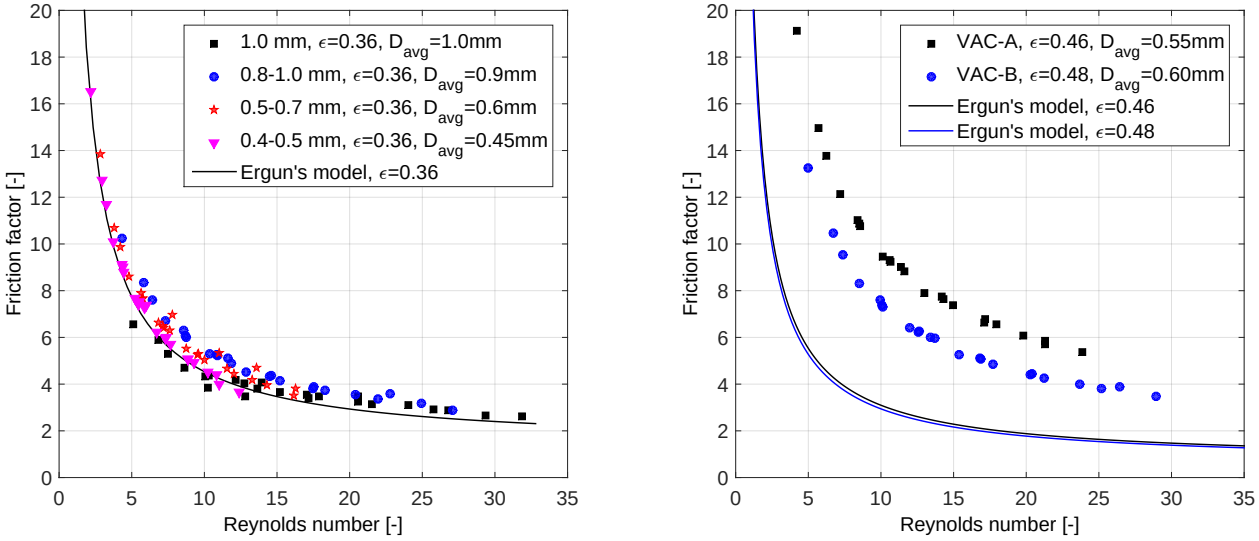

(a) Packed SS particle beds

(b) Epoxy bonded $La(Fe,Mn,Si)_{13}H_y$ beds

Fig. 6.7: Estimated friction factors of packed particle beds and epoxy bonded beds based on the experimental measurements and the Ergun equation.

6.1.2 Effectiveness and heating power

Based on Eqns. 5.9, 5.10 and 5.12, the effectiveness and utilization ratio for different regenerators are calculated and presented in this section. To obtain the utilization ratio, the average specific heat capacity of the fluid is used according to the temperature dependence curve in Figure 5.11. For $La(Fe,Mn,Si)_{13}H_y$, the temperature dependence of the specific heat capacity c_s (as seen in Ref. [11]) is also considered. The average c_s about 540 J/(kg·K) is used for a temperature span from 22 to 42 °C.

As shown in Figure 5.4, three thermocouples are set at each end to ensure the reliability of temperature measurements. Figure 6.8 presents the variation in effectiveness based on measurements of different thermocouples. Here, the regenerator packed with 0.5-0.7 mm SS particles is used and the operating frequency is 1 Hz. The error bars represent the variation in five cycles as shown in Figure 5.10. The results show a relatively small variation in the effectiveness, meaning that the measurements are relatively reliable. In the following figures, only the average value of effectiveness is presented.

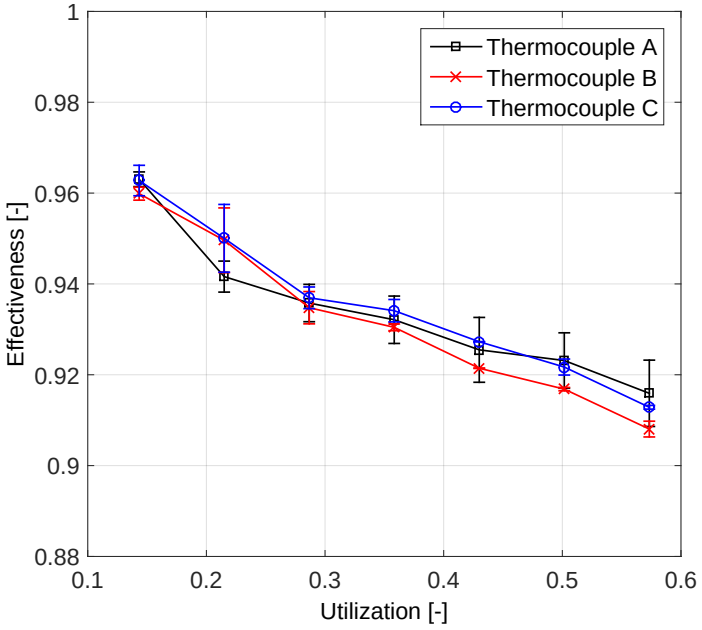

Fig. 6.8: Variation in effectiveness based on the measurements of three thermocouples.

As opposed to stainless steel, the specific heat capacity of $La(Fe,Mn,Si)_{13}H_y$ is strongly temperature dependent near the magnetic transition temperature. This could lead to a considerable change in the total solid heat mass during the two blow periods, which affects the effectiveness correspondingly. Trevizoli et al. [115] studied the effectiveness imbalance in gadolinium regenerator. In all tests in this primary study, the cold end temperature is around 22-24 °C, which is higher than the Curie temperature 20 °C of $La(Fe,Mn,Si)_{13}H_y$. In this op-

erating condition, there will be only a small temperature dependence in c_s and thus small effectiveness imbalance between two blow periods. Figure 6.9 presents the effectiveness during the two blow periods, showing the deviation is relatively small in these tests.

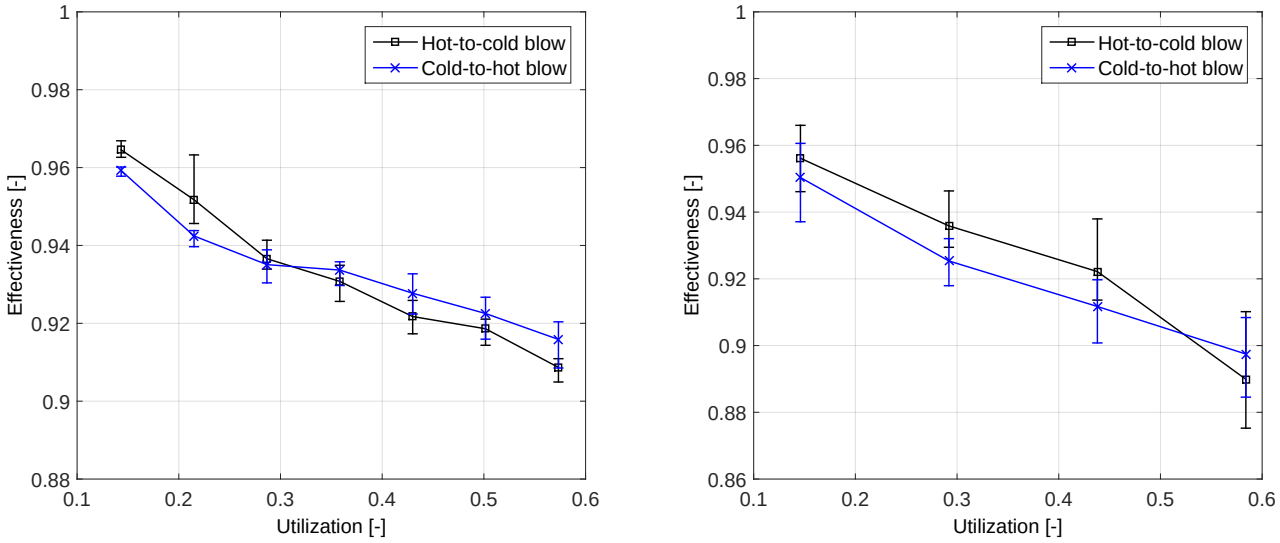

(a) Packed bed loaded with 0.5-0.7 mm SS particles

(b) Epoxy bonded $La(Fe,Mn,Si)_{13}H_y$ bed (VAC-A)

Fig. 6.9: Effectiveness of packed particle bed and epoxy bonded bed in two blow periods.

Figure 6.10 shows the average effectiveness of regenerators packed with different SS particles and epoxy bonded $La(Fe,Mn,Si)_{13}H_y$. For the packed particle beds, smaller particles exhibits higher effectiveness at the same utilization ratio, which could be attributed to higher NTU due to higher Reynolds number and larger specific surface area. A high NTU regenerator is always preferable for the AMR design; however, it requires smaller channel size in return, which raises the pressure drop. The simulation results presented in Chapter 4 also reveal the importance of the trade-off between the flow and heat transfer performance.

Figure 6.10 (b) gives the effectiveness of the two epoxy bonded beds. Although less material is consumed, the utilization ratios in the new regenerators are similar to those in Figure 6.10 (a). This is because both solid and fluid heat mass are considered during calculation of the utilization ratio based on Eqn. 5.12 . VAC-A packed with irregular particles exhibits a slightly higher effectiveness than VAC-B with spherical particles, while presenting much higher pressure drop as shown in Figure 6.6. Note that the two curves in Figure 6.10 (b) are close to each other and the error bars even cross, indicating the overall heat transfer performance of the two epoxy bonded beds are similar. In addition, the performances are approximately equivalent to the beds packed with 0.5-0.7 and 0.8-1.0 mm particles. However, smaller particle diameter as 0.2-0.3 mm is promising in some AMR designs shown in Chapter 4. Therefore, both VAC-A and VAC-B should be further improved by adjusting the particle size distribution, irregularity and bonded structures.

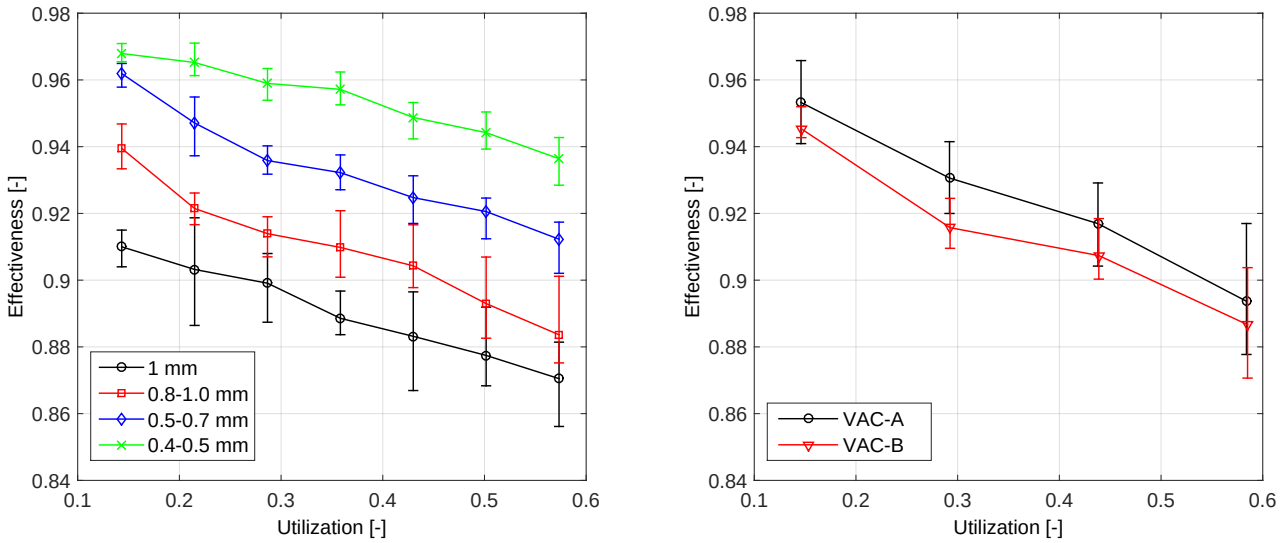

(a) Packed SS particle beds

(b) Epoxy bonded $La(Fe,Mn,Si)_{13}H_y$ beds

Fig. 6.10: Effectiveness of different regenerators as a function of utilization ratio.

Another index for evaluating the overall heat transfer performance is the heating power applied on the hot side of the regenerators. Theoretically, the heating power represents the total enthalpy difference at the hot end and it is inversely proportional to the effectiveness. The heating power here includes the heat transport through the regenerator and the inevitable heat loss in the whole system. The measurement of heating power has high accuracy as described in Chapter 5. Therefore, this parameter can be used to estimate the overall heat transfer performance by direct comparison, which is also one of the objectives of this test apparatus. Figure 6.11 presents the applied heating power at different temperature spans and strokes for regenerators packed with different SS particles. In general, large stroke, i.e., high utilization ratio, and large temperature span require more heating power. For larger particles, larger heating power is required to keep the same temperature span, due to the lower effectiveness presented in Figure 6.10 (a).

Based on the same idea, the heating power applied on epoxy bonded beds is presented in Figure 6.12. For VAC-B, a slightly higher heating power is necessary to build up the same temperature span compared to VAC-A, which is also reflected by slightly lower effectiveness as shown in Figure 6.10 (b).

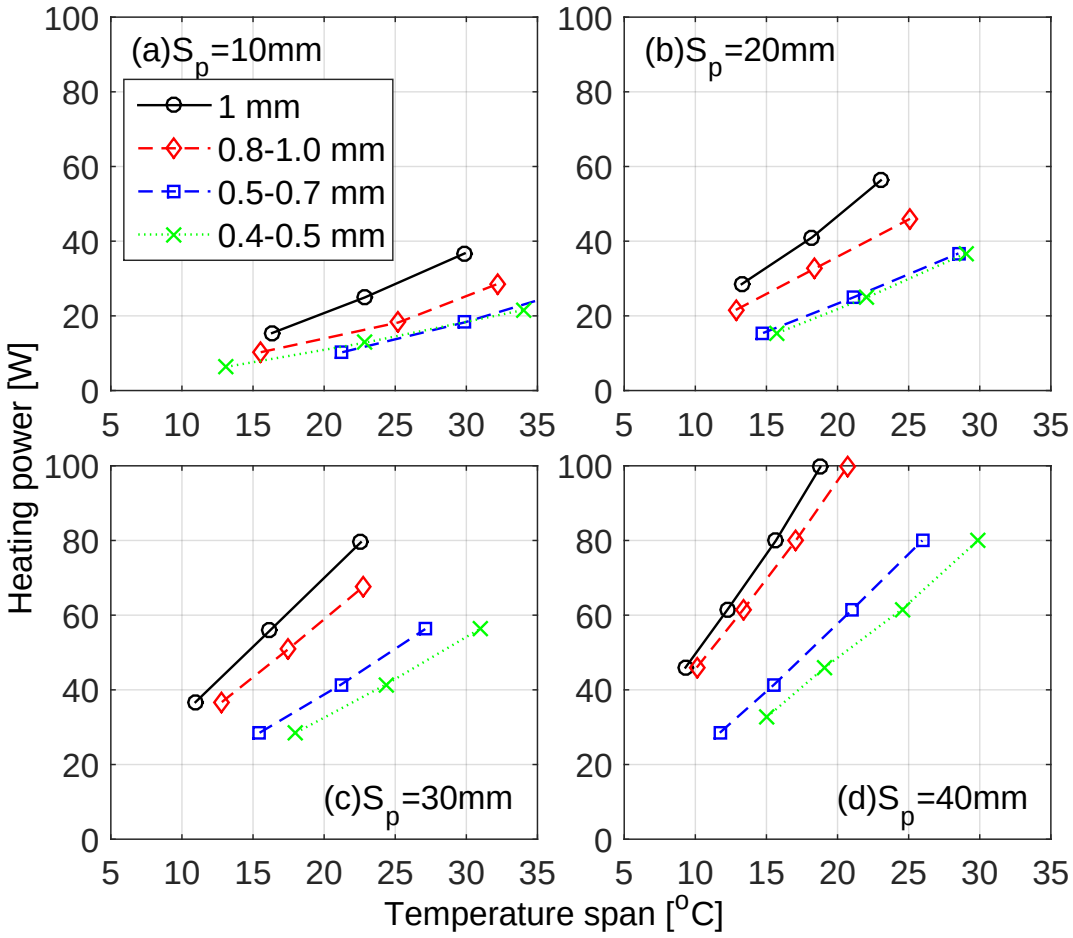

Fig. 6.11: Heating power applied on regenerators using packed particle beds at different temperature spans and strokes.

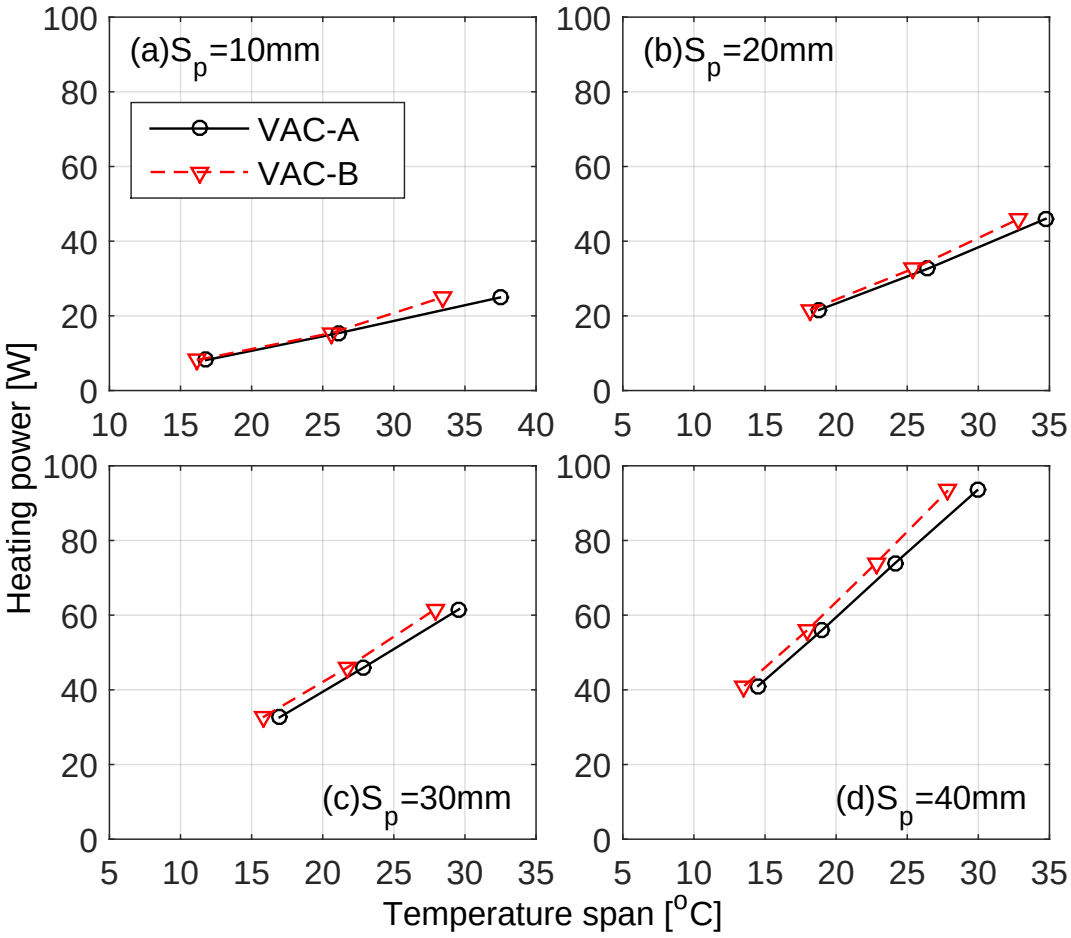

Fig. 6.12: Heating power applied on regenerators using epoxy bonded beds at different temperature spans and strokes.

6.1.3 Impact of frequency

For the packed particle bed, the effectiveness at different frequencies are also presented in Figure 6.13. Here the stroke is held at 40 mm, i.e., constant utilization ratio, and the temperature span varies according to the applied heating power. The same conclusion that smaller particles can realize higher effectiveness can be drawn from the results in Figure 6.13. Besides, the impact of frequency on the effectiveness is not significant in this study. The effectiveness only increases slightly with the increasing frequency when bigger particles (1 mm SS balls) are used, which could be attributed to the small variation in frequency from 0.5 to 1.0 Hz. Note the variation in effectiveness becomes larger for bigger particles, meaning that the overall NTU of the regenerator loaded with larger particles is more sensitive to the frequency. The increased effectiveness indicates that the enthalpy difference at the hot end becomes less in one cycle. Therefore, increasing the frequency from 0.5 to 1.0 Hz would not double the heating power. In addition, the actual operating frequency is lower than the desired value as seen in Figure 6.13, which further decreases the applied heating power. This is verified in Figure 6.14 that the heating power increases slower with increasing frequency.

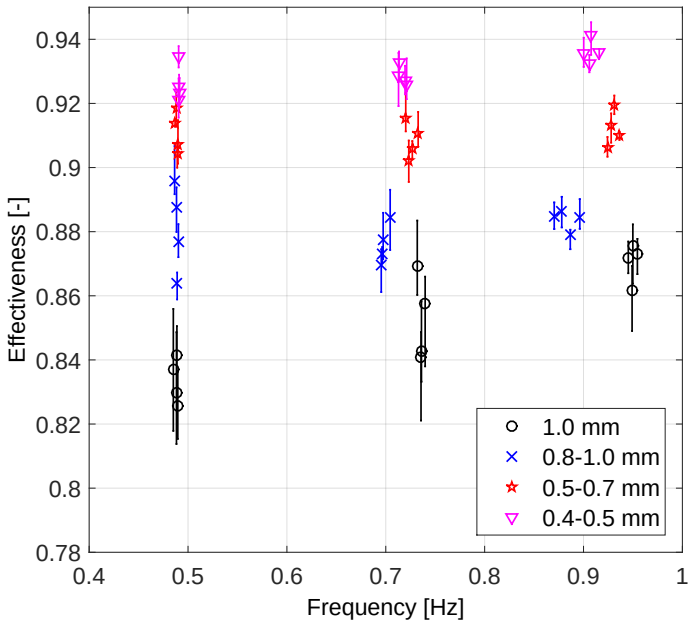

Fig. 6.13: Effectiveness of regenerators using packed particle beds when the stroke is 40 mm and the frequency ranges from 0.50 to 1.00 Hz.

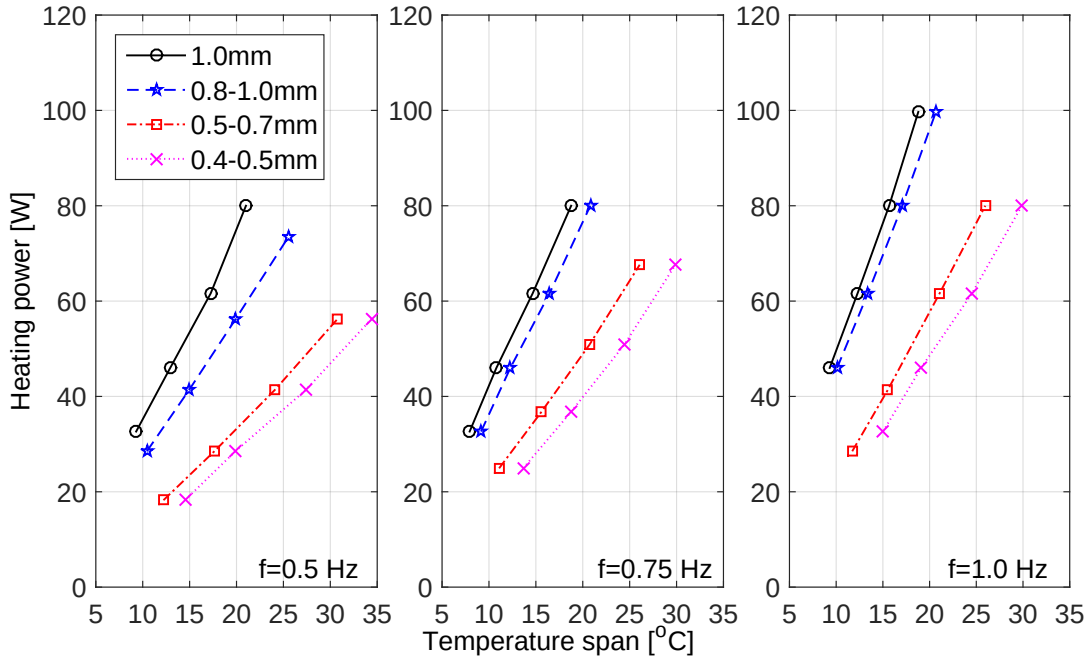

Fig. 6.14: Heating power applied on regenerators packed with different particles when the stroke is 40 mm and the frequency ranges from 0.5 to 1.0 Hz.

6.1.4 Overall Nusselt number

The overall Nusselt number is calculated based on Eqn. 5.19 and presented in Figure 6.15. The mean Reynolds number based on the hydraulic diameter and mean superficial velocity is re-defined as:

$$\overline{\mathrm{Re}_h} = \frac{\rho_f \overline{v_s} D_h}{\mu_f} \tag{6.3}$$

where $\overline{v_s}$ is the mean superficial velocity of an approximate sine wave movement.

For the regenerators using packed particle beds, the overall Nusselt number with oscillating flow increases with the increasing mean Reynolds number. The trends of four curves are similar to each other, which could form a consistent correlation. Some scatting points are found in the curves representing 0.4-0.5 mm and 0.5-0.7 mm particles. A similar trend in the overall Nusselt number is observed in the epoxy bonded beds. It must be noted again that there is a huge uncertainty in the estimated Nu_o of epoxy bonded beds. Engelbrecht [2] presented a correlation of the Nusselt number for a packed bed by the single blow test. The Nusselt number is described as:

$$\mathrm{Nu} = 0.7\mathrm{Pr}^{0.23}\mathrm{Re}_h^{0.6} \tag{6.4}$$

where the Reynolds number Re_h based on the hydraulic diameter and superficial velocity is used.

Both plots in Figure 6.15 show that the experimental curves in this study follow the trend of Engelbrecht's correlation, and in this study the overall Nusselt number is lower. Note that the experiments here are implemented with an oscillating flow condition. The mean Reynolds number is used which is different from the single blow test for obtaining Eqn. 6.4. As the estimation of the hydraulic properties in packed particle beds is relatively accurate, the results in Figure 6.15 (a) are considered close to the real conditions.

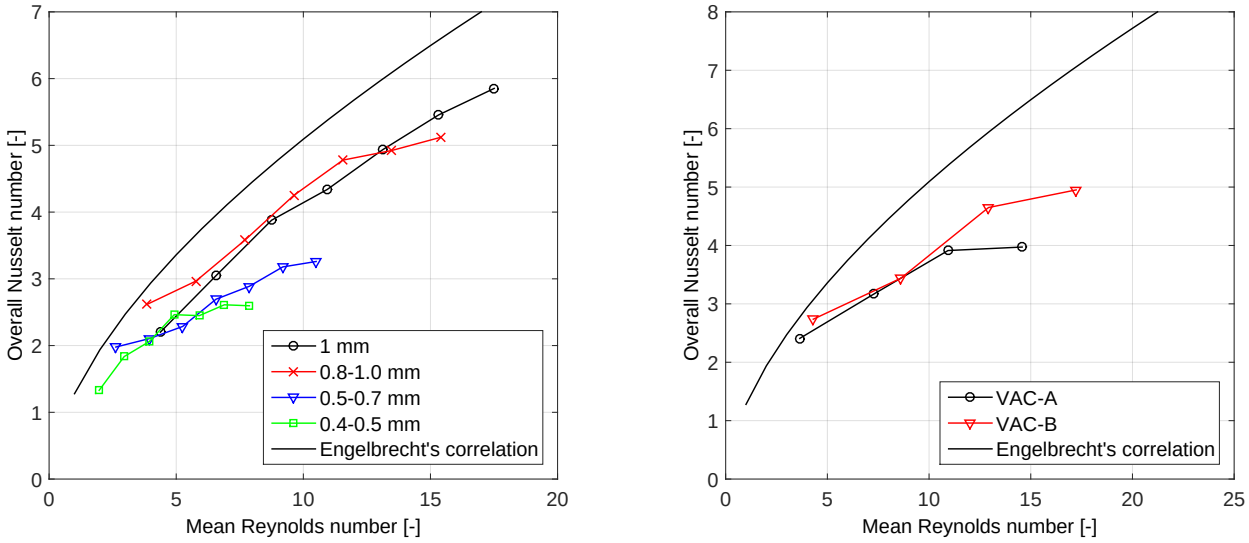

(a) Packed SS particle beds

(b) Epoxy bonded $La(Fe,Mn,Si)_{13}H_y$ beds

Fig. 6.15: Overall Nusselt number as a function of mean Reynolds number for regenerators using packed particle beds and epoxy bonded beds.

6.2 Test of heat transfer fluids

In magnetic refrigeration systems, an aqueous solution with anti-corrosion / anti-freeze additives is commonly used as the heat transfer fluid. This kind of heat transfer liquid usually has a relatively high Prandtl number and high viscosity larger than 1 mPa·s. It is also worth noting that the thermal mass of the fluid in the porous bed is in the same order of that of the solid bed, due to the high specific heat capacity. Choosing heat transfer fluids with proper thermal properties, low viscosity and high corrosion resistance is thus vital to realize a high performance magnetic refrigerator.

The properties of different heat transfer fluids are summarized in Table 2. All the density

and dynamic viscosity are measured by a commercial viscometer (Anton Paar DMA 4500M / Lovis 2000 M) at DTU. The thermal conductivity λ and specific heat capacity c_p of the ethylene glycol aqueous solutions are calculated based on the commercial software EES. ENTEK FNE is a commercial anti-corrosion additive but the formulation is not given [44, 131]. A low concentration (1-2 v/v %) [131] is enough to well protect the magnetocaloric materials, which may bring benefits such as low viscosity and high thermal conductivity. However, the composition of ENTEK FNE and the solution properties including λ and c_p are not specified. In this study, λ is estimated to be 0.5 W/(m·K) and the specific heat capacity is calculated based on the volume fraction assuming $c_{p,ENTEK}$= 2000 J/(kg·K). Note that these uncertainties will lead to certain errors during calculating the dimensionless parameter.

Table 6.2: Properties of different heat transfer fluids at 20 °C.

Fluids	Density [kg/m^3]	Dynamic viscosity [mPa·s]	Thermal conductivity [W/(m·K)]	Specific heat capacity [J/(kg·K)]
Water	998	1.00	0.586* [1]	4186*
10 v/v% ethylene glycol solution	1015	1.43	0.548*	4031*
20 v/v% ethylene glycol solution	1031	1.77	0.500*	3866*
30 v/v% ethylene glycol solution	1041	2.31	0.455*	3672*
2 v/v% ENTEK FNE solution	1001	1.07	0.5	4138**[2]
5 v/v% ENTEK FNE solution	1003	1.15	0.5	4066**
10 v/v% ENTEK FNE solution	1008	1.34	0.5	3948**

6.2.1 Pressure drop and friction factor

The pressure drop data over the regenerators using different heat transfer fluids are presented in Figures 6.16 and 6.17. The pressure drop increases when the solution with a higher concentration is used, due to the increase in dynamic viscosity. Moreover, EG solutions have a slightly higher pressure drop than the ENTEK FNE solutions and water always gives the lowest value. Figure 6.18 shows the re-calculated friction factor based on the pressure drop data in Figures 6.16 and 6.17. Although the experimental data fit the trend of the theoretical prediction, the scattering indicates that the measurement error is relatively large. The reasons may be the fluid property changes due to the temperature variation and few bubbles in the system (especially with the ENTEK FNE solutions).

[1] * Calculated based on the commercial software EES.
[2] ** Calculated based on the volume fraction assuming $c_{p,ENTEK}$= 2000 J/(kg·K).

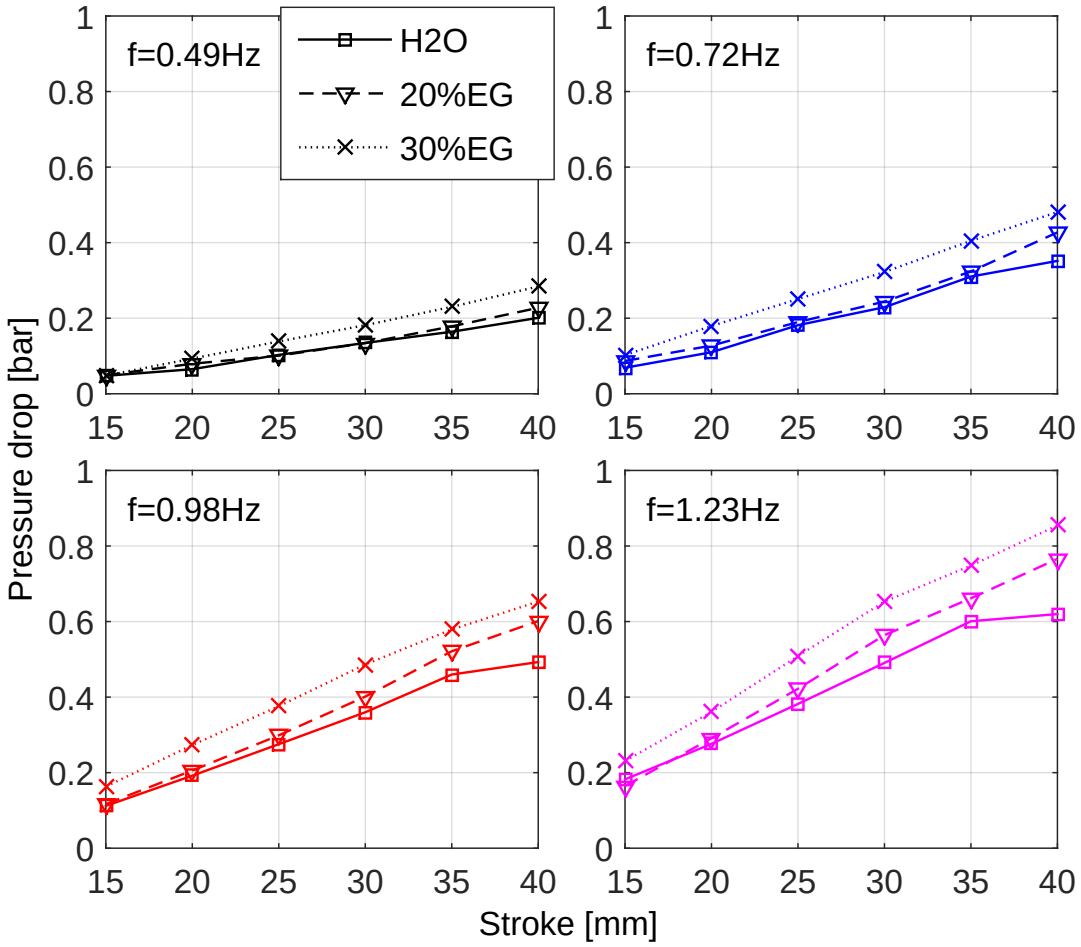

Fig. 6.16: Maximum pressure drop over regenerators using the ethylene glycol aqueous solutions at different strokes and frequencies.

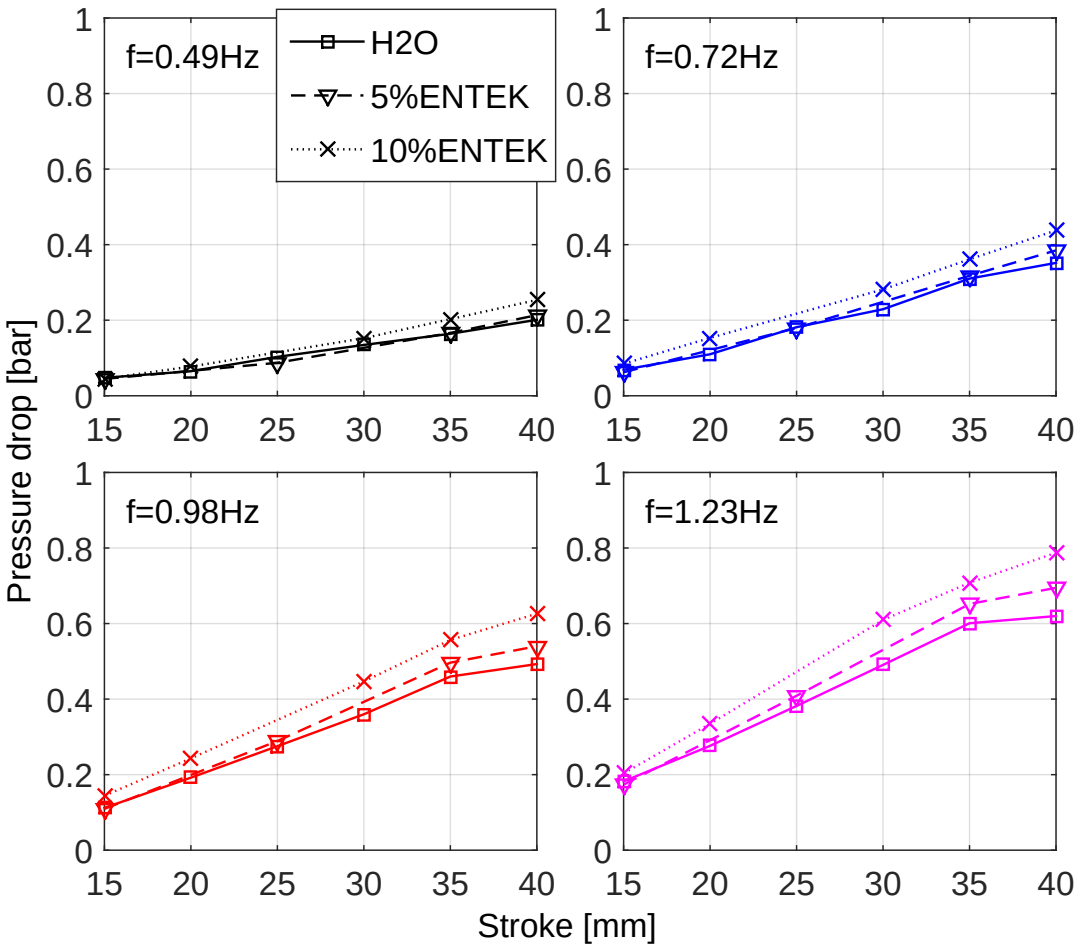

Fig. 6.17: Maximum pressure drop over regenerators using the ENTEK FNE aqueous solutions at different strokes and frequencies.

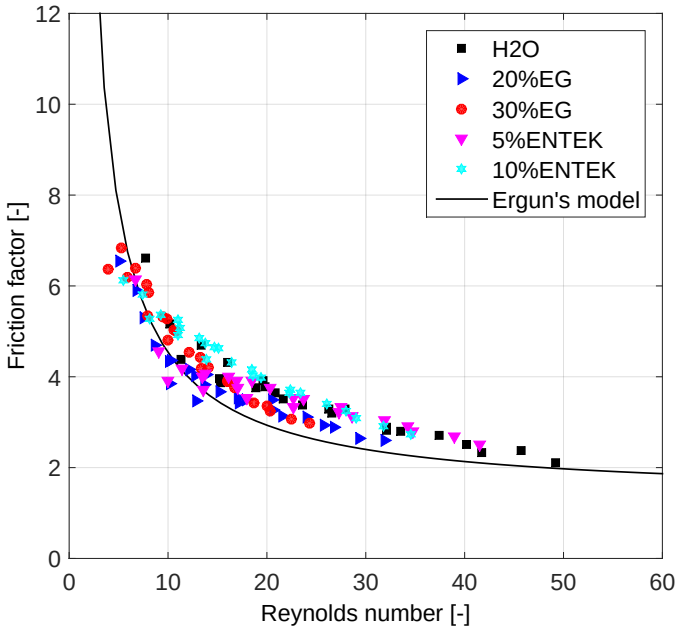

Fig. 6.18: Friction factor as a function of Reynolds number for different heat transfer fluids based on the experimental measurements and the Ergun equation.

6.2.2 Effectiveness and heating power

The effectiveness of regenerators using different heat transfer fluids are summarized in Figure 6.19. Here 1 mm stainless steel balls are used as the regenerator material; the operating frequency is 1 Hz; and the utilization ratio is adjusted by using different piston strokes. The results show that the water always exhibits a higher effectiveness than the others. Between the other heat transfer fluids, the effectiveness are similar and the variation is difficult to identify. The results in Figure 6.20 show that less heating power is required to build up the same temperature span for water, while the heating powers required for the other fluids are similar, which reflects the results from Figure 6.19.

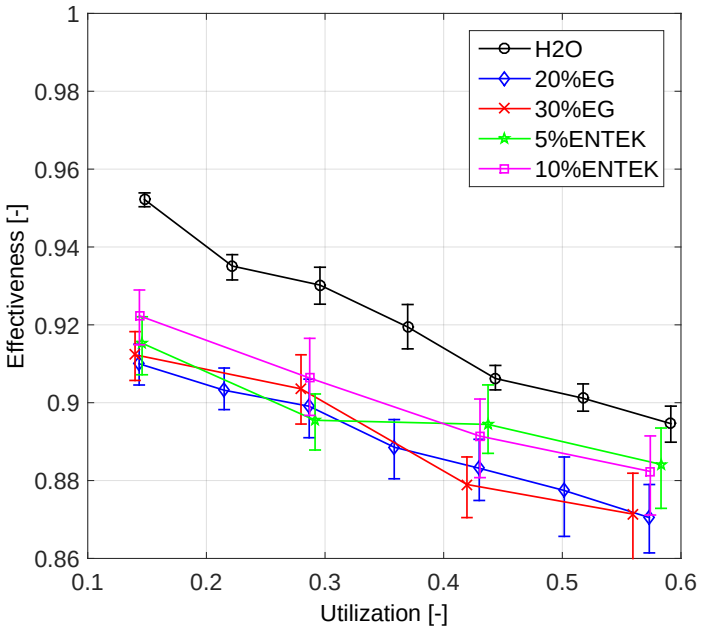

Fig. 6.19: Effectiveness of a regenerator using different heat transfer fluids as a function of utilization ratio.

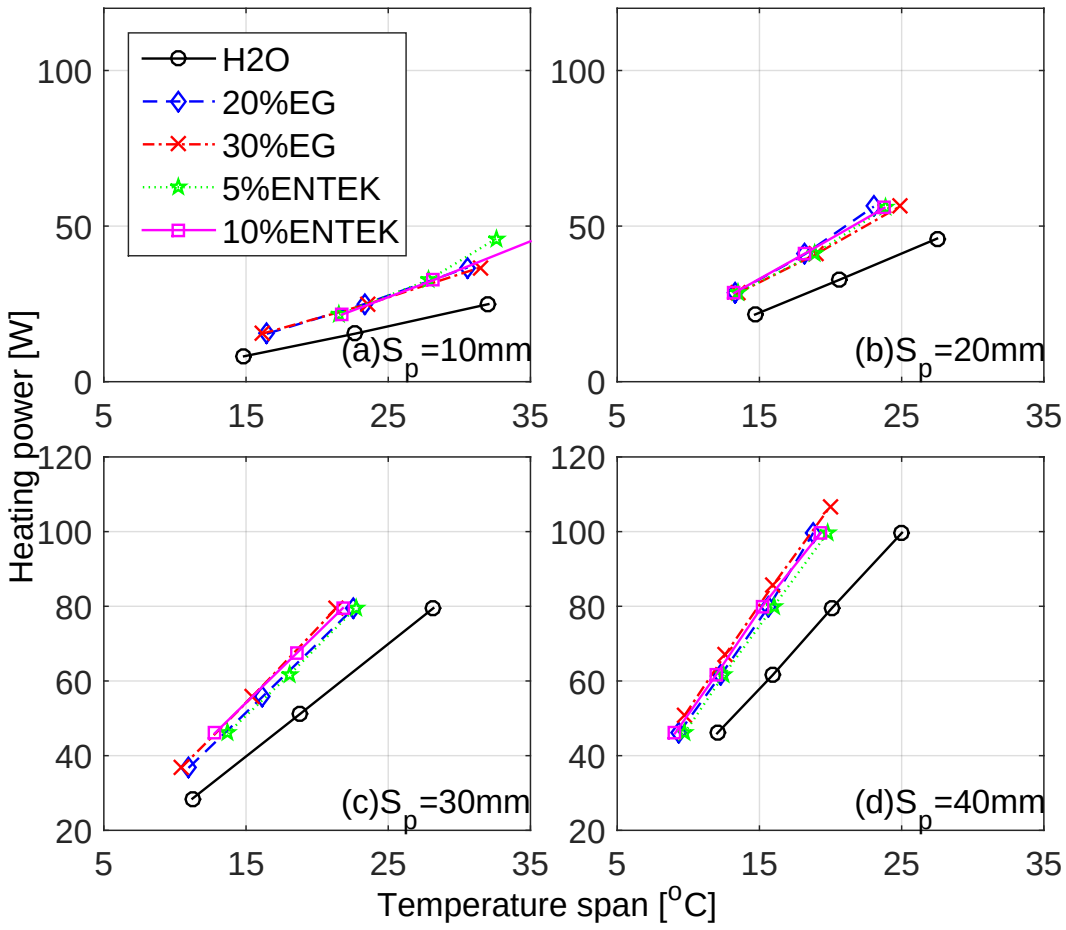

Fig. 6.20: Heating power applied on a regenerator using various heat transfer fluids at different temperature spans and strokes.

6.2.3 Overall Nusselt number

Based on the effectiveness presented in Figure 6.19, the overall Nusselt number is calculated and plotted in Figure 6.21 (a). The measured or estimated properties of heat transfer fluids at room temperature are used as shown in Table 6.2. The data show relatively large deviation from each other, which may due to the variation in the Prandtl number for different heat transfer fluids. This effect is taken out by dividing Nu_o with a ratio of $Pr^{0.23}$ and the results are further presented in Figure 6.21 (a). For different heat transfer fluids, the $Nu_o/Pr^{0.23}$ ratios give a consistent trend, which are lower than the prediction based on Engelbrecht's correlation.

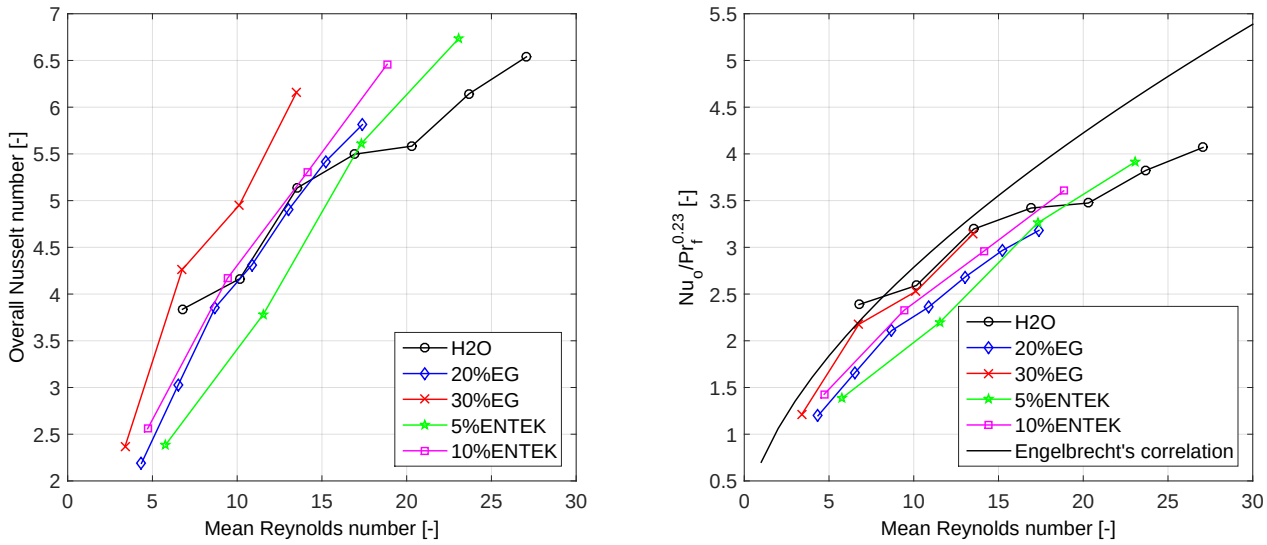

(a) Overall Nusselt number Nu_o

(b) $Nu_o/Pr^{0.23}$

Fig. 6.21: Overall Nusselt number and $Nu_o/Pr^{0.23}$ as functions of mean Reynolds number in a regenerator using different heat transfer fluids.

6.3 Summary

This chapter presents a thorough experimental study of passive regenerators, including emerging regenerator geometries and heat transfer fluids for future design. Different indicators, including the pressure drop, friction factor, effectiveness, heating power and overall Nusselt number, are presented to investigate the flow and heat transfer characteristics of different regenerators with an oscillating flow. The experiments run in the low Reynolds number region with high Prandtl number fluid.

Six regenerators, which are two epoxy bonded $La(Fe,Mn,Si)_{13}H_y$ beds and four packed SS particle beds are tested in Section 6.1 In general, smaller SS particles lead to high effectiveness with an increasing pressure drop over the regenerator. Additionally, the measured friction factors well fit the classic Ergun correlation, regardless of the variation in particle sizes. The overall Nusselt number of the packed particle bed is lower than the theoretical estimation based on the correlation from Ref. [2], which has relatively high accuracy. For the epoxy bonded beds, VAC-A loaded with bonded irregular particles exhibits much higher pressure drop and slightly higher effectiveness than VAC-B with spherical particles. The friction factor and overall Nusselt number of the epoxy bonded beds are presented, noting that the unknown hydraulic diameter and the impact of epoxy could lead to a large error in dimensionless parameters predictions. The pressure drop data can be directly used for designing AMRs for a upcoming magnetic heat pump system. The improvement of the effectiveness is expected by adjusting the particle size and the irregularity for the epoxy bonded beds.

The heating powers are presented to reflect the overall heat transfer performance for different regenerators, which sometimes are more intuitive and accurate for comparison. In addition, the test apparatus runs at different frequencies below 1.5 Hz, and the impact of the frequency on the effectiveness is small.

The regenerators using different heat transfer fluids are tested and evaluated in Section 6.2. The predicted friction factors have a relatively large deviation when comparing with the Erguns model, which may be due to the temperature induced property change and high measurement error. Water realizes the highest effectiveness, while the other fluids show similar effectiveness, which is also verified by the heating power data. The estimated overall Nusselt number is also lower than the correlation from Ref. [2].

CHAPTER 7

Conclusions and perspectives

The general purpose of this thesis is to investigate different concepts and designs for future AMRs. Various topics are investigated and analyzed based on the numerical modeling of active magnetic regenerators and experimental investigation of passive regenerators. In this chapter, the findings of the studies are summarized and discussed, covering the following issues:

1. Improve the numerical tool for modeling different regenerators;
2. Explore strategies on how to layer different FOPT and SOPT materials;
3. Analyze loss mechanisms inside AMRs;
4. Optimize regenerator geometries and operation;
5. Experimentally investigate the flow and heat transfer characteristics of different regenerators.

Furthermore, perspectives and some suggestions for future work are provided based on the research in this thesis.

7.1 Conclusions

Improvements in a 1D AMR model

In Chapter 2, several improvements of a one dimensional AMR model are presented. A new discretization scheme using the MC limiter is introduced to avoid spurious temperature oscillation in the numerical solution. Based on this modification, the accuracy of the numerical model is improved, which is verified with the previously used central difference scheme. Theoretically the new scheme can handle high CFL condition (coarse temporal grid) and save computation time. However, low CFL number (dense temporal grid) is still used, as the magnetocaloric properties of the FOPT materials are highly nonlinear. Improvements are also implemented for simulating tapered regenerators, heat loss through the housing wall and regenerators using mixed materials, which are applied in other investigations in this thesis.

Multi-layer AMRs using the FOPT and SOPT materials

Magnetocaloric materials with large isothermal entropy change ΔS_{iso} attract a lot of attention [14, 70], while the influences of adiabatic temperature change ΔT_{ad} and shape factor γ describing the temperature dependence of the MCE are sometimes underestimated. Based on

artificially built magnetocaloric properties, a simulation study is presented in Section 3.1. to show the combined influences of ΔS_{iso}, ΔT_{ad} and γ. The results show that all those parameters should be equally emphasized. Although FOPT materials exhibit larger ΔS_{iso}, they sometimes only produce equivalent cooling performance compared to SOPT materials due to a similar or lower ΔT_{ad} and smaller shape factor γ. For materials with small γ, i.e., narrow working temperature region, more layers are needed to achieve a desired cooling power compared to those with larger γ.

In Section 3.2, another investigation is done to investigate how to design multi-layer AMRs using typical FOPT or SOPT materials, e.g., La(Fe,Mn,Si)$_{13}$H$_y$ or Gd-like materials, respectively. The simulations show that La(Fe,Mn,Si)$_{13}$H$_y$ regenerators could realize higher specific cooling power than those using Gd-like materials, but many more layers are needed at the same time. From a practical point, around 10 to 12 layers may be suitable for a temperature span of 30 K with the FOPT material La(Fe,Mn,Si)$_{13}$H$_y$. Besides, AMRs using La(Fe,Mn,Si)$_{13}$H$_y$ are more sensitive to the working temperature and the Curie temperature variation, which describes the degree of deviating from an even Curie temperature distribution. To improve the stability of those regenerators using La(Fe,Mn,Si)$_{13}$H$_y$, a concept of mixing FOPT and SOPT materials is investigated. Compared to FOPT materials, the required number of layers is significantly reduced with the mixed materials. In addition, the performance degradation becomes smaller when faced with fluctuating working temperatures and the random variations in the Curie temperature distribution.

This study is not limited to La(Fe,Mn,Si)$_{13}$H$_y$ and Gd-like materials. It shows a general approach for choosing and layering different FOPT or SOPT materials in a proper way. Except for the system design and prototype fabrication, this work also provides useful information for material development, such as the necessary accuracy of controlling Curie temperature and the importance of ΔT_{ad} and γ.

The findings here are directly applied in the performance prediction for a small test machine (Section 3.3) and the design of an efficient magnetocaloric heat pump at DTU (Section 3.4), which is the final product of the project. In the design, the multi-layer regenerators using FOPT materials are supposed to provide 2 kW heating power with COP$_{HP}$ of 5, fulfilling the heating demand in a typical Danish house.

Loss mechanisms inside AMRs, heat loss through the housing wall and dead volume effect

A multi-parameter optimization of an AMR is presented in Section 4.1, combined with the analysis of the main loss mechanisms. The entropy production rates are calculated to quantify the weighing factors of different losses inside the AMR. In detail, the entropy production rates due to the three main loss mechanisms: insufficient heat transfer, viscous dissipation and axial conduction, are compared and discussed. The results show that insufficient heat transfer is more sensitive to the frequency, while the viscous dissipation is more affected by the aspect ratio. The conduction loss becomes significant when the aspect ratio is less than 1.0. Comparison also indicates insufficient heat transfer and the viscous dissipation are the two main losses

in most practical cases. At the optimal point, both the minimum total entropy production rate and the maximum COP are observed, that is a direct application of entropy production minimization.

The heat loss through the housing is also studied in Section 4.2 by introducing the energy equation describing the housing wall. In fact, there are more losses involved in this issue, including the heat transfer between the fluid and wall, heat transfer between the wall and ambient and axial heat conduction through the wall. Different conditions can be simulated by varying the heat transfer coefficients. The results show that both specific cooling power and COP are reduced by this effect.

By illustrating the temperature curves, the phenomenon of the dead volume is explained to reveal how it affects the system performance. With increased dead volume ratio, both specific cooling power and COP decreases significantly. A tolerant maximum dead volume ratio of 0.10 is suggested for maintaining the cooling performance in Section 4.3.

This part of the work serves to understand the impacts of different losses inside AMRs and to investigate the ways to reduce the overall loss.

Optimization of regenerator geometries and operation

A thorough study of optimizing regenerator geometries and operation is implemented for maximizing the COP in Section 4.4. In this multi-parameter optimization, four geometries, including the packed sphere bed, parallel plate matrix, micro-channel matrix and packed screen bed, are investigated.

A general study shows that both the optimal frequency and aspect ratio would change for different hydraulic diameters. For small hydraulic diameter (small channel size), the COP is more sensitive to the aspect ratio but does not change much with frequency. In contrast, the COP is more sensitive to the frequency rather than the aspect ratio for large hydraulic diameters.

For different geometries, the optimal hydraulic diameter, aspect ratio and frequency are summarized and presented for further comparison. The parallel plate matrix and micro-channel matrix and packed screen bed show better performance than the packed sphere bed at the optimal point. However, producing an ideal parallel plate matrix or micro-channel matrix is difficult, due to the limits of the fabrication technology and the related flow mal-distribution problem. In contrast, the packed screen bed or similar matrix structure such as a packed wire bed could realize a high homogeneity, which is a promising geometry, considering the tradeoff between the pressure drop and the heat transfer performance.

Passive regenerator test

The flow and heat transfer characteristics of the emerging regenerator geometry, epoxy bonded bed, are not well investigated. Therefore, Chapters 5 and 6 develop an experimental apparatus to test those geometries passively with oscillating flow, which is similar to the operating condition in a real AMR. Different indicators, including the pressure drop, friction factor, effectiveness ratio, heating power and overall Nusselt number, are presented and analyzed.

Four packed SS particle beds and two epoxy bonded La(Fe,Mn,Si)$_{13}$H$_y$ beds are tested. For the packed beds, smaller SS particles realize higher effectiveness ratios with also high pressure drop. The calculated friction factors fit the Ergun model well and the predicted overall Nusselt number is lower than the correlation from Ref. [2]. The epoxy bonded regenerator VAC-A, which is loaded with La(Fe,Mn,Si)$_{13}$H$_y$ irregular particles, exhibits much higher pressure drop and slightly higher effectiveness ratio than VAC-B with spherical particles. Although the friction factor and overall Nusselt number are presented, the unknown hydraulic diameter and the impact of epoxy would lead to huge uncertainty when deducing the dimensionless indices. Moreover, the heating power data are also presented, which provides a relatively accurate approach for comparing the overall heat transfer performance.

The tests of heat transfer fluids show that water always gives the highest effectiveness ratio compared with the other heat transfer fluids with anti-corrosion additives. The predicted friction factors fit the trend of the Ergun model with a relatively large deviation.

7.2 Perspectives and suggestions

There are still a lot of unfinished work in this thesis. The study also raises some interesting questions to be addressed in future work. In order to further improve magnetic refrigeration technology, the following investigations are suggested:

1. Development of a non-uniform time grid to handle the nonlinear magnetocaloric properties and to save computation time.

2. Testing of more multi-layer AMRs actively and verify the layering strategy.

3. Experimental investigation on the impact of uneven Curie temperature distribution on the AMR performance.

4. Verification of the design in the upcoming ENOVHEAT magnetic heat pump.

5. Study on how to optimize the layer thickness in the multi-layer regenerators.

6. Testing of more regenerator geometries actively and passively. Although many attempts have been done to fabricate new porous geometries by using the fugitive porous scaffold, most of the sintered samples fail to form a stable porous structure with high mechanical strength. Long term investigation is needed due to lack of experience. Gd mirco-wire is a good candidate to perform a packed wire bed.

7. Improvement on the epoxy bonded beds by adjusting the particle size distribution and epoxy formulation.
8. Study on the transient behavior of AMRs combined with research on the control strategy of magnetic refrigerators / heat pumps.

Bibliography

[1] T. E. W. Schumann. Heat transfer: A liquid flowing through a porous prism. *Journal of the Franklin Institute*, 208(3):405–416, 1929.

[2] K. Engelbrecht. *A Numerical Model of an Active Magnetic Regenerator Refrigerator with Experimental Validation*. PhD thesis, University of Wisconsin - Madison, 2008.

[3] A. Smith. Who discovered the magnetocaloric effect? *Eur. Phys. J. H.*, 38(4):507–517, 2013.

[4] W. F. Giauque. A thermodynamic treatment of certain magnetic effects. a proposed method of producing temperatures considerably below 1 absolute. *Journal of the American Chemical Society*, 49(8):1864–1870, 1927.

[5] W. F. Giauque and D. P. MacDougall. Attainment of temperatures below 1 k absolute by demagnetization of $Gd_2(SO_4)_3 \cdot 8H_2O$. *Physical Review*, 43(9):768, 1933.

[6] G. V. Brown. Magnetic heat pumping near room temperature. *Journal of Applied Physics*, 47:3673–3680, 1976.

[7] D. Harvey. *A handbook on low-energy buildings and district-energy systems: fundamentals, techniques and examples*. Routledge, 2012.

[8] V. K. Pecharsky, K. A. Gschneidner, A. Pecharsky, and A. Tishin. Thermodynamics of the magnetocaloric effect. *Physical Review B*, 64(14):144406, 2001.

[9] A. Smith, C. R. H. Bahl, R. Bjørk, K. Engelbrecht, K. K. Nielsen, and N. Pryds. Materials challenges for high performance magnetocaloric refrigeration devices. *Advanced Energy Materials*, 2(11):1288–1318, 2012.

[10] S. Jeppesen, S. Linderoth, N. Pryds, L. T. Kuhn, and J. B. Jensen. Indirect measurement of the magnetocaloric effect using a novel differential scanning calorimeter with magnetic field. *Review of Scientific Instruments*, 79(8):083901, 2008.

[11] V. Basso, M. Kupferling, C. Curcio, C. Bennati, A. Barzca, M. Katter, M. Bratko, E. Lovell, J. Turcaud, and L. F. Cohen. Specific heat and entropy change at the first order phase transition of $La(Fe - Mn - Si)_{13} - H$ compounds. *Journal of Applied Physics*, 118(5):053907, 2015.

[12] K. K. Nielsen, H. N. Bez, L. von Moos, R. Bjørk, D. Eriksen, and C. R. H. Bahl. Direct measurements of the magnetic entropy change. *Review of Scientific Instruments*, 86(10):103903, 2015.

[13] L. von Moos. *Hysteresis in Magnetocaloric Materials: An experimental and modelling approach*. PhD thesis, Technical University of Denmark, 2014.

[14] W. Brey, G. Nellis, and S. Klein. Thermodynamic modeling of magnetic hysteresis in amrr cycles. *International Journal of Refrigeration*, 47:85–97, 2014.

[15] S. M. Benford and G. V. Brown. T-s diagram for gadolinium near the curie temperature. *J. Appl. Phys.*, 52:2110–2112, 1981.

[16] A. R. Dinesen, S. Linderoth, and S. Morup. Direct and indirect measurement of the magnetocaloric effect in $La_{0.67}Ca_{0.33-y}Sr_xMnO_{3\pm\sigma}$. *Journal of Physics: Condensed Matter*, 17(39):6257, 2005.

[17] C. Zimm, A. Boeder, J. Chell, A. Sternberg, A. Fujita, S. Fujieda, and K. Fukamichi. Design and performance of a permanent-magnet rotary refrigerator. *International Journal of Refrigeration*, 29(8):1302–1306, 2006.

[18] G. Green, J. Chafe, J. Stevens, and J. Humphrey. A gadolinium-terbium active regenerator. In *Advances in Cryogenic Engineering*, pages 1165–1174. Springer, 1990.

[19] D. Eriksen, K. Engelbrecht, C. R. H. Bahl, R. Bjørk, K. K. Nielsen, A. R. Insinga, and N. Pryds. Design and experimental tests of a rotary active magnetic regenerator prototype. *International Journal of Refrigeration*, 58:14–21, 2015.

[20] V. K. Pecharsky and K. A. Gschneidner Jr. Giant magnetocaloric effect in $Gd_5(Si_2Ge_2)$. *Physical review letters*, 78(23):4494, 1997.

[21] K. A. Gschneidner Jr. and V. K. Pecharsky. Magnetocaloric materials. *Annu. Rev. Mater. Sci.*, 30:387–429, 2000.

[22] F. Hu, B. Shen, J. Sun, and J. Zhang. Great magnetic entropy change in $La(Fe,M)_{13}(M = Si, Al)$ with co doping. *Chinese Physics*, 9(7):550, 2000.

[23] B. G. Shen, J. R. Sun, F. X. Hu, H. W. Zhang, and Z. H. Cheng. Recent progress in exploring magnetocaloric materials. *Advanced Materials*, 21(45):4545–4564, 2009.

[24] E. Bruck, M. Ilyn, A. M. Tishin, and O. Tegus. Magnetocaloric effects in $MnFeP_{1-x}As_x$-based compounds. *J. Magn. Magn. Mater.*, 290:8–13, 2005.

[25] R. Bjørk, C. R. H. Bahl, and M. Katter. Magnetocaloric properties of $LaFe_{13-x-y}Co_xSi_y$ and commercial grade Gd. *Journal of Magnetism and Magnetic Materials*, 322(24):3882–3888, 2010.

[26] S. Taskaev, K. Skokov, D. Karpenkov, V. Khovaylo, V. Buchelnikov, D. Zherebtsov, M. Ulyanov, D. Bataev, M. Drobosyuk, and A. Pellenen. Magnetocaloric properties of severe plastic deformed $Gd_{100-x}Y_x$ alloys. *Acta Physica Polonica A*, 127(2):641–643, 2015.

[27] S. L. Russek and C. B. Zimm. Potential for cost effective magnetocaloric air conditioning systems. *International Journal of Refrigeration*, 29(8):1366–1373, 2006.

[28] J. Kastil, P. Javorsky, J. Kamarad, and E. Santava. Magnetocaloric effect of gd-tb alloys: influence of the sample shape anisotropy. *Applied Physics A*, 104(1):205–209, 2011.

[29] A. Fujita, S. Fujieda, Y. Hasegawa, and K. Fukamichi. Itinerant-electron metamagnetic transition and large magnetocaloric effects in $La(Fe_xSi_{1-x})_{13}$ compounds and their hydrides. *Physical Review B*, 67(10):104416, 2003.

[30] F. X. Hu, J. Gao, X. L. Qian, M. Ilyn, A. M. Tishin, J. R. Sun, and B. G. Shen. Magnetocaloric effect in itinerant electron metamagnetic systems $La(Fe_{1-x}Co_x)_{11.9}Si_{1.1}$. *Journal of Applied Physics*, 97(10):10M303, 2005.

[31] J. Shen, B. Gao, Q. Dong, Y. Li, F. Hu, J. Sun, and B. Shen. Magnetocaloric effect in $La_{1-x}Pr_xFe_{10.7}Co_{0.8}Si_{1.5}$ compounds near room temperature. *Journal of Physics D: Applied Physics*, 41(24):245005, 2008.

[32] M. Manekar and S. B. Roy. Reproducible room temperature giant magnetocaloric effect in fe-rh. *Journal of Physics D: Applied Physics*, 41(19):192004, 2008.

[33] F. Hu, B. Shen, J. Sun, and G. Wu. Large magnetic entropy change in a heusler alloy $Ni_{52.6}Mn_{23.1}Ga_{24.3}$ single crystal. *Physical Review B*, 64(13):132412, 2001.

[34] K. A. Gschneidner Jr. and V. K. Pecharsky. Thirty years of near room temperature magnetic cooling: where we are today and future prospects. *Int. J. Refrigeration*, 31:945–961, 2008.

[35] B. Yu, M. Liu, P. W. Egolf., and A. Kitanovski. A review of magnetic refrigerator and heat pump prototypes built before the year 2010. *Int. J. Refrigeration*, 33:1029–1060, 2010.

[36] A. Kitanovski, J. Tusek, and A. Poredosc. *Magnetocaloric energy conversion*. Springer, 2015.

[37] R. Bjørk, C. R. H. Bahl, A. Smith, and N. Pryds. Review and comparison of magnet designs for magnetic refrigeration. *International Journal of Refrigeration*, 33(3):437–448, 2010.

[38] S. Jacobs, J. Auringer, A. Boeder, J. Chell, L. Komorowski, J. Leonard, S. Russek, and C. Zimm. The performance of a large-scale rotary magnetic refrigerator. *International Journal of Refrigeration*, 37:84–91, 2014.

[39] D. S. Arnold, A. Tura, and A. Rowe. Experimental analysis of a two-material active magnetic regenerator. *International Journal of Refrigeration*, 34(1):178–191, 2011.

[40] D. S. Arnold, A. Tura, A. Ruebsaat-Trott, and A. Rowe. Design improvements of a permanent magnet active magnetic refrigerator. *Int. J. Refrigeration*, 37:99–105, 2014.

[41] J. Tušek, A. Kitanovski, U. Tomc, and C. Favero. Experimental comparison of multilayered la-fe-co-si and single-layered gd active magnetic regenerators for use in a room-temperature magnetic refrigerator. *International Journal of Refrigeration*, 37:117–126, 2014.

[42] K. Engelbrecht, D. Eriksen, C. R. H. Bahl, R. Bjørk, J. Geyti, J. A. Lozano, K. K. Nielsen, F. Saxild, A. Smith, and N. Pryds. Experimental results for a novel rotary active magnetic regenerator. *International Journal of Refrigeration*, 35(6):1498–1505, 2012.

[43] D. Eriksen, K. Engelbrecht, C. R. H. Bahl, and R. Bjørk. Exploring the efficiency potential for an active magnetic regenerator. *Science and Technology for the Built Environment*, 22(5):527–533, 2016.

[44] H. Neves Bez, K. Navickaite, T. Lei, K. Engelbrecht, A. Barcza, and C. R. H. Bahl. Epoxy-bonded $La(Fe,Mn,Si)_{13}H_z$ as a multi-layered active magnetic regenerator. In *The 7th IIF-IIR International Conference on Magnetic Refrigeration at Room Temperature*, 2016.

[45] K. Engelbrecht, C. R. H. Bahl, and K. K. Nielsen. Experimental results for a magnetic refrigerator using three different types of magnetocaloric material regenerators. *International Journal of Refrigeration*, 34(4):1132–1140, 2011.

[46] T. Okamura, R. Rachi, N. Hirano, and S. Nagaya. Improvement of 100w class room temperature magnetic refrigerator. *Proceedings of the 2nd International Conference of Magnetic Refrigeration at Room Temperature*, pages 377–382, 2007.

[47] M. S. Capovilla, J. A. Lozano, P. V. Trevizoli, and J. R. Barbosa Jr. Performance evaluation of a magnetic refrigeration system. *Science and Technology for the Built Environment*, 22:534–543, 2016.

[48] P. V. Trevizoli, J. R. Barbosa, and R. T. S. Ferreira. Experimental evaluation of a gd-based linear reciprocating active magnetic regenerator test apparatus. *International Journal of Refrigeration*, 34(6):1518–1526, Sep 2011.

[49] J. A. Lozano, K. Engelbrecht, C. R. H. Bahl, K. K. Nielsen, D. Eriksen, U. L. Olsen, J. R. Barbosa, A. Smith, A. T. Prata, and N. Pryds. Performance analysis of a rotary active magnetic refrigerator. *Applied Energy*, 111:669–680, 2013.

[50] J. M. Gatti, C. Muller, C. Vasile, G. Brumpter, P. Haegel, and T. Lorkin. Magnetic heat pumps: Configurable hydraulic distribution for a magnetic cooling system. *International Journal of Refrigeration*, 37:165–175, 2014.

[51] K. Engelbrecht and C. R. H. Bahl. Evaluating the effect of magnetocaloric properties on magnetic refrigeration performance. *J. Appl. Phys.*, 108:123918, 2010.

[52] B. Van Leer. Towards the ultimate conservative difference scheme iii. upstream-centered finite-difference schemes for ideal compressible flow. *Journal of Computational Physics*, 23:263–275, 1977.

[53] B. Torregrosa-Jaime, K. Engelbrecht, and Paya J. A new numerical scheme for the simulation of active magnetic regenerators. In *Proceedings of the 6th IIF-IIR international Conference on Magnetic Refrigeration*, 2014.

[54] K. K. Nielsen, J. Tušek, K. Engelbrecht, S. Schopfer, A. Kitanovski, C. R. H. Bahl, A. Smith, N. Pryds, and A. Poredos. Review on numerical modeling of active magnetic regenerators for room temperature applications. *Int. J. Refrigeration*, 34:603–616, 2011.

[55] L. D. Kirol and J. I. Mills. Numerical analysis of thermomagnetic generators. *J. Appl. Phys.*, 56:824–828, 1984.

[56] J. W. Johnson and C. B. Zimm. Performance modeling of a 4 k active magnetic regenerative refrigerator. *Journal of Applied Physics*, 79(5):2171–2175, 1996.

[57] P. Li, M. Gong, and J. Wu. Geometric optimization of an active magnetic regenerative refrigerator via second-law analysis. *J. Appl. Phys.*, 104(10):103536, 2008.

[58] A. Sarlah. *Thermohydraulic properties of heat regenerators in magnetic refrigerators*. PhD thesis, University of Ljubljana, Slovenia, 2008.

[59] J. Tušek, A. Kitanovski, and A. Poredoš. Geometrical optimization of packed-bed and parallel-plate active magnetic regenerators. *Int. J. Refrigeration*, 36(5):1456–1464, 2013.

[60] T. F. Petersen, N. Pryds, A. Smith, J. Hattel, and H. Schmidt. Two-dimensional mathematical model of a reciprocating room-temperature active magnetic regenerator. *International Journal of Refrigeration*, 31(3):432–443, 2008.

[61] K. K. Nielsen. *Numerical modeling and analysis of the active magnetic regenerator*. PhD thesis, Technical University of Denmark, 2010.

[62] P. A. Oliveira, P. Trevizoli Jr., and Prata A. T. Numercial analsysis of a reciprocating active magnetic regenerator. In *Proceedings of the 3rd International Conference on Magnetic Refrigeration at Room Temperature*, 2009.

[63] K. K. Nielsen, G. F. Nellis, and S. A. Klein. Numerical modeling of the impact of regenerator housing on the determination of nusselt numbers. *International Journal of Heat and Mass Transfer*, 65:552–560, 2013.

[64] K. K. Nielsen, K. Engelbrecht, and C. R.H. Bahl. The influence of flow maldistribution on the performance of inhomogeneous parallel plate heat exchangers. *Int. J. Heat Mass Transf.*, 60:432–439, 2013.

[65] T. Lei, K. K. Nielsen, K. Engelbrecht, C. R. H. Bahl, H. Neves Bez, and C. T. Veje. Sensitivity study of multi-layer active magnetic regenerators using first order magnetocaloric material $\mathrm{La(FeMnSi)_{13}H}_y$. *J. Appl. Phys.*, 118(1):014903, 2015.

[66] D. R. Durran. *Numerical methods for fluid dynamics: With applications to geophysics*. Springer Science & Business Media, 2010.

[67] P. K. Sweby. High resolution schemes using flux limiters for hyperbolic conservation laws. *SIAM J. Numer. Anal.*, 21(5):995–1011, 1984.

[68] S. Jacobs. Modeling and optimal design of a multi-layer active magnetic refrigeration system. In *Proceedings of the 3rd International Conference on Magnetic Refrigeration at Room Temperature*, 2009.

[69] C. Aprea, A. Greco, and A. Maiorino. The use of the first and of the second order phase magnetic transition alloys for an amr refrigerator at room temperature: A numerical analysis of the energy performances. *Energy Conversion and Management*, 70:40–55, 2013.

[70] V. K. Pecharsky and K. A. Gschneidner Jr. Advanced magnetocaloric materials: What does the future hold? *Int. J. Refrig.*, 29:1239–1249, 2006.

[71] K. Morrison, K. G. Sandeman, L. F. Cohen, C. P. Sasso, V. Basso, A. Barcza, M. Katter, J. D. Moore, K. P. Skokov, and O. Gutfleisch. Evaluation of the reliability of the measurement of key magnetocaloric properties: A round robin study of $La(Fe, Mn, Si)H$ conducted by the sseec consortium of european laboratories. *International Journal of Refrigeration*, 35(6):1528–1536, 2012.

[72] S. Fujieda, Y. Hasegawa, A. Fujita, and K. Fukamichi. Thermal transport properties of magnetic refrigerants $La(Fe_xSi_{1-x})_{13}$ and their hydrides, and $Gd_5Si_2Ge_2$ and MnAs. *Journal of Applied Physics*, 95(5):2429–2431, 2004.

[73] P. V. Trevizoli and J. R. Barbosa. Entropy generation minimization analysis of oscillating-flow regenerators. *International Journal of Heat and Mass Transfer*, 87:347–358, 2015.

[74] N. Pryds, F. Clemens, M. Menon, P. H. Nielsen, K. Brodersen, R. Bjørk, C. R. H. Bahl, K. Engelbrecht, K. K. Nielsen, and A. Smith. A monolithic perovskite structure for use as a magnetic regenerator. *J. Am. Ceram. Soc*, 94(8):2549–2555, 2011.

[75] J. D. Moore, D. Klemm, D. Lindackers, S. Grasemann, R. Träger, J. Eckert, L. Löber, S. Scudino, M. Katter, and A. Barcza. Selective laser melting of $La(FeCoSi)_{13}$ geometries for magnetic refrigeration. *J. Appl. Phys.*, 114(4):043907, 2013.

[76] R. Radebaugh and B. Louie. A simple, first step to the optimization of regenerator geometry. In *Proceedings of the 3rd Cryocooler Conference*, volume 1, pages 177–198, 1985.

[77] J. A. Barclay and S. Sarangi. Selection of regenerator geometry for magnetic refrigerator applications. *Technical Report, Los Alamas National Laboratory, U.S.*, 1984.

[78] D. Vuarnoz and T. Kawanami. Numerical analysis of a reciprocating active magnetic regenerator made of gadolinium wires. *Appl. Therm. Eng.*, 37:388–395, 2012.

[79] J. Li, T. Numazawa, K. Mastumoto, Y. Yanagisawa, and H. Nakagome. A modeling study on the geometry of active magnetic regenerator. In *Advances in Cryogenic Engineering*, volume 1434, pages 327–334. AIP Publishing, 2012.

[80] R. F. Benenati and C. B. Brosilow. Void fraction distribution in beds of spheres. *AIChE J.*, 8(3):359–361, 1962.

[81] R. F Barron, G. F. Nellis, and J. M. Pfotenhauer. *Cryogenic heat transfer*. CRC Press, 1999.

[82] J. C. Armour and J. N. Cannon. Fluid flow through woven screens. *AIChE J.*, 14(3):415–420, 1968.

[83] S. Ergun and A. A. Orning. Fluid flow through randomly packed columns and fluidized beds. *Ind. Eng. Chem.*, 41(6):1179–1184, 1949.

[84] M. Kaviany. *Principles of heat transfer in porous media*. Springer-Verlag, 1991.

[85] L. G. Gibilaro, R Di Felice, S. P. Waldram, and P. U. Foscolo. Generalized friction factor and drag coefficient correlations for fluid-particle interactions. *Chem. Eng. Sci.*, 40(10):1817–1823, 1985.

[86] W. M. Kays and A. L. London. *Compact Heat Exchangers*. Krieger Publishing Company, 1984.

[87] N. Wakao, S. Kaguei, and T. Funazkri. Effect of fluid dispersion coefficients on particle-to-fluid heat transfer coefficients in packed beds: correlation of nusselt numbers. *Chem. Eng. Sci.*, 34(3):325–336, 1979.

[88] A. Bejan. *Entropy generation minimization: the method of thermodynamic optimization of finite-size systems and finite-time processes*. CRC press, 1995.

[89] R. K. Shah and A. L. London. *Laminar flow forced convection in ducts: a source book for compact heat exchanger analytical data*. Academic press, 1978.

[90] M. Nickolay and H. Martin. Improved approximation for the nusselt number for hydrodynamically developed laminar flow between parallel plates. *Int. J. Heat Mass Transf.*, 45(15):3263–3266, 2002.

[91] W. M. Kays, M. E. Crawford, and B. Weigand. *Convective heat and mass transfer*. Tata McGraw-Hill Education, 2012.

[92] M. Asadi, G. Xie, and B. Sunden. A review of heat transfer and pressure drop characteristics of single and two-phase microchannels. *Int. J. Heat Mass Transf.*, 79:34–53, 2014.

[93] K. V. Sharp and R. J. Adrian. Transition from laminar to turbulent flow in liquid filled microtubes. *Exp. Fluids*, 36(5):741–747, 2004.

[94] P. Wibulswas. *Laminar-flow heat-transfer in non-circular ducts.* PhD thesis, University of London, 1966.

[95] H. Hausen, M. S. Sayer, and A. J. Willmott. *Heat Transfer in counterflow, parallel flow and cross flow*. McGraw-Hill New York, 1983.

[96] P. S. Lee, S. V. Garimella, and D. Liu. Investigation of heat transfer in rectangular microchannels. *Int. J. Heat Mass Transf.*, 48(9):1688–1704, 2005.

[97] M. Tanaka, I. Yamashita, and F. Chisaka. Flow and heat transfer characteristics of the stirling engine regenerator in an oscillating flow. *JSME Int. J.*, 33(2):283–289, 1990.

[98] D. Gedeon and J. G. Wood. Oscillating-flow regenerator test rig: Hardware and theory with derived correlations for screens and felts. *Technical Report, NASA, U.S.*, 1996.

[99] J. R. Sodre and J. A. R. Parise. Friction factor determination for flow through finite wire-mesh woven-screen matrices. *J. Fluids Eng.*, 119(4):847–851, 1997.

[100] J. W. Park, D. Ruch, and R. A. Wirtz. Thermal/fluid characteristics of isotropic plain-weave screen laminates as heat exchange surfaces. *Proceed. 40th AIAA Aerosp. Sci. Meeti. Exhibit.*, 208:2002–0208, 2002.

[101] K. Hamaguchi, S. Takahashi, and H. Miyabe. Thermal performance of regenerator matrix. *Trans. Jpn. Soc. Mech. Eng.*, 49(445):2001–2010, 1983.

[102] S. Isshiki, A. Sakano, I. Ushiyama, and N. Isshiki. Studies on flow resistance and heat transfer of regenerator wire meshes of stirling engine in oscillatory flow. *JSME Int. J.*, 40(2):281–289, 1997.

[103] Z. C. Chang and P. H. Chen. Flow channeling effect on a regenerator's thermal performance. *Cryogenics*, 38(2):191–196, 1998.

[104] G. R. Hadley. Thermal conductivity of packed metal powders. *Int. J. Heat Mass Transf.*, 29(6):909–920, 1986.

[105] U. H. Kurzweg and M. J. Jaeger. Thermal pulse propagation and dispersion in laminar flow within conduits of finite wall conductivity. *Int. J. Heat Mass Transf.*, 40(6):1391–1400, 1997.

[106] W. S. Chang. Porosity and effective thermal conductivity of wire screens. *J. Heat Transf.*, 112(1):5–9, 1990.

[107] R. Radebaugh. Development of the pulse tube refrigerator as an efficient and reliable cryocooler. In *Proceedings of Institute of Refrigeration*, volume 96, pages 1999–2000. Citeseer, 2000.

[108] L. Chen, Y. Li, F. Sun, and C. Wu. Power optimization of open-cycle regenerator gas-turbine power-plants. *Applied Energy*, 78(2):199–218, 2004.

[109] C. W. Park and M. Kaviany. Evaporation-combustion affected by in-cylinder, reciprocating porous regenerator. *Journal of Heat Transfer*, 124(1):184, 2002.

[110] K. Daou, R. Wang, and Z. Xia. Desiccant cooling air conditioning: a review. *Renewable and Sustainable Energy Reviews*, 10(2):55–77, 2006.

[111] E. Barbour, D. Mignard, Y. Ding, and Y. Li. Adiabatic compressed air energy storage with packed bed thermal energy storage. *Applied Energy*, 155:804–815, 2015.

[112] G. L. Morini. Single-phase convective heat transfer in microchannels: a review of experimental results. *International Journal of Thermal Sciences*, 43(7):631–651, 2004.

[113] P. J. Heggs and D. Burns. Single-blow experimental prediction of heat transfer coefficients: A comparison of four commonly used techniques. *Experimental Thermal and Fluid Science*, 1(3):243–251, 1988.

[114] S. Schopfer. *Experimental and numerical determination of thermohydraulic properties of regenerators subjected to oscillating flow*. PhD thesis, University of Victoria, 2011.

[115] P. Trevizoli, Y. Liu, A. Tura, A. Rowe, and J. Barbosa. Experimental assessment of the thermal-hydraulic performance of packed-sphere oscillating-flow regenerators using water. *Experimental Thermal and Fluid Science*, 57:324–334, 2014.

[116] K. Vafai. Convective flow and heat transfer in variable-porosity media. *Journal of Fluid Mechanics*, 147(1):233–259, 1984.

[117] M. Frischmann, K. Engelbrecht, G. Nellis, and S. Klein. Heat transfer coefficient in a packed sphere regenerator for use in active magnetic regenerative refrigeration. In *International Refrigeration and Air Conditioning Conference*, 2008.

[118] J. E. Coppage and A. L. London. Heat transfer and flow friction characteristics of porous media. *Chem. Eng. Prog.*, 52:57–63, 1956.

[119] F. W. Schmidt and A J. Willmott. *Thermal energy storage and regeneration*. Hemisphere Publishing Corporation Washington, 1981.

[120] R. A. Ackermann. *Cryogenic regenerative heat exchangers*. Springer Science & Business Media, 2013.

[121] D. S. Beck. Regenerator effectiveness during transient operation. *Journal of Engineering for Gas Turbines and Power*, 118(3):661, 1996.

[122] D. E. Daney. Regenerator performance with sinusoidal flow. *Cryogenics*, 31(9):839–841, 1991.

[123] M. Golombok, H. Jariwala, and L. C. Shirvill. Gas-solid heat exchange in a fibrous metallic material measured by a heat regenerator technique. *International Journal of Heat and Mass Transfer*, 33(2):243–252, 1990.

[124] Y. Ju and Q. Shen. Comparative study of oscillating flow characteristics of cryocooler regenerator at low temperatures. *Frontiers of Energy and Power Engineering in China*, 3(1):80–84, 2009.

[125] OMEGA. Thermocouple response time. Technical report, OMEGA Engineering Inc., 2016.

[126] R. K. Shah and D. P. Sekuli. *Fundamentals of Heat Exchanger Design*. Wiley-Blackwell, 2003.

[127] EES. Engineering equation solver. Technical report, F-Chart Software, LLC., 2016.

[128] M. Katter, V. Zellmann, G. W. Reppel, and K. Uestuener. Magnetocaloric properties of $La(Fe, Co, Si)_{13}$ bulk material prepared by powder metallurgy. *IEEE Transactions on Magnetics*, 44(11):3044–3047, 2008.

[129] J. Lanzarini, T. Barriere, M. Sahli, J. C. Gelin, A. Dubrez, C. Mayer, M. Pierronnet, and P. Vikner. Thermoplastic filled with magnetocaloric powder. *Materials & Design*, 87:1022–1029, 2015.

[130] L. H. S. Roblee, R. M. Baird, and J. W. Tierney. Radial porosity variations in packed beds. *AIChE J.*, 4:460–464, 1958.

[131] D. Velazquez, M. Castro, and Palacios E. Practical properties of lafecosi materials to be used in magnetic cooling regenerators. In *Proceedings of 6th IIF-IIR International Conference on Magnetic Refrigeration at Room Temperature*, 2014.

Appendix A

Published or submitted papers

A.1 Sensitivity study of multi-layer active magnetic regenerators using first order magnetocaloric material $La(Fe,Mn,Si)_{13}H_y$

T. Lei, K. K. Nielsen, K. Engelbrecht, C. R. H. Bahl, H. Neves Bez and C. T. Veje, Sensitivity study of multi-layer active magnetic regenerators using first order magnetocaloric material $La(Fe,Mn,Si)_{13}H_y$, *Journal of Applied Physics*, **118**, 014903, (2015).

JOURNAL OF APPLIED PHYSICS **118**, 014903 (2015)

Sensitivity study of multi-layer active magnetic regenerators using first order magnetocaloric material $La(Fe,Mn,Si)_{13}H_y$

Tian Lei,[1,a)] Kaspar K. Nielsen,[1] Kurt Engelbrecht,[1] Christian R. H. Bahl,[1]
Henrique Neves Bez,[1] and Christian T. Veje[2]
[1]*Department of Energy Conversion and Storage, Technical University of Denmark, Frederiksborgvej 399, DK 4000 Roskilde, Denmark*
[2]*Mærsk Mc-Kinney Møller Instituttet, University of Southern Denmark, DK 5230 Odense M, Denmark*

(Received 27 February 2015; accepted 21 June 2015; published online 6 July 2015)

We present simulation results of multi-layer active magnetic regenerators using the solid-state refrigerant $La(Fe,Mn,Si)_{13}H_y$. This material presents a large, however quite sharp, isothermal entropy change that requires a careful choice of number of layers and working temperature for multi-layer regenerators. The impact of the number of layers and the sensitivity to the working temperature as well as the temperature span are quantified using a one dimensional numerical model. A study of the sensitivity of variation in Curie temperature through a uniform and normal distribution is also presented. The results show that the nominal cooling power is very sensitive to the Curie temperature variation in the multi-layer regenerators. A standard deviation of the Curie temperature variation for a normal distribution less than 0.6 K is suggested in order to achieve sufficient performance of a 15-layer regenerator with Curie temperature spacing of 2 K. © *2015 AIP Publishing LLC*.
[http://dx.doi.org/10.1063/1.4923356]

I. INTRODUCTION

Magnetic refrigeration is a promising technology compared to vapor-compression systems due to the use of environmentally friendly heat transfer fluids and solid-state refrigerants, as well as a potentially high efficiency. With various improvements in magnetocaloric materials (MCMs), system design, and fluid control, the magnetic refrigeration technique has recently undergone a rapid development and several kilowatt class prototypes have emerged.[1,2] MCMs exhibit a temperature rise due to adiabatic magnetization, or temperature decrease when adiabatically demagnetized. The magnetocaloric effect has a peak near the Curie temperature T_C of the MCM, and T_C is the temperature at which the transition from ferro- to paramagnetic phase takes place. With permanent magnets producing fields on the order of 1.5 T, the adiabatic temperature change of the best performing material will be about 5 K,[3] which may not be sufficient for practical applications. To achieve a large temperature span, the concepts of active magnetic regeneration (AMR)[4] and multi-layer regenerators are widely used in the design of existing machines.[2,5,6] An AMR regenerator has a similar porous structure and oscillating flow pattern as some passive regenerative heat exchangers, but uses the MCM to transfer magnetic work into the regenerator, allowing it to absorb a cooling power over a useful temperature span.

A typical AMR cycle[7] starts from the adiabatic magnetization process, which causes the solid temperature to increase. Then the heat transfer fluid flows through the porous bed from the cold to the hot end and is heated by the solid. At the hot end, the fluid rejects excess heat to the ambient. Followed by the adiabatic demagnetization and a temperature decrease of the MCM, the hot-to-cold flow will reject heat to the solid and reach a lower temperature than the initial condition. Then the fluid absorbs heat, i.e., a cooling load, at the cold end. After several cycles, a temperature gradient is achieved along the axial direction and the regenerator reaches a periodic steady state. The net enthalpy flows at the ends are the heating and cooling power (Q_h and Q_c), respectively.

The material's performance has significant effect on the cooling power and the regenerator efficiency. Recent research has presented various interesting materials with compelling performance;[2,6,8] especially, MCMs with a first-order phase transition at the Curie temperature have a large isothermal entropy change ΔS_{mag}. It is defined as

$$\Delta S_{mag}(T, H_i : H_f) \equiv S(T, H_f) - S(T, H_i), \tag{1}$$

with H and T denoting magnetic field and temperature, respectively, and the subscripts i and f denoting initial and final state, respectively. The isothermal entropy change of these first-order transition materials is often large compared to MCMs with a pure second order transition like gadolinium (Gd). $La(Fe,Mn,Si)_{13}H_y$ is an attractive first order material and is subject to extensive research due to the high values of ΔS_{mag}, a small hysteresis effect, adjustable T_C, relatively high thermal conductivity, and high stability.[9–11] The material was developed from $La(Fe_xSi_{1-x})_{13}$, where the Curie temperature can be tuned by the addition of hydrogen.[12] Barcza *et al.*[10] pointed out that it is difficult to control partial hydrogenation on the industrial level with high accuracy; therefore, a method of substituting Fe with Mn[13] was used. With this method, the material is always fully hydrogenated while the Mn content tunes T_C.

Although it is anticipated that large ΔS_{mag} will improve the regenerator performance, it decreases quickly at temperatures away from its T_C. A sharp peak may prevent the

[a)]Electronic mail: tile@dtu.dk

material from working in the optimal temperature region. Multi-layer regenerators, in which each layer is aligned to make sure the T_C of each material follows the temperature gradient, can be a solution to this issue. Larger temperature spans as well as cooling capacities are expected in multi-layer regenerators using first order materials compared to single-material regenerators.

Smith *et al.*[14] pointed out that for first order materials, the peak in the specific heat will move significantly with the applied field, and in reality the ΔS_{mag} peaks also show similar shift to higher temperature in a high applied field.[11] It is implied that the best working temperature for the first order material is expected to be higher than the Curie temperature. Therefore, multi-layer regenerators could be sensitive to the working temperature and a study of how a regenerator bed should be layered is therefore presented here.

Moreover, it may be difficult to control the T_C of each material to a high accuracy when fabricating a layered regenerator. Actual regenerator beds will have some arrangements in which T_C deviates from the intended design. This paper investigates how random variations in T_C affect the AMR performance. First, the impact of the Curie temperature variation of a single layer in each position is investigated. Then a more general study is carried out, where each layer in the regenerator deviates from the desired T_C according to either a uniform distribution or a normal distribution with a set standard deviation σ.

II. ONE DIMENSIONAL NUMERICAL MODEL OF AMR

A one-dimensional transient numerical model for simulating the AMR regenerators has been developed based on the work presented by Engelbrecht *et al.*[8] The energy equations for the fluid and solid in the transient model[8,15] can be written as

$$\frac{\partial}{\partial x}\left(k_{disp}A_c\frac{\partial T_f}{\partial x}\right)-\dot{m}c_f\frac{\partial T_f}{\partial x}-\frac{Nuk_f}{d_h}a_sA_c(T_f-T_r)+\left|\frac{\partial P}{\partial x}\frac{\dot{m}}{\rho_f}\right|=\rho_fA_c\varepsilon c_f\frac{\partial T_f}{\partial t}, \quad (2)$$

$$\frac{\mathrm{Nu}k_f}{d_h}a_sA_c(T_f-T_r)+\frac{\partial}{\partial x}\left(k_{stat}A_c\frac{\partial T_r}{\partial x}\right)+(1-\varepsilon)A_c\rho_rT_r\left(\frac{\partial s_r}{\partial H}\right)_T\frac{\partial H}{\partial t}=\rho_r(1-\varepsilon)A_cc_{r,H}\frac{\partial T_r}{\partial t}, \quad (3)$$

where k, T, ρ, c, and s are the thermal conductivity, temperature, density, specific heat, and specific entropy; A_c, d_h, a_s, and ε are the cross section area, hydraulic diameter, specific area, and porosity, which reflect the geometry characteristics of a regenerator; x, t, $\dot{m}$, and H are the axial position, time, mass flow rate, and internal magnetic field. The subscripts f and r represent fluid and solid refrigerant, respectively. More details for the expressions of thermal conductivity due to fluid dispersion k_{disp}, static thermal conductivity k_{stat}, pressure drop $\frac{\partial P}{\partial x}$, and Nusselt number Nu are presented by Nielsen *et al.*[16] It should be noted that k_{disp} and k_{stat} are already scaled to fit the cross-sectional area; therefore, the porosity is not included in the conduction terms. From left to right in the fluid energy equation, the thermal dispersion, convection, heat transfer between solid and fluid, viscous dissipation, and energy storage are considered; the terms for the energy equation of the solid side are the heat transfer between solid and fluid, axial heat conduction, magnetic work, and energy storage.

In each AMR cycle, the fluid is assumed to enter the packed bed with a constant temperature T_{hot} at the hot end during the hot-to-cold blow, and T_{cold} at the cold end during cold-to-hot blow, synchronized with a periodically varying magnetic field. The temperature span is $\Delta T = T_{\mathrm{hot}} - T_{\mathrm{cold}}$ and the heating and cooling powers are

$$Q_h=\int|\dot{m}|_f(h_{f,x=0}-h_{f,T_{\mathrm{hot}}})dt \quad \text{when} \quad \dot{m}<0, \quad (4)$$

$$Q_c=\int|\dot{m}|_f(h_{f,T_{\mathrm{cold}}}-h_{f,x=L})dt \quad \text{when} \quad \dot{m}>0, \quad (5)$$

where $h_{f,x=0}$ and $h_{f,x=L}$ are the specific enthalpies of the fluid flowing out of the hot and cold end; $h_{f,T_{\mathrm{hot}}}$ and $h_{f,T_{\mathrm{cold}}}$ are the specific enthalpies of the fluid at T_{hot} and T_{cold}.

In the numerical model, the central difference and implicit time schemes are used for discretizing the partial differential equations presented above in both space and time. By solving the coupled discretized equations, the temperature gradient can be calculated after each time step given an initial condition, and the model will output the performance indices after reaching the steady state with a tolerance. The main modeling parameters are presented in Table I. The regenerator geometry is kept fixed as a packed bed, and the number of layers, the material, the averaged mass flow rate, as well as the temperature span vary in different cases.

For modeling multi-layer regenerators using $La(Fe,Mn,Si)_{13}H_y$, the magnetocaloric properties, mainly the entropy data as a function of the internal magnetic field and temperature, of numerous materials with different T_C are needed. However, existing measurements are limited. Based on the observation that $La(Fe,Mn,Si)_{13}H_y$ materials behave quite similarly under the magnetization process and the peaks of both ΔS_{mag} and specific heat c_H are similar in magnitude and shape for a range of T_C,[11] it is assumed that the properties

TABLE I. Main parameters input in the numerical model.

Parameter	Value	Unit
Maximum applied magnetic field	1.2	T
Cross sectional area	225×10^{-6}	m^2
Length	0.100	m
Frequency	2	Hz
Regenerator bed number	20	…
Bed geometry	Packed sphere bed	…
Sphere diameter	0.0003	m
Porosity	0.36	…
MCM mass	2.01	kg
MCM thermal conductivity	8	W/(mK)
MCM density	7000	kg/m^3

of the materials with different T_C other than the characterized material can be approximated by shifting one group of experimental data according to T_C. The material has a T_C of 305.0 K, and it is provided by Vacuumschmelze GmbH, Germany. The measured data of the specific heat at zero field and the absolute value of ΔS_{mag} presented in Fig. 1 are obtained from the Lake Shore 7407 Vibrating Sample Magnetometer (VSM) and a Differential Scanning Calorimeter (DSC) at the Technical University of Denmark.[17] The density of $La(Fe,Mn,Si)_{13}H_y$ is measured in a X-ray Diffraction (XRD). The thermal conductivity k_r of $La(Fe,Mn,Si)_{13}H_y$ is assumed as 8 W/(mK), which is close the measured k_r data of LaFeSi and LaFeSiH at the ambient temperature.[9]

III. RESULTS AND DISCUSSION

A. Impact of layer number and sensitivity to working temperature

Compared to second order materials, a distinguishing feature of first order materials is the shape of the ΔS_{mag} curves with respect to temperature. The sharp peak in ΔS_{mag} makes a multi-layer design necessary for regenerators using first order materials. In this section, the impact of the number of layers in the regenerator is quantitatively studied. An N_l-layer regenerator is modeled here while operating over a temperature span of 30 K, and N_l is the number of layers. The material in the n^{th} layer is assumed to have $T_{C,n} = 305 - 30(2n-1)/2n$ $(n = 1, ..., N_l)$. That is, the $T_{C,n}$ follows a linear arrangement along the temperature gradient from 305 to 275 K. Taking a 15-layer regenerator, for example, the $T_{C,n}$ $(n = 1, ..., 15)$ varies from 304 to 276 K with an interval of 2 K according to the expression above.

It is shown in Fig. 1 that the temperature, at which the peak value of ΔS_{mag} occurs, shifts to higher values as the magnetic field increases. Due to this effect, the material is predicted to perform better when the working temperature is higher than the Curie temperature. To estimate the sensitivity to the working temperature, the hot and cold end temperatures (T_{hot} and T_{cold}) are shifted at the same time by −2 to 8 K in the simulation, while the temperature span ΔT is held fixed at 30 K and $T_{C,n} = 305 - 30(2n-1)/2n$.

Fig. 2 presents the impact of the number of layers N_l and the working temperature T_w on the nominal cooling power $\eta_1 = \frac{Q_{c,T_w,N_l}}{Q_{c,T_w=307-277K,N_l=60}}$, where the denominator $Q_{c,T_w=307-277K,N_l=60}$ is the cooling power of a 60-layer regenerator under T_w of 307–277 K (also the maximum value in the figure) and Q_{c,T_w,N_l} is the cooling power of the N_l-layer regenerator working with a specific T_w. It should be noted that the averaged flow rate is optimized to get the maximum cooling power in each case.

It is shown that the nominal cooling power, η_1, increases significantly with the number of layers from 4 to 20 and approaches the maximum value when the number of layers exceeds 20 for each working temperature. The maximum number of layers in this study is 60, since a regenerator with more than 60 layers will only lead to a minimal increase in the nominal cooling power according to the results in Fig. 2. 10–15 layers may be practical considering a balance between obtaining the maximum cooling performance and the difficulty of construction. It can be observed that the performance of a multi-layer regenerator is quite sensitive to the absolute working temperature, although the temperature span is fixed. The best T_w is 307–277 K, which is 2 K higher than the

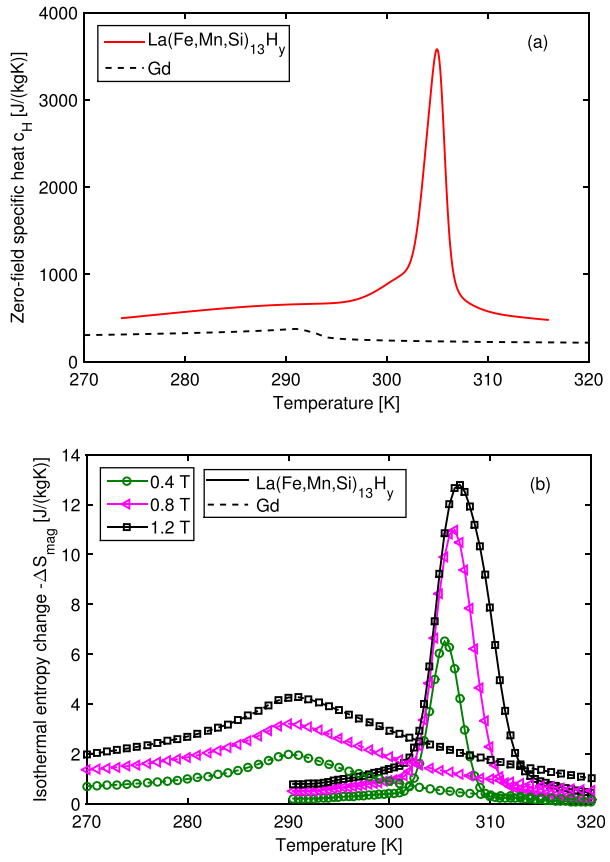

FIG. 1. The specific heat c_H at zero field (a) and the absolute value of isothermal entropy change $-\Delta S_{mag}$ (b) of $La(Fe,Mn,Si)_{13}H_y$ and Gd[18] as a function of temperature.

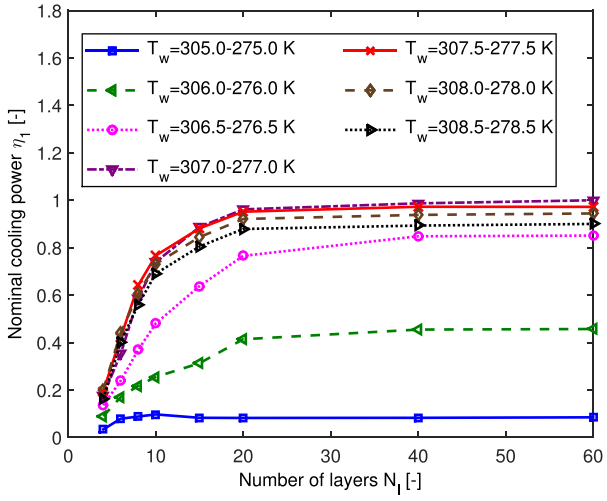

FIG. 2. Impact of number of layers N_l on nominal cooling power $\eta_1 = \frac{Q_{c,T_w,N_l}}{Q_{c,T_w=307-277K,N_l=60}}$ of N_l-layer regenerators with constant temperature span of 30 K.

initially guessed temperature span of 305–275 K. This is explained by the fact that the temperature that corresponds to the peak of ΔS_{mag} rises with increasing magnetic field. The optimal averaged mass flow rate increases with the cooling power, although the data are not presented here.

More detailed results are shown in Fig. 3, and they reveal that the multi-layer regenerators have considerable dependence on the working temperature T_w for fixed $\Delta T = 30$ K. Although both the hot and cold end temperatures are shifted, the horizontal axis only shows the hot end temperature T_{hot}. η_1 reaches the maximum value when T_w is close to 307–277 K and decreases rapidly with changes of T_w to either hot or cold region. Moreover, the nominal cooling power of the multi-layer regenerators decreases much faster when T_w is shifted lower, since the total magnetocaloric effect becomes smaller in a lower T_w region due to the shift of ΔS_{mag} curves. Flat peaks in η_1 curves are observed in the regenerators with fewer layers, which mean the sensitivity is smaller; however, much less nominal cooling power is obtained.

Fig. 4 presents the corresponding results of the coefficient of performance (COP), which is defined as $\text{COP} = \frac{Q_c}{Q_h - Q_c}$. Higher COP can be obtained in the regenerators with more layers, and the peak of the COP appears at T_w of 308.5–278.5 K, which is even higher than the guessed temperature region. The results imply that the design of the multi-layer regenerator with the first order materials is challenging, and the number of layers as well as the working temperature should be carefully chosen to achieve desired cooling power and COP.

B. Sensitivity to temperature span ΔT

Another interesting question is how multi-layer regenerators perform under different temperature spans. For the regenerators using the second order materials, the performance curves of cooling power to temperature span in the experiments[1] show a linear shape. However, with the first order materials with a narrow peak in ΔS_{mag}, the multi-layer regenerator, designed for a temperature span of 30 K, probably cannot produce more cooling power when the temperature span is decreased, because in certain layers the material may work outside its respective optimal working temperature.

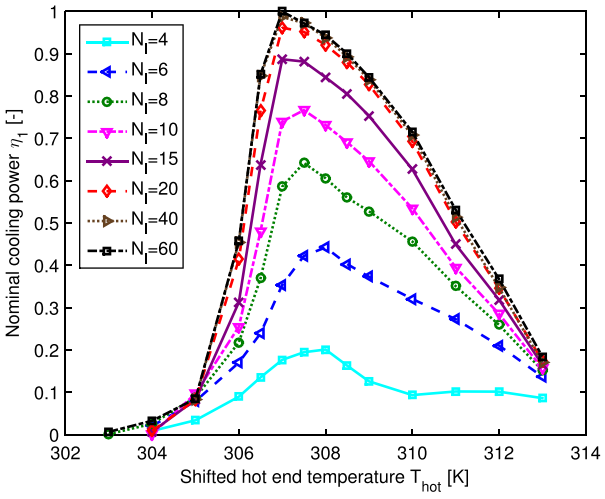

FIG. 3. Impact of working temperature T_w (from T_{hot} to $T_{\text{hot}} - 30$ K) on nominal cooling power η_1 of N_l-layer regenerators when temperature span is 30 K.

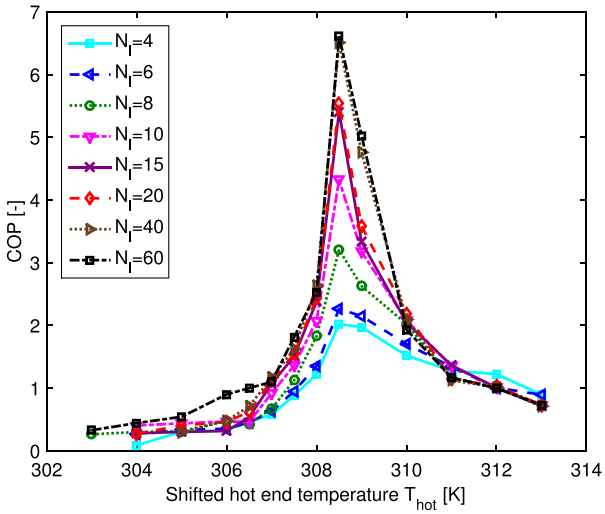

FIG. 4. Impact of working temperature T_w (from T_{hot} to $T_{\text{hot}} - 30$ K) on COP of N_l-layer regenerators when temperature span is 30 K.

To investigate this impact, the N_l-layer ($N_l = 4 - 60$) regenerators with $T_{C,n} = 305 - 30(2n-1)/2n$ K ($n = 1,...,N_l$) are chosen as the simulation targets. The hot end temperature T_{hot} is fixed at 308 K, which is close to the optimal value for most cases as found in the previous study; whereas the cold end temperature T_{cold} is varied from 278 K to 298 K with an interval of 5 K, corresponding to temperature spans ΔT from 30 K to 10 K.

The results illustrated in Fig. 5 show the impact of ΔT on nominal cooling power $\eta_2 = \frac{Q_{c,\Delta T,N_l}}{Q_{c,\Delta T=10\text{K},N_l=60}}$ of the N_l-layer regenerators. Although the temperature span is decreased, the increment in the nominal cooling power η_2 is much smaller compared to the behaviors of the regenerators using

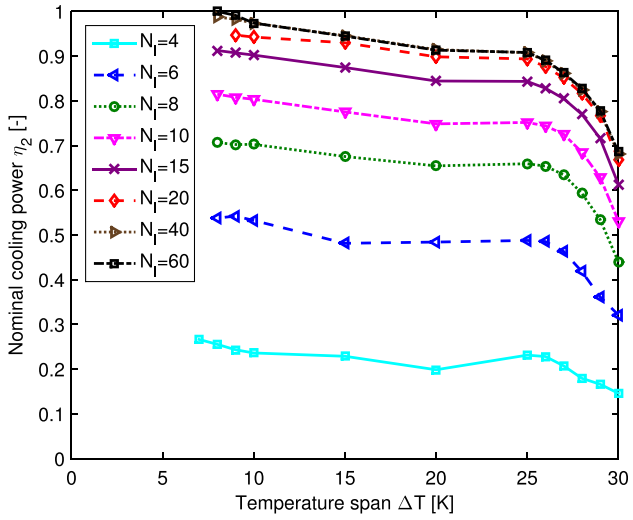

FIG. 5. Impact of temperature span ΔT on nominal cooling power $\eta_2 = \frac{Q_{c,\Delta T,N_l}}{Q_{c,\Delta T=10\text{K},N_l=60}}$ of N_l-layer regenerators with a fixed $T_{C,n}$ arrangement of $305 - 30(2n-1)/2n$.

Gd.[1] It should be noted that there is a limited temperature range for the measured material properties used in these simulations. In this case, when the temperature span falls below 7 K, the material with the lowest Curie temperature starts to operate outside of the measured property range. Here, the simulations are no longer valid and the corresponding points are not shown in Fig. 5. The results also agree well with the findings presented by Jacobs *et al.*[2] where similar performance curves can be observed for a refrigerator using a 6-layer regenerator was studied.

Moreover, to account for different temperature spans, the N_l-layer regenerators can be optimized by fitting the Curie temperature of each layer to the specific temperature span ΔT, that is, $T_{C,n} = 305 - \Delta T(2n-1)/2n$. This means that a different regenerator is modeled for each temperature span. The results of the nominal cooling power for each temperature span $\eta_3 = \frac{Q_{c,\Delta T,N_l}}{Q_{c,\Delta T,N_l=60}}$, where $Q_{c,\Delta T,N_l=60}$ is the cooling power of a 60-layer regenerator over the temperature span of ΔT, are presented in Fig. 6. The impact of the layer number is similar to the results in Fig. 2; however for a smaller temperature span, the regenerators reach the maximum cooling performance much faster, meaning fewer layers are needed to reach a cooling power near the maximum. This is because the ΔS_{mag} curves for each material have a certain width of best working temperature region and fewer layers are needed to cover a smaller temperature span.

The inset in Fig. 6 shows the number of layers when the cooling power reaches 90% of the maximum value ($\eta_3 = 0.9$) as a function of temperature span. The curve shows an approximately linear relation and gives a slope of 2.24 layers per 5 K temperature span, which can be used as a reference for choosing the number of layers when constructing layered regenerators with $La(Fe,Mn,Si)_{13}H_y$.

The results of the nominal cooling power $\eta_4 = \frac{Q_{c,\Delta T,N_l}}{Q_{c,\Delta T=5K,N_l=60}}$ produced by the multi-layer regenerators with optimized $T_{C,n}$ arrangement are presented in Fig. 7. The performance curves of the N_l-layer regenerators now behave in

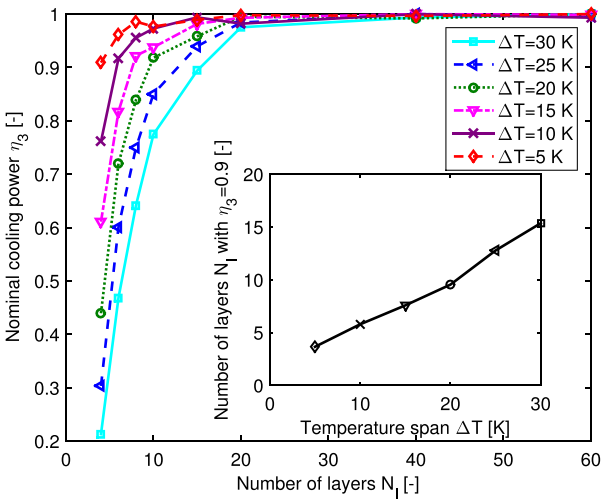

FIG. 6. Impact of number of layers N_l on nominal cooling power $\eta_3 = \frac{Q_{c,\Delta T,N_l}}{Q_{c,\Delta T,N_l=60}}$ of N_l-layer regenerators with optimized $T_{C,n}$ arrangement of $305 - \Delta T(2n-1)/2n$.

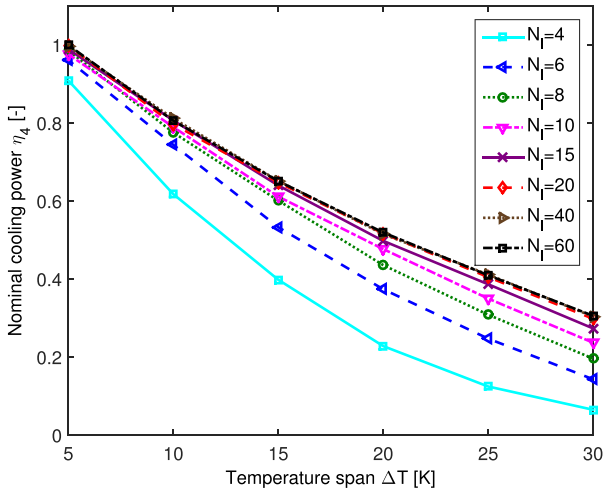

FIG. 7. Impact of temperature span ΔT on nominal cooling power $\eta_4 = \frac{Q_{c,\Delta T,N_l}}{Q_{c,\Delta T=5K,N_l=60}}$ of N_l-layer regenerators with optimized $T_{C,n}$ arrangement of $305 - \Delta T(2n-1)/2n$.

a more linear manner, which is different than those with fixed $T_{C,n}$ arrangement shown in Fig. 5. The curves split out when the temperature span becomes larger, meaning that more layers are needed to approach the maximum performance, which also reflects the conclusions drawn before.

C. Impact of Curie temperature variation in specific positions

There will always be some manufacturing variation in the Curie temperature T_C for the materials studied here, meaning the ideal T_C arrangement is quite difficult to achieve. The effect of Curie temperature variation in layered regenerators is not well understood and this will be quantified in the following study. A straightforward way to investigate this is to study the impact of the variation in the Curie temperature $\Delta T_{C,n}$, which is $T_{C,n,real} - T_{C,n,base}$ in the n^{th} layer. $T_{C,n,real}$ and $T_{C,n,base}$ are the real and base Curie temperature of every material for constructing a layered regenerator, and positive $\Delta T_{C,n}$ means shifting $T_{C,n,real}$ of the n^{th} layer to a higher temperature, and vice versa.

In the simulation, a 15-layer regenerator, in which the n^{th} layer has the Curie temperature $T_{C,n,base} = 305 - 30(2n-1)/2n$ K (n = 1…15), is used as the baseline for comparison, and in this case $\Delta T_{C,n} = 0$. Then one at a time, $T_{C,n}$ of every individual layer in the 15-layer regenerator is shifted by the variation $\Delta T_{C,n}$, which is considered to vary from −1.6 to 1.6 K with a step of 0.4 K. The temperature span is held constant at 307–277 K, and it is close to the best working temperature according to the previous study. As the number of layers and the working temperature are fixed, the optimal averaged mass flow rate for each case is close to each other, and a constant value is used in the rest of this study. The impact of $\Delta T_{C,n}$ in a single layer-n is shown in Fig. 8. The nominal cooling power η_5 is $\frac{Q_{c,\Delta T_{C,n}}}{Q_{c,\Delta T_{C,n}=0}}$, where $Q_{c,\Delta T_{C,n}=0}$ is the cooling power of the base regenerator with $\Delta T_{C,n} = 0$, meaning an even Curie temperature arrangement, and $Q_{c,\Delta T_{C,n}}$ is the cooling power of a regenerator with certain $\Delta T_{C,n}$ in the n^{th} layer. For most cases, the maximum value of η_5 is close

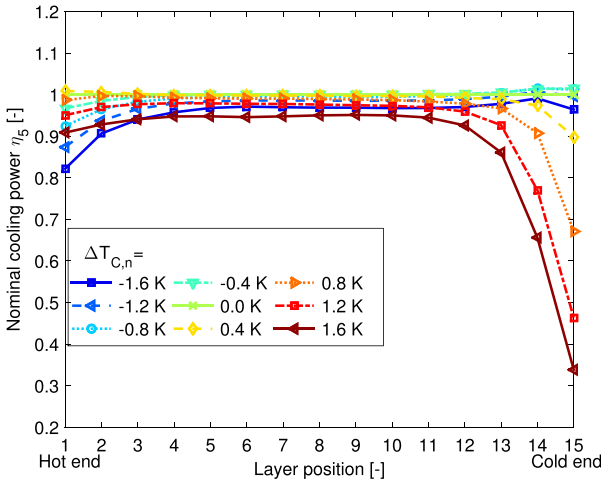

FIG. 8. Impact of Curie temperature variation $\Delta T_{C,n}$ of every individual layer on nominal cooling power $\eta_5 = \frac{Q_{c,\Delta T_{C,n}}}{Q_{c,\Delta T_{C,n}=0}}$.

to 1, which shows that the base regenerator with $\Delta T_{C,n} = 0$ is the best choice, that is, an even Curie temperature arrangement produces a cooling power close to the maximum value. It can be seen that the performance is most sensitive to $\Delta T_{C,n}$ for the cases of shifting the layers close to the hot or cold ends. Especially when shifting the layer-13, 14, and 15 to the hot region, η_5 decreases dramatically, which means that the regenerators are more sensitive to $\Delta T_{C,n}$ in the layers close to the cold end.

D. Impact of Curie temperature variations following statistical distributions

To reflect the impact of production uncertainties, it is necessary to model layered regenerators where the Curie temperature $T_{C,n}$ of each layer may vary according to a uniform distribution or a normal distribution; the latter is expected to be closer to reality. Therefore, in this section, the acceptable degree of the Curie temperature variation $\Delta T_{C,n}$ is investigated by running a batch of simulations and reflecting on the range of AMR performance that can arise from assuming $\Delta T_{C,n}$, to be a stochastic variable. The method used to generate the new regenerators assumes that the $\Delta T_{C,n}$ follows a uniform distribution first. The base regenerator is still the one presented in Sec. III C, and each layer of the new 15-layer regenerator has a random shift that is modeled in four magnitudes: ± 0.5, ± 1, ± 2, and ± 3.5 K. The uniform distribution makes sure the probability that $\Delta T_{C,n}$ of each layer appears inside the defined region is the same. For each magnitude, 200 such combinations are generated randomly and the nominal cooling powers are compared. The root mean square deviation $RMSD = \sqrt{\frac{\sum_{n=1}^{15} \Delta T_{C,n}^2}{15}}$ is utilized to present the degree of overall variation in $T_{C,n}$. *RMSD* close to 0 means near to the even $T_{C,n}$ arrangement, conversely large values mean higher average degrees of variation in $T_{C,n}$, in other words, uneven $T_{C,n}$ arrangement.

Fig. 9 shows four groups of data and the markers represent different magnitudes. Here, negative nominal cooling power is still presented for statistical purposes. It can be seen that the maximum nominal cooling power η_5 is close to 1 and η_5 decreases rapidly with the RMSD of $\Delta T_{C,n}$ in total, which means the regenerators can only tolerate relatively small $\Delta T_{C,n}$ on the order of ± 0.5 K without significant loss in cooling power. With a variation larger than ± 1 K, η_5 is away from the median value, which implies that larger variation adds considerable difficulty to realize designed cooling power of the multi-layer regenerators in the real construction.

In the following studies, we present the sensitivity of the multi-layer regenerators when $\Delta T_{C,n}$ follows a normal distribution with a mean value μ and standard deviation σ. In the simulations, $\mu = 0$ and σ is set from 0.3 K to 3 K with steps of 0.3 K. For each σ, 200 regenerators are simulated (in total 2000 cases). The results of the nominal cooling power are presented in Fig. 10. It can be seen that the impact of σ is significant. For $\sigma = 0.3$ K, the median value of the nominal cooling power is 0.960, and the 25%–75% box shows the

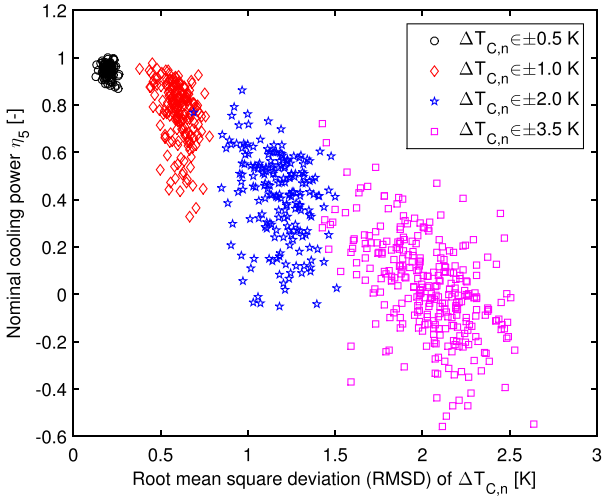

FIG. 9. Impact of *RMSD* of $\Delta T_{C,n}$ on nominal cooling power η_5 when $\Delta T_{C,n}$ follows a uniform distribution.

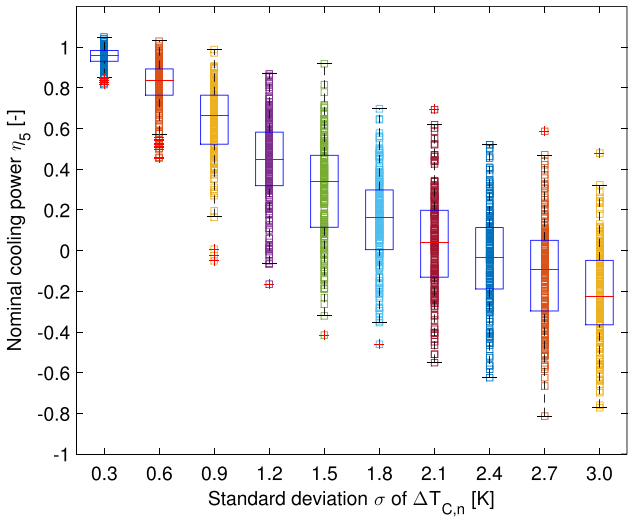

FIG. 10. Impact of standard deviation σ of $\Delta T_{C,n}$ on nominal cooling power η_5 when $\Delta T_{C,n}$ follows a normal distribution. The central mark of the 25%–75% box is the median value of η_5 for each σ, and the edges of the box are the 25th and 75th percentiles. The whiskers show the most extreme data points without outliers, and the outliers are plotted individually in red cross.

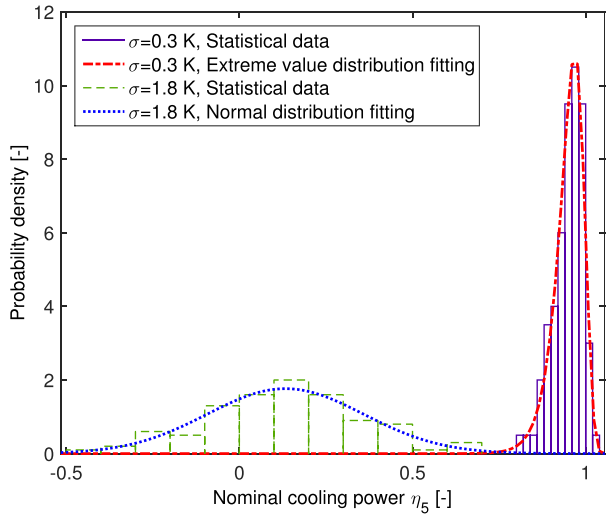

FIG. 11. Distribution fittings of statistical data of nominal cooling power η_5 when $\sigma = 0.3$ K and $\sigma = 1.8$ K. For $\sigma = 0.3$ K, the expectation and standard variation of η_5 are $\mu_{\eta_5} = 0.969$ and $\sigma_{\eta_5} = 0.034$; for $\sigma = 1.8$ K, they are $\mu_{\eta_5} = 0.133$ and $\sigma_{\eta_5} = 0.226$.

upper limit of 0.984 and the low limit of 0.931, which implies that the regenerator performance will lie in this region with a probability of 50%. However, with increasing σ, the median value decreases dramatically and the 25%–75% box becomes bigger, meaning there is larger uncertainty in η_5. It can be seen that $\sigma > 0.6$ K will lead to at least 16.6% performance reduction in the median value and η_5 varies in quite a large range, which means a risk of getting vastly different performance from two regenerators built in the same way.

Fig. 11 presents the histogram and probability density of η_5 when $\sigma = 0.3$ K and $\sigma = 1.8$ K. It can be observed that in each case η_5 follows the extreme value distribution and the normal distribution, respectively. Besides the obvious difference in median values, the case $\sigma = 0.3$ K shows a concentrated distribution and there is a much smaller calculated

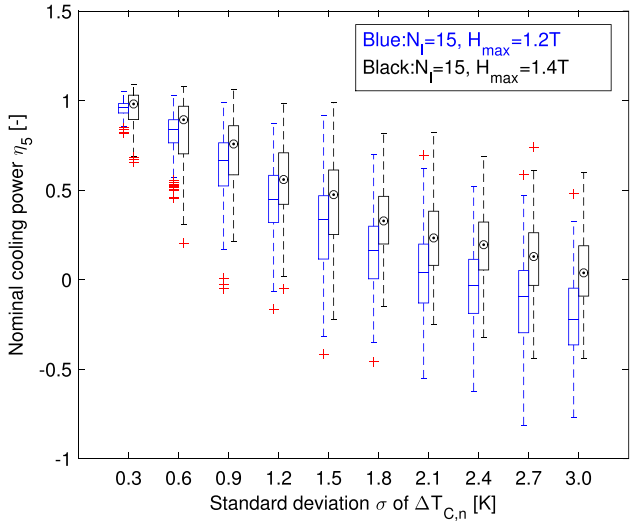

FIG. 12. Sensitivity of nominal cooling power η_5 to standard deviation σ of $\Delta T_{C,n}$ with $H_{max} = 1.2$ T and $H_{max} = 1.4$ T. The line insides the box represents the median value of η_5 when $H_{max} = 1.2$ T, and the spot for $H_{max} = 1.4$ T.

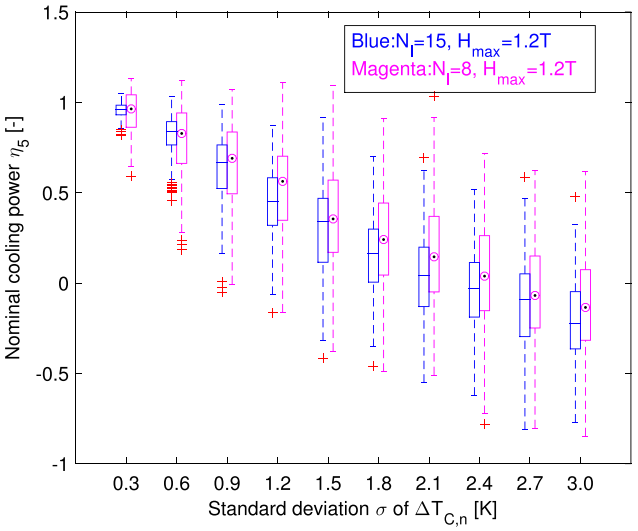

FIG. 13. Sensitivity of nominal cooling power η_5 to standard deviation σ of $\Delta T_{C,n}$ with $N_l = 15$ and $N_l = 8$. The line insides the box represents the median value of η_5 when $N_l = 15$, and the spot for $N_l = 8$.

standard deviation in the nominal cooling power σ_{η_5} of 0.034, compared to $\sigma_{\eta_5} = 0.226$ of the wide distribution when $\sigma = 1.8$ K. It is also reflected in Fig. 10 in the type of wider box and region of extreme values.

As the ΔS_{mag} curve tends to be wider when the internal magnetic field increases, it is hypothesized that the multi-layer regenerators should be less sensitive to Curie temperature variation $\Delta T_{C,n}$ with a larger applied field. This is verified in Fig. 12. The results from the maximum applied field of 1.2 T and 1.4 T are compared, and it shows that not only the median cooling power is higher at larger σ but also the variation of the nominal cooling power is lower at higher applied field, that is, the regenerators become less sensitive to σ with an increase of the maximum applied field from 1.2 T to 1.4 T.

The sensitivity of an 8-layer regenerator is also investigated. Fig. 13 shows that the median value of η_5 from the 8-layer regenerator has a smaller slope with increasing σ compared to that of the 15-layer regenerators; however, the deviation in the nominal cooling power becomes larger, which indicates the regenerators with more layers are less sensitive and can reduce the risk of the performance degradation. It should be noted that, generally, the regenerators with more layers and larger maximum applied field will produce more cooling power; therefore, the base values for calculating η_5 in Figs. 12 and 13 are different.

IV. CONCLUSION

Multi-layer regenerators using the first order material series $La(Fe,Mn,Si)_{13}H_y$ were investigated. The impact of the number of layers N_l, the sensitivity to the working temperature T_w, and the sensitivity to the variations in the Curie temperature $\Delta T_{C,n}$ were presented. The results showed that the nominal cooling power increases significantly with N_l, and from a practical point, around 10 to 15 layers may be suitable for a temperature span ΔT of 30 K given an applied field of

1.2 T. Meanwhile, multi-layer regenerators are quite sensitive to T_w and the best temperature region is 307–277 K. With a non-optimized $T_{C,n}$ arrangement, the performance increases slowly with decreasing ΔT. It was also shown that fewer layers are needed for a smaller ΔT with optimized $T_{C,n}$ arrangement, and around 2.24 layers are necessary for every 5 K ΔT to get 90% of the maximum performance.

Moreover, Curie temperature variations $\Delta T_{C,n}$ in the layers close to the cold or hot end have significant impact on the system performance, which is most sensitive to $\Delta T_{C,n}$ of layers close to the cold end. Furthermore, AMR performance with $\Delta T_{C,n}$ that varies according to a uniform or normal distribution was predicted for a population of randomly generated layers. The results showed that multi-layer regenerators are considerably sensitive to RMSD of $\Delta T_{C,n}$ for a uniform distribution, and the standard deviation σ of $\Delta T_{C,n}$ for a normal distribution. In the latter case, $\sigma > 0.6$ K will cause at least 16.6% decrease in the median value of the nominal cooling power η_5 and increase in the uncertainty of η_5, which implies that there may be huge difference in the performance of two regenerators built from materials with the same accuracy in Curie temperature. It is also predicted that larger applied field and layer number will decrease the sensitivity of the multi-layer regenerator to $\Delta T_{C,n}$.

ACKNOWLEDGMENTS

This work was financed by the ENOVHEAT project which is funded by Innovation Fund Denmark (Contract No. 12-132673). The authors would like to thank Vacuumschmelze GmbH, Germany for providing the $La(Fe,Mn,Si)_{13}H_y$ material.

[1]K. Engelbrecht, D. Eriksen, C. R. H. Bahl, R. Bjørk, J. Geyti, J. A. Lozano, K. K. Nielsen, F. Saxild, A. Smith, and N. Pryds, "Experimental results for a novel rotary active magnetic regenerator," Int. J. Refrig. **35**, 1498–1505 (2012).

[2]S. Jacobs, J. Auringer, A. Boeder, J. Chell, L. Komorowski, J. Leonard, S. Russek, and C. Zimm, "The performance of a large-scale rotary magnetic refrigerator," Int. J. Refrig. **37**, 84–91 (2014).

[3]S. Y. Dan'Kov, A. Tishin, V. Pecharsky, and K. Gschneidner, "Magnetic phase transitions and the magnetothermal properties of gadolinium," Phys. Rev. B **57**, 3478–3490 (1998).

[4]J. A. Barclay, "The theory of an active magnetic regenerative refrigerator," NASA STI/Recon Technical Report No. 83 (1982), p. 34087.

[5]J. Tušek, A. Kitanovski, U. Tomc, C. Favero, and A. Poredoš, "Experimental comparison of multi-layered LaFeCoSi and single-layered Gd active magnetic regenerators for use in a room-temperature magnetic refrigerator," Int. J. Refrig. **37**, 117–126 (2014).

[6]A. Rowe and A. Tura, "Experimental investigation of a three-material layered active magnetic regenerator," Int. J. Refrig. **29**, 1286–1293 (2006).

[7]A. Rowe, "Thermodynamics of active magnetic regenerators: Part I," Cryogenics **52**, 111–118 (2012).

[8]K. Engelbrecht, K. K. Nielsen, C. R. H. Bahl, C. P. Carroll, and D. van Asten, "Material properties and modeling characteristics for $MnFeP_{1-x}As_x$ materials for application in magnetic refrigeration," J. Appl. Phys. **113**, 173510 (2013).

[9]S. Fujieda, Y. Hasegawa, A. Fujita, and K. Fukamichi, "Thermal transport properties of magnetic refrigerants $La(Fe_xSi_{1-x})_{13}$ and their hydrides, and $Gd_5Si_2Ge_2$ and MnAs," J. Appl. Phys. **95**, 2429–2431 (2004).

[10]A. Barcza, M. Katter, V. Zellmann, S. Russek, S. Jacobs, and C. Zimm, "Stability and magnetocaloric properties of sintered La(Fe, Mn, Si)H alloys," IEEE Trans. Magn. **47**, 3391–3394 (2011).

[11]K. Morrison, K. Sandeman, L. Cohen, C. Sasso, V. Basso, A. Barcza, M. Katter, J. Moore, K. Skokov, and O. Gutfleisch, "Evaluation of the reliability of the measurement of key magnetocaloric properties: A round robin study of La(Fe, Mn, Si)H conducted by the SSEEC consortium of European laboratories," Int. J. Refrig. **35**, 1528–1536 (2012).

[12]A. Fujita, S. Fujieda, Y. Hasegawa, and K. Fukamichi, "Itinerant-electron metamagnetic transition and large magnetocaloric effects in $La(Fe_xSi_{1-x})_{13}$ compounds and their hydrides," Phys. Rev. B **67**, 104416 (2003).

[13]C. Wang, Y. Long, T. Ma, B. Fu, R. Ye, Y. Chang, F. Hu, and J. Shen, "The hydrogen absorption properties and magnetocaloric effect of $La_{0.8}Ce_{0.2}(Fe_{1-x}Mn_x)_{11.5}Si_{1.5}H_y$," J. Appl. Phys. **109**, 07A910 (2011).

[14]A. Smith, C. R. H. Bahl, R. Bjørk, K. Engelbrecht, K. K. Nielsen, and N. Pryds, "Materials challenges for high performance magnetocaloric refrigeration devices," Adv. Energy Mater. **2**, 1288–1318 (2012).

[15]T. Lei, K. K. Nielsen, and K. Engelbrecht, "Modelling and simulation of regenerators with complex flow arrangements for active magnetocaloric refrigeration," in *ASME 12th Biennial Conference on Engineering Systems Design and Analysis* (2014), Vol. 3, p. V003T12A007.

[16]K. K. Nielsen, G. Nellis, and S. Klein, "Numerical modeling of the impact of regenerator housing on the determination of Nusselt numbers," Int. J. Heat Mass Transfer **65**, 552–560 (2013).

[17]S. Jeppesen, S. Linderoth, N. Pryds, L. T. Kuhn, and J. B. Jensen, "Indirect measurement of the magnetocaloric effect using a novel differential scanning calorimeter with magnetic field," Rev. Sci. Instrum. **79**, 083901 (2008).

[18]R. Bjørk, C. R. H. Bahl, and M. Katter, "Magnetocaloric properties of $LaFe_{13-x-y}Co_xSi_y$ and commercial grade Gd," J. Magn. Magn. Mater. **322**, 3882–3888 (2010).

A.2 Study of geometries of active magnetic regenerators for room temperature magnetocaloric refrigeration

T. Lei, K. Engelbrecht, K. K. Nielsen and C. T. Veje, Study of geometries of active magnetic regenerators for room temperature magnetocaloric refrigeration, *Applied Thermal Engineering*, in press, (2015).

Applied Thermal Engineering ■■ (2015) ■■–■■

Contents lists available at ScienceDirect

Applied Thermal Engineering

journal homepage: www.elsevier.com/locate/apthermeng

Research Paper

Study of geometries of active magnetic regenerators for room temperature magnetocaloric refrigeration

Tian Lei [a,*], Kurt Engelbrecht [a], Kaspar K. Nielsen [a], Christian T. Veje [b]

[a] Department of Energy Conversion and Storage, Technical University of Denmark, Frederiksborgvej 399, DK 4000 Roskilde, Denmark
[b] Mærsk Mc-Kinney Møller Institute, University of Southern Denmark, DK 5230 Odense M, Denmark

HIGHLIGHTS

- Entropy generation minimization was used to optimize an active magnetic regenerator.
- Range of geometries studied included micro-channel and packed screens.
- AMRs can be more efficient using alternative geometries except packed spheres.
- Practical difficulties in implementing new geometries were discussed.

ARTICLE INFO

Article history:
Received 10 October 2015
Accepted 21 November 2015
Available online

Keywords:
Magnetic refrigeration
Active magnetic regenerator
Regenerator geometry
Heat transfer

ABSTRACT

Room temperature magnetic refrigeration has attracted substantial attention during the past decades and continuing to increase the performance of active magnetic regenerators (AMR) is of great interest. Optimizing the regenerator geometry and related operating parameters is a practical and effective way to obtain the desired cooling performance. To investigate how to choose and optimize the AMR geometry, a quantitative study is presented by simulations based on a one-dimensional (1D) numerical model. Correlations for calculating the friction factor and heat transfer coefficient are reviewed and chosen for modeling different geometries. Moreover, the simulated impacts of various parameters on the regenerator efficiency with a constant specific cooling capacity are presented. An analysis based on entropy production minimization reveals how those parameters affect the main losses occurring inside the AMR. In addition, optimum geometry and operating parameters corresponding to the highest efficiency for different geometries are presented and compared. The results show that parallel plate and micro-channel matrices show the highest theoretical efficiency, while the packed screen and packed sphere beds are possibly more practical from the application point of view.

1. Introduction

Room temperature magnetocaloric refrigeration (MCR) has developed rapidly in recent years and many prototypes with significant cooling capacity have emerged [1–3]. Okamura et al. [4] in 2007 presented a rotary active magnetocaloric refrigerator, which provided 540 W maximum cooling power and a largest temperature span of 21 K. In 2012, a rotary prototype exhibiting a no-load temperature span of over 25 K and maximum cooling power of 1010 W using gadolinium (Gd) spheres was developed by Engelbrecht et al. [5]. Arnold et al. [6] reported on a compact magnetocaloric refrigerator in 2014, realizing a no-load temperature span of 33 K using 650 g of Gd. In 2014, Jacobs et al. [7] built a rotary prototype using six layers of LaFeSiH particles, producing 3042 W of cooling power at zero temperature span and 2502 W over a span from 32 to 44 °C with a coefficient of performance (COP) around 2. However, in Europe and North America commercial residential air-conditioners generally have COPs of 2.5–3.5 over a temperature span of 20–30 °C and a clear gap still exists between these conventional cooling devices and available MCR systems. To improve the performance, researchers have focused on various techniques, such as developing novel magnetocaloric materials [1–3], increasing the maximum applied magnetic field of the permanent magnet, reducing the parasitic losses by using novel designs and optimizing the regenerator geometry as well as related operating parameters. The last approach is of substantial interest to many machine designers since it is practical and important to get close to the best performance with existing materials and techniques.

The AMR is a porous media made of magnetocaloric material (MCM), which is the active solid refrigerant. The porous structure allows the heat transfer fluid to flow through and transfer heat with the solid at the same time. As shown in Fig. 1, a typical AMR cycle

* Corresponding author. Tel.: +4551308382.
E-mail address: tile@dtu.dk (T. Lei).

http://dx.doi.org/10.1016/j.applthermaleng.2015.11.113
1359-4311/

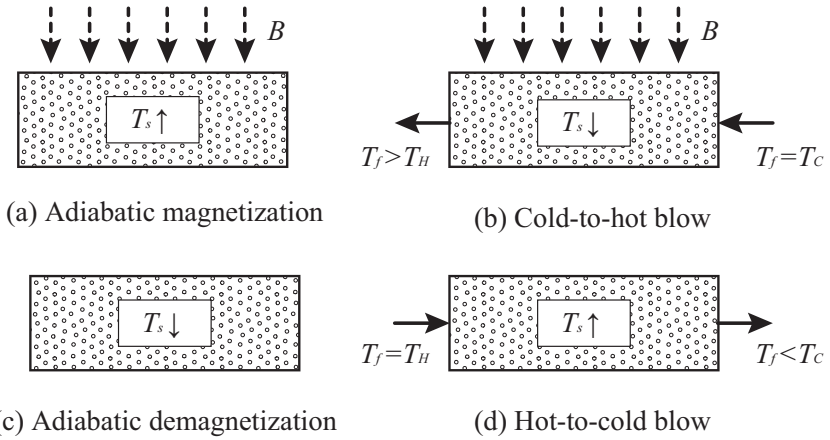

Fig. 1. Active magnetic regeneration cycle consisting of four processes: (a) adiabatic magnetization; (b) cold-to-hot blow; (c) adiabatic demagnetization; (d) hot-to-cold blow.

is comprised of four processes. Starting with the adiabatic magnetization process, the temperature of the MCM increases and the heat transfer fluid is successively heated by the solid refrigerant during the cold-to-hot blow. The fluid exiting the regenerator then rejects heat to the hot reservoir. This is followed by the adiabatic demagnetization process that results in a decrease in the solid temperature and the hot-to-cold blow allows a cooling load to be absorbed in the cold reservoir. The temperature of the regenerator increases back to its original temperature, thus completing the cycle. In each AMR cycle, the fluid is assumed to enter the packed bed with a constant temperature T_H at the hot end during the hot-to-cold blow, or T_C at the cold end during the cold-to-hot blow. The temperature span is $\Delta T = T_H - T_C$. The heating power, the cooling power and the COP are defined as:

$$\dot{Q}_H = \int_0^\tau |\dot{m}_f| (h_{f,x=0} - h_{f,T_H}) dt \quad \text{when} \quad \dot{m}_f < 0 \tag{1}$$

$$\dot{Q}_C = \int_0^\tau |\dot{m}_f| (h_{f,T_C} - h_{f,x=L}) dt \quad \text{when} \quad \dot{m}_f > 0 \tag{2}$$

$$COP = \frac{\dot{Q}_C}{\dot{Q}_H - \dot{Q}_C} \tag{3}$$

where $\dot{m}_f$, τ and t is the mass flow rate, cycle time and time; $h_{f,x=0}$ and $h_{f,x=L}$ are the specific enthalpies of the fluid flowing out of the hot and cold end in each blow period; h_{f,T_H} and h_{f,T_C} are the specific enthalpies of the fluid at T_H and T_C. The two blow processes are synchronized with a periodically varying magnetic field, and the four processes may overlap in timing sequence in a real prototype.

From a thermodynamic viewpoint, the most obvious causes of reduced cooling capacity or efficiency of the AMRs include insufficient heat transfer between the fluid and solid refrigerant, viscous dissipation due to the pump work, axial conduction, and heat loss to the ambient. The last issue is not discussed here, while we mainly focus on the other three irreversible mechanisms, which are directly or indirectly related to the regenerator geometry and operating parameters. For example, smaller flow channels in a porous regenerator have a higher heat transfer coefficient than larger channels; however, they also lead to an increase in the pressure drop and the viscous dissipation. Moreover, large power density requires high frequency operation, which may oppositely increase the risk of insufficient heat transfer due to the reduced blow time. Important parameters related to the regenerator geometry include the regenerator type, hydraulic diameter, porosity, and aspect ratio. In addition, the frequency, average mass flow rate, temperature span and applied magnetic field are the key operating parameters. Since those parameters simultaneously affect the regenerator performance, the choice and optimization should be carefully done for achieving desired cooling performance.

In general, a good regenerator geometry requires sufficient heat transfer between fluid and porous solid matrix, low pressure drop, and small axial conduction. Among these issues, the insufficient heat transfer and the viscous dissipation are two major loss mechanisms, while the axial conduction should be stressed when dealing with short and bulky regenerators. In various prototypes, which were well reviewed in References 1–3, the packed particle bed and parallel plate matrix were two commonly used geometries. Due to the advantages of easy construction and good heat transfer performance, the packed particle beds were widely implemented. However, the pressure drop over the packed particle beds and the viscous dissipation loss are relatively large, which may cause a reduction in regenerator efficiency. Although the parallel plate matrix has much lower frictional pressure drop compared with the former, high heat transfer coefficient is hard to obtain in experiments due to the limitation of fabricating small channels [8]. The micro-channel matrix for MCR application, which consists of numerous micro channels through a monolithic block, has been presented in a few papers [9,10].

Radebaugh and Louie [11] presented a comparison study on different regenerator geometries for regenerative refrigerators. For various geometries, the ratios of heat transfer modulus to friction factor $StPr^{2/3}/f_F$, where St, Pr, and f_F are the Stanton number, Prandtl number, and friction factor respectively, were compared. The Stanton number is the ratio of the heat transferred into fluid to the thermal capacity of fluid. Their study showed that the parallel plate and micro-channel matrices were preferable concerning a balance between heat transfer and pressure drop. The worst group included the rod bundle matrix, packed screen bed and packed sphere bed. The authors also debated that the parallel plate or micro-channel matrices were not suitable for the cryogenic regenerators because of their relatively large longitudinal conduction. In reality, the packed screen bed and packed sphere bed are widely used in regenerative heat engines or refrigerators instead of the parallel plate or micro-channel matrices. Barclay and Sarangi [12] compared four different geometries for MCR application by using a simplified model, which included the packed sphere bed, parallel plate matrix, and micro-channel matrix. The study presented optimal characteristic dimension and aspect ratio for different regenerator geometries at three frequencies. More recently, Li et al. [13] presented the optimization of the sphere diameter and aspect ratio for AMR using the packed sphere bed by a one-dimensional model. Vuarnoz and Kawanami [14] simulated the AMRs using a stacked wire matrix, and compared the results with the packed sphere bed. Li et al. [15]

Please cite this article in press as: Tian Lei, Kurt Engelbrecht, Kaspar K. Nielsen, Christian T. Veje, Study of geometries of active magnetic regenerators for room temperature magnetocaloric refrigeration, Applied Thermal Engineering (2015), doi: 10.1016/j.applthermaleng.2015.11.113

compared the regenerators with the packed sphere bed and parallel plate matrix by simulation, and the latter showed smaller total entropy production rate and better performance. Tušek et al. [16] presented the optimization of an AMR with a packed sphere bed and parallel plate matrix in two operating frequencies based on a 1D model.

The study on the AMR geometry is insufficient and interesting geometries like packed screen beds are not included. In the following, a general analysis of the regenerator geometries is presented. The correlations for estimating friction factor and heat transfer coefficient of different geometries are reviewed and proper ones are chosen for modeling. By using a one-dimensional model, the synthetic impacts of various parameters on regenerator performance are quantified and analyzed. Moreover, the entropy production rates due to different loss mechanisms inside the AMRs are calculated and compared. Assuming a constant specific cooling power, which is ratio of the cooling power to the mass of solid refrigerant $\dot{q}_C = \dot{Q}_C / \dot{m}_s$, the maximum COP of regenerators using different geometries and the optimum geometry and operating parameters are compared.

2. Geometry comparison

2.1. Geometry characterization

In this section, five regenerator geometries, which are the packed sphere bed, parallel plate matrix, circular micro-channel matrix, rectangular micro-channel matrix and packed screen bed, are discussed. The correlations for the friction factor and heat transfer coefficient are briefly reviewed. The schematic diagrams of the different regenerator geometries are shown in Fig. 2, where the dark area represents solid refrigerant and the remaining white space is the flow channel, where the flow direction is perpendicular to the schematic diagram except Fig. 2 (e-2). Table 1 gives the important dimensions and the expressions of various characterizing parameters for different geometries, which include porosity ε, hydraulic diameter D_h and volumetric surface area a_s. The porosity is the void fraction of the porous regenerator; the hydraulic diameter is the ratio of the cross sectional area to the wetted perimeter of the cross-section of a flow channel times four; the volumetric surface area is the amount of surface area per unit volume.

Here we use the "packed sphere bed" instead of the packed particle bed, although the regenerator beds are typically packed with irregular particles in existing prototypes, since in this study all particles are assumed spherical with the same size. This kind of geometry can be easily constructed by packing small spheres into a regenerator housing. In addition, the porosity is assumed constant equal to 0.36 since the sphere diameter is much smaller than the housing diameter [17]. Therefore, the sphere diameter is the single characterizing parameter for the packed sphere bed. Under this assumption, the boundary effects are neglected, which means that the flow is assumed uniform in the cross section and in particular that no channeling of the fluid occurs. It can be seen that the hydraulic diameter of a packed sphere bed is proportional to

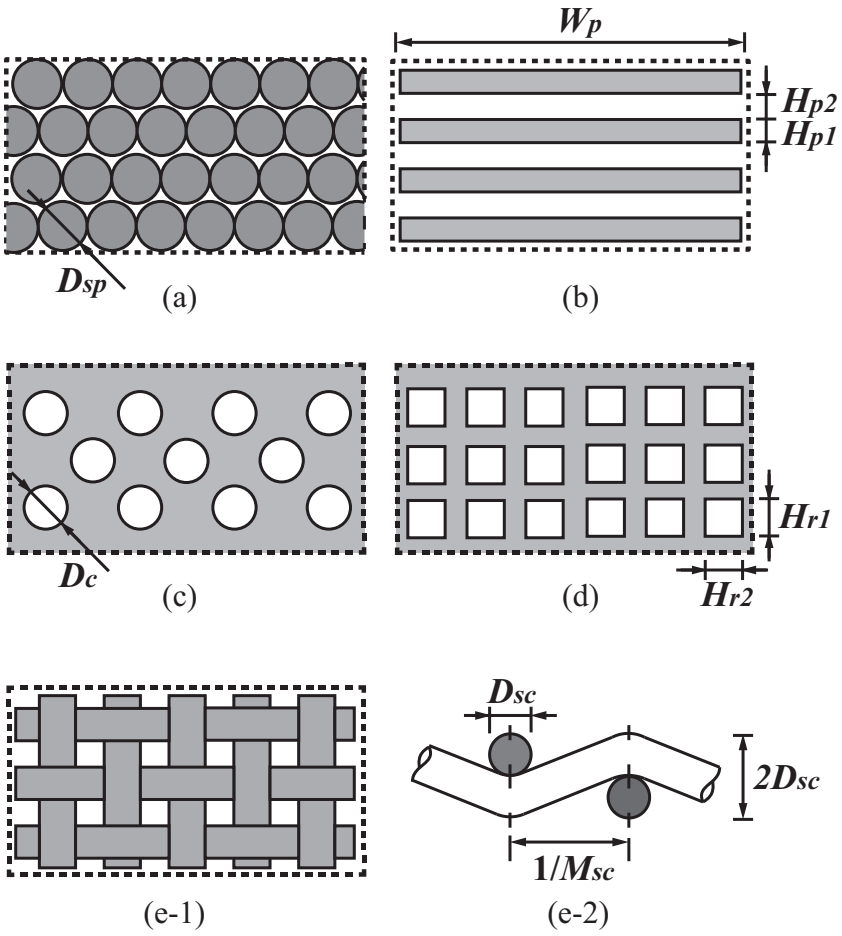

Fig. 2. Schematic diagram of different regenerator geometries including: (a) packed sphere bed; (b): parallel plate matrix; (c): circular micro-channel matrix; (d): rectangular micro-channel matrix; (e-1) and (e-2): top and side views of packed screen bed. Except (e-2), the flow direction is perpendicular to the schematic diagram. The dark region represents solid refrigerant, i.e., magnetocaloric material, and the rest of the region represents flow channel.

Please cite this article in press as: Tian Lei, Kurt Engelbrecht, Kaspar K. Nielsen, Christian T. Veje, Study of geometries of active magnetic regenerators for room temperature magnetocaloric refrigeration, Applied Thermal Engineering (2015), doi: 10.1016/j.applthermaleng.2015.11.113

Table 1
Parameters for characterizing different regenerator geometries.

Geometry	Dimensions	Porosity	Hydraulic diameter	Specific surface area
Packed sphere bed	D_{sp}	$\varepsilon = 0.36$	$D_h = \frac{2\varepsilon}{3(1-\varepsilon)} D_{sp}$	$a_s = \frac{4\varepsilon}{D_h} = \frac{6(1-\varepsilon)}{D_{sp}}$
Parallel plate matrix	H_{p1}, H_{p2}	$\varepsilon = \frac{H_{p2}}{H_{p1}+H_{p2}}$	$D_h = 2H_{p2}$	$a_s = \frac{4\varepsilon}{D_h} = \frac{2}{H_{p1}+H_{p2}}$
Circular micro-channel matrix	D_c	ε	$D_h = D_c$	$a_s = \frac{4\varepsilon}{D_h} = \frac{4\varepsilon}{D_c}$
Rectangular micro-channel matrix	H_{r1}, H_{r2}	ε	$D_h = \frac{2H_{r1}H_{r2}}{H_{r1}+H_{r2}}$	$a_s = \frac{4\varepsilon}{D_h} = \frac{2\varepsilon(H_{r1}+H_{r2})}{H_{r1}H_{r2}}$
Packed screen bed	M_{sc}, D_{sc}	$\varepsilon = 1 - \frac{\pi D_{sc} M_{sc}^2 \sqrt{D_{sc}^2 + M_{sc}^{-2}}}{4}$	$D_h = \frac{4\varepsilon}{\alpha_s}$	$a_s = \pi M_{sc}^2 \sqrt{D_{sc}^2 + M_{sc}^{-2}}$

the sphere diameter D_{sp}, and the volumetric surface area has an inverse relationship with D_{sp} [18].

The parallel plate matrix can be built by stacking thin plates with a specified spacing from each other, and the main dimensions are the plate thickness H_{p1} and flow channel height H_{p2}. The porosity and volumetric surface area is a function of H_{p1} and H_{p2}, assuming the plate width is much bigger than the channel size. For the circular micro-channel matrix, the hydraulic diameter is the same as the channel diameter D_c and the specific surface area can be calculated from the hydraulic diameter and porosity. The hydraulic diameter of the rectangular micro-channel matrix is related to the height and width of the flow channel (H_{r1} and H_{r2}). A square channel with $H_{r1} = H_{r2} = H_r$ gives $D_h = H_r$. Woven screens have been used for catalytic reaction for a long time, since they have highly ordered structures, high heat transfer rates, and moderate flow resistances. Armour and Cannon [19] presented the equations for calculating different parameters by using a wire diameter D_{sc} and mesh number per meter M_{sc}, as shown in Table 1. Only the packed sphere bed can be characterized by only one parameter, and the other geometries need two variables for full identification. Therefore, in this study we use two parameters, the hydraulic diameter and the porosity, to characterize the AMR geometries for reasonable comparison.

2.2. Flow and heat transfer correlations

As numerous flow and heat transfer correlations for different geometries exist and there are few universally applicable correlations for modeling AMRs, a brief review of correlations is provided in the following. In a typical AMR, Gd is used as the solid refrigerant, while the heat transfer fluid could be aqueous solution with anti-freeze, which has a high Prandtl number around 5–7. Low Reynolds number (<100) flow is predicted as the typical operating condition [20], which is considered in choosing the correlations.

The Ergun equation [21] is generally used to calculate the friction factor in a packed sphere bed, and the expression includes both viscous and kinetic effects as shown in Table 2. More correlations [30–32] are compared with the Ergun equation, and it turns out the latter presents a good estimation. Wakao et al. [33] in 1979 presented an expression for estimating the Nusselt number for the packed sphere bed. Engelbrecht [25] considered the internal temperature gradient inside the solid, and further correlated Wakao et al.'s correlation with the Biot number Bi, which is used in this study. The Fanning friction factor for laminar flow through the parallel plates was presented as $f_F = 24/\mathrm{Re}$ [22], and a similar expression can be found in Reference 24. Different correlations for the heat transfer coefficient of the parallel plates were presented in References 24, 26, and 28. Among those, Nickolay and Martin [26] presented a correlation of overall Nusselt number and it gave a good estimation compared with the others. Nielsen [34] found that the Biot number for a parallel plate matrix is much less than 1, which means the heat transfer inside the plate is faster than that across the boundary layer. Therefore, the correlation is not further modified here.

The Poiseuille law and its modified form [23,35,36] are generally used to calculate the friction factor for laminar flow through the micro-channel matrix. Comparing References 24, 27, 35, and 37 shows that Hausen et al.'s correlation [27] is the best for calculating the heat transfer coefficient of the circular channel, and the one presented by Kays et al. [28] is used for the rectangular channel. Armour and Cannon [19] developed a flow friction correlation applicable to the flow through the most types of woven metal screens with different porosities. It gave the best estimation in contrast to References 38–40. Park et al. [29] presented a heat transfer correlation based on experiments and it is chosen by comparing with other references [41–43].

The details of correlation comparison will not be presented in this paper to avoid tedious enumeration. Only chosen correlations for different geometries are presented and compared. Figure 3a and b shows the friction factor f_F and Nusselt number Nu as a function of Reynolds number Re_h for different geometries, when the porosity is 0.36 and the hydraulic diameter is 0.20 mm. Here the friction factor, Nusselt number, and Reynolds number based on the hydraulic diameter and the superficial velocity v_s are:

$$f_F = \frac{dP}{dx}\frac{2D_h}{\rho_f v_s^2} \tag{4}$$

$$\mathrm{Nu} = \frac{hD_h}{k_f} \tag{5}$$

$$\mathrm{Re}_h = \frac{\rho_f v_s D_h}{\mu_f} \tag{6}$$

$$v_s = \frac{\dot{m}_f}{\rho_f A_c} \tag{7}$$

where dP/dx, D_h, ρ_f, v_s, h, k_f, μ_f, $\dot{m}_f$ and A_c, are pressure drop over unit length, hydraulic diameter, density, superficial velocity, heat transfer coefficient, thermal conductivity of fluid, dynamic viscosity, mass flow rate and cross sectional area, respectively.

Fig. 3a shows that the packed sphere bed exhibits the largest friction factor, and the second largest is the packed screen bed, whereas the other three have much lower flow resistance. On the contrary, higher Nusselt numbers can be observed in the packed sphere bed and packed screen bed than the other three geometries as shown in Fig. 3b. Since higher Nusselt number Nu and lower friction factor f_F are desirable, the ratio of Nusselt number to friction factor Nu/f_F (see Fig. 3c) is utilized to evaluate the regenerator geometries. The parallel plate matrix gives the highest Nu/f_F in this comparison, and the lowest value is observed in the packed sphere bed. It is found that the circular and rectangular micro-channel matrices yield virtually the same friction factor and Nusselt number; therefore in this study we only present the results of the circular micro-channel matrix and denote them as "micro-channel matrix". Since the static and dispersion conduction is relatively small, the related

Please cite this article in press as: Tian Lei, Kurt Engelbrecht, Kaspar K. Nielsen, Christian T. Veje, Study of geometries of active magnetic regenerators for room temperature magnetocaloric refrigeration, Applied Thermal Engineering (2015), doi: 10.1016/j.applthermaleng.2015.11.113

Table 2
Chosen correlations for different regenerator geometries.

Reference	Geometry	Characteristic dimension length	Reynolds number	Friction factor	Pressure drop	Remarks
Ergun and Orning [21]	Packed sphere bed	$D_L = D_{sp}$			$\frac{dP}{dx} = 2\alpha\frac{(1-\varepsilon)^2}{\varepsilon^3}\frac{\mu v_s S_v^2}{\varepsilon^3} + \frac{\beta}{8}\frac{(1-\varepsilon)\rho v_s^2 S_v}{\varepsilon^3}$ $\alpha = (\pi/2)^2 \approx 2.5$, $\beta = 2.4$ and $S_v = 6/D_L$	Laminar and turbulent flow
Bejan [22]	Parallel plate matrix	$D_L = 2H_{p2}$	$\mathrm{Re} = \frac{\rho(v_s/\varepsilon)D_L}{\mu_f}$	$f_F = 24/\mathrm{Re}$	$\frac{dP}{dx} = 4f_F\left[\frac{\rho(v_s/\varepsilon)^2}{2D_L}\right]$	Laminar flow
Poiseuille law (Asadi et al.) [23]	Circular micro-channel matrix	$D_L = D_c$	$\mathrm{Re} = \frac{\rho(v_s/\varepsilon)D_L}{\mu_f}$	$f_F = 64/\mathrm{Re}$	$\frac{dP}{dx} = f_F\left[\frac{\rho(v_s/\varepsilon)^2}{2D_L}\right]$	Laminar flow
Shah and London [24]	Rectangular micro-channel matrix	$D_L = \frac{2H_1 H_2}{H_1+H_2}$	$\mathrm{Re} = \frac{\rho(v_s/\varepsilon)D_L}{\mu_f}$	$f_F = 24(1-1.3553\alpha+1.9467\alpha^2-1.7012\alpha^3+0.9564\alpha^4-0.2537\alpha^5)/\mathrm{Re}$ $\alpha = H_{c1}/H_{c2}$	$\frac{dP}{dx} = 4f_F\left[\frac{\rho(v_s/\varepsilon)^2}{2D_L}\right]$	Laminar flow
Armour and Cannon [19]	Packed screen bed	$D_L = \frac{1-M_{sc}D_{sc}}{M_{sc}}$	$\mathrm{Re} = \frac{\rho v_s}{d_{sf}\mu_f D_L}$	$f_F = \frac{64}{\mathrm{Re}} + 0.52$	$\frac{dP}{dx} = f_F\left[\frac{\rho(v_s/\varepsilon)^2}{D_L}\right]$	$0.35 < \varepsilon < 0.76$ $0.1 < \mathrm{Re} < 1000$
Reference	Geometry	Characteristic dimension length	Reynolds number	Nusselt number	Heat transfer coefficient	Remarks
Engelbrecht [25]	Packed sphere bed	$D_L = D_{sp}$	$\mathrm{Re} = \frac{\rho v_s D_{sp}}{\mu_f}$	$\mathrm{Nu} = \frac{2+1.1\mathrm{Pr}^{1/3}\mathrm{Re}^{0.6}}{1+2\mathrm{Bi}/3}$	$h_f = \frac{\mathrm{Nu}k_f}{D_L}$	Laminar flow
Nickolay and Martin [26]	Parallel plate matrix	$D_L = 2H_{p2}$		$\mathrm{Nu} = \left[7.541^n + (1.841\mathrm{Gz}^{1/3})^n\right]^{(1/n)}$ $\mathrm{Gz} = \frac{2v_s A_c \rho c_f D_L}{k_f W_p L}$ and $n = 3.592$	$h_f = \frac{\mathrm{Nu}k_f}{D_L}$	$\mathrm{Gz} < 10^5$
Hausen et al. [27]	Circular micro-channel matrix	$D_L = D_c$	$\mathrm{Re} = \frac{\rho(v_s/\varepsilon)D_L}{\mu_f}$	$\mathrm{Nu} = 3.657 + 0.19\mathrm{C}^{0.8}/(1+0.117\mathrm{C}^{0.467})$ $\mathrm{C} = \mathrm{RePr}D_L/L$	$h_f = \frac{\mathrm{Nu}k_f}{D_L}$	Laminar flow and constant wall temperature
Kays et al. [28]	Rectangular micro-channel matrix	$D_L = \frac{2H_1 H_2}{H_1+H_2}$		$\mathrm{Nu} = 8.235(1-1.883/\alpha+3.767/\alpha^2-5.814/\alpha^3+5.361/\alpha^4-2/\alpha^5)$	$h_f = \frac{\mathrm{Nu}k_f}{D_L}$	$\mathrm{Re} < 2200$
Park et al. [29]	Packed screen bed	$D_L = \frac{\varepsilon}{1-\varepsilon}D_{sc}$	$\mathrm{Re} = \frac{\rho(v_s/\varepsilon)D_L}{\mu_f}$	$\alpha = H_{c1}/H_{c2}$ $\mathrm{Nu} = 1.315\mathrm{Pr}^{1/3}\mathrm{Re}^{0.35\left(\frac{1-\varepsilon}{\varepsilon}\right)^{0.2}}$	$h_f = \frac{\mathrm{Nu}k_f}{D_L}$	$0.40 < \varepsilon < 0.84$ $10 < \mathrm{Re} < 500$

correlations for different geometries are not compared in this study and they can be found in References 30, 39, and 44–46.

3. Simulation model

To study the AMRs using different geometries, a 1D transient numerical model developed at the Technical University of Denmark [47,48] is used. The energy equations for the heat transfer liquid and solid refrigerant [25] can be expressed as:

$$A_c\frac{\partial}{\partial x}\left(k_{disp}\frac{\partial T_f}{\partial x}\right) - \dot{m}_f c_f\frac{\partial T_f}{\partial x} - \frac{\mathrm{Nu}k_f}{D_h}a_s A_c(T_f - T_s) + \left|\frac{\partial P}{\partial x}\frac{\dot{m}_f}{\rho_f}\right| = \varepsilon\rho_f A_c c_f\frac{\partial T_f}{\partial t} \tag{8}$$

$$\frac{\mathrm{Nu}k_f}{D_h}a_s A_c(T_f - T_s) + A_c\frac{\partial}{\partial x}\left(k_{stat}\frac{\partial T_s}{\partial x}\right) + (1-\varepsilon)\rho_s A_c T_s\left(\frac{\partial s_s}{\partial H}\right)_T\frac{\partial H}{\partial t} = (1-\varepsilon)\rho_s A_c c_H\frac{\partial T_s}{\partial t} \tag{9}$$

where k, T, ρ, c, and s are the thermal conductivity, temperature, density, specific heat, and specific entropy; A_c, x, t, $\dot{m}_f$, and H are the cross sectional area, axial position, time, mass flow rate and internal magnetic field. The subscripts f and s represent fluid and solid refrigerant, respectively. Table 2 presents the correlations for calculating the pressure drop $\partial P/\partial x$, and the Nusselt number Nu. In this numerical model, the mass flow and applied magnetic field are given as functions of time. The central difference and implicit time schemes are used for discretizing the energy equations in both space and time. In the simulation, the number of the space and time nodes N_x and N_t are 100 and 4000 respectively. By solving the discretized equations, the temperature gradient can be calculated after each time step, given an initial condition. The model outputs the performance indices after reaching the cyclical steady state with a tolerance.

Moreover, entropy production minimization is a powerful tool for quantitatively analyzing different loss mechanisms inside a thermal system. The second law of thermodynamics requires the entropy production in a natural process to be positive, and entropy production minimization can be used to obtain the optimal theoretical performance. This approach can also be used to quantify the irreversibility of various processes in the AMRs. The four main irreversible processes are summarized: (1) insufficient heat transfer process between fluid and solid refrigerant, as well as insufficient heat transfer processes at the hot or cold reservoirs; (2) viscous dissipation through the porous bed due to the flow resistance; (3) axial conduction through the bed and conduction due to fluid thermal dispersion; (4) other mechanisms such as irreversibility related to magnetization and demagnetization processes. The last issue is not discussed since it has less relation to this study. The following equations are used to calculate the entropy production rates for different irreversible processes based on the 1D numerical model [13]:

$$\dot{S}_{p,ht} = \frac{1}{\tau}\int_0^\tau\int_0^L h a_s A_c\frac{(T_f - T_s)^2}{T_f T_s}dxdt + \frac{1}{\tau}\int_0^\tau|\dot{m}_f|c_f\left(\ln\frac{T_C}{T_{f,x=L}} + \frac{T_{f,x=L} - T_C}{T_C} + \ln\frac{T_H}{T_{f,x=0}} + \frac{T_{f,x=0} - T_H}{T_H}\right)dt \tag{10}$$

$$\dot{S}_{p,vd} = \frac{1}{\tau}\int_0^\tau\int_0^L\frac{|\dot{m}_f|}{\rho_f T_f}\frac{\partial P}{\partial x}dxdt \tag{11}$$

$$\dot{S}_{p,ac} = \frac{1}{\tau}\int_0^\tau\int_0^L\left[k_{stat}A_c\frac{1}{T_s^2}\left(\frac{dT_s}{dx}\right)^2 + k_{disp}A_c\frac{1}{T_f^2}\left(\frac{dT_f}{dx}\right)^2\right]dxdt \tag{12}$$

$$\dot{S}_{p,tot} = \dot{S}_{p,ht} + \dot{S}_{p,vd} + \dot{S}_{p,ac} \tag{13}$$

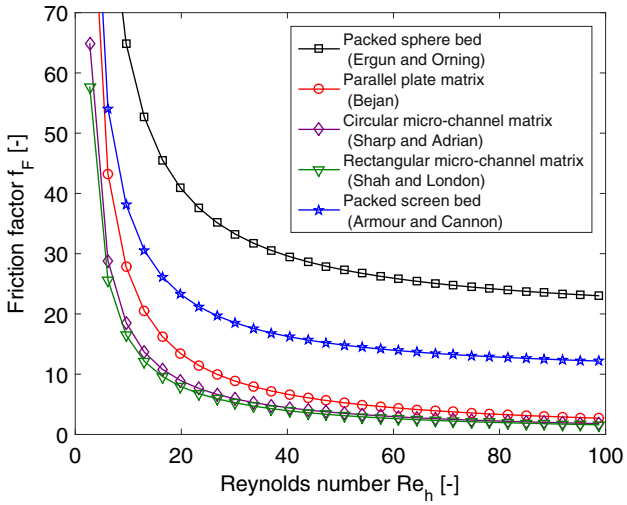

(a) Friction factor f_F

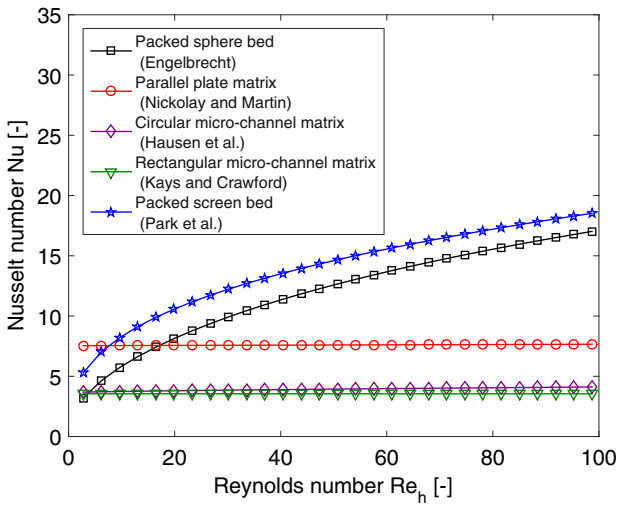

(b) Nusselt number Nu

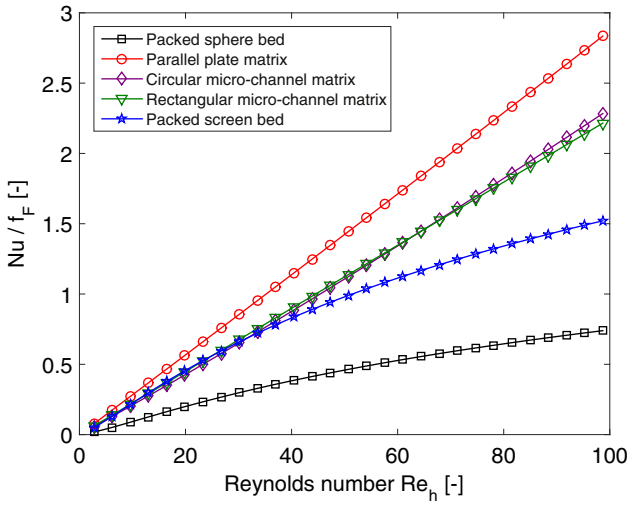

(c) Nu / f_F

Fig. 3. Nusselt number Nu, friction factor f_F, and ratio of Nusselt number to friction factor Nu/f_F as a function of Reynolds number Re_h for different geometries when porosity ε is 0.36 and hydraulic diameter D_h is 0.20 mm.

where $\dot{S}_{p,ht}$, $\dot{S}_{p,vd}$ and $\dot{S}_{p,ac}$ represent the entropy production rates due to insufficient heat transfer, viscous dissipation, and axial conduction, respectively; $\dot{S}_{p,tot}$ is the total entropy production rate; L and τ are the regenerator length and the period of one cycle. By comparing those entropy production rates, we can quantitatively measure the three loss mechanisms.

Table 3 shows the details of the modeling parameters. In the simulation, Gd is used as the refrigerant and water mixture with 20% v/v ethylene glycol as the heat transfer fluid. The magnetocaloric properties of Gd was presented in Reference 49. We keep the regenerator volume $V_r = LA_c$ constant; therefore, the aspect ratio $R_a = L/\sqrt{A_c}$ can fully describe the regenerator shape. The temperature span is fixed from 280 to 300 K. The profiles of the applied magnetic field and the nominal mass flow rate are shown in Fig. 4. The optimization objectives usually include the specific cooling power $\dot{q}_C$, and the COP. In this paper we focus on maximizing COP for obtaining a constant specific cooling power. In a typical condition, the specific cooling power increases with the increment of averaged mass flow rate until reaching the maximum value. Therefore, the averaged mass flow rate can be specified when the specific cooling power is kept constant. Correspondingly the COP data are

Table 3
Main modeling parameters.

Parameter	Value
Maximum applied magnetic field B	1.2 T
Regenerator volume V_r	2.25×10^4 mm^3
Number of regenerator beds N_r	20
Temperature span ΔT	280–300 K
Aspect ratio R_a	0.1–8
Frequency f	0.3–10 Hz
Regenerator geometry	Packed sphere bed Parallel plate matrix Micro-channel matrix Packed screen bed
Hydraulic diameter D_h	0.05–0.20 mm
Porosity ε	0.36, 0.50 and 0.64
Heat transfer fluid	Aqueous solution with 20% v/v ethylene glycol
MCM	Gadolinium
MCM thermal conductivity k_s	11 W/(m·K)
MCM density ρ_s	7900 kg/m^3

Please cite this article in press as: Tian Lei, Kurt Engelbrecht, Kaspar K. Nielsen, Christian T. Veje, Study of geometries of active magnetic regenerators for room temperature magnetocaloric refrigeration, Applied Thermal Engineering (2015), doi: 10.1016/j.applthermaleng.2015.11.113

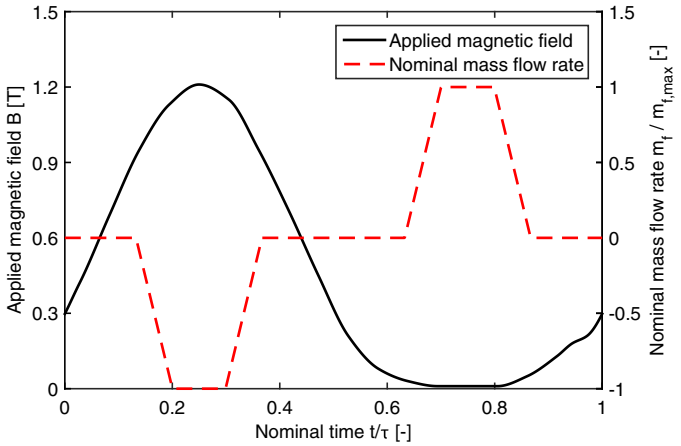

Fig. 4. Applied magnetic field B and nominal mass flow rate $\dot{m}_f/\dot{m}_{f,max}$ as a function of nominal time t/τ.

presented and compared. In this way, the frequency becomes the only operating parameter to be optimized.

4. Results and discussion

The performance of an AMR using four different geometries is presented and discussed in this section. For a reasonable comparison, the results for a desired specific cooling capacity of 100 W/kg of regenerator material are compared and the corresponding COPs are presented below.

4.1. Packed sphere bed

Fig. 5 shows how COP of regenerators using packed sphere bed vary with the frequency f and the aspect ratio R_a. Four subgraphs represent different hydraulic diameters from 0.05 to 0.20 mm, which are corresponding to the sphere diameters from 0.14 to 0.57 mm. For each case, the frequency ranges from 0.3 to 10 Hz, and the aspect ratio from 0.1 to 8. In total, about 1800 simulations were done to present the synthetic impacts of those three variables.

In general, it is found that not only the maximum COP, but also optimum frequency and aspect ratio vary with the hydraulic

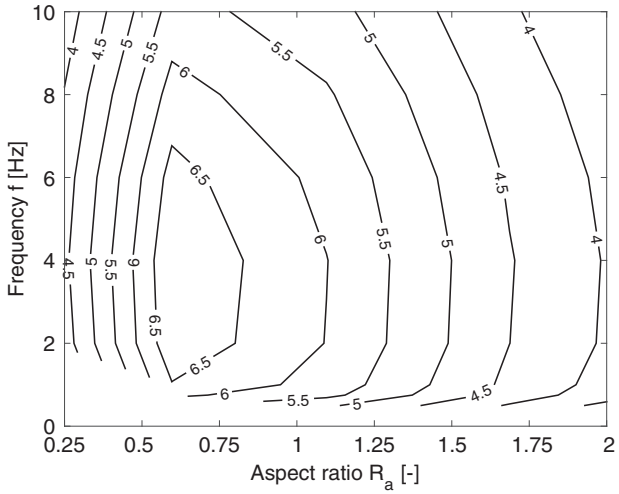

(a) $D_h = 0.05$ mm

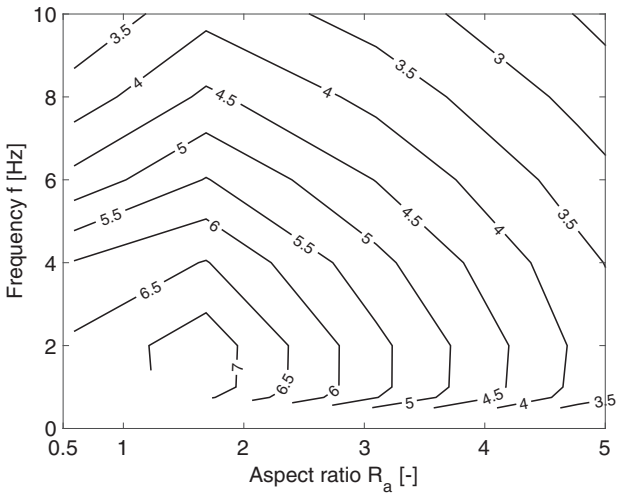

(b) $D_h = 0.10$ mm

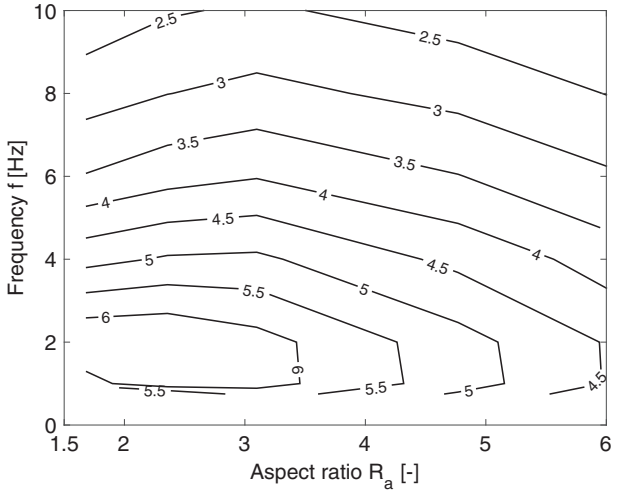

(c) $D_h = 0.15$ mm

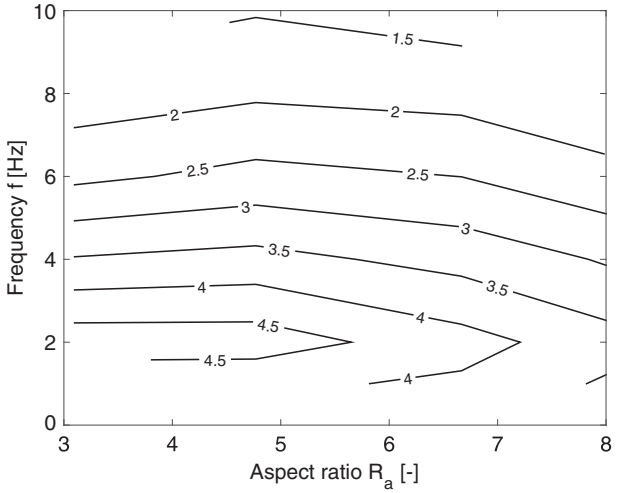

(d) $D_h = 0.20$ mm

Fig. 5. COP as a function of frequency f and aspect ratio R_a for regenerators using packed sphere bed.

Please cite this article in press as: Tian Lei, Kurt Engelbrecht, Kaspar K. Nielsen, Christian T. Veje, Study of geometries of active magnetic regenerators for room temperature magnetocaloric refrigeration, Applied Thermal Engineering (2015), doi: 10.1016/j.applthermaleng.2015.11.113

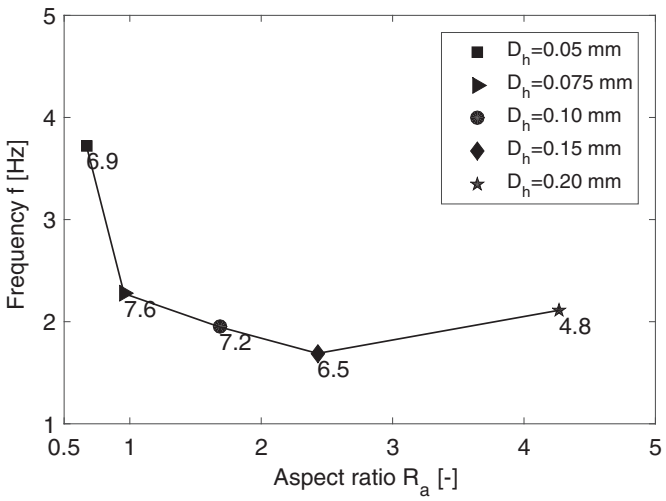

Fig. 6. Maximum COP (sidenoted numbers) as well as optimum frequency f (vertical coordinate) and aspect ratio R_a (horizonal coordinate) for regenerators using packed sphere bed with different hydraulic diameter D_h.

diameter in Fig. 5a–d. For the packed sphere bed with a hydraulic diameter of 0.05 mm, the maximum COP is around 6.9 when the frequency is 3.7 Hz and the aspect ratio is 0.7 as shown in Fig. 5a. Too large or small frequency and aspect ratio can lead to a decrease in COP. The spindle shaped contour reveals that COP changes significantly with the aspect ratio; in contrast, it is less sensitive to the frequency. Fig. 5b–d shows that the maximum COP becomes 7.2, 6.5 and 4.8 when the hydraulic diameters are 0.10, 0.15, and 0.20 mm, respectively. Simultaneously the optimum frequency shifts to a lower value and the optimum aspect ratio becomes larger. In the case of a small hydraulic diameter, the pressure drop per unit length is relatively high; therefore, a small aspect ratio is necessary in order to prevent the viscous dissipation from dominating. On the other hand, larger hydraulic diameter allows longer regenerator, which in turn increases the risk of insufficient heat transfer. As a result, a relatively low frequency is desired in order to increase the heat transfer time and number of transfer units (NTU), defined as the ratio of the amount of heat transferred between solid and fluid to the thermal mass of the fluid moved. When the hydraulic diameter is larger than or equal to 0.15 mm, the COP becomes more sensitive to frequency instead of aspect ratio, as shown in Fig. 5c and d.

Fig. 6 summarizes the maximum COP and shows how optimum frequency and aspect ratio shift with the hydraulic diameter, by extracting the information from Fig. 5a–d. The largest COP is 7.6 when the hydraulic diameter, frequency, and aspect ratio are 0.075 mm, 2.3 Hz, and 1.0, respectively.

Fig. 7a shows the total entropy production rates $\dot{S}_{p,tot}$ as a function of frequency and aspect ratio, which has a reversed pattern compared to the results of COP in Fig. 5b. The minimum total production rate is found when the frequency is around 2.0 Hz and the aspect ratio is 1.7, which fits the position of the maximum COP. As seen in Fig. 7b, the entropy production rates due to insufficient heat transfer are strongly related to the frequency rather than the aspect ratio, In a typical case where the frequency increases from 0.3 to 10 Hz, the averaged mass flow rate only decreases slightly less than 15% for obtaining a constant specific cooling power. It leads to about 8% decrease in the averaged heat transfer coefficient h. It is observed that the average value of $\frac{(T_f - T_s)^2}{T_f T_s}$ decreases slightly with increasing frequency when f < 1 Hz, due to a relatively higher heat transfer coefficient. However, for f > 1 Hz this term increases significantly, which is caused by the decreasing heat transfer time. As a result, $\dot{S}_{p,ht}$ decreases slightly when the frequency is less than 1 Hz, while it increases dramatically with a further increasing frequency. In contrast, $\dot{S}_{p,vd}$ in Fig. 7c is more sensitive to the aspect ratio than the frequency, which is reflected by the equations for calculating the pressure drop through the bed. Since the axial conduction loss increases when the cross sectional area becomes larger and the length shorter, $\dot{S}_{p,ac}$ increases significantly with decreasing aspect ratio; however, the frequency does not affect $\dot{S}_{p,ac}$ much. In most cases, the entropy production rates representing insufficient heat transfer and viscous dissipation contribute most to the total entropy production rate, whereas the entropy production rate due to axial conduction becomes significant when the aspect ratio is smaller than 1.0. At the point of minimum total entropy production rate, the viscous dissipation contributes the most, the second is insufficient heat transfer, while the last is axial conduction.

4.2. Parallel plate matrix

In contrast to the packed sphere bed, the porosity of the parallel plate matrix can be adjusted by changing the plate thickness and flow channel height. Therefore we study three porosities 0.36, 0.50 and 0.64, and present the results of optimum frequency and aspect ratio for different hydraulic diameters in Fig. 8. The curve representing the porosity of 0.36 shows a similar pattern to that of the packed sphere bed. The optimum aspect ratio increases with the hydraulic diameter, while the optimum frequency decreases to a minimum and then increases. The maximum COP is around 9.0, which is higher than that of the packed sphere bed, when the hydraulic diameter is 0.10 mm, the frequency is 4.7 Hz, and the aspect ratio is 2.1. It is found that higher frequency is preferable for the parallel plate matrix compared with the packed sphere bed.

In general, the maximum COP increases and the optimum frequency becomes smaller with the increase of porosity, which can also be seen in some results from Reference 16. The highest COPs of regenerators using a parallel plate matrix are 10.0 and 11.2 for the porosities of 0.50 and 0.64, respectively, corresponding to optimum hydraulic diameters of 0.10 and 0.15 mm. With the same hydraulic diameter, increased porosity will lead to a decrease in the plate thickness and solid mass, where a smaller mass flow rate is needed and this may make the COP higher with the same specific cooling power. However, the porosity should not be too high in a real design, because the power density per unit volume is decreased, which reversely requires a large magnet apparatus to obtain the same cooling power.

The optimum hydraulic diameter for a parallel plate matrix is around 0.10–0.15 mm, and the corresponding flow channel height ranges from 0.05 to 0.075 mm. Besides, a uniform channel size in the parallel plate matrix is desired, otherwise the flow maldistribution may reduce the overall heat transfer coefficient and efficiency significantly [8]. Those requirements make the fabrication difficult and become the barriers for applying the parallel plate matrix in the real prototypes.

4.3. Micro-channel matrix

Since the circular and rectangular micro-channel matrices have similar characteristics, we only present the simulation results of the circular micro-channel matrix. Fig. 9 shows that the micro-channel matrix exhibits similar behavior as the parallel plate matrix. However, the best COP is lower, which is 7.8, 9.0 and 10.1 for different porosities. This is expected since the micro-channel matrix provides slightly smaller Nu/f_F compared to the parallel plate matrix. The optimum hydraulic diameter is 0.075 or 0.10 mm, which is also the optimal diameter of the circular channels.

Please cite this article in press as: Tian Lei, Kurt Engelbrecht, Kaspar K. Nielsen, Christian T. Veje, Study of geometries of active magnetic regenerators for room temperature magnetocaloric refrigeration, Applied Thermal Engineering (2015), doi: 10.1016/j.applthermaleng.2015.11.113

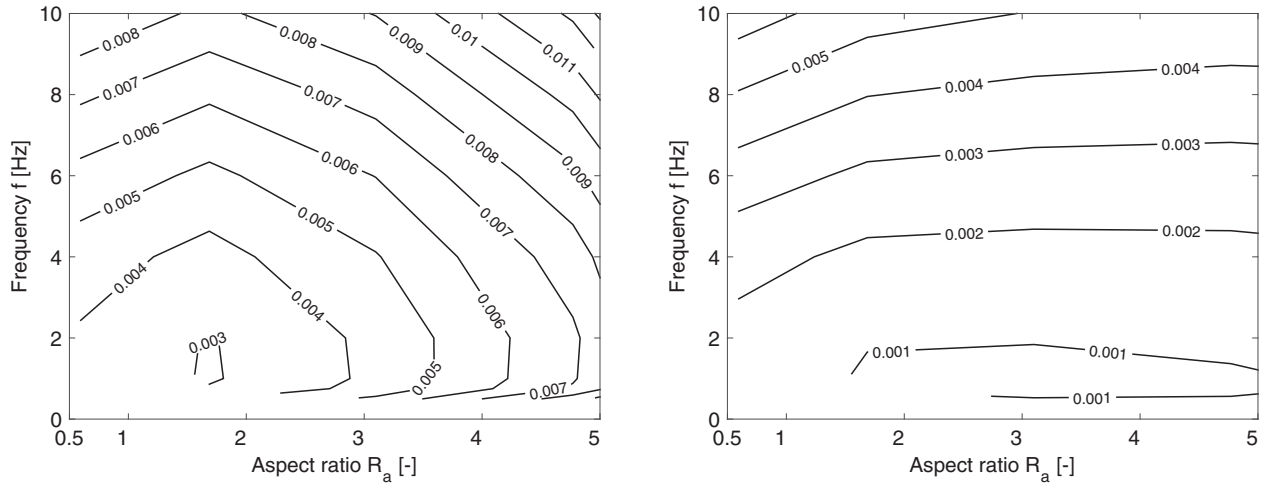

(a) Total entropy production rate consisted by three parts $\dot{S}_{p,tot}$

(b) Entropy production rate due to insufficient heat transfer $\dot{S}_{p,ht}$

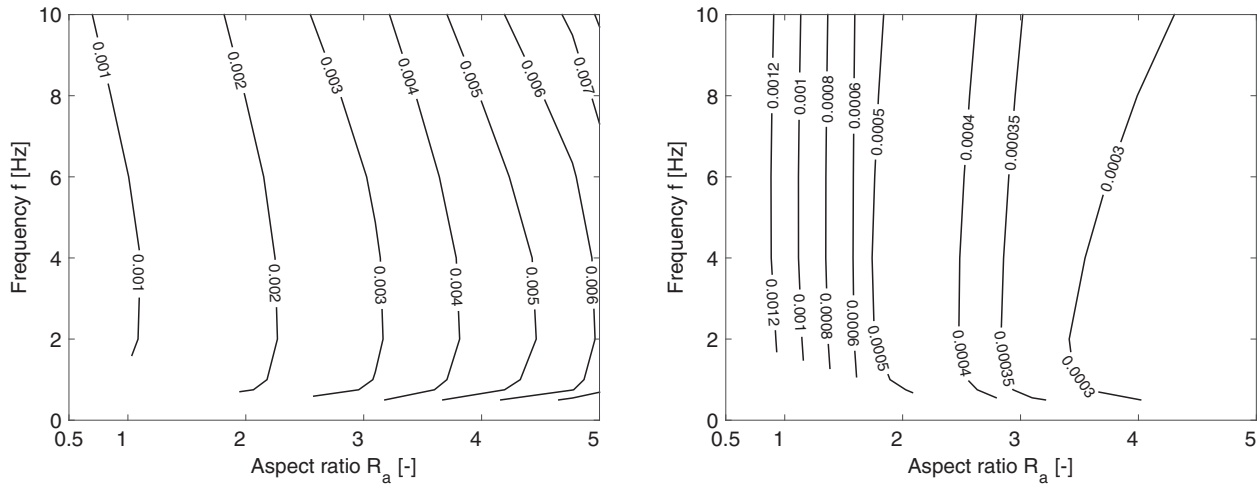

(c) Entropy production rate due to viscous dissipation $\dot{S}_{p,vd}$

(d) Entropy production rate due to axial conduction $\dot{S}_{p,ac}$

Fig. 7. Corresponding entropy production rate as a function of frequency f and aspect ratio R_a of AMRs using packed sphere bed with $D_h = 0.10$ mm (in the case of Fig. 5b).

Like the parallel plate matrix, the problems of fabrication and long term durability also exist. A regenerator with a monolithic perovskite structure fabricated by extrusion process has been tested [9] with a channel size around 1 mm. This was much larger than the optimum channel size in this study and in addition it revealed a problem of structure collapsing during sintering. Moore et al. [10] used selective laser melting technology to fabricate a wavy-channel block and an array of fin-shaped rods. The minimum channel diameter was around 0.8 mm and a corrosion problem existed.

4.4. Packed screen bed

Compared with the packed sphere bed, the channels in the packed screen bed are more structured, giving an equivalent heat transfer performance but significantly lower pressure drop, as shown in Fig. 3c. The tortuous structure is capable of relieving the problem of the flow mal-distribution as compared to the parallel plates. Another advantage of the packed screen bed is relatively low axial conduction due to the stacked structure, which is not discussed in detail here. Fig. 10 shows the performance of AMRs using a packed screen bed. It can be seen that the optimum frequency approaches that of the packed sphere bed, which is lower compared with the parallel plate and micro-channel matrices. With a porosity of 0.36, the packed screen bed could provide the best COP around 7.7, which is higher than the packed sphere bed. At this point, the optimum frequency is 2.0 Hz and the aspect ratio is 3.3. With increased porosity, the best COP increases considerably to 8.9 and 9.6 for the porosities of 0.50 and 0.64, respectively. Although it is difficult to fabricate the woven screens with existing MCM materials like Gd or ceramics, there is a probability of producing a similar geometry like packed felt bed in the future. Table 4 summarizes the best COP of regenerators using different geometries and it is clearly seen that the other three geometries could provide higher efficiency at the optimum points compared with the packed sphere bed.

Please cite this article in press as: Tian Lei, Kurt Engelbrecht, Kaspar K. Nielsen, Christian T. Veje, Study of geometries of active magnetic regenerators for room temperature magnetocaloric refrigeration, Applied Thermal Engineering (2015), doi: 10.1016/j.applthermaleng.2015.11.113

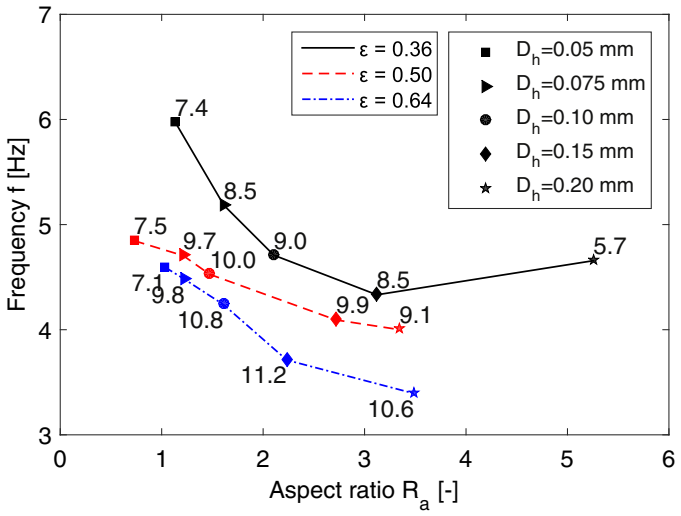

Fig. 8. Maximum COP (sidenoted numbers) as well as optimum frequency f (vertical coordinate) and aspect ratio R_a (horizonal coordinate) for regenerators using parallel plate matrix under different hydraulic diameters D_h and porosities ε.

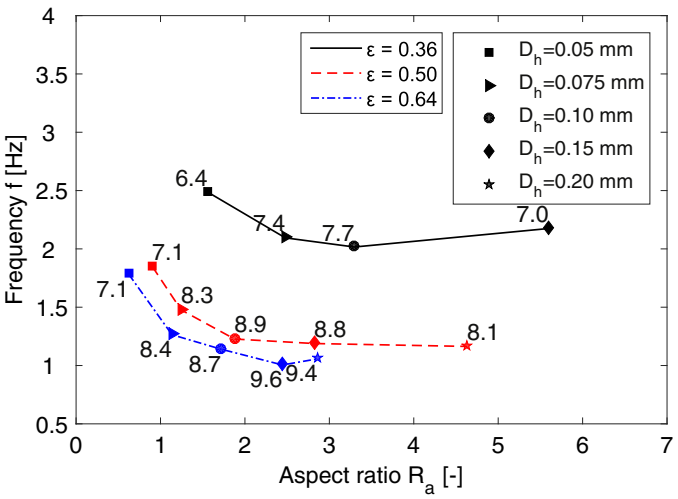

Fig. 10. Maximum COP (sidenoted numbers) as well as optimum frequency f (vertical coordinate) and aspect ratio R_a (horizonal coordinate) for regenerators using packed screen bed under different hydraulic diameters D_h and porosities ε.

5. Conclusions

We have presented a study on regenerator geometries for application in magnetocaloric refrigeration based on a 1D numerical model. The simulation results show that with a specific cooling power of 100 W/kg, the maximum COP of regenerators using a packed sphere bed varies with the hydraulic diameter: The optimum frequency decreases and optimum aspect ratio increases as the hydraulic diameter increases. For a small hydraulic diameter of 0.05 mm, the COP changes significantly with the aspect ratio while it is less sensitive to the frequency. In contrast, the COP becomes more sensitive to the frequency when the hydraulic diameter is equal to or larger than 0.15 mm. For the packed sphere bed, the best COP is 7.6 when the hydraulic diameter, frequency, and aspect ratio are 0.075 mm, 2.3 Hz, and 1.0, respectively. The entropy production rates due to the three main loss mechanisms, insufficient heat transfer, viscous dissipation, and axial conduction, as well as the total entropy production rates, are calculated and compared. They show that the insufficient heat transfer is more sensitive to the frequency while the viscous dissipation is more affected by the aspect ratio. The conduction loss becomes significant when the aspect ratio is less than 1.0. It is also found that the minimum total entropy production rate fits the maximum COP concurrently.

In general, the parallel plate matrix, micro-channel matrix, and packed screen bed show better performance than the packed sphere bed. With a constant porosity, the optimum aspect ratio increases with the hydraulic diameter and the optimum frequency decreases in most cases. Higher porosity may lead to an increase in the maximum COP and the optimum frequency becomes smaller. Although the regenerators based on parallel plates or micro-channels provide higher theoretical efficiency compared to packed sphere beds, the fabrication of small channel size and the effect of flow mal-distribution may become barriers to a real application. In contrast, the packed screen bed or similar matrix structure could be a promising geometry. The practical challenge in general is clearly to fabricate the required structures with the often very brittle composite magnetocaloric materials.

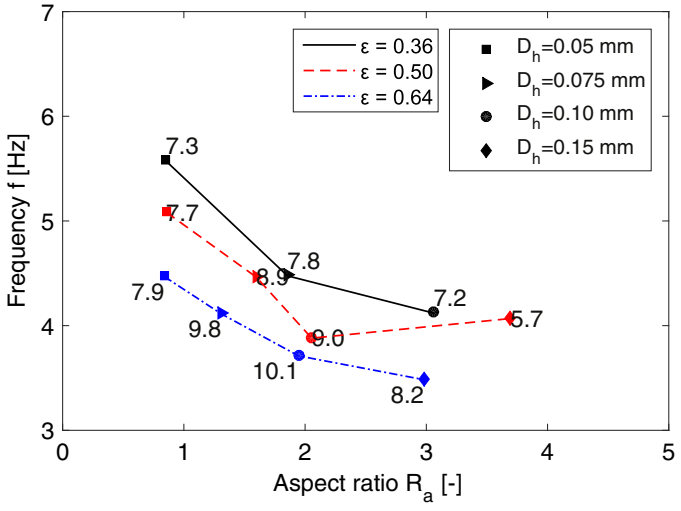

Fig. 9. Maximum COP (sidenoted numbers) as well as optimum frequency f (vertical coordinate) and aspect ratio R_a (horizonal coordinate) for regenerators using micro-channel matrix under different hydraulic diameters D_h and porosities ε.

Acknowledgements

This work was financed by the ENOVHEAT project which is funded by Innovation Fund Denmark (contract no. 12-132673). Tian Lei wishes to thank the Otto Mønsteds Fund for financial support.

Table 4
Best performance and optimum parameters for different regenerator geometries.

Geometry	Porosity ε	Hydraulic diameter D_h	Aspect ratio R_a	Frequency f	COP
Packed sphere bed	0.36	0.075	1.0	2.3	7.6
Parallel plate matrix	0.36	0.10	2.1	4.7	9.0
	0.50	0.10	1.5	4.5	10.0
	0.64	0.15	2.2	3.7	11.2
Micro-channel matrix	0.36	0.075	1.9	4.5	7.8
	0.50	0.10	2.1	3.8	9.0
	0.64	0.10	2.0	3.7	10.1
Packed screen bed	0.36	0.10	3.3	2.0	7.7
	0.50	0.15	1.9	1.2	8.9
	0.64	0.15	2.4	1.0	9.6

Please cite this article in press as: Tian Lei, Kurt Engelbrecht, Kaspar K. Nielsen, Christian T. Veje, Study of geometries of active magnetic regenerators for room temperature magnetocaloric refrigeration, Applied Thermal Engineering (2015), doi: 10.1016/j.applthermaleng.2015.11.113

Nomenclature

a_s	Specific surface area [1/m]
A_c	Cross sectional area [m^2]
B	Applied magnetic field [Tesla]
Bi	Biot number
c_f	Specific heat capacity of fluid [J/(kg·K)]
c_H	Specific heat capacity of MCM at constant magnetic field [J/(kg·K)]
D_c	Micro-channel diameter [m]
D_h	Hydraulic diameter [m]
D_L	Characteristic dimension length [m]
D_{sc}	Wire diameter of woven screen [m]
D_{sp}	Sphere diameter [m]
f_F	Friction factor
Gz	Graetz number
h	Heat transfer coefficient [W/(m^2·K)]
h_f	Specific enthalpy of fluid [J/kg]
H_{p1}	Plate thickness of parallel plate matrix [m]
H_{p2}	Flow channel height of parallel plate matrix [m]
H_{r1}	Flow channel height of rectangular micro-channel matrix [m]
H_{r2}	Flow channel width of rectangular micro-channel matrix [m]
k_{disp}	Thermal conductivity of the fluid due to axial dispersion [W/(m·K)]
k_f	Thermal conductivity of fluid [W/(m·K)]
k_s	Thermal conductivity of MCM [W/(m·K)]
k_{stat}	Static thermal conductivity of regenerator and fluid [W/(m·K)]
L	Regenerator length [m]
$\dot{m}_f$	Mass flow rate [kg/s]
M_{sc}	Mesh number of woven screen [1/m]
N_r	Number of regenerator beds
N_t	Number of time steps
Nu	Nusselt number
N_x	Number of axial nodes
P	Pressure [Pa]
Pr	Prandtl number
$\dot{q}_C$	Specific cooling power [W/kg]
$\dot{Q}_C$	Cooling power [W]
$\dot{Q}_H$	Heating rejection [W]
R_a	Aspect ratio
Re	Reynolds number
$\mathrm{Re_h}$	Reynolds number based on hydraulic diameter
s_s	Specific entropy of solid refrigerant [J/(kg·K)]
$S_{p,ac}$	Entropy production rate due to axial conduction [W/K]
$S_{p,ht}$	Entropy production rate due to insufficient heat transfer [W/K]
$S_{p,vd}$	Entropy production rate due to viscous dissipation [W/K]
$S_{p,tot}$	Total entropy production rate [W/K]
St	Stanton number
t	Time [s]
T	Temperature [K]
T_C	Cold end temperature [K]
T_f	Fluid temperature [K]
T_s	Solid temperature [K]
T_H	Hot end temperature [K]
u	Specific internal energy [J/kg]
v_s	Superficial velocity [m/s]
V_r	Regenerator volume [m^3]
W_p	Plate width [m]
x	Axial position [m]

Abbreviations

AMR	Active magnetic regenerator
COP	Coefficient of performance
MCM	Magnetocaloric material
MCR	Magnetocaloric refrigeration
NTU	Number of transfer units

Greek letters

α	Aspect ratio of micro-channel
ε	Porosity of regenerator bed
μ_f	Dynamic viscosity [Pa·s]
ρ_f	Density of fluid [kg/m^3]
ρ_s	Density of MCM kg/m^3]
χ	Correlation factor of internal temperature gradient in Reference 25

References

[1] K.A. Gschneidner Jr., V.K. Pecharsky, Thirty years of near room temperature magnetic cooling: where we are today and future prospects, Int. J. Refrigeration 31 (2008) 945–961, doi:10.1016/j.ijrefrig.2008.01.004.
[2] B. Yu, M. Liu, P.W. Egolf, A. Kitanovski, A review of magnetic refrigerator and heat pump prototypes built before the year, Int. J. Refrigeration 33 (2010) (2010) 1029–1060, doi:10.1016/j.ijrefrig.2010.04.002.
[3] A. Kitanovski, J. Tusek, A. Poredosc, Magnetocaloric Energy Conversion, Springer, 2015.
[4] T. Okamura, R. Rachi, N. Hirano, S. Nagaya, Improvement of 100w class room temperature magnetic refrigerator, Proceedings of the 2nd International Conference of Magnetic Refrigeration at Room Temperature 2007, pp. 377–382.
[5] K. Engelbrecht, D. Eriksen, C.R.H. Bahl, R. Bjørk, J. Geyti, J.A. Lozano, et al., Experimental results for a novel rotary active magnetic regenerator, Int. J. Refrigeration 35 (6) (2012) 1498–1505, doi:10.1016/j.ijrefrig.2012.05.003.
[6] D. Arnold, A. Tura, A. Ruebsaat-Trott, A. Rowe, Design improvements of a permanent magnet active magnetic refrigerator, Int. J. Refrigeration 37 (2014) 99–105, doi:10.1016/j.ijrefrig.2013.09.024.
[7] S. Jacobs, J. Auringer, A. Boeder, J. Chell, L. Komorowski, J. Leonard, et al., The performance of a large-scale rotary magnetic refrigerator, Int. J. Refrigeration 37 (2014) 84–91, doi:10.1016/j.ijrefrig.2013.09.025.
[8] K.K. Nielsen, K. Engelbrecht, C.R. Bahl, The influence of flow maldistribution on the performance of inhomogeneous parallel plate heat exchangers, Int. J. Heat Mass Transf. 60 (2013) 432–439, doi:10.1016/j.ijheatmasstransfer.2013.01.018.
[9] N. Pryds, F. Clemens, M. Menon, P.H. Nielsen, K. Brodersen, R. Bjrk, et al., A monolithic perovskite structure for use as a magnetic regenerator, J. Am. Ceram. Soc. 94 (8) (2011) 2549–2555, doi:10.1111/j.1551-2916.2011.04398.x.
[10] J. Moore, D. Klemm, D. Lindackers, S. Grasemann, R. Trger, J. Eckert, et al., Selective laser melting of $La(FeCoSi)_{13}$ geometries for magnetic refrigeration, J. Appl. Phys. 114 (4) (2013) 043907, doi:10.1063/1.4816465.
[11] R. Radebaugh, B. Louie, A simple, first step to the optimization of regenerator geometry, in: Proceedings of the Third Cryocooler Conference, vol. 1, 1985, pp. 177–198.
[12] J.A. Barclay, S. Sarangi, Selection of regenerator geometry for magnetic refrigerator applications, Tech. Rep., Los Alamos Nat. Lab (1984).
[13] P. Li, M. Gong, J. Wu, Geometric optimization of an active magnetic regenerative refrigerator via second-law analysis, J. Appl. Phys. 104 (10) (2008) 103536, doi:10.1063/1.3032195.
[14] D. Vuarnoz, T. Kawanami, Numerical analysis of a reciprocating active magnetic regenerator made of gadolinium wires, Appl. Therm. Eng. 37 (2012) 388–395, doi:10.1016/j.applthermaleng.2011.11.053.
[15] J. Li, T. Numazawa, K. Mastumoto, Y. Yanagisawa, H. Nakagome, A modeling study on the geometry of active magnetic regenerator, in: Advances in Cryogenic Engineering, vol. 1434, AIP Publishing, 2012, pp. 327–334.
[16] J. Tušek, A. Kitanovski, A. Poredo, Geometrical optimization of packed-bed and parallel-plate active magnetic regenerators, Int. J. Refrigeration 36 (5) (2013) 1456–1464, doi:10.1016/j.ijrefrig.2013.04.001.
[17] R.F. Benenati, C.B. Brosilow, Void fraction distribution in beds of spheres, AIChE J. 8 (3) (1962) 359–361, doi:10.1002/aic.690080319.
[18] R.F. Barron, G. Nellis, J.M. Pfotenhauer, Cryogenic Heat Transfer, CRC Press, 1999.
[19] J.C. Armour, J.N. Cannon, Fluid flow through woven screens, AIChE J. 14 (3) (1968) 415–420.
[20] K.K. Nielsen, G. Nellis, S. Klein, Numerical modeling of the impact of regenerator housing on the determination of Nusselt numbers, Int. J. Heat Mass Transf. 65 (2013) 552–560, doi:10.1016/j.ijheatmasstransfer.2013.06.032.
[21] S. Ergun, A.A. Orning, Fluid flow through randomly packed columns and fluidized beds, Ind. Eng. Chem. 41 (6) (1949) 1179–1184.
[22] A. Bejan, Entropy Generation Minimization: The Method of Thermodynamic Optimization of Finite-size Systems and Finite-time Processes, CRC Press, 1995.
[23] M. Asadi, G. Xie, B. Sunden, A review of heat transfer and pressure drop characteristics of single and two-phase microchannels, Int. J. Heat Mass Transf. 79 (2014) 34–53, doi:10.1016/j.ijheatmasstransfer.2014.07.090.
[24] R.K. Shah, A.L. London, Laminar Flow Forced Convection in Ducts: A Source Book for Compact Heat Exchanger Analytical Data, Academic Press, 1978.

Please cite this article in press as: Tian Lei, Kurt Engelbrecht, Kaspar K. Nielsen, Christian T. Veje, Study of geometries of active magnetic regenerators for room temperature magnetocaloric refrigeration, Applied Thermal Engineering (2015), doi: 10.1016/j.applthermaleng.2015.11.113

[25] K. Engelbrecht, A numerical model of an active magnetic regenerator refrigerator with experimental validation (Ph.D. thesis), University of Wisconsin – Madison, 2008.
[26] M. Nickolay, H. Martin, Improved approximation for the Nusselt number for hydrodynamically developed laminar flow between parallel plates, Int. J. Heat Mass Transf. 45 (15) (2002) 3263–3266, doi:10.1016/S0017-9310(02)00028-5.
[27] H. Hausen, M. Sayer, A.J. Willmott, Heat Transfer in Counterflow, Parallel Flow and Cross Flow, McGraw-Hill New York, 1983.
[28] W.M. Kays, M.E. Crawford, B. Weigand, Convective Heat and Mass Transfer, Tata McGraw-Hill Educ., 2012.
[29] J.-W. Park, D. Ruch, R. Wirtz, Thermal/fluid characteristics of isotropic plain-weave screen laminates as heat exchange surfaces, Proceed. 40th AIAA Aerosp. Sci. Meeti. Exhibit 208 (2002) 2002–2008.
[30] M. Kaviany, Principles of Heat Transfer in Porous Media, Springer-Verlag, 1991.
[31] L. Gibilaro, R. Di Felice, S. Waldram, P. Foscolo, Generalized friction factor and drag coefficient correlations for fluid-particle interactions, Chem. Eng. Sci. 40 (10) (1985) 1817–1823, doi:10.1016/0009-2509(85)80116-0.
[32] W. Kays, A. London, Compact Heat Exchangers, Krieger Publishing Company, 1984.
[33] N. Wakao, S. Kaguei, T. Funazkri, Effect of fluid dispersion coefficients on particle-to-fluid heat transfer coefficients in packed beds: correlation of Nusselt numbers, Chem. Eng. Sci. 34 (3) (1979) 325–336, doi:10.1016/0009-2509(79)85064-2.
[34] K.K. Nielsen, Numerical modeling and analysis of the active magnetic regenerator (Ph.D. thesis), Technical University of Denmark 2010.
[35] K.V. Sharp, R.J. Adrian, Transition from laminar to turbulent flow in liquid filled microtubes, Exp. Fluids 36 (5) (2004) 741–747, doi:10.1007/s00348-003-0753-3.
[36] P. Wibulswas, Laminar-flow heat-transfer in non-circular ducts (Ph.D. thesis), University of London 1966.
[37] P.S. Lee, S.V. Garimella, D. Liu, Investigation of heat transfer in rectangular microchannels, Int. J. Heat Mass Transf. 48 (9) (2005) 1688–1704, doi:10.1016/j.ijheatmasstransfer.2004.11.019.
[38] M. Tanaka, I. Yamashita, F. Chisaka, Flow and heat transfer characteristics of the Stirling engine regenerator in an oscillating flow, JSME Int. J. 33 (2) (1990) 283–289.
[39] D. Gedeon, J. Wood, Oscillating-flow regenerator test rig: hardware and theory with derived correlations for screens and felts, Tech. Rep. NASA, USA (1996).
[40] J. Sodre, J. Parise, Friction factor determination for flow through finite wire-mesh woven-screen matrices, J. Fluids Eng. 119 (4) (1997) 847–851, doi:10.1115/1.2819507.
[41] K. Hamaguchi, S. Takahashi, H. Miyabe, Thermal performance of regenerator matrix, Trans. Jpn. Soc. Mech. Eng. 49 (445) (1983) 2001–2010.
[42] S. Isshiki, A. Sakano, I. Ushiyama, N. Isshiki, Studies on flow resistance and heat transfer of regenerator wire meshes of Stirling engine in oscillatory flow, JSME Int. J. 40 (2) (1997) 281–289.
[43] Z.-C. Chang, P.-H. Chen, Flow channeling effect on a regenerator's thermal performance, Cryogenics 38 (2) (1998) 191–196, doi:10.1016/S0011-2275(97)00133-1.
[44] G.R. Hadley, Thermal conductivity of packed metal powders, Int. J. Heat Mass Transf. 29 (6) (1986) 909–920, doi:10.1016/0017-9310(86)90186-9.
[45] U. Kurzweg, M. Jaeger, Thermal pulse propagation and dispersion in laminar flow within conduits of finite wall conductivity, Int. J. Heat Mass Transf. 40 (6) (1997) 1391–1400, doi:10.1016/S0017-9310(96)00196-2.
[46] W.S. Chang, Porosity and effective thermal conductivity of wire screens, J. Heat Transf. 112 (1) (1990) 5–9, doi:10.1115/1.2910365.
[47] K. Engelbrecht, K.K. Nielsen, C.R.H. Bahl, C.P. Carroll, D. van Asten, Material properties and modeling characteristics for MnFeP1-xAsx materials for application in magnetic refrigeration, J. Appl. Phys. 113 (17) (2013) 173510, doi:10.1063/1.4803495.
[48] T. Lei, K.K. Nielsen, K. Engelbrecht, C.R.H. Bahl, H. Neves Bez, C.T. Veje, Sensitivity study of multi-layer active magnetic regenerators using first order magnetocaloric material $La(FeMnSi)_{13}H_y$, J. Appl. Phys. 118 (1) (2015) 014903, doi:10.1063/1.4923356.
[49] R. Bjørk, C.R.H. Bahl, M. Katter, Magnetocaloric properties of $LaFe_{13-x-y}Co_xSi_y$ and commercial grade Gd, J. Magnet. Magn. Mater. 322 (24) (2010) 3882–3888, doi:10.1016/j.jmmm.2010.08.013.

Please cite this article in press as: Tian Lei, Kurt Engelbrecht, Kaspar K. Nielsen, Christian T. Veje, Study of geometries of active magnetic regenerators for room temperature magnetocaloric refrigeration, Applied Thermal Engineering (2015), doi: 10.1016/j.applthermaleng.2015.11.113

A.3 Study of multi-layer active magnetic regenerators using magnetocaloric materials with a first and second order phase transition

T. Lei, K. Engelbrecht, K. K. Nielsen, H. Neves Bez and C. R. H. Bahl, Study of multi-layer active magnetic regenerators using magnetocaloric materials with a first and second order phase transition, *Journal of Physics D: Applied Physics*, **49**, 345001, (2016).

IOP Publishing Journal of Physics D: Applied Physics
J. Phys. D: Appl. Phys. **49** (2016) 345001 (10pp) doi:10.1088/0022-3727/49/34/345001

Study of multi-layer active magnetic regenerators using magnetocaloric materials with first and second order phase transition

T Lei, K Engelbrecht, K K Nielsen, H Neves Bez and C R H Bahl

Department of Energy Conversion and Storage, Technical University of Denmark, 4000 Roskilde, Denmark

E-mail: tile@dtu.dk

Received 22 April 2016, revised 20 June 2016
Accepted for publication 29 June 2016
Published 27 July 2016

Abstract

Magnetocaloric materials (MCM) with a first order phase transition (FOPT) usually exhibit a large, although sharp, isothermal entropy change near their Curie temperature, compared to materials with a second order phase transition (SOPT). Experimental results of applying FOPT materials in recent magnetocaloric refrigerators (MCR) demonstrated the great potential for these materials, but a thorough study on the impact of the moderate adiabatic temperature change and strong temperature dependence of the magnetocaloric effect (MCE) is lacking. Besides, comparing active magnetic regenerators (AMR) using FOPT and SOPT materials is also of fundamental interest. We present modeling results of multi-layer AMRs using FOPT and SOPT materials based on a 1D numerical model. First the impact of isothermal entropy change, adiabatic temperature change and shape factor describing the temperature dependence of the MCE are quantified and analyzed by using artificially built magnetocaloric properties. Then, based on measured magnetocaloric properties of $La(Fe,Mn,Si)_{13}H_y$ and Gd, an investigation on how to layer typical FOPT and SOPT materials with different temperature spans is carried out. Moreover, the sensitivity of variation in Curie temperature distribution for both groups of AMRs is investigated. Finally, a concept of mixing FOPT and SOPT materials is studied for improving the stability of layered AMRs with existing materials.

Keywords: magnetic refrigeration, active magnetic regenerator, magnetocaloric material, magnetic phase transition

(Some figures may appear in colour only in the online journal)

1. Introduction

Since a regenerative magnetic refrigerator was first demonstrated by Brown in 1976 [1], many improvements in room temperature magnetic refrigeration have been presented. Many early MCR systems used gadolinium (Gd) or Gd alloys, which are typical SOPT materials, as the solid refrigerant. During the ferromagnetic to paramagnetic transition, the magnetization of SOPT materials goes continuously to zero as the temperature approaches the Curie temperature T_{Curie} [2]. SOPT materials exhibit a moderate isothermal entropy change ΔS_{iso} and adiabatic temperature change ΔT_{ad}, which are the two most commonly used parameters for evaluating MCMs. For FOPT materials, the magnetization changes discontinuously and a latent heat is associated with the magnetic phase transition. In the characterization of a real FOPT material, the impurities and spatial variations in the stoichiometry may blur the first-order/second-order distinction [2] and the measured properties are always continuous. FOPT materials usually exhibit much larger peak values in ΔS_{iso} than SOPT materials and have equivalent or lower ΔT_{ad} at the same time. For example, the maximum $|\Delta S_{\mathrm{iso}}|$ of the typical SOPT material Gd is around 5 J kg^{-1} K^{-1} and the peak of ΔT_{ad} is around 4 K for a magnetic field change of 1.5 T [3],

while the values are 10–20 J kg^{-1} K^{-1} and 4 K for an FOPT material La(Fe,Mn,Si)$_{13}$H$_y$ [4]. Much research effort has been applied to develop FOPT materials, such as $Gd_5Si_2Ge_2$ [5], La(Fe,Si)$_{13}$ [6] and MnFe(P,As) [7], or to apply FOPT materials in an MCR prototype. Jacobs *et al* [8] presented a rotary MCR device using six-layer LaFeSiH and it produced a cooling power of around 2500 W over a span of 11 K with a coefficient of performance (COP) around 2, which demonstrates the significant potential of FOPT materials.

A distinguishing difference between the two groups of materials is that both ΔS_{iso} and ΔT_{ad} of FOPT materials will decrease much faster as the temperature deviates from T_{Curie}, displaying that the proper working temperature region is thus much narrower than that for SOPT materials. It indicates that a single-layer AMR using an FOPT material is unable to realize a large temperature span ΔT. In order to improve ΔT, a multi-layer design is required, in which MCMs with different Curie temperatures are aligned along the regenerator bed following the temperature gradient. Although the large ΔS_{iso} of FOPT materials is reported and emphasized extensively, the influence of moderate (or even lower) ΔT_{ad} and 'sharp' temperature dependence of the magnetocaloric effect on the AMR performance are not well investigated. Engelbrecht and Bahl [9] studied the individual impact of ΔS_{iso} or ΔT_{ad} by holding the other parameter constant, and they concluded that ΔT_{ad} can be more important than ΔS_{iso} in certain conditions. Brey *et al* [10] evaluated the influence of ΔS_{iso} and ΔT_{ad} on the cooling power of a continuously layered AMR by scaling measured properties. However, the temperature dependence of the MCE, which differs a lot between FOPT and SOPT materials, has not been taken into account when evaluating AMRs in previous studies. To further the understanding, this paper studies how the combination of ΔS_{iso}, ΔT_{ad} and the temperature dependence of the MCE affect the cooling performance of multi-layer AMRs, based on artificially built magnetocaloric properties and a 1D numerical model.

Comparing AMRs using FOPT and SOPT materials are of significant importance for choosing proper materials for future MCRs. Aprea *et al* [11] investigated AMRs using four kinds of FOPT and SOPT materials based on a simplified model. Lei *et al* [12] presented a study on multi-layer regenerators only using FOPT materials and the results suggested building an AMR with 2.2 layers FOPT materials per 5 K temperature span. However, the studies are still insufficient. Therefore, for AMRs using typical FOPT and SOPT materials, the influence of the number of layers, temperature span and variation in the Curie temperature distribution are presented here based on measured magnetocaloric properties of La(Fe,Mn,Si)$_{13}$H$_y$ and Gd. A concept of mixing FOPT and SOPT materials are also investigated, which is expected to bring benefits in certain conditions.

2. 1D numerical model of AMR

A modern MCR generally includes four main sections: permanent magnets generating the high and low magnetic field region, AMRs filled with a porous matrix of MCM, a mechanical system generating a relative movement between the permanent magnet and AMR, as well as a flow control system. A typical four-step cycle is shown in figure 1, and this AMR consists of six layers of MCMs with different Curie temperatures as seen in figure 1(e). In operation, the MCMs are periodically magnetized and demagnetized with an associated temperature increase and decrease. During the intervals, a heat transfer fluid is blown through the porous AMR bed to transport heat with the solid refrigerant, and the arrows in figures 1(b) and (d) show the flow directions during the blow period. At the hot end, the outflow has a higher temperature than that of the hot end reservoir T_h, and rejects the excess heat $\dot{Q}_h$ to the reservoir. While the outflow at the cold end absorbs heat, that is cooling power $\dot{Q}_c$, from the cold end reservoir with T_c due to a temperature difference. The temperature span is $\Delta T = T_h - T_c$ and the COP is defined as $\dot{Q}_c/(\dot{Q}_h - \dot{Q}_c)$ [13].

The approach of numerical modeling provides a complimentary tool to study the AMR performance. Besides a number of effective thermodynamic analysis tools [14, 15], one and 2D models of the AMR have also been developed [13, 16, 17]. This paper uses a 1D numerical model to investigate AMRs using FOPT and SOPT materials. The model is generally build on two energy equations for the solid refrigerant and fluid [12, 13] as shown in (1) and (2), which have been widely used to predict the AMR performance. The fluid is incompressible and the regenerator housing is adiabatic in this model.

$$\frac{\partial}{\partial x}\left(k_{stat}\frac{\partial T_s}{\partial x}\right)A_c + \frac{Nuk_f}{d_h}a_s A_c(T_f - T_s) = A_c(1-\varepsilon)\rho_s\left[c_H\frac{\partial T_s}{\partial t} + T_s\left(\frac{\partial s_s}{\partial H}\right)_{T_s}\frac{\partial H}{\partial t}\right] \quad (1)$$

$$\frac{\partial}{\partial x}\left(k_{disp}\frac{\partial T_f}{\partial x}\right)A_c - \dot{m}_f c_f\frac{\partial T_f}{\partial x} - \frac{Nuk_f}{d_h}a_s A_c(T_f - T_s) + \left|\frac{\partial P}{\partial x}\frac{\dot{m}_f}{\rho_f}\right| = A_c\varepsilon\rho_f c_f\frac{\partial T_f}{\partial t}. \quad (2)$$

The energy storage and magnetic work terms are rewritten as shown in the left side of the solid energy equation (1), which can be calculated only through the specific entropy data s_s of the MCM, since $c_H = T_s(\partial s_s/\partial T_s)_H$. The two terms on the left hand side represent the thermal conduction through the regenerator bed and the heat transfer between solid and fluid. For the fluid equation, the thermal conduction, enthalpy flow, heat transfer with the solid, viscous dissipation and energy storage are considered and expressed from left to right in (2). Both equations are coupled by the heat transfer term, and they are solved numerically by discretizing in time and spatial domains. More details of the model and related expression of each term has been reviewed in literature [10, 13, 17]. The number of time and spatial nodes are 6000 and 120, respectively, for realizing a good numerical accuracy. The performance indices such as cooling power and COP will be output after hundreds or thousands of iterations until reaching a numerical tolerance.

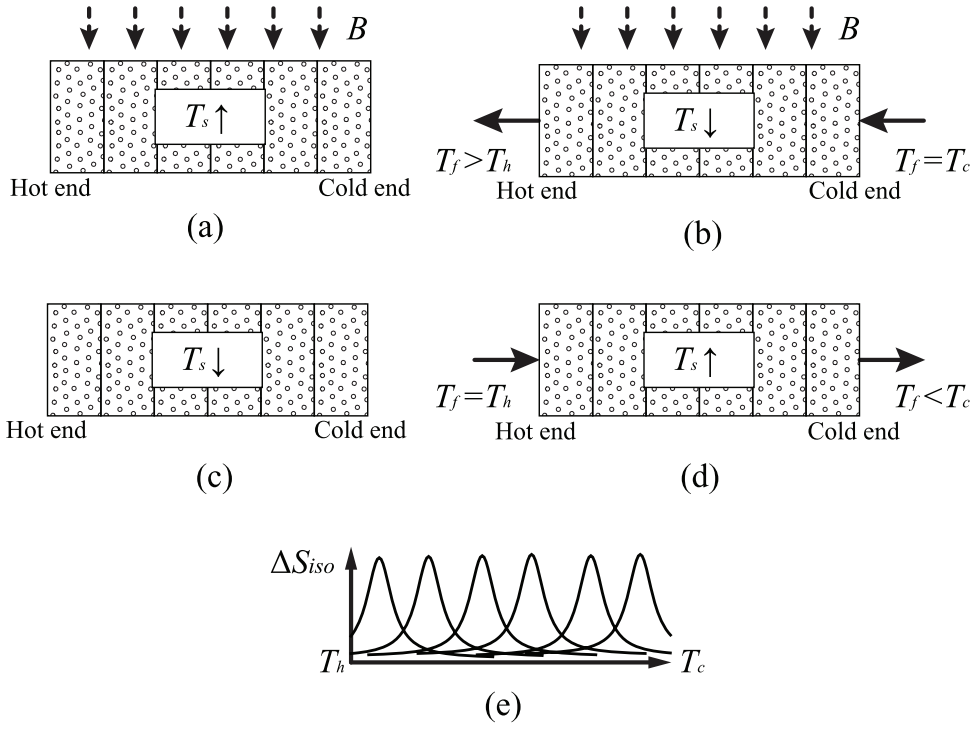

Figure 1. Schematic diagram of a multi-layer active magnetic regenerator undergoing a four-step refrigeration process and ΔS_{iso} of each layer: (a) adiabatic magnetization, (b) cold-to-hot blow, (c) adiabatic demagnetization, (d) hot-to-cold blow, (e) ΔS_{iso} of each layer as a function of T.

3. Material properties

As discussed in section 2, for modeling multi-layer AMRs using FOPT and SOPT materials, mainly the entropy data as a function of the internal magnetic field and temperature are needed. The two important parameters, isothermal entropy change ΔS_{iso} and adiabatic temperature change ΔT_{ad} of an MCM are also tightly connected and they are both derived from the entropy data by [2, 18]:

$$\begin{aligned}\Delta S_{\mathrm{iso}}(T_{\mathrm{s}};H_{\mathrm{f}},H_{\mathrm{i}}) &= \int_{H_{\mathrm{i}}}^{H_{\mathrm{f}}}\left(\frac{\partial S_{\mathrm{s}}}{\partial H}\right)_{T_{\mathrm{s}}}\mathrm{d}H \\ &= \int_0^{T_{\mathrm{s}}}\frac{c_{\mathrm{H}}(T_{\mathrm{s}},H_{\mathrm{f}})}{T_{\mathrm{s}}}\mathrm{d}T_{\mathrm{s}} - \int_0^{T_{\mathrm{s}}}\frac{c_{\mathrm{H}}(T_{\mathrm{s}},H_{\mathrm{i}})}{T_{\mathrm{s}}}\mathrm{d}T_{\mathrm{s}}\end{aligned} \tag{3}$$

$$\begin{aligned}\Delta T_{\mathrm{ad}}(T_{\mathrm{s}};H_{\mathrm{f}},H_{\mathrm{i}}) &= -\int_{H_{\mathrm{i}}}^{H_{\mathrm{f}}}\left(1/\left(\frac{\partial s_{\mathrm{s}}}{\partial T_{\mathrm{s}}}\right)_{\mathrm{H}}\right)\left(\frac{\partial S_{\mathrm{s}}}{\partial H}\right)_{T_{\mathrm{s}}}\mathrm{d}H \\ &= -\int_{H_{\mathrm{i}}}^{H_{\mathrm{f}}}\frac{T_{\mathrm{s}}}{c_{\mathrm{H}}(T_{\mathrm{s}},H)}\left(\frac{\partial S_{\mathrm{s}}}{\partial H}\right)_{T_{\mathrm{s}}}\mathrm{d}H\end{aligned} \tag{4}$$

where T_{s}, H_{f} and H_{i} are the solid temperature, final magnetic field and initial magnetic field. In order to study the impacts of ΔS_{iso} and ΔT_{ad} as a combination, empirical methods, including holding one parameter constant [9] and scaling ΔS_{iso} or ΔT_{ad} [10], have been developed. However, the strong temperature dependence of MCE is not taken in account, which loses important information of FOPT and SOPT materials. Therefore, we use the following equation to calculate isothermal entropy change upon an increase of magnetic field from 0 to 1.5 T:

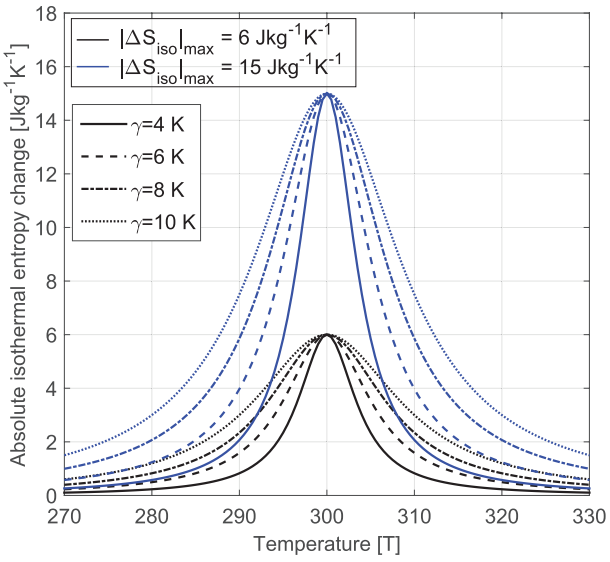

Figure 2. Absolute isothermal entropy change $|\Delta S_{\mathrm{iso}}|$ based on (5) as a function of temperature T for different shape factors γ upon a field change of 1.5 T, when the maximum absolute isothermal entropy change $|\Delta S_{\mathrm{iso}}|_{\mathrm{max}}$ is 6 and 15 J kg^{-1} K^{-1}, respectively.

$$\Delta S_{\mathrm{iso,\,1.5\,T}}(T_{\mathrm{s}}) = -|\Delta S_{\mathrm{iso}}|_{\mathrm{max}}\frac{\gamma^2}{(T_{\mathrm{s}}-T_{\mathrm{Curie}})^2+\gamma^2} \tag{5}$$

where $|\Delta S_{\mathrm{iso}}|_{\mathrm{max}}$, T_{Curie} and γ are the maximum absolute isothermal entropy change, Curie temperature and shape factor

Table 1. Parameters for modeling AMRs using FOPT and SOPT materials.

Parameter	Value
Maximum applied magnetic field	1.4 T
Heat transfer fluid	Aqueous solution with 20% v/v ethylene glycol
Cross sectional area of regenerator bed	625 mm^2
Number of regenerator beds	12
Length of regenerator bed	50 mm
Sphere diameter	0.3 mm
Geometry of regenerator bed	Packed sphere bed
Porosity of regenerator bed	0.36
Frequency	2 Hz
Number of layers	1–40
Temperature span	1–30 K
Thermal conductivity of $La(Fe,Mn,Si)_{13}H_y$	8 W m^{-1} K^{-1}
Density of $La(Fe,Mn,Si)_{13}H_y$	6900 kg m^{-3}
Thermal conductivity of Gd	11 W m^{-1} K^{-1}
Density of Gd	7900 kg m^{-3}

of ΔS_{iso} curve. Figure 2 presents the absolute value of isothermal entropy change based on (5) for $|\Delta S_{iso}|_{max}$ of 6 and 15 J kg^{-1} K^{-1} as well as γ from 4 to 10 K. The shape factor γ is introduced to adjust the temperature distribution and the shape of ΔS_{iso} curve. Smaller γ could lead to sharper ΔS_{iso} curve around the Curie temperature and then narrower working temperature region, which is similar to the case with FOPT materials. The isothermal entropy change upon a magnetic field change of H is calculated by:

$$\Delta S_{iso,H}(T_s) = \left(\frac{H}{1.5}\right)^{2/3} \Delta S_{iso,1.5\,T}(T_s) \tag{6}$$

where the scaling coefficient $(H/1.5)^{2/3}$ is used due to the nonlinear magnetic field dependence of ΔS_{iso} [2].

The specific heat at zero magnetic field as a function of temperature is defined as:

$$c_{H,0\,T}(T_s) = c_{H,max}\frac{\gamma^2}{(T_s - T_{Curie})^2 + \gamma^2} + c_{H,base} \tag{7}$$

where $c_{H,max}$ and $c_{H,base}$ are the maximum and background value of the specific heat at zero magnetic field.

Combining (6) and (7) gives the entropy data as a function of the internal magnetic field and temperature and the adiabatic temperature change ΔT_{ad} can be further calculated by (4). For a combination of ΔS_{iso} and ΔT_{ad}, $|\Delta S_{iso}|_{max}$ is given and the desired ΔT_{ad} is obtained by iteration with adjusted $c_{H,max}$. Note the temperature dependent curve of ΔT_{ad} also presents a sharp peak around the preset Curie temperature for a small γ, which is close to the real situation. By using this method, the magnetocaloric properties with different combinations of ΔS_{iso}, ΔT_{ad}, γ and T_{Curie} are obtained, which cover most of FOPT and SOPT materials applied in room temperature MCRs.

In the simulation, the measured magnetocaloric properties are also used for evaluating multi-layer AMRs using typical FOPT and SOPT materials, which is the second part of this work. Since the measurements of materials with different T_{Curie} are limited, an approach of shifting one group of experimental data according to designed T_{Curie} [12] is used. It is implemented based on an observation that materials behave quite similarly under the magnetization process and the peaks of ΔS_{iso} are similar in magnitude and shape for a range of T_{Curie}. For simulating FOPT and SOPT materials with different T_{Curie}, $La(Fe,Mn,Si)_{13}H_y$ with $T_{Curie} = 305$ K and Gd are used as the bases, respectively. The influence brought by magnetic hysteresis of $La(Fe,Mn,Si)_{13}H_y$ is also included in the simulation, using the method of irreversible magnetization presented by Brey *et al* [10]. Note this effect is ignored when using the artificially built magnetocaloric properties. The details of the magnetocaloric properties of $La(Fe,Mn,Si)_{13}H_y$ and Gd can be reviewed in [4, 12, 19].

4. Results and discussion

In the simulations, each regenerator has a length of 50 mm and a cross section of 625 mm^2. Packed spherical particle beds are used and the particle diameter is 0.3 mm. The maximum applied magnetic field is 1.4 T. The other operating and geometry parameters are listed in table 1.

For multi-layer AMRs, we assume that each layer is aligned evenly without special description. The thickness of each layer is the same and the Curie temperature of the material in each layer follows:

$$T_{Curie,n} = T_h - (T_h - T_c)\frac{2n-1}{2n} \tag{8}$$

where n denotes the sequence number of each layer.

4.1. Impact of isothermal entropy change, adiabatic temperature change and shape factor

Figure 3 shows the impact of ΔS_{iso} and ΔT_{ad} on the specific cooling power $\dot{q}_c$, which is the cooling power generated with 1 kg MCM, of AMRs using materials with different shape factors when the COP is 5. The temperature span is fixed at 20 K and the mass flow is always optimized to reach the targeted COP while the frequency is held constant at 2 Hz. Here we assume the density and the thermal conductivity of these materials are 7400 kg m^{-3} and 9.5 W m^{-1} K^{-1}, which are averaged based on those of $La(Fe,Mn,Si)_{13}H_y$ and

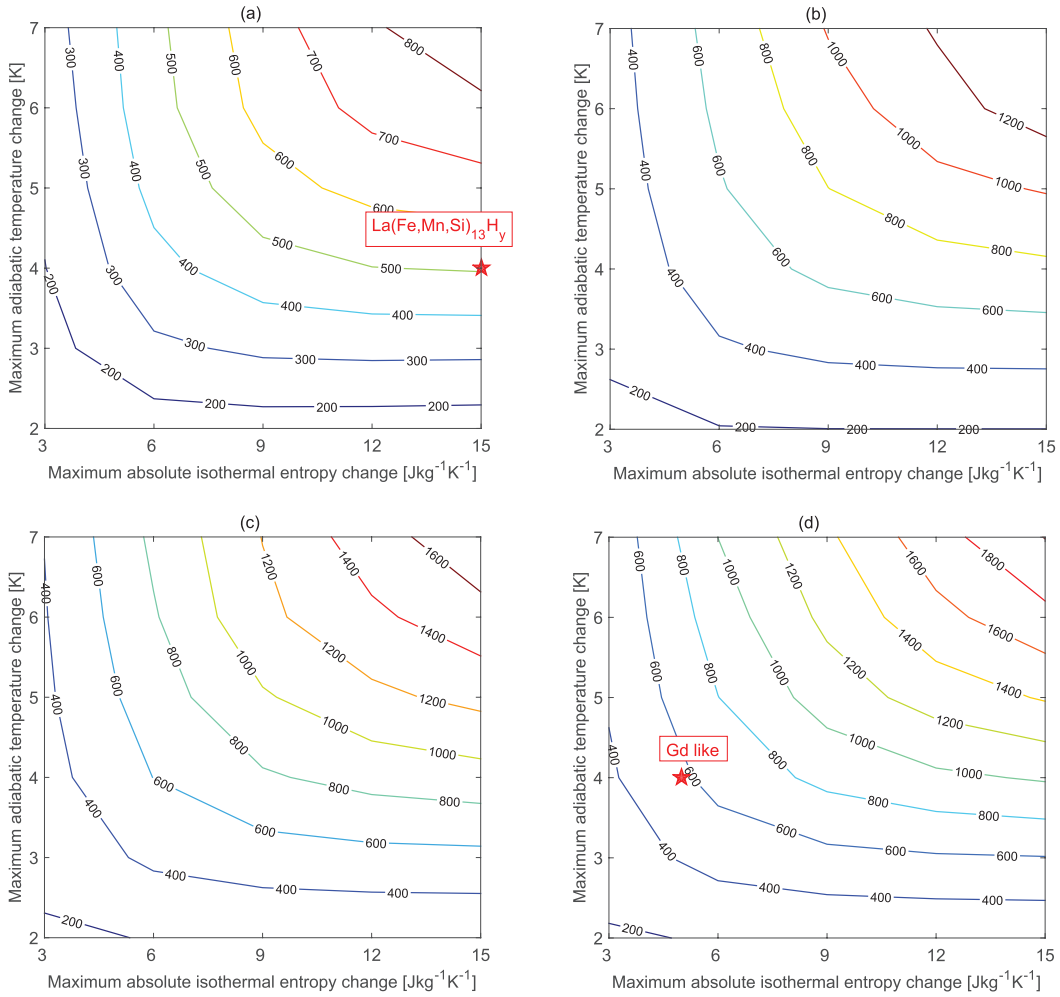

Figure 3. Impact of maximum absolute isothermal entropy change $|\Delta S_{\mathrm{iso}}|_{\mathrm{max}}$ and maximum adiabatic temperature change $\Delta T_{\mathrm{ad,max}}$ on specific cooling power $\dot{q}_{\mathrm{c}}$ (contour lines) of AMRs using materials with different shape factors: (a) $\gamma = 4$ K; (b) $\gamma = 6$ K; (c) $\gamma = 8$ K; (d) $\gamma = 10$ K, when the COP is fixed at 5.

Gd [4, 12, 19] as shown in table 1. The number of layers N_{L} is 40, which ensures that the overall magnetocaloric effect varies along the regenerator quasi continuously and ideally. Since further increasing N_{L} does not improve the AMR performance much, N_{L} of 40 is chosen considering the computation time. The results presented in figures 3(a)–(d) show that both ΔS_{iso} and ΔT_{ad} exert significant impact on the specific cooling power and $\dot{q}_{\mathrm{c}}$ increases with larger ΔS_{iso} and ΔT_{ad} generally. Note that when one of the two parameters is relatively small, increasing the other does not improve the performance much, which implies that both ΔS_{iso} and ΔT_{ad} should be emphasized equally.

An interesting trend with different shape factors γ is observed. A smaller shape factor, which means sharper MCE curve and narrower working temperature region, will lead to a decrease in $\dot{q}_{\mathrm{c}}$ even with the same $|\Delta S_{\mathrm{iso}}|_{\mathrm{max}}$ and $\Delta T_{\mathrm{ad,\,max}}$. The maximum $\dot{q}_{\mathrm{c}}$ of figure 3(d) is about 1900 W kg^{-1}, which is about twice of that in the case of figure 3(a), showing the significant impact brought by variation in γ.

The position representing materials similar to La(Fe,Mn,Si)$_{13}$H$_y$ or Gd are marked in figures 3(a) and (d), respectively. Here approximate values of ΔS_{iso}, ΔT_{ad} and γ for both materials are used for a theoretical study. AMR using LaFeMnSiH-like materials gives a theoretical specific cooling power around 510 W kg^{-1}, which is close to the value of 580 W kg^{-1} for AMRs using Gd-like materials, although the former presents much larger peak value in ΔS_{iso}. This may be attributed to the close ΔT_{ad} for both materials and the difference in the shape factors. Compared to the results from [10], the influence of ΔT_{ad} is further emphasized here due to the introduction of the shape factor γ, which is closer to the real situation. The results show that not only the peak value of ΔS_{iso}, but also ΔT_{ad} and the shape factor γ, which did not attract enough attentions in the existing literature, are also important for improving the AMR performance.

4.2. Impact of temperature span and number of layers

The continuously layered AMR is difficult to construct due to limits of fabricating the materials and tuning the Curie temperature. Besides investigating the theoretical maximum cooling

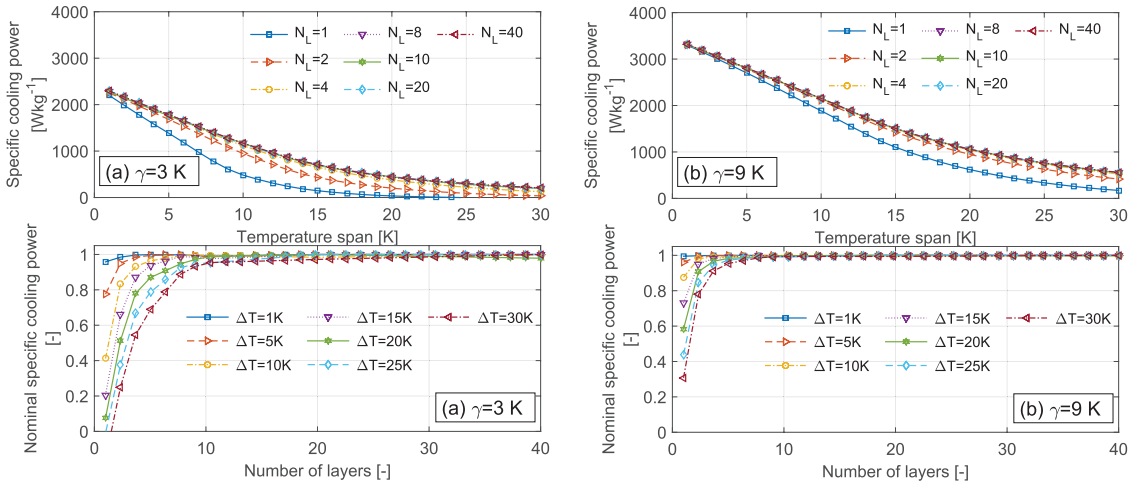

Figure 4. Impacts of temperature span ΔT and number of layers N_{L} for multi-layer AMRs using materials with different shape factors: (a) $\gamma = 3$ K and (b) $\gamma = 9$ K, where $|\Delta S_{\mathrm{iso}}|_{\mathrm{max}}$ and $\Delta T_{\mathrm{ad,max}}$ are 15 J kg^{-1} K^{-1} and 4 K respectively.

performance, it is also interesting to explore how to layer the regenerators and how many layers are needed in a real AMR. Figure 4 presents a study on the impacts of number of layers for AMRs operating under different temperature spans. In the following studies, the mass flow is optimized for obtaining the highest specific cooling power. The Curie temperature of each layer is distributed evenly according to (6). The maximum $|\Delta S_{\mathrm{iso}}|$ and ΔT_{ad} are 15 J kg^{-1} K^{-1} and 4 K, respectively, upon a filed change of 1.5 T. Two shape factors, 3 and 9 K, are used. The specific cooling power decreases quickly with an increase in the temperature span and $\dot{q}_c$ increases with the number of layers for both cases. However, for the materials with a larger shape factor of 9 K, the maximum specific cooling power (when $N_{\mathrm{L}} = 40$) is much larger, due to the widely distributed magnetocaloric properties. The subplots at the bottom of figures 4(a) and (b) directly show the impact of the number of layers on the nominal cooling power $\dot{q}_{\mathrm{c}}/\dot{q}_{\mathrm{c},N_{\mathrm{L}}=40}$, which is the ratio of the specific cooling power to the maximum value when N_{L} is 40. Comparison shows that a smaller shape factor requires more layers to get close to the theoretical maximum performance, increasing the difficulties of constructing the multi-layer AMRs using the materials with small γ.

Based on the method presented in [12], figure 5 summarizes the value of 90% of the theoretical maximum specific cooling power and the corresponding number of layers needed to achieve that performance. It is aimed at proposing a reasonable number of layers without losing too much theoretical cooling capacity. Two more shape factors $\gamma = 5$ and 7 K are simulated and added in figure 5. The corresponding number of layers is obtained by interpolating the performance curve as a function of N_{L}, which could be a non-integer, and the minimum N_{L} is 1. With increasing temperature span, the needed N_{L} becomes larger with a significant decrease in the specific cooling power in all cases. At the same time, smaller shape factors present lower cooling performance and larger necessary number of layers. For a temperature span of 30 K, about 7.6, 5.2, 4.0, 3.2 layers are needed to achieve the theoretical performance for $\gamma = 3$, 5, 7 and 9 K, respectively. It shows the importance of the shape factor and its strong influence on the system performance even with the same values of ΔS_{iso} and ΔT_{ad}.

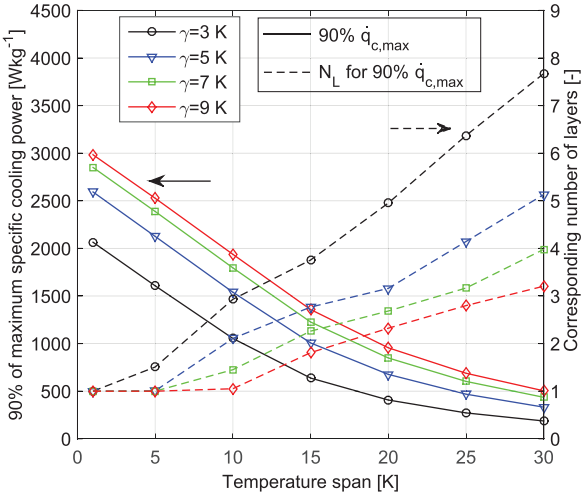

Figure 5. 90% of the maximum specific cooling power $\dot{q}_{\mathrm{c,max}}$ and corresponding number of layers N_{L} as functions of temperature span ΔT for a multi-layer AMR using materials with different shape factors γ, where $|\Delta S_{\mathrm{iso}}|_{\mathrm{max}}$ and $\Delta T_{\mathrm{ad,\ max}}$ are 15 J kg^{-1} K^{-1} and 4 K, respectively.

4.3. Multi-layer AMRs using La(Fe,Mn,Si)$_{13}$H$_y$ or Gd-like materials

In sections 4.1 and 4.2 we discuss the impact of different parameters on the system performance by using synthesized properties based on (5)–(7). We also investigate the performance of AMRs using FOPT and SOPT materials based on measured properties. As mentioned in section 3, La(Fe,Mn,Si)$_{13}$H$_y$ and Gd are chosen as typical materials with first and second order phase transition. Although Gd has a fixed Curie temperature, its magnetocaloric properties are used to simulate similar materials with tunable T_{Curie}, e.g. Gd-Y alloys.

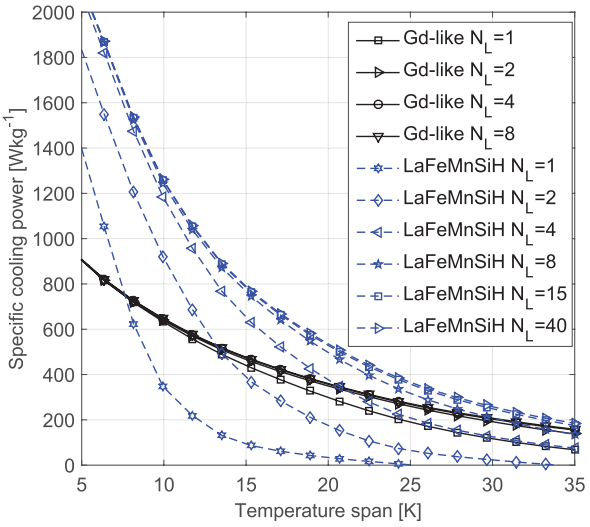

Figure 6. Impacts of temperature span ΔT and number of layers N_L on maximum specific cooling power $\dot{q}_{c,max}$ of multi-layer AMRs using La(Fe,Mn,Si)$_{13}$H$_y$ or Gd-like materials, where LaFeMnSiH denotes La(Fe,Mn,Si)$_{13}$H$_y$.

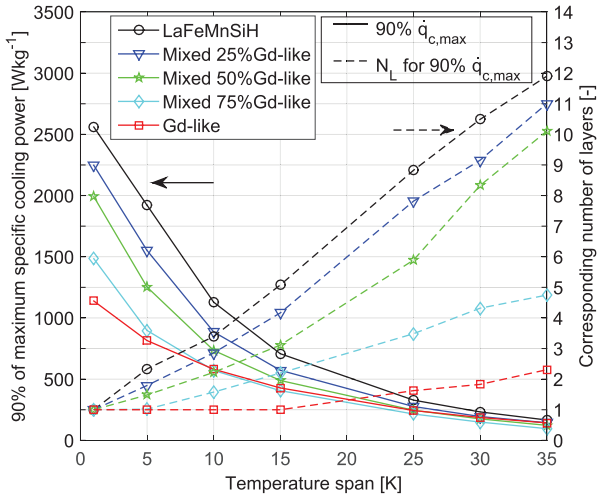

Figure 7. 90% of the maximum specific cooling power $\dot{q}_{c,max}$ and corresponding number of layers N_L as functions of temperature span ΔT for multi-layer AMR using La(Fe,Mn,Si)$_{13}$H$_y$, Gd-like or mixed materials.

4.3.1. Impact of number of layers and temperature span. The impact of the number of layers and the temperature span for multi-layer AMRs using La(Fe,Mn,Si)$_{13}$H$_y$ or Gd-like materials is presented in figure 6. Increasing the number of layers or decreasing the temperature span leads to a higher specific cooling power for both cases generally. Although the maximum cooling power of AMRs using FOPT materials like La(Fe,Mn,Si)$_{13}$H$_y$ is larger than that with Gd-like materials, more layers are needed to approach the theoretical performance. It is preferable to use FOPT materials for obtaining a higher specific cooling power when the temperature span is less than 30 K, while the benefits become smaller when $\Delta T > 30$ K. Note that Gd has superior magnetocaloric properties compared with most other SOPT materials with tunable Curie temperatures. Therefore the real performance of AMRs using Gd-like materials will be somewhat lower than the theoretical prediction here.

As shown in figure 7, 90% of the theoretical maximum specific cooling power and corresponding number of layers for AMRs using La(Fe,Mn,Si)$_{13}$H$_y$ or Gd-like materials are presented. Higher cooling performance is observed in AMRs using La(Fe,Mn,Si)$_{13}$H$_y$. However, only 2–3 layers are needed for Gd-like materials to get close to the maximum performance when the temperature span is 30 K, while about 12 layers are required for La(Fe,Mn,Si)$_{13}$H$_y$. A concept of mixing FOPT and SOPT materials is proposed and further investigated here. La(Fe,Mn,Si)$_{13}$H$_y$ and Gd-like materials are mixed by volume fraction in each layer and their Curie temperatures are assumed the same. The results show that the number of layers could be reduced by sacrificing specific cooling power with the method of mixing more Gd-like materials. Although lower cooling performance is obtained, this concept could still bring certain benefits to the system design, which will be discussed in the following sections.

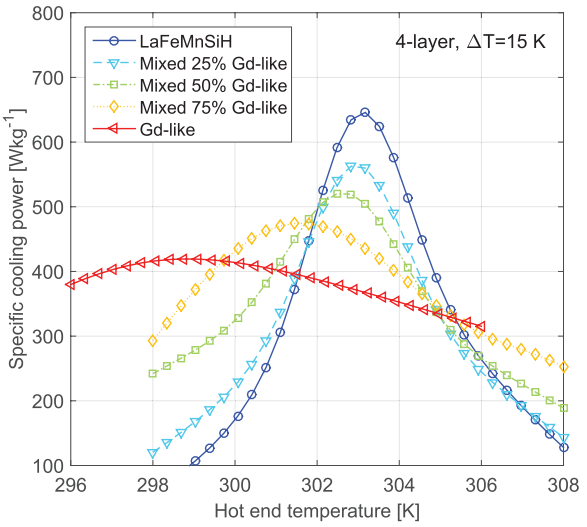

Figure 8. Impact of working temperature (represented only by the hot end temperature T_h due to a fixed ΔT) on specific cooling power $\dot{q}_c$ of multi-layer AMRs using La(Fe,Mn,Si)$_{13}$H$_y$, Gd-like or mixed materials.

4.3.2. Sensitivity to working temperature. For most refrigeration devices, the system stability under fluctuating ambient temperatures is quite important, which depends on the climate and region. These varying operating conditions can cause performance issues for AMRs using FOPT materials, due to their relatively narrow MCE curve. To investigate this effect, we simulate AMRs using FOPT, SOPT or mixed materials and the results are presented in figure 8. The number of layers is fixed at 4, and the Curie temperature distribution is calculated based on (8). The working temperature region is changed by shifting both cold and hot end temperatures, while the temperature span is kept constant at 15 K. In this way, the performance of AMRs using La(Fe,Mn,Si)$_{13}$H$_y$ degrades fastest when the

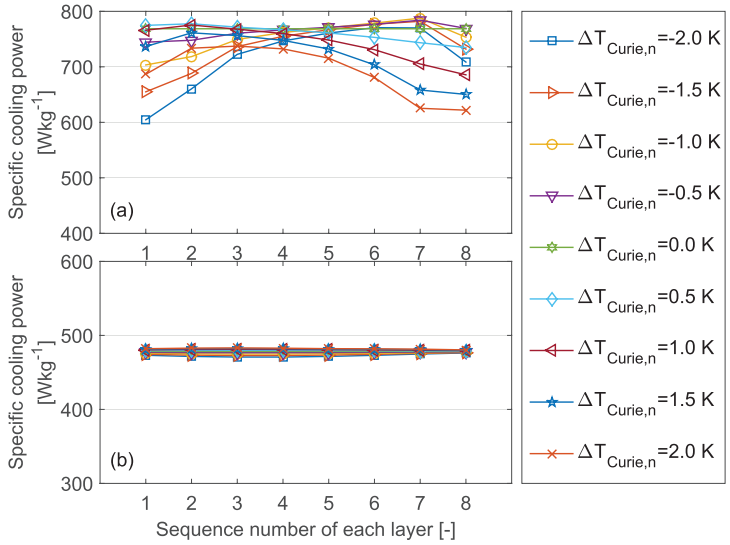

Figure 9. Impact of Curie temperature deviation $\Delta T_{\mathrm{Curie},n}$ of each layer on specific cooling power $\dot{q}_c$ of multi-layer AMRs using La(Fe,Mn,Si)$_{13}$H$_y$ or Gd-like materials. (a) LaFeMnSiH, (b) Gd-like.

working temperature deviates from the designed region. Even a change of ~2–3 K will result in a significant decrease in performance. With an increased volume fraction of Gd, the sensitivity of AMRs to the working temperature becomes smaller, although the peak performance decreases. Therefore, mixing FOPT and SOPT materials may be beneficial for resisting the variation in the ambient temperature and obtaining better performance than using only the SOPT materials. It can also be seen that the optimum working temperature regions are slightly different from that of the AMRs using different materials.

4.3.3. Impact of Curie temperature distribution. It is known that accurately tuning the Curie temperature during the manufacture of MCMs is difficult, and the impact of the Curie temperature deviation is of interest for designing multi-layer AMRs. Although this topic has been discussed in [12] for FOPT materials, the comparison between the FOPT and SOPT or mixed materials has not yet been presented. We start from studying the deviation of T_{Curie} in a single layer, that is, the Curie temperature of a single layer will be shifted with a deviation of $\Delta T_{\mathrm{Curie},n}$ and the Curie temperature is not evenly distributed anymore. That is, $T_{\mathrm{Curie},n} = T_h - (T_h - T_c)(2n-1)/2n + \Delta T_{\mathrm{Curie},n}$.

The deviation $\Delta T_{\mathrm{Curie},n}$ ranges from -2 to 2 K with an interval of 0.5 K, and a positive value means shifting to a higher temperature and vice versa. The number of layers is 8 and the temperature span is 15 K. Comparison between figures 9(a) and (b) shows that Gd-like materials can resist deviations in the Curie temperature much better than FOPT materials like La(Fe,Mn,Si)$_{13}$H$_y$, and the performance change is less than 8%. For the AMRs using La(Fe,Mn,Si)$_{13}$H$_y$, both positive and negative deviation will result in lower cooling performance. And this influence becomes more sensitive when shifting the layers close to either end of the AMR, which should be more

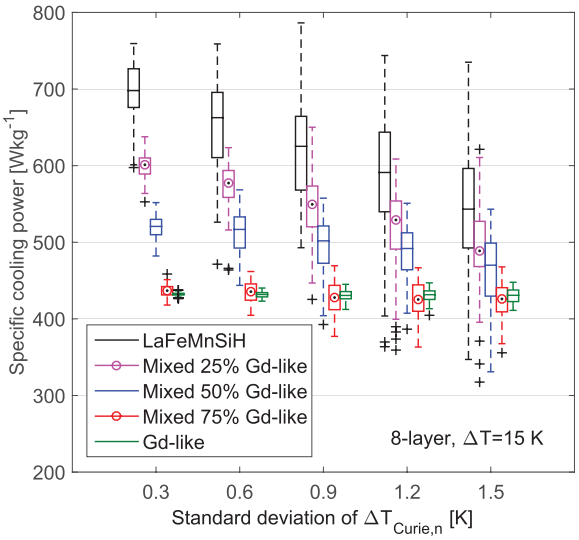

Figure 10. Impact of standard deviation σ of $\Delta T_{\mathrm{Curie},n}$ on specific cooling power $\dot{q}_c$ of multi-layer AMRs using La(Fe,Mn,Si)$_{13}$H$_y$, Gd-like or mixed materials when $\Delta T_{\mathrm{Curie},n}$ follows a normal distribution.

carefully handled than the layers in the middle. In both cases, the maximum cooling powers can be obtained with an approximately even Curie temperature distribution, which are around 790 W kg^{-1} and 470 W kg^{-1} for each group.

A further study is carried out based on the assumption that the Curie temperature deviation follows a normal distribution, and $\Delta T_{\mathrm{Curie},n}$ of each layer has a random deviation following the normal distribution. In this way, the standard deviation σ of Curie temperature variations could be utilized to describe how much $T_{\mathrm{Curie},n}$ deviates from the designed value and also the overall degree of deviating from an even distribution. The median of the normal distribution is 0 K. This treatment allows that there is a small random deviation in each layer,

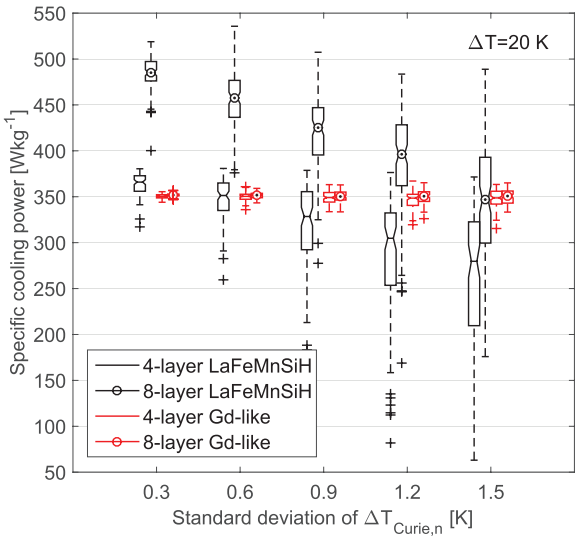

Figure 11. Impacts of number of layers N_L and standard deviation σ of $\Delta T_{Curie,n}$ on specific cooling power $\dot{q}_c$ of multi-layer AMRs using $La(Fe,Mn,Si)_{13}H_y$ or Gd-like materials.

and makes the simulation more representative as real conditions for a commercial AMR. For each standard deviation, we randomly build 500 AMRs with different Curie temperature distributions and the results are presented in figure 10 using a box plot to show the probability of generated specific cooling powers. The concept of mixing materials is also studied. In figure 10, the central mark of the box plot is the median value of a group of specific cooling powers for each standard deviation, and the box edges are the 25th and 75th percentiles. The whiskers show the most extreme data points without outliers and the crosses show the outliers. It can be seen that increasing the standard deviation reduces the median value of the specific cooling power significantly and also increases the risk of performance fluctuations for AMRs using $La(Fe,Mn,Si)_{13}H_y$. As the volume faction of Gd increases in AMRs using mixed materials, the median value of $\dot{q}_c$ decreases, however the fluctuation in $\dot{q}_c$ becomes smaller. The results show that mixing FOPT and SOPT materials helps to improve the system stability regarding deviations in the Curie temperature.

Figure 11 shows the combined impact of number of layers and the standard deviation. Both FOPT and SOPT materials are simulated for 4 and 8 layers. As the number of layers increases, the performance fluctuation decreases and the median value increases significantly for AMRs using $La(Fe,Mn,Si)_{13}H_y$. Therefore it is suggested to increase the number of layers as much as possible for improving the system stability. For Gd-like materials, the performance fluctuation is much smaller for both $N_L = 4$ and 8, but the cooling capacity does not improve much.

5. Conclusion

AMRs using FOPT and SOPT materials are investigated based on a 1D numerical model. The results show that not only the isothermal entropy change ΔS_{iso}, but also the adiabatic temperature change ΔT_{ad} and the shape factor γ of MCE, have significant influence on the AMR performance. Although FOPT materials exhibit higher ΔS_{iso}, they sometimes could only produce equivalent performance to SOPT materials due to a close or lower ΔT_{ad} and smaller shape factor γ. For materials with small γ, more layers are needed to achieve a high cooling power compared to those with larger γ.

The simulated results of multi-layer AMRs using typical $La(Fe,Mn,Si)_{13}H_y$ or Gd-like materials are presented and a concept of mixing FOPT and SOPT materials is investigated. Although $La(Fe,Mn,Si)_{13}H_y$ could realize higher specific cooling powers than Gd-like materials, many more layers are needed to achieve the desired performance. At the same time, AMRs using typical FOPT materials are more sensitive to the working temperature and the Curie temperature variation. Mixing FOPT and SOPT could significantly reduce the required number of layers, better resist fluctuating working temperatures, and be more robust to variations in the Curie temperature compared to FOPT materials, while realizing higher specific cooling powers than SOPT materials.

Acknowledgments

This work was financed by the ENOVHEAT project which is funded by Innovation Fund Denmark (contract no 12-132673). The authors would like to thank Vacuumschmelze GmbH, Germany for providing the $La(Fe,Mn,Si)_{13}H_y$ material. T Lei wishes to thank the Otto Mønsteds Fund for financial support.

References

[1] Brown G V 1976 Magnetic heat pumping near room temperature *J. Appl. Phys.* **47** 3673–80
[2] Smith A, Bahl C R H, Bjørk R, Engelbrecht K, Nielsen K K and Pryds N 2012 Materials challenges for high performance magnetocaloric refrigeration devices *Adv. Energy Mater.* **2** 1288–318
[3] Benford M and Brown G V 1981 T-s diagram for gadolinium near the Curie temperature *J. Appl. Phys.* **52** 2110–2
[4] Basso V, Küpferling M, Curcio C, Bennati C, Barzca A, Katter M, Bratko M, Lovell E, Turcaud J and Cohen L F 2015 Specific heat and entropy change at the first order phase transition of La(Fe–Mn–Si)$_{13}$-H compounds *J. Appl. Phys.* **118** 053907
[5] Gschneidner K A Jr and Pecharsky V K 2000 Magnetocaloric materials *Annu. Rev. Mater. Sci.* **30** 387–429
[6] Fujita A, Fujieda S, Hasegawa Y and Fukamichi K 2003 Itinerant-electron metamagnetic transition and large magnetocaloric effects in $La(Fe_xSi_{1-x})_{13}$ compounds and their hydrides *Phys. Rev.* B **67** 104416
[7] Brück E, Ilyn M, Tishin A M and Tegus O 2005 Magnetocaloric effects in $MnFeP_{1-x}As_x$-based compounds *J. Magn. Magn. Mater.* **290** 8–13
[8] Jacobs S, Auringer J, Boeder A, Chell J, Komorowski L, Leonard J, Russek S and Zimm C 2014 The performance of a large-scale rotary magnetic refrigerator *Int. J. Refrig.* **37** 84–91
[9] Engelbrecht K and Bahl C R H 2010 Evaluating the effect of magnetocaloric properties on magnetic refrigeration performance *J. Appl. Phys.* **108** 123918

[10] Brey W, Nellis G and Klein S 2014 Thermodynamic modeling of magnetic hysteresis in AMRR cycles *Int. J. Refrig.* **47** 85–97

[11] Aprea C, Greco A and Maiorino A 2013 The use of the first and of the second order phase magnetic transition alloys for an AMR refrigerator at room temperature: a numerical analysis of the energy performances *Energy Convers. Manage* **70** 40–55

[12] Lei T, Nielsen K K, Engelbrecht K, Bahl C R H, Neves Bez H and Veje C T 2015 Sensitivity study of multi-layer active magnetic regenerators using first order magnetocaloric material $La(Fe,Mn,Si)_{13}H_y$ *J. Appl. Phys.* **118** 014903

[13] Engelbrecht K 2008 *A Numerical Model of an Active Magnetic Regenerator Refrigerator with Experimental Validation* (Madison, WI: University of Wisconsin Press) pp 43–7

[14] Yan Z and Chen J 1992 The effect of field-dependent heat capacity on the characteristics of the ferromagnetic Ericsson refrigeration cycle *J. Appl. Phys.* **72** 1–5

[15] Rowe A M and Barclay J A 2003 Ideal magnetocaloric effect for active magnetic regenerators *J. Appl. Phys.* **93** 1672–6

[16] Kirol L D and Mills J I 1984 Numerical analysis of thermomagnetic generators *J. Appl. Phys.* **56** 824–8

[17] Nielsen K K, Engelbrecht K and Bahl C R H 2013 The influence of flow maldistribution on the performance of inhomogeneous parallel plate heat exchangers *Int. J. Heat Mass Transfer* **60** 432–9

[18] Pecharsky V K and Gschneidner K A Jr 2006 Advanced magnetocaloric materials: what does the future hold? *Int. J. Refrig.* **29** 1239–49

[19] Bjørk R, Bahl C R H and Katter M 2010 Magnetocaloric properties of $LaFe_{13-x-y}Co_xSi_y$ and commercial grade Gd *J. Magn. Magn. Mater.* **322** 3882–8

A.4 Analysis and comparison of novel phase shifters for Stirling pulse tube cryocooler

T. Lei, J. M. Pfotenhauer, W. Zhou, Analysis and comparison of novel phase shifters for Stirling pulse tube cryocooler, *Cryogenics*, under review, (2016).

Analysis and Comparison of Different Phase Shifters for Stirling Pulse Tube Cryocooler

Tian Lei[a,*], John M. Pfotenhauer[b], Wenjie Zhou[b]

[a] *Department of Energy Conversion and Storage, Technical University of Denmark, Denmark*
[b] *Solar Energy Lab., College of Engineering, University of Wisconsin-Madison, USA*

Abstract

Researches on phase shifters and power recovery mechanism are of sustainable interest for developing Stirling pulse tube cryocoolers (SPTC) with higher power density, more compact design and higher efficiency. Gas-liquid and spring-oscillator phase shifters are investigated for the purpose of minimizing the size of the phase shifter without sacrificing the cooling performance and the system simplicity. Based on simulation with a distributed model, the phase shifting capacity and the acoustic power dissipation of these two compact phase shifters are analyzed and compared with the traditional inertance tube phase shifter. The results show that both phase shifters have the distinctive capacity of phase shifting with a much more compact design. To investigate the performance of these three different phase shifters and a power recovery displacer, a distributed model of the SPTC is developed. The cooling performance of a SPTC using different phase shifters are simulated and typical phase relations are presented and analyzed. Comparison reveals that the power recovery displacer with a more complicated configuration provides the highest efficiency. The gas-liquid and spring-oscillator phase shifters show advantages of compactness and simplicity, presenting equivalent efficiency compared with the inertance tube phase shifter. Approximately 10%-20% of the acoustic power is dissipated by the phase shifters without power recovery, while 15-20% of the acoustic power can be recovered by the power recovery displacer, leading to a maximum coefficient of performance (COP) around 0.14.

Keywords: Stirling pulse tube cryocooler, phase shifter, gas-liquid phase shifter, spring-oscillator phase shifter, power recovery

1. Introduction

In recent decades, the SPTC has attracted substantial attention due to the advantages of avoiding moving parts at cryogenic temperature, low vibration and reliable operation. 80 K SPTCs with higher efficiency and more compact designs are expected to fulfil the increas-

*Corresponding author, E-mail:tile@dtu.dk

ing demand of cooling electronic devices such as infrared detectors and high temperature superconductors [1, 2, 3]. Derived from the orifice configuration [4], several phase shifting approaches including double-inlet configuration and inertance tube-reservoir phase shifter (hereinafter to be referred as inertance tube phase shifter), have been developed to provide favorable phase relations between the pressure and mass flow oscillations inside a SPTC [3]. In order to supply sufficient acoustic inertance, a thin and several meters long inertance tube has to be used [5], which raises the risk of high viscous resistance from oversizing the inertance tube. The inertance tube inevitably dissipates an amount of acoustic power, which makes the tradeoff between suitable phase shifting and the dissipation loss particularly important in a real design. Many studies of the inertance tube phase shifter have been carried out to improve the cooling performance [3, 6] or to enhance the operation [7].

In theory, a liquid column could provide considerable acoustic inertance due to a larger density compared with the pressurized gas. For example, in the Stirling engines with liquid pistons [8] and some thermoacoustic engines [9, 10], the liquid column has been introduced into the gas oscillation systems for tuning the acoustic impedance. The spring-oscillator configuration is commonly seen in the linear motors or Stirling engines, which has also been used as a power recovery displacer for SPTCs in a few published cases [11, 12]. Due to a much higher density, the solid oscillator can provide equivalent inertance with an even smaller size than liquid or pressurized gas. Therefore, it is anticipated that a liquid column loaded in a U-shaped tube or a spring-oscillator installed between the hot end of the pulse tube and the gas reservoir can be utilized as a phase shifter in the SPTC system. Although standard liquids like water are impossible for use in the cryogenic systems, ionic liquids [13] with vapor pressures near zero show the possibility of being applied at the ambient region of a SPTC. It is expected that both phase shifters, especially the spring-oscillator phase shifter, could supply sufficient phase shifting capacity with decreased size and the possibility of reduced dissipative losses.

In contrast to the three phase shifters mentioned above, the power recovery displacer provides both functions of phase shifting and power recovery. It is normally located between the hot end of the pulse tube and the back pressure cavity of the compressor or the compression chamber [11, 12]. Similar examples include a transmission tube between the hot ends of the regenerator and the pulse tube presented by Swift et al. [14], the power recovery displacers in a Stirling-engine-type pressure wave generator by Sugita et al. [15], and a gas-driven displacer between the regenerator inlet and the pulse tube outlet by Zhu and Nogawa [11]. Wang et al. presented a coaxial pulse tube cryocooler with power recovery displacers and it realized a cooling power of 26.4 W at 80 K with a relative Carnot efficiency of 24.2%. It is noted that this configuration increases the system complexity and requires a

relatively complicated modification to the SPTC and the compressor.

To investigate the pros and cons of different phase shifters and concepts, we present a theoretical study by simulation. Based on Swift's thermoacoustic theory and the electro-acoustic analogy [14], distributed models of different phase shifters and a SPTC are developed. The impact of inertia component dimensions on the phase shifting capacity as well as the acoustic power dissipation are presented and discussed for the inertance tube, gas-liquid and spring-oscillator phase shifters, respectively. In addition, the SPTCs using three phase shifters without power recovery and a power recovery displacer are optimized for maximizing the refrigeration efficiency. The performance and typical phase diagrams for various designs are compared and analyzed.

2. Distributed Models

There are several approaches, such as the enthalpy flow model [3] and the thermoacoustic theory [16], available for investigating SPTCs using different phase shifters. Among those, the thermoacoustic theory is capable of simulating small wave oscillations in the acoustic network in an intuitive and effective way, which is used in this paper. In this section, the distributed models of different phase shifters and corresponding SPTCs are presented.

2.1. Thermoacoustics and Electro-acoustic Analogy

According to Swift's thermoacoustic theory and the electro-acoustic analogy, the small wave oscillation in a short channel with a temperature gradient can be described by the following complex equations [16], which have been extensively used and proven to be effective tool [14, 10, 17].

$$d\hat{p} = -(i\omega l dx + r_\nu dx)\hat{U} \tag{1}$$

$$d\hat{U} = -(i\omega c dx + \frac{dx}{r_\kappa})\hat{p} + g dx \hat{U} \tag{2}$$

$$l = \frac{\rho_m}{A}\frac{1-\mathrm{Re}[f_\nu]}{|1-f_\nu|^2} \tag{3}$$

$$r_\nu = \frac{\omega\rho_m}{A}\frac{\mathrm{Im}[-f_\nu]}{|1-f_\nu|^2} \tag{4}$$

$$c = \frac{A}{\gamma\rho_m}(1+(\gamma-1)\mathrm{Re}[f_\kappa]) \tag{5}$$

$$r_\kappa = \frac{\gamma p_m}{(\gamma-1)A\omega\mathrm{Im}[-f_\kappa]} \tag{6}$$

$$g = \frac{f_\kappa - f_\nu}{(1-f_\nu)(1-\sigma)}\frac{1}{T_m}\frac{dT_m}{dx} \tag{7}$$

where $\hat{p}$ and $\hat{U}$ represent the pressure oscillation and volumetric flow oscillation, respectively. They are expressed in the complex form, while the actual pressure and volumetric flow rate

are $p = p_m + \mathrm{Re}[|\hat{p}|\, e^{i\omega t}]$ and $U = \mathrm{Re}[|\hat{U}|e^{i\omega t}]$, where p_m is the mean pressure and the other two terms represent the oscillation quantities. l, r_ν, c, r_κ and g are the inertance, viscous resistance, compliance, thermal relaxation resistance and complex gain factor per unit length. ω, ρ_m, A, γ, σ, T_m and dT_m/dx are the angular frequency, mean density, cross sectional area, specific heat ratio, Prandtl number, mean temperature and temperature gradient. i, Re and Im mean the imaginary unit, the real or the imaginary part of a complex quantity. f_ν and f_κ are viscous and thermal functions for different channel geometries, which were presented in Reference [16]. Based on the electro-acoustic analogy, a short channel can be analogized as a circuit consisting of five impedances as mentioned above, which are strongly related to the channel geometry and operating parameters as seen in the equations. With known $\hat{p}_1$ and $\hat{U}_1$ at the inlet as well as dT_m/dx along a short channel, $\hat{p}_2$ and $\hat{U}_2$ at the outlet can be calculated by solving the combined equations. This approach provides a fast and intuitive way to learn the details of the wave oscillation inside various regenerative engines and refrigerators without fully solving the time domain under reasonable assumptions, especially for the phase analysis and primary design.

In a qualitative analysis, the inertance tube phase shifter can be analogized as a resistance-inertance-compliance circuit for simplification. Its total impedance is $Z = \hat{p}_1/\hat{U}_1 = R_\nu + i[\omega L - (1/\omega(C + C_r))]$, where L, R_ν, C and C_r are the inertance, viscous resistance and compliance of the inertance tube, as well as the compliance of the gas reservoir. In an efficient regenerator of the SPTC, the phase of the pressure oscillation is expected to locate between the phases of the volumetric flow oscillations at both ends [14]. Since the phase change of pressure oscillations through the regenerator and pulse tube is relatively small, the phase of the volumetric flow oscillation usually leads the pressure oscillation in phase at the hot end of the regenerator and lags at the hot end of the pulse tube, which is also the inlet of the phase shifter. This phase relation requires the impedance of a phase shifter to satisfy $phase[Z] = phase[\hat{p}_1/\hat{U}_1] > 0°$ and then the imaginary part $\omega L - 1/\omega(C + C_r) > 0$, as R_ν is always positive [5]. In the following analysis, positive phase difference $phase[\hat{p}/\hat{U}]$ means the pressure oscillation leads the volumetric flow oscillation, and vice versa. The total acoustic inertance of the inertance tube is $L = \int l dx$ and it can be increased by either reducing the tube diameter or extending the tube length based on Eqns. 1 and 3. Therefore suitable phase relation at the inlet of the inertance tube phase shifter could be obtained by adjusting the inertance tube. However, a certain amount of acoustic power $\dot{W}_a = \frac{1}{2}\mathrm{Re}[\hat{p}_1\widetilde{\hat{U}_1}]$ will be dissipated along the inertance tube due to the viscous resistance, which should be taken into consideration in the actual design in terms of the total efficiency. The overhead wave symbol in $\widetilde{\hat{U}_1}$ means to take the complex conjugate of $\hat{U}_1$.

A distributed model as shown in Figure 1 (a) is developed to predict the pressure and

volumetric flow oscillations along the inertance tube as well as the total impedance. In this model, the acoustic component is divided into numerous connected nodes and each node is analogized as a combination of five micro impedances. The wave oscillation along the circuit can be calculated by solving the governing equations with the pre-set boundary conditions. Since the combined equations are implicit with an unknown volumetric flow oscillation at the inlet of the phase shifter, an iterative solver based on the numerical computing environment MATLAB is used and the convergence is reached when the impedance of the gas reservoir is satisfied, that is, $\hat{p}_2/\hat{U}_2 = 1/i\omega C_r$ as shown in Figure 1 (a).

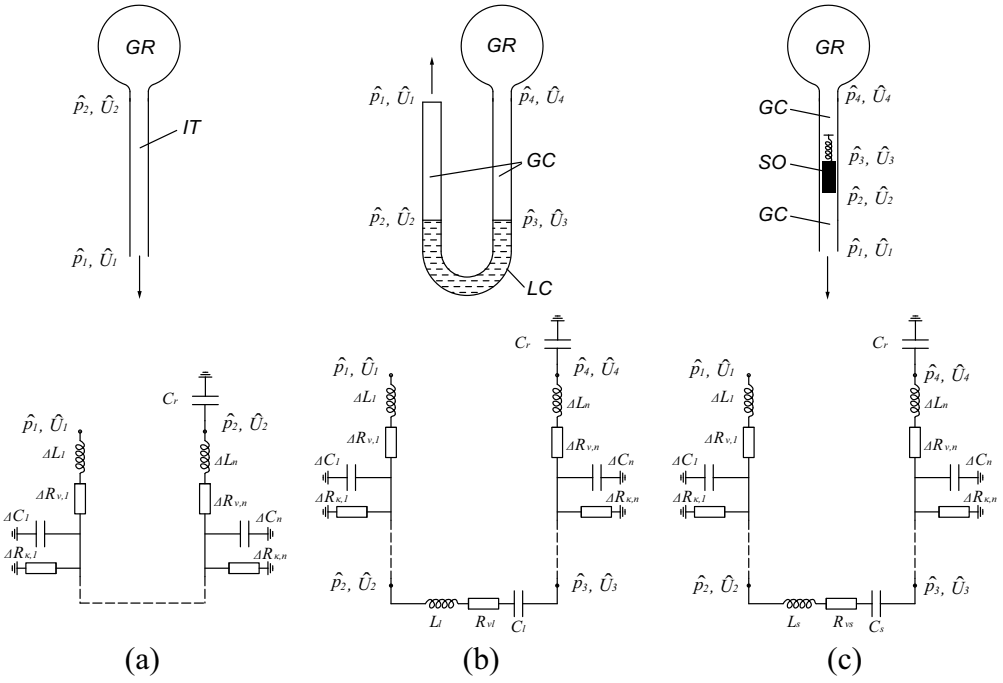

Figure 1: Schematic diagrams and electro-acoustic analogy of three phase shifters: (a) inertance tube phase shifter; (b) gas-liquid phase shifter; (c) spring-oscillator phase shifter. The symbols represent different components: GC gas column; GR gas reservoir; IT inertance tube; LC liquid column; SO spring-oscillator, where the dashed lines mean repetitive nodes and the arrow shows the position connected to the hot heat exchanger of the pulse tube in a SPTC.

2.2. Models of Different Phase Shifters and SPTCs

The schematic diagrams and the equivalent impedance circuit of the gas-liquid and spring-oscillator phase shifters are shown in Figure 1 (b) and (c). The gas-liquid phase shifter consists of a U shaped tube filled with ionic liquid and a gas reservoir. Some spaces at both ends of the liquid column are left for oscillation. The force balance equation of the

liquid column is described by [10]:

$$Adp = -\Big(\rho_l dx \frac{dU}{dt} + 2\rho_l g_a \int U dt + \frac{\xi}{A} U\Big) \tag{8}$$

where dp, U, A, ρ_l, g_a and ξ are the pressure difference between both ends of the liquid column, volumetric flow rate, cross sectional area, liquid density, gravity acceleration and friction factor of the liquid column with a unit of N·s/m. Considering the oscillating wave, this equation can be rewritten as:

$$d\hat{p} = -\Big(i\omega L_l + \frac{1}{i\omega C_l} + R_{\nu,l}\Big)\hat{U} \tag{9}$$

$$L_l = \frac{\rho_l x_l}{A} \tag{10}$$

$$C_l = \frac{A}{2\rho_l g_a} \tag{11}$$

$$R_{\nu,l} = \frac{\xi}{A^2} = \frac{\omega \rho_l x_l}{A} \frac{\mathrm{Im}[-f_{\nu,l}]}{|1 - f_{\nu,l}|^2} \tag{12}$$

where L_l, C_l, and $R_{\nu,l}$ are the inertance, compliance and resistance of the liquid column. The second term in the multiplier of Eqn. 9 has a similar format as the acoustic compliance. Therefore, this term is named as compliance of the liquid column, although it derives from the pressure difference due to the relative displacement of both liquid levels. Due to this definition, the compliance of the liquid column is connected in series as shown in Figure 1 (b). The volumetric flow oscillations are the same at both ends of the liquid column because it is incompressible. Note that the acoustic inertance is proportional to the density of the liquid, thus only a short liquid column is needed in order to provide the same inertance as the pressurized gas. For example, the ionic liquid [emim][BF_4] named 1-ethyl-3-methylimidazolium tetrafluoroborate [18], has a density of 1289 kg/m^3, which is hundreds of times larger than 3.18 kg/m^3 for the pressurized helium gas at 2.0 MPa and 300 K. The gas reservoir is analogized as an acoustic compliance and the gas columns are divided into numerous nodes.

Moreover, the model of the spring-oscillator phase shifter, which shares the same principle as the gas-liquid phase shifter, is presented. The force balance equation of the spring-oscillator, which is driven by the pressure difference between both ends, is formulated as:

$$Adp = -\Big(\frac{M_s}{A}\frac{dU}{dt} + \frac{K_s}{A}\int U dt + \frac{F_s}{A} U\Big) \tag{13}$$

where M_s, F_s and K_s are the oscillator mass, friction coefficient with a unit of N·s/m and elastic coefficient of the spring with a unit of N/m. Rewriting the force balance equation

under the wave oscillation gives:

$$d\hat{p} = -\Big(i\omega L_s + \frac{1}{i\omega C_s} + R_{\nu,s}\Big)\hat{U} \tag{14}$$

$$L_s = \frac{\rho_s x_s}{A} \tag{15}$$

$$C_s = \frac{A^2}{K_s} \tag{16}$$

$$R_{\nu,s} = \frac{F_s}{A^2} \tag{17}$$

where L_s, C_s, $R_{\nu,s}$, ρ_s and x_s are the acoustic inertance, acoustic compliance, acoustic resistance, solid density and length of the oscillator. The analogized circuit and the solution solving procedure of the spring-oscillator phase shifter are similar to the gas-liquid phase shifter. However, the compliance of the spring-oscillator phase shifter is contributed by the flexible spring.

As discussed above, $\hat{p}$ and $\hat{U}$ along the phase shifters, as well as the total impedance, can be solved by numeric iterations, given the amplitude and phase of the pressure oscillation at the inlet of the phase shifters. During iterations, the volumetric flow oscillation at the inlet of phase shifters will be adjusted until $\hat{p}_4/\hat{U}_4 = 1/i\omega C_r$ at the inlet of the gas reservoir as shown in Figure 1 (b) and (c).

The schematic diagrams and the analogized circuits of SPTCs using various phase shifters are presented in Figure 2 (a)-(c). The single stage cryocooler consists of three heat exchangers, one regenerator and one pulse tube, which are separated into numerous respective nodes in the model. However, only one node circuit is shown in the dashed-line frame for simplification. The inertance tube phase shifter is connected to the second hot heat exchanger and then the hot end of the pulse tube as shown in Figure 2 (a). In Figure 2 (b) and (c), only the gas-liquid and spring-oscillator phase shifters are illustrated and the SPTCs as well as the corresponding analogized circuit are omitted to avoid repetition. Since the influence of the heat exchangers on the wave oscillation is relatively small, $\hat{p}_{ph}$ and $\hat{U}_{ph}$ are named pressure and volumetric flow oscillations at the hot end of the pulse tube, although the real position is after the second hot heat exchanger at the hot end of the pulse tube. Similarly, the subscribe rh represents the hot end of the regenerator, while the marked position is before the first hot heat exchanger at the regenerator's hot end. For the models from Figure 2 (a) to (c), the calculation starts from the pressure oscillation at the hot end of the regenerator, and the volumetric flow oscillation at the inlet is solved by iterations until the end impedance is satisfied. The preset pressure oscillation and the total impedance of the SPTC determine the volumetric flow oscillation and the acoustic power input, which vary in different cases. Therefore, the focus is mainly on comparison of the efficiency rather

than the cooling capacity of the SPTC with different phase shifters. Additionally, optimized coupling between the SPTC system and the compressor is not emphasized in this study and the geometric and operation parameters of the SPTC are constant.

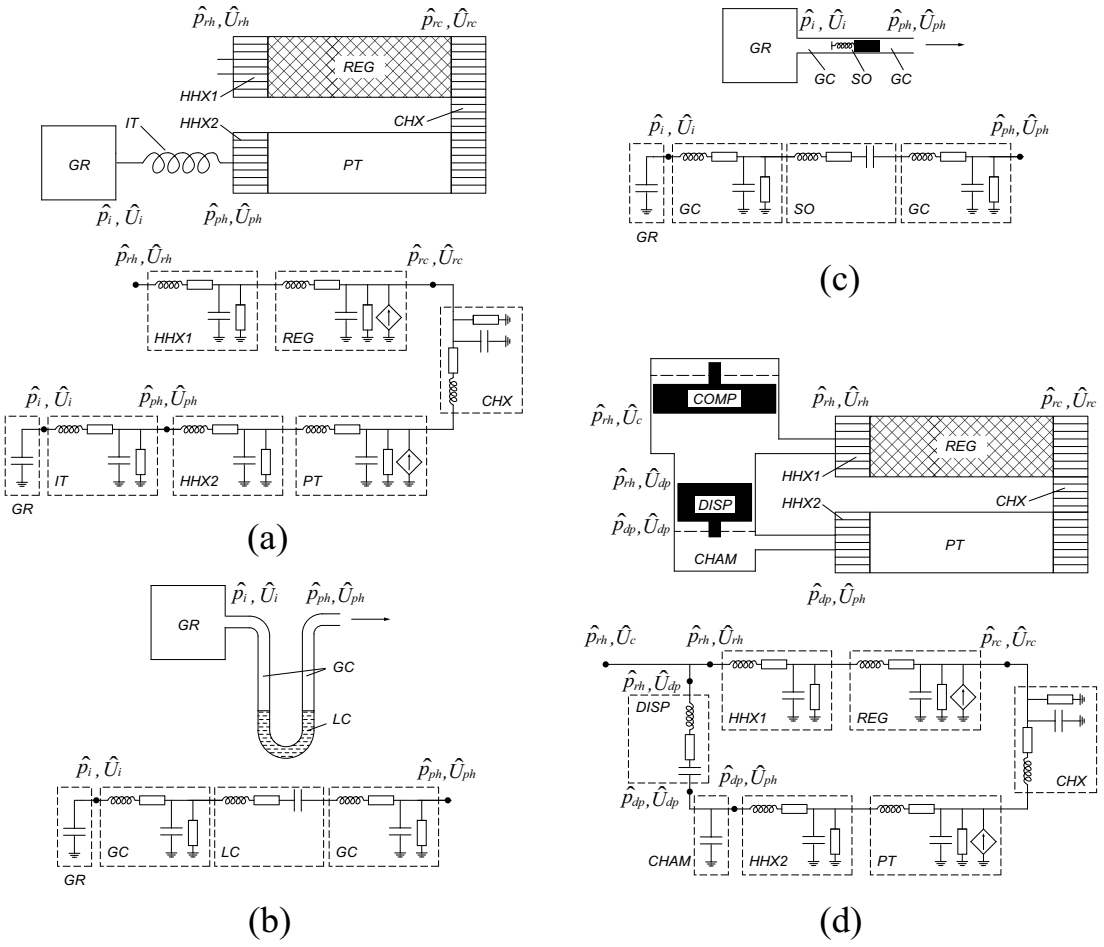

Figure 2: Schematic diagrams and electro-acoustic analogy of the SPTCs using different phase shifters: (a) SPTC using the inertance tube phase shifter; (b) SPTC using the gas-liquid phase shifter; (c) SPTC using the spring-oscillator phase shifter; (d) SPTC using the power recovery displacer. The symbols represent different components: CHAM chamber before displacer; CHX cold heat exchanger; COMP compression piston; DISP power recovery displacer; GC gas column; GR gas reservoir; HHX1 first hot heat exchanger; HHX2 second hot heat exchanger; IT inertance tube; LC liquid column; PT pulse tube; REG regenerator; SO spring-oscillator. The subscripts represent different positions in the SPTC: c compression piston; dp power recovery displacer; i inlet of the reservoir; ph hot end of the pulse tube; rc cold end of the regenerator; rh hot end of the regenerator. The arrow shows the position connected to the hot heat exchanger of the pulse tube in a SPTC.

As seen in Figure 2 (d), the power recovery displacer is set between the compression chamber and the hot end of the pulse tube, which has a one-piston configuration. In actual design, a dual-piston design is more favorable for reducing vibration. The force balance equation of the power recovery displacer has the same expression as Eqn. 14, where

$d\hat{p} = \hat{p}_{rh} - \hat{p}_{dp}$ and each acoustic impedance can be calculated based on Eqns. 15 - 17. $\hat{p}_{rh}$ and $\hat{p}_{dp}$ are the pressure oscillations at the regenerator's hot end and the displacer chamber, respectively.

For the displacer chamber between the power recovery displacer and the hot end of the pulse tube, we have:

$$\hat{U}_{dp} - \hat{U}_{ph} \quad = \quad -i\omega C_{dc}\hat{p}_{dp} \tag{18}$$

where $\hat{U}_{dp}$, $\hat{U}_{ph}$, $\hat{p}_{dp}$ and C_{dc} are the volumetric flow oscillation of the displacer, the volumetric flow oscillation at the hot end of the pulse tube, the pressure oscillation in the chamber, and the compliance of the displacer chamber. The analogized circuit of the SPTC with the power recovery displacer becomes a loop as shown in Figure 2 (d). The volumetric flow oscillation at the regenerator hot end consists of two parts:

$$\hat{U}_{rh} = \hat{U}_c + \hat{U}_{dp} \tag{19}$$

where $\hat{U}_c$ and $\hat{U}_{dp}$ are the volumetric flow oscillation of the compression piston and the power recovery displacer, respectively. For solving the analogized circuit in Figure 2 (d), the pressure oscillation at the hot end of the regenerator will be kept as the same as previous cases; however, the constrained condition is different, that is, the impedance of the power recovery displacer must be fulfilled, rather than the end impedance of the gas reservoir. The change in the total power $\dot{H}$ between the regenerator and the cold heat exchanger represents the cooling power $\dot{Q}_C$ [16]:

$$\dot{Q}_C \quad = \quad \dot{H}_{rc} - \dot{H}_{chx} \tag{20}$$

where $\dot{H}_{rc}$ and $\dot{H}_{chx}$ are the total power at the cold end of the regenerator and the inlet of the cold heat exchanger, respectively. The expression of $\dot{H}$ can be found in Reference [16]. The input acoustic power $\dot{W}_a$ for the SPTCs using the power recovery displacer is:

$$\dot{W}_a = \frac{1}{2}\mathrm{Re}[\hat{p}_{rh}\widetilde{\hat{U}_c}] \tag{21}$$

Because the compression chamber can be viewed as a typical acoustic compliance leading to zero acoustic power loss, $\dot{W}_a$ for the SPTCs using the other three phase displacers can be calculated by using the pressure and volumetric flow oscillations at the inlet of the

regenerator:

$$\dot{W}_a = \frac{1}{2}\mathrm{Re}[\hat{p}_{rh}\widetilde{\hat{U}_{rh}}] \tag{22}$$

The coefficient of performance (COP) is defined as:

$$\mathrm{COP} = \frac{\dot{Q}_C}{\dot{W}_a} \tag{23}$$

3. Results and Discussion

3.1. Inertance Tube Phase Shifter

The distributed model in Figure 1 (a) is initially used to investigate the impacts of the inertance tube geometries on the phase shifting capacity and the acoustic power dissipation. In the simulation, the gas reservoir has a volume of 3×10^{-4} m^3 and the phase shifter operates under the conditions listed in Table 1. The diameter of the inertance tube varies from 0.001 to 0.005 m and the length varies from 0.2 to 7 m. The amplitude and phase of the pressure oscillation at the phase shifter inlet are 0.3 MPa and 0°, respectively. Figure 3 illustrates the phase difference between the pressure and volumetric flow oscillations at the inlet of the inertance tube (solid line contour) and the acoustic power dissipation (dashed line contour) as functions of the diameter and length of the inertance tube. In this case, the inertance tube phase shifter could provide a positive phase difference at the inlet of the inertance tube up to 50°. Also, the acoustic power dissipation increases significantly as the tube diameter increases and the tube length decreases, due to the varying volumetric flow oscillation. However, too long or too short of an inertance tube will cause a negative phase difference, which is represented by the blank area. The inertance tube unavoidably dissipates dozens of watts when it produces a positive phase difference larger than 30°. It implies that the choice and optimization of the inertance tube should be considered carefully. Since the SPTC is not specified, a coupled optimization will be required during the design of the whole refrigeration system.

The details of the acoustic power and the phase difference along the inertance tube are shown in Figure 4 (a). In this specific case, the length and diameter of the inertance tube are 5.0 and 0.0035 m, respectively. It shows that a positive phase difference of 20.9° at the inlet of the inertance tube is obtained, and the acoustic power input is around 28 W. The acoustic power is dissipated along the inertance tube and it becomes zero where the inertance tube connects to the reservoir. The phase difference varies continuously and becomes -90° at the end of the inertance tube due to the compliance impedance of the gas reservoir.

Table 1: Parameters for modeling different phase shifters

	Parameter	Value
General parameters	Frequency	44 Hz
	Working gas	Helium gas at 300 K
	Mean pressure	3.3 MPa
	Amplitude and phase of the pressure oscillation at the phase shifter inlet	0.3 MPa, 0°
	Volume of gas reservoir	3×10^{-4} m^3
Inertance tube phase shifter	Length of inertance tube	0.2-7.0 m
	Diameter of inertance tube	0.001-0.005 m
Gas-liquid phase shifter	Length of left and right gas column	0.1 m
	Diameter of left and right gas column	0.01m
	Length of liquid column	0.05-0.80 m
	Diameter of liquid column	0.005-0.05 m
	Liquid	[emim][BF_4] ionic liquid
	Dynamic viscosity of liquid	0.033 Pa·s
	Liquid density	1289 kg/m^3
	Gravity	9.8 m/s^2
Spring-oscillator phase shifter	Length of left and right gas column	0.1 m
	Diameter of left and right gas column	0.01 m
	Length of oscillator	0.005-0.06 m
	Diameter of oscillator	0.005-0.06 m
	Density of solid	7900 kg/m^3
	Spring coefficient	100 N/m
	Friction factor	1 N·s/m

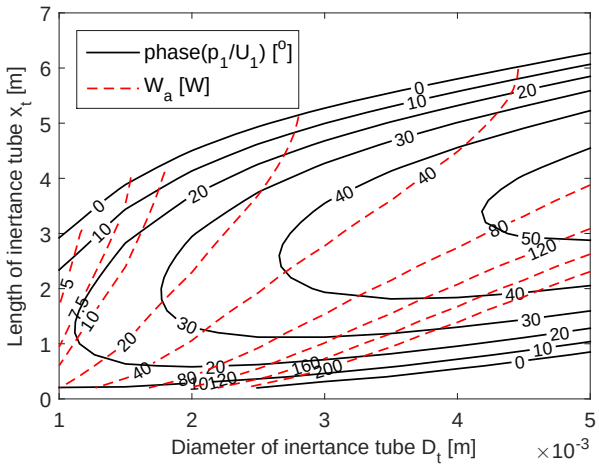

Figure 3: Phase difference between the pressure and volumetric flow oscillations at the inlet of the inertance tube phase shifter (solid line contour) and acoustic power dissipation (dashed line contour).

3.2. Gas-liquid Phase Shifter

Due to a high density, the liquid column is able to provide sufficient inertance with a much shorter length, which may be beneficial for a compact phase shifter design. The parameters for simulating the gas-liquid phase shifter are listed in Table 1. As shown in

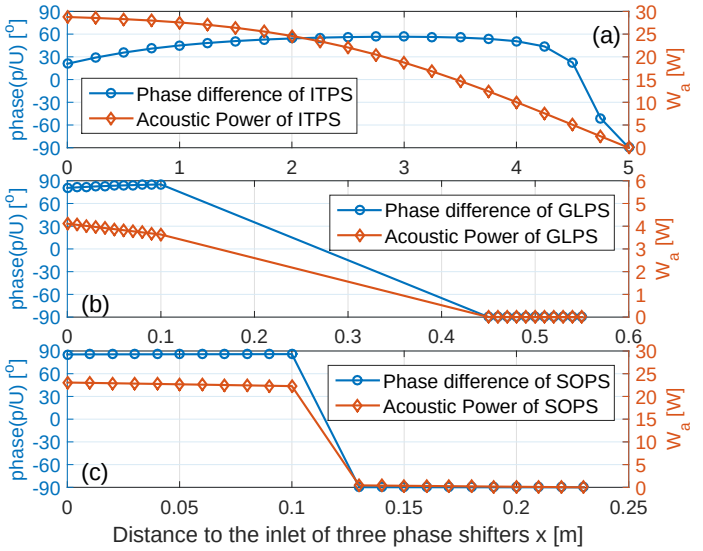

Figure 4: Acoustic power and phase difference between the pressure and volumetric flow oscillations along the inertance tube, gas-liquid and spring-oscillator phase shifters (ITPS, GLPS and SOPS). The length and diameter of the inertance tube are 5.0 and 0.0035 m; the length and diameter of the liquid column are 0.35 and 0.012 m; the length and diameter of the oscillator are 0.03 and 0.02 m.

Figure 1 (b), the gas-liquid phase shifter is comprised of a U-shaped tube loaded with the liquid column and a gas reservoir. The ionic liquid [emim][BF_4] is chosen as the working liquid. The inlet condition and the gas reservoir are the same as those in the inertance tube phase shifter. The phase difference and the acoustic power dissipation at the inlet of the gas-liquid phase shifter are presented in Figure 5. The results show that the gas-liquid phase shifter can produce a positive phase difference up to 80° at the phase shifter inlet. The acoustic power dissipation increases with larger liquid column diameter and shorter length. A notable reduction in the size of the phase shifter can be obtained in this configuration with a maximum length, including the two gas columns, less than 1.0 m, which is much shorter than the inertance tube presented in Figure 3.

A significant change in the pressure oscillation is expected due to the impedance of the liquid column. Therefore, we further present the phase difference and the acoustic power dissipation along the gas-liquid phase shifter as shown in Figure 4 (b) when the length and diameter of the liquid column are 0.35 and 0.012 m. It is noticeable that both the acoustic power and the phase difference exhibit a sudden change through the liquid column, which is different from the continuously changing pattern in the inertance tube phase shifter. The acoustic power reduces significantly across the liquid column, and most of the acoustic power is dissipated by the liquid column, which may be attributed to the relatively high viscosity of the ionic liquid. Simultaneously, a significant change of about 170° in the phase difference

is observed due to the impedance of the liquid column.

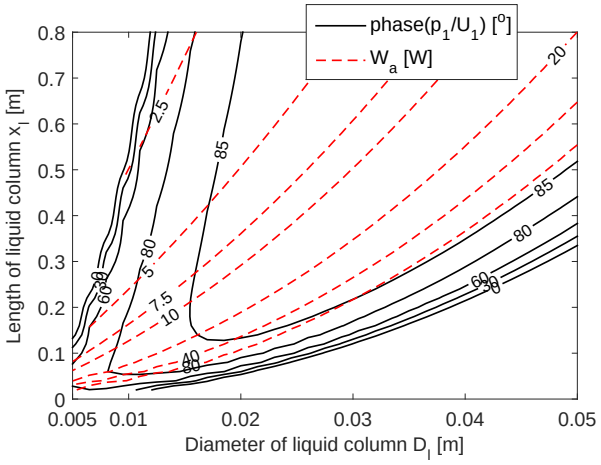

Figure 5: Phase difference between the pressure and volumetric flow oscillations at the inlet of the gas-liquid phase shifter (solid line contour) and acoustic power dissipation (dashed line contour).

3.3. Spring-oscillator Phase Shifter

Figure 6 shows the phase difference between the pressure and volumetric flow oscillations at the inlet of the spring-oscillator phase shifter and the corresponding acoustic power dissipation. In the simulation, the spring coefficient is 100 N/m and the friction factor is 1 N·s/m. Both the diameter and length of the oscillator range from 0.005 to 0.06 m. The region representing a positive phase difference has the shape of an inverted triangle similar to that of the gas-liquid configuration. A positive phase difference larger than 60° can be obtained by suitable geometries with the spring-oscillator phase shifter. The acoustic power dissipation increases with larger diameter and shorter length in the plotted area.

Further details of the pressure and volumetric flow oscillation along the spring-oscillator phase shifter are presented in Figure 4 (c). The spring-oscillator phase shifter also exhibits a significant capacity for phase shifting and the system design is much more compact with a total length of 0.23 m, in which the oscillator is only 0.03 m long. Note that the gas column length could be further decreased due to an expected small impact. Moreover, the spring-oscillator phase shifter maintains the same operation in low or zero gravity environments, which expands its applicability compared with the gas-liquid phase shifter.

3.4. Power Recovery Displacer

In comparison with the three phase shifters mentioned above, the feedback configuration of the power recovery displacer is more complicated. A distributed model of this SPTC system as shown in Figure 2 (d) is necessary for investigating the power recovery displacer.

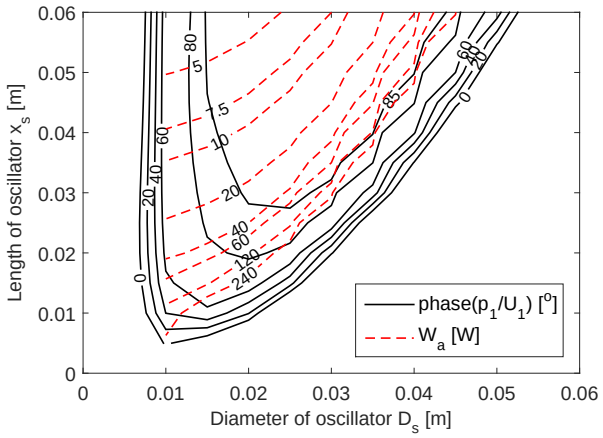

Figure 6: Phase difference between the pressure and volumetric flow oscillations at the inlet of the spring-oscillator phase shifter (solid line contour) and acoustic power dissipation (dashed line contour).

Here, a single stage SPTC is used and main parameters are listed in Table 2. The pressure amplitude at the hot end of the regenerator is fixed at 0.3 MPa and the phase of the pressure oscillation is set to 0°. In the simulation model, only the regenerator and pulse tube exhibit temperature gradients, therefore, the source term is considered for these two components. Additionally, the refrigeration temperature is 80 K, and the ambient temperature is kept 300 K. Along the regenerator or pulse tube, a linear temperature gradient is assumed. The spring coefficient is 8000 N/m and the friction factor is 1 N·s/m. The optimization of the displacer geometry for maximizing the COP is implemented and the results are shown in Figure 7a. The highest COP of approximately 0.14 is obtained when the diameter and length of the power recovery displacer are 0.0195 and 0.043 m, respectively. In this case, the relative Carnot efficiency is 38.5%. The optimum diameter and length of the oscillator display an inverse relationship and the design region for obtaining a sufficient COP larger than 0.10 is relatively narrow. Figure 7b illustrates the cooling power, COP and acoustic power in three locations when the displacer diameter is 0.0195 m. The maximum COP is found when the length of the displacer is around 0.042 - 0.043 m. In the simulation, the compression acoustic power is $1/2\mathrm{Re}[\hat{p}_{rh}\widetilde{\hat{U}_c}]$ and the recovered acoustic power is $1/2\mathrm{Re}[\hat{p}_{rh}\widetilde{\hat{U}_{dp}}]$. The comparison in Figure 7b shows that as much as 15-20% of the acoustic power is recovered.

3.5. Comparison of Stirling Pulse Tube Cryocoolers using Different Phase Shifters

The distributed models presented in Figure 2 (a)-(c) are used to simulate the SPTCs using three different phase shifters without power recovery. The results are used to compare the performance of those configurations with that of the SPTC using the power recovery displacer. More modeling parameters are listed in Table 2 and the same SPTC is used

Table 2: Parameters for modelling the SPTCs using different phase shifters

	Parameter	Value
Parameters of the SPTC	Frequency	44 Hz
	Gas	Helium
	Refrigeration temperature	80 K
	Mean pressure	3.3 MPa
	Amplitude and phase of the pressure oscillation at the hot end of the regenerator	0.3 MPa, 0°
	Regenerator diameter	0.03 m
	Regenerator length	0.16 m
	Hydraulic radius of regenerator	2.3×10^{-5} m
	Pulse tube diameter	0.02 m
	Pulse tube length	0.20 m
	Gas reservoir volume	3×10^{-4} m^3
Inertance tube phase shifter	Length of inertance tube	5.0-9.0 m
	Diameter of inertance tube	0.006-0.012 m
Gas-liquid phase shifter	Length of liquid column	0-0.05 m
	Diameter of liquid column	0.003-0.008 m
Spring-oscillator phase shifter	Length of oscillator	0.01 - 0.03 m
	Diameter of oscillator	0.008 - 0.018 m
Power recovery displacer	Volume of chamber before power recovery displacer	2×10^{-5} m^3
	Spring coefficient	8000 N/m
	Friction factor	1 N·s/m
	Length of displacer	0.03 - 0.06 m
	Diameter of displacer	0.017 - 0.022 m

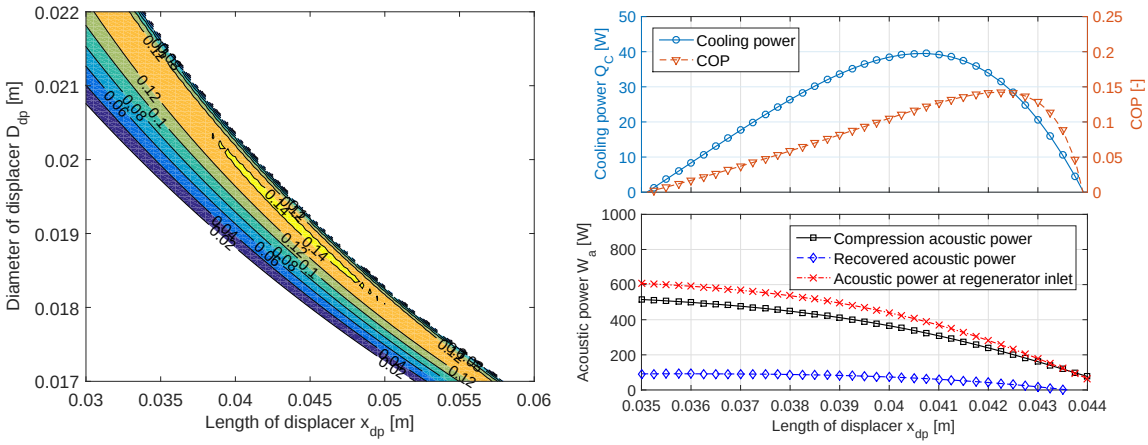

(a) COP of SPTC using the power recovery displacer

(b) Performance parameters with displacer diameter D_{dp} =0.0195 m

Figure 7: COP of SPTC using the power recovery displacer as a function of the displacer dimensions and performance parameters with displacer diameter D_{dp} =0.0195 m.

for comparison. Figure 8a, 8c and 8e show the COP of SPTCs using three different phase shifters, respectively. The impacts of both the length and diameter of the core inertial components in the phase shifters, which are gas column, liquid column and oscillator, are investigated. It is observed that the maximum COP is around 0.125 for the three phase shifters. In general, the optimum diameter increases with the optimum length of the inertial components in different phase shifters, but the overall dimensions differ from each other. The optimum inertance tube length and diameter are around 6.0 - 8.0 m and 0.008 - 0.010 m. For the liquid column, these optimum parameters are about 0.03 m and 0.06 m; while an oscillator with a length of 0.03 m and a diameter of 0.02 m gives the best performance. Significant reduction in the size of phase shifter can be observed in the gas-liquid or spring-oscillator phase shifters without efficiency reduction. The results in Figure 8b, 8d and 8f show the acoustic power input and dissipation with a fixed diameter of the inertial component. The losses due to the high viscosity of liquid and the friction factor of the oscillator are of the same order of magnitude as that in the long inertance tube. About 10%-20% of the acoustic power is dissipated by these phase shifters, which reduces the total efficiency of the refrigeration system compared with the one using the power recovery displacer. Replotting the COP as a function of the cooling power in Figure 9 reveals that the power recovery displacer can achieve the highest efficiency, while the peak efficiencies for the other three phase shifters are close.

Figure 10 shows the phase diagrams of the SPTCs using the four different phase shifters at their optimal points with highest efficiency in Figure 9. The horizontal and vertical axes represent the imaginary and real parts of the complex, respectively. The vectors marked by the star symbol show the phase relations of the normalized pressure and volumetric flow oscillations at different positions in the SPTCs. They are normalized by $|\hat{p}_{rh}|$ and $|\hat{U}_{rh}|$, respectively. Therefore, we have $|\hat{p}^*_{rh}| = 1$ and $|\hat{U}^*_{rh}| = 1$. The length of other vectors represented the relative amplitude of corresponding pressure or volumetric flow oscillation. In the SPTC using the inertance tube, the volumetric flow oscillation at the reservoir inlet $\hat{U}_i$ differs a lot from $\hat{U}_{ph}$, which is the volumetric flow oscillation at the hot end of the pulse tube. However, in the SPTCs using the gas-liquid or spring-oscillator phase shifter, the volumetric flow oscillations through the liquid column or the oscillator do not change and they are relatively small compared with the case of the inertance tube. For the SPTC using the power recovery displacer, the volumetric flow oscillation at the hot end of the regenerator $\hat{U}_{rh}$ is the sum of $\hat{U}_{dp}$ and $\hat{U}_c$, and the volumetric flow oscillation of the displacer, $\hat{U}_{dp}$ lags the pressure oscillation $\hat{p}_{dp}$ by around 70°.

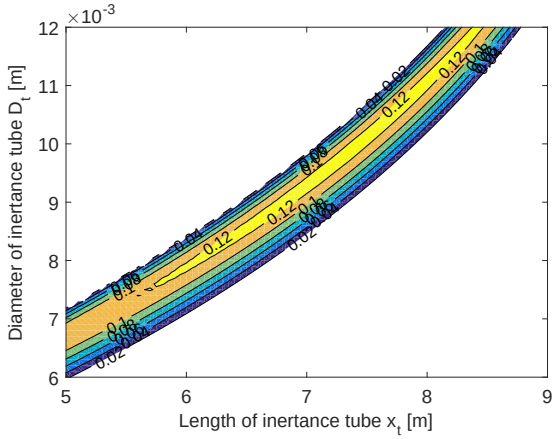

(a) COP of SPTC using the inertance tube phase shifter

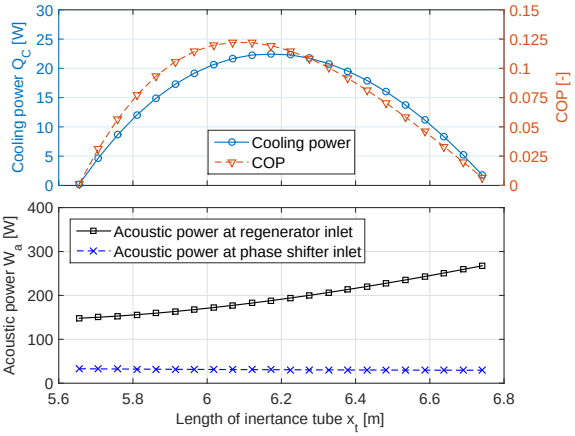

(b) Performance parameters with tube diameter D_t =0.008 m

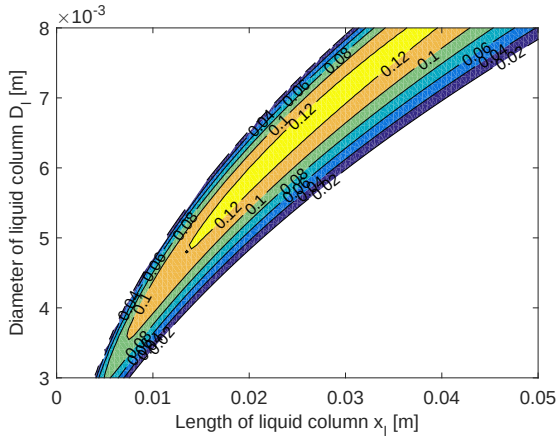

(c) COP of SPTC using the gas-liquid phase shifter

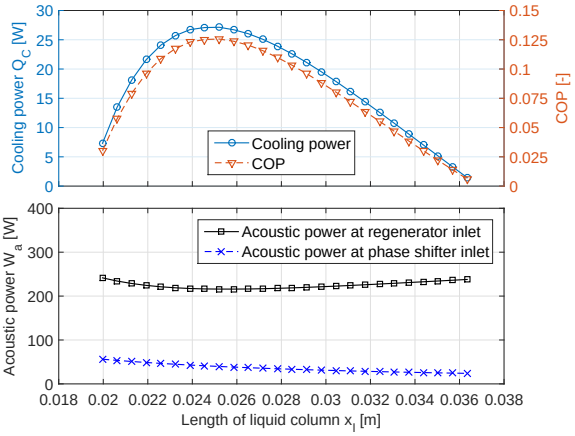

(d) Performance parameters with liquid column diameter D_l = 0.0065 m

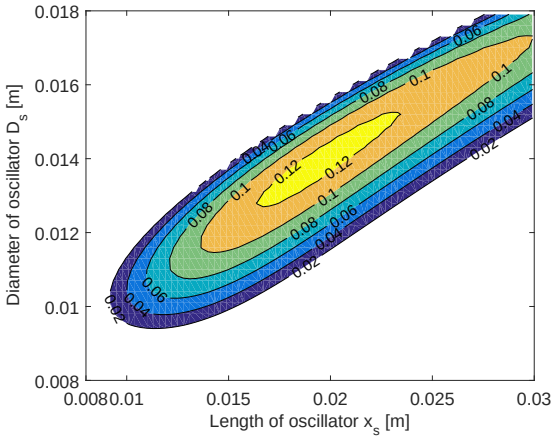

(e) COP of SPTC using the spring-oscillator phase shifter

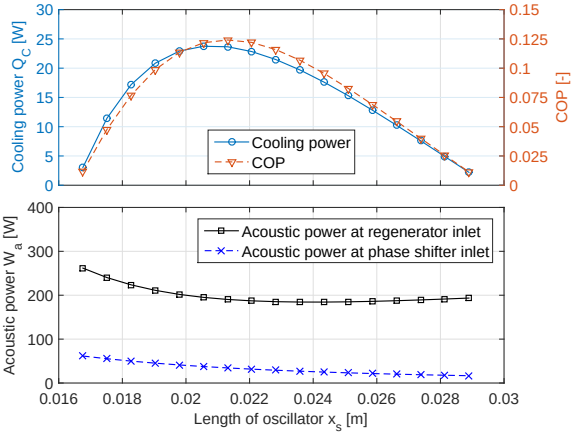

(f) Performance parameters with oscillator diameter D_s =0.0146 m

Figure 8: COP as a function of phase shifter dimensions and performance parameters with specific conditions for SPTCs using three phase shifters without power recovery.

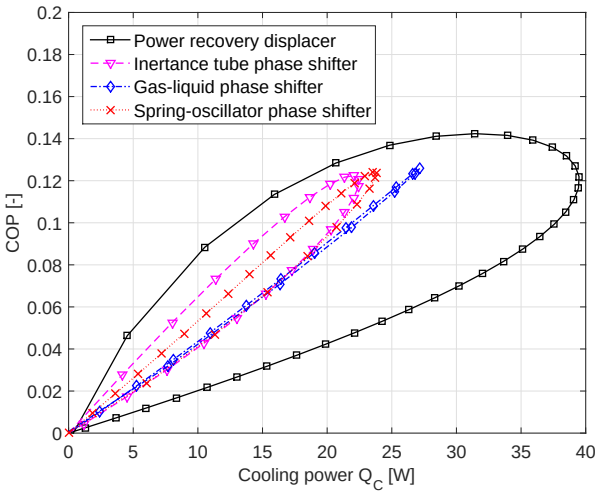

Figure 9: COP as a function of cooling power for SPTCs using different phase shifters.

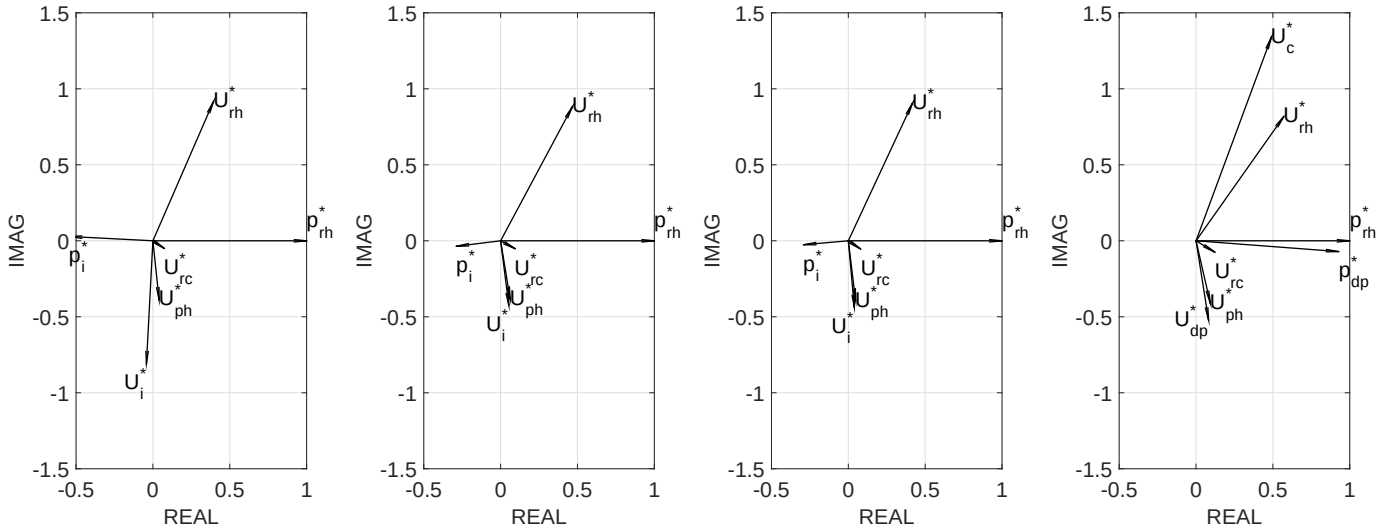

(a) Inertance tube phase shifter (b) Gas-liquid phase shifter (c) Spring-oscillator phase shifter (d) Power recovery displacer

Figure 10: Phase diagrams of SPTCs using different phase shifters. The subscripts represent various positions inside the SPTCs: c compression piston; dp power recovery displacer; i inlet of the reservoir; ph hot end of the pulse tube; rc cold end of the regenerator; rh hot end of the regenerator.

4. Conclusions

Aiming at minimizing the size of the phase shifter without sacrificing the refrigeration performance and the system simplicity, the gas-liquid and spring-oscillator phase shifters have been investigated, based on the thermoacoustic theory and the electro-acoustic analogy. Compared with the conventional inertance tube phase shifter, these two compact phase

shifters demonstrate an equivalent capacity for phase shifting with a much smaller size. Due to the incompressibility of the liquid and solid, the pressure oscillation changes dramatically through the liquid column or the oscillator, which leads to a significant change in the phase difference. Also, the acoustic resistance associated with the liquid column or the oscillator dissipates most of the acoustic power transported to the phase shifter.

In addition, a distributed model of the Stirling-type pulse tube cryocooler has been developed to evaluate the performance of the various phase shifters. The results show that the highest COP of around 0.14 is achieved by the power recovery displacer. In this case, about 15-20% of the acoustic power recovered when the diameter and length are 0.0195 and 0.043m, respectively. For the other three phase shifters without power recovery, the highest COP is around 0.12, and the acoustic resistance along these three phase shifters dissipates about 10%-20% of the acoustic power. A characteristic analysis is implemented and presented in Table 3. The spring-oscillator phase shifter and the power recovery displacer exhibit the highest compactness, while the efficiency of the latter is higher. However, the power recovery displacer increases the complexity of the refrigeration system and requires relatively more modifications to the SPTC systems. Replacing and tuning the other phase shifters is comparably easier. It is noted that only the gas-liquid phase shifter must be operated in a non-zero gravity environment and the risk of contaminating the refrigeration system due to escaping into the regenerator is relatively high. A potential solution for this issue is to use the elastic membranes or flexible balloons at both ends of the liquid column to avoid spilling out [17]. The spring-oscillator phase shifter also holds the potential of loss reduction, due to short channel and low volumetric flow in a real SPTC system. Comparison of the different phase shifters reveals that the power recovery displacer provides the highest efficiency, while the gas-liquid and the spring-oscillator phase shifters offer favorable alternatives when system compactness and simplicity are emphasized.

Table 3: Merit analysis of different phase shifters

Merit	Inertance tube phase shifter	Gas-liquid phase shifter	Spring-oscillator phase shifter	Power recovery displacer
Compactness	Poor	Fair	Good	Good
Efficiency	Fair	Fair	Fair	Good
Simplicity	Good	Good	Good	Poor
Gravity independence	Fair	Poor	Fair	Fair
Reliable operation	Good	Fair	Good	Good
Low cost and easy maintenance	Good	Good	Good	Poor

Acknowledgements

This work was financed by the ENOVHEAT project which is funded by Innovation Fund Denmark (contract no. 12-132673). The authors would like to thank Prof. G. F. Nellis from University of Wisconsin-Madison for the valuable comments. Tian Lei wishes to thank the Otto Mønsteds Fund for financial support.

Nomenclature

A Area [m^2]

c Compliance per unit length [m^2/Pa]

C Compliance [m^3/Pa]

f Frequency [Hz]

f_κ Thermal functions for different channel geometries [-]

f_ν Viscous functions for different channel geometries [-]

F_s Friction coefficient [N·s/m]

g Complex gain factor [1/m]

g_a Gravity acceleration [m/s^2]

$\dot{H}$ Total power [W]

i Imaginary unit $\sqrt{-1}$

k Thermal conductivity [W/(m·K)]

K_s Coefficient of the spring [N/m]

l Inertance per unit length [kg/m^5]

L Inertance [kg/m^4]

M_s Solid mass [kg]

p Pressure [Pa]

$\hat{p}$ Pressure oscillation in the complex form [Pa]

$\dot{Q}_C$ Cooling power [W]

r_κ Thermal relaxation resistance per unit length [Pa·s/m^2]

r_ν Viscous resistance per unit length [Pa·s/m^4]

R_ν Viscous resistance [Pa·s/m^3]

t Time [s]

T_m Mean temperature [K]

U Volumetric flow rate [m^3/s]

$\hat{U}$ Volumetric flow oscillation in the complex form [m^3/s]

$\dot{W}_a$ Acoustic power [W]

x Displacement or length [m]

Z Total impedance [Pa·s/m^3]

Abbreviations

COP Coefficient of performance

GLPS Gas-liquid phase shifter

ITPS Inertance tube phase shifter

SOPS Spring-oscillator phase shifter

SPTC Stirling pulse tube cryocooler

Greek letters

γ Specific heat ratio [-]

ρ Density [kg/m^3]

σ Prandtl number [-]

ω Angular frequency [1/s]

ξ Friction factor of liquid column [N·s/m]

Superscripts

$\hat{}$ Pressure or volumetric flow oscillation in the complex form

$\tilde{}$ Complex conjugate

* Normalized parameter

Subscripts

c Compression chamber

C Cold end

chx Cold heat exchanger

dc Displacer chamber

dp Power recovery displacer

i Inlet of the reservoir

l Liquid column

m Mean value

ph Hot end of the pulse tube

r Reservoir

rc Cold end of the regenerator

rh Hot end of the regenerator

s Solid oscillator

t Inertance tube

κ Thermal

ν Viscous

References

[1] R. Radebaugh, Development of the pulse tube refrigerator as an efficient and reliable cryocooler, in: Proceedings of the Institute of Refrigeration, London, Vol. 96IIR, 2000, p. 1131.

[2] X. Luo, J. Wang, M. Dooner, J. Clarke, Overview of current development in electrical energy storage technologies and the application potential in power system operation, Applied Energy 137 (2015) 511–536. doi:10.1016/j.apenergy.2014.09.081.

[3] R. Radebaugh, M. Lewis, E. Luo, J. Pfotenhauer, G. Nellis, L. Schunk, Inertance tube optimization for pulse tube refrigerators, in: Advances in Cryogenic Engineering, Vol. 823, AIP Publishing, 2006, pp. 59–67.

[4] E. Mikulin, A. Tarasov, M. Shkrebyonock, Low-temperature expansion pulse tubes, in: Advances in Cryogenic Engineering, Vol. 29, Springer, 1984, pp. 629–637.

[5] D. Gardner, G. Swift, Use of inertance in orifice pulse tube refrigerators, Cryogenics 37 (2) (1997) 117–121. doi:10.1016/S0011-2275(96)00107-5.

[6] P. R. Roach, A. Kashani, Pulse tube coolers with an inertance tube: theory, modeling, and practice, in: Advances in Cryogenic Engineering, Vol. 43, Springer, 1998, pp. 1895–1902.

[7] W. Zhou, J. M. Pfotenhauer, G. F. Nellis, Comparison of three adjustable inertance tubes, in: Advances in Cryogenic Engineering, Vol. 1573, AIP Publishing, 2014, pp. 994–1001. doi:10.1063/1.4860814.

[8] C. D. West, Liquid piston Stirling engines, Oak Ridge National Lab., 1983.

[9] A. A. Castrejn-Pita, G. Huelsz, Heat-to-electricity thermoacoustic-magnetohydrodynamic conversion, Applied Physics Letters 90 (17) (2007) 174110. doi:10.1063/1.2733026.

[10] K. Tang, T. Lei, T. Jin, X. G. Lin, Z. Z. Xu, A standing-wave thermoacoustic engine with gas-liquid coupling oscillation, Applied Physics Letters 94 (25) (2009) 254101. doi:10.1063/1.3157920.

[11] S. Zhu, M. Nogawa, Pulse tube stirling machine with warm gas-driven displacer, Cryogenics 50 (5) (2010) 320–330. doi:10.1016/j.cryogenics.2010.01.011.

[12] X. Wang, Y. Zhang, H. Li, W. Dai, S. Chen, G. Lei, E. Luo, A high efficiency hybrid stirling-pulse tube cryocooler, AIP Advances 5 (3) (2015) 037127. doi:10.1063/1.4915900.

[13] R. D. Rogers, Chemistry: Ionic liquids–solvents of the future?, Science 302 (5646) (2003) 792–793. doi:10.1126/science.1090313.

[14] G. W. Swift, D. L. Gardner, S. Backhaus, Acoustic recovery of lost power in pulse tube refrigerators, The Journal of the Acoustical Society of America 105 (2) (1999) 711. doi:10.1121/1.426262.

[15] H. Sugita, Y. Matsubara, A. Kushino, T. Ohnishi, H. Kobayashi, W. Dai, Experimental study on thermally actuated pressure wave generator for space cryocooler, Cryogenics 44 (6-8) (2004) 431–437. doi:10.1016/j.cryogenics.2004.02.014.

[16] G. W. Swift, Thermoacoustics: a unifying perspective for some engines and refrigerators, Acoustical Society of America, 2002.

[17] J. Hu, E. Luo, S. Li, B. Yu, W. Dai, Heat-driven thermoacoustic cryocooler operating at liquid hydrogen temperature with a unique coupler, Journal of Applied physics 103 (10) (2008) 104906. doi:10.1063/1.2926348.

[18] J. Fuller, The room temperature ionic liquid 1-ethyl-3-methylimidazolium tetrafluoroborate: Electrochemical couples and physical properties, J. Electrochem. Soc. 144 (11) (1997) 3881. doi:10.1149/1.1838106.

A.5 Operational test of bonded magnetocaloric plates

C. R. H. Bahl, K. Navickaité, H. Neves Bez, **T. Lei**, K. Engelbrecht, R. Bjørk, K. Li, Z. Li, J. Shen, W. Dai, J. Jia, Y. Wu, Y. Long, F. Hu, B. Shen, Operational test of bonded magnetocaloric plates, *International Journal of Refrigeration*, under review, (2016).

Operational test of bonded magnetocaloric plates

Christian R.H. Bahl, Kristina Navickaitė, Henrique Neves Bez, Tian Lei, Kurt Engelbrecht, Rasmus Bjørk

Department of Energy Conversion and Storage, Technical University of Denmark, Frederiksborgvej 399, DK-4000 Roskilde, Denmark

Ke Li, Zhenxin Li, Jun Shen, Wei Dai

Technical Institute of Physics and Chemistry, Chinese Academy of Sciences, Beijing 100190, China

Jichen Jia, Yuanyuan Wu, Yi Long

University of Science and Technology Beijing, Beijing 100083, China

Fengxia Hu, Baogen Shen

Institute of Physics, Chinese Academy of Sciences, Beijing 100190, China

Abstract

Bonded plates made by hot pressing $La_{0.85}Ce_{0.15}Fe_{11.25}Mn_{0.25}Si_{1.5}H_y$ particles and resin have been tested as active magnetic regenerators in a small scale magnetocaloric device. Firstly the plates were carefully characterised magnetically and thermally. The plates were prepared with 5 wt% resin, and from density measurements it was found that the volume ratio of the magnetocaloric material was 0.53, due to the resin and porosity. The best operating conditions for the plate regenerator were determined at which a temperature span of 6.4 K was measured along the plates.

Keywords: Magnetocaloric, Magnetic refrigerator, Regenerator, Resin bonding

Nomenclature

Abbreviations	
AMR	Active manetic regenerator
DSC	Differential scanning calorimeter
EDS	Energy-dispersive X-ray spectroscopy
Gd	Gadolinium
PPMS	Physical properties measurement system
SEM	Scanning electron microscope
TTO	Thermal transport option
VSM	Vibration sample magnetometer

Variables	
C	Specific heat
C	Specific heat at constant magnetic field
m	Mass
T_{hot}	Hot end temperature
ΔS_{M}	Magnetic isothermal entropy change
ΔT_{ad}	Adiabatic temperature change
$\Delta T_{\text{effective}}$	Effective adiabatic temperature change
ΔT_{span}	Temperature span
ϕ	Utilisation

Subscripts	
f	Fluid
MCM	Magnetocaloric material
resin	Resin binder material
s	Solid

1. Introduction

For the past decade significant progress has been made in bringing magnetic refrigeration towards commercialisation. New magnetocaloric materials have been developed and magnetocaloric demonstration devices become ever more powerful and efficient (Kitanovski et al., 2015). Most of these devices have employed the so called active magnetic regenerator (AMR) cycle as a method of utilising the magnetocaloric effect in a device. Here the temperature of a porous regenerator structure is increased and decreased by applying and removing a magnetic field, while a heat transfer fluid is reciprocated back and forth in order to build up a temperature gradient. Keys to utilising the AMR concept are firstly to have a magnetocaloric material, or a cascade of such, with high magnetocaloric effect, and secondly, to shape this material in a way that there is good thermal contact between solid and fluid, allowing an effective heat transfer.

Many magnetocaloric materials have been studied and considered for application in devices (Smith et al., 2012). Recently a lot of research has been done on materials that undergo a first order magnetic phase transition, so-called first order materials, as they have a very high magnetic entropy change ΔS_{M} around the phase transition. An important example of this class of materials is the intermetallic $\mathrm{La(Fe,Si)_{13}H}_y$, which has been studied with a number of different elements doped into the Fe and Si sites (Zhang et al., 2013). In general this material series has a high magnetocaloric effect, a tunable Curie temperature and only a small amount of undesirable thermal hysteresis. The disadvantage of these materials is the lack of structural stability due to the volume change at the phase transition (Lyubina et al., 2010).

Recently, different strategies for shaping these and similar magnetocaloric materials into the desired shapes have been proposed and tested. Polymer bonding and pressing to plates has been demonstrated for first order materials (Skokov et al., 2014; Radulov et al., 2015) and second order materials of the same type (Pulko et al., 2015). Other methods of producing structures have also been presented, such as injection moulding (Lanzarini et al., 2015), hot pressing with Cu (Liu et al., 2015) and extrusion into monoliths Pryds et al. (2011). Actual AMR performance in a test device has only been reported for the second order bonded plates (Pulko et al., 2015). However, porous particle based regenerators where the particles are bonded for stability have been presented, most notably by Jacobs et al. (2014) using

$La(Fe,Si)_{13}H_y$.

Here we demonstrate in a small versatile AMR device the performance of plates of first order materials bonded with resin and cured during pressing.

2. Experimental

A $La_{0.85}Ce_{0.15}Fe_{11.25}Mn_{0.25}Si_{1.5}$ ingot was prepared in an induction furnace. The purity of the raw materials was at least 99.9 wt%. The annealed ingots were crushed into particles less than 0.35 mm in size for the hydrogenation process. These were annealed in a high purity hydrogen atmosphere until saturation. The structure of the hydrides was confirmed by x-ray powder diffraction. The hydrogen concentration y of $La_{0.85}Ce_{0.15}Fe_{11.25}Mn_{0.25}Si_{1.5}H_y$ (referred to as LaFeSiH in the following) was estimated to be 2.0 wt% by the inert gas pulse infrared absorption method. When vacuum annealing under 350 °C for 2 hours a sharp decrease of the Curie temperature was observed due to the escape of H.

2.1. Processing the plates

The resulting powder was mixed with a phenolic resin system in a mass ratio of 20:1. The mixed powders were pressed into plate shape under pressure of 20 MPa and then solidified at 150 °C for 10 minutes, as shown in Figure 1. The plates were prepared in the size 25 mm by 40 mm, in order to fit into the regenerator test device, with a thickness of 0.5 mm. Measuring the specific heat shows that the Curie temperature does not change during the resin curing process, indicating that the LaFeSiH is unaffected by this treatment.

2.2. Characterisation of the plates

Thermal conductivity was measured at 300 K using a Thermal Transport Option (TTO) on a Quantum Design physical property measurement system (PPMS). The density of the plates was measured using AccuPyc 1340 helium pycnometer repeating each measurement 10 times, and the density of the resin was measured with a Pentapyc5200e Auto Density Analyzer. The magnetic properties were analysed in a LakeShore 7407 vibrating sample magnetometer (VSM). The sample was measured in the temperature range 270 K - 306 K at applied fields up to 1.5 T. The specific heat of the sample was measured using a custom built differential scanning calorimeter (DSC), allowing the applied field to be varied in the range 0-1.6 T at a fixed

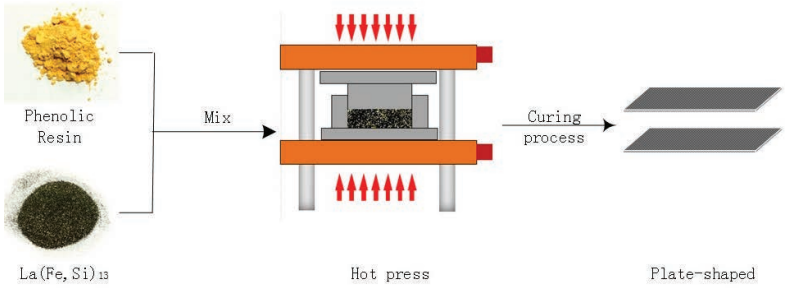

Fig. 1: Illustration of the fabrication process, showing the mixing of powder with resin, hot pressing and the final plates.

orientation relative to the sample (Jeppesen et al., 2008). An scanning electron microscope (SEM), Hitachi TM3000, equipped with a Bruker Quantax Energy-dispersive X-ray spectroscopy detector (EDS) was used to analyse the microstructure of a piece of one of the plates.

3. Results

3.1. Physical properties of the plates

Figure 2 shows the structure of a plate. It consists of irregular particles of LaFeSiH with a broad size range. There is a significant porosity between the particles. Using EDS mapping we can probe the presence of the resin by isolating the carbon signal, as this will be unique to the resin. As shown in Figure 3 the resin covers large areas binding together the particles, but there are still significant volumes of porosity between particles. So the system can be considered as a mixture of three phases, LaFeSiH, resin and pores.

A representative density value of 5721 ± 3 kgm^{-3} was measured based on pieces of plates weighing in total 2.3947 g. The mass fraction of magnetocaloric material is 0.95 and the mass fraction of resin is 0.05. Based on the structural symmetry and lattice parameters the density of the LaFeSiH, ρ_{LaFeSiH}, is 7207 kgm^{-3} and the density of the resin, ρ_{resin}, is 1166 kgm^{-3} found by crushing down a sample of pure resin into a powder and measuring the density. Assuming that there are no pores closed to helium penetration, the weighted average density of the LaFeSiH and the resin is 5724 kgm^{-3}, very close to the measured value.

Geometrically measuring and weighing a plate gave a density of approximately 4000 kgm^{-3}, which includes all pores. From this we can calculate the

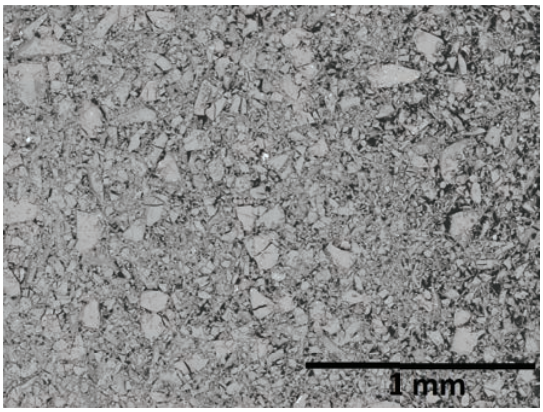

Fig. 2: Backscattered SEM image of an area of a plate. The image shows the surface of the plate as prepared.

porosity of the plates as 0.30. Thus the volume fractions of LaFeSiH, resin and pores are approximately 0.53, 0.17 and 0.30, respectively.

Based on the mass fractions of LaFeSiH and resin the reduction in effective adiabatic temperature change due to the presence of resin is quite limited. The actual temperature change $\Delta T_{\text{effective}}$ will be given by:

$$\Delta T_{\text{effective}} = \frac{\Delta T_{\text{ad}} c_{\text{H,MCM}}}{0.95 c_{\text{H,MCM}} + 0.05 c_{\text{H,resin}}} \approx 0.94 \Delta T_{\text{ad}}, \tag{1}$$

where $c_{\text{H,MCM}}$ and $c_{\text{H,resin}}$ are the specific heats of LaFeSiH (500 $\text{Jkg}^{-1}\text{K}^{-1}$) and resin (1200 $\text{Jkg}^{-1}\text{K}^{-1}$), respectively. As the peak of specific heat in LaFeSiH is very narrow and field dependent we use the background value away from the peak. Closer to the peak $\Delta T_{\text{effective}}$ will be even closer to ΔT_{ad}.

Magnetisation measurements were used to calculate the magnetic entropy change, ΔS_{M}, in the conventional way described by Pecharsky and Gschneidner Jr. (1999b). A 11.76 mg piece of one of the plates was used. This piece seemed free of resin, but there may be a little resin included. This would slightly change the level reached by the peak, but not the profile shape. The data was corrected for demagnetisation approximating the sample to a prism and using the expression by Aharoni (1998).

To probe for the presence of hysteresis the magnetic entropy was measured both during cooling and during heating. Between each measurement the sample was 'reset' at an equilibrium temperature far above or below

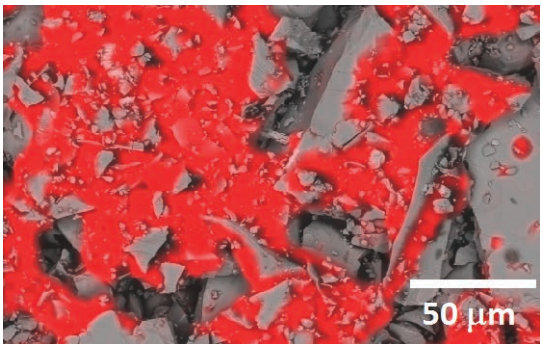

Fig. 3: EDS filtered to show carbon. The resin is observed to bind together the particles, but there is also a significant porosity remaining as discussed in the text.

the measurement range, for cooling and heating, respectively (Caron et al., 2009). The ΔS_{M} values are consistent with those found in literature (Zhang et al., 2013). Figure 4 shows that the hysteresis at the phase transition is very low. In order to further probe the presence of hysteresis the specific heat of the sample was measured during heating and cooling at different temperature ramp rates in the range 1 Kmin^{-1} to 5 Kmin^{-1}. By applying a linear regression of the peak temperatures with respect to the temperature rates, the hysteresis is found to be 0.4 ± 0.2 K, consistent with the magnetisation data, as shown in Figure 5.

When applying a magnetic field the temperature of the peaks of the specific heat increase at a rate of about 4.3 KT^{-1}. Also, the peak goes from being very sharp to becoming more broad, as shown in Figure 6, consistent with the results reported by Basso et al. (2015). Due to the very low value of the hysteresis and the errors on the lines fitted to the peak temperatures, determining the critical field at which the hysteresis vanishes cannot be done with confidence.

3.2. Regenerator testing

A stack of 25 plates was tested as an AMR in a small scale test device at the Technical University of Denmark. The stack was prepared as described in Engelbrecht et al. (2011) by layering the plates with ø0.25 mm metal wire as spacers. The sides were then sealed with epoxy before removing the metal wire. This resulted in a 20.5 mm tall stack, 25 mm wide and 40 mm long, which was then mounted in a cylindrical regenerator housing using silicone

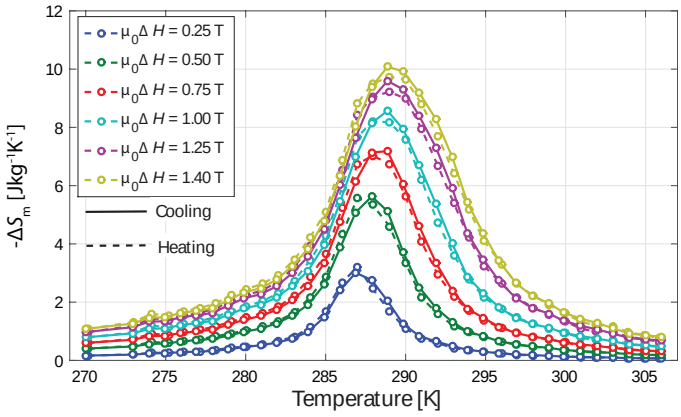

Fig. 4: Measured entropy change of a sample of one of the plates. Both the heating and cooling curves are shown, and the hysteresis is observed to be small.

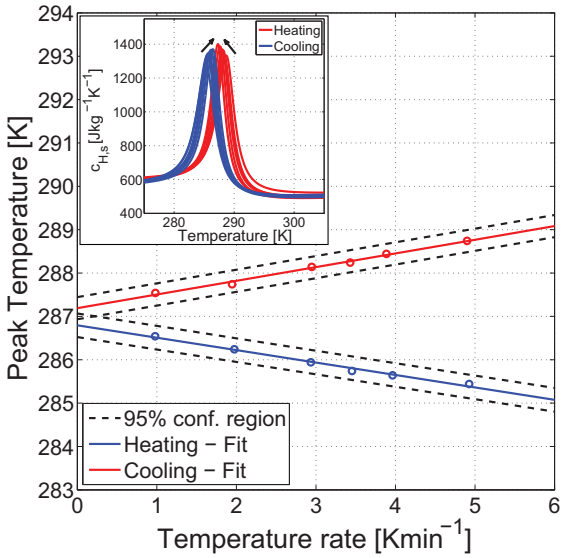

Fig. 5: The peak temperature of the specific heat measured at different ramp rates in the DSC. Both the heating peak and the cooling peak have been measured, as shown in the inset. Extrapolating to zero ramp rate gives a measure of the hysteresis.

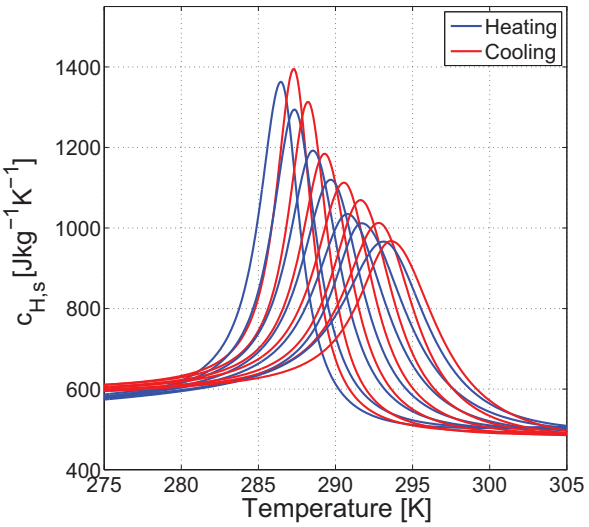

Fig. 6: Field dependence of the peak in specific heat, for cooling and heating. Applied fields of 0, 0.25, 0.50, 0.75, 1.00, 1.25 and 1.50 T are shown, with the peak moving up in temperature and broadening as the field increases.

around the border of the stack. The mass of each plate was approximately 2 g, so the mass of the regenerator was 50 g.

The glued stack, before being mounted in the regenerator housing, is shown in Figure 7. The channels between the plates are clearly seen, but close inspection reveals that with the chosen plate spacing the unevenness of the plates becomes significant. Thus the actual channel height varies significantly across the regenerator. The effect of this will be discussed later.

Testing of the regenerator was done in the versatile test device described previously (Bahl et al., 2008; Engelbrecht et al., 2011). Here the cylindrical regenerator housing moves in and out of the bore of a 1.1 T permanent magnet Halbach cylinder. A ø18 mm reciprocating piston forces the heat transfer fluid through the regenerator to perform the well known four steps of the AMR cycle (Pecharsky and Gschneidner Jr., 1999a). Demineralised water, mixed with 2 vol% of ENTEK FNE corrosion inhibitor, as recommended for a similar material by Velazquez et al. (2014), was used as the heat transfer fluid.

Three parameters were varied in the testing of the regenerator, the fluid velocity, the length the piston is moved, and the ambient temperature. A

Fig. 7: The stack of plates used in the regenerator before being mounted in the cylindrical regenrator housing.

heat exchanger at the hot end of the regenerator keeps the temperature of this close to that of the temperature controlled cabinet, in which the device is mounted. The length the piston moves is conventionally expressed as the utilisation, ϕ, defined as

$$\phi = \frac{m_{\mathrm{f}} c_{\mathrm{f}}}{m_{\mathrm{s}} c_{\mathrm{H,s}}} \tag{2}$$

where m_{f} is the mass of the fluid pushed through the regenerator in one blow, c_{f} is the specific heat of the fluid, m_{s} is the mass of the solid regenerator and $c_{\mathrm{H,s}}$ is the specific heat of the bonded plates. m_{f} is found from the movement of the ø18 mm piston, c_{f} is set as the textbook value of 4200 $\mathrm{Jkg^{-1}K^{-1}}$, ignoring the small amount of corrosion inhibitor, m_{s} is 50 g and for $c_{\mathrm{H,s}}$ the background value of 600 $\mathrm{Jkg^{-1}K^{-1}}$ is used, as found from Figure 6, including the resin.

Starting at an ambient temperature of 290 K and a utilisation of 0.23, the AMR cycle is repeated until the temperature difference between the cold end and the hot end, known as the temperature span, ΔT_{span}, reached a constant value. Different values of the fluid velocity were tested recording the achieved ΔT_{span}, as shown in Figure 8. Note that the fluid velocity reported is the velocity in the channels, not the piston velocity. It is observed that the highest values of the span are found in a broad optimum around about 7 $\mathrm{mms^{-1}}$, which is consistent with that previously found for plates of a similar material (Engelbrecht et al., 2011). The plates in Engelbrecht et al. (2011) were somewhat thicker and cut from blocks made of different $\mathrm{La(Fe,Co,Si)_{13}}$ compounds, all with a second order phase transition. Using this fluid velocity of 7 $\mathrm{mms^{-1}}$ and staying at an ambient temperature of 290 K the utilisation was varied to find the best performance, as shown in Figure 9. Again a broad peak of ΔT_{span} is observed, the utilisation giving the highest values

being about 0.23, similar to Engelbrecht et al. (2011); Bahl et al. (2012). Due to the change in the distance and velocity of the piston movement the cycle time varies in the range of 5 to 24 s in Figure 8 and in the range 5.5 - 12 s in Figure 9.

The magnetocaloric effect in materials with a first order magnetic phase transition occurs over a narrow range of temperatures, as shown in Figure 4. Thus it is very important when utilising these materials in a device that the span of the device is across the peak in magnetocaloric effect. Figure 10 shows the achieved span of the device as the hot end temperature is changed, while keeping a utilisation of 0.23 and a fluid velocity of 7 mms^{-1}. The cycle time remains constant at about 9 s. We observe a relatively narrow peak that drops off sharply at 293 K, which is a few degrees above the peak temperature of ΔS_{M} in a 1 T field. The maximum ΔT_{span} was 6.4 K, which is around double the maximum adiabatic temperature change of such a material in this applied field, see e.g. Basso et al. (2015), demonstrating the AMR cycle in the regenerator. The maximum span is lower than the 10.2 K span achieved using plates of the benchmark material Gd (Engelbrecht et al., 2011), but comparable to the spans achieved using plates of a single second order LaFeCoSi material or the single perovskite type material $\mathrm{La_{0.67}Ca_{0.26}Sr_{0.07}Mn_{1.05}O_3}$ (Pulko et al., 2015; Engelbrecht et al., 2011). When grading the regenerator to two similar materials with Curie temperatures close to each other the span can be significantly increased for both the LaFeCoSi type materials (Engelbrecht et al., 2011) and the perovskite type materials (Bahl et al., 2012). Layering materials is key to the success of first order materials, due to the narrow peaks of the magnetocaloric effect, so it is clearly expected that if a regenerator were constructed with a number of different Curie temperatures along the flow direction significantly higher performance could be reached. However, as shown recently it is extremely important to have the correct spacing of the Curie temperatures, as the performance can easily be significantly reduced if this is not the case (Lei et al., 2015).

4. Discussion

The measured maximum temperature span of 6.4 K is relatively low compared to other reported spans from this and similar devices. But when using just a single first order material, there is a natural limit to the achievable span, due to the very narrow ΔS_{M} peak. This span may be expanded by

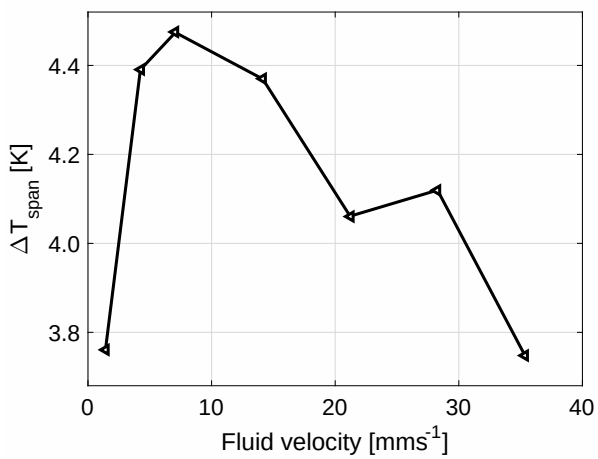

Fig. 8: The steady state temperature span between the hot and the cold end as a function of the velocity of the fluid being pushed between the plates.

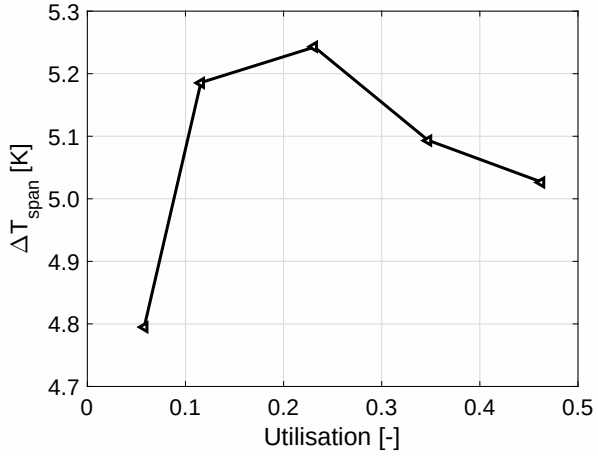

Fig. 9: The steady state temperature span between the hot and the cold end as a function of the utilisation.

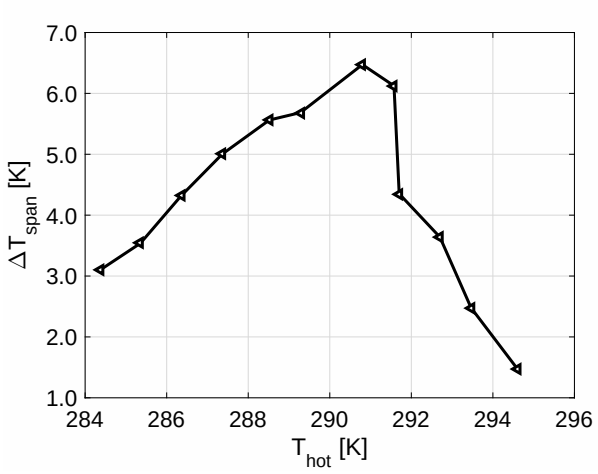

Fig. 10: The steady state temperature span between the hot and the cold end as a function of the constant hot end temperature.

layering materials with slightly different Curie temperatures, as done by Jacobs et al. (2014). Previously it has been shown how thin plates consisting of a number of magnetocaloric materials have been produced by tape casting (Bulatova et al., 2015). A similar production technique could be imagined for hot-pressing single plates consisting of multiple materials.

Regenerator performance is heavily influenced by the morphology of the regenerator. In the present study flat parallel plates were chosen, giving a regenerator with a significantly reduced pressure drop compared to an equivalent packed bed one. Lower pressure drop leads to higher efficiency, although this is not measured in the device used here. The disadvantage of plates is the demand for thin very parallel plates with small plate spacing, which is often hard to realise. The increase of the Biot number for thicker plates will result in a slower heat transfer to the surrounding fluid, preventing fast operation and high performance. A higher thermal conductivity will allow for the use of thicker plates. The thermal conductivity of the plates tested here has been measured to be 3.13 $\mathrm{Wm^{-1}K^{-1}}$, reduced from the generally accepted value of about 9 $\mathrm{Wm^{-1}K^{-1}}$ for this type of material (Fujieda et al., 2004), due to porosity and the presence of resin in the plates. In order to realise the full potential of plates with this relatively low thermal conductivity the thickness would have to be significantly reduced, and the channel thicknesses be reduced accordingly.

In addition to the challenges of producing significantly thinner plates the flatness requirement of such plates will also become more critical. The reduction in regenerator performance due to a maldistribution of the plate spacings has been shown both by modelling and experimentally (Nielsen et al., 2012; Engelbrecht et al., 2013). Even seemingly insignificant variation in the channel thicknesses can have a large impact. With sub-millimeter plates a requirement of less than 10% variation in spacing, in accordance with the general recommendation in Nielsen et al. (2012), will necessitate very accurate production techniques.

Although the addition of the low mass fraction resin hardly influences ΔS_{M} per unit mass, the volumetric ΔS_{M} decreases from about 70 $\mathrm{mJcm^{-3}K^{-1}}$ to about 40 $\mathrm{mJcm^{-3}K^{-1}}$ due to the porous structure of the bonded material under a changing magnetic field of 1.4 T. From a practical point of view, the volumetric ΔS_{M} is of more importance (Gschneidner Jr. et al., 2005), since the magnetic system is the most expensive part and the magnetic field volume is thus limited. This is a challenge when making bonded plates and reducing the amount of resin to the minimum amount that will still maintain the structural integrity of the plates should be considered. Also, the 0.30 volume fraction of pores could possibly be reduced by improving the processing route.

5. Conclusion

We have shown that it is possible to use resin bonded plates of the magnetocaloric material $\mathrm{La_{0.85}Ce_{0.15}Fe_{11.25}Mn_{0.25}Si_{1.5}H_{\mathit{y}}}$ as regenerators in a small scale magnetocaloric testing device. The plates were characterised thermally and magnetically to determine the magnetic entropy change, the heat capacity and the hysteresis. The maximum achieved temperature span was 6.4 K. Increasing this span may be achieved by layering materials, reducing the amount of resin and pores or by manufacturing thinner and flatter plates.

Acknowledgements

The authors acknowledge the International Network Programme: Rare-earth/transition-metal oxides and compounds for environment friendly energy science and technology (grant no 4070-00047) from The Danish Agency for Science, Technology and Innovation. This work is supported by National Natural Science Foundation of China (51322605, 51571018, 51531008) and

also partly financed by the ENOVHEAT project which is funded by Innovation Fund Denmark (contract no 12-132673).

Aharoni, A., 1998. Demagnetizing factors for rectangular ferromagnetic prisms. J. Appl. Phys. 83, 3432.

Bahl, C. R. H., Petersen, T. F., Pryds, N., Smith, A., 2008. A versatile magnetic refrigeration test device. Rev. Sci. Instrum. 79, 093906.

Bahl, C. R. H., Velazquez, D., Nielsen, K., Engelbrecht, K., Andersen, K., Bulatova, R., Pryds, N., 2012. High performance magnetocaloric perovskites for magnetic refrigeration. Appl. Phys. Lett. 100, 121905.

Basso, V., Küpferling, M., Curcio, C., Bennati, C., Barzca, A., Katter, M., Bratko, M., Lovell, E., Turcaud, J., Cohen, L., 2015. Specific heat and entropy change at the first order phase transition of La(Fe-Mn-Si)$_{13}$-H compounds. J. Appl. Phys 118, 053907.

Bulatova, R., Bahl, C. R. H., Andersen, K. B., Theil Kuhn, L., Pryds, N., 2015. Functionally graded ceramics fabricated with side-by-side tape casting for use in magnetic refrigeration. Int. J. Appl. Ceram. Technol 12, 891898.

Caron, L., Ou, Z., Nguyen, T., Thanh, D. C., Tegus, O., Brück., E., 2009. On the determination of the magnetic entropy change in materials with firstorder transitions. J. Magn. Magn. Mater. 321, 35593566.

Engelbrecht, K., Bahl, C., Nielsen, K., 2011. Experimental results for a magnetic refrigerator using three different types of magnetocaloric material regenerators. International Journal of Refrigeration 34, 1132–1140.

Engelbrecht, K., Tusek, J., Nielsen, K., Kitanovski, A., Bahl, C., Poredos, A., 2013. Improved modelling of a parallel plate active magnetic regenerator. J. Phys. D.: Appl. Phys 46, 255002.

Fujieda, S., Hasegawa, Y., Fujita, A., 2004. Thermal transport properties of magnetic refrigerants La(Fe$_x$Si$_{1-x}$)$_{13}$ and their hydrides, and Gd$_5$Si$_2$Ge2 and MnAs. J. Appl. Phys. 95, 24292431.

Gschneidner Jr., K. A., Pecharsky, V. K., Tsokol, A. O., 2005. Recent developements in magnetocaloric materials. Rep. Prog. Phys. 68, 1479.

Jacobs, S., Auringer, J., Boeder, A., Chell, J., Komorowski, L., Leonard, J., Russek, S., Zimm, C., 2014. The performance of a large-scale rotary magnetic refrigerator. Int. J. Refrigeration 37, 84–91.

Jeppesen, S., Linderoth, S., Pryds, N., Kuhn, L. T., Jensen, J. B., 2008. Indirect measurement of the magnetocaloric effect using a novel differential scanning calorimeter with magnetic field. Review of Scientific Instruments 79 (8), 083901.

Kitanovski, A., Tusek, J., Tomc, U., Plaznik, U., Ozbolt, M., Poredos, A., 2015. Magnetocaloric Energy Conversion: From Theory to Applications. Springer International Publishing, New York.

Lanzarini, J., Barriere, T., Sahli, M., Gelin, J., Dubrez, A., C.Mayer, Pierronnet, M., Vikner, P., 2015. Thermoplastic filled with magnetocaloric powder. Materials and Design 87, 1022–1029.

Lei, T., Nielsen, K., Engelbrecht, K., Bahl, C., Bez, H. N., Veje, C., 2015. Sensitivity study of multi-layer active magnetic regenerators using first order magnetocaloric material La(Fe,Mn,Si)$_{13}$H$_y$. J. Appl. Phys 118, 014903.

Liu, J., Zhang, M., Shao, Y., Yan, A., 2015. LaFe$_{11.6}$ Si$_{1.4}$/Cu Magnetocaloric Composites Prepared by Hot Pressing. IEEE Trans. Magn. 51, 2501502.

Lyubina, J., Schäfer, R., Martin, N., Schultz, L., Gutfleisch, O., 2010. Novel Design of La(Fe,Si)$_{13}$ Alloys Towards High Magnetic Refrigeration Performance. Advanced Materials 22, 3735–3739.

Nielsen, K., Engelbrecht, K., Christensen, D., Jensen, J., Smith, A., Bahl, C., 2012. Degradation of the performance of microchannel heat exchangers due to flow maldistribution. Appl. Therm. Engineer 40, 236.

Pecharsky, V. K., Gschneidner Jr., K. A., 1999a. Magnetocaloric affect and magnetic refrigeration. J. Magn. Magn. Mater. 200, 44.

Pecharsky, V. K., Gschneidner Jr., K. A., 1999b. Magnetocaloric effect from indirect measurements: Magnetization and heat capacity. J. Appl. Phys. 86, 565–575.

Pryds, N., Clemens, F., Menon, M., Nielsen, P. H., Brodersen, K., Bjørk, R., Bahl, C. R. H., Engelbrecht, K., Nielsen, K. K., Smith, A., 2011. A monolithic perovskite structure for use as a magnetic regenerator. Journal of the American Ceramic Society 94, 2549–2555.

Pulko, B., Tusekek, J., J.D.Moore, Weise, B., Skokov, K., Mityashkin, O., Kitanovski, A., Favero, C., Fajfar, P., Gutfleisch, O., Waske, A., Poredos, A., 2015. Epoxy-bondedlafecosi magnetocaloricplates. J. Magn. Magn 375, 65–73.

Radulov, I., Skokov, K., nad T. Braun, D. K., Gutfleisch, O., 2015. Polymer-Bonded La(Fe,Mn,Si)$_{13}$H$_x$ Plates for Heat Exchangers. IEEE Trans. Magn. 51, 2501204.

Skokov, K. P., Karpenkov, D., Kuzmin, M. D., Radulov, I., Gottschall, T., Kaeswurm, B., Fries, M., Gutfleisch, O., 2014. Heat exchangers made of polymer-bonded La(Fe,Si)$_{13}$. J. Appl. Phys 115, 17A941.

Smith, A., Bahl, C., Bjørk, R., Engelbrecht, K., Nielsen, K., Pryds, N., 2012. Materials challenges for high performance magnetocaloric refrigeration devices. Advanced Energy Materials 2, 1288–1318.

Velazquez, D., Castro, M., Palacios, E., Burriel, R., 2014. Practical properties of lafecosi materials to be used in magnetic cooling regerators. Proceedings 6th IIF-IIR International Conference on Magnetic Refrigeration, Victoria, BC, 7-10 September 2014.

Zhang, H., Hu, F., Sun, J., Shen, B., 2013. Effects of interstitial H and/or C atoms on the magnetic and magnetocaloric properties of La(Fe, Si)$_{13}$-based compounds. Science China Physics, Mechanics and Astronomy 56, 2302–2311.

A.6 Optimization of multi-layer active magnetic regenerator towards compact and efficient refrigeration

T. Lei, K. Engelbrecht, K. K. Nielsen, et al., Optimization of multi-layer active magnetic regenerator towards compact and efficient refrigeration, *The 29th International Conference on Efficiency, Cost, Optimisation, Simulation and Environmental Impact of Energy Systems*, Portorož, (2016).

Optimization of Multi-layer Active Magnetic Regenerator towards Compact and Efficient Refrigeration

Tian Lei[a], Kurt Engelbrecht[a], Kaspar K. Nielsen[a], Henrique Neves Bez[a], Christian T. Veje[b], Christian R. H. Bahl[a]

[a] *Technical University of Denmark, Roskilde, Denmark, tile@dtu.dk*
[b] *University of Southern Denmark, Odense, Denmark*

Abstract:

Magnetic refrigerators can theoretically be more efficient than current vapor compression systems and use no vapor refrigerants with global warming potential. The core component, the active magnetic regenerator (AMR) operates based on the magnetocaloric effect of magnetic materials and the heat regeneration processes of periodic fluid blows. Magnetocaloric materials with a first order phase transition (FOPT) are suitable to realize a higher cooling capacity than commonly used gadolinium, but layering such materials is necessary, due to a large isothermal entropy change (ΔS_m) in a narrow region around their Curie temperature. Simulations are implemented to investigate how to layer the FOPT materials for obtaining higher cooling capacity. Moreover, based on entropy generation minimization, optimization of the regenerator geometry and related operating parameters is presented for improving the AMR efficiency. In addition, simulations are carried out to investigate the potential of applying nanofluid in future magnetic refrigerators.

Keywords:

Magnetic refrigeration, Magnetocaloric material, Regenerator optimization, Nanofluid

1. Introduction

Room temperature magnetocaloric refrigerators (MCR) operate based on the magnetocaloric effect (MCE) and principle of heat regeneration. Compared to a vapor compression refrigerator, MCRs exhibits advantages such as high theoretical efficiency, avoiding use of vapor refrigerants, and easy integration with distributed heat exchangers. Therefore, an MCR is considered to be a compact and efficient refrigeration technology and attracts a lot of attentions in recent decades. Tura and Rowe presented the improvements of a prototype, which can realize a maximum no-load temperature span of 29 ºC and a cooling power of 50W at 2 ºC temperature span [1]. Engelbrecht et al. [2] built a rotary MCR and it exhibits a no-load temperature span of over 25 ºC and a maximum cooling power of 1010 W using gadolinium (Gd) spheres. Jacobs et al. [3] presented a rotary prototype using six layers of LaFeSiH particles, producing 3042 W cooling power at zero temperature span and 2502 W over a span of 12ºC with a coefficient of performance (COP) around 2. A compact rotary MCR presented by Eriksen et al. [4] could realize a temperature span of 10.2 ºC at a cooling load of 103 W and a COP of 3.1. More prototypes and materials are reviewed in References [5-7].

The magnetocaloric effect can be explained from the viewpoint of thermodynamics. Upon an increase in the applied magnetic field, the magnetic contribution to the entropy (S_m) of the magnetocaloric material (MCM) will decrease. Under an adiabatic condition, this magnetization process leads to an increase in temperature, which is so called adiabatic temperature change ΔT_{ad}, since the lattice and/or electronic contributions to the entropy must increase to hold the total entropy constant [6]. While in an isothermal process, the total entropy change of MCM is equal to the magnetic entropy change ΔS_m. The intensity of the MCE is largest when the temperature approaches the material's Curie temperature T_{Curie} and increases with increasing magnetic field

change. Assuming no magnetic hysteresis, the magnetization and demagnetization processes are considered reversible, which indicates that an MCR can realize high theoretical efficiency.

Permanent magnets are commonly used in existing room temperature MCR devices and the reachable magnetic field of a typical permanent magnet is of the order 1.5 T. Upon this magnetic field change, the adiabatic temperature change for the best performing materials will be about 5 ºC [6,7]. It is, however, not enough for most applications, such as domestic refrigeration. Therefore, the principle of heat regeneration and the AMR [8] are necessary to increase the temperature span to an applicable level. An AMR is a solid porous matrix consisting of the magnetocaloric materials, where a heat transfer fluid may flow through and exchange heat with the solid. As shown in Figure 1, a typical AMR cycle comprises four steps: (a) adiabatic magnetization associated with an increase in the solid temperature T_s; (b) cold-to-hot blow, where T_s decreases due to heat transfer with the fluid; (c) adiabatic demagnetization, and T_s further decreases below the initial state; (d) hot-to-cold blow, and the solid absorbs heat from the heat transfer fluid, leading to a lower temperature in the outflow than the load temperature at the cold end. Driven by this temperature difference, the fluid can absorb a certain amount of heat, i.e., cooling power, from the load. After several cycles, a temperature gradient larger than ΔT_{ad} can be built up between the hot and cold ends, and the magnetocaloric materials along the regenerator work in different temperature regions based on location.

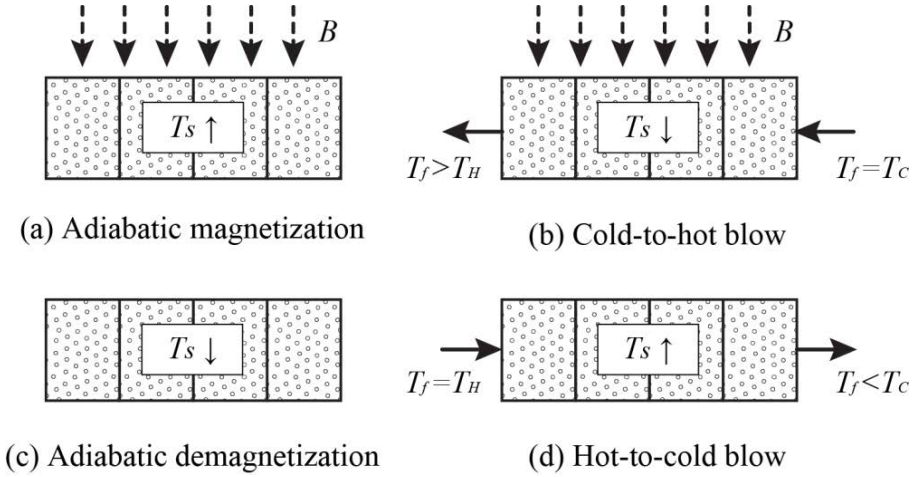

Figure 1. A typical cycle of multi-layer magnetic regenerator

Materials with a large MCE are key factors for an MCR to realize compact and efficient refrigeration. Compared with magnetocaloric materials with a second order phase transition (SOPT) such as Gd, MCMs with a first order phase transition (FOPT) exhibit a larger peak value in ΔS_m near T_{Curie}. This may be beneficial for elevating the specific cooling power, which is the cooling power per kilogram of MCM. Applying FOPT materials in future prototypes is promising; however, a previous study [9] showed that 2.2 layers per 5 ºC temperature span are needed for regenerators using the FOPT material $La(Fe,Mn,Si)_{13}H_y$. Comparing AMRs using first and second order magnetocaloric materials is thus of substantial interest and we present a study by simulation based on a one dimensional (1D) model. The influences of the number of layers and the temperature span on the specific cooling power are quantified. Based on analysis, a practical number of layers is proposed to reach 90% of the theoretical specific cooling power.

Besides maximizing the magnetocaloric properties, minimizing the losses inside the AMR is important for improving the refrigeration efficiency. According to a previous study [10], the main losses are caused by the insufficient heat transfer between the fluid and solid refrigerant as well as at the hot or cold heat exchangers, viscous dissipation due to the pump work and axial conduction.

These three loss mechanisms are directly or indirectly related to the regenerator geometry and operating parameters, including the frequency, fluid flow rate, aspect ratio and hydraulic diameter. To minimize the total loss and maximize the COP, a multi-parameter optimization of AMRs using a packed sphere bed is presented. Furthermore, entropy production rates are calculated and compared for quantitative analysis of the impacts of different loss mechanisms.

Aqueous solutions with anti-corrosion additives are widely used in existing MCR devices as heat transfer fluids, and the additives usually have a lower thermal conductivity and higher viscosity than water, which reduces efficiency. Although many studies have been carried out to enhance the heat transfer performance using nanofluids [11], which is produced by suspending nanoparticles in base fluids, investigation of applying nanofluids in the regenerator or the AMR is rarely reported. In this study, the performance of an AMR using nanofluid containing titania nanosheets (TNS) is predicted and compared with water and aqueous solution with 20% v/v ethylene glycol (EG) based on simulation.

2. Numerical model

To investigate the active magnetic regenerator, a one dimensional transient numerical model [10] is used. Considering the conduction, enthalpy flow, heat transfer between fluid and solid, viscous dissipation, energy storage and magnetic work, the governing equations for the heat transfer liquid and solid refrigerant are:

$$\frac{\partial}{\partial x}\left(k_{disp}\frac{\partial T_f}{\partial x}\right)A_c - \dot{m}_f c_f \frac{\partial T_f}{\partial x} - \frac{Nuk_f}{d_h}a_s A_c\left(T_f - T_r\right) + \left|\frac{\partial P}{\partial x}\frac{\dot{m}_f}{\rho_f}\right| = \rho_f A_c \varepsilon c_f \frac{\partial T_f}{\partial t} \quad (1)$$

$$\frac{\partial}{\partial x}\left(k_{stat}\frac{\partial T_r}{\partial x}\right)A_c + \frac{Nuk_f}{d_h}a_s A_c\left(T_f - T_r\right) = A_c(1-\varepsilon)\rho_r\left[c_{\mu_0 H}\frac{\partial T_r}{\partial t} + T_r\left(\frac{\partial s_r}{\partial H}\right)_T\frac{\partial H}{\partial t}\right] \quad (2)$$

where k, T, ρ, c and s are the thermal conductivity, temperature, density, specific heat and specific entropy; A_c, x, t, $\dot{m}_f$ and H are the cross sectional area, axial position, time, mass flow rate and internal magnetic field. The subscripts f and s represent fluid and solid refrigerant, respectively.

The central difference and implicit time schemes are used for discretizing the governing equations in both space and time domains. Given the initial temperature, mass flow rate and applied magnetic field, the fluid and solid temperatures can be solved at each time step. After reaching a periodical steady state with a specified tolerance, the simulation will be terminated and the indices, such as cooling power and COP, are output. In the simulation, the number of the space and time nodes is 100 and 4000 respectively. More details for the expressions of thermal conductivity due to fluid dispersion, static thermal conductivity, pressure drop and Nusselt number are described in Ref. [12].

According to the second law of thermodynamics, the entropy production of an irreversible thermal process $\dot{S}_p$ is larger than zero, and for a reversible process $\dot{S}_p = 0$. The entropy production can be used to evaluate the irreversibility and the method of entropy production minimization is widely utilized to optimize the thermal system. Considering an amount of heat $\Delta Q = kAdT/dx$ is transferred between two adjacent elements with temperature T_1 and T_2 ($T_1 > T_2$). The entropy changes in both sides are $-\Delta Q/T_1$ and $\Delta Q/T_2$, resulting in a total entropy change of $-\Delta Q/T_1 + \Delta Q/T_2 = \Delta Q(T_1 - T_2)/T_1 T_2$, which is also the entropy production of this process for an isolated system. Based on the numerical model, the entropy production due to insufficient heat transfer, viscous dissipation and axial conduction are calculated in Eqns. 3-6[10,13]:

$$\dot{S}_{p,ht} = \frac{1}{\tau}\int_0^\tau\int_0^L h a_s A_c \frac{\left(T_f - T_s\right)^2}{T_f T_s}dxdt + \frac{1}{\tau}\int_0^\tau \left|\dot{m}_f\right| c_f\left(\ln\frac{T_C}{T_{f,x=L}} + \frac{T_{f,x=L} - T_C}{T_C} + \ln\frac{T_H}{T_{f,x=0}} + \frac{T_{f,x=0} - T_H}{T_H}\right)dt \quad (3)$$

$$\dot{S}_{p,vd} = \frac{1}{\tau}\int_0^{\tau}\int_0^{L}\frac{|\dot{m}_f|}{\rho_f T_f}\frac{\partial P}{\partial x}dxdt \quad (4)$$

$$\dot{S}_{p,ac} = \frac{1}{\tau}\int_0^{\tau}\int_0^{L}\left[k_{stat}A_c\frac{1}{T_s{}^2}\left(\frac{dT_s}{dx}\right)^2 + k_{disp}A_c\frac{1}{T_f{}^2}\left(\frac{dT_f}{dx}\right)^2\right]dxdt \quad (5)$$

$$\dot{S}_{p,tot} = \dot{S}_{p,ht} + \dot{S}_{p,vd} + \dot{S}_{p,ac} \quad (6)$$

where $\dot{S}_{p,ht}$, $\dot{S}_{p,vd}$ and $\dot{S}_{p,ac}$ are the entropy production rates due to insufficient heat transfer, viscous dissipation and axial conduction, respectively; $\dot{S}_{p,tot}$ is the total entropy production rate; L and τ are the regenerator length and the cycle period.

3. Results and discussion

3.1. Multi-layer regenerator using magnetocaloric material with FOPT or SOPT

In a multi-layer AMR, various magnetocaloric materials with different T_{Curie} are aligned along the regenerator following the temperature gradient. For modeling such a multi-layer AMR, the entropy data as a function of the internal magnetic field and temperature of numerous materials are needed. It is assumed that those entropy data can be obtained by shifting the measured data of the base material according to the designed T_{Curie}. Here La(Fe,Mn,Si)$_{13}$H$_y$ with T_{Curie}=31.8 ºC and Gd are the base materials for the FOPT and SOPT materials respectively, and the isothermal entropy change of two materials [9] are presented in Figure 2. Here an even Curie temperature distribution, $T_{Curie,n} = T_H - (T_H - T_C)(2n-1)/2n$ where n is the layer number, is expected. That is, the T_{Curie} difference between each layer is the same. Table 1 summarizes the parameters for modeling AMRs using the FOPT or SOPT materials.

Figure 3 shows the specific cooling power of the multi-layer AMRs using the FOPT or SOPT materials. Here the specific cooling power is the maximum value obtained with optimum mass flow rate. For two groups of AMRs, the specific cooling power generally increases with decreased temperature span or increased layers. Compared to the SOPT materials, although the ΔS_m peak of

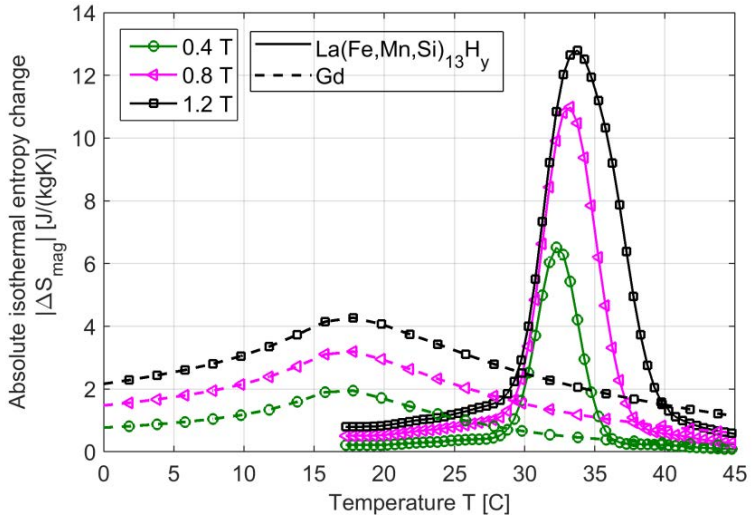

Figure 2. The absolute value of isothermal entropy change $|\Delta S_m|$ of La(Fe,Mn,Si)$_{13}$H$_y$ and Gd as a function of temperature [9]

Table 1. Parameters for modeling AMRs using the FOPT or SOPT materials

Parameter	Value
Maximum applied field	1.4 T
Temperature span	5-35 ºC
Frequency	2 Hz
Number of layers	1-40
Regenerator bed number	12
Cross sectional area of regenerator	625 mm^2
Regenerator length	50 mm
Bed geometry	Packed spheres
Sphere diameter	0.3 mm
Porosity	0.36
Heat transfer fluid	Aqueous solution with 20% v/v ethylene glycol
Thermal conductivity of $La(Fe,Mn,Si)_{13}H_y$	8 W/(m·K)
Density of $La(Fe,Mn,Si)_{13}H_y$	7000 kg/m^3
Thermal conductivity of Gd	11 W/(m·K)
Density of Gd	7900 kg/m^3

FOPT materials is much larger, ΔS_m rapidly decreases when the working temperature is away from T_{Curie}. Due to this, more layers are needed to cover a certain temperature span for the FOPT materials, which is also reflected in Figure 3. For AMRs using the FOPT materials more layers are necessary to get close to the theoretical specific cooling power, which is achieved when $N_L = 40$, while for the SOPT materials $N_L = 8$. However, the theoretical specific cooling power reachable with the FOPT materials is larger, especially when the temperature span is relatively small.

To show the influence of number of layers, the specific cooling power is further normalized to the theoretical specific cooling power and presented in Figure 4. Here the theoretical specific cooling power is obtained with $N_L = 40$ or $N_L = 8$ for two groups of AMRs, since little improvement is expected with even more layers. It shows that the nominal cooling power increases significantly with an increase in the number of layers, and fewer layers are needed for smaller temperature span, for both groups. It is clear, that more layers are desired for the FOPT materials to approach the maximum performance.

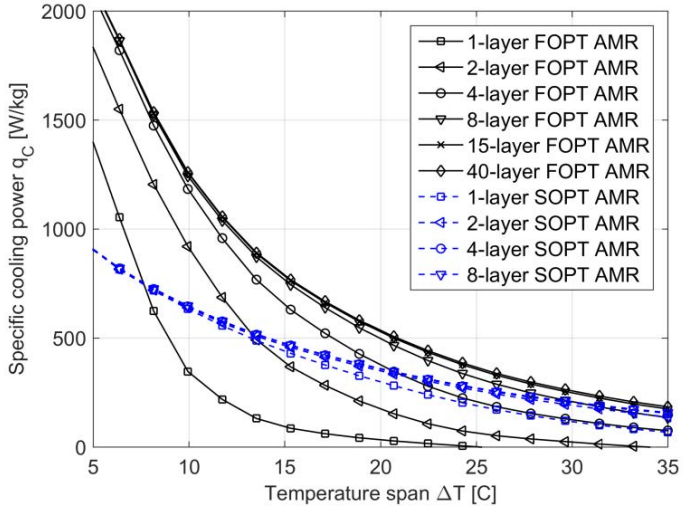

Figure 3. Specific cooling power of the multi-layer AMRs using the FOPT or SOPT materials as a function of temperature span

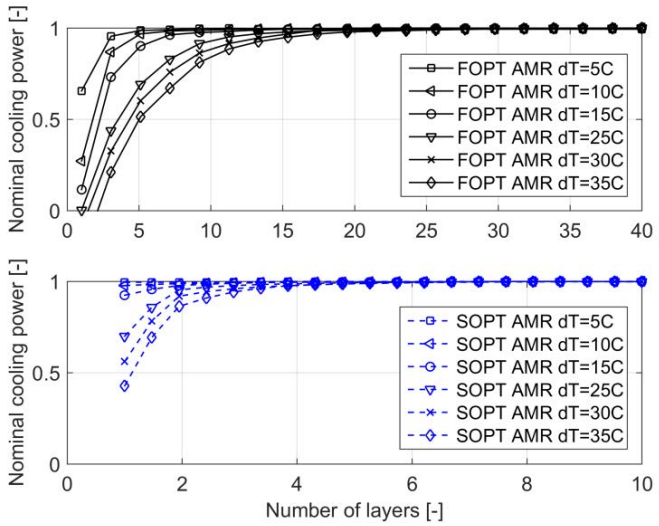

Figure 4. Nominal specific cooling power of the multi-layer AMRs using the FOPT or SOPT materials as a function of number of layers

However, building a regenerator with 40 layers may not be practical and tuning the Curie temperature with high accuracy is also difficult. Therefore, reasonable number of layers is proposed to get 90% of the theoretical specific cooling power, as shown in Figure 5. For the FOPT material, the curves of number of layers show an approximately linear relation and about 12 layers are needed with a temperature span of 35 ºC for realizing 90% maximum performance, while only 1-2 layers are necessary for the SOPT materials. It is also clear, larger specific cooling power can be obtained with the FOPT materials, and a specific cooling power of about 500 W/kg can be obtained when the temperature span is 20 ºC, while 330 W/kg for the SOPT materials.

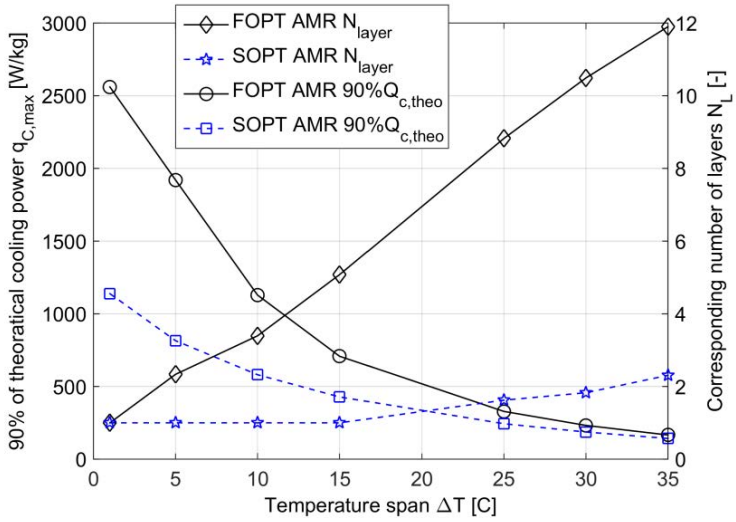

Figure 5. 90% of the theoretical maximum specific cooling power and corresponding number of layers as functions of temperature span.

3.2. Optimization of regenerator geometry and operation

In this section, we present an investigation of the influence of different geometry and operating parameters, including the aspect ratio and frequency, on the AMR performance and various loss mechanisms. Table 2 shows the modelling parameters in the simulation. Gd is used as the refrigerant and water mixture with 20 % v/v ethylene glycol as the heat transfer fluid. Here the

regenerator volume is held constant and the aspect ratio $R_a = L/\sqrt{A_c}$ can fully describe the regenerator shape. The flow rate is always optimized to get the specific cooling power of 100 W/kg for maximum the efficiency. In this way, the frequency becomes the only operating parameter to be optimized.

Table 2. Parameters for optimizing AMR geometry and operation

Parameter	Value
Maximum applied field	1.2 T
Temperature span	7 - 27 ºC
Frequency	0.3 - 10 Hz
Regenerator volume	2.25×10^4 mm^3
Bed geometry	Packed sphere
Number of regenerator beds	20
Aspect ratio	1.5 - 6
Hydraulic diameter	0.15 mm
Porosity	0.36
Heat transfer fluid	Aqueous solution with 20% v/v ethylene glycol
MCM	Gd

Figure 6 shows the COP of AMRs using a packed sphere bed as a function of the frequency and aspect ratio. The hydraulic diameter is 0.15 mm, corresponding to a sphere diameter of 0.43 mm. The aspect ratio ranges from 1.5 to 6 and the frequency from 0.3 to 10 Hz. It is found that the maximum COP of 6.5 can be obtained when the aspect ratio and frequency are 2.5 and 1.9 Hz, respectively. Too large or small frequency and aspect ratio leads to a significant decrease in COP.

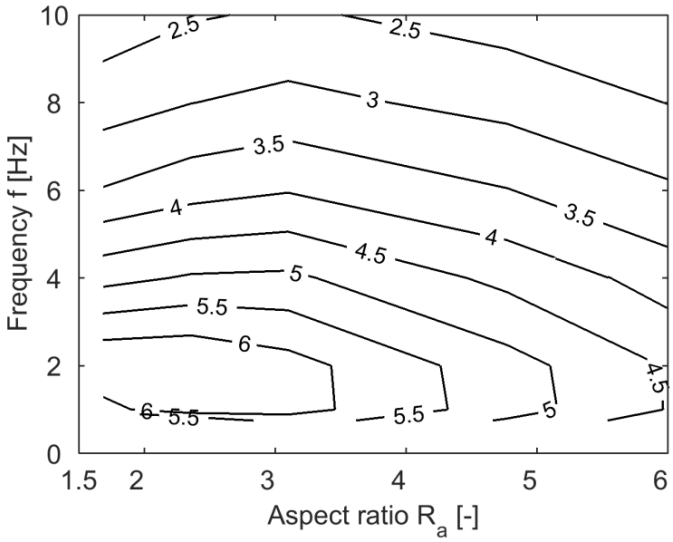

Figure 6. COP as a function of frequency and aspect ratio for AMRs using packed sphere bed with a hydraulic diameter of 0.15 mm

Figure 7a shows the total entropy production rates $\dot{S}_{p,tot}$ as a function of frequency and aspect ratio, which has a reversed pattern compared to the results of COP in Figure 6. The minimum total production rate is found at the position where the maximum COP appears. As seen in Figure 7b, the entropy production rates due to insufficient heat transfer $\dot{S}_{p,ht}$ is strongly related to the frequency rather than the aspect ratio. In contrast, the entropy production rate due to viscous dissipation $\dot{S}_{p,vd}$ in Figure 7c is more sensitive to the aspect ratio than the frequency. Since the axial conduction loss

increases when the cross sectional area becomes larger and the length shorter, $\dot{S}_{p,ac}$ increases significantly with decreasing aspect ratio, however the frequency does not affect $\dot{S}_{p,ac}$ much. In most cases, the entropy production rates representing insufficient heat transfer and viscous dissipation contribute most to the total entropy production rate, whereas the entropy production rate due to axial conduction becomes significant when the aspect ratio is smaller than 2.0. At the point of minimum total entropy production rate, the insufficient heat transfer contributes the most; the second is the viscous dissipation, while the last is axial conduction.

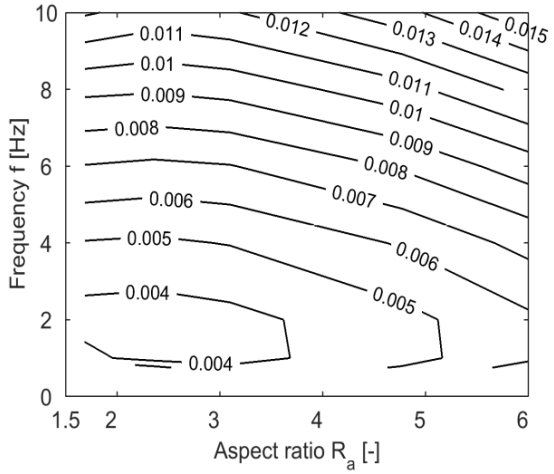

(a) Total entropy production rate consisted by three parts $\dot{S}_{p,tot}$

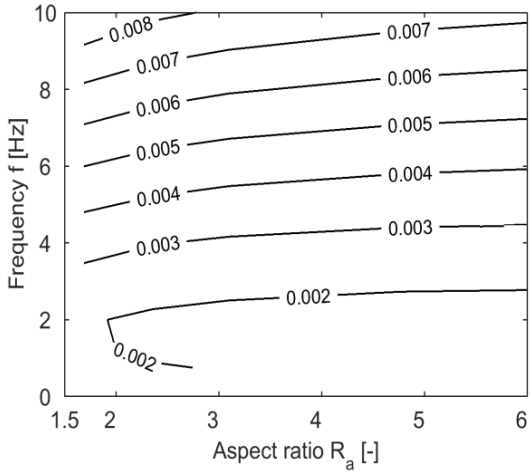

(b) Entropy production rate due to insufficient heat transfer $\dot{S}_{p,ht}$

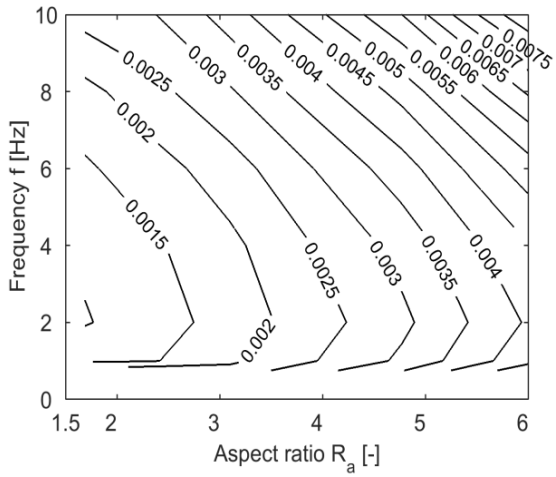

(c) Entropy production rate due to viscous dissipation $\dot{S}_{p,vd}$

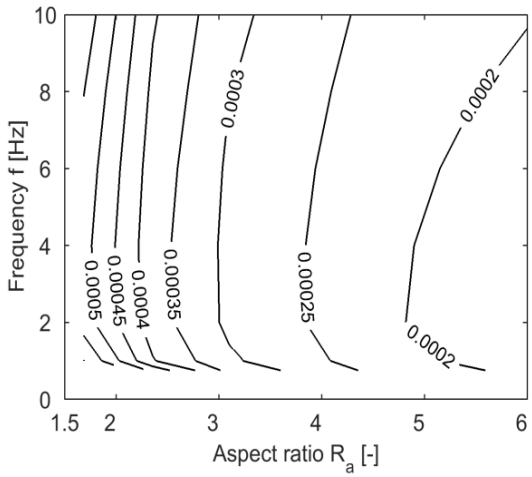

(d) Entropy production rate due to axial conduction $\dot{S}_{p,ac}$

Figure 7. Entropy production rates as a function of frequency and aspect ratio of AMRs using packed sphere bed with a hydraulic diameter of 0.15 mm

3.3. Optimization of heat transfer fluids

Increasing the heat transfer coefficient is beneficial for improving the AMR performance. In general reducing the hydraulic diameter of the regenerator bed could increase the overall heat transfer coefficient; however, it raises the risk of high viscous dissipation and overpressure due to too small channels. An alternative approach is to use a heat transfer fluid with high conductivity and low viscosity. Compared to aqueous solution with anti-corrosion additives and pure water, nanofluids may have higher thermal conductivity and convective heat transfer coefficient [11]. By adjusting the concentration of particles, the dynamic viscosity of a nanofluid can be controlled to an acceptable level. In this section, the performance of AMRs using different heat transfer fluids; water, aqueous solution with 20% v/v ethylene glycol and nanofluid containing TNS, are presented and compared.

The modeling parameters are presented in Table 1 and an AMR using a one-layer Gd regenerator is simulated. The temperature span and the frequency are 20 ºC and 2 Hz, respectively. Ref. [14] shows that the enhancement in heat transfer coefficient with nanofluids compared to water lies between 10 to 15% in the packed bed. Therefore, in the simulation, the heat transfer coefficient with nanofluid is assumed 1.1 times that of the original correlations as shown in Ref. [12]. The thermal conductivity and the dynamic viscosity of nanofluid are considered 0.6 W/(m·K) and 0.001 Pa·s respectively. The predicted specific cooling powers of AMRs using different heat transfer fluids are presented in Figure 8. The results show that the nanofluid presents the best performance with a peak value of 341 W/kg, which is higher than 325 or 302 W/kg for the other two fluids. Correspondingly, Figure 9 shows the COP of AMRs using three heat transfer fluids, and the nanofluid also exhibits the highest efficiency. Combined with the anti-corrosion additives, the nanofluid could be a promising heat transfer fluid for further improving the AMR performance.

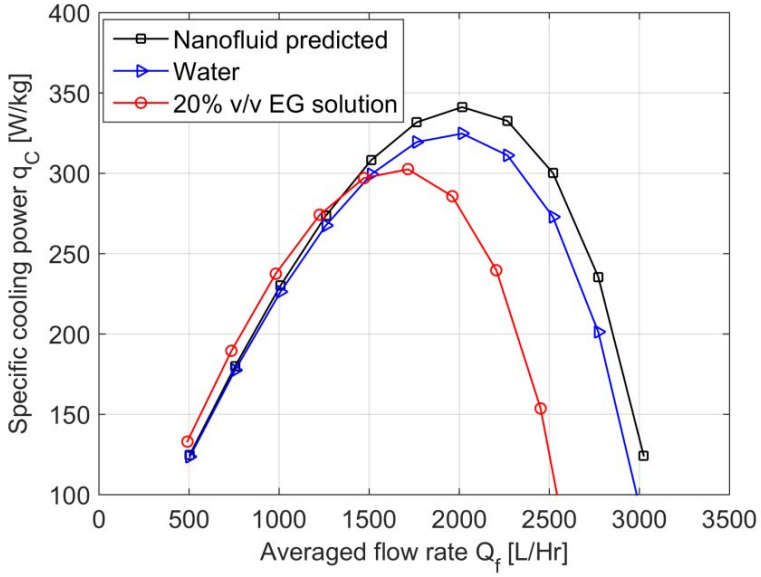

Figure 8. Specific cooling power as a function of average flow rate for AMRs using different heat transfer fluids

4. Conclusions

A 1D transient numerical model for simulating the multi-layer AMRs and an experiment apparatus for testing the heat transfer fluids in passive regenerators were developed and presented. Based on

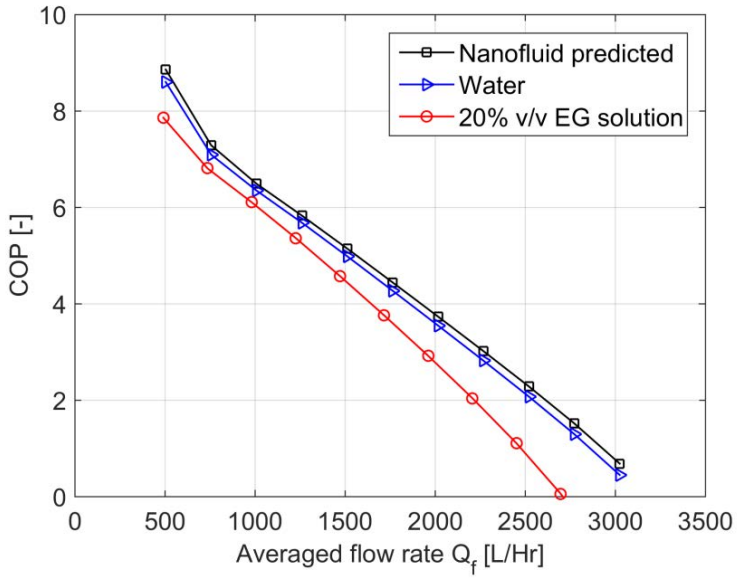

Figure 9. COP as a function of average flow rate for AMRs using different heat transfer fluids

the simulation, the influences of the number of layers and temperature span on the performance of AMRs using the FOPT or SOPT materials are quantified and compared. The results show that more layers are necessary to approach the theoretical specific cooling power for AMRs using the FOPT materials. The theoretical specific cooling power reachable with the FOPT materials is significantly lager, especially when the temperature span is relatively small, which is important for designing a compact refrigeration system. Further, a reasonable number of layers, that is 12 layers for a temperature span of 35 ºC, is proposed to get 90% of the theoretical specific cooling power for AMRs using the FOPT material. A multi-parameter optimization for maximizing the efficiency is presented combined with the method of entropy production minimization. It shows the insufficient heat transfer and viscous dissipation contribute the most and the axial conduction is less important. The performance of AMRs using three heat transfer fluids, which are water, aqueous solution with 20% v/v ethylene glycol and nanofluid, are predicted and compared. The results of the specific cooling power and the COP show that the nanofluid presents the best performance, which indicates that nanofluid could be a promising heat transfer fluid for future MCR devices.

Acknowledgments

This work was financed by the ENOVHEAT project which is funded by Innovation Fund Denmark (contract no 12-132673). The authors would like to thank Vacuumschmelze GmbH & Co., Germany for providing the $La(Fe,Mn,Si)_{13}H_y$ material.

Nomenclature

a_s	specific surface area, 1/m
A_c	cross sectional area, m^2
B	applied magnetic field, tesla
c	specific heat capacity, J/(kg·K)
c_H	specific heat capacity of magnetocaloric material at constant magnetic field, J/(kg·K)
d_h	hydraulic diameter, m
f	frequency, Hz
h	specific enthalpy, J/kg
H	internal magnetic field, tesla
k	thermal conductivity, W/(m·K)

k_{disp} thermal conductivity of the fluid due to axial dispersion, W/(m·K)
k_{stat} static thermal conductivity of regenerator and fluid, W/(m·K)
L regenerator length, m
$\dot{m}_f$ mass flow rate, kg/s
n layer number
N_L number of layers
Nu Nusselt number
P pressure, Pa
$\dot{q}_C$ specific cooling power, W/kg
$\dot{Q}_f$ average flow rate, L/Hr
R_a aspect ratio
s_s specific entropy of solid refrigerant, J/(kg·K)
S Entropy
$\dot{S}_{p,ac}$ entropy production rate due to axial conduction, W/K
$\dot{S}_{p,ht}$ entropy production rate due to insufficient heat transfer, W/K
$\dot{S}_{p,vd}$ entropy production rate due to viscous dissipation, W/K
$\dot{S}_{p,tot}$ total entropy production rate, W/K
t Time, s
T temperature, ºC
u specific internal energy, J/kg
V_r regenerator volume, m^3
x axial position, m

Abbreviations

AMR active magnetic regenerator
COP coefficient of performance
FOPT first order phase transition
MCM magnetocaloric material
MCR magnetocaloric refrigeration
NTU number of transfer units
SOPT second order phase transition

Greek symbols

μ dynamic viscosity, mPa·s
ρ density, kg/m^3
ε porosity
τ cycle period, s
Δ increment

Subscripts and superscripts

ad adiabatic process
Curie Curie temperature
C cold end
f fluid
H hot end
m magnetic
s solid

References

[1] Tura A., Rowe A., Progress in the characterization and optimization of a permanent magnet magnetic refrigerator. Proceedings of the Third International Conference on Magnetic Refrigeration at Room Temperature, 2009.

[2] Engelbrecht K., Eriksen D., Bahl C. R. H., Bjørk R., Geyti J., Lozano J. A., Nielsen K. K., Saxild F., Smith A., Pryds N., Experimental results for a novel rotary active magnetic regenerator. International Journal of Refrigeration 2012;(35): 1498-1505.

[3] Jacobs S., Auringer J., Boeder A., Chell J., Komorowski L., Leonard J., Russek S., Zimm C., The performance of a large-scale rotary magnetic refrigerator. International Journal of Refrigeration 2014;(37):84-91.

[4] Eriksen D., Engelbrecht K., Bahl C. R. H., Bjørk R., Nielsen K. K., Insinga A. R., Pryds N., Design and experimental tests of a rotary active magnetic regenerator prototype. International Journal of Refrigeration 2015;(58):14-21.

[5] Kitanovski A., Tušek J., Tomc U., Plaznik M., Ozbolt M., Poredoš A., Magnetocaloric Energy Conversion: From Theory to Applications. Springer 2014.

[6] Gschneidner Jr. K. A., Pecharsky V. K., Tsokol A. O., Recent developments in magnetocaloric materials. Reports on Progress in Physics 2005;(68):1479-1539.

[7] Smith A., Bahl C. R. H., Bjørk R., Engelbrecht K., Nielsen K. K., Pryds N., Materials challenges for high performance magnetocaloric refrigeration devices. Advanced Energy Materials 2012;(11):1288-1318.

[8] Barclay J. A., Theory of an active magnetic regenerative refrigerator. NASA Conference Publication, 1983:375-387.

[9] Lei T., Nielsen K. K., Engelbrecht K., Bahl C. R. H., Neves Bez H., Veje C. T., Sensitivity study of multi-layer active magnetic regenerators using first order magnetocaloric material $La(Fe,Mn,Si)_{13}H_y$. Journal of applied physics 2015;118(1):014903.

[10] Lei T., Engelbrecht K., Nielsen K. K., Veje C. T., Study of geometries of active magnetic regenerators for room temperature magnetocaloric refrigeration. Applied Thermal Engineering, 2015, in print.

[11] Wang X., Mujumdar, A. S., Heat transfer characteristics of nanofluids: a review. International journal of thermal sciences 2007;(46):1-19.

[12] Nielsen K. K., Engelbrecht K., Bahl C. R. H., The influence of flow maldistribution on the performance of inhomogeneous parallel plate heat exchangers. International Journal of heat and Mass transfer 2013;(60):432-439.

[13] Li P., Gong M., Wu J., Geometric optimization of an active magnetic regenerative refrigerator via second-law analysis. Journal of applied physics 2008;104(10):103536.

[14] Srinivasa Rao G., Sharma K. V., Chary S. P., Bakar R. A., Rahman M. M., Kadirgama K., Noor M. M., Experimental study on heat transfer coefficient and friction factor of Al_2O_3 nanofluid in a packed bed column. Journal of Mechanical Engineering and Sciences 2011;(1): 1-15.

A.7 Modelling and simulation of regenerators with complex flow arrangements for active magnetocaloric refrigeration

T. Lei, K. K. Nielsen, K. Engelbrecht, et al., Modelling and simulation of regenerators with complex flow arrangements for active magnetocaloric refrigeration, *Proceedings of the ASME 12th Biennial Conference on Engineering Systems Design and Analysis*,Copenhagen, (2014).

Proceedings of 12th Biennial Conference on Engineering Systems Design and Analysis
ESDA 2014
June 25-27, 2014, Copenhagen, Denmark

ESDA2014-20146

MODELLING AND SIMULATION OF REGENERATORS WITH COMPLEX FLOW ARRANGEMENTS FOR ACTIVE MAGNETOCALORIC REFRIGERATION

Tian Lei, Kaspar K. Nielsen and Kurt Engelbrecht
DTU Energy Conversion
Technical University of Denmark
Frederiksborgvej 399
4000 Roskilde, Denmark
Email: tile@dtu.dk

ABSTRACT

Compared to a conventional vapor compression refrigeration system, a magnetocaloric refrigerator has many advantages, such as potentially high efficiency, low vibration and avoidance of refrigerants that deplete the ozone layer and cause the greenhouse effect. As a main component of the active magnetic regenerative refrigerator, the regenerator plays an important role in the cooling performance and efficiency of the whole system. However, the regenerator design is constrained by several external factors, such as the geometry of the magnetic field source and flow resistance.

In this work, novel regenerators with complex flow arrangements, providing high performance at lower pressure drop, are investigated. Correspondingly a one dimensional model is presented and comparative studies between novel and conventional regenerators are carried out by simulation. The effect of regenerator geometries and different flow arrangements on the cooling performance, pressure drop and efficiency are investigated. In particular, the effect of so-called dead volume on the performance of a regenerator is researched.

NOMENCLATURE

a_s specific surface area (m^2/m^3)
A_c cross section area (m^2)
AMR active magnetic regeneration
c specific heat capacity (J/kg-K)
$c_{\mu_o H}$ specific heat capacity at constant magnetic field (J/kg-K)
COP coefficient of performance
d_h hydraulic diameter (m)
dP pressure drop (Pa)
h heat transfer coefficient (W/m^2-K) or enthalpy (J/kg-K)
I flow direction judgement index
k thermal conductivity (W/m-K)
k_{disp} thermal conductivity of the fluid due to axial dispersion (W/m-K)
k_{eff} effective static thermal conductivity of regenerator and fluid (W/m-K)
L length (m)
MC monotonized centered
MCE magnetocaloric effect
$\dot{m}$ mass flow rate (kg/s)
Nt number of steps used in numerical solution
Nu Nusselt number
Nx number of axial control volumes used in numerical solution
NTU number of transfer units
P pressure (Pa)
R dead volume ratio
R_{area} non-dimensional cross sectional area
s entropy (J/kg-K)
t time (s)
v fluid velocity (m/s)
T temperature (K)
TVD total variation diminishing
u specific internal energy (J/kg)
x axial position (m)

Greek
ε porosity of the regenerator bed
μ magnetic permeability (H/m)
$\mu_o H$ applied field (Tesla)
σ monotonized centered limiter
θ dimensional temperature difference
ρ density (kg/m^3)
Δx length of control volume (m)
Δt time step (s)
Δs magnetic entropy change (J/kg-K)

Subscripts
area cross section area
C cold or refrigeration temperature
eff effective
f fluid
H hot or heat rejection temperature
i spatial subscript
j temporal subscript
L left
new new regenerator
r regenerator material
reg regenerator
R right
s surface

INTRODUCTION

Magnetic refrigeration is a technology based on the magnetocaloric effect (MCE), which appears in magnetic materials. When varying an externally applied magnetic field to any magnetic material the magnetic contribution to the entropy of the system will change (for ferro- and paramagnets it will decrease upon an increase in field). Under adiabatic conditions this is associated with an increase in temperature since the lattice and electronic contributions to the entropy must increase for the process to be adiabatic. In soft ferromagnets the process is reversible, and thus the temperature will decrease upon reduction of the externally applied magnetic field. When applying / removing the external magnetic field isothermally, the total entropy of the system will change with an amount equivalent to the magnetic entropy change, Δs_{m}.

The magnetic entropy change is a function of magnetic field and temperature, with a peak in the vicinity of the Curie, or magnetic ordering, temperature of the material. Generally, the magnetic entropy change increases with the magnitude of the applied field. The magnitude of the magnetic entropy change varies from material to material as does the Curie temperature, specific heat and thus adiabatic temperature change. It is, however, a common factor that in magnetic fields reachable with conventional permanent magnets (of the order 1.5 T) the adiabatic temperature change will be about 5 K at the peak for the best performing materials (see, e.g., Refs. [1, 2] for reviews).

In order to achieve useful temperature spans for applications such as domestic refrigeration or heat pumps, it is therefore necessary to apply the regeneration principle [3]. In this way the magnetocaloric material is arranged as a solid porous matrix through which a heat transfer fluid may flow in a periodic manner. The principle is called an active magnetic regeneration (AMR) and may be considered as a process consisting of four steps: i) adiabatic magnetization, where the temperature increases. ii) fluid flow from cold to hot end, and fluid rejects excess heat to the ambient. iii) adiabatic demagnetization, and the temperature decreases below the initial state and iv) fluid flow from the hot to the cold end while fluid absorb heat, i.e. cooling load, at the cold end.

The AMR process cannot be described in a single T-S diagram since each differential element throughout the regenerator undergoes its own unique cycle due to the fact that a temperature gradient exists between the hot and cold ends. In order to predict and understand the behavior of a device utilizing the AMR process it is therefore necessary to apply a thermal regenerator model with a model of the magnetocaloric effect including the behavior of the magnetic field. In the simplest form the adiabatic temperature change may be considered to be constant (with a slightly temperature-dependent specific heat) and the applied field to be constant in space while changing instantaneously when magnetizing / demagnetizing. More advanced and detailed models solve for the local magnetic field through each time step as well as include the MCE in a realistic way based on experimental data [4].

There are many aspects to an AMR system. One of these is the configuration of the regenerator, which may affect the overall performance significantly. And it is also restricted by the magnetized volume of a magnet assembly, where the regenerators are installed. In various existing prototypes, generally the magnetized volume of the magnet assembly shows an elongated shape with different cross section configurations. In the magnet for the prototype at Technical University of Denmark (DTU), an external radius of the inner magnet of 70 mm and an internal radius of the outer magnet of 100 mm were chosen, and a ring of 24 regenerators was installed in the magnetized volume between the inner and outer magnets. The maximum regenerator length that the magnet can accommodate is 250 mm, although the current regenerator length is only 100 mm and the cross sectional area of each regenerator is 238 mm^2 [5]. For such a long regenerator with packed gadolinium (Gd) spheres the pressure drop is considerable. However, to get a magnet with a large magnetized volume will raise the cost a lot and make the device uneconomic.

The performance of an AMR refrigerator can be analyzed by using the following time-average equation. In Eqn. 1, each term is the time-average cooling power, heat rejection, pump power

consumption, motor power consumption, and total loss including axial conduction and heat loss to the environment, etc. The pump in an AMR system provides sufficient head to overcome the flow resistance of a regenerator and cycle the heat transfer fluid continuously, and the pump work $\langle \dot{W}_{pump} \rangle$ is a large part of work input. It is noticed that large pressure drop will cause a substantial viscous dissipation loss and make $\langle \dot{W}_{pump} \rangle$ raise, which reduces the coefficient of performance (COP), shown as Eqn. 2. Meanwhile, it also brings some problems such as resistance to pressure and seals, etc., in the real design.

$$\langle \dot{Q}_H \rangle = \langle \dot{Q}_C \rangle + \langle \dot{W}_{pump} \rangle + \langle \dot{W}_{motor} \rangle + \langle \dot{Q}_{loss} \rangle \quad (1)$$

$$COP = \frac{\langle \dot{Q}_C \rangle}{\langle \dot{W}_{pump} \rangle + \langle \dot{W}_{motor} \rangle} \quad (2)$$

Aiming at an efficient and compact regenerator with lower pressure drop, this paper proposes a group of new regenerators with complex flow arrangements. In order to investigate new regenerators systematically, a detailed one dimensional model is presented first. Then the impact of different cross section areas is studied to show the original idea of the new regenerators. Moreover three new regenerators with complex flow arrangements, which could have improved performance, are simulated and compared to the conventional one. Furthermore, the effect of dead volume which is supposed to exist in the new regenerators is researched and a tolerance dead volume ratio is proposed.

NEW REGENERATORS WITH COMPLEX FLOW ARRANGEMENTS

The new regenerators with complex flow arrangements are shown in Fig. 1. It is emphasized that the new regenerator (b) - (d) have the same amount of Gd spheres (0.116 kg) as the conventional regenerator (a) does, which has a length of 100 mm and a cross sectional area of about 238 mm^2. However, in the new regenerators separating walls are installed to force the heat transfer liquid flow through a larger cross sectional area, which are 1.32, 1.65, and 2.20 times of the original, respectively. By this method the flow inside the regenerator is re-distributed and it will flow through the whole regenerator with a lower flow resistance, which may reduce the viscous dissipation loss and improve the regenerator efficiency.

Moreover, to make the heat transfer fluid flow smoothly between regenerator compartments and reduce the flow resistance, empty ducts are assumed to connect these chambers, which are set to take a total volume ratio of 5%, as shown in Fig.1. These empty ducts can also be seen as dead volume, where an amount of fluid not in contact with the solid regenerator material is left after the cold / hot blow period. Due to this, the dead volume will cause a regenerator loss. This effect will be researched in following.

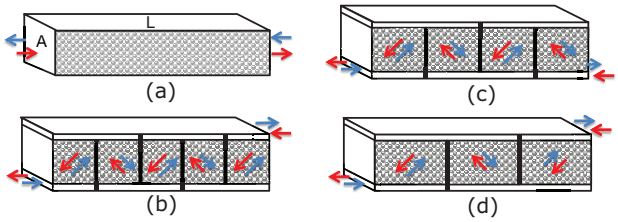

FIGURE 1. THE NEW REGENERATORS WITH COMPLEX FLOW ARRANGEMENTS: (A) THE CONVENTIONAL REGENERATOR; (B) 5-COMPARTMENT REGENERATOR; (C) 4-COMPARTMENT REGENERATOR; (D) 3-COMPARTMENT REGENERATOR.

These new regenerators maintain compactness and can be used in the prototype at DTU [5]. In this system, also the simulation model presented below, a ring of 24 regenerators is rotated in the gap of the concentric cylindrical magnet assembly, and the rotation will make each regenerator experience high and low magnetic field regions periodically. Synchronized with that, the heat transfer fluid flow is controlled by two rotary multi-channel valves to flow from hot-to-cold while in a low field region and from cold-to-hot while in a high field region. The Gd spheres and water mixed with 25% ethylene glycol are chosen as the solid material and heat transfer fluid, separately. The magnetocaloric properties have been presented previously [6].

MODEL

This section presents a detailed one dimensional transient numerical model for simulating the new magnetocaloric regenerators, based on the model developed by Engelbrecht [7]. Considering heat transfer via conduction and convection in a regenerator bed, the partial differential equations of the heat transfer fluid and magnetocaloric material can be written as:

$$k_{disp}A_c\frac{\partial^2 T_f}{\partial x^2} - \dot{m}\frac{\partial h_f}{\partial x} - \frac{Nuk_f}{d_h}a_sA_c(T_f - T_r) + \left|\frac{\partial P}{\partial x}\frac{\dot{m}}{\rho_f}\right| = \rho_f A_c \varepsilon \frac{\partial u_f}{\partial t} \quad (3)$$

$$\frac{Nuk_f}{d_h}a_sA_c(T_f - T_r) + k_{stat}A_c\frac{\partial^2 T_r}{\partial x^2} + A_c(1-\varepsilon)\mu_o H\frac{\partial M}{\partial t} = \rho_r A_c(1-\varepsilon)\frac{\partial u_r}{\partial t} \quad (4)$$

where subscripts f and r represents the heat transfer fluid and regenerator material respectively. For a given control volume, fluid takes a fraction of $\varepsilon = 0.36$ which is the porosity, and the rest of the volume is solid.

From left to right, the term of Eqn. 4 is axial conduction, enthalpy flow, heat transfer, viscous dissipation and energy storage on the fluid side separately, and for solid governing equation, i.e., Eqn. 4, the terms are heat transfer, axial conduction, magnetic work, and energy storage respectively. The fluid and solid domains are coupled through the convective heat transfer term.

In seeking a numerical solution for these partial differential equations, discretizations have to be done in both space and time domains. In Engelbrecht's model [7], the central difference and implicit time schemes were utilized to discretize the equations in spatial and temporal domain respectively. However, facing with a discontinuity problem, e.g., the large temperature difference between incoming flow from the cold / hot reservoir and existing fluid in the regenerator bed, the solution of conventional method, like central difference scheme, shows spurious oscillation. The flux limiter method can be employed to capture sharper shock predictions without any misleading oscillations that would otherwise occur with high order spatial discretization schemes. Using a flux limiter, like the monotonized centered (MC) limiter [8], can make the solutions total variation diminishing (TVD) [9]. In this paper, the MC limiter is used to discretize the partial differential equations in space domain, and implicit time discretization method is utilized as the previous model did. The governing equations for liquid can be rewritten as follows.

If $\dot{m}(t_j) > 0$, i.e. the fluid flows from the cell 1 to N_x, then,

$$
\begin{aligned}
(T_{fi,j+1} - T_{fi,j})\rho_f A_{ci}\varepsilon_i c_{fi,j}\frac{\Delta x}{\Delta t} = \\
-\dot{m}_j c_{fi,j}\Bigg[T_{fi,j} - T_{fi-1,j} \\
+\Big(\frac{1}{2} - \frac{1}{2}\frac{|v_{i,j}|\Delta t}{\varepsilon_i \Delta x}\Big)\big(\sigma_{Ri,j}(T_{fi+1,j} - T_{fi,j}) - \sigma_{Li,j}(T_{fi,j} - T_{fi-1,j})\big)\Bigg] \\
+\frac{k_{dispi,j}A_{ci}}{\Delta x}(T_{fi-1,j+1} - 2T_{fi,j+1} + T_{fi+1,j+1}) \\
+h_{i,j}a_{si}A_{ci}\Delta x(T_{ri,j+1} - T_{fi,j+1}) + \frac{dP_{i,j}|\dot{m}_j|}{\rho_f} \quad (5)
\end{aligned}
$$

If $\dot{m}(t_j) < 0$, the discretized equation for fluid will be:

$$
\begin{aligned}
(T_{fi,j+1} - T_{fi,j})\rho_f A_{ci}\varepsilon_i c_{fi,j}\frac{\Delta x}{\Delta t} = \\
-\dot{m}_j c_{fi,j}\Bigg[T_{fi+1,j} - T_{fi,j} \\
+\Big(\frac{1}{2} - \frac{1}{2}\frac{|v_{i,j}|\Delta t}{\varepsilon_i \Delta x}\Big)\big(\sigma_{Li,j}(T_{fi,j} - T_{fi-1,j}) - \sigma_{Ri,j}(T_{fi+1,j} - T_{fi,j})\big)\Bigg] \\
+\frac{k_{dispi,j}A_{ci}}{\Delta x}(T_{fi-1,j+1} - 2T_{fi,j+1} + T_{fi+1,j+1}) \\
+h_{i,j}a_{si}A_{ci}\Delta x(T_{ri,j+1} - T_{fi,j+1}) + \frac{dP_{i,j}|\dot{m}_j|}{\rho_f} \quad (6)
\end{aligned}
$$

And $\sigma_{Li,j}$ and $\sigma_{Ri,j}$ are the MC limiters:

$$\sigma_{Li,j} = Max\Big(0, Min\Big(\frac{1+\theta_{Li,j}}{2}, 2, 2\theta_{Li,j}\Big)\Big), \quad (7a)$$

$$\theta_{Li,j} = \frac{T_{fI,j} - T_{fI-1,j}}{T_{fi,j} - T_{fi-1,j}}, \quad (7b)$$

$$\sigma_{Ri,j} = Max\Big(0, Min\Big(\frac{1+\theta_{Ri,j}}{2}, 2, 2\theta_{Ri,j}\Big)\Big), \quad (7c)$$

$$\theta_{Ri,j} = \frac{T_{fI+1,j} - T_{fI,j}}{T_{fi+1,j} - T_{fi,j}}, \quad (7d)$$

$$I = i-1, \text{if } \dot{m}(t_j) > 0, \quad (7e)$$

$$I = i+1, \text{if } \dot{m}(t_j) < 0. \quad (7f)$$

For the solid, the discretized equation is the same as shown in Ref. [7]. By using Eqns. 5 - 6 combined with the discretized equation for solid, the temperature profiles on both fluid and solid sides can be computed after each time step. At the beginning of the computation, the initial fluid and solid temperature is set to follow a linear distribution between the hot and cold reservoir temperature. The heat transfer fluid flows through the regenerator bed periodically, synchronized with the changing magnetic field. In the positive / negative blow period, the inflow temperature from the hot / cold reservoir is set to be constant, and the difference between these two temperatures is the temperature span of the magnetocaloric regenerator. The computation is terminated when cyclical steady state has been reached with a numerical tolerance. Finally, the cooling power and heat rejection can be calculated by the periodical enthalpy flux at both sides. Also the indexes like pressure drop and COP will be output at the end.

RESULTS AND DISCUSSION

Impact of non-Dimensional Cross Sectional Area

The efficiency of a regenerator largely depends on the heat transfer performance and loss reduction. The heat transfer performance can be improved by raising flow velocity, because the heat transfer coefficient h and Nusselt number $\mathrm{Nu} = hL/k$ have positive correlations with flow velocity. However, correspondingly the viscous dissipation loss will increase. Therefore, usually there will be an optimal flow rate to get the best performance of a regenerator. It can therefore be conceived that the efficiency of the regenerator can be improved by enlarging the cross sectional area optimally, where a reduced pressure drop can be achieved and the heat transfer is still sufficient and not degrading largely with the reduced velocity due to larger cross sectional area.

To verify this, a group of regenerators with larger cross sectional area and shorter length, which are packed with the same amount of Gd spheres are simulated and compared with the regenerator (a). In this paper, the frequency is set to be 2 Hz,

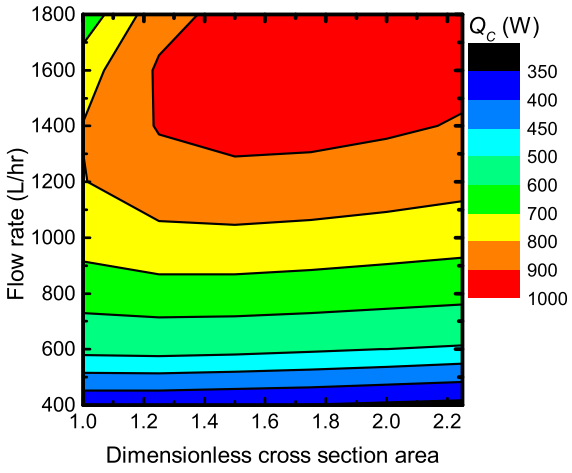

FIGURE 2. THE IMPACT OF DIMENSIONLESS CROSS SECTIONAL AREA AND FLOW RATE ON THE COOLING POWER WHEN THE TEMPERATURE SPAN IS 5 K.

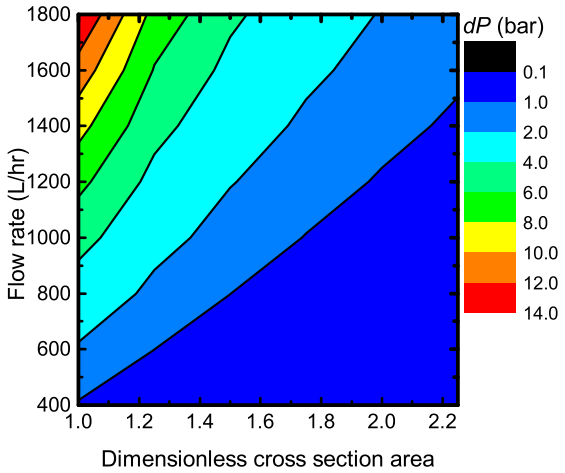

FIGURE 3. THE IMPACT OF DIMENSIONLESS CROSS SECTIONAL AREA AND FLOW RATE ON THE PRESSURE DROP WHEN THE TEMPERATURE SPAN IS 5 K.

and hot reservoir temperature is 300 K. Fig.2 shows the impact of the dimensionless cross sectional area, which is defined as $R_{area} = A_{new}/A_{reg(a)} = L_{reg(a)}/L_{new}$, on cooling power at different flow rates, when the temperature span is 5 K. Correspondingly, the results of pressure drop and COP are shown in Figs. 3 and 4. It can be seen that, although the cooling power does not change much with changing R_{area}, when the flow rate is relatively low and commonly seen in the AMR system, the pressure drop is reduced considerably and a larger COP is achieved when $R_{area} > 1$. For this reason the new regenerators with complex flow arrangements as shown in Fig. 1 show a potential for improved performance. Moreover, with a continuously raising flow rate, the cooling power when $R_{area} = 1$ fells after reaching a peak, because of the rapid increasing pressure drop as Fig.3 shown.

Regenerator Performance

The cooling power, pressure drop and COP of the new regenerators are presented in Figs. 5 - 6. The cooling power of regenerator (a) has a peak at about 1400 L/hr, whereas a monotonously increasing cooling power is observed in the new regenerators (b) - (d) with R_{area} of 1.32, 1.65, and 2.20, respectively. The rapidly increasing pressure drop, which brings large viscous dissipation loss, is the reason why the cooling power of regenerator (a) has an optimum at a significantly smaller flow rate than the regenerators (b) - (d) (see Figs. 5 - 6). In the low flow rate region which is usually applied, a lower pressure drop and larger COP can be achieved with the new regenerators although the cooling power decreases somewhat.

The cooling power and COP obtained in the new regenerators are shown in Fig. 7. It can be seen that at a low flow rate the

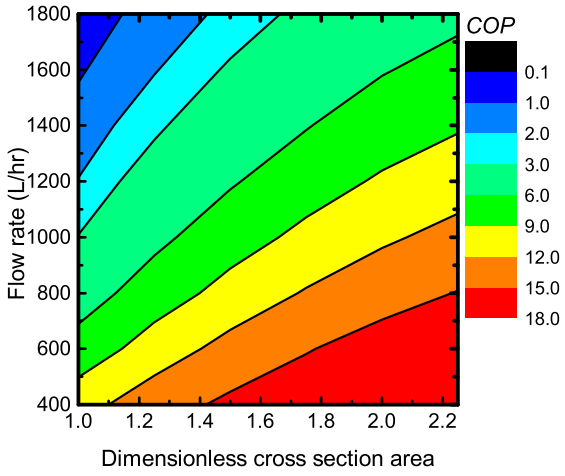

FIGURE 4. THE IMPACT OF DIMENSIONLESS CROSS SECTIONAL AREA AND FLOW RATE ON COP WHEN THE TEMPERATURE SPAN IS 5 K.

COP of the new regenerators is much higher at the same cooling power as compared to the original regenerator (a) in the top half of Fig. 7. It is noted that the flow rates are generally not coinciding for the four regenerators at a given set of cooling power and COP values.

The results of a temperature span of 15 K are shown in Figs. 8 - 10. Though the cooling power of the new regenerator is lower than the conventional regenerator (a) at the same flow rate, the trends of COP still show that the efficiency of the new regener-

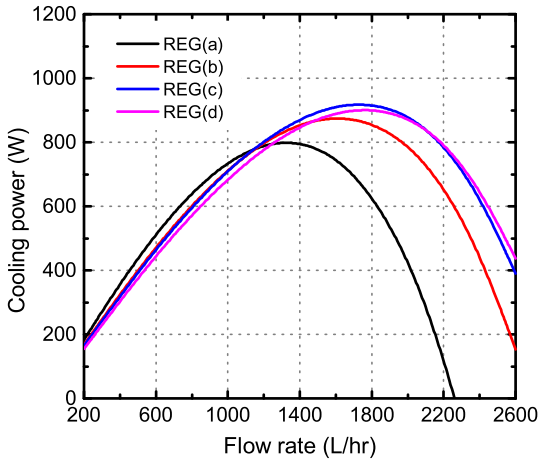

FIGURE 5. THE COOLING POWER OF REGENERATORS AS A FUNCTION OF FLOW RATE WHEN THE TEMPERATURE SPAN IS 5 K.

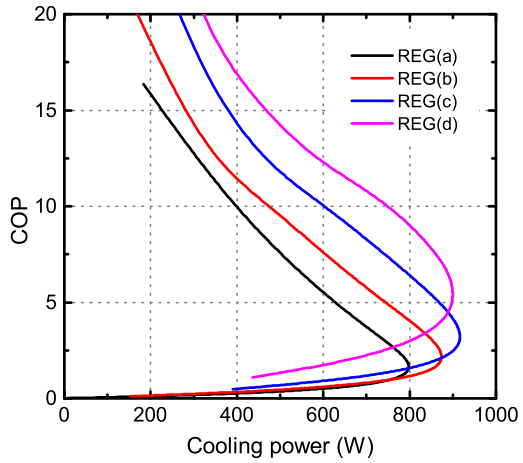

FIGURE 7. THE RELATIONSHIP OF COOLING POWER AND COP OF NEW REGENERATORS WHEN THE TEMPERATURE SPAN IS 5 K.

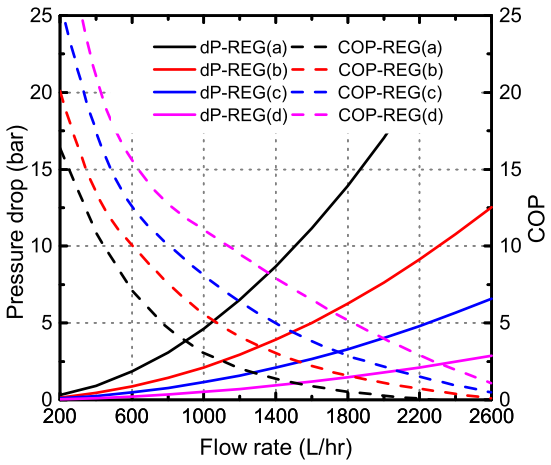

FIGURE 6. THE PRESSURE DROP AND COP OF REGENERATORS AS FUNCTIONS OF FLOW RATE WHEN THE TEMPERATURE SPAN IS 5 K.

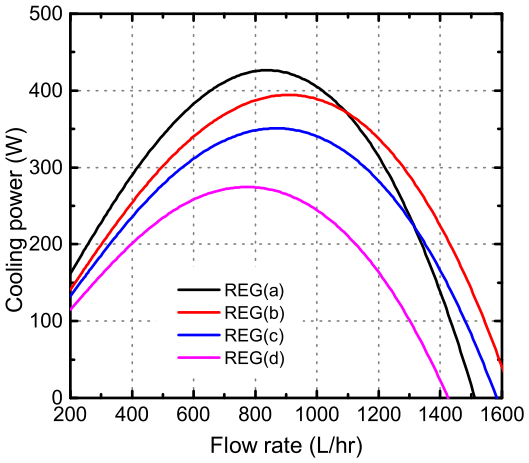

FIGURE 8. THE COOLING POWER OF REGENERATORS AS A FUNCTION OF FLOW RATE WHEN THE TEMPERATURE SPAN IS 15 K.

ator is larger and the pressure drop is lower, which is similar to the results presented in Fig. 6. It is seen that the performance of regenerator (b) is close to that of regenerator (a) in the top half of Fig. 10, while the efficiencies of (c) and (d) are reduced significantly. This suggests that regenerator (b) is the best choice between the four regenerators compared in this study.

Effect of Dead Volume

Empty ducts occupying a 5% of total volume are used to connect the regenerator compartments (see Fig. 1). These connecting chambers can be viewed as so-called dead volumes. Usually at the fluid inlet / outlet there will be a small mixing chamber where the cold inlet / outlet fluid streams mix (and similarly at the hot end), which could cause a substantial loss. From a regenerator stand-point it is clear that such zones should be minimized. It had previously been shown [10] that the performance of an AMR

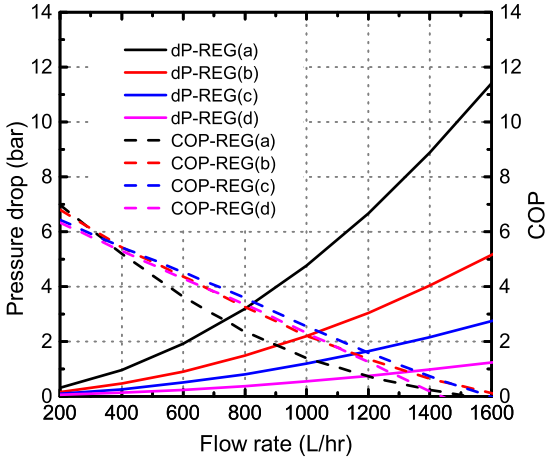

FIGURE 9. THE PRESSURE DROP AND COP OF REGENERATORS AS FUNCTIONS OF FLOW RATE WHEN THE TEMPERATURE SPAN IS 15 K.

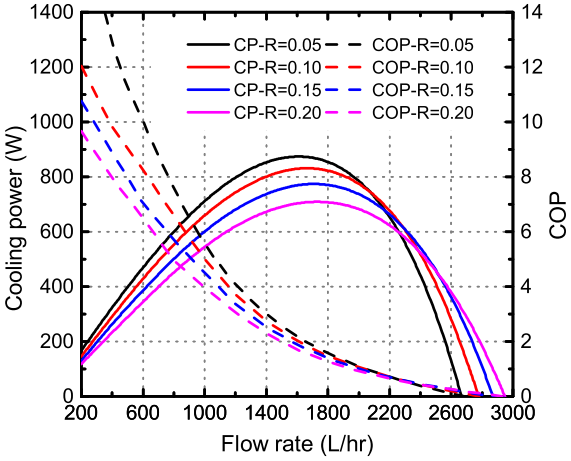

FIGURE 11. THE COOLING POWER AND COP OF REGENERATOR (B) WITH DIFFERENT DEAD VOLUME RATIOS AS FUNCTIONS OF FLOW RATE WHEN THE TEMPERATURE SPAN IS 5 K.

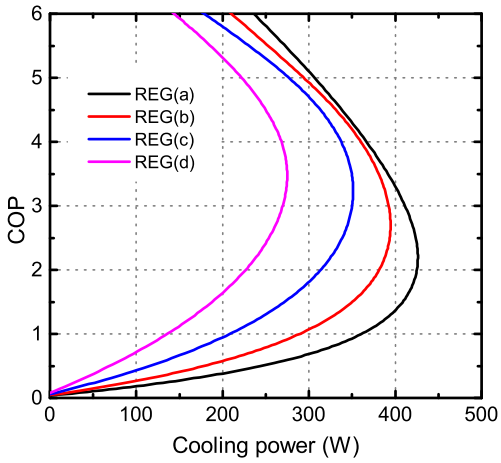

FIGURE 10. THE RELATIONSHIP OF COOLING POWER AND COP OF NEW REGENERATORS WHEN THE TEMPERATURE SPAN IS 15 K.

decreases as a function of the ratio R between dead volume and regenerator volume. In the new regenerators, the question is, from a practical point of view, how much dead volume can be tolerated in terms of the impact on performance.

In order to investigate this, a dead volume ratio R of 0.05 - 0.20 are assumed to exist in the regenerator (b), and comparison study is carried out. Figs. 11 and 12 show the performance of regenerator (b) with different dead volume ratios when the temperature span is 5 K and 15 K respectively. Both cooling power and COP decrease with an increasing dead volume ratio when the flow rate is relatively low. With the dead volumes existing in the regenerator, the heat transfer liquid, which is left in the dead volume after hot / cold period, does not transfer heat in demagnetization / magnetization process because it is not in contact with magnetocaloric material, therefore this part of heat transfer liquid has a higher / lower temperature than that of the upcoming cold / hot flow, which reduces enthalpy flux at each end and the effectiveness of the regenerator. The trend of cooling power curve runs into an opposite way after reaching the peak, however such an high flow rate is not commonly seen in real application. Also the COP turns to be a little higher when the flow rate is larger than 1100 L/hr. It can be concluded that the performance will degrade severely with a dead volume larger than 0.05.

CONCLUSIONS

The new regenerators with complex flow arrangements are demonstrated in the article. To simulate the performance of the new regenerators, a one dimensional model of a magnetocaloric regenerator is presented, using the MC limiter to discretize partial differential equations. And the new approach can eliminate spurious oscillation in the solution facing with the discontinuity problem of ramping flow through a regenerator bed.

By employing the improved one dimensional model, the impact of dimensional cross section area R_{area}, the performance of new regenerators, and the effect of dead volume ratio R, are studied. It can be seen that, although the cooling power does not change much with changing R_{area}, when the flow rate is rela-

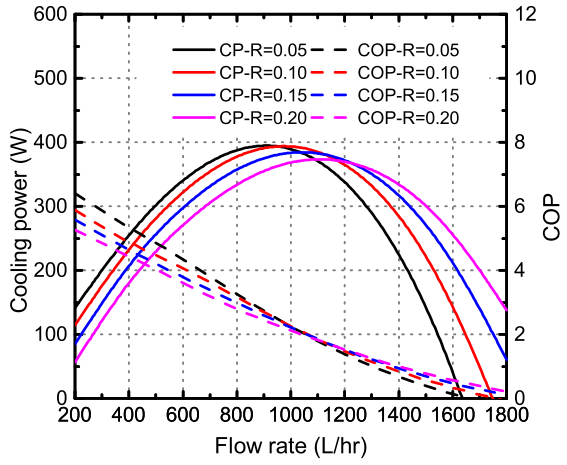

FIGURE 12. THE COOLING POWER AND COP OF REGENERATOR (B) WITH DIFFERENT DEAD VOLUME RATIOS AS FUNCTIONS OF FLOW RATE WHEN THE TEMPERATURE SPAN IS 15 K.

tively low, the pressure drop is reduced significantly and a larger COP is achieved at $R_{area} > 1$. Therefore the efficiency of the regenerator can be improved by enlarging the cross sectional area optimally. Compared to the conventional regenerator (a), a lower pressure drop and larger COP can be achieved with the new regenerators (b)-(d) with R_{area} of 1.32, 1.65, and 2.20, although the cooling power decreases somewhat at the same flow rate when the temperature span is 5 K. The results of a temperature span of 15 K show that the efficiency of the new regenerator is larger and the pressure drop is lower, and at low flow rates the cooling power of regenerator (b) is close to that of regenerator (a). This suggests that regenerator (b) is the best choice between the four regenerators compared in this study. A dead volume ratio R of 0.05 - 0.20 are assumed to exist in the regenerator (b), and comparison study is carried out in order to investigate this effect. The results show that both cooling power and COP decrease with an increasing dead volume ratio when the temperature span is 5 K. The performance degrades a lot with dead volume and it should be minimized in practical application. It is recommended that the dead volume should not be larger than 0.05 in the new regenerators.

ACKNOWLEDGMENT

This work was (in part) financed by the ENOVHEAT project which is funded by the Danish Council for Strategic Research (contract no 12-132673) within the Programme Commission on Sustainable Energy and Environment.

We would like to thank Barbara T. Jaime from Universidad Politecnica De Valencia for private communication about the model. [11]

REFERENCES

[1] Gschneidner Jr, K. A., Pecharsky, V. K., and Tsokol, A. O., 2005. "Recent developments in magnetocaloric materials". *Rep. Prog. Phys.,* ***68***, pp. 1479–1539.

[2] Smith, A., Bahl, C. R. H., Bjørk, R., Engelbrecht, K., Nielsen, K. K., and Pryds, N., 2012. "Materials challenges for high performance magnetocaloric refrigeration devices". *Adv. Energy Mater.,* ***2***(11), pp. 1288–1318.

[3] Barclay, J. A., 1983. "Theory of an active magnetic regenerative refrigerator". *NASA Conference Publication*, pp. 375–387.

[4] Nielsen, K. K., Tusek, J., Engelbrecht, K., Schopfer, S., Kitanovski, A., Bahl, C. R. H., Smith, A., Pryds, N., and Poredos, A., 2011. "Review on numerical modeling of active magnetic regenerators for room temperature applications". *Int. J. Refrig.,* ***34***, pp. 603–616.

[5] Engelbrecht, K., Eriksen, D., Bahl, C., Bjørk, R., Geyti, J., Lozano, J., Nielsen, K. K., Saxild, F., Smith, A., and Pryds, N., 2012. "Experimental results for a novel rotary active magnetic regenerator". *Int. J. Refrig.,* ***35***, pp. 1498–1505.

[6] Bjørk, R., Bahl, C. R. H., and Katter, M., 2010. "Magnetocaloric properties of $LaFe_{13-x-y}Co_xSi_y$ and commercial grade Gd". *J. Magn. Magn. Mater.,* ***322***, pp. 3882–3888.

[7] Engelbrecht, K., 2008. "A numerical model of an active magnetic regenerator refrigerator with experimental validation". PhD thesis, University of Wisconsin - Madison.

[8] Van Leer, B., 1977. "Towards the ultimate conservative difference scheme iii. upstream-centered finite-difference schemes for ideal compressible flow". *J. Comput. Phys.,* ***23***, pp. 263–275.

[9] Durran, D., 2010. *Numerical Methods for Fluid Dynamics: With Applications to Geophysics*. Springer.

[10] Jacobs, S., 2009. "Modeling and optimal design of a multilayer active magnetic refrigeration system". *Proceedings of the 3rd International Conference on Magnetic Refrigeration at Room Temperature, Des Moines, Iowa, USA*, pp. 267–274.

[11] Jaime, B. T., Salvador, J. M. C., and Herrero, J. P., 2013. A numerical scheme for the simulation of active magnetic regenerators. Tech. rep., Instituto Ingeniera Energetica, Universidad Politecnica De Valencia.

A.8 Modelling and comparison studies of packed screen regenerators for active magnetocaloric refrigeration

T. Lei, K. Engelbrecht, K. K. Nielsen, et al., Modelling and comparison studies of packed screen regenerators for active magnetocaloric refrigeration, *Proceedings of the 6th IIF-IIR International Conference on Magnetic Refrigeration*, Victoria, (2014).

Modelling and comparison studies of packed screen regenerators for active magnetocaloric refrigeration

Lei, Tian; Engelbrecht, Kurt; Nielsen, Kaspar Kirstein; Veje, Christian T.; Tusek, Jaka; Bahl, Christian

Published in:
Proceedings of the 6th IIF-IIR international Conference on Magnetic Refrigeration

Publication date:
2014

6th IIF-IIR International Conference on Magnetic Refrigeration
Victoria, BC, 7-10 September 2014

MODELLING AND COMPARISON STUDIES OF PACKED SCREEN REGENERATORS FOR ACTIVE MAGNETOCALORIC REFRIGERATION

T. LEI[(a)], K. ENGELBRECHT[(a)], K.K. NIELSEN[(a)], C.T. VEJE[(b)], J. TUŠEK[(a)], C.R.H. BAHL[(a)]

[(a)]Department of Energy Conversion and Storage, Technical University of Denmark
Roskilde, DK 4000, Denmark, tile@dtu.dk, kuen@dtu.dk, kaki@dtu.dk, jatu@dtu.dk, chrb@dtu.dk
[(b)]Institute for Technology and Innovation, University of Southern Denmark
Odense M, DK 5230, Denmark, veje@iti.sdu.dk

ABSTRACT — In active magnetic regeneration (AMR) systems, not only the magnetocaloric properties of materials, but also the regenerator geometry plays an important role in the system performance. Packed sphere regenerators are often employed in existing prototypes, however, the characteristics such as relatively large pressure drop and almost fixed porosity make loss reductions and further optimization challenging. This paper proposes and focuses on packed screen regenerators, which may exhibit lower pressure drop and equivalent heat transfer performance to packed sphere regenerators. A 1D AMR model is improved and applied to simulate the regenerators. The performance of the new regenerators is studied and compared with that of the packed sphere regenerators. Possible fabrication methods of the packed screen regenerators are also discussed.

1. INTRODUCTION

In recent years, magnetocaloric refrigeration based on the AMR cycle has attracted the interest of many researchers, as the AMR systems have high theoretical efficiency, and use environmentally friendly working fluids. Given the limited magnetic flux density and magnetized volume, efficient regenerator design is important for the overall performance of the AMR system. In most current prototypes, packed spheres and parallel plates are the most common regenerator geometries. The packed sphere regenerators are somewhat easy to construct and have demonstrated relatively high performance in AMR devices. However, they exhibit relatively large pressure drop, and a nearly fixed porosity around 0.36, which make loss reductions and further optimization challenging. Alternatively, parallel plate regenerators have much lower pressure drop, but the geometry requires very small plate thickness and plate spacing to behave as efficient regenerators. The small dimensions required make fabrication of high performance regenerators sensitive to manufacturing tolerances and difficult to fabricate [1]. In many research and industrial applications, wire screens have been applied in regenerative heat engines, catalytic reactors, etc. [2], as they have highly ordered structures, high heat transfer rates, and moderate flow resistance. Screens with different materials are commercially available and the mesh number (the number of wires per inch) ranges into hundreds, correspondingly the pore diameter ranges from several millimeters to dozens of microns. The porosity can be adjusted by varying the wire diameter, and the stacking technique can reduce axial conduction losses. These qualities give regenerator optimization more flexibility. In this paper, packed screen regenerators are simulated and researched by using a 1D numerical model.

2. SIMULATION MODEL

To simulate the packed screen regenerator, an existing 1D model [3] has been modified. In the model, the heat transfer fluid flows through 24 regenerator beds periodically, which is synchronized with the changing magnetic field. The regenerator material is gadolinium (Gd) and the heat transfer fluid is water mixed with 20% ethylene glycol by volume. By solving discretized energy equations of liquid and solid, the temperature profiles, cooling power, heat rejection, pressure drop and COP etc., can be calculated once the model has converged to cyclical steady state. A detailed model is described in Ref. [4]. To estimate the friction factor and heat transfer performance of packed screens, Armour and Park's correlations [2, 5], which cover the range of Reynolds number, Prandtl number, porosity and mesh number in this study, are used (see (1) and (2)).

$$\Delta P = (8.61/\mathrm{Re}_{\mathrm{Armour}} + 0.52)\, L\, u_0^2\, \rho_f / [\, \varepsilon^2 (1/M_w - D_w)], \text{ where } \mathrm{Re}_{\mathrm{Armour}} = \rho_f\, u_0/[\mu A_w^2 (1/M_w - D_w)] \text{ and } 0.1 < \mathrm{Re}_{\mathrm{Armour}} < 1000 \quad (1)$$

$$\mathrm{Nu} = 1.315\, \mathrm{Pr}^{0.33}\, \mathrm{Re}_{\mathrm{Park}}^{0.35}\, [(1-\varepsilon)/\varepsilon]^{0.2}, \text{ where } \mathrm{Re}_{\mathrm{Park}} = \rho_f\, u_0/\mu\, A_w, \text{ and } 30 < \mathrm{Re}_{\mathrm{Park}} < 500 \quad (2)$$

In this study, each regenerator bed has a length of 150 mm and a cross sectional area of 250 mm^2. We consider six groups of screens with a mesh number range of 25 – 600 wires/inch and porosity ε from 0.36 to 0.71, which are adjusted by changing wire diameter for a given mesh number. The screens are stacked with random orientation and are close packed. For comparison, a group of packed sphere regenerators with sphere diameter ranging from 0.7 to 0.2 mm, which means the flow channel is smaller, is simulated. A typical 75 wires/inch screen has on average 2.95 pores in 1 mm distance, and wire diameter can vary from 0.118 mm to 0.229 mm. This means the porosity changes from 0.71 to 0.36 and specific surface area from 9824 to 11193 m^{-1}. Comparatively the packed sphere bed has a fixed porosity of 0.36 and a specific surface area of 9600 m^{-1} when the sphere diameter is 0.4 mm. The temperature span is fixed from 275 to 305 K.

3. RESULTS AND DISCUSSION

Figs. 1 - 3 show the cooling power, pressure drop and COP of packed screen regenerators with variable mesh numbers (bottom axis), compared to packed sphere regenerators with different sphere diameters (top axis). The flow rate is 800 liters/hr. With increasing mesh number, both cooling power and COP reach a peak (see Figs. 1 and 3) and consequently reduce, whereas the pressure drop (shown in Fig. 2) increases continuously. It can be seen that there is an optimal mesh number between 75 - 100 wires/inch for all groups of packed screen regenerators. The heat transfer performance is enhanced by increasing the mesh number, because the channel size becomes smaller and the heat transfer area increases. This effect increases the enthalpy flow in the cold blow period, i.e. cooling power, at the cold end of regenerator. However, the rising viscous dissipation, represented by the pressure drop, will degrade the performance considerably. Therefore, packed screen regenerators with an approximate mesh number between 75 - 100 wires/inch, providing sufficient heat transfer and moderate pressure drop, gives the best performance. The COP can be increased by reducing the porosity, however cooling power behaves oppositely, which may be due to a reduction in Gd mass and larger utilization of the regenerator. The maximum cooling power is 471.5 W when the porosity is 0.36, while the maximum COP is 5.2 when the porosity is 0.71. The results of packed sphere regenerators with different sphere diameters from 0.7 - 0.2 mm are also shown in Figs. 1 - 3. The optimal sphere diameter is between 0.3 to 0.4 mm and the maximum cooling power and COP are 291.9 W and 0.9, respectively. Compared to packed sphere regenerators, packed screen regenerators with mesh numbers between 50 and 250 wires/inch can achieve larger cooling power and COP, as well as lower pressure drop. Even with a porosity larger than 0.50, meaning that less Gd is used, better performance can be observed in the packed screen regenerators.

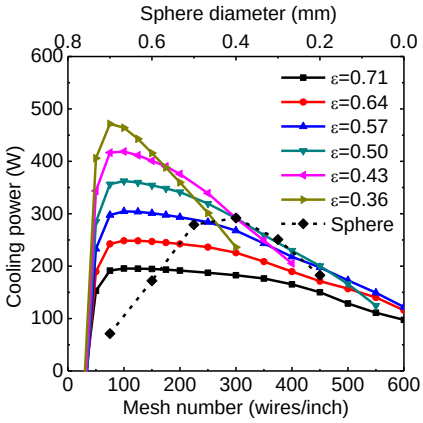

Fig.1 The cooling power

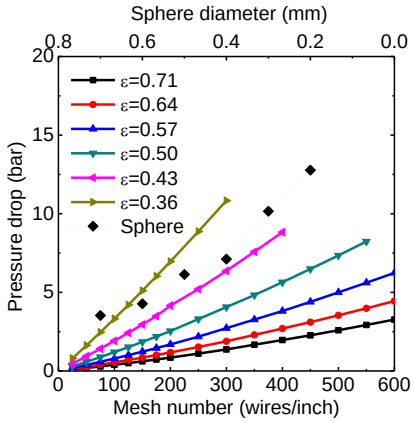

Fig.2 The pressure drop

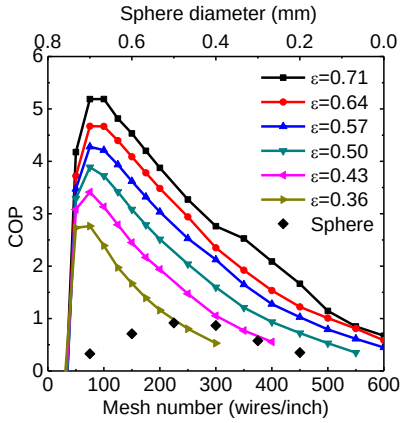

Fig.3 The COP

4. POSSIBLE FABRICATION METHODS

Although the performance of the AMR system may be increased by utilizing a packed screen regenerator compared with a packed sphere regenerator, it is difficult to manufacture screens from many magnetocaloric materials. Therefore, in this study we present some alternative methods for fabricating regenerators with a similar structure as the packed screen regenerator. The first method is electro-spinning processing, in which ceramic fine fibers (typically on the micro or nano-scale) can be drawn out from the solution, and deposited as porous media on a collector by using high electrical charge. It is possible to fabricate such a porous ceramic regenerator, with the same structure of randomly packed wires as packed screen bed. Another choice is co-extrusion fabrication, which can also be used to fabricate ceramic fibers on the micro scale. A proper wire diameter may be achieved after extruding repeatedly, and a packed bed with a porous structure can be realized by depositing the fibers randomly.

This work was financed by the ENOVHEAT project which is funded by the Danish Council for Strategic Research (contract no 12-132673) within the Programme Commission on Sustainable Energy and Environment.

REFERENCES

[1] K.K. Nielsen, K. Engelbrecht, C.R.H. Bahl, "The influence of flow maldistribution on the performance of inhomogeneous parallel plate heat exchangers," 2013, Int. J. Heat Mass Tran., vol. 60, pp. 432-439.

[2] J.C. Armour and J.N. Cannon, "Fluid flow through woven screens," J. AIChE, vol. 14, pp. 415–420.

[3] K. Engelbrecht, J. Tušek, K.K. Nielsen, et al., "Improved modelling of a parallel plate active magnetic regenerator," J. Phys. D: Appl. Phys., vol. 46, 255002.

[4] T. Lei, K.K. Nielsen and K. Engelbrecht, "Modeling and simulation of regenerators with complex flow arrangements for active magnetocaloric refrigeration," 12th Biennial Conference on Engineering Systems Design and Analysis, Denmark, 2014.

[5] J.W. Park, D. Ruch and R. Wirtz, "Thermal / fluid characteristics of isotropic plain-weave screen laminates as heat exchange surfaces," 40th AIAA Aerospace Sciences Meeting & Exhibit, vol. 208, A02-13700.

A.9 Computationally efficient model of an active magnetocaloric regenerator

M. Tahavori, C. Veje, **T. Lei**, K. K. Nielsen and K. Engelbrecht, Computationally efficient model of an active magnetocaloric regenerator. *Proceedings of the 5th IEEE International Conference on Control Systems, Computing and Engineering*, Batu Ferringhi, (2015).

Computationally Efficient Model of an Active Magnetic Regenerator

Maryamsadat Tahavori and Christian Veje
Center for Energy Informatics
The Maersk Mc-Kinney Moller Institute
University of Southern Denmark
Odense, Denmark
Email: mta,veje@mmmi.sdu.dk

Tian Lei, Kaspar K. Nielsen and Kurt Engelbrecht
The Department of Energy Conversion and Storage
Technical University of Denmark
Roskilde, Denmark
Email: tile,kaki,kuen@dtu.dk

***Abstract*—Active magnetic regenerator refrigeration is an alternative refrigeration technology to conventional vapor-compression refrigeration. This technology has potential for higher efficiency and less environmental impact in comparison to conventional vapor-compression refrigeration. In recent years substantial amount of studies have been done on modeling of active magnetic regenerators. Some of these models are time dependent models and consequently computation time is relatively high and therefore not suitable for online applications, advanced optimization and control of such a system. In this paper, a computationally efficient model of an active magnetic regenerator is derived and validated. The derived model is based on a data-based modeling technique not previously implemented for active magnetic regenerators. The derived model is numerically more efficient and computation time for system analysis, simulation, optimization and control reduces significantly by using this model. The results show that this model can capture the local nonlinear behavior of the system, and it is validated by comparing predicted performance with the full dynamic model.**

I. Introduction

During the last century, conventional vapor-compression refrigeration has been widely used in a daily life. However, it has some disadvantages. It not only has relatively low efficiency, but the refrigerants used in some of the implementations have high global warming potentials, and for older systems even ozone depleting substances [1] - [2]. In order to solve these problems several studies have been carried out on high efficiency and environmentally friendly refrigeration technologies. Active magnetic refrigeration is an alternative refrigeration technology to conventional compressor refrigeration. This technology is based on the magnetocaloric effect and uses magnetization and demagnetization to generate a cooling effect [3]. Because of the reversible nature of the magnetocaloric effect it can be used as an efficient thermodynamic cycle. It has also no ozone depleting potential and no direct global warming potential [4].

The room-temperature magnetic refrigerator was studied by Brown in 1976 for the first time [3] and since then it has developed quickly. Since the Active Magnetic Regenerator (AMR) involves solid state physics, thermodynamics, fluid dynamics and magnetism a wide range of physical interactions affects the performance of such a system [1]. To better understand, to control, and to optimize the process it is important to have a suitable model of the process to predict system performance. A comprehensive review on different numerical models of AMR can be found in [1]. In [5] and [6] general reviews of room temperature magnetic refrigeration are given.

The AMR cycle consists of four phases, which can overlap [7]. First phase is magnetization, where the field is applied to the solid regenerator material and causes a temperature increase. Magnetization is followed by a fluid flow from the cold fluid heat exchanger to the hot fluid heat exchanger. This is the phase in which heat is rejected to the surroundings via the hot heat exchanger. During demagnetization the applied field is removed and causes a temperature decrease. Finally in phase four, there is fluid flow from the hot heat exchanger to the cold, and a cooling load is accepted, see Figure 1.

There are different categories of models for AMR in the literature. The first category are steady state models which are relatively simple models and are time independent. In these models the performance of AMR can be estimated in terms of cooling power versus temperature span as a function of e.g. the geometry of the AMR [1]. Different steady state models of AMR can be found in [8] - [13]. The second category of AMR models are time-dependent models which provide a more complex description of the AMR [1]. The change of the magnetic field and the fluid flow is time dependent in these models. Fluid flow is coupled with heat transfer between the fluid and solid. These models represent the physics on a more fundamental level. A number of works have been done on time-dependent models of AMR during last decades [14] - [19]. In these models the geometry of the regenerator is also considered. In most of the models the finite element or finite difference approaches are used to solve the problem numerically. These models are complex and one is faced with a relatively larger computational burden. This limits the application of these models in practice. In particular for online applications, advanced optimization and control it is very important to develop models which are computationally efficient. In this paper such an efficient model is derived using the data-based technique: system identification. To the best of our knowledge data-based modeling technique has not been used for modeling of AMR.

The rest of the paper is organized as follows: In section II a data-based modeling technique is reviewed. The computationally efficient model of AMR using data-based modeling technique is presented in section III and the results are shown. The last section concludes the paper.

978-1-4799-8252-3/15/$31.00 ©2015 IEEE

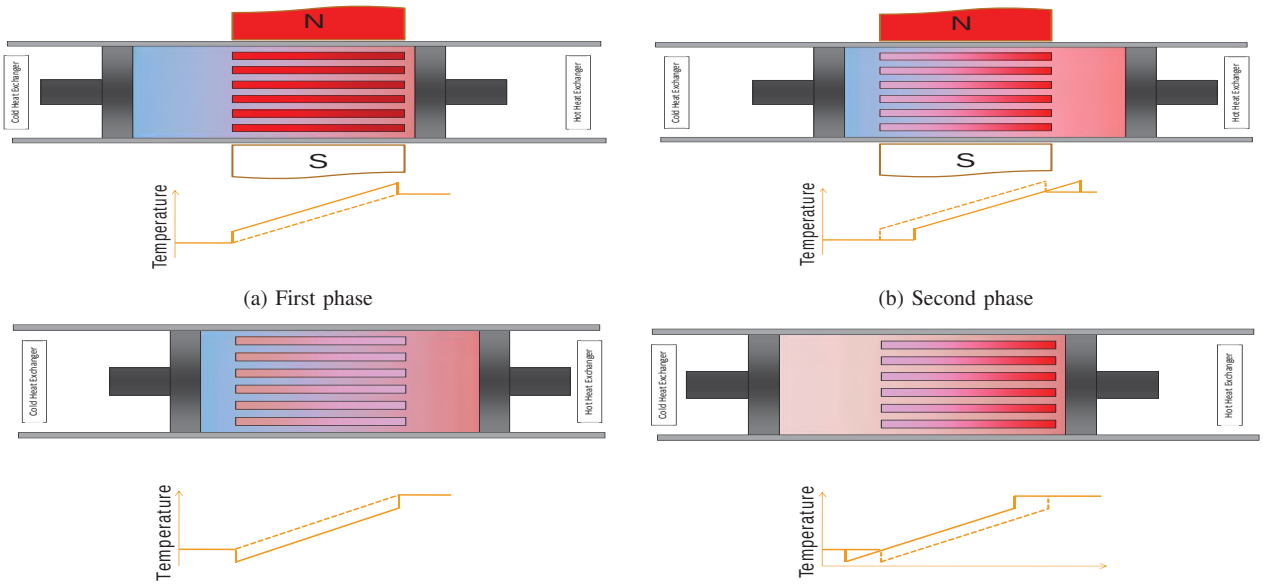

(a) First phase

(b) Second phase

(c) Third phase

(d) Fourth phase

Fig. 1: Schematic of four phases in each AMR cycle [7]

II. Data-Based Modeling

In this section data-based modeling techniques are reviewed. System identification is used to drive an efficient model of an AMR in section III.

Modeling is an important step in analysis, optimization and control of processes and systems. Obtaining the dynamic model of a complex dynamical system is often difficult due to the complexity involved in behavior of the system. The result of the modeling process in this case is often too complex, results in computational burden and compromises the efficiency of the analysis, optimization and control. To cope with the problem of complexity, simplification techniques such as model reduction have gained a lot of attention over the last few decades [20] - [21]. These methods reduce the order of the describing model of the dynamic system to maintain tractability. However, to be able to use model reduction methods, a dynamic model of the system in the explicit state-space form is required which is not always easy to obtain. This paper uses system identification as a powerful data-based tool to develop an efficient model.

In system identification, a dynamic model of a system is identified by using a set of measured inputs and outputs. In the process of identifying a system model, a mathematical function that correlates inputs and outputs is estimated. The identified model is an approximation of the original system and it can be in different forms such as state space model, nonlinear model, etc. The identified model is not unique and there can be more than one model which can fit the input-output data set. System identification is a very popular data-based modeling method for advanced optimization and control.

Real word systems are usually nonlinear and a lot of phenomena are described with nonlinear dynamics. Therefore nonlinear system identification techniques are very useful for optimization and control of such systems. The nonlinear system identification techniques based on only input-output data set are: nonlinear autoregressive exogenous (ARX) model and Hammerstein-Wiener model. In this paper the nonlinear ARX model is used.

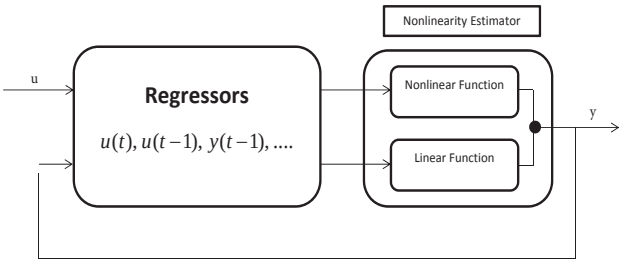

Fig. 2: The structure of a nonlinear ARX model

The structure of the nonlinear ARX model is presented in Figure 2. In this model the nonlinearity is described using a parallel combination of both linear and nonlinear functions. These functions are expressed in terms of variables called regressors. The nonlinear ARX model computes regressors from the current and past input and past output data. In the most simple case the regressors are delayed inputs and outputs.

III. Efficient Modeling of Active Magnetic Regenerator

The data which used in this paper are generated using the 1D model developed in [19]. In [19] a one dimensional

transient numerical model for the AMR prototype which has a length of 100 mm and cross sectional area of 238 mm^2 is presented. A ring of 24 regenerators was installed in the magnetized volume between inner and outer magnets. Gadolinium (Gd) spheres and water mixed with 25 % ethylene glycol are chosen as the solid material and heat transfer fluid in the prototype. This model is highly nonlinear and it is not easy to simulate it numerically.

Experimental validation with good results were done on the 1D model [22]. The disadvantage of this model is that the computation time is too high and it imposes a large computational burden for dynamic control as mentioned above. Therefore it is not suitable for advanced control and optimization of AMR sytems. In this paper, an AMR system consisting of four inputs and three outputs is considered to obtain an efficient model of the AMR, see Figure 3.

Fig. 3: An AMR system model with 4 inputs and 3 outputs

In Figure 3, T_c^i and T_c^o are the inlet and outlet temperatures of the cold side of AMR in $[K]$. T_h^i and T_h^o are the inlet and outlet temperatures of the hot side of AMR in $[K]$. f is the AMR frequency $[Hz]$, $\dot{m}$ is the mass flow rate $[\frac{kg}{s}]$, and COP is the AMR coefficient of performance.

To have a general model of the AMR a lot of data such as cooling power, heat rejection, frequency, mass flow rate, heat capacity, the average hot and cold end temperatures of an AMR have been collected from the model developed in [19]. To generate these data the AMR was simulatd with a fixed hot end temperature, a cycle frequency of $0.1, 0.5, 1, 2, 3$ and 4 $[Hz]$ with different temperature spans (average temperature difference between hot and cold side of AMR) of $0.5, 5, 10, 20$ and 30 $[K]$.

To obtain the inlet and outlet temperatures in both hot and cold side of the AMR the equations below have been used:

$$\dot{Q}_h = \frac{1}{\tau}\int_{\tau} \dot{m}(t)c_f(T_h^o(t) - T_h^i)dt, \quad (1)$$

$$\dot{Q}_c = \frac{1}{\tau}\int_{\tau} \dot{m}(t)c_f(T_c^i - T_c^o(t))dt, \quad (2)$$

$$T_c = T_c^i, \quad (3)$$

$$T_h = T_h^i, \quad (4)$$

where $\dot{Q}_h$ is heat rejected, $\dot{Q}_c$ is cooling power, c_f is heat capacity of fluid, τ is the AMR cycle time, T_c is cold end temperature and T_h is hot end temperature. By using the above equations we have all necessary data to system identification model of the system.

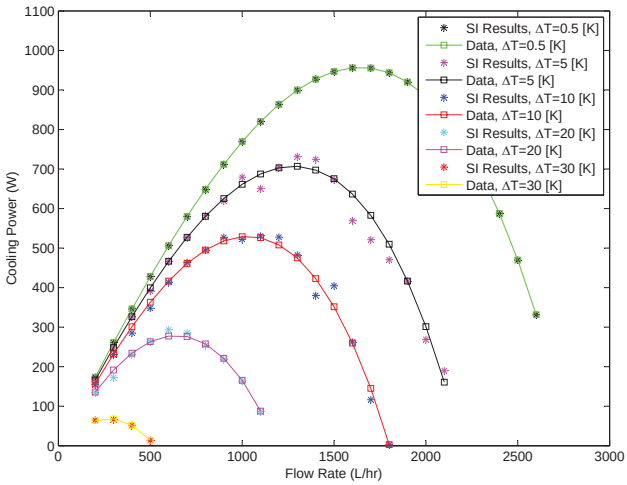

Fig. 4: The cooling power of regenerator vs flow rate at different temperature span.

All the collected data have been used to derive an efficient model based on system identification. The model derived using the system identification approach is a nonlinear ARX model.

Figure 4 - Figure 6 show the behaviour of the system by using system identification approach. Figure 4 shows the changes of cooling power of regenerator with respect to flow rate at fixed frequency of 2 $[Hz]$ and at different temperature span. Figure 5 - Figure 6 show how the regenerator COP will change with respect to the regenerator cooling power and mass flow rate at fixed frequency of 2 $[Hz]$ and at different temperature span respectively.

As the results show the model obtained from system identification fits well with the actual data. The 1D model in [19] was simulated with hot end temperature of 302 $[K]$ and the temperature span of 5 $[K]$ at cycle frequency of 3 $[Hz]$. The computation time was around 6603 seconds. Afterwards the obtained nonlinear ARX model was run at exactly the same condition as above. The computation time was around 1 second by using this model. This model is numerically more efficient compared to 1D model in [19] and reduces the computations significantly.

To validate the derived model, a new set of data are generated by using the 1D model in [19]. This new set of data is for the temperature span of 15 $[K]$ at cycle frequency of $0.1, 0.5, 1, 2, 3$ and 4 $[Hz]$. These data are given as inputs to the model derived using system identification technique. The changes of cooling power and COP data with respect to cooling power and COP of system identification model is plotted and shown in Figures 7 and 8. As these figures show the model obtained using system identification predict the new set of data very well. The changes of cooling power data and COP data with respect to cooling power and COP of system identification model is a line with slope 1. This shows that the

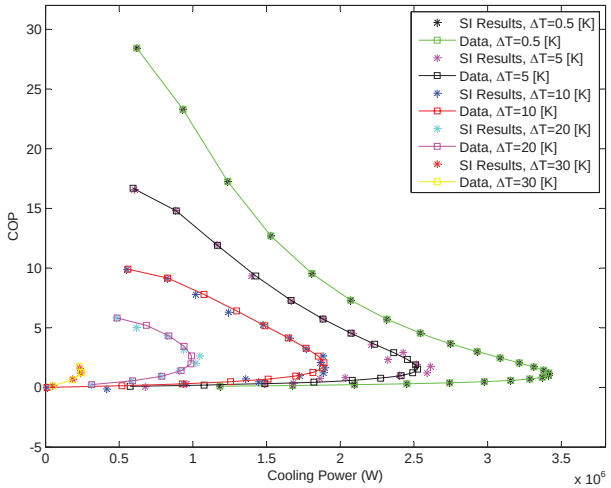

Fig. 5: The COP of regenerator vs cooling power at different temperature span.

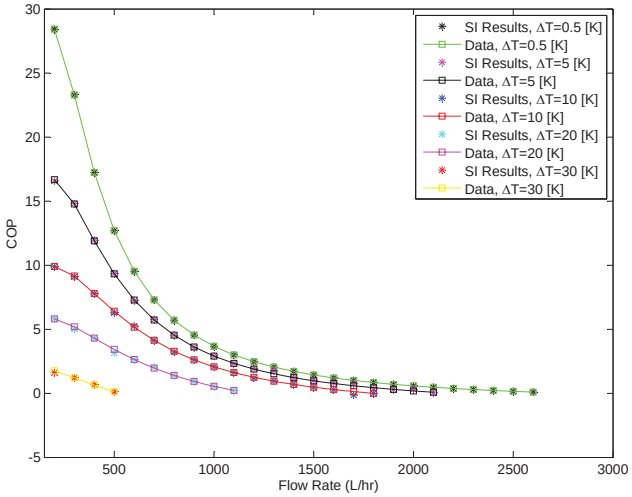

Fig. 6: The COP of regenerator vs flow rate at different temperature span.

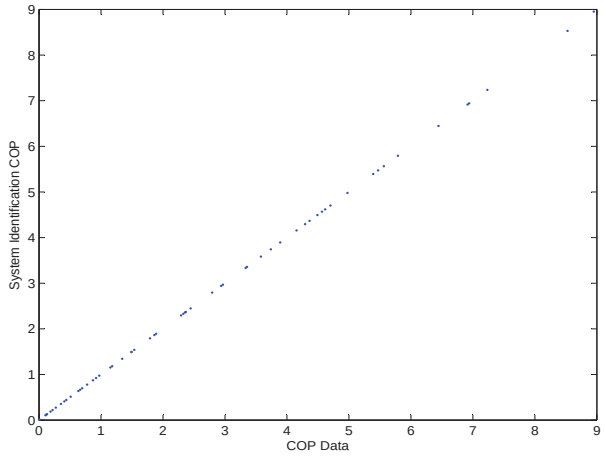

Fig. 7: COP of regenerator vs system identification COP at the temperature span of 15 $[K]$ and cycle frequency of $0.1, 0.5, 1, 2, 3$ and 4 $[Hz]$

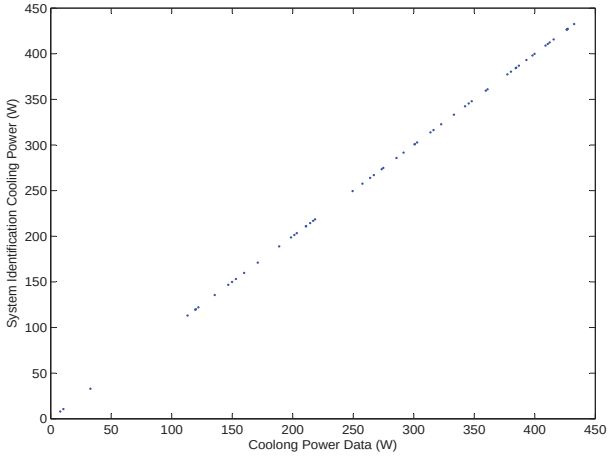

Fig. 8: The regenerator cooling power vs system identification cooling power at the temperature span of 15 $[K]$ and cycle frequency of $0.1, 0.5, 1, 2, 3$ and 4 $[Hz]$

output obtained from system identification model is equal to the data which is used for validation, see Figure 9.

IV. Conclusion

An efficient model of an active magnetic regenerator is presented in this paper. The presented model is based on the data-based modeling technique: system identification. To the best of our knowledge a data-based modeling technique has not been used for modeling an active magnetic regenerator. Compared to the models which are developed for active magnetic regenerator in the literature this model is numerically more efficient. The computation time for simulation, control and optimization reduces significantly by using this model. Therefore it is suitable for advanced optimization and control of such a system. The results show that this model can capture the local nonlinear behavior of the system very well. The validation shows that the model from system identification fits well with the data used for validation. The future work includes using the model obtained from system identification for optimization and control of magnetocaloric heat pump.

Acknowledgment

This work was (in part) financed by the ENOVHEAT project which is funded by Innovation Fund Denmark (contract no 12-132673).

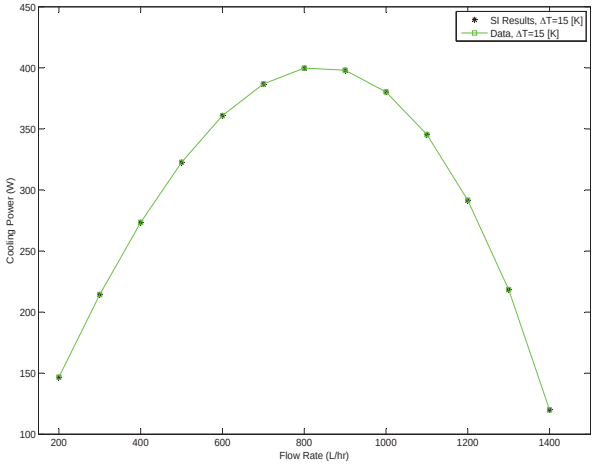

(a) The cooling power of regenerator vs flow rate

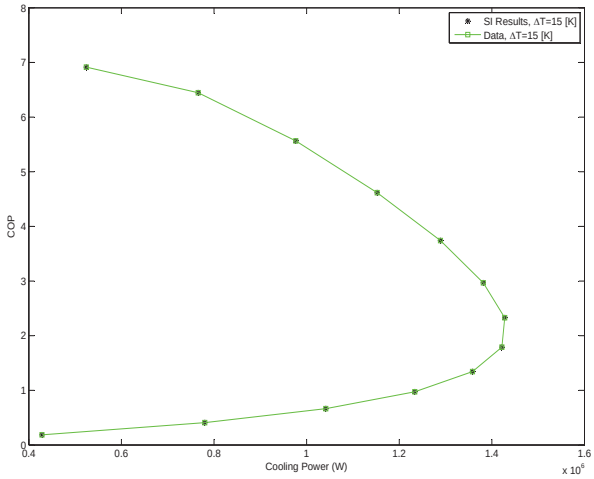

(b) The COP of regenerator vs cooling power

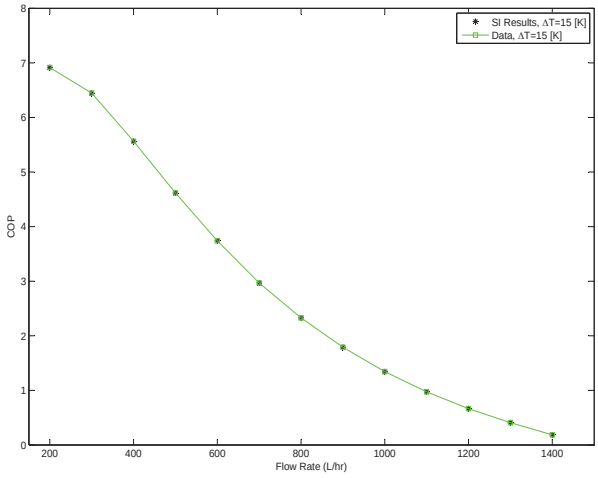

(c) The COP of regenerator vs flow rate

Fig. 9: Identified model vs validation data at cycle frequency of 2 $[Hz]$.

REFERENCES

[1] K. K. Nielsen, J. Tusek, K. Engelbrecht, S. Schopfer, A. Kitanovski, C. R. H. Bahl, A. Smith, N. Pryds and A. Poredos, "Review On Numerical Modeling Of Active Magnetic Regenerators For Room Temperature Applications", *International Journal of Refrigeration*, 34(3):603-616, 2011.

[2] D. Vuarnoz and T. Kawanami, "Modeling And Experimental Validation Of A Flat-Parallel-Plate Active Magnetic Regenerator Made Of Gadolinium", *International Conference on Magnetic Refrigeration at Room Temperature, Thermag V*, 493-500, 2012

[3] G. V. Brown, "Magnetic Heat Pumping Near Room Temperature", *Journal of Applied Physics*, 47(8):3673-3680, 1976.

[4] K. Engelbrecht, D. Eriksen, C. R. H. Bahl, R. Bjrk, J. Geyti, J. A. Lozano, K. K. Nielsen, F. Saxild, A. Smith, N. Pryds, "Experimental Results For A Novel Rotary Active Magnetic regenerator", *International Journal of Refrigeration*, 35(6):1498-1505, 2012.

[5] B. Yu, Q. Gao, B. Zhang, X. Meng, and Z. Chen, "Review On Research Of Room Temperature Magnetic Refrigeration", *International Journal of Refrigeration*, 26:622-636, 2003.

[6] K. L. Engelbrecht, G. F. Nellis, S. A. Klein and C. H. Zimm, "Review Article: Recent Developments In Room Temperature Active Magnetic Regenerative Refrigeration", *HVAC and R Research*, 13(4), 2007.

[7] K. K. Nielsen, *Numerical Modeling And Analysis Of The Active Magnetic Regenerator*, P.h.D Thesis, Technical University Of Denmark, Denmark, 2010.

[8] L. Zhang, S. A. Sherif, A. J. DeGregoria, C. B. Zimm and T. N. Veziroglu, "Design And Optimization Of A 0.1 Ton/Day Active Magnetic Regenerative Hydrogen Liquifier", *Cryogenics*, 40:269-278, 2000.

[9] J. He, J. Chen and C. Wu, "The Influence Of Heat-Transfer Laws On The Performance Of A Magnetic Stirling Refrigeration Cycle", *International Journal of Ambient Energy*, 24(2):75-82, 2003.

[10] Z. Yan and J. Chen, "The Characteristics Of Polytropic Magnetic Refrigeration Cycles", *Journal of Applied Physics*, 70(4):1911-1914, 1991.

[11] Z. Yan and J. Chen, "The Effect Of Field-Dependent Heat Capacity On The Characteristics Of The Ferromagnetic Ericsson Refrigeration Cycle", *Journal of Applied Physics*, 72(1):1-5, 1992.

[12] F. Shir, L. YaniK, L. H. Bennet, E. D. Torre and R. D. Shull, "Room Temperature Active Regenerative Magnetic Refrigeration: Mag-

netic Nanocomposites", *Journal of Applied Physics*, 93(10):8295-8297, 2003.

[13] A. Rowe and J. Barclay, "Ideal Magnetocaloric Effect For Active Magnetic Regenerators", *Journal of Applied Physics*, 93(3):1672-1676, 2003.

[14] K. Engelbrecht, *A Numerical Model Of An Active Magnetic Regenerator Refrigerator With Experimental Validation*, P.h.D thesis, University of Wisconsin, Madison, 2008.

[15] T. F. Petersen, N. Pryds, A. Smith, J. Hattel, H. Schmidt, and H. Knudsen, "Two-Dimensional Mathematical Model Of A Reciprocating Room-Temperature Active Magnetic Regenerator", *International Journal of Refrigeration*, 31:432-443, 2008.

[16] K. K. Nielsen, C. R. H. Bahl, A. Smith, R. Bjrk, N. Pryds and J. Hattel, "Detailed Numerical Modeling Of A Linear Parallel-Plate Active Magnetic Regenerator", *International Journal of Refrigeration*, 32(6):1478-1486, 2009.

[17] K. K. Nielsen, K. Engelbrecht, C. R. H. Bahl, A. Smith, N. Pryds and J. Hattel, "umerical Modeling Of Multi-Material Active Magnetic Regeneration", *The 7th World Conference on Experimental Heat Transfer, Fluid Mechanics and Thermodynamics*, 515–522, 2009.

[18] J. Bouchard, H. Nesreddine, and N. Galanis, " Model Of A Porous Regenerator Used For Magnetic Refrigeration At Room Temperature", *International Journal of Heat and Mass Transfer*, 52(5-6):1223-1229, 2009.

[19] T. Lei, K. K. Nielsen and K. Engelbrecht, "Modelling And Simulation Of Regenerators With Complex Flow Arrangements For Active Magnetocaloric Regrigeration", *Proceedings of the ASME 2014 12th Biennial Conference on Engineering Systems Design and Analysis*, 2014.

[20] A. C. Antoulas, "Approximation of Large-Scale Dynamical Systems", *Advances in Design and Control*, SIAM, Philadelphia, 2005.

[21] H. R. Shaker, and M. Tahavori, "Time-Interval Model Reduction of Bilinear Systems", *International Journal of Control*, 87(8):1487-1495, 2014.

[22] J. A. Lozano, K. Engelbrecht, C. R. H. Bahl, K. K. Nielsen, J. R. Barbosa, A. T. Prata and N. Pryds, "Experimental And Numerical Results Of A high Frequency Rotating Active Magnetic Refrigerator", *International Journal of Refrigeration*, 37:92-98, 2014.

A.10 Epoxy-bonded $La(Fe,Mn,Si)_{13}H_z$ as a multi-layered active magnetic regenerator

H. Neves Bez, K. Navickaité, **T. Lei**, K. Engelbrecht, A. Barcza and C. R. H. Bahl, Epoxy-bonded $La(Fe,Mn,Si)_{13}H_z$ as a multi-layered active magnetic regenerator, *The 7th IIF-IIR International Conference on Magnetic Refrigeration at Room Temperature*, Turin, (2016).

EPOXY-BONDED $La(Fe,Mn,Si)_{13}H_z$ AS A MULTI LAYERED ACTIVE MAGNETIC REGENERATOR

Henrique Neves Bez[(a)], Kristina Navickaitė [(a)], Tian Lei[(a)], Kurt Engelbrecht[(a)], Alexander Barcza[(b)], Christian R. H. Bahl[(a)*]

[(a)] *Department of Energy Conversion and Storage – Technical University of Denmark, Frederiksborgvej 399, Roskilde, Denmark*

[(b)] *Vacuumschmelze GmbH & Co. KG, D-63450 Hanau, Germany*

[*]Corresponding author. E-mail: chrb@dtu.dk

ABSTRACT

The high magnetocaloric effect and tunability of the Curie temperature over a broad range makes $La(Fe,Mn,Si)_{13}H_z$ a promising magnetocaloric material for applications. Due to a volume change across the transition and the brittleness of the material as well as erosion due to fluid flow, the particles of the material may break apart during operation. In this context, we studied epoxy-bonded $La(Fe,Mn,Si)_{13}H_z$ regenerators, in a small versatile active magnetic regeneration (AMR) test device with a 1.1 T permanent magnet source. The magnetocaloric material was in the form of packed irregular particles (250-500 µm), which were mechanically held in place by an epoxy matrix connecting the particles, improving the mechanical integrity, while allowing a continuous porosity for the fluid flow. Water with 2 wt% ENTEK FNE as anti-corrosion additive was used as the heat transfer fluid for the epoxy-bonded regenerators. A series of AMRs was evaluated by varying the epoxy content in the range 1-4 wt%.

Keywords: Magnetocaloric, refrigeration, epoxy-bonded, layered regenerator, AMR.

1. INTRODUCTION

Since the discovery of a material with a giant magnetocaloric effect two decades ago[1] there has been a desire to translate the very high entropy change observed into an increased performance in a magnetocaloric device. Since the first room temperature device presented by Brown in 1976[2] most magnetocaloric devices have used materials with a second order phase transition (SOPT). In these materials the transition between the ferromagnetic and the paramagnetic phase results in a smooth entropy change across a broad temperature range. Contrary to this, the discontinuous transition in materials with a first order phase transition (FOPT) results in a very sharp and narrow entropy change. However, the peak values of the entropy change are in general several times higher than those found in SOPT materials.

In order to improve performance, first order magnetic phase transition magnetocaloric materials may be used in the AMR. One of the most promising FOPT materials' series is $La(Fe,Mn,Si)_{13}H_z$[3]. This material has the Curie temperature, T_C, near room temperature, while it can be finely tuned by the Fe/Mn/Si ratio. Still, using FOPT materials instead of SOPT ones is not trivial and further considerations must be taken. Firstly, FOPT materials exhibit hysteresis [4], although it has been shown that for the $La(Fe,Mn,Si)_{13}H_z$ series it is rather small and in the range of 1 K [5]. Additionally, by definition FOPT materials exhibit a discontinuous phase transition over temperature and field, which is the reason that they exhibit large magnetocaloric effect. Nevertheless, the temperature range where there is a significant magnetocaloric effect is much narrower for FOPT materials. For example, the full width at half maximum of the Δs peak of Gd is about 30 K [6] for a field change of 1 T, while for $La(Fe,Mn,Si)_{13}H_z$ it can be as low as 7 K [5]. This brings forth the necessity of layering the regenerator with $La(Fe,Mn,Si)_{13}H_z$ with slightly different compositions along the direction of the temperature span, in such a way that the working temperature of each layer is optimized. This engineering is not straightforward and many complications have been shown elsewhere [7]. Furthermore, due to the necessity of interstitial H in order to bring the T_C to near room temperature without significant changes of the magnetocaloric properties, the shapeability of the material is compromised, as the hydrogenation process must be performed while the material is in the powder form and further sintering options remain limited [8].

Moreover, this material undergoes a volume change of ~0.9 vol% during the magnetic phase transition [8,9]. Given the brittleness of the material, microstructure and secondary phases, the volume change may lead to

cracking [10,11]. A method proposed to avoid cracking and erosion of the material under application is to bond the particles of the magnetocaloric material with epoxy, increasing the mechanical stability of the regenerator while still maintaining a continuous porosity [12].

In this context, we evaluate the performance of $La(Fe,Mn,Si)_{13}H_z$ epoxy-bonded double layer AMRs. The factors investigated here are: the effect of epoxy content; the heat transfer fluid; the effect of layering; and the utilization.

2. EXPERIMENTAL PROCEDURE

Fine particles of five slightly different compositions of $La(Fe,Mn,Si)_{13}H_{1.65}$ were used to make regenerators. The materials were produced by the same processing route[3] and will in the following be identified by their Curie temperature, measured by magnetometry.

Two types of regenerators were made: one with loose particles, held in place mechanically with a mesh at either end and a second where the particles were bonded together by a small amount of epoxy. In both cases the regenerators were cylindrical and made to fit into the versatile test device described previously[13,14]. The regenerator moves in and out of the 40 mm diameter bore of a 1.1 T permanent magnet Halbach cylinder. The device is placed in a temperature controlled cabinet, and the hot end temperature, T_{hot}, is fixed by a heat exchanger to be slightly above the ambient temperature in the cabinet, T_{amb}.

A table listing the regenerators tested is given below. The particle sizes were in a range of 250-500 µm and the regenerators had a porosity of 55%. The relatively high porosity is due to the relatively high irregularity of the shape of the particles, leading to a low packing density. The epoxy bonded regenerators were all fixed in 40 mm long pieces of Perspex tube, as shown in Fig. 1 all with masses of 95 g. The non-bonded regenerators were held in a custom container allowing filling with different amounts of material. Additionally, the viscosity and density of the transfer fluids were evaluated in an Anton Paar Lovis 2000 M/ME viscometer.

Name	**Description**	T_C	**Mass**
Single	Single layer regenerator with no epoxy	23.3 ºC	48 g
Double	Double layer regenerator with no epoxy	19.2 and 23.3 ºC	25 g each
Single4wt%	Single layer regenerator with 4 wt.% epoxy	22 ºC	95 g
Double1wt%	Double layer regenerator with 1 wt.% epoxy	23 and 26.6 ºC	95 g
Double2wt%	Double layer regenerator with 2 wt.% epoxy	23 and 26.6 ºC	95 g
Double4wt%	Double layer regenerator with 4 wt.% epoxy	23 and 26.6 ºC	95 g

Table 1: Description and properties of the regenerators for each given name.

Fig. 1 : Photo of an epoxy bonded regenerator, pen top for scale.

3. RESULTS AND DISCUSSION

For the regenerator tests we used two different corrosion protection additives, which have previously been shown to be effective for $La(Fe,Mn,Si)_{13}H_z$ type material, namely ethylene glycol based automotive antifreeze (EG) and Entek FNE (NT) [15]. Viscosity and density of water with different amounts of these additives were measured and compared to pure water, as shown in Fig. 2. The measurements were done at 20 ºC, which is close to the range the regenerators are tested in. Previous experience has shown that a concentration of around 15% of EG is needed for good corrosion protection, while concentrations in the order of 1-2% are sufficient when using NT. It is observed in Fig. 2 that the effect of the additive on the density and viscosity is much less for NT than for EG, presumably due to the much smaller concentrations. It can be noted that the change in viscosity per percent of additive is approximately the same while the effect on density is higher per percent of EG than NT. Also, while there is a significant change in the absolute viscosity of about 50% for EG and 20% for NT, the difference in density is only of the order of 3% for EG and less than 1% for NT.

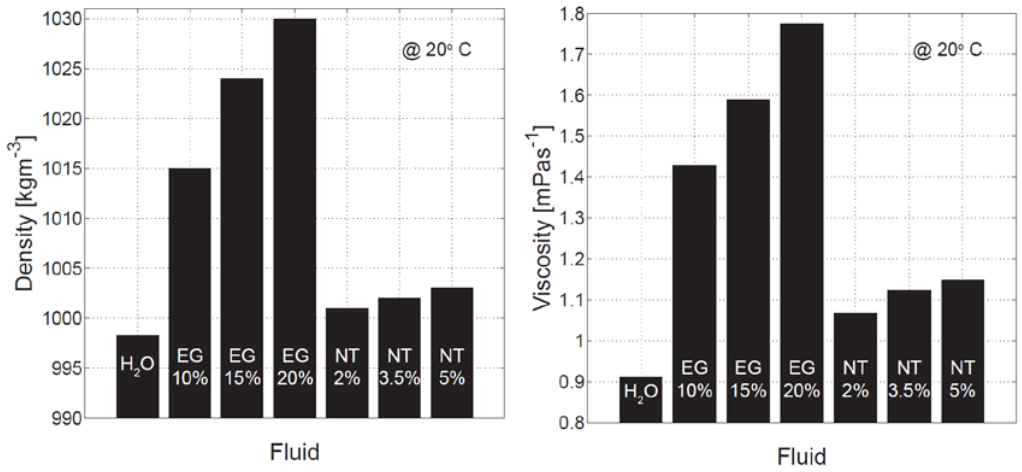

Fig. 2 : (a) The density and (b) the viscosity of the different fluids.

The apparent mechanical strength of the regenerators is generally good. However, during the regenerative tests the *Double1wt%* regenerator with just 1 wt.% of epoxy could not withstand the forces during operation and the regenerator broke apart.

We initiate the investigation of the regenerative performances by evaluating the influence of the utilization at a T_{hot} in the region of the maximum temperature span. The utilization, ϕ, is defined as

$$\phi = \frac{m_f c_f}{m_s c_s} \quad (1)$$

where m_f is the mass of the fluid pushed through the regenerator in one direction, c_f is the specific heat of the fluid, m_s is the mass of the solid regenerator and c_s is the specific heat of the regenerator material. The values used for c_s and c_f are 480 [5] and 4200 $Jkg^{-1}K^{-1}$, respectively.

Since the utilization is linearly proportional to the blown fluid mass, m_f, in Fig. 3 ΔT_{span} is shown as a function of the blown fluid mass. One can see that the trend of the span versus the m_f is approximately the same for the two regenerators without epoxy, independent of the number of layers and amount of material. The epoxy bonded regenerators have the peak at the same blown fluid mass as the ones without epoxy. Nonetheless, the mass of the solid regenerator is basically double of the ones without epoxy, and as we can see in equation (1) the effect will be to decrease the utilization by half.

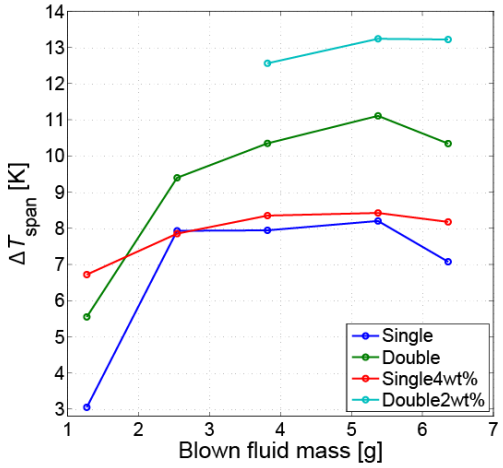

Fig. 3 : Temperature span as a function the blown fluid mass for three different regenerator at the region of maximum temperature span.

The temperature span as a function of the hot end temperature is shown in Fig. 4, where the left graph shows the results of the material without epoxy, while the right shows the results of the material with epoxy. It should be noted that the results of the regenerators without epoxy were done with water and 15 vol.% EG as the heat transfer fluid, while for the epoxy containing ones the fluid was changed to water with 2 vol.% NT. As discussed above these additives do change the viscosity, but only have a weak impact on the density. Due to the low frequency (0.13 Hz) the viscous dissipation is small when pushing the fluid through the regenerator, so even for the EG this will not have a large influence on the results. The regenerators were operated with the best resulting m_f, 5.4 g, which due to the difference of mass in the regenerators lead to different utilizations: 0.5 for the epoxy-bonded regenerators while those without epoxy were operated at a utilization of 0.9, in accordance with the results found in Fig. 3.

A feature common in all the results is a steady increase of temperature span with increasing T_{hot} up to a maximum at a temperature about 3-5 K above the highest T_C, then the span sharply decreases at higher hot end temperatures[7]. Additionally, it is observed that increasing the number of layers, from one to two, significantly increases the span, as expected. The measured temperature spans in the regenerators were not affected much by the epoxy-bonding. In fact they increased a little, as the dashed lines in Fig. 4 suggest. This, however, could be a combined effect of the different heat transfer fluids, differences in the mass of magnetocaloric materials and effects related to the epoxy itself. Additionally, the T_C spacing of the double layer regenerator without epoxy and the ones epoxy-bonded is slightly different. As it is shown in the literature[7], the temperature span can be heavily influenced by this spacing.

Although good performance was observed in the regenerators without epoxy, these regenerators were not mechanically stable. After three weeks of measurements, the regenerators started to release some very fine particles to the heat transfer fluid. These fine particles are believed to be the corners of the irregular particles, which are more susceptible to cracking. We believe that erosion during the fluid blow periods, coupled with the ~0.9% volume change that the material experiences at the transition [9, 11] result in breaking apart of the particles. Additionally, once this breaking apart starts, the packing of the regenerators is lost, and the particles are free to move inside the regenerator housing leading to further degradation of the regenerators. Indeed, this is what was observed. Shortly after the first fine particles were observed the number of particles in the fluid increased until the whole regenerators broke apart.

The reason for introducing the epoxy into the regenerator matrix was to enhance the mechanical stability and prevent breaking apart of the regenerators. As expected, the mechanical stability of the regenerators was increased significantly by epoxy bonding the particles. No degradation related to particles breaking was observed, even after 5 weeks of testing. By comparing the temperature span of regenerators *Double2wt%* and *Double4wt%* in Fig. 4 it is observed that increasing the amount of epoxy was detrimental to the span. So when epoxy bonding it is important to find the minimum amount of epoxy that can be used while still

maintaining the structural integrity of the regenerator. As discussed above the regenerator *Double1wt%* broke apart during initial testing, so the minimum amount of epoxy to avoid this seems to be 2 vol.%.

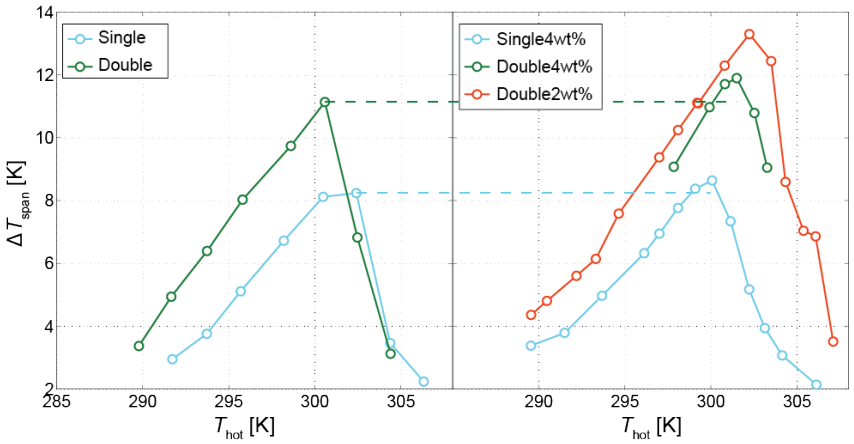

Fig. 4 : Temperature span as a function of the hot end temperature for different regenerators. The Dashed line is a guide to the eye.

4. CONCLUSIONS

The performance of La(Fe,Mn,Si)$_{13}$H$_z$ as an active magnetic regenerator is evaluated in a custom-built device. The results show that irregular particles of La(Fe,Mn,Si)$_{13}$H$_z$ deteriorate during application which would limit the use of this material as an AMR. By epoxy bonding the particles, the mechanical stability of the regenerators increased significantly and no deterioration due to particles breaking was observed. The temperature span reached by the epoxy-bonded regenerators suggest that 2 wt.% of epoxy maximizes the span, while still maintaining the mechanical integrity. The characterization of the transfer fluid showed that the Entek solutions have a lower viscosity and density then the ethylene glycol ones. Although the effect of a lower viscosity does not influence of the tests here done since the frequency is relatively low, this might play a very important role under high frequency operations.

ACKNOWLEDGMENTS

This work was financed by the ENOVHEAT project which is funded by Innovation Fund Denmark (contract no 12-132673). The authors are grateful to Vacuumschmelze GmbH for providing the samples.

REFERENCES

[1] V. K. Pecharsky and K. A. Gschneidner, Jr., "Giant Magnetocaloric Effect in $Gd_5Si_2Ge_2$," *Phys. Rev. Lett.*, vol. **78**, no. 23, pp. 4494–4497, 1997.

[2] G. V. Brown, "Magnetic heat pumping near room temperature," *J. Appl. Phys.*, vol. **47**, no. 8, p. 3673, 1976.

[3] A. Barcza, M. Katter, V. Zellmann, S. Russek, S. Jacobs, C. Zimm, "Stability and Magnetocaloric Properties of Sintered La(Fe, Mn, Si)$_{13}$H$_z$ Alloys," *IEEE Trans. Magn.*, vol. **47**, no. 10, pp. 3391–3394, 2011.

[4] L. von Moos, C. R. H. Bahl, K. K. Nielsen, and K. Engelbrecht, "The influence of hysteresis on the determination of the magnetocaloric effect in $Gd_5Si_2Ge_2$," *J. Phys. D. Appl. Phys.*, vol. **48**, no. 2, p. 025005, 2015.

[5] V. Basso, M. Küpferling, C. Curcio, C. Bennati, A. Barzca, M. Katter, M. Bratko, E. Lovell, J. Turcaud, and L. F. Cohen, "Specific heat and entropy change at the first order phase transition of La(Fe-Mn-Si)$_{13}$-H compounds," *J. Appl. Phys.*, vol. **118**, no. 5, p. 053907, 2015.

[6] K. K. Nielsen, H. N. Bez, L. von Moos, R. Bjørk, D. Eriksen, and C. R. H. Bahl, "Direct measurements of the magnetic entropy change," *Rev. Sci. Instrum.*, vol. **86**, no. 10, p. 103903, 2015.

[7] T. Lei, K. K. Nielsen, K. Engelbrecht, C. R. H. Bahl, H. Neves Bez, and C. T. Veje, "Sensitivity study of multi-layer active magnetic regenerators using first order magnetocaloric material

$La(Fe,Mn,Si)_{13}H_y$," *J. Appl. Phys.*, vol. **118**, no. 1, p. 014903, 2015.
[8] S. Fujieda, a. Fujita, K. Fukamichi, Y. Yamazaki, and Y. Iijima, "Giant isotropic magnetostriction of itinerant-electron metamagnetic $La(Fe_{0.88}Si_{0.12})_{13}H_y$ compounds," *Appl. Phys. Lett.*, vol. **79**, no. 5, p. 653, 2001.
[9] H. N. Bez, K. K. Nielsen, P. Norby, A. Smith, and C. R. H. Bahl, "Magneto-elastic coupling in $La(Fe, Mn, Si)_{13}H_y$ within the Bean-Rodbell model," *AIP Adv.*, vol. **6**, no. 5, p. 056217, 2016.
[10] J. Lyubina, R. Schäfer, N. Martin, L. Schultz, and O. Gutfleisch, "Novel design of $La(Fe,Si)_{13}$ alloys towards high magnetic refrigeration performance.," *Adv. Mater.*, vol. **22**, no. 33, pp. 3735–9, 2010.
[11] A. Waske, L. Giebeler, B. Weise, A. Funk, M. Hinterstein, M. Herklotz, K. Skokov, S. Fähler, O. Gutfleisch, and J. Eckert, "Asymmetric first-order transition and interlocked particle state in magnetocaloric $La(Fe,Si)_{13}$," *Phys. status solidi - Rapid Res. Lett.*, vol. **9**, no. 2, pp. 136–140, 2015.
[12] J. Lanzarini, T. Barriere, M. Sahli, J. C. Gelin, A. Dubrez, C. Mayer, M. Pierronnet, and P. Vikner, "Thermoplastic filled with magnetocaloric powder," *Mater. Des.*, vol. **87**, pp. 1022–1029, 2015.
[13] K. Engelbrecht, K. K. Nielsen, and N. Pryds, "An experimental study of passive regenerator geometries," *Int. J. Refrig.*, vol. **34**, pp. 1817–1822, 2011.
[14] C. R. H. Bahl, T. F. Petersen, N. Pryds, and a Smith, "A versatile magnetic refrigeration test device.," *Rev. Sci. Instrum.*, vol. **79**, no. 9, p. 093906, 2008.
[15] D. Velázquez, M. Castro, E. Palacios, and R. Burriel, "Pratical Properties of LaFeCoSi Materials to Be Used in Magnetic Cooling Applications," in *Proceedings of Thermag VI*, 2014, pp. 133–134.

A.11 A cascading model of an active magnetic regenerator system

M. Tahavori, K. Filonenko, C. T. Veje, **T. Lei**, K. Engelbrecht and C. R. H. Bahl, A cascading model of an active magnetic regenerator system, *The 7th IIF-IIR International Conference on Magnetic Refrigeration at Room Temperature*, Turin, (2016).

A CASCADING MODEL OF AN ACTIVE MAGNETIC REGENERATOR SYSTEM

M. Tahavori[(a)], K. Filonenko[(a)*], C. T. Veje[(a)], T. Lei[(b)], K. Engelbrecht[(b)], C. R. H. Bahl[(b)]

[(a)] *The Maersk Mc-Kinney Moller Institute, University of Southern Denmark, Campusvej 55, DK – 5230 Odense, Denmark*

[(b)] *Department of Energy Conversion and Storage, Technical University of Denmark, Frederiksborgvej 39, DK – 4000 Roskilde, Denmark*

[*]Corresponding author. E-mail: kfi@mmmi.sdu.dk

ABSTRACT

In recent years, significant amounts of studies have been done on modeling and analysis of active magnetic regenerators (AMRs). Depending on the AMR geometry and the magnetocaloric material being modeled, the AMR may not be able to provide the required performance demanded by practical applications. Some AMR models in the literature predict high performance but with relatively low temperature spans at either end of the AMR. Therefore, they may not be sufficient for practical applications, such as providing the heat exchanger temperature spans required for residential and commercial space air conditioning. To remedy this, one solution is cascading of multiple single layer AMRs. In this work, a cascading AMR model is presented and studied. In a cascade configuration, *N* number of single layer AMRs are connected. The results show that higher hot and cold side temperature differences may be achieved compared to the ones obtained with a single AMR rendering the solution more suitable for use in residential and commercial space conditioning.

Keywords: cascading model, active magnetic regenerator, magnetocaloric material, temperature span, practical applications.

1. INTRODUCTION

Modeling and analysis of AMRs have received a lot of attention recently [1-6]. By reversing the refrigeration cycle, the resulting device can be operated as a heat pump with improved residential and commercial space-heating capabilities. Our primary focus is a particular implementation of the latter device depicted in Fig. 1a, however, the results can be useful for refrigeration applications also.

The AMR itself, as the main component of the heat pump, requires a detailed mathematical model. Here we adopt the 1D transient model developed in [2], where it is applied to several AMR geometries. Generally such models predict relatively low temperature differences on both hot and cold sides of AMR made of Gd spheres and utilizing water with 25 % ethylene glycol as a heat transfer fluid, Figs. 1b and 1c. In building applications such low temperature differences will require unrealisticly high massflows to provide the required capacity. This will hamper the system performance through increased viscous dissipation and pressure loss. Depending on the geometry of the magnetocaloric material, the AMR may not be able to provide sufficient coefficient of performance (COP), heating power, temperature spans, etc. required for building heating. One way to increase temperature differences and enhance AMR performance would be to use first order materials with higher magnetocaloric effect [5].

In this paper, we propose a different solution: cascading of multiple single-layer AMRs. We show that the requirements for the conventional building heating can be met in cascading geometry even without layering of the magnetocaloric material. Magnetocaloric cascading systems is a subject of active research, but concerns mainly AMRs connected in series [6-8]. Such configuration leads to a larger temperature span across the device. Our goal, on the other hand, is to demonstrate an increase in temperature difference on either side of the system. For this purpose, we present a modified configuration detailed in the next section.

2. CASCADING AMR MODEL

A single-layer AMR 1D model developed in [2], is modified such that it can be used in a cascade system

configuration. Fig. 1b shows a modified 1D AMR with T_C^i and T_C^o (T_H^i and T_H^o) as inlet and outlet temperatures of the cold (hot) side, respectively, f as the AMR frequency and $\dot{m} = \rho_f \dot{V}$ as the mass flow rate defined through volumetric flow rate $\dot{V}$ and fluid density ρ_f. As opposed to the temperature span across the regenerator, $T_H^i - T_C^i$, we will call the difference between the input and the output temperatures at cold (hot) end, $\Delta T_C = T_C^i - T_C^o(t)$ ($\Delta T_H = T_H^o(t) - T_H^i$), a cold (hot) end span. In the case of multiple regenerators, the temperatures are enumerated by index n, e.g. $\Delta T_H = T_H^{o(n)}(t) - T_H^{i(n)}$.

The cascading system shown in Fig. 2a consists of N number of single-layer modified 1D AMRs. Neighbouring regenerators are connected through their hot ends and separately through their cold ends in contrast to hot-to-cold and cold-to-hot connections for AMRs in series [8]. The total COP at the hot side of the cascading AMR model is defined as COP = $Q_H / (Q_H - Q_C)$ with $Q_X = Q_{X,1} + Q_{X,2} + \ldots + Q_{X,N}$ where $Q_{X,n} = \frac{1}{\tau}\int \dot{m}(t)\, c_f\, \Delta T_X\, dt$ have the meaning of cooling load and heating power of the *n*'th regenerator for $X \equiv C$ and $X \equiv H$, respectively. Here, τ is AMR cycle time and c_f is fluid heat capacity.

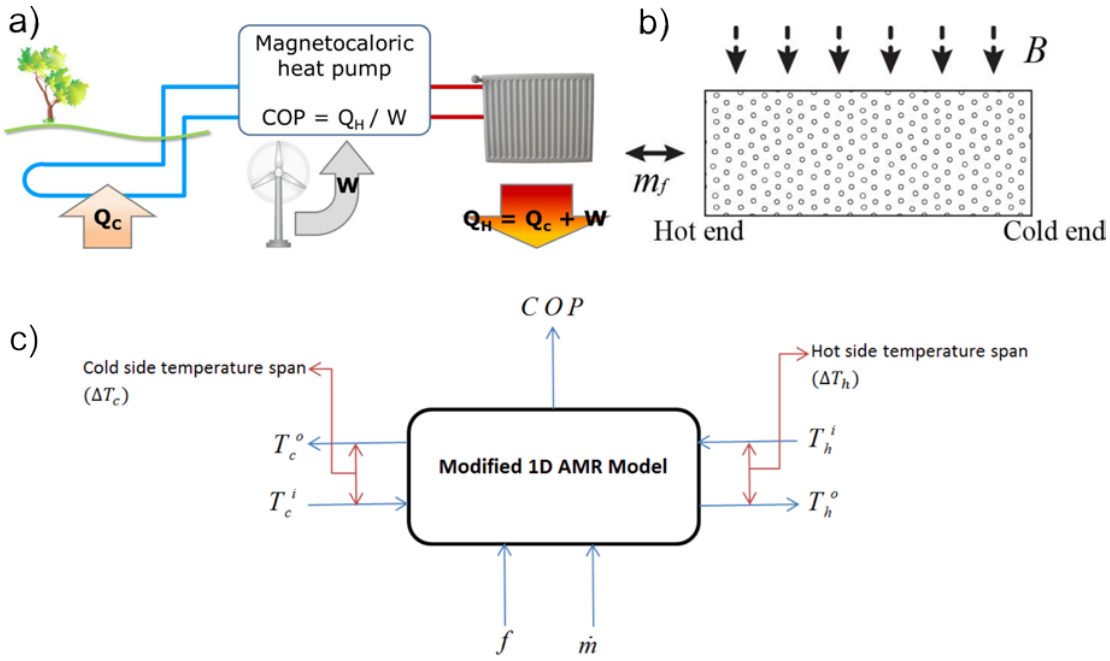

Figure 1. a) Magnetocaloric heat pump: the cold and hot ends are connected to the ambient and residential/commercial building, respectively; b) geometry of AMR made of Gd spheres; c) modified 1D AMR model to be implemented in a cascading configuration.

3. TEMPERATURE SPAN IN AMR CASCADING

In order to demonstrate the possibility of the substantial increase of the temperature span in a cascading configuration in comparison to the single regenerator model, a preliminary study is described in this section. We fix volumetric flow rate in all regenerators at $\dot{V}$ = 2.23 m^3/hr corresponding to a heating power of approximately 2 kW for a single regenerator. By adding consecutively identical regenerators to the system, we follow in Fig. 2b how the cold and hot end temperature differences change with number of regenerators. The calculations are made for two regenerator masses: 33.6 kg and 50.2 kg. Obviously, the total mass values are considerably larger compared to those used in conventional heat pumps. In subsequent research the required mass can be reduced through optimization with respect to both material properties, e.g. by layering each regenerator, and to device specifications, e.g. by varying operating frequency and regenerator aspect ratio. Here we are interested in illustrating the concept of cascading and therefore not concerned with

keeping the regenerator size small. From Fig.2b the expected growth of temperature spans is observed: for a six-regenerator cascading system, ΔT_H is in the range of 4-5 K, whereas ΔT_C has a value between 3 K and 4 K. This comes together with high enough heating power Q_H=1.6 kW and COP=3-4, which makes the six-regenerator cascade a viable device for building heating.

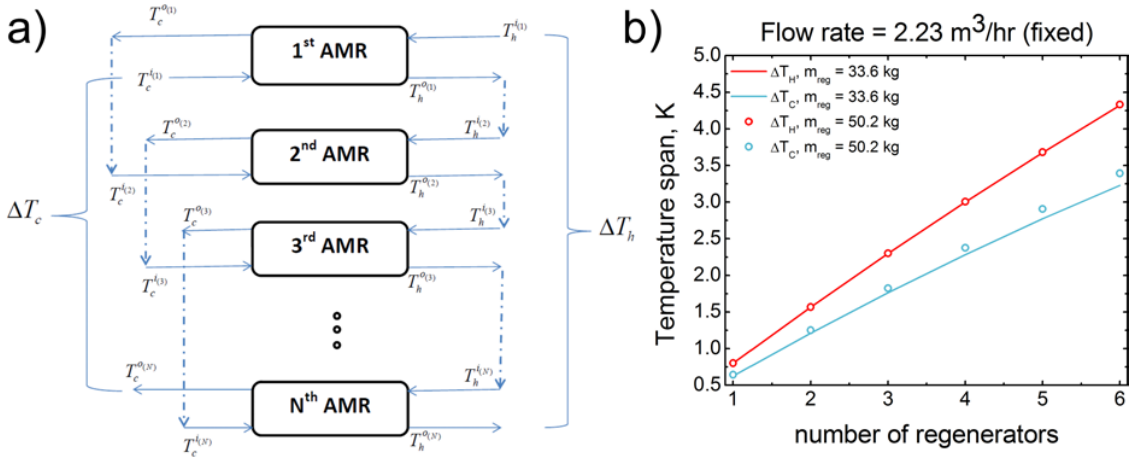

Figure 2. Cascading AMR model: a) schematic drawing of a cascading system, b) temperature span vs. number of AMRs which are all identical and have masses 33,6 kg or 50,2 kg each with $\dot{V}$ fixed at 2.23 m^3/hr in all regenerators.

4. MATCHING RESIDENTIAL HEATING REQUIREMENTS

With respect to in-house heating conditions we assumed that:

1. The amount of heating power which is required in a residential/commercial building is about 2 kW;
2. We aim for COP = 5;
3. The amount of temperature difference which is required on the hot side of AMR is about 4-5 K.

In this section, we limit ourselves to three regenerators and to moderate temperature spans below 3 K keeping in mind that the analysis can be generalized by increasing the number of regenerators. This allows us to match the system parameters for the first two heating requirements, while keeping computation time relatively small.

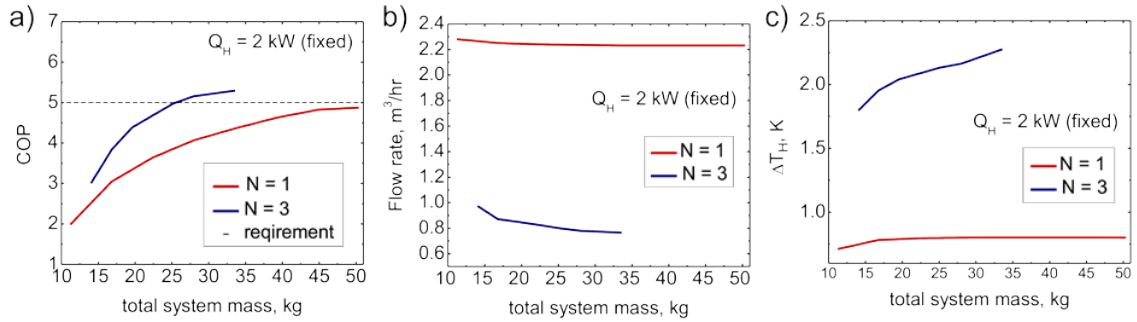

Figure 3. Optimization of AMR cascading for N = 1, 3: a) COP , b) volumetric flow rate and b) temperature spans vs. total cascading system mass.

Parameters of the cascading system with one and three AMRs are analyzed in Fig. 3 as functions of total system mass m_{tot} under condition that the overall heating power has a fixed value $Q_H = 2$ kW in all calculations. All regenerators in a cascading system are assumed to be identical and have the same aspect ratio AR = 6.6 independent of the number of regenerators and m_{tot}. Constant AR allows to relate the regenerator length L and cross-section area Ac to those of an arbitrary regenerator chosen as a reference. We

choose the reference regenerator with mass m_{reg} =2.8 kg, length L_0 = 100 mm, cross-section area A_0 = 229.25 mm^2 and geometry of regenerators inside the cascading system is given by $L_{reg} = L_0 (M/N)^{1/3}$ and $A_{reg} = A_0 (M/N)^{2/3}$, where $M = m_{tot}/m_0$. Red and blue curves in Fig. 3 correspond to N = 1 and N = 3, respectively, and the dashed line in Fig. 3a represents the requirement of COP = 5. It can be concluded that the COP gets and stays larger for N>1, which is also supported by the calculations made for N > 3 (not shown here). Beyond total mass values approximately equal to 25 kg COP gets larger than 5 thereby fulfilling the second requirement for building heating. As is expected, the flow rate decreases and temperature difference increases with increasing total mass and number of regenerators.

5. CONCLUSIONS

Through numerical analysis of AMR cascades we showed that cascading increases both temperature difference and COP showing the possibility for fulfilling the requirements on heating power, COP and temperature span imposed by the residential/commercial heating. Unlike in non-optimized case discussed in Sec. 3, the 3-regenerator cascade discussed in Sec. 4 needs much less total cascade mass compared to the single-regenerator case to achieve the same (and even higher) COP. Although we have fulfilled first two requirements separately from the third, we have shown that the temperature span increases together with number of regenerators. Therefore, it is possible to fulfil all three requirements by performing time-consuming calculations.

Authors realize that the regenerator masses used in the paper are considerably larger than the masses of currently used AMR prototypes and produced heat pumps. However, the goal in the present manuscript was to explore methodology and check the hypothesis concerning the influence of cascading on AMR performance and temperature span. Therefore, the single-layer Gd was used to simplify consideration. In future research, this issue will be addressed and the required mass can be sufficiently reduced by layering the AMRs in the cascading geometry. The cascading technique described in this paper will allow a further increase of efficiency and temperature span of AMR and in combination with other techniques will bring closer the industrial realization of commercial AMR- based devices.

ACKNOWLEDGMENTS

We are grateful for financial support provided by the ENOVHEAT project funded by Innovation Fund Denmark (contract no 12-132673).

REFERENCES

[1] A. Kitanovski, P. W. Egolf, “Thermodynamics of magnetic refrigeration”, *International Journal of Refrigeration* **29**, 3 (2006).
[2] K. Engelbrecht, “A Numerical Model of an Active Magnetic Regenerator Refrigerator with Experimental Validation”, *Ph.D. thesis*, University of Wisconsin (2008).
[3] K. K. Nielsen et al., “Review on Numerical Modeling of Active Magnetic Regenerators for Room Temperature Applications”, *International Journal of Refrigeration* **34**, 603 (2011).
[4] A. Rowe, “Thermodynamics of active magnetic regenerators”, *Cryogenics* **52**, 111 (2012).
[5] T. Lei et al., “Sensitivity study of multi-layer active magnetic regenerators using first order magnetocaloric material La(Fe,Mn,Si)13Hy”, *Journal of Applied Physics* **118**, 014903 (2015).
[6] P. J. Shirron, “Applications of the Magnetocaloric effect in Single-Stage, Multi-Stage and Continuous Adiabatic Demagnetization Refrigerators”, *Cryogenics* **62**, 130 (2014).
[7] P. Shirron, “Optimization strategies for single-stage, multi-stage and continuous ADRs”, *Cryogenics* **62**, 140 (2014).
[8] P.W. Egolf, A. Kitanovski, D. Vuarnoz, M. Diebold, C. Besson, “An introduction to magnetic refrigeration” [Online]. Available: http://www.centrogalileo.it/nuovapa/Articoli%20tecnici/INGLESE CONVEGNO/XII%20Convegno%20English/II%20SESSIONE/Egolf%201_eng.pdf, (2008).